Understanding Complex Systems

Springer : COMPLEXITY

Juan F. R. Archilla
Faustino Palmero
M. Carmen Lemos
Bernardo Sánchez-Rey
Jesús Casado-Pascual *Editors*

Nonlinear Systems, Vol. 2

Nonlinear Phenomena in Biology, Optics and Condensed Matter

Springer

Springer Complexity

Springer Complexity is an interdisciplinary program publishing the best research and academic-level teaching on both fundamental and applied aspects of complex systems—cutting across all traditional disciplines of the natural and life sciences, engineering, economics, medicine, neuroscience, social and computer science.

Complex Systems are systems that comprise many interacting parts with the ability to generate a new quality of macroscopic collective behavior the manifestations of which are the spontaneous formation of distinctive temporal, spatial or functional structures. Models of such systems can be successfully mapped onto quite diverse "real-life" situations like the climate, the coherent emission of light from lasers, chemical reaction-diffusion systems, biological cellular networks, the dynamics of stock markets and of the Internet, earthquake statistics and prediction, freeway traffic, the human brain, or the formation of opinions in social systems, to name just some of the popular applications.

Although their scope and methodologies overlap somewhat, one can distinguish the following main concepts and tools: self-organization, nonlinear dynamics, synergetics, turbulence, dynamical systems, catastrophes, instabilities, stochastic processes, chaos, graphs and networks, cellular automata, adaptive systems, genetic algorithms and computational intelligence.

The three major book publication platforms of the Springer Complexity program are the monograph series "Understanding Complex Systems" focusing on the various applications of complexity, the "Springer Series in Synergetics", which is devoted to the quantitative theoretical and methodological foundations, and the "Springer Briefs in Complexity" which are concise and topical working reports, case studies, surveys, essays and lecture notes of relevance to the field. In addition to the books in these two core series, the program also incorporates individual titles ranging from textbooks to major reference works.

Editorial and Programme Advisory Board

Understanding Complex Systems

Founding Editor: S. Kelso

Future scientific and technological developments in many fields will necessarily depend upon coming to grips with complex systems. Such systems are complex in both their composition–typically many different kinds of components interacting simultaneously and nonlinearly with each other and their environments on multiple levels–and in the rich diversity of behavior of which they are capable.

The Springer Series in Understanding Complex Systems series (UCS) promotes new strategies and paradigms for understanding and realizing applications of complex systems research in a wide variety of fields and endeavors. UCS is explicitly transdisciplinary. It has three main goals: First, to elaborate the concepts, methods and tools of complex systems at all levels of description and in all scientific fields, especially newly emerging areas within the life, social, behavioral, economic, neuro- and cognitive sciences (and derivatives thereof); second, to encourage novel applications of these ideas in various fields of engineering and computation such as robotics, nano-technology, and informatics; third, to provide a single forum within which commonalities and differences in the workings of complex systems may be discerned, hence leading to deeper insight and understanding.

UCS will publish monographs, lecture notes, and selected edited contributions aimed at communicating new findings to a large multidisciplinary audience.

More information about this series at http://www.springer.com/series/5394

Juan F. R. Archilla · Faustino Palmero
M. Carmen Lemos · Bernardo Sánchez-Rey
Jesús Casado-Pascual
Editors

Nonlinear Systems, Vol. 2

Nonlinear Phenomena in Biology, Optics and Condensed Matter

Springer

Editors
Juan F. R. Archilla
Departamento de Fisica Aplicada I, ETSI Informática
Universidad de Sevilla
Sevilla
Spain

Bernardo Sánchez-Rey
Departamento de Fisica Aplicada I, EPS
Universidad de Sevilla
Sevilla
Spain

Faustino Palmero
Departamento de Fisica Aplicada I, ETSI Informática
Universidad de Sevilla
Sevilla
Spain

Jesús Casado-Pascual
Departamento de Física Atómica, Molecular y Nuclear
Universidad de Sevilla
Sevilla
Spain

M. Carmen Lemos
Departamento de Física de la Materia Condensada
Universidad de Sevilla
Sevilla
Spain

ISSN 1860-0832 ISSN 1860-0840 (electronic)
Understanding Complex Systems
ISBN 978-3-319-72217-7 ISBN 978-3-319-72218-4 (eBook)
https://doi.org/10.1007/978-3-319-72218-4

Library of Congress Control Number: 2017960294

Printed on acid-free paper

This Springer imprint is published by Springer Nature
The registered company is Springer International Publishing AG
The registered company address is: Gewerbestrasse 11, 6330 Cham, Switzerland

To Prof. Francisco Romero Romero, founder and head during twenty years of the Group of Nonlinear Physics of the Universidad de Sevilla. He was responsible for the incorporation of all group members, most of them former students of his lectures in N-body quantum mechanics and other subjects at the Physics Faculty. He always worked to keep the group together and to develop the scientific capability and friendship of its members. He was Ph.D. supervisor of two editors of this book (JFRA and FP) and one editor of Nonlinear systems. Vol. 1. (JC).

Preface

This book commemorates the conference Nonlinear 2016: International Conference on Nonlinear Mathematics and Physics, that took place in Sevilla, Spain, from July 7 to 10, 2016. There were delegates from many different countries in Europe and also three other continents.

At the end of the conference, the decision was taken of writing a book to provide the readers with a landscape of the many different fields in which nonlinear science is being developed with great success. Contributions would not be proceedings but present an introduction to the different subjects, provide context, and present the state of art and certainly the own research of the authors in the field.

Although the mathematics and physics of nonlinear systems are closely intertwined, it has been considered convenient to divide the matter into two volumes:

- Nonlinear Systems; Volume 1. Mathematical Theory and Computational Methods in Nonlinear Systems, edited by Victoriano Carmona-Centeno, Jesús Cuevas-Maraver, Fernando Fernández-Sánchez and Elisabeth García-Medina
- Nonlinear Systems. Volume 2. Nonlinear Phenomena in Biology, Optics and Condensed Matter, edited by Juan F. R. Archilla, Faustino Palmero, M. Carmen Lemos, Bernardo Sánchez-Rey and Jesús Casado-Pascual

The present book is the second volume and it is dedicated to nonlinear physics. This is a very large area of research including subjects as regulation and morphogenesis of living systems, nonlinear hydrodynamic waves, gravitational waves, ocean circulation, drug resistance, black holes, brain tumors, antifreeze proteins, dark matter waves, neural communication, ionic channels, Bose–Einstein condensates, charge transport in ionic crystals, acoustic metamaterials, breathers and kinks in crystals, surface reactions, electro-polarons, repelling lattices, transition state theory, layered media, interstitial loops, political conversations, accelerator physics, and photonic fibers, to name a few.

Each field would require several books; therefore, in this one we only intend to present the reader some chapters in a few different fields which can be useful to understand how nonlinear physics is used in such different systems.

We concentrate in some examples of three applications in biology, as protein folding, morphogenesis, and neural communication; three chapters on optics Bose-Eisntein condesates suppressed; and seven very different chapters in condensed matter, from graphene to annealing, from layered silicates to superfluid helium, and from kinks and solitons to breathers. The outline of the book is as follows:

1. *Biology*

   - Protein folding in vivo: from Anfinsen back to Levinthal by Leonor Cruzeiro ……. p. 3
   - Patterning, dynamics, and evolution in the ocellar complex of the fruit fly by Daniel Aguilar-Hidalgo, Fernando Casares, and M. Carmen Lemos ……. p. 39
   - Computation of invariant curves in the analysis of periodically forced neural oscillators by Alberto Pérez-Cervera, Gemma Huguet, and Tere M-Seara ……. p. 63

2. *Optics*

   - Solitary waves on graphene superlattices by Francisca Martín-Vergara, Francisco Rus and Francisco R. Villatoro ……. p. 85
   - Nonlinear vortex light beams supported and stabilized by dissipation by Angel A. Porras, Carlos Ruiz-Jiménez and Marcio, Carvalho ……. p. 111
   - Spatial solitons in nonlinear photonic crystal fibers by José R. Salgueiro and Albert Ferrando ……. p. 139

3. *Crystals, metamaterials, and other condensed matter*

   - Nonlinear excitations in graphene and other carbon nano-polymorphs by Sergey V. Dmitriev, Julia A. Baimova, Elena A. Korznikova, and Alexander P. Chetverikov ……. p. 175
   - A cellular automaton model for the catalytic oxidation of CO including CO desorption and diffusion by Francisco Jiménez-Morales and M. Carmen Lemos ……. p. 197
   - Transmission of thermal phonons in superfluid helium through nonlinear meta-interface with a solid by Yuriy A. Kosevich, Olena Yu. Tkachenko, and Eugenii S. Syrkin ……. p. 221
   - Transport properties of quodons in muscovite by F. Michael Russell ……. p. 241
   - Kinks in a lattice of repelling particles by Ahmed Mehrem, Luis J. Salmerón-Contreras, Noé Jiménez, Víctor J. Sánchez-Morcillo, Rubén Picó, Luis M. García-Raffi, Juan F. R. Archilla, and Yuriy A. Kosevich ……. p. 261

Chapters will provide an opportunity for the readers to understand subjects which are normally dispersed in different journals for specialists. We expect them to feel the fascination of nonlinear physics and its broad applicability, stimulating their curiosity and perhaps extending their own research to unexpected territory.

Sevilla, Spain
June 2017

Juan F. R. Archilla
Faustino Palmero
M. Carmen Lemos
Bernardo Sánchez-Rey
Jesús Casado-Pascual

Prof. Francisco Romero Romero, head from 1997 to 2017 of the Group of Nonlinear Physics, Full Professor of Theoretical Physics in the Physics Faculty of the Universidad de Sevilla, Spain

Acknowledgements

I am grateful to all the editors of this book for the kind dedicatory. I have had the pleasure to work with them in different forms.

I would like to express my deep gratitude to all the members of the Group of Nonlinear Physics, with which I have had such a fruitful and pleasant scientific collaboration.

Specially, I would like to thank J. F. R. Archilla and F. Palmero which were co-founders of our group in 1997. Without their enthusiasm, dedication, and hard work, the enterprise would have never been possible.

I also wish to acknowledge the Universidad de Sevilla, which has helped us so much along our scientific careers.

Sevilla, Spain
June 2017

Francisco Romero Romero
Professor in Theoretical Physics
Universidad de Sevilla

Contents

Contributors

Daniel Aguilar-Hidalgo Max Plank Institute for the Physics of Complex Systems, Dresden, Germany

Juan F. R. Archilla Instituto de Instrumentación para Imagen Molecular, Consejo Superior de Investigaciones Científicas, Universitat Politècnica de València, Valencia, Spain

Julia A. Baimova Institute for Metals Superplasticity Problems of RAS, Ufa, Russia; M.N. Mikheev Institute of Metal Physics of the Ural Branch of RAS, Ekaterinburg, Russia

Pavel M. Bokov Radiation Science Department, The South African Nuclear Energy Corporation SOC Ltd (Necsa), Pretoria, South Africa

Márcio Carvalho Grupo de Sistemas Complejos, ETSI Agronómica, Alimentaria y de Biosistemas, Universidad Politécnica de Madrid, Madrid, Spain

Fernando Casares CABD (Andalusian Centre for Development Biology), CSIC - UPO -JA, Campus Universidad Pablo de Olavide, Sevilla, Spain

Alexander P. Chetverikov Saratov State University, Saratov, Russia

Leonor Cruzeiro Centro de Ciências do Mar and Faculdade de Ciências e Tecnologia, Universidade do Algarve, Campus de Gambelas, Faro, Portugal

Sergey V. Dmitriev Institute for Metals Superplasticity Problems of RAS, Ufa, Russia; National Research Tomsk State University, Tomsk, Russia

Albert Ferrando Departament d'Òptica, Interdisciplinary Modeling Group InterTech, Universitat de València, Burjassot (València), Spain

Luis M. García-Raffi Instituto Universitario de Matemática Pura y Aplicada, Universitat Politècnica de Valencia, Valencia, Spain

Gemma Huguet Dept. Matemàtica Aplicada, Universitat Politècnica de Catalunya Avda., Barcelona, Spain

Noé Jiménez LUNAM Université, Université du Maine, CNRS, Le Mans, France; Semenov Institute of Chemical Physics, Russian Academy of Sciences, Moscow, Russia

Francisco Jiménez-Morales Departamento de Física de la Materia Condensada, Universidad de Sevilla, Sevilla, Spain

Elena A. Korznikova Institute for Metals Superplasticity Problems of RAS, Ufa, Russia

Yuriy A. Kosevich Group of Nonlinear Physics, Department of Applied Physics I, Universidad de Sevilla, ETSII, Sevilla, Spain; Semenov Institute of Chemical Physics, Russian Academy of Sciences, Moscow, Russia

M. Carmen Lemos Department of Condensed Matter Physics, Universidad de Sevilla, Sevilla, Spain; Departamento de Física de la Materia Condensada, Universidad de Sevilla, Sevilla, Spain

Tere M-Seara Dept. Matemàtica Aplicada, Universitat Politècnica de Catalunya Avda., Barcelona, Spain

Francisca Martin-Vergara Dept. Lenguajes y Ciencias de la Computación, Escuela de Ingenierías Industriales, Universidad de Málaga, Málaga, Spain

Ahmed Mehrem Instituto de Investigación para la Gestión Integrada de las Zonas Costeras, Universitat Politècnica de València, Grao de Gandia, Spain

Alberto Pérez-Cervera Dept. Matemàtica Aplicada, Universitat Politècnica de Catalunya Avda., Barcelona, Spain

Rubén Picó Instituto de Investigación para la Gestión Integrada de las Zonas Costeras, Universitat Politècnica de València, Grao de Gandia, Spain

Miguel A. Porras Grupo de Sistemas Complejos, ETSI de Minas y Energía, Universidad Politécnica de Madrid, Madrid, Spain

Carlos Ruiz-Jiménez Grupo de Sistemas Complejos, ETSI Agronómica, Alimentaria y de Biosistemas, Universidad Politécnica de Madrid, Madrid, Spain

Francisco Rus Dept. Lenguajes y Ciencias de la Computación, Escuela de Ingenierías Industriales, Universidad de Málaga, Málaga, Spain

F. Michael Russell Group of Nonlinear Physics, Department of Applied Physics I, Universidad de Sevilla, ETSII, Sevilla, Spain

José R. Salgueiro Departamento de Física Aplicada, Universidade de Vigo, Escola de Enxeñaría Aeronáutica e do Espazo, Ourense, Spain

Luis J. Salmerón-Contreras Instituto Universitario de Matemática Pura y Aplicada, Universitat Politècnica de València, Valencia, Spain

Víctor J. Sánchez-Morcillo Instituto de Investigación para la Gestión Integrada de las Zonas Costeras, Universitat Politècnica de València, Grao de Gandia, Spain

Pavel A. Selyshchev Department of Physics, University of Pretoria, Hatfield, South Africa

Ivan O. Starodub Bogolyubov Institute for Theoretical Physics, National Academy of Sciences of Ukraine, Kiev, Ukraine

Eugenii S. Syrkin B. I. Verkin Institute of Low-Temperature Physics and Engineering, National Academy of Sciences of Ukraine, Kharkov, Ukraine

Olena Yu. Tkachenko V. N. Karazin Kharkov National University, Kharkov, Ukraine

Francisco R. Villatoro Dept. Lenguajes y Ciencias de la Computación, Escuela de Ingeniereas Industriales, Universidad de Málaga, Málaga, Spain

Yaroslav Zolotaryuk Bogolyubov Institute for Theoretical Physics, National Academy of Sciences of Ukraine, Kiev, Ukraine

Part I
Biology

Protein Folding in Vivo: From Anfinsen Back to Levinthal

Leonor Cruzeiro

Abstract In this chapter two visions of the protein folding process are confronted. The first is based on the thermodynamic hypothesis and the second is based on the kinetic hypothesis. Experimental results in support of each of the theories are reviewed and in some cases re-interpreted. While the thermodynamic hypothesis has been dominant since the 1970s, here it is argued that the experimental evidence favours the kinetic hypothesis, particularly in what concerns folding in vivo. A specific kinetic process, designated as the VES KM, is proposed. According to the VES KM the structure that *all* proteins have as they emerge from the ribosome is helical and the first step in folding is the bending of this helix at specific amino acid sites (i.e. the location of the bending sites depends on the protein sequence). Results from molecular dynamics simulations on a small all-α protein demonstrate the theoretical viability of the VES KM. The chapter ends with a discussion on the state of the art in protein folding from the point of view of the VES KM and with proposals for future work.

Keywords Protein folding · Kinetic hypothesis · Nascent chain · VES hypothesis

1 The Protein Folding Problem

Proteins are the macromolecules that mediate most of the processes that take place in a living cell: they regulate the intracellular medium, pass signals from the outside to the inside of a cell (and vice-versa), transport organelles from one region of a cell to another, catalyze chemical reactions like the synthesis and hydrolysis of adenosinetriphosphate (ATP) and provide basic structure. Given that even a small protein with some sixty amino acids has approximately one thousand atoms, and thus three thousand degrees of freedom, one main question, known as *the protein folding problem*, is how each protein, after its synthesis in cells, most of the times, manages

L. Cruzeiro (✉)
Centro de Ciências do Mar and Faculdade de Ciências e Tecnologia,
Universidade do Algarve, Campus de Gambelas, 8005-139 Faro, Portugal
e-mail: lhansson@ualg.pt

J. F. R. Archilla et al. (eds.), *Nonlinear Systems, Vol. 2*, Understanding
Complex Systems, https://doi.org/10.1007/978-3-319-72218-4_1

to reach the one three-dimensional structure it needs to have to function properly (its native structure). In this chapter we are concerned with two very different solutions to the protein folding problem both of which were first proposed in the late 1960s: one solution is known as Anfinsen's thermodynamic hypothesis [3] (see Sect. 3) and the other is Levinthal's kinetic hypothesis [91] (see Sect. 4). One important message in this chapter is that although the former has until now been the mainstream hypothesis, there are good reasons to think that the latter will be mainstream in the future.

There are two distinct protein folding problems [80]: one that consists of devising a set of rules to obtain the three dimensional structure from its amino acid sequence, and a second problem that consists of the identification of the physical mechanisms/forces that take a protein to its native state. The first is equivalent to building a black box which, upon being fed the primary sequence of a protein, would turn out the full three dimensional structure of that protein. Even if this black box leaves us ignorant about the physical mechanisms that drive folding it will still be very useful for progress in Biology and Medicine and for practical applications in the pharmaceutical and biotechnological industries. On the other hand, the knowledge of the physical mechanisms responsible for protein folding constitutes the complete answer and should allow us to build the black box as well. Both of these protein folding problems have been, and are being pursued by the protein folding community. Here we are mostly concerned with the second protein folding problem and one important purpose of this chapter is to put forward a specific (kinetic) mechanism for protein folding (see Sects. 4–6).

Protein folding research started in the 1950s and, since then, it has never ceased to be the object of intensive study. It has thus generated a vast literature. It is not the purpose of this chapter to attempt to review all of it. Indeed, there are many reviews that describe the progress that has been made so far (see e.g. [45, 46, 48, 51, 64, 69, 83, 87, 114, 124]) but here, instead of focusing on the successes achieved in protein folding, the remaining weaknesses will be emphasized in order to build a case for a new (or actually, old) line of research. Therefore, newcomers to this field should beware of the bias towards the kinetic hypothesis that permeates this whole chapter. On the other hand, I have endeavoured to make, not a complete because that is impossible, but rather a self-contained description of the protein folding problem. To that end, the features of protein structure that are necessary to follow the different protein folding theories are presented in the next section. Section 3 deals with theories and experimental evidence related to the thermodynamic hypothesis, and Sect. 4 deals with the kinetic hypothesis, its relations to folding in vivo and the experimental data that support it. In Sect. 5 a particular kinetic mechanism for folding is described, which is illustrated by computer simulations reported in Sect. 6. Finally, in Sect. 7 an evaluation of the status of the thermodynamic hypothesis and of the kinetic hypothesis is made, and in Sect. 8 suggestions for future work within the kinetic hypothesis, as well as predictions and suggestions of experiments capable of distinguishing between the two hypotheses, are put forward.

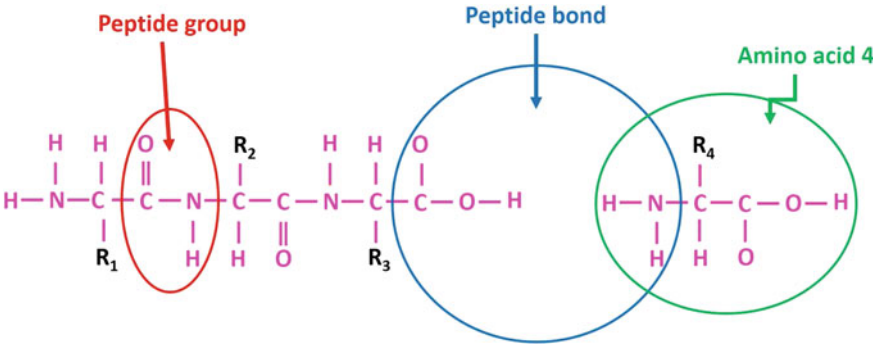

Fig. 1 Protein synthesis or amino acid polymerization. Four amino acids are shown, the first three of which have already been polymerized. In pink are shown the atoms of the protein backbone, with the side-chains or residues in black. Protein synthesis consists in the reaction of the carboxylic group of one amino acid with the amine group of the amino acid that is being added, as highlighted by the blue oval

2 Protein Structure

In this section, the essentials of protein structure are briefly described. Physically, proteins are polymers whose units are the amino acids. The so-called primary structure of proteins consists simply of the specification of its number of the amino acids and of their order of appearance. All amino acids have a part that is equal for all of them (plotted in pink in Fig. 1) and which leads to the so-called protein backbone, and another part, represented by $R_i, i = 1, \ldots, 4$ in the figure, which differentiates them. The differentiating groups R_i are the side-chains or residues of the amino acids and can be constituted by more than one atom even if they are represented by a single letter in Fig. 1. The green oval which circles one amino acid not yet polymerized shows that isolated amino acids have two sides, one with an amine (NH_2) group and the other with a carboxylic (COOH) group. Protein synthesis (or polymerization), which in cells is mediated by the ribosomes, consists in the chemical reaction of the carboxylic group of amino acid i with the amine group of the amino acid $i + 1$, thus creating the peptide bond C-N, and the peptide group (CONH) which is highlighted by a red oval in Fig. 1. Notice that in each peptide group, the C=O (carbonyl) group comes from amino acid i and the NH group comes amino acid $i + 1$ in the protein sequence. The ultimate aim in the protein folding problem consists in devising a method to determine the shape assumed by the protein backbone from the knowledge of its primary structure.

One remarkable feature of protein structure is its hierarchical character. Indeed, the analysis of the known protein structures (on the 8th September 2016 there were 113586 protein structures deposited in the protein data bank (PDB) [14]) shows that the backbone of proteins can assume two types of structures: helical (most of which are the so-called α-helices) and β-sheets. These are known as protein's secondary structures and are shown in Fig. 2. Helices are stabilized by hydrogen bonds between

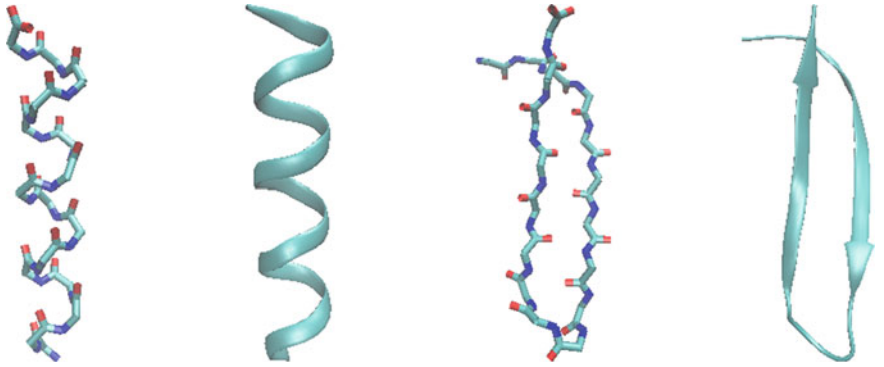

Fig. 2 Protein secondary structures. The first two pictures on the left are representations of the α-helix and the two on the right are representations of the β-sheet (see text). For each secondary structure type, the first picture shows an atomic representation of the backbone, with the links between atoms represented by lines (cyan being for carbon atoms, blue for nitrogen and red for oxygen), and the second is the corresponding cartoon representation. These figures were prepared with VMD [75]

the C=O groups of one amino acid, i, and the NH group of another amino acid, j, forming a hydrogen-bonded chain that runs parallel to the helix axis with the following composition: $\cdots$ H-N-C=O $\cdots$ H-N-C=O $\cdots$ H-N-C=O $\cdots$ In the case of α-helices $j = i + 4$ and the helix is stabilized by three such hydrogen-bonded chains. β-sheets, on the other hand, as can be seen in Fig. 2, are also stabilized by the same type of hydrogen-bonded chains, but their orientation is perpendicular to main chain axis. A third type are structures that connect the first two, like turns and loops, which are essentially structure-less parts. The full three-dimensional structure of proteins (designated as the tertiary structure) results from the packing of regions with either helical or sheet structure. Some proteins are formed by more than one unit (a unit being a chain of sequentially covalently linked amino acids as shown in Fig. 1), in which case one can also define the *quaternary* structure, constituted by the packing of the different units with respect to one another. Here we restrict ourselves to protein monomers (i.e. proteins formed by just one unit).

Analysis of the known structures shows that all proteins fall into just four different classes [107], as illustrated in Fig. 3: (1) mainly-α, in which most of the secondary structure is formed by α-helices (as seen in the first picture of Fig. 3), mainly-β in which most of the secondary structure is formed by β-sheets (as seen in second picture of Fig. 3), α/β in which both α-helices and β-sheets are found in approximately equal proportion (as seen in the third picture of Fig. 3), few secondary structures in which most of the protein is unstructured (as seen in the fourth picture of Fig. 3). The essence of the protein folding problem is to understand how the different amino acid sequences determine the different protein structures. Related questions are why proteins have a hierarchical structure and why they do not show a much greater variety of structures. We shall come back to these questions in Sect. 7.

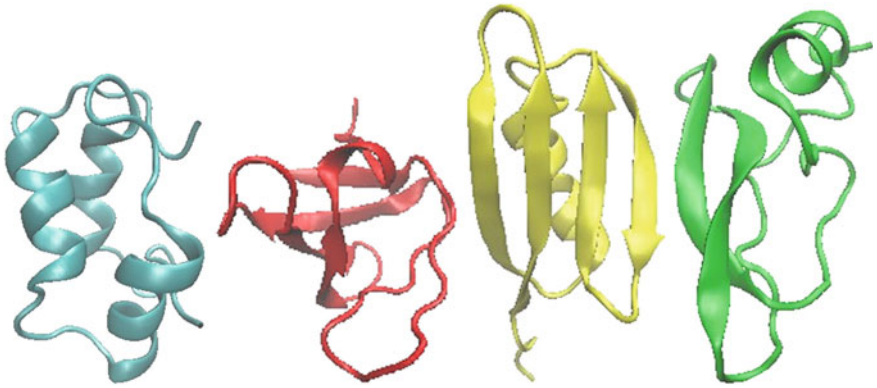

Fig. 3 The four CATH protein structural classes: (first, cyan) mainly-α (PDB1BDD [68]), (second, red) mainly-β (PDB1J08 [60]), (third, yellow) α/β (PDB1IGD [65]), and (fourth, green) few secondary structures (PDB1AAP [76]). These figures were prepared with VMD [75]

3 Anfinsen's Thermodynamic Hypothesis

Since the 1970s much of the efforts to solve each of the two protein folding problems mentioned in Sect. 1 have been guided by Anfinsen's thermodynamic hypothesis [3] according to which the native state of a protein is the global (free) energy minimum. Curiously, Anfinsen who, in the mid 1950s, was studying the relationship between structure and function in enzymes, first concluded that the structure of enzymes was irrelevant for their activity [5]! As stated by Anfinsen himself [4], he then spent another 15 years proving precisely the reverse.

Anfinsen's experiments on protein denaturation and re-folding were the basis for his formulation of the thermodynamic hypothesis. Indeed, Anfinsen and co-workers showed that two proteins, namely, bovine pancreatic ribonuclease A (RNase A) and *staphylococcal* nuclease, after denaturation in, respectively, 8 M urea and acid solutions, could recover their native states when normal physiological conditions were restored [3, 123]. Although the methods used to monitor the state of the proteins as a function of the concentration of urea and of acidity were biological activity and fluorescence emission, which could not say anything about what was happening to the structure of the proteins as they denatured, it was assumed that when the solutions were very different from the normal cellular conditions the protein structure was completely disrupted. If so, these experiments seemed to demonstrate that the native (biologically active) state of a protein can be reached from *any* initial structure so that the amino acid sequence is the sole determinant of the native structure. The matter was considered settled when Gutte and Merrifield were able to synthesize, in the absence of the cellular machinery and by a solid phase method, a 124 amino acid fragment of RNase A with an activity largely indistinguishable from the natural one [70, 100]. Anfinsen received a Nobel prize in Chemistry in 1972 "for his work on ribonuclease, especially concerning the connection between the amino acid

sequence and the biologically active conformation" and since then the thermodynamic hypothesis has been the dominant guide in the search for a solution to the protein folding problem.

In the next subsection, a critical appraisal is made of the theoretical developments made within the thermodynamic hypothesis.

3.1 The Funnel Model and "Landscape Theory"

The first theoretical development within the thermodynamic hypothesis came from statistical approaches within polymer physics: Dill [44] modelled a protein as a polymer constituted by hydrophobic (H) and polar (P) amino acids (considered as beads in a lattice) in which folding is driven by the tendency for hydrophobic beads to cluster together, something that is opposed by entropy. The overall result was that the number of stable compact, low energy, states is much smaller than the number of extended, high energy, states, leading to the concept of a funnel-shaped free energy landscape.

In lattice models the native state is, by definition, the state with the lowest energy and the observed uniqueness of the native state corresponds to a well defined ground state whose existence, in such models, is assumed a priori [44, 85]. However, if those models are to obey the thermodynamic hypothesis they *must* possess only one, well defined, ground state. A boost to the lattice models came from calculations with the HP model which suggested that, as the number of amino acids increases, the probability that a given sequence has more than one ground state decreases [47, 88]. However, recent studies in which lattices much larger than those considered before were used, have demonstrated that the probability that an HP sequence has a unique ground state decreases exponentially with increasing chain length [126, 127]. These latter studies weaken the theoretical case for funnel-shaped energy landscapes and for the thermodynamic hypothesis.

A concurrent theoretical development within the thermodynamic hypothesis borrowed the concept of frustration from spin glasses [23]. In the context of protein folding, frustration can be qualitatively defined as the impossibility for any conformation to simultaneously optimize all the types of interactions present in a protein, and the native states of proteins can be conceived as those which minimize frustration [23, 106]. While most protein sequences may not obey the principle of minimal frustration, it has been proposed that evolution has selected the protein sequences that possess a single, well defined state in which frustration is minimized [147].

An aspect that is shared by the two theoretical approaches mentioned above is that the (free) energy landscape of proteins is funnel-shaped [23, 44, 45, 80, 147]. This shape is thought to provide the solution to a problem raised already in the end of the 1960s by Levinthal [92]. Indeed, Levinthal pointed out that if a protein with some 2000 atoms must explore the more than 10^{300} different conformations it potentially can have to find its native state, it should take much longer to fold than the time measured in re-folding experiments, which range from sub-microseconds

to hours [98, 110] and in some cases, days [120] (in the experiments by Anfinsen it was minutes [67]). This so-called "Levinthal paradox" was eventually solved by the proposal that the (free) energy landscape of proteins is funnel-shaped, with unfolded states located at the rim and the native state at the bottom of the funnel [23, 44, 45, 80]. In such a landscape, the number of available states decreases as the energy approaches that of the native state and the second law of thermodynamics may suffice to explain reproducible folding in a reasonable time. In Sect. 4 the other, very different solution proposed by Levinthal [91, 92] is described.

Another idea that emerged from the theories described above is that hydrophobic interactions are the main drivers for the formation of initial compact protein structures [48, 87]. This idea has been criticized by Ben-Naim [13] who claims that hydrophilic forces are more important for protein folding. Ben-Naim also criticizes the concept of free energy landscape [12] and suggests instead the use of the distribution of the protein conformations (DPC) (see also [23, 51]). He points out that, in an equilibrium process, the free energy is minimized with respect to this distribution, which in principle may have any form, with or without minima and maxima (see [12], p. 118). Following Ben-Naim [12, 13], instead of referring to the shape of the energy landscape, we shall henceforth talk about the shape of the DPC at equilibrium. With this formalism, the thermodynamic hypothesis (a well defined ground state) and a funnel-shaped free energy landscape correspond to an equilibrium DPC with a clear (single) peak. On the other hand, an equilibrium distribution of conformations with n peaks of approximately equal height and area corresponds to the potential existence of more than one conformation in the same thermodynamic conditions, as first proposed by Levinthal [91] (see Sect. 4 below). Furthermore, hierarchies of protein motion and protein intermediates [63] lead to roughness within the corresponding peak. Although in previous works the expression "multi-funnel free energy landscape" was used [32, 34, 39], in what follows we shall prefer the point of view of the DPC at equilibrium [37, 38].

Until now, the search, in silico, for the native states of specific sequences has been made under the umbrella of the thermodynamic hypothesis according to which the DPC has a single dominant peak with a clear maximum. Most of the times, that search consists just of looking for the minimum of the *potential* energy. The acknowledged problems of determining protein structure with such a strategy are the enormous size of protein conformational space, as first pointed out by Levinthal [92], which is very difficult to cover in the available computer time, and inaccuracies in the force fields which may steer proteins into non-native regions of their conformational space. The efforts to solve these problems have led to the development of more accurate force fields [21, 25, 29], of fast molecular dynamics (MD) programs [16, 21, 25, 29], of efficient methods to navigate the conformational space, such as targeted MD [125], steered MD [95], accelerated MD [71], and transition path sampling [15, 43], and even to the building of more powerful computers [2, 129]. However, in spite of all this progress, the protein folding problem remains a challenge.

An evaluation of the state of the art in the prediction of protein structures from their amino acid sequence is made every two years in the Critical Assessment of protein Structure Prediction (CASP) exercises (found at www.predictioncenter.org).

Having started in 1994 and being held every two years, the CASP exercises let groups around the world predict, from their sequences, the structures of proteins which have not yet been made public. The analysis of these predictions shows that while in the first CASP exercises there was general progress in the accuracy of protein structure prediction [18, 48], in more recent years this progress seems to be levelling off [46]. In particular, ab initio predictions in which only force fields to describe the atomic interactions are used, and de novo prediction in which statistical distributions derived from known protein structures are used, as well as protein structure refinement [115] turn out to be especially challenging [124].

In spite of these difficulties, computational studies of changes in protein stability after selected mutations have led to a few successes in the prediction of sequences which lead to proteins with varying degrees of stability or folding rates [87] and, in some cases, to the increase in the accuracy of structure prediction [114]. Most importantly, using the new computer ANTON [129] and the fast program Desmond [16], Shaw and co-workers have succeeded in making MD simulations of 12 small proteins for up to 100 milliseconds! In these time periods, and at temperatures such that the population of the folded state is 30% on average, they have observed that the 12 proteins unfolded and re-folded repeatedly [78, 94, 130]. These results, which are the best numerical mimics of reversible thermal unfolding experiments, have been thought to provide theoretical support for the thermodynamic hypothesis [78, 94, 130]. Indeed, they seem to show that, with sufficient computer time and sufficiently accurate potentials, it is possible to fold proteins in silico.

Curiously, other simulations which started from protein structures obtained using templates consistently deviated from the native fold, something that was considered to be due to inaccuracies in the force field [115]. However, the fact that we can change 65% of the amino acids of a protein and, with high probability, still get another protein with the same backbone fold as the original one [61] means that small inaccuracies in the force field cannot matter much. Thus, let me suggest another explanation. In most MD simulations the initial structure is either the native structure (obtained from the PDB [14]) or a structure obtained by heating the latter (mildly or less mildly). Although it may not seem so from indicators like the RMSD (with respect to the native state) or the radius of gyration, or just visual inspection, those heated structures may keep crucial features of the native state and will thus tend to drift back to the native state. In the language of the DPC, although those changes take the protein away from the center of the native peak, they do not take it outside that peak. On the other hand, structures built from templates may not possess such hidden native features, i.e., they start in a non-native peak of the DPC and will tend to drift towards the center of that non-native peak, and to a structure different from the native.

In interpreting their results Shaw and co-workers [94, 115] implicitly assume that the DPC is characterized by a main peak, corresponding to the native state. On the other hand, a cursory study of the DPC at equilibrium which has been performed for a total of six proteins indicates that the DPC of all of them is multi-peaked, i.e., apart from the peak associated with the native state, there are many other peaks corresponding to as many structures that are as stable as the native [32, 34, 37–39] (see Sect. 4.2). These simulations indicate that the difficulty in finding the native state

in silico is not due either to the size of the conformational space or to inaccuracies in the protein force fields but to the real multitude of possible structures proteins can have that are as stable as the native state, in the same thermodynamic conditions.

3.2 *Experimental Evidence for the Thermodynamic Hypothesis*

The thermodynamic hypothesis was not initially based on theory but rather on the success of Anfinsen's re-folding experiments described above [3, 123] and of the chemical synthesis by Gutte and Merrifield [70, 100]. Since then, innumerable studies of reversible protein unfolding of various proteins have been performed, with other denaturing conditions like changes in ionic strength, increases or decreases in temperature or pressure, and mutations of specific amino acids. Several types of techniques, like hydrogen exchange, fluorescence labeling, Fourier Transform Infrared spectroscopy, Circular Dichroism, Nuclear Magnetic Resonance and, more recently, single molecule methods, have been applied to monitor protein states and the results have largely been interpreted to provide extra experimental support to the thermodynamic hypothesis [46, 48, 51, 69, 83, 98].

A critical assumption to infer the thermodynamic hypothesis from the reversible unfolding experiments is that the denatured states of the proteins are completely unstructured. However, what was directly monitored by Anfinsen was the biological activity or the fluorescence emission of the proteins in the denatured states, and even now, that other techniques that can monitor structure in a more direct way have been used, this assumption is still far from proved [17]. While one study showed that the dimensions of denatured proteins have a sequence size dependence that is very similar to that of random coils [86], another study showed that the radius of gyration of unfolded protein ensembles in which the native secondary structure is preserved is also very similar to that of random coils [62]. Thus, both fully random structures and structures that preserve native secondary structure are theoretically possible in denatured states.

Another experimental finding is that the refolding times for the same protein vary with the denaturing conditions imposed on it [109]. If denatured states corresponded to completely random structures, all denatured ensembles would be equivalent and the refolding times should be, on average, independent of the denaturing conditions. The fact that refolding times for the same protein vary with the denaturing conditions means that there is a residual structure in denatured states and that residual structure is dependent on the denaturing conditions. Furthermore, there is, in many cases, direct experimental evidence of residual native secondary structure in the denatured ensemble [17, 22, 26, 116, 131, 132], something that was first envisaged by Lumry and Eyring who suggested that reversible unfolding occurs when denaturation leads to changes mainly to the tertiary structure, while irreversible unfolding is due to changes in the secondary structure as well [96].

Following theoretical studies within the funnel model that suggested that folding times should correlate with protein sequence size [146], Plaxco and co-workers [109] looked for correlations between the folding rates and protein characteristics such as the thermodynamic stability of the native state, the sequence size and the relative contact order (defined as the average sequence separation between spatially neighbouring residues in the native state, normalized by the sequence size). The only correlation they found was between the folding rate and the relative contact order [109]. This finding led to the optimistic view "that a general and quantitative theory of protein folding rates and mechanisms (as opposed to unfolding rates and thus protein stability) may be near on the horizon" [110]. Although those expectations are yet to be fulfilled as far as protein folding mechanisms are concerned, the prediction of re-folding rates is arguably the part of current protein folding theories that has met with the greatest success until now.

4 Levinthal's Kinetic Hypothesis

As pointed out in [121] there are two types of protein stability: the thermodynamic stability which is related to the free energy difference between the (natively) folded and unfolded/misfolded states, and the kinetic stability which depends on how fast the transition from native to other states is. Even if the native state of a protein is not thermodynamically particularly stable (i.e. even if there are many alternative conformations with approximately the same free energy), the population of the native state and its lifetime may still be large enough for the protein to fulfill its function in the cell if the energetic (kinetic) barrier that it must overcome to undergo a harmful conformational change is sufficiently high. In this case, the native state will just be one of the many kinetic traps in which the same protein may find itself, in the same thermodynamic conditions.

For protein function it is important to ensure that a large part of the population of cell proteins is in the native state at all times, something that requires a strong thermodynamic stability. However, experimental data show that proteins are, thermodynamically, only marginally stable [122, 139]. On the other hand, a high population of natively folded states can also be achieved if, (1) after synthesis most proteins follow a pathway that takes them to the native basin and (2) if the kinetic barriers surrounding the native basin are sufficiently high. The kinetic mechanism for folding described in Sect. 5 follows this second possibility.

The hypothesis that native states are only kinetic traps and that, therefore, protein folding is a kinetic process was first put forward by Levinthal, in what constituted his own solution [92] to the so-called "Levinthal paradox" (see Sect. 3.1). Indeed, at the same time that Anfinsen made the experiments that led to the thermodynamic hypothesis [3], Levinthal proposed that the native state of proteins is just one of the many kinetic traps in which they may fall. In Levinthal's view the time it takes for a protein to fold is short because proteins follow specific pathways and thus explore very few of the conformations potentially available to them [92]. Pathways are

deterministic trajectories in conformational space and Levinthal suggested that relative pauses in those trajectories will lead to specific protein folding intermediates which have been found in many cases [20, 55, 56, 113, 117]. But the first experimental evidence of a protein whose native state is a kinetic trap was found by Levinthal himself and is reported in a reference, [91], that only includes the summary (and which, at the end, states in French that the text of the manuscript did not arrive). Reference [91] reports on experiments that show that the protein alkaline phosphatase when synthesized and folded at 44 °C assumes a shape that is inactive, and when synthesized and folded at 25 °C assumes a shape that is active, *also when it is heated above* 44 °C. I.e., short as [91] is, it shows that alkaline phosphatase can have at least two stable structures at 44 °C, one of which is active and another which is not.

Since this seminal work by Levinthal, direct evidence of proteins whose native state is a kinetic trap has been accumulating [9, 66, 102, 111, 121, 137, 140]. Prions [111, 112] are perhaps the most famous but other examples are metamorphic proteins, known to fluctuate between very different conformations in native conditions [140]. Also, while most papers report cases of reversible unfolding, which support the thermodynamic hypothesis, cases of irreversible protein unfolding, which support the kinetic hypothesis, have also been found [77, 102, 103]. Moreover, the proteins that have been used in protein reversible unfolding studies are only a select set, which constitute a poor representation of the whole protein universe, and the conditions under which they unfold reversibly are far from being generic [19]. This suggests that reversible unfolding, instead of being the norm, may rather be the exception.

One more argument in favour of the kinetic hypothesis is the aggregated state. While reversible unfolding is found only for a small set of proteins, most proteins when taken out of the cell and denatured, form aggregates that do not re-fold back to the native state [19]. This shows that for most proteins the aggregated state is the true global free energy minimum. The aggregated state was first identified in proteins associated with misfolding diseases [111, 112] but was afterwards also found to occur with myoglobin [58] and "it now seems to be a generic feature of polypeptide chains" [50]. The existence of this aggregated state and the fact that in cells proteins, most of the time, avoid falling into it, is perhaps the best argument for that the native state is merely a kinetic trap, as first proposed by Levinthal [91].

The purpose here is to build on Levinthal's and others perspective that protein folding is a kinetic process [8, 20, 55, 56, 91, 136]. The specific pathway described in Sect. 5 and illustrated in Sect. 6 includes the idea that the starting structure in a folding process conditions the final structure, something that was not considered by Levinthal [91, 92] and which is still absent in other proposals, like the foldon [56]. One consequence of taking into account the starting structure is that folding in vivo can and will tend to be fundamentally different from re-folding in vitro. As explained in detail in Sect. 7, according to the kinetic hypothesis the only protein folding problem likely to possess a unique solution is folding in vivo which constitutes our main interest and which is the subject of the next subsection.

4.1 Protein Folding in Vivo

As mentioned above, most proteins, when denatured outside the cell, will not re-fold to the native state, when brought back to buffers that are meant to mimic normal physiological conditions [19, 119]. Instead, most proteins denatured in those in vitro conditions aggregate. One reason why the same proteins may fold in the crowded environment found in cells is thought to be chaperones [119]. The role usually attributed to chaperones is solely the increase of the rate of folding, thereby preventing aggregation and increasing folding efficiency. However, recent experiments have shown that many of the proteins that under stress conditions are substrates of the chaperones, do not require them for efficient folding in normal cellular conditions [19]. Furthermore, there is evidence that chaperones can influence the structural outcome of the folding process, e.g. in the absence of its own chaperones the protein actin from plasmodium can remain incompletely folded [105]. But, in spite of many studies, the mechanism by which chaperones assist folding remains unknown. While a usual picture is that their substrates fold inside the chaperone cavities [119], there is also evidence of a protein that folds outside the chaperone GROEL [27], a process that resembles the folding process after protein synthesis by the ribosome.

While the focus in this subsection is folding in vivo, until now most experiments on protein folding have been in vitro re-folding experiments [19]. In the latter experiments, the starting point is a denatured state of a natively folded protein whose subsequent re-folding is monitored. Just as different denaturing conditions induce different conformational ensembles [17, 22, 26, 116, 131, 132], the structure of proteins as they emerge from the ribosome may be (and probably is) very different from those sampled in re-folding experiments. According to the thermodynamic hypothesis the influence of the unfolded protein states is only on the corresponding folding time, since the final folded structure is supposed to be always the same for a given amino acid sequence. On the other hand, according to kinetic hypothesis, a different starting structure will not only influence the folding time but, more importantly, it may also lead to different final (native) structures. Thus, for the kinetic hypothesis it is very important to know the shape of the starting structure (i.e. the structure of the nascent chain).

Just as it was initially thought that denatured proteins were completely devoid of structure [3, 86] it was also thought that the structure protein chains have as they leave the ribosome is completely random. However, recent experiments of folding in vivo have shown that this is not the case. The ribosomal exit tunnel is a tube with a length between 80 and 100 Å and with a width between 10 and 20 Å [10] and specific secondary structures, namely, α-helices, have been detected in different parts of it [148]. Thus, the initial structures in cells are far from random.

The recent in vivo evidence also indicates that the ribosome's role is not limited to synthesis and to defining the initial structure, but it extends to the folding process itself. Indeed, while the dimensions of the exit tunnel seem to preclude tertiary folding inside it [143], there is plenty of evidence for tertiary folding while the nascent chain is still tethered to the ribosome and for a determining role of the ribosome on the

conformations sampled by the nascent chain [54, 57, 79, 84, 138, 141, 143, 145, 148]. Moreover, it has been found that when the rate of synthesis is modulated by silent codon changes (changes in the DNA and messenger RNA sequences that do not affect the amino acid sequence), the folding efficiency changes [104]. This direct effect of the time it takes to synthesize a protein on its final structure is yet another evidence that folding in vivo is a kinetic process, that the native state is a kinetic trap and that the ribosome, apart from being a synthesizing machine, also acts like a chaperone.

In summary, the recent experiments of folding in vivo have not only given extra support to the kinetic hypothesis but have also indicated that, at least in some cases, the nascent chain is helical. In Sect. 5 a specific kinetic mechanism for protein folding in vivo is described which is based on the idea that the nascent chains of *all* proteins is helical.

4.2 Exploring the DPC at Equilibrium

Within the thermodynamic hypothesis, the search for the native state of a protein is equivalent to the search for the main peak in the DPC (which in most studies translates to trying to find the global free energy minimum or even just the global potential energy minimum). However, in spite of several decades of attempting to predict the native structure in this manner, it is still not possible to do it with a sufficient degree of accuracy, in the absence of templates [46]. One reason commonly invoked for this failure is that, in spite of the progress made in the development of the force fields used for protein dynamics, there are inaccuracies in those force fields [115]. However, if force fields possess a particular bias, it should be to favour the native states, from whose knowledge they originate [21, 25, 29]. A second reason invoked for the failure is the size of the conformational space that even a small protein can access. The argument is that, even if the probability for the native state is much larger than for any other state, it remains difficult to locate it among the zillions of possible conformations. Even when using the most advanced sampling techniques like accelerated MD [71], replica exchange [28, 74] and others [124] and with ever more powerful computers [2, 129], it is still very difficult to find the native state with the (computer) time available.

On the other hand, within the kinetic hypothesis, the reason for the failure to determine the structure of the native state solely from the primary sequence, using the thermodynamic hypothesis, is much more fundamental: it is the fact that the native state is not the only well defined peak in the DPC. According to the kinetic hypothesis the DPC does not possess a dominant peak and, on the contrary, it includes numerous peaks of similar height and width. One of these peaks corresponds to the native state and the other peaks correspond to non-native, alternative states, kinetically separate from the native, structurally very different from it, and yet as thermodynamically stable as the native state. If the DPC does have this multi-peak shape then it is

impossible to find a dominant peak, putatively corresponding to the native state, even with the most accurate force fields and with the most powerful computers.

There are now more than hundred thousand proteins whose native structure is known [14] and for those it is possible to compare the stability of the native structure with the stability of other structures that they may potentially have. One advantage of the kinetic hypothesis is that to prove it, i.e. to prove the existence of more than one stable structure for the same protein, it is not necessary to sift through the whole conformational space of that protein. We can take a protein whose native structure is known and just need to show that same protein can have other, different structures, that are as stable as the native, in the same thermodynamic conditions. This was done in [34, 37–39] for six different proteins, two of which were common to all studies.

In [37] four proteins were selected: PDB1BDD [68], whose CATH [107] class is mainly-α, PDB1J08 [60], a mainly-β protein, PDB1IGD [65], an α/β protein, and PDB1AAP [76], a few secondary structures protein. These four proteins, whose structures are displayed in Fig. 3, are representative of the four CATH classes [107] that have been identified by analysing all the protein structures in the PDB [14]. The coordinates for the native structures of these proteins were taken from the PDB and for each of them, three alternative structures were built by imposing on its backbone the shape of backbone of the other three. For example, 1BDD has 60 amino acids [68], and 1J08 has 58 amino acids [60]. To generate one of the alternative conformations for the mainly-β protein 1J08, the backbone fold of the first 58 amino acids of the mainly-α protein 1BDD was imposed onto the 58 amino acids of 1J08 and, vice versa, to generate an alternative conformation for the mainly-α protein 1BDD, the backbone fold of the 58 amino acids of 1J08 was imposed onto the first 58 amino acids of 1I0S, while the remaining 2 amino acids were allowed to keep their native fold [37]. As the class is the main distinction between protein structures in the CATH classification scheme [107] the alternative structures created in this manner constitute some of the most artificial structures that can be imagined for each of the proteins. In a single peak DPC (that is, in a funnel-shaped energy landscape) these alternative structures should be highly unstable. However, the simulations, done in a explicit water bath, at a temperature of 298 K, for 500 nanoseconds, show that many of them are as stable as their native counterparts [37]. Moreover, those that are not stable, do not evolve to the native basin but rather to other basins at least 15 Å away from the native [37].

The results in [34, 37–39] indicate that, at least for the 6 proteins studied, the DPC, apart from the peak corresponding to the native basin, includes at least three more peaks corresponding to different average structures that are as stable as the native. This happens because protein structures are stabilized by a large amount of weak interactions and there are many structural combinations for which the intensity of attractive interactions compensates the intensity of repulsive ones leading to the same overall stability. It may be argued that 6 is a small number and that a more thorough coverage of the protein universe might lead to different conclusions, particularly since, as happens in most in silico studies, also the proteins selected in [34, 37–39] are small proteins. However, apart from their smallness, there is nothing particularly special about the proteins selected, and since the same potential energy functions

apply to large proteins as well, we expect that larger proteins will have an even greater number of conformations with a combination of interactions that leads to the same overall energy. I.e., the atomic constitution of proteins and the nature of their intramolecular interactions leads to that the DPC of *most* proteins has a multi-peak structure, or, in the language of "energy landscapes", we can expect that the energy landscape of most proteins has not one funnel, but many. Although not often reported in the literature, similar results, in qualitative terms, have been obtained by other researchers [19, 89, 144].

If indeed the generic DPC is multi-peaked, why has this characteristic not been detected in many other proteins? Within the kinetic hypothesis the answer is that, in spite of all the techniques used experimentally [46, 48, 51, 69, 83, 98] and in spite of all the advances in computer power [2, 129] and in sampling techniques [28, 71, 74, 124], only a very restricted part of the conformational space potentially available to each protein has been explored. On the other hand, while each trajectory in [37–39] is restricted, particularly when compared with millisecond simulations [78, 94, 115, 130], taken together, the four 500 ns trajectories generated for the four proteins cover a larger part of the conformational space because each starts from a very different part of the conformational space of the given protein. The non-native, alternative structures used in [37–39] are not visited by proteins in their lifetime in cells (which can be hours, days or years [49]) and even less in the millisecond simulations, or less, that start from natively folded structures, or distortions thereof. In fact, what the simulations in [37–39] also indicate is that, once folded, either natively or otherwise, most proteins, in the absence of triggers, in normal physiological conditions, never stray very far from that structure.

The second law of thermodynamics tells us that isolated systems tend to the minimum of their free energies which is reached at equilibrium. But cells are not isolated systems and are not at equilibrium. In vitro experiments are isolated systems, so they may reach equilibrium. But the second law of thermodynamics does not specify the time it can take for a system to reach equilibrium and does not rule out the existence of long-lived metastable states. The thermodynamic hypothesis claims that there is only one such long-lived state and is at odds with the results in [34, 37–39]. On the other hand, the kinetic hypothesis proposes that native states are one of the many long-lived metastable states that a given sequence of amino acids may take and is in agreement with those results.

In spite of the large number of articles that proclaim the funnel-shaped energy landscape [46, 48, 51, 64, 69, 87, 114, 124], Dill, in [46], states that there is "little experimental knowledge of protein-folding energy landscapes". The results in [19, 34, 37–39, 89, 90, 144] and the experimental evidence described in Sect. 4.1 suggest that the current notion of a DPC with a dominant peak (or, in another language, of a funnel-shaped energy landscape) should be revised.

5 A Kinetic Mechanism for Folding and the VES Hypothesis

The specific kinetic mechanism that is the subject of this section was first described in [34] and a preliminary (successful) feasibility test was reported in [35]. For reasons that will be clear below, let us call it the VES kinetic mechanism (VES KM) for folding. As explained in the previous section, if folding is a kinetic process, re-folding in vitro can be substantially different from folding in vivo because of the difference in the starting structures. Thus, it must be emphasized that the VES KM proposed here aims at describing folding in vivo. One application of this model has appeared in [36] and a second one is described in Sect. 6.

We can divide the VES KM into three main steps. **A first step** of the VES KM is the emergence of the polypeptides from the ribosome and the assumption is that the nascent structure of *all* proteins is helical. This defines the starting structure.

A second step is the bending of the initial helix at specific amino acid sites. This bending is the structure-determining step and is assumed to be driven by quantum vibrational excited states (VES). As explained in greater detail below, the idea is that VES are the means by which proteins store and transport energy from active sites, where the energy is generated, to other regions where the energy is used for work. When the quantum VES decay, it is further assumed that the energy they carry is released as classical kinetic energy of the same atoms that carried it, i.e. VES are transformed into classical kicks applied to the atoms which carried that quantum vibrational mode. In this view, *protein conformational changes associated with the early stages of folding are driven by quantum VES* and will not take place in their absence. On the other hand, the response to those initial kicks is governed by the classical interactions included in traditional force fields such as AMBER [25], GROMOS [29] and CHARMM [21]. From the point of view of the DPC, the second step is also that in which the native peak is selected from among all the other peaks, i.e. the initial atomic kick pushes the protein (or, for a larger protein which is synthesized in sections, the protein domain) towards the conformational area of the native peak.

The third step in the VES KM consists of a stochastic trajectory that takes the protein from the edges of the native peak to its central area, where the DPC has a local maximum. This third step is very similar to the diffusion claimed to take place, from the very start, in funnel theories. Indeed, the VES KM shares with the funnel model the idea that the folding rate is determined by this third diffusional step, the difference being that, according to VES KM, the native structure is defined by the first step mentioned above, which is a deterministic step driven by quantum VES. The fact that an initial helical structure and VES have not been considered until now may explain the lack of success in determining structures from sequence alone [46, 124], and the fact that the final stochastic trajectory in the native basin, ruled by the classical interactions, is the rate limiting step in folding, may explain the success in correlating in vitro folding rates with native topologies [109].

The hypothesis that quantum VES play a role in protein function (the VES hypothesis [32]) has a long history [41, 99, 128]. Indeed, in a meeting on bioenergetics, in 1973, and with the purpose of solving what was then described as a "crisis in bioenergetics", McClare proposed that energy can be stored in proteins in the form of "excimers", i.e. resonances between excited states [99]. In the last page of his paper, McClare further suggests that a possible candidate for an excited state in living systems is the first overtone of the amide I band which, as he notes, corresponds to two quanta of the bending mode of water [99]. This suggestion was picked up by Davydov, a Ukrainian solid state physicist, who applied it to muscle contraction [41]. Davydov's analytical studies [42], together with Scott and co-workers numerical work [128] led to a great interest in this field in the 1980s and 1990s. The main question then was whether VES assumed the form of solitons, as Davydov [41, 42] and Scott and many others thought [128], and how long the solitons lasted. Computer simulations have shown that, at biological temperatures, VES share with solitons the attribute of being localized but instead of moving coherently (as solitons do), they hop stochastically from peptide group to peptide group [31, 33, 36, 40]. Furthermore, experimental evidence indicates that the lifetime of VES is a few picoseconds [52, 72].

One important question is how VES are generated. Davydov [41, 42] assumed that the energy released in the hydrolysis of ATP is stored in the form of amide I excitations (that energy is sufficient to create two quanta of amide I). On the other hand, Careri and Wyman have calculated that the binding of ions to a protein corresponds to an energy input also sufficient to create two amide I excitations [24] and it has also been proposed that they can be transferred from excitations of the bending mode of water [31, 32], which resonates with the amide I mode and for which there is experimental evidence [133]. In fact, it is not unreasonable that, apart from chemical reactions, VES can be locally generated by the binding of ligands to proteins.

While most authors have been interested in the effect of the amide I on protein dynamics, the VES KM proposed here focuses instead on the effect of its *annihilation* on protein dynamics. Thus, while other authors consider a lifetime of a few picoseconds the amide I excitation too short for the purposes they have in mind [7, 52, 72], computer simulations show that in that time scale amide I excitations can move from the active site, where they are generated, to other regions of the protein where they are used for work [30–32, 39, 40]. The amide I vibration consists essentially in the stretching of the C=O bond of the O-C-N-H peptide group (marked with a red oval in Fig. 1) and one assumption of the VES KM is that when the amide I decays, its energy is converted into classical kinetic energy of the peptide group that was excited at the moment of annihilation, something that may result in the breaking of the hydrogen bond that connects that group to another group.

Both amide I and amide II are routinely used in the laser ablation of lesions [53, 142], with their energy being ultimately converted to local heat. Recently, however, it has been shown that irradiation with amide I can break protein aggregates back into soluble monomers [81, 82]. In the latter studies the effect was frequency dependent and found to occur with amide I excitations only. As protein aggregates are kept by hydrogen bonds, the experiments in [81, 82] indicate that amide I exci-

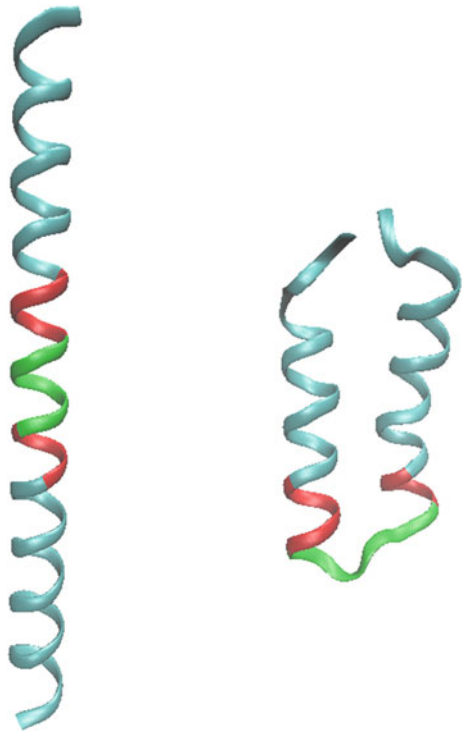

Fig. 4 The right panel shows the known native structure of protein PDB2HEP [14]. The left panel shows the initial conformation of the protein which in the VES KM is assumed to be an α-helix. The amino acids whose amide groups suffer the initial kicks (see Sect. 5 and text below) are highlighted in red and green, the latter colour signalling also the location of the loop that connects the two helices in the native state

tations can lead to the breaking of hydrogen bonds and to a conformational change, as postulated by the VES KM.

6 The Folding of a Small All-Alpha Protein

To illustrate the kinetic folding mechanism proposed in the previous section, as in [36], a small all-α protein was selected from the PDB [14], namely, protein PDB2HEP [6]. The PDB conformation was first energy minimized with the AMBER force field FF03SB [25] and the resulting structure is displayed in the right panel of Fig. 4. On the left panel of this figure is the same protein in the conformation of an α-helix, which, as explained in Sect. 5, is assumed to be the starting structure for protein folding in vivo.

A crucial aspect of the VES KM is that the energy stored in quantum amide I vibrations drive the first step in protein folding. While the amide I propagation is a quantum event, a conformational change of a protein, which involves the motion of a large number of atoms, can be considered a classical event. There is experimental evidence that amide I vibrations can propagate from one α-helix to another in a protein

[59], and there is also experimental evidence for the use of the amide I energy to generate a conformational change [81, 82], but there is not yet any knowledge about the classical state that arises in a protein after the decay of an amide I excitation. As was done in [36] also here it will be assumed that the energy released in the annihilation of an amide I excitation is transferred to the momenta of the atoms where the quantum excitation was originally localized, the CONH atoms of the peptide group that was excited when the annihilation took place. Since the amide I excitation consists essentially of the stretching of the CO bond, the direction of those extra momenta in the CONH atoms will be the same as that of the CO bond and the sense will be from O $\rightarrow$ C. The aim of the simulations reported in this section is to evaluate the efficiency with which a localized kick to just four atoms of the α-helix displayed in the left panel of Fig. 4 can bend the helix to its native shape, shown in the right panel.

The influence on the folding efficiency, of the location of the initial kick and of its intensity, is investigated. The locations i, where i designates the amino acid number in the primary sequence, for the initial kicks in the CO(i)NH($i+1$) groups are signalled by the red and green colours in Fig. 4. The amino acids in green have $i = 19, \ldots, 23$ and the amino acids in red have $i = 15, \ldots, 18$ in the first helix of the native structure (see the right panel of Fig. 4), and $i = 24, \ldots, 26$ in the second helix. The impulse was the same for all of the four atoms of the group CONH and its sense, from O $\rightarrow$ C, tended to break the hydrogen bond between the CO of CO(i)NH($i+1$) to the NH of CO($i+3$)NH($i+4$), in the initial α-helix.

As described below, the kick that made the initial helix evolve to a structure closest to the native state was at $i = 23$, and the final structure obtained can be seen in second picture of Fig. 5. Figure 5 illustrates the influence of the relative intensity of the initial impulse (measured in multiples of the amide I energy) when the location of the initial impulse was kept fixed at $i = 23$. It shows that for weaker kicks in which the kinetic energy of the kick is $n = 32$ or below, the helix bends but does not close and keeps a V-like architecture throughout the rest of the 1 ns trajectory. On the other hand, for stronger kicks in which $n > 100$, the final structure is compact but has several types of distortion with respect to the native, like longer loops, greater twists between the helices and distortions in the helices themselves, such as even the generation of helical bundles (not shown). Thus, Fig. 5 shows that there is a range of energies in which the initial impulse can drive the helix to the vicinity of the native state. Indeed, for $50 < n < 75$ the final structures obtained were quite close to the native structure (compare the middle structures in Fig. 5 with the native structure in Fig. 4). In the structure obtained with the $n = 51$ kick, the loop is shifted towards the C-end, when compared to the native structure, but the root mean square deviation (RMSD) with respect to the native state is the lowest (close to 3 Å when all backbone atoms are taken into account, see Fig. 6 and text below). On the other hand, in the structure obtained with the $n = 74$ kick, the loop is in the correct place but the two helices have a slight twist with respect to each other that is not present in the native structure.

In Fig. 6 are compared the results of simulations in which 4 different intensities of the initial impulses and 12 different locations for them were considered. Also, in order

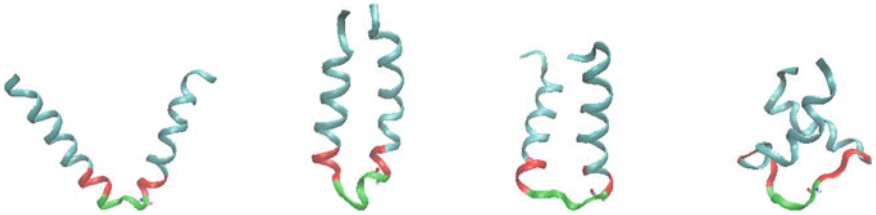

Fig. 5 Final structures obtained after impulses of increasing intensities on the group CO(23)NH(24) that is shown as the atoms that stick out of the backbone at the end of the green portion. From left to right, the total kinetic energy in the initial impulse, in units of amide I energy, is n = 32, 51, 74, 101, respectively. The green colour shows the position of the loop in the native state

to check the influence of variations in the coordinates of the atoms which is expected in a statistical ensemble at finite temperature, 6 slightly different initial helices were taken. Notice that if the CO bond directions vary, also the direction of the initial kick varies and thus the 6 slightly different initial helices will also have slightly different initial kicks, even if the kick is applied at the same peptide group with the same intensity. A much greater difference between the trajectories obtained from each of the 6 initial structures is, however, due to the fact that the velocities *on the other atoms*, which number 688 in protein PDB2HEP [6], were different in each of the 6 trajectories and obeyed a Maxwell–Boltzmann distribution at $T = 298$ K. Another very important point is that all the simulations were made in the microcanonical ensemble (i.e. with option NTT = 0, in the AMBER package [25]). There were two reasons for this. One reason is that the usual Langevin terms, with the default frequency coupling to the thermal bath of 5 ps^{-1}, lead to a fast dissipation of any energy input and prevent conformational changes such as the bending of the initial helix that is aimed at here. It was verified that this coupling must be reduced by a factor of at least 10 for the conformational changes to take place. A second reason is that Langevin dynamics or any other form of coupling to a thermal bath leads to random variations between the trajectories which muddle the comparisons aimed at here.

In Fig. 6 the results of 288 simulations (4 different intensities of the initial impulses $\times$ 12 different locations $\times$ 6 different initial conditions for each of the previous) are displayed. Each rectangle has an abscissa that goes from zero to 1 ns (the total duration of each of the trajectories) and an ordinate that goes from 3 to 6 Å. The lines are the RMSD, with respect to the native state, of each conformation in a trajectory. The colours identify each of 6 different initial structures, i.e. all lines of the same colour correspond to trajectories that start with the same initial helix, with the same random velocities in all atoms, except for the velocities of 4 atoms in the group CO(i)NH($i + 1$)at which the initial impulse is applied. The trajectories are only visible in the rectangles when the conformations sampled in them are within 6 Å of the native structure. Empty rectangles correspond to kick locations and/or to kick intensities that led to conformations that were further away than 6 Å from the native structure, throughout the 1 ns trajectory. Figure 6 clearly shows that there is

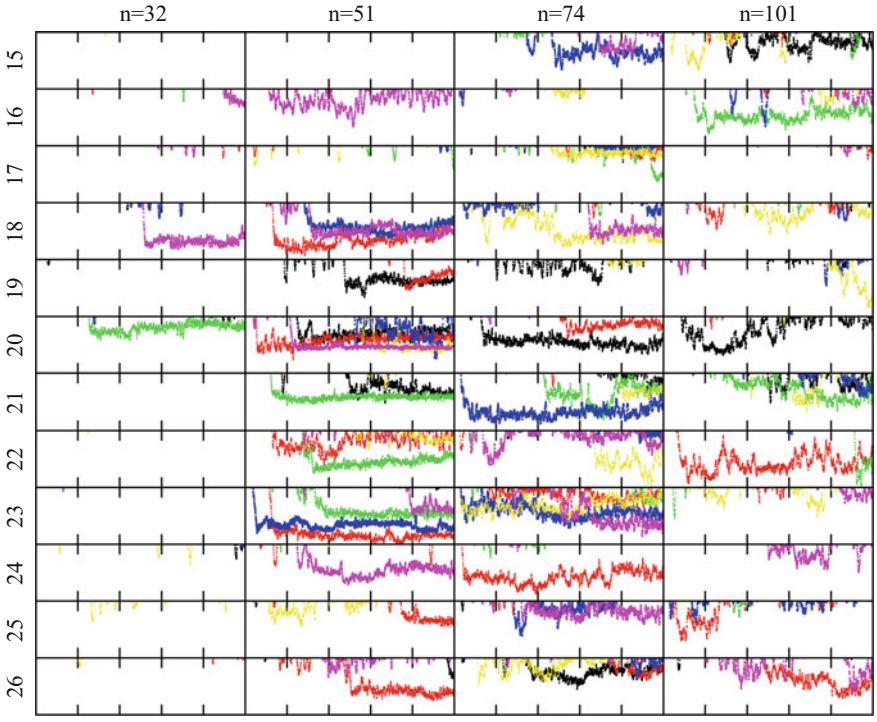

Fig. 6 In each rectangle is plotted the RMSD versus time of each conformation in a trajectory, using the native structure as a reference. In each rectangle, time goes from 0 to 1 ns and the RMSD is between 3 and 6 Å. I.e., when the conformations approach the native state (with RMSD smaller or equal to 6 Å), they appear in the rectangle. All the trajectories in each row started with kicks at the same CO(i)NH($i + 1$) atoms of the helix displayed in the left panel of Fig. 4. The label in front of each row specifies the value of i for that row. The labels n on top of each column specify the value of the kinetic energy of the initial kick in the corresponding atoms, in units of amide I energy. For each i and each n, i.e., for each rectangle, 6 different trajectories were run whose initial velocities in the CO(i)NH($i + 1$) atoms were equal but whose velocities for the other atoms were different and obeyed a Maxwell–Boltzmann distribution for T = 298 K (see also text)

a minimum intensity of the kick below which it is not possible to drive to bend the initial helix, as well as a maximum: the density of lines increases above $n = 32$ and by $n = 101$ it has already started to decrease again. Inspection of Fig. 6 also shows that there are many impulses capable of driving the initial helix into the vicinity of the native state (many different pathways, in the language of the funnel model). But not all kicks are as efficient as the others and looking for the location and intensity that leads to the trajectories that come closer to the native, we identify the kick at $i = 23$, with $n = 51$, as the best, since 4 of the 6 random trajectories come close to 3 Å of the native state. Notice though that their folding times are different: the blue and the red trajectory "fold" in less than 200 ps, while the green takes 400 ps and the pink takes 800 ps. In decreasing order of folding efficiency, $i = 23$ is the

best location for a kick, followed by $i = 20$ (which is hydrogen bonded to $i = 23$!), followed by $i = 18, 21, 22$, all equally less efficient. Figure 6 also shows that none of the kicks tried lead to folding in all the 6 random initial conditions, i.e., all of the kicks show some sensitivity to noise.

A general conclusion from these simulations is that it has been demonstrated that a kick in just 4 covalently bonded atoms *can* drive the conformational change from the initial helix to the native state of protein PDB2HEP [6]. On the other hand, it cannot be said that the right kick, capable of surviving the noisy environment that exists in a living cell, and capable of folding the helix in a fully reproducible manner (i.e. for all the 6 trajectories and more), has yet been found. Another problem is that the minimum energy of the initial kick is rather high ($n = 51$ amide I excitations!), something that is expected to improve when more efficient kicks are found.

7 Discussion

The question of whether protein folding is a thermodynamic or a kinetic process is as old as the protein folding problem. As detailed in Sect. 3, the thermodynamic hypothesis has been the leading guide to the protein folding problem since the 1970s. According to the thermodynamic hypothesis, the DPC has one predominant peak and folding is a stochastic process in which proteins, in a step by step fashion, move towards the center of that peak. In this picture, the final (native) structure is only dependent on the protein sequence, the starting structure only influences the folding time and the driver of protein folding is random thermal agitation.

The main arguments in favour of the thermodynamic hypothesis were outlined, and criticized, in Sect. 3 and the case for the kinetic hypothesis was put forward in Sect. 4. According to the kinetic hypothesis, apart from the native peak, the DPC possesses many other peaks of similar width and height, each corresponding to a different structure of the same protein, potentially available in normal cell conditions, and as stable as the native.

According to Levinthal's kinetic hypothesis the native state is reached in a reproducible manner, not because it is the most probable one, but because the pathway that takes a newly synthesized sequence to it is essentially the same every time [91, 92]. Within the specific kinetic mechanism described in Sect. 5, designated as VES KM, the pathway is as follows. The starting structure *all* proteins have as they emerge from the ribosome is helical. When this helix emerges from the ribosome, the binding of water molecules, ions and other ligands, or a chemical reaction like the hydrolysis of ATP, generate energy in the form of quantum vibrations (VES). These quantum vibrations hop stochastically from peptide group to peptide group and concentrate at specific amino acid sites in the helix, the bending sites. Once a sufficient number of VES has accumulated at a bending site, the quantum state becomes unstable and decays, releasing its energy in the form of kicks to the atoms of the amino acid where it was located. The simulations reported in Sect. 6 show that such kicks can bend a helix and produce two helices connected by a loop (see Fig. 5). Then two possibilities

arise. Either the interactions between the side chains that are brought into contact by the bending of the helix are globally attractive, in which case the helix bundle is stable and the corresponding region will be mainly-α, or they are globally repulsive, and the helices will tend to distort into extended chains which can pair up as β-sheets. In the case of large proteins, for which synthesis suffers occasional pauses [54, 104, 145], this folding process applies to each of the regions of the protein that is successively synthesized, with the previously synthesized and folded regions influencing those that are synthesized and folded later. Within the thermodynamic hypothesis, such an influence of the synthesis on the native structure of the protein should not take place because all initial structures should tend to the same final structure, in the same thermodynamic conditions. On the other hand, in the VES KM, the pauses and their duration will affect the three dimensional structure of the incomplete protein and thereby may affect the folding efficiency, as is observed experimentally [104].

Protein folding is dependent on the interactions that drive folding. As mentioned in Sect. 3.1, it has been suggested that hydrophobic interactions are the drivers of the initial compact structures [48, 87]. Instead, the VES KM described in Sect. 5 follows Ben-Naim who proposes that hydrophilic interactions are much more important [13]. In particular, it is assumed that what water molecules do is to generate VES in proteins, which they can do in two ways: one is by direct transfer of energy from the bending mode of water to the amide I excitation of a peptide group in the protein, something that has been observed experimentally [133], and explored as one cause of misfolding diseases [31, 32], and a second way is by forming a hydrogen bond with a group in a protein which leads to an energy input of the amount needed to create an amide I excitation, something that can also happen with the binding of other ligands [24]. Thus, the suggestion here is that the hydrophobic interactions will only manifest themselves *after* two parts of the protein have been brought together by other causes (like the bending of an helix at a specific site) and have little influence in *producing* that compaction in the first place.

It should be emphasized that the VES KM includes both a kinetic step and a thermodynamic step. The kinetic step is the bending of the initial helix at a specific site. In terms of the DPC, this step corresponds to the selection of one of the peaks in the DPC (in cells, the peak selected will be the native peak, most of the times). Once a peak is selected, the diffusion towards the center of the peak is similar to what is postulated to occur, from the very start, in the thermodynamic hypothesis. The difference is that in the thermodynamic hypothesis the native structure is defined by this diffusive process while in the kinetic hypothesis the selection of the peak (the kinetic step) is the structure defining step. According to the thermodynamic hypothesis protein misfolding should not exist. On the other hand, according to the VES KM, misfolding should be improbable but it will occur when a non-native peak of the DPC is selected, for instance, because the bending of the initial helix took place at a different site.

7.1 The DPC and Evolution

It is sometimes recognized that, given the nature of the interactions that stabilize protein structure, it is in fact probable for their DPC to have a multi-peak shape, and it has been suggested that does not happen for the proteins found in living cells because evolution has led to the selection of very specific sequences whose DPC has a single dominant peak corresponding to the native state (or, in another language, evolution has led to the selection of sequences that have funnel-shaped energy landscapes and are good folders) [69, 147]. In Sect. 4.2 results were described that suggest that the DPC of *most* existing proteins is multi-peaked, i.e. that most proteins can assume many, very different conformations that are as stable as the native. That being so, if we could look at the full conformational space of real proteins, their DPCs would be very similar to one another in that all of them would be constituted by many peaks, some with extra structure (correspondent to rougher free energy surfaces) and others smoother. Thus, I would argue that, except in very special cases like in polypeptides made of a single amino acid, evolution does not and cannot mold the whole DPC of a protein and the only thing it can do is limit the part of the conformational space that is accessible to that protein when it folds in a cell. I.e., what evolution does is select the sequence whose folding process in a living cell will lead to a specific final structure capable of realizing a necessary function. As emphasized in [73] the cellular and organismal fitness of the native state of a new protein is the really important factor for its evolutionary selection, not the shape of its DPC (or of its energy landscape).

Ultimately what the views expressed here mean is that there is *not* a one to one correspondence between an amino acid sequence and its three dimensional structure, as assumed in the thermodynamic hypothesis. Therefore, the problem of determining the three dimensional structure that a given sequence will adopt in normal physiological conditions has no answer, because there is an immense number of possibilities. I would argue that this is the main reason why the prediction of the native structure, solely by looking for the maximum in the DPC, has met with very little success, in spite of all the progress made so far [46]. The only question that can have a unique answer is “What is what the three dimensional structure of a protein that has a given sequence when this protein is synthesized by a ribosome in normal cellular conditions”. For the existing proteins, the answer is the native structure and that should be predictable from the amino acid sequence. Indeed, cells do it all the time and the proposal is that we must apply the VES KM to understand how they do it.

7.2 Protein Structure

Proteins are very large molecules. Even a small protein, with 60 amino acids, has approximately a thousand atoms. Since the order of magnitude of the interactions between atoms that are close in space is similar for many of them, if their structures were acquired from random initial conditions, in a series of steps driven by thermal

agitation, we should expect a great variety of structures, possibly with quite a few of them being like convoluted wool yarns. Instead, the analysis of structures in the PDB [14] shows that all of them have a hierarchical and modular structure, in which we can distinguish a primary structure (the polymer-like chain of the amino acids), the secondary structure (which is already a three-dimensional arrangement of the chain into helices or sheets), the tertiary structure (which is the full three-dimensional structure formed by the packing of the different secondary structures) and, when there is more than one monomer, the quaternary structure (which is the formed by the packing of the monomers). According to the thermodynamic hypothesis this hierarchical structure is in a sense fortuitous as it is deemed to arise, step by step, from structures that can be completely random initially. On the other hand, in the VES KM, the hierarchical nature of proteins is imprinted on the initial condition (all nascent chains are helical) and on the subsequent pathway that proteins follow in cells (starting with bending at a specific helical site). If proteins did not start from this specific structure, and if they did not follow that specific pathway, their structure would be much more varied.

The analysis of known protein structures has led to the identification of two main secondary structures, namely the helix (mostly α-helix) and the β-strands (turns, loops and random coil can be seen as essentially lack of structure, see Sect. 2). However, while the helices can exist in isolation, β-strands can only exist in association, thus, contrary to the usual views, I would argue that there is only *one* fundamental secondary structure: the helix (in its different varieties). This makes it natural for it to be the selected initial condition for the folding events in cells. According to the VES KM, the other secondary structures arise only as distortions of the initial helix, which occur when, along the pathway towards the stable final (native or other) protein structure, the helices that are brought together by the bending of the initial helix at a specific site, are unstable, wholly or in part. If two neighboring helices, or part of them, become extended, the two extended structures can form a β-sheet, whose chains will be linked by turns or loops. The latter can also form if one helix only, or part of it, is unstable and becomes extended. The tertiary structure results from a stable packing of the different modules (which can have helices, sheets or loops). Thus, the limited variety of protein structures can be understood from the point of view of the VES KM, as a result of a specific initial structure and of a folding pathway that greatly limit the conformational space covered by proteins. If proteins could indeed follow all possible pathways from all possible initial conditions they would be able to assume a much larger variety of structures (as seems to happen in part with prions, which are known to be differentiated in several strains related to as many conformations [112]).

Although the notion that proteins are tightly packed and that their density resembles that of solids is widespread, recent studies suggest that this too needs to be revised [11, 93, 108, 118]. Indeed, the internal density of proteins is not uniform, with cavities found at all depths, and many times filled with water [118]. Also, while hydrophobic forces are often invoked as the driving forces for folding [48, 87] (see Sect. 3.1), the conclusion from another study is that in fact hydrophobicity is far from being optimized in protein structure [11, 108]. Finally, in [11, 108] it is concluded

that, instead of being dense like solids, proteins are more like sponges, and should be characterized by a fractal dimension. Also, normalized unfolding enthalpies and heat capacities were found not to correlate with packing densities, something that indicates that folding is not driven by van der Waals interactions. These findings agree with the VES KM according to which folding is driven by the decay of VES, with the classical interatomic potential only being responsible for the favourable or unfavourable interactions between amino acid pairs that have been pushed together (see Sects. 5 and 6).

As mentioned above, it is thought that protein structure is controlled by hydrophobic interactions. On the other hand, the prediction of protein structures using templates is based on the knowledge that two proteins with just 30% of sequence homology have a strong probability of sharing the same structure [61, 101]. I.e., it is possible to change 70% of the amino acids of a protein and still get proteins with the same structure as the original one. On the contrary, sometimes the mutation of a single amino acid can lead to a substantial structural change [1, 101]. Furthermore, the percentage of amino acids that must be conserved to maintain the same protein structure *decreases* as the sequence size increases [61]. This suggests that protein structure is controlled by a small number of amino acids. From the point of view of the thermodynamic hypothesis it is difficult to explain how changing one amino acid can have a stronger effect on hydrophobic (or any other) interactions than changing 70%, or more, of the amino acids. On the other hand, from the point of view of the VES KM the amino acids that control the native structure are those at the bending sites. Mutations at other sites may be structurally silent, but mutations that move the bending site will have a strong structural effect. As the number of bending sites does not grow appreciably with the sequence size, they will constitute an ever diminishing proportion of the total number of amino acids, as observed experimentally [61].

8 Future Work

At the end of his review on the advances made in protein folding research in the last fifty years, Dill makes a list that is a measure of the undiscovered country in this area: “we have little experimental knowledge of protein-folding energy landscapes; we cannot consistently predict the structures of proteins to high accuracy; we do not have a quantitative microscopic understanding of the folding routes or transition states for arbitrary amino acid sequences; we cannot predict a proteins propensity to aggregate, which is important for aging and folding diseases; we do not have algorithms that accurately give the binding affinities of drugs and small molecules to proteins; we do not understand why a cellular proteome does not precipitate, because of the high density inside a cell; we know little about how folding diseases happen, or how to intervene” [46]. In the two final subsections below proposals and predictions for future theoretical and experimental work, inspired by the VES KM, are made, some at the level of the black box approach (see Sect. 1) and others aiming at the

physical mechanism behind protein folding, all in order to try to clear at least a few of the unknowns mentioned in Dill's list.

8.1 Theoretical Projects

According to the thermodynamic hypothesis, given sufficient time, proteins should reach their native state from any initial condition, whether it is extended or not. In this case, it is possible to speak of the propensities for each amino acid to form an α-helix, or a β-sheet, or a turn, etc. On the other hand, according to the VES KM (see Sect. 5), such propensities have little meaning because the native structure of a protein is the result of one initial condition and one pathway, which, if changed, will lead to different conformations, with equal probability. Some specific amino acids, like proline or glycine, may destabilize an α-helix, but most of them, in isolated helices that are neither too short nor too long, will not. Assuming that the VES KM is valid, what is important to determine from known protein structures are the locations of the bending sites and the directions along which the initial helix bends into two helices. If, for each sequence, we know how to characterize this bending process we will know which side chains of that sequence will be brought together. According to the VES KM it is the overall stability of those side chain interactions that will decide whether the two-helix bundle so formed will survive much as it is, or not. Thus, another statistics that is important from the point of view of the VES KM is that of *which such amino acid pairs are not found in neighbouring helices*. Those missing pairs can be the destabilizing pairs that lead to denaturation of the helical bundle and to the formation of β-strands.

More generally, and if the previous statistical approach is not productive, the theoretical exercise that can be done to find the rules for a black box approach to protein folding is to determine the steps that, for a protein of known structure, take the corresponding initial helix to its native state. I.e., look at the initial helix and at the native state and, using the VES KM as a guide, try to infer the pathway that would bring the former to the latter. The aim of such a study is to identify common features in the folding pathways of many proteins. This is easier to do when the native state does not stray too far from the initial helical conformation, and thus a set of all-α proteins should be used first, preferably starting with helical hairpins like PDB2HEP [6] and later proceeding to multi-helix bundles. Once the necessary and sufficient folding rules have been established for all-α proteins, we can move to α/β proteins. With some luck, the folding rules determined by following the previous procedures will lead, in the case of α/β proteins, to helical bundles with some of the destabilizing pairs mentioned in the preceding paragraph and will make it easier to predict the evolution of the two unstable helices into extended chains and β-sheets. If not, one can also use the structure with the two-helix bundle as an initial condition in an MD simulation and verify whether the classical potentials [21, 25, 29] predict a trajectory that turns the helices, or part of them, into β-sheets. When we know how to fold mainly-α and α/β proteins we can look at the two other CATH [107] classes:

mainly-β and few secondary structures. While the attempts to fold proteins, namely at CASP exercises (see Sect. 3.1), have been made with proteins across all classes, the VES KM suggests that a more fruitful approach may be to first restrict the search for general rules to one particular class and follow a step by step development, as outlined here. Furthermore, chaperones provide further restrictions to the in vivo folding pathway, too complex to envisage at this stage. Thus, the set of proteins used to infer protein folding rules should include only proteins able to fold in the absence of chaperones.

In Sect. 4.2 it was suggested that the reason why non-native structures have not been found for most proteins is that most simulations and experiments on protein unfolding and re-folding are made in conditions that do not take proteins away from the native basin. On the other hand, in [34, 37–39] many of the simulations started from structures that were away from the native and did not approach the native basin. However, it may be argued that this is because half a microsecond is not long enough for such an evolution to take place. A stronger case for the VES KM can be built by running this kind of simulations for longer times, like the millisecond trajectories in [78, 94, 115, 130].

In Sect. 6 the folding of the protein PDB2HEP [6] from an initial α-helix to its native state was achieved by specific kicks to the peptide group of just one amino acid. One problem with these folding simulations is that the kinetic energy input was too high, namely, an amide I state with 51 quanta was necessary to produce folding. Although other simulations with non-conservative Davydov-Scott Hamiltonians have shown that it is indeed theoretically possible for amide I states to accumulate to similar high quantum numbers [134, 135], it is worth to test different initial conditions, like excitations spread on more than one site (and thus kicks to more than one amino acid), different directions of the kick, more related to the direction of the hydrogen bond that is broken, etc., in order to see whether lower energy kicks that can also be efficient in folding.

Finally, from a more physical perspective, a model of the decay of quantum VES is also an open issue and one that is critical for the assumption that the energy stored in the quantum states is released in the form of classical kicks to specific atoms. Thus, the development of such decay models should also be pursued.

8.2 Experimental Projects

According to the VES KM (see Sect. 5) the starting structure for folding in vivo is always a helix while the in vitro refolding experiments start from structures that are obtained by denaturing already folded proteins. I would suggest that the great variety of folding rates [109] measured in in vitro experiments is a reflection of a concomitant variety of starting structures. **One prediction** from the VES KM is that the distribution of in vivo folding rates will be much more uniform than the re-folding rates of the same set of proteins measured in vitro. A **second prediction** is that, for proteins of the same class, a strong correlation will be found between the

in vivo folding rate and sequence size, contrary to what happens in in vitro folding experiments [109].

As discussed in Sect. 7, following the VES KM, the helix is the primary secondary structure in proteins (it is there from the very start) and all the other secondary structures only arise when this primary structure is unstable. Thus, a **third prediction** is that, for proteins of similar size, the in vivo folding rate will vary with protein class in the following manner: all-α > mainly-α > α/β, $\alpha+\beta$ > mainly-β.

It is known that protein folding takes place concurrently with synthesis, and that the folding rate influences folding efficiency [54, 57, 79, 84, 104, 138, 141, 143, 148], which constitutes another indication that folding is a kinetic process (see Sect. 4.1). It has also been suggested that folding can take place *inside* the ribosome, something that would explain the pull exerted by the part of the protein that is inside the ribosome on the part that is already outside [97]. However, the size of the exit tunnel seems to preclude it [143] and the *proposal* here is that that pull may be due to a conformational change from a thinner helical structure (like a 3_10 helix, capable of fitting within the inner tunnel of the ribosome) to a broader helix (like the α-helix) which can fit within the exit tunnel.

According to the thermodynamic hypothesis the reason why the unfolding of proteins is sometimes irreversible is protein aggregation (see also Sect. 4). If proteins did not aggregate, it is argued, no matter what the initial conformation is, most proteins would refold to the native state, when the native conditions are restored. On the other hand, according to the kinetic hypothesis, proteins only refold to the native state from very special initial conditions. The two theories can be distinguished in another single molecule experiment. Take a protein that, after being heated to a given unfolding temperature, aggregates when normal conditions are restored. Heat this protein to this same temperature in a single molecule experiment. According to the thermodynamic hypothesis this isolated protein should refold to the native state while according to the kinetic hypothesis it will most probably not.

According to the VES KM, the drivers of protein conformational changes are quantum VES (see Sect. 5). This possibility has been experimentally validated in experiments in which irradiation of light with the amide I frequency (and only with this frequency) was shown to revert protein aggregates back into protein monomers [81, 82]. Other experiments of this kind, with aggregates of other proteins, will provide further support to the VES KM.

Summing up: it is hoped that this chapter will encourage other researchers to investigate protein folding from the point of view of the VES KM. The idea is that with present-day computers and force fields it is possible to solve the protein folding problem in vivo, which is the only one that is solvable, i.e., it is the only one for which there is a one to one correspondence between sequence and native state. Cells demonstrate it repeatedly and the VES KM is at least one example of how it can be done.

Acknowledgements L.C. received national funds from FCT - Foundation for Science and Technology, Portugal, through the project UID/Multi/04326/2013. The author also acknowledges the

Laboratory for Advanced Computing at University of Coimbra (http://www.lca.uc.pt) for providing HPC computing resources that have contributed to the research results reported within this paper.

References

1. Alexander, P.A., He, Y., Chen, Y., Orban, J., Bryan, P.N.: A minimal sequence code for switching protein structure and function. P. Natl. Acad. Sci. USA **106**, 21149–21154 (2009)
2. Allen, F., Almasi, G., Andreoni, W., Beece, D., Berne, B.J., Bright, A., Brunheroto, J., Cascaval, C., Castanos, J., Coteus, P., Crumley, P., Curioni, A., Denneau, M., Donath, W., Eleftheriou, M., Fitch, B., Fleischer, B., Georgiou, C.J., Germain, R., Giampapa, M., Gresh, D., Gupta, M., Haring, R., Ho, H., Hochschild, P., Hummel, S., Jonas, T., Lieber, D., Martyna, G., Maturu, K., Moreira, J., Newns, D., Newton, M., Philhower, R., Picunko, T., Pitera, J., Pitman, M., Rand, R., Royyuru, A., Salapura, V., Sanomiya, A., Shah, R., Sham, Y., Singh, S., Snir, M., Suits, F., Swetz, R., Swope, W.C., Vishnumurthy, N., Ward, T.J.C., Warren, H., Zhou, R.: Blue gene: a vision for protein science using a petaflop computer. IBM Syst. J. **40**, 310–327 (2001)
3. Anfinsen, C.B.: Principles that govern the folding of protein chains. Science **181**(4096), 223–230 (1973)
4. Anfinsen, C.B.: Commentary by C.B. Anfinsen, on "Studies on the structural basis of ribonuclease activity", by Anfinsen, C.B., Harrington, W.F., Hvidt, A., Linderstrom-Lang, K., Ottesen, M., SchellmanJ. Biochim. Biophys. Acta **17**, 141–142 (1955). Biochim. Biophys. Acta **1000**, 197–199 (1989)
5. Anfinsen, C.B., Harrington, W.F., Hvidt, A., Linderstrom-Lang, K., Ottesen, M., Schellman, J.: Studies on the structural basis of ribonuclease activity. Biochim. Biophys. Acta **17**, 141–142 (1955)
6. Aramini, J., Sharma, S., Huang, Y., Swapna, G., Ho, C., Shetty, K., Cunningham, K., Ma, L., Zhao, L., Owens, L., Jiang, M., Xiao, R., Liu, J., Baran, M., Acton, T., Rost, B., Montelione, G.: Solution NMR structure of the SOS response protein YnzC from Bacillus subtilis. Proteins **72**, 526–530 (2008)
7. Austin, R.H., Xie, A., Fu, D., Warren, W.W., Redlich, B., van der Meer, L.: Tilting after Dutch windmills: probably no long-lived Davydov solitons in proteins. J. Biol. Phys. **35**, 91–101 (2009)
8. Baker, D., Agard, D.A.: Kinetics versus thermodynamics in protein folding. Biochemistry **356**, 263–265 (1994)
9. Baker, D., Sohl, J.L., Agard, D.A.: A protein-folding reaction under kinetic control. Nature **356**, 263–265 (1992)
10. Ban, N., Nissen, P., Hansen, J., Moore, P.B., Steitz, T.A.: The complete atomic structure of the large ribosomal subunit at 2.4 A resolution. Science **289**, 905–920 (2000)
11. Banerji, A., Ghosh, I.: Revisiting the myths of protein interior: studying proteins with mass-fractal hydrophobicity-fractal and polarizability-fractal dimensions. PLoS ONE **4**, e7361 (2009)
12. Ben-Naim, A.: Levinthal's question revisited, and answered. J. Biomol. Struct. Dyn. **30**, 113–124 (2012)
13. Ben-Naim, A.: Myths and Verities in Protein Folding Theories, 1st edn. World Scientific, Singapore (2016)
14. Berman, H.M., Westbrook, J., Feng, Z., Gilliland, G., Bhat, T.N., Weissig, H., Shindyalov, I.N., Bourne, P.E.: The protein data bank. Nucleic Acids Res. **28**, 235–242 (2000)
15. Bolhuis, P.G., Chandler, D., Geissler, P.L.: Transition path sampling: throwing ropes over rough mountain passes, in the dark. Annu. Rev. Phys. Chem. **53**, 291–318 (2002)
16. Bowers, K.J., Chow, E., Xu, H., Dror, R.O., Eastwood, M.P., Gregersen, B.A., Klepeis, J.L., Kolossvary, I., Moraes, M.A., Sacerdoti, F.D., Salmon, J.K., Shan, Y., Shaw, D.E.: Scalable

algorithms for molecular dynamics simulations on commodity clusters. In: Proceedings of the ACM/IEE Conference on Supercomputing, SC'06, pp. 84:1–84:13. ACM, New York (2006)
17. Bowler, B.E.: Residual structure in unfolded proteins. Curr. Opin. Struc. Biol. **22**, 4–13 (2012)
18. Bradley, P., Misura, K.M.S., Baker, D.: Toward high-resolution de novo structure prediction for small proteins. Science **309**, 1868–1871 (2005)
19. Braselmann, E., Chaney, J.L., Clark, P.L.: Folding the proteome. Trends Biochem. Sci. **38**, 337–344 (2013)
20. Brockwell, D.J., Radford, S.E.: Intermediates: ubiquitous species on folding energy landscapes? Curr. Opin. Struc. Biol. **17**, 30–37 (2007)
21. Brooks, B.R., Brooks III, C.L., Mackerell Jr., A.D., Nilsson, L., Petrella, R.J., Roux, B., Won, Y., Archontis, G., Bartels, C., Boresch, S., Caflisch, A., Caves, L., Cui, Q., Dinner, A.R., Feig, M., Fischer, S., Gao, J., Hodoscek, M., Im, W., Kuczera, K., Lazaridis, T., Ma, J., Ovchinnikov, V., Paci, E., Pastor, R.W., Post, C.B., Pu, J.Z., Schaefer, M., Tidor, B., Venable, R.M., Woodcock, H.L., Wu, X., Yang, W., York, D.M., Karplus, M.: CHARMM: the biomolecular simulation program. J. Comput. Chem. **30**, 1545–1614 (2009)
22. Brown, M.C., Mutter, A.C., Koder, R.L., JiJia, R.D., Cooleya, J.W.: Observation of persistent a-helical content and discrete types of backbone disorder during a molten globule to ordered peptide transition via deep-UV resonance Raman spectroscopy. J. Raman Spectrosc. **44**, 957–962 (2013)
23. Bryngelson, J.D., Wolynes, P.G.: Spin glasses and the statistical mechanics of protein folding. P. Natl. Acad. Sci. USA **84**(21), 7524–7528 (1987)
24. Careri, G., Wyman, J.: Soliton-assisted unidirectional circulation in a biochemical cycle. P. Natl. Acad. Sci. USA **81**, 4386–4388 (1984)
25. Case, D.A., Cheatham, T.E.I., Darden, T., Gohlke, H., Luo, R., Merz, K.M.J., Onufriev, A., Simmerling, C., Wang, B., Woods, R.: The AMBER biomolecular simulation programs. J. Comput. Chem. **26**(16), 1668–1688 (2005)
26. Chatterjee, A., Kumar, A., Chugh, J., Srivastava, S., Bhavesh, N.S., Hosur, R.V.: NMR of unfolded proteins. J. Chem. Sci. **117**(1), 3–21 (2005)
27. Chaudhuri, T.K., Farr, G.W., Fenton, W.A., Rospert, S., Horwich, A.L.: GroEL/GroES-mediated folding of a protein too large to be encapsulated. Cell **107**, 235–246 (2001)
28. Cheng, X., Cui, G., Hornak, V., Simmerling, C.: Modified replica exchange simulation methods for local structure refinement. J. Phys. Chem. B **109**, 8220–8230 (2005)
29. Christen, M., Hünenberger, P.H., Bakowies, D., Baron, R., Bürgi, R., Geerke, D.P., Heinz, T.N., Kastenholz, M.A., Kräutler, V., Oostenbrink, C., Peter, C., Trzesniak, D., van Gunsteren, W.F.: The GROMOS software for biomolecular simulation: GROMOS05. J. Comput. Chem. **26**(16), 1719–1751 (2005)
30. Cruzeiro, L.: Influence of the nonlinearity and dipole strength on the amide I band of protein α-helices. J. Chem. Phys. **123**, 234909 (2005)
31. Cruzeiro, L.: Why are proteins with Glutamine- and Asparagine-rich regions associated with protein misfolding diseases? J. Phys-Condens. Mat. **17**, 7833–7844 (2005)
32. Cruzeiro, L.: Protein's multi-funnel energy landscape and misfolding diseases. J. Phys. Org. Chem. **21**, 549–554 (2008)
33. Cruzeiro, L.: The Davydov/Scott model for energy storage and transport in proteins. J. Biol. Phys. **35**, 43–55 (2009)
34. Cruzeiro, L.: Protein folding. In: Springborg, M. (ed.) Chemical Modelling, pp. 89–114. Royal Society of Chemistry, London (2010)
35. Cruzeiro, L.: A kinetic mechanism for in vivo protein folding. Bio-Algorithms Med-Syst. **10**(3), 117–127 (2014)
36. Cruzeiro, L.: The VES hypothesis and protein conformational changes. Z. Phys. Chem. **230**, 743–776 (2016)
37. Cruzeiro, L., Degrève, L.: What is the shape of the distribution of protein conformations at equilibrium? J. Biomol. Struct. Dyn. **33**(7), 1539–1546 (2015)
38. Cruzeiro, L., Degrève, L.: Exploring the Levinthal limit in protein folding. J. Biol. Phys. **43**(1), 15–30 (2016)

39. Cruzeiro, L., Lopes, P.A.: Are the native states of proteins kinetic traps? Mol. Phys. **107**(14), 1485–1493 (2009)
40. Cruzeiro-Hansson, L., Takeno, S.: Davydov model: the quantum, mixed quantum-classical, and full classical systems. Phys. Rev. E **56**, 894–906 (1997)
41. Davydov, A.S.: The theory of contraction of proteins under their excitation. J. Theor. Biol. **38**, 559–569 (1973)
42. Davydov, A.S.: Solitons in Molecular Systems, 2nd edn. Kluwer Academic publication, Dordrecht (1991)
43. Dellago, C., Bolhuis, P.G., Csajka, F.S., Chandler, D.: Transition path sampling and the calculation of rate constants. J. Chem. Phys. **108**, 1964–1977 (1998)
44. Dill, K.A.: Theory for the folding and stability of globular proteins. Biochemistry **24**, 1501–1509 (1985)
45. Dill, K.A., Chan, H.S.: From Levinthal to pathways to funnels. Nat. Struct. Biol. **4**, 10–19 (1997)
46. Dill, K.A., MacCallum, J.L.: The protein-folding problem, 50 years on. Science **338**, 1042–1046 (2012)
47. Dill, K.A., Bromberg, S., Yue, K., Fiebig, K.M., Yee, D.P., Thomas, P.D., Chan, H.S.: Principles of protein folding: a perspective from simple exact models. Protein Sci. **4**, 561–602 (1995)
48. Dill, K.A., Ozkan, S.B., Shell, M.S., Weikl, T.R.: The protein folding problem. Annu. Rev. Biophys. **37**, 289–316 (2008)
49. Dobson, C.M.: Protein-misfolding diseases: getting out of shape. Nature **418**, 729–730 (2002)
50. Dobson, C.M.: Protein folding and misfolding. Nature **426**, 884–890 (2003)
51. Echenique, P.: Introduction to protein folding for physicists. Contemp. Phys. **48**, 81–108 (2007)
52. Edler, J., Hamm, P.: Self-trapping of the amide I band in a peptide model crystal. J. Chem. Phys. **117**, 2415–2424 (2002)
53. Edwards, G., Logan, R., Copeland, M., Reinisch, L., Davidson, J., Johnson, B., Maciunas, R., Mendenhall, M., Ossoff, R., Tribble, J., Werkhaven, J., O'Day, D.: Tissue ablation by a free-electron laser tuned to the amide II band. Nature **371**, 416–419 (1994)
54. Ellis, J.P., Bakke, C.K., Kirchdoerfer, R.N., Jungbauer, L.M., Cavagnero, S.: Chain dynamics of nascent polypeptides emerging from the ribosome. ACS Chem. Biol. **3**, 555–566 (2008)
55. Englander, S.W.: Protein folding intermediates and pathways studied by hydrogen exchange. Annu. Rev. Bioph. Biom. **29**, 213–238 (2000)
56. Englander, S.W., Mayne, L., Kan, Z.Y., Hu, W.: Protein folding: how and why: by hydrogen exchange, fragment separation, and mass spectrometry. Annu. Rev. Biophys. **45**, 135–152 (2016)
57. Evans, M.S., Sander, I.M., Clark, P.L.: Cotranslational folding promotes beta-helix formation and avoids aggregation in vivo. J. Mol. Biol. **383**, 683–692 (2008)
58. Fändrich, M., Fletcher, M.A., Dobson, C.M.: Amyloid fibrils from muscle myoglobin. Nature **410**, 165–166 (2001)
59. Fang, C., Senes, A., Cristian, L., DeGrado, W.F., Hochstrasser, R.M.: Amide vibrations are delocalized across the hydrophobic interface of a transmembrane helix dimer. P. Natl. Acad. Sci. USA **103**, 16740–16745 (2006)
60. Fazi, B., Cope, M.J., Douangamath, A., Ferracuti, S., Schirwitz, K., Zucconi, A., Drubin, D.G., Wilmanns, M., Cesareni, G., Castagnoli, L.: Unusual binding properties of the $SH3$ domain of the yeast actinbinding protein Abp1: structural and functional analysis. J. Biol. Chem. **277**, 5290–5298 (2002)
61. Fersht, A.: Structure and Mechanism in Protein Science: A Guide to Enzyme Cataysis and Protein Folding, 2nd edn. W. H. Freeman and Company, New York (1999)
62. Fitzkee, N.C., Rose, G.D.: Reassessing random-coil statistics in unfolded proteins. P. Natl. Acad. Sci. USA **101**, 12497–12502 (2004)
63. Frauenfelder, H., Sligar, S.G., Wolynes, P.G.: The energy landscapes and motions of proteins. Science **254**, 1598–1603 (1991)

64. Freddolino, P.L., Harrison, C.B., Liu, Y., Schulten, K.: Challenges in protein-folding simulations. Nat. Phys. **6**, 751–758 (2010)
65. Gallagher, T., Alexander, P., Bryan, P., Gillilan, G.L.: Two crystal structures of the B1 immunoglobulinbinding domain of streptococcal protein G and comparison with NMR. Biochemistry **33**, 4721–4729 (1994)
66. Gettins, P.G.W.: Serpin structure, mechanism, and function. Chem. Rev. **102**, 4751–4803 (2002)
67. Givol, D., De Lorenzo, F., Goldberger, R.F., Anfinsen, C.B.: Dissulfide interchange and the three dimensional structure of proteins. Biochemistry **53**, 676–684 (1965)
68. Gouda, H., Torigoe, H., Saito, A., Sato, M., Arata, Y., Shimada, I.: Three-dimensional solution structure of the B domain of staphylococcal protein A: comparisons of the solution and crystal structures. Biochemistry **31**, 9665–9672 (1992)
69. Gruebele, M., Dave, K., Sukenik, S.: Globular protein folding in vitro and in vivo. Annu. Rev. Biophys. **45**, 233–251 (2016)
70. Gutte, B., Merrifield, R.B.: The synthesis of ribonuclease A. J. Biol. Chem. **246**, 1922–1940 (1971)
71. Hamelberg, D., Mongan, J., McCammon, J.A.: Accelerated molecular dynamics: a promising and efficient simulation method for biomolecules. J. Chem. Phys. **120**, 11919–11929 (2004)
72. Hamm, P.: Femtosecond IR pump-probe spectroscopy of nonlinear energy localization in protein models and model proteins. J. Biol. Phys. **35**, 17–30 (2009)
73. Hingorani, K.S., Gierasch, L.M.: Comparing protein folding in vitro and in vivo: foldability meets the fitness challenge. Curr. Opin. Struc. Biol. **24**, 81–90 (2014)
74. Hukushima, K., Nemoto, K.: Exchange Monte Carlo method and application to spin glass simulations. J. Phys. Soc. Jpn. **65**, 1604–1608 (1996)
75. Humphrey, W., Dalke, A., Schulten, K.: VMD: visual molecular dynamics. J. Mol. Graphics. **14**, 33–38 (1996)
76. Hynes, T.R., Randal, M., Kennedy, L.A., Eigenbrot, C., Kossiakoff, A.A.: X-ray crystal structure of the protease inhibitor domain of Alzheimer's amyloid betaprotein precursor. Biochemistry **29**, 10018–10022 (1990)
77. Ishikawa, H., Shimoda, M., Yonekura, A., Mishima, K., Matsumoto, K., Osajima, Y.: Irreversible unfolding of myoglobin in an aqueous solution by supercritical carbon dioxide. J. Agr. Food Chem. **48**, 4535–4539 (2000)
78. Jiang, F., Wu, Y.D.: Folding of fourteen small proteins with a residue-specific force field and replica-exchange molecular dynamics. J. Am. Chem. Soc. **136**, 9536–9539 (2014)
79. Kaiser, C.M., Goldman, D.H., Chodera, J.D., Tinoco Jr., I., Bustamante, C.: The ribosome modulates nascent protein folding. Science **334**, 1723–1727 (2011)
80. Karplus, M.: The Levinthal paradox: yesterday and today. Fold. Des. **2**, S69–S75 (1997)
81. Kawasaki, T., Fujioka, J., Imai, T., Tsukiyama, K.: Effect of midinfrared free-electron laser irradiation on refolding of amyloid-like fibrils of lysozyme into native form. Protein J. **31**, 710–716 (2012)
82. Kawasaki, T., Fujioka, J., Imai, T., Torigoe, K., Tsukiyama, K.: Mid-infrared free-electron laser tuned to the amide I band for converting insoluble amyloid-like protein fibrils into the soluble monomeric form. Laser Med. Sci. **29**, 1701–1707 (2014)
83. Kim, P.S., Baldwin, R.L.: Intermediates in the folding reactions of small proteins. Annu. Rev. Biochem. **59**, 631–660 (1990)
84. Kimchi-Sarfaty, C., Oh, J.M., Kim, I.W., Sauna, Z.E., Calcagno, A.M., Ambudkar, S.V., Gottesman, M.M.: A "silent" polymorphism in the MDR1 gene changes substrate specificity. Science **315**(5811), 525–528 (2007)
85. Klimov, D.K., Thirumalai, D.: Factors governing the foldability of proteins. Proteins: Struct. Funct. Genet. **26**, 26,411–26,441 (1996)
86. Kohn, J.E., Millett, I.S., Jacob, J., Zagrovic, B., Dillon, T.M., Cingel, N., Dothager, R.S., Seifert, S., Thiyagarajan, P., Sosnick, T.R., Hasan, M.Z., Pande, V.S., Ruczinski, I., Doniach, S., Plaxco, K.W.: Random-coil behavior and the dimensions of chemically unfolded proteins. P. Natl. Acad. Sci. USA **101**, 12491–12496 (2004)

87. Kuhlman, B., Baker, D.: Exploring folding free energy landscapes using computational protein design. Curr. Opin. Struc. Biol. **14**, 89–95 (2004)
88. Lau, K.F., Dill, K.A.: A lattice statistical mechanics model of the conformational and sequence spaces of proteins. Macromolecules **22**, 3986–3997 (1989)
89. Lazaridis, T., Karplus, M.: "New view" of protein folding reconciled with the old through multiple unfolding simulations. Science **278**, 1928–1931 (1997)
90. Lazaridis, T., Karplus, M.: Hidden complexity of free energy surfaces for peptide (protein) folding. P. Natl. Acad. Sci. USA **101**, 14766–14770 (2004)
91. Levinthal, C.: Are there pathways for protein folding? J. Chim. Phys. **65**, 44–45 (1968)
92. Levinthal, C.: How to fold graciously. In: DeBrunner, J.T.P., Munck, E. (eds.) Mossbauer Spectroscopy in Biological Systems: Proceedings of a meeting held at Allerton House, Monticello, Illinois, vol. 22, pp. 22–24. University of Illinois Press (1969)
93. Liang, J., Dill, K.A.: Are proteins well-packed? Biophys. J. **81**, 751–766 (2001)
94. Lindorff-Larsen, K., Piana, S., Dror, R.O., Shaw, D.E.: How fast-folding proteins fold. Science **334**, 517–520 (2011)
95. Lu, H., Isralewitz, B., Krammer, A., Vogel, V., Schulten, K.: Unfolding of titin immunoglobulin domains by steered molecular dynamics simulation. Biophys. J. **75**, 662–671 (1998)
96. Lumry, R., Eyring, H.: Conformation changes of proteins. J. Phys. Chem. **58**, 110–120 (1954)
97. Marino, J., von Heijne, G., Beckmann, R.: Small protein domains fold inside the ribosome exit tunnel. FEBS Lett. **590**, 655–660 (2016)
98. Maxwell, K.L., Wildes, D., Zarrine-Afsar, A., De Los Rios, M.A., Brown, A.G., Friel, C.T., Hedberg, L., Horng, J.C., Bona, D., Miller, E.J., Vallée-Bélisle, A., Main, E.R., Bemporad, F., Qiu, L., Teilum, K., Vu, N.D., Edwards, A.M., Ruczinski, I., Poulsen, F.M., Kragelund, B.B., Michnick, S.W., Chiti, F., Bai, Y., Hagen, S.J., Serrano, L., Oliveberg, M., Raleigh, D.P., Wittung-Stafshede, P., Radford, S.E., Jackson, S.E., Sosnick, T.R., Marqusee, S., Davidson, A.R., Plaxco, K.W.: Protein folding: defining a "standard" set of experimental conditions and a preliminary kinetic data set of two-state proteins. Protein Sci. **14**(3), 602–616 (2005)
99. McClare, C.W.F.: Resonance in bioenergetics. Ann. N.Y. Acad. Sci. **227**, 74–97 (1974)
100. Merrifield, R.B.: The synthesis of ribonuclease A. Protein Sci. **5**, 1947–1951 (1996)
101. Meyerguz, L., Kleinberg, J., Elber, R.: The network of sequence flow between protein structures. P. Natl. Acad. Sci. USA **104**, 11627–11632 (2007)
102. Mitra, R.K., Sinha, S.S., Pal, S.K.: Hydration in protein folding: thermal unfolding/refolding of human serum albumin. Langmuir **23**, 10224–10229 (2007)
103. Mukherjee, S., Sharma, S., Kumar, S., Guptasarma, P.: Slow irreversible unfolding of Pyrococcus furiosus triosephosphate isomerase: separation and quantitation of conformers through a novel electrophoretic approach. Anal. Biochem. **347**, 49–59 (2005)
104. O'Brien, E.P., Ciryam, P., Vendruscolo, M., Dobson, C.M.: Understanding the influence of codon translation rates on cotranslational protein folding. Acc. Chem. Res. **47**, 1536–1544 (2014)
105. Olshina, M.A., Baumann, H., Willison, K.R., Baum, J.: Plasmodium actin is incompletely folded by heterologous protein-folding machinery and likely requires the native Plasmodium chaperonin complex to enter a mature functional state. FASEB J. **30**(1), 405–416 (2016)
106. Onuchic, J.N., Luthey-Schulten, Z., Wolynes, P.G.: Theory of protein folding: the energy landscape perspective. Annu. Rev. Phys. Chem. **48**, 545–600 (1997)
107. Orengo, C.A., Michie, A.D., Jones, S., Jones, D.T., Swindells, M.B., Thornton, J.M.: CATH-a hierarchic classification of protein domain structures. Sructure **5**, 1093–1108 (1997)
108. Paola, L.D., Paci, P., Santoni, D., Ruvo, M.D., Giuliani, A.: Proteins as sponges: a statistical journey along protein structure organization principles. J. Chem. Inf. Model. **52**, 474–482 (2012)
109. Plaxco, K.W., Simons, K.T., Baker, D.: Contact order, transition state placement and the refolding rates of single domain proteins. J. Mol. Biol. **277**, 985–994 (1998)
110. Plaxco, K.W., Simons, K.T., Ruczinski, I., Baker, D.: Topology, stability, sequence, and length: defining the determinants of two-state protein folding kinetics. Biochemistry **39**, 11177–11183 (2000)

111. Prusiner, S.B.: Novel proteinaceous infectious particles cause scrapie. Science **216**, 136–144 (1982)
112. Prusiner, S.B., McCarty, M.: Discovering DNA encodes heredity and prions are infectious proteins. Annu. Rev. Genet. **40**, 25–45 (2006)
113. Ptitsyn, O.B.: How the molten globule became. Trends Biochem. Sci. **20**, 376–379 (1995)
114. Qian, B., Raman, S., Das, R., Bradley, P., McCoy, A.J., Read, R.J., Baker, D.: High-resolution structure prediction and the crystallographic phase problem. Nature **450**, 259–264 (2007)
115. Raval, A., Piana, S., Eastwood, M.P., Dror, R.O., Shaw, D.E.: Refinement of protein structure homology models via long, all-atom molecular dynamics simulations. Proteins: Struct. Funct. Bioinform. **80**, 2071–2079 (2012)
116. Religa, T.L., Markson, J.S., Mayor, U., Freund, S.M.V., Fersht, A.R.: Solution structure of a protein denatured state and folding intermediate. Nature **437**, 1053–1056 (2005)
117. Roder, H., Colón, W.: Kinetic role of early intermediates in protein folding. Curr. Opin. Struc. Biol. **7**, 15–28 (1997)
118. Rother, K., Preissner, R., Goede, A., Frömmel, C.: Inhomogeneous molecular density: reference packing densities and distribution of cavities within proteins. Bioinformatics **19**, 2112–2121 (2003)
119. Rothman, J.E., Schekman, R.: Molecular mechanism of protein folding in the cell. Cell **146**, 851–854 (2011)
120. Rumfeldt, J.A., Stathopulos, P.B., Chakrabarrty, A., Lepock, J.R., Meiering, E.M.: Mechanism and thermodynamics of guanidinium chloride-induced denaturation of ALS-associated mutant Cu,Zn superoxide dismutases. J. Mol. Biol. **355**, 106–123 (2006)
121. Sanchez-Ruiz, J.M.: Protein kinetic stability. Biophys. Chem. **148**, 1–15 (2010)
122. Savage, H.J., Elliot, C.J., Freeman, C.M., Finney, J.L.: Lost hydrogen-bonds and buried surface-area: rationalizing stability in globular-proteins. J. Chem. Soc., Faraday Trans. **89**, 2609–2617 (1993)
123. Schechter, A.N., Chen, R.F., Anfinsen, C.B.: Kinetics of folding of staphylococcal nuclease. Science **167**, 886–887 (1970)
124. Schlick, T., Collepardo-Guevara, R., Halvorsen, L.A., Jung, S., Xiao, X.: Biomolecular modeling and simulation: a field coming of age. Q. Rev. Biophys. **44**, 191–228 (2011)
125. Schlitter, J., Engels, M., Kruger, P.: Targeted molecular-dynamics - a new approach for searching pathways of conformational transitions. J. Mol. Graphics **12**, 84–89 (1994)
126. Schram, R.D., Schiessel, H.: Exact enumeration of Hamiltonian walks on the $4 \times 4 \times 4$ cube and applications to protein folding. J. Phys. A-Math. Theor. **46**, 485001 (2013)
127. Schram, R.D., Schiessel, H.: Corrigendium: Exact enumeration of Hamiltonian walks on the $4 \times 4 \times 4$ cube and applications to protein folding (J. Phys. A: Math. Theor. **46**, 485001, 2013). J. Phys. A-Math. Theor. **49**, 369501 (2016)
128. Scott, A.: The Davydov soliton revisited. Phys. Rep. **217**, 1–67 (1992)
129. Shaw, D.E., Dror, R.O., Salmon, J.K., Grossman, J.P., Mackenzie, K.M., Bank, J.A., Young, C., Deneroff, M.M., Batson, B., Bowers, K.J., Chow, E., Eastwood, M.P., Ierardi, D.J., Klepeis, J.L., Kuskin, J.S., Larson, R.H., Lindorff-Larsen, K., Maragakis, P., Moraes, M.A., Piana, S., Shan, Y., Towles, B.: Millisecond-scale molecular dynamics simulations on Anton. In: Proceedings of the Conference on High Performance Computing Networking, Storage and Analysis, SC'09, pp. 65:1–65:11. ACM, New York (2009)
130. Shaw, D.E., Maragakis, P., Lindorff-Larsen, K., Piana, S., Dror, R.O., Eastwood, M.P., Bank, J.A., Jumper, J.M., Salmon, J.K., Shan, Y., Wriggers, W.: Atomic-level characterization of the structural dynamics of proteins. Science **330**, 341–346 (2010)
131. Shi, Z., Chen, K., Liu, Z., Kallenbach, N.R.: Conformation of the backbone in unfolded proteins. Chem. Rev. **106**, 1877–1897 (2006)
132. Shortle, D., Ackerman, M.S.: Persistence of native-like topology in a denatured protein in 8 M urea. Science **293**, 487–489 (2001)
133. Sieler, G., Schweitzer-Stenner, R.: The amide I mode of peptides in aqueous solution involves vibrational coupling between the peptide group and water molecules of the hydration shell. J. Am. Chem. Soc. **119**, 1720–1726 (1997)

134. Silva, P.A.S., Cruzeiro-Hansson, L.: A reduced set of exact equations of motion for a non-number-conserving Hamiltonian. Phys. Lett. A **315**(6), 447–451 (2003)
135. Silva, P.A.S., Cruzeiro-Hansson, L.: Dynamics of a nonconserving Davydov monomer. Phys. Rev. E **74**, 021920 (2006)
136. Skolnick, J.: Putting the pathway back into protein folding. P. Natl. Acad. Sci. USA **102**(7), 2265–2266 (2005)
137. Sohl, J.L., Jaswal, S.S., Agard, D.A.: Unfolded conformations of α-lytic protease are more stable than its native state. Nature **395**, 817–819 (1998)
138. Spencer, P.S., Siller, E., Anderson, J.F., Barral, J.M.: Silent substitutions predictably alter translation elongation rates and protein folding efficiencies. J. Mol. Biol. **422**, 328–335 (2012)
139. Taverna, D.M., Goldstein, R.A.: Why are proteins marginally stable? Proteins: Struct. Funct. Genet. **46**, 105–109 (2002)
140. Tuinstra, R.L., Peterson, F.C., Kutlesa, S., Elgin, E.S., Kron, M.A., Volkman, B.F.: Interconversion between two unrelated protein folds in the lymphotactin native state. P. Natl. Acad. Sci. U.S.A. **105**, 5057–5062 (2008)
141. Ugrinov, K.G., Clark, P.L.: Cotranslational folding increases GFP folding yield. Biophys J. **98**, 1312–1320 (2010)
142. Vogel, A., Venugopalan, V.: Mechanisms of pulsed laser ablation of biological tissues. Chem. Rev. **103**, 577–644 (2003)
143. Voss, N.R., Gerstein, M., Steitz, T.A., Moore, P.B.: The geometry of the ribosomal polypeptide exit tunnel. J. Mol. Biol. **360**, 893–906 (2006)
144. Wales, D.J.: Energy landscapes: some new horizons. Curr. Opin. Struc. Biol. **20**, 3–10 (2010)
145. Wilson, D.N., Beckmann, R.: The ribosomal tunnel as a functional environment for nascent polypeptide folding and translational stalling. Curr. Opin. Struc. Biol. **21**, 274–282 (2011)
146. Wolynes, P.G.: Folding funnels and energy landscapes of larger proteins within the capillarity approximation. P. Natl. Acad. Sci. USA **94**, 6170–6175 (1997)
147. Wolynes, P.G.: Evolution, energy landscapes and the paradoxes of protein folding. Biochimie **119**, 218–230 (2015)
148. Zhang, G., Ignatova, Z.: Folding at the birth of the nascent chain: coordinating translation with co-translational folding. Curr. Opin. Struc. Biol. **21**, 25–31 (2011)

Patterning, Dynamics and Evolution in the Ocellar Complex of the Fruit Fly

Daniel Aguilar-Hidalgo, Fernando Casares and M. Carmen Lemos

Abstract One of the most intriguing aspects in developing tissues is the emergence of chemical patterns with the capability to drive cellular differentiation, provide positional information and stimuli or inhibit growth. Among these features, the study of cell specificity driven by chemical patterns requires the coupling of positional information mechanisms with the dynamics of complex genetic networks. In this work, we follow such approach to study the formation of the ocellar complex in the fruit fly *Drosophila melanogaster*. We present a theoretical model that fits experimental observations in both patterning and molecular regulation, and derive a simplified model, which not only recapitulates patterning features but also predicts that differences in the size of the ocellar complex among fly species might depend on differential biochemical regulation of an evolutionarily fixed regulatory network. Moreover, we discuss how this regulatory network can generate sustained spatiotemporal oscillations of some of the network's components. We also find that these oscillations can become highly complex in the presence of another oscillator, with parameter-dependent regions of multi-periodic and quasiperiodic regimes.

Keywords Pattern formation · Morphogen · Ocellar development · Mathematical model · Reaction-diffusion system · Gene regulatory network · Oscillatory behavior

D. Aguilar-Hidalgo (✉)
Max Plank Institute for the Physics of Complex Systems, Nöthnitzer Straße 38,
01187 Dresden, Germany
e-mail: daguilar@pks.mpg.de

F. Casares
CABD (Andalusian Centre for Development Biology), CSIC -UPO -JA,
Campus Universidad Pablo de Olavide, 41013 Sevilla, Spain
e-mail: fcasfer@upo.es

M.C. Lemos
Department of Condensed Matter Physics, Universidad de Sevilla,
Avda Reina Mercedes s/n, 41012 Sevilla, Spain
e-mail: lemos@us.es

J. F. R. Archilla et al. (eds.), *Nonlinear Systems, Vol. 2*, Understanding Complex Systems, https://doi.org/10.1007/978-3-319-72218-4_2

1 Introduction

During animal development, a fertilized egg contains an increasing number of identical pluripotent cells. This early stage, in which the embryo grows by increasing the number of pluripotent cells, is followed by a period in which pluripotent cells start a process of cellular differentiation, to build orientational body-axes, and generate different types of tissues that will lately define organs of specific size and shape. Organogenesis, (that combines cell differentiation, tissue patterning and morphogenesis) has fascinated scientists from Aristotle to our days. Indeed, how a developing organ grows to attain a specific size and shape is one of the most intriguing questions in the field of Developmental Biology as well as in the emerging fields of Biological Physics and Mathematical and Theoretical Biology.

In order to start looking at morphogenesis from a theoretical perspective, we have to go back exactly 100 years to 1917, when D'Arcy Thomsom rationalized this concept in his master piece *On growth and Form* [37]. However, we do not find a first formalism for a mechanism able to explain morphogenesis based on physico-chemical grounds until 1952 in Turing's seminal paper *The Chemical Basis of Morphogenesis* [40]. In this paper, Turing introduces the idea that two coupled biochemical species with diffusible properties, termed morphogens, can produce spatial concentration patterns.

The theoretical implications of morphogens on tissue patterning have been debated since Lewis Wolpert introduced the idea of positional information provided by a concentration gradient of a chemical (the "morphogen") that is generated by the production and diffusion of that chemical across a developing field of cells [43]. This idea poses that cell would use the chemical concentration of the diffusible chemical to take decisions on, for example, different fates at distinct concentration thresholds (*french flag model* [43]).

Lately, and clearly inspired by the ideas of Turing and Wolpert, many others, starting with Meinhardt and Koch [25], have revealed the increasing variety of morphological features that may potentially arise as an effect of morphogen dynamics in tissues, e.g. patterning, cellular differentiation and tissue specificity, genetic regulation, tissue growth and growth control [9, 16, 18, 21, 23, 28, 33, 41, 42].

Coming back to Wolpert's positional information idea, we understand that a specific morphogen concentration can lead to a specific cellular fate, this is, a cell will chose among a number of choices a particular differentiation pathway and thus a function. But, how is this specification process performed? The idea that comes out from the *french flag model* is that different morphogen concentrations trigger different genetic programs in a cascade of switching on and off specific genes, through intracellular biochemical (signaling) cascades, that will lately end in cellular differentiation in a spatially patterned tissue. The network representation of biochemical activities (including signaling cascades and gene regulatory events) involved in generating patterned cell differentiation during development is commonly termed as Gene Regulatory Network (GRN) [8]. GRNs can be formed by several interconnected genes, where the nodes represent the genes and their links their genetic or biochemical coupling. GRNs are dynamical networks that change the

number and activity (whether they are switched on or off) of both nodes and links with developmental time. This makes their analysis from both experimental and theoretical perspectives cumbersome. Despite the high complexity of these networks, many authors study the dynamics of GRNs by means of simplified systems and/or the use of evolutionary and inference algorithms [2, 5, 14, 23, 27, 36].

In this work, we report recent advances on our understanding of the development of the ocellar complex of Drosophila, through the modeling and analysis of its GRN, as an entry point into the development of more complex visual structures. To do this, we will analyze, in an experimentally supported manner, the formation of the ocellar complex as a morphogen-patterned tissue, and how an intricate GRN leads to a compartmentalized tissue with distinct cellular fates. Later on, we will theoretically minimize the patterning model to a simpler network motif that is a recurrent regulatory subnetwork [7], typically formed by a small number of nodes. This simplification confirms that the ocellar region is specified as a *french flag model*, and clarifies that this pattern is driven by a negative regulatory feedback, which may lead to parameter dependent regions of stationary dynamics as well as self-sustained oscillatory domains. Finally we will study these oscillations as an autonomous system, and analyze the complex dynamics that arise when we couple this dynamical system to another potential oscillatory network.

2 The Ocellar Complex: The Biology

The ocelli, or more precisely the ocellar complex, is a light-detecting organ widely present in insects. It comprises three small eyelets, or ocelli, located at the vertices of a triangular patch of cuticle on the insect's forehead Fig. 1a, b. Ocelli and the more conspicuous (and better studied) compound eyes were present in arthropods since, at least, the middle Cambrian, about 500 Myrs [31]. Therefore, the ocellar complex is an ancient component of the light-detecting system in this animal group. Each ocellus is formed by a retina capped with a large lens. The proximity of the lens to the retinal cells, the photoreceptors, is such that the focus of the image lies well behind the retina. Therefore, the image at the retina is blurred: the ocelli do not form good images, but instead are very sensitive to light. The retinal photoreceptors are enwrapped in a pigment layer, that shields them optically except from the light entering through the lens, so that direction of light can be perceived. The photoreceptors connect with a small number of large second order neurons, which then transmit the information from the ocelli to other brain nuclei. These neurons have axons of large diameter and thereby this transmission is very fast. The high sensitivity and fast transmission of ocelli allow the insect to respond to sudden changes in light intensity, and is used to ensure maneuverability and stability during flight and in triggering an escape reflex in response to looming objects [26, 30].

The development of the ocellar complex is best understood in the higher dipteran *Drosophila melanogaster*, the vinegar fly. The head of the adult fly derives from two symmetrical (left and right) epithelial discs. During metamorphosis (the transition

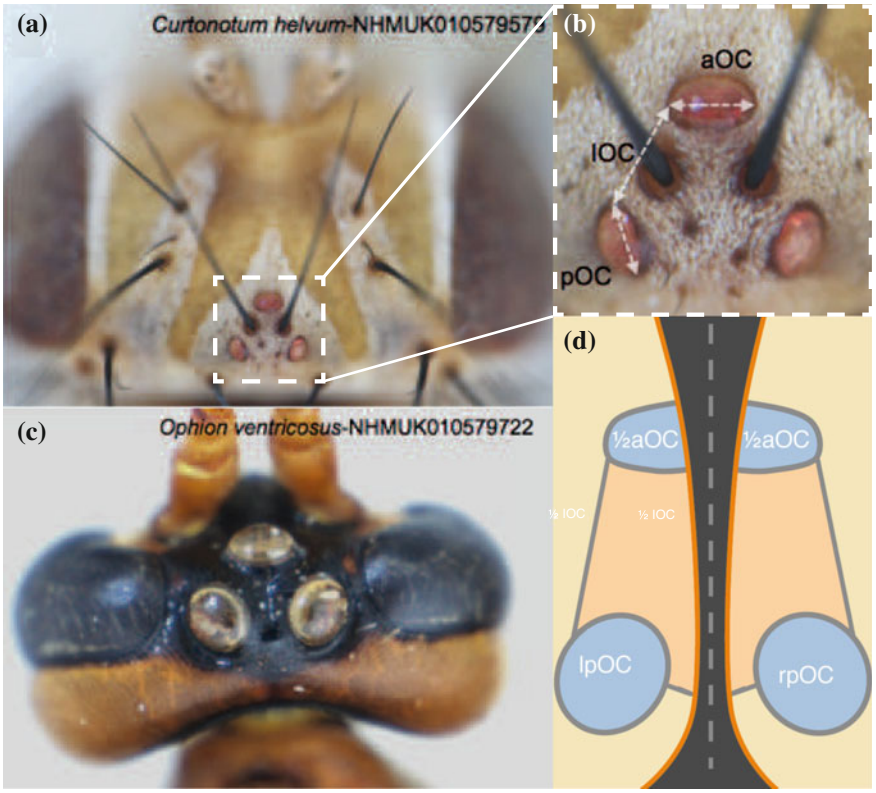

Fig. 1 Morphology of the ocellar complex. Dorsal views of the heads of a fly (**a**: Curtonotum helvum) and a wasp (**c**: Ophion ventricosus), showing the triangular arrangement of ocellar lenses. The close-up in **b** shows a detail of the ocellar complex and the linear dimension used to define the ocellar complex morphology. "aOC": anterior ocellus; "pOC": posterior ocellus; "IOC": interocellar distance. Codes ("NHMUK") are specimen codes of the Natural History Museum, London, UK. **d** Schematic representation of the fusion of the two eye imaginal discs, thus promoting the formation of two posterior ocelli, left-lpOC ad right-rpOC, and one anterior ocellus, aOC. Panel taken from [1]. Licensed under CC BY 4.0

from the larva into a flying, sexually mature adult) the two halves fuse to give rise to the eyes, antennae, maxillary sense organs, the head capsule and, on the anterior dorsal head capsule, the ocellar complex [24]. In each disc, the prospective ocellar complex is genetically specified by a series of transcription factors [10–12, 17, 34]. Once specified, this territory is further subdivided into three subdomains. The central subdomain produces the signaling molecule *hedgehog* (Hh), the founding member of the Hh family of morphogens [22]. The term "morphogen", as used by Wolpert (see above), denotes a molecule (in this case Hh), produced locally at a source and dispersing from it, that triggers different responses in receiving cells depending on its concentration. This translates into cells located at different distances

relative to the morphogen's source (and thereby receiving different concentrations) activating different target genes [43]. During the development of the ocellar complex, from the central Hh-producing domain, Hh disperses. Upon binding to its membrane receptor *patched* (*ptc*), the Hh cascade is activated, resulting in the stabilization and activation of the Gli-type transcription factor *cubitus interruptus* (*ci*), thus increasing the concentration of CiA, the transcriptional activator form of Ci. Otherwise, Ci is cleaved into the transcriptional repressor form, CiR [6]. Hh signaling then activates two major target genes. The repressor transcription factor *engrailed* (*en*) is a low sensitivity target and therefore is only activated by maximal Hh signaling levels. This results in En being expressed almost coincidentally with the Hh-producing cells [3, 35]. The retinal determination gene *eyes absent* is a higher sensitivity target, i.e. Hh triggers its expression also at lower concentrations, so that *eya* expression is activated in cells farther away from the Hh-producing domain [3, 11]. The fact that En represses the expression of *ci* causes the loss of Eya in the Hh-producing cells, as this cells can no longer transduce Hh signal. The resulting gene expression pattern is a central domain of Hh-producing, En-expressing cells and two adjacent domains expressing Eya. This basic pattern prefigures the adult ocellar complex pattern (see below). Although biologically this gene expression pattern is stable, the fact that En is activated by and represses the Hh signaling pathway simultaneously would turn the system unstable. Genetic experiments show that this potentially instability is eliminated by En expression becoming fixed, once initiated, through the action of the *Delta*(*Dl*)/*Notch* signaling pathway [3]. Another important issue is that of the size of the Eya domains. These domains specify the cells that will be developing the ocelli. The regulation of the final size of the Eya domains depend positively on Hh signaling, but is negatively modulated by the Wnt signaling (*wingless*, *wg*) and the transcription factor *homothorax* (*hth*): Both in *wg* and *hth* mutants, the size of the ocelli increases [12, 29, 39]. Therefore, ocellar size depends on the balance between Hh and Wnt/hth signaling. Genetic studies have proposed that these two domains (the Eya/So and Hh domains, (So, *sine oculis*; a Six2-type transcription factor)), once established, become fixed through positive feedback loops [3, 10, 12, 17].

By the end of larval development, each (left and right) head epithelial discs show a central Hh domain flanked by two adjacent Eya/So domains. During metamorphosis, the fusion of these two contralateral discs will lead to the fusion of the two anterior Eya patches, giving rise to the anterior ocellus (aOC). The two posterior Eya patches will remain separate and will become the (left and right) posterior ocelli. The intervening Hh-domain will for the triangular interocellar cuticle, see Fig. 1. The simplicity of the ocellar complex pattern (one Hh-producing domain flanked by two Eya-expressing regions) and its genetic accessibility makes it an excellent model to study how gene regulatory networks controlled by a morphogen (Hh) regulate morphological patterns in animals. Recently, our groups, taking advantage of the wealth of biological knowledge accumulated during the past years, have generated and analyzed a complex gene regulatory model including all known interactions, see [3] and Fig. 2. To deepen the analysis of this system, we then further simplified the gene network model to one that still is able to recapitulate the pattern (the "3-node" network; see [4] and Fig. 5).

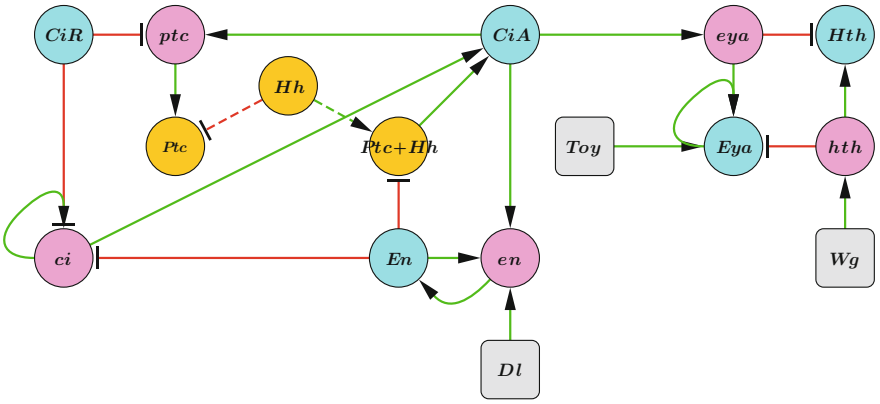

Fig. 2 Network diagram of a GRN for the formation of the ocellar complex in the fruit fly. Round nodes represent variables of the system. Light blue nodes show transcription factors that regulate gene (pink nodes) expression. Rounded square nodes represent functional behaviors such as conditions or constant inputs. Green and red links indicate positive and negative coupling, respectively. Dashed lines between Hh node and both Ptc and Ptc+Hh nodes represent the binding process between Hh and Ptc

3 GRN Models for the Formation of the Ocellar Complex

The study of morphogenetic processes requires extensive experimental research to find the molecular components and their genetic interactions controlling morphogenesis. In general, the integration of these components and their interactions as a GRN allows a global view of the process and its analysis as a whole. In many cases, GRNs show a high complexity revealing the holistic view of the process they define.The further theoretical analysis of these complex networks helps to understand the process itself, by identifying key components during the process and/or revealing missing and unnecessary components and interactions [2, 5, 14, 23, 27, 36].

3.1 Analysis of a Complex GRN for the Formation of the Ocellar Complex

During morphogenesis of the ocellar complex, as commented above, many molecular components have been identified as well as some of their relations. We can represent such components and relations in a networked manner, see Fig. 2. This network can be then modelled using a variety of techniques to analyse its dynamics and stability. Here, we decided to model the system as a set of kinetic equations. To do this, we make the following considerations. First, we model the ocellar complex in a developmental time previous to the fusion of the two eye imaginal discs, see

above. This allows a one-dimensional representation of the ocellar complex where the interocellar region (IOC; the domain of Hh production is flanked by two ocellar domains (OC) and these are surrounded by the periocellar domain (POC) -this latter the most "external" region of the ocellar complex, which would give rise to the head cuticle surrounding the ocellar complex in the adult animal, see Fig. 1. We further consider that the ocellar complex is symmetrical with respect to the center of the IOC, though recent research determined that anterior and posterior ocelli are both morphological and molecularly distinct [17]. We also consider that the source for Hh is constant, and that tissue growth is negligible during the time of observation, so that we can neglect convection and advection in the system. With this, we can model the network in Fig. 2 as a system of reaction equations coupled to the spatial dynamics of a reaction-diffusion equation in Hh, see Eqs. 1–14, with small concentration as initial condition for all variables of the system and reflecting boundary conditions [3].

$$\partial_t\, Hh = D\frac{\partial^2 Hh}{\partial x^2} + \delta(x)\alpha_{hh} - \gamma_{Ptc-Hh}\, Ptc \cdot Hh - \beta_{Hh} Hh \tag{1}$$

$$\partial_t\, ptc = \kappa_0\, \beta_{ptc}\Big(\big(\alpha_{ptc} + \kappa_{Ciptc}\, \phi(CiA\, \psi(CiR, k_{CiR}, n_{CiR}), k_{CiA}, n_{CiA})\big) \cdot \psi(En, k_{En-ptc}, n_{En-ptc}) - ptc\Big) \tag{2}$$

$$\partial_t\, Ptc = \theta_{ptc}\, ptc - \gamma_{Ptc-Hh}\, Ptc \cdot Hh - \beta_{Ptc} Ptc \tag{3}$$

$$\partial_t\, PtcHh = \gamma_{Ptc-Hh}\, Ptc \cdot Hh - \beta_{PtcHh}\, PtcHh \tag{4}$$

$$\partial_t\, ci = \kappa_0\, \beta_{ci}\, \big(\alpha_{ci}\, \phi(\psi(En, k_{En-ci}, n_{En-ci}), k_{ci}, n_{ci}) - ci\big) \tag{5}$$

$$\partial_t\, CiA = \kappa_0\, \beta_{CiA}\, (\theta_{ci}\, ci - CiA) - \kappa_{Ci}\, \phi(CiA\, \psi(\frac{PtcHh}{Ptc}, k_{PH}, n_{PH}), k_{CiA}, n_{CiA}) \tag{6}$$

$$\partial_t\, CiR = \kappa_{Ci}\, \phi(CiA\, \psi(\frac{PtcHh}{Ptc}, k_{PH}, n_{PH}), k_{CiA}, n_{CiA}) - \kappa_0\, \beta_{CiR}\, CiR \tag{7}$$

$$\partial_t\, en = \kappa_0\, \beta_{en}\Big(\alpha_{en} + \phi(CiA\psi(CiR, k_{CiR}, n_{CiR}), k_{CiA}, n_{CiA}) + \kappa_{En}\, \phi(En, k_{DlEn}, n_{En}) - en\Big) \tag{8}$$

$$\partial_t\, En = \theta_{en}\, en - \beta_{En} En \tag{9}$$

$$\partial_t\, eya = \kappa_0\, \beta_{eya}\Big(\alpha_{eya} + \alpha_{Toy}\, \phi(CiA\psi(Hth, k_{Hth-eya}, n_{Hth}), k_{CiA-eya}, n_{CiA}) + \phi(Eya, k_{Eya}, n_{Eya}) - eya\Big) \tag{10}$$

$$\partial_t\, Eya = \theta_{eya}\, eya - \beta_{Eya} Eya \tag{11}$$

$$\partial_t\, hth = \kappa_0\, \beta_{hth}\, \big(\alpha_{hth} + \alpha_{Wg}\, \phi(\psi(Eya, k_{Eya-hth}, n_{Eya}), k_{Wg}, n_{Wg}) - hth\big) \tag{12}$$

$$\partial_t\, Hth = \theta_{hth}\, hth - \beta_{Hth} Hth \tag{13}$$

$$\delta(x) = \begin{cases} 1 \text{ if } x \in hh - \text{expressing cells} \\ 0 \text{ if } x \notin hh - \text{expressing cells} \end{cases} \tag{14}$$

where $\phi(X,k,n) = \frac{X^n}{k^n+X^n}$ and $\psi(X,k,n) = 1-\phi(X,k,n)$, with X any system variable. The model contains different parameter types: α_X for the basal transcription rates, β_X for the degradation rates, k_X for the Hill equation transcriptional regulators, n_X for the Hill coefficients, θ_X for the translation rates; γ_X for protein complex formation. The non-dimensional parameters κ_0, κ_{Ci}, κ_{En} and α_{ci} are used for changing the scale of different terms and D is the diffusion coefficient. Subscript X-Y, with X and Y system variables, indicates a regulation from X to Y. Among the equations describing the system, we can observe high non-linear coupling, which describes the complexity in the transcriptional regulation. As an example, the formation of the PtcHh complex, Eq. 4, requires the coupling between Hh, Eq. 1, and Ptc, Eq. 3, which influences back Hh. Ptc is promoted by Eq. 2, ptc, which is positively regulated by CiA, Eq. 6 and negatively by CiR, Eq. 7. Additionally, equation for CiA and CiR are negatively and positively regulated, respectively, by the ratio of bound and unbound Ptc, PtcHh/Ptc.

For parameter choice in [3], we numerically find dynamical solutions for all the variables of the system that qualitatively match with experimental observations, see Fig. 3 and [3] for details. These results show the gradient formation in Hh, which drives the shape of the rest of the variables in the system. We observe that the negative repression of En blocks the activation of CiA and, consequently, of Eya, forming the IOC in the region of maximum Hh concentration. Furthermore, the mutual repression between Eya and Hth operates as a activation-repression switch, where low concentrations of one of the two species promotes the activation of the other.

Interestingly, this set of equations provided testable predictions for different experiments related to the patterning effect under certain mutant conditions [3]. Among these, we observed that the IOC is lost if En concentration is reduced, for instance, by blocking the action of *Dl* on *en* self-regulation, see [3] and Fig. 4a; and OC is lost if *Dl* action is increased, see Fig. 4b. We also observed that the size of the ocelli could be parametrically modified. One simple case is the variation of Hth activity, see Fig. 4c, d.

This observation of parameter-dependent size prompted an interesting idea. As commented above, the ocellar complex is present in many different species of insects, including different species of flies. Could it be possible the differences in size of OC and IOC observed in different fly species are explained by the same GRN? And, if so, which constraints on the potential morphological evolution of the ocellar complex may be imposed by the structure of the GRN? We will discuss these question further in Sect. 4.

By analysing the network structure of the GRN (see Fig. 2 and the resulting pattern, see Fig. 3), we observe that the profile of Eya expression follows that of CiA. We will describe next how the OC/IOC pattern can also be generated by a resulting pattern in CiA. We will describe that correct OC and IOC pattern distribution can be achieved by a simplified GRN (3-node GRN) driven by a concentration graded Hh input.

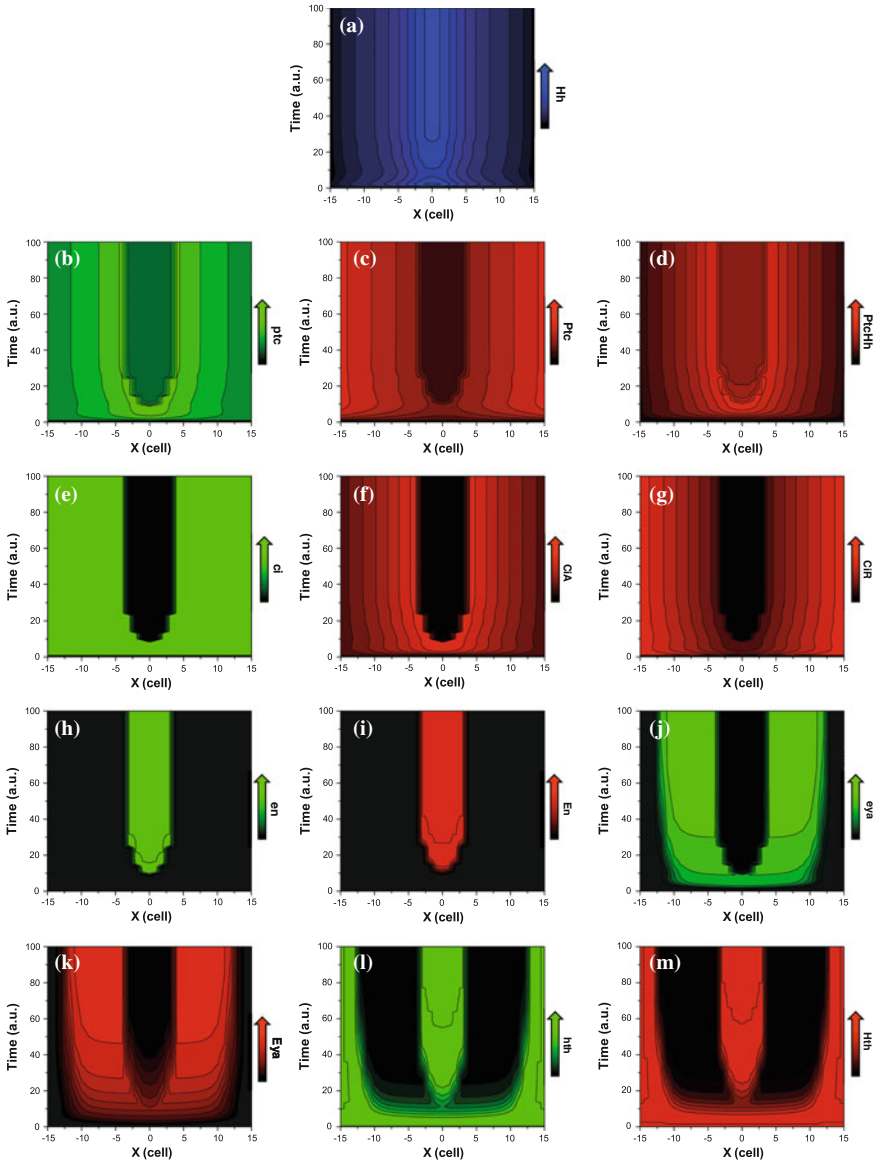

Fig. 3 Spatiotemporal dynamic of every variable in the system, the brighter the color the higher the concentration. Panel letter corresponds to equation number in main text

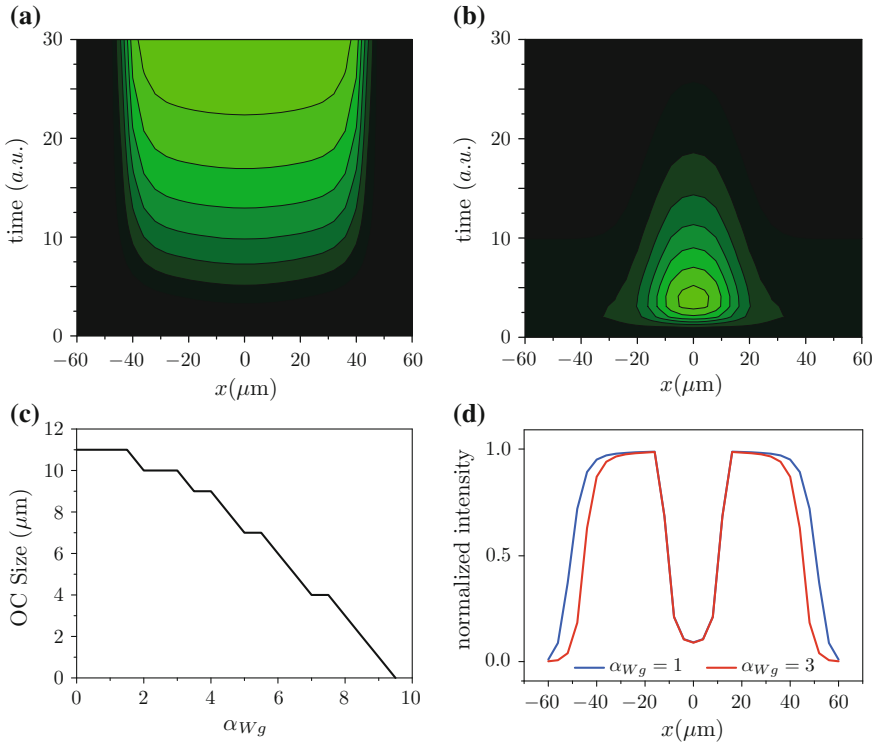

Fig. 4 Numerical results under mutant conditions. **a** Spatio-temporal profile of Eya with loss of IOC when self-activation of En is not produced, $k_{DlEn} = 2$. **b** Spatio-temporal profile of Eya with loss of OC when self-activation of En is more easily satisfied, $k_{DlEn} = 0.1$. **c** Dependence of OC size with regulation of transcription of hth, parameter α_{Wg}. **d** Instances of Eya for values of $\alpha_{Wg} = 1$ (larger OC) and $\alpha_{Wg} = 3$ (smaller OC)

3.2 The Ocellar Pattern in a Simplified 3-Node Network

The study of the GRN for the formation of the ocellar complex, Fig. 2, reveals a subnetwork as responsible for the initial patterning of the ocellar complex that starts from the extracellular Hh gradient and ends in the pattern of CiA. From this pattern, the mutual coupling between Eya and Hth leads to the addition of the POC to the final ocellar complex pattern. As commented above, the negative repression performed by En is responsible for the IOC-OC distinction. Thus, we wonder whether a simplified model, containing just the basic information of the spatial graded profile of Hh and the negative repression from En could yield a correct CiA pattern.

We introduce a simplified 3-node GRN, see Fig. 5, that we can model as a set of three ordinary differential equations of the reaction type with a constant in time input of a $Hh(x)$ spatial-dependent graded concentration profile, see Eqs. 15–17 and [4] for details and parameters choice.

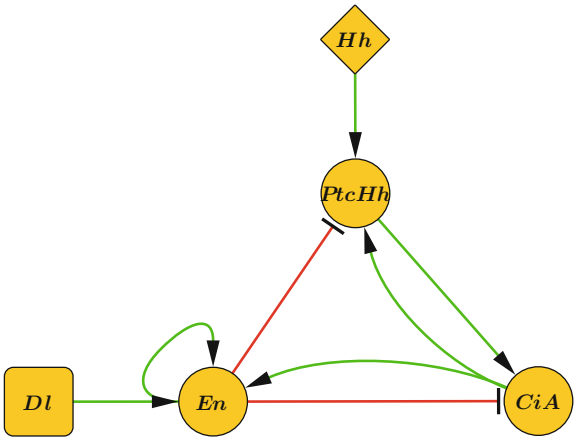

Fig. 5 Network diagram of a simplified GRN for the patterning of the ocellar complex. Round nodes represent variables of the system. Rounded square node *Dl* represent conditional self-activation for En. Square node Hh represent a constant in time input of a spatial graded concentration profile. Green and red links indicate positive and negative coupling, respectively

$$\partial_t\, PtcHh = (\alpha_{Hh-PtcHh}\, Hh(x) + \alpha_{CiA-PtcHh}\, CiA - \alpha_{En-PtcHh}\, En) \cdot \Theta\left(En^{crit} - En\right) - \beta_{PtcHh}\, PtcHh \tag{15}$$

$$\partial_t\, CiA = \frac{\frac{\gamma_{PtcHh-CiA}}{1+\phi_{En-CiA}\, En}\, (\phi_{PtcHh-CiA}\, PtcHh)^{n_C}}{k_{m_C}^{n_C} + (\phi_{PtcHh-CiA}\, PtcHh)^{n_C}} - \beta_{CiA}\, CiA \tag{16}$$

$$\partial_t\, En = \frac{\gamma_{CiA-En}\, (\phi_{CiA-En}\, CiA)^{n_E}}{k_{m_E}^{n_E} + (\phi_{CiA-En}\, CiA)^{n_E}} + \alpha_{En-En}\, En\, Dl(\zeta_{En}, \zeta_t, t_{\zeta_{En}}) - \beta_{En}\, En \tag{17}$$

$$Dl(\zeta_{En}, \zeta_t, t_{\zeta_{En}}) = \begin{cases} Dl \text{ if } En \geq \zeta_{En},\ \forall t \in \left[t_{\zeta_{En}},\ t_{\zeta_{En}} + \zeta_t\right] \\ 0 \quad \text{otherwise} \end{cases} \tag{18}$$

with $En^{crit} = (\alpha_{Hh-PtcHh}\, Hh(x) + \alpha_{CiA-PtcHh}\, CiA)/\alpha_{En-PtcHh}$ a spatial dependent critical value for En concentration at which En switches off PtcHh effective production, and Θ the Heaviside step function. En is self-maintained if its concentration exceeds a certain threshold, ζ_{En}, for a time interval, ζ_t, starting from the time point when En reaches the concentration threshold, $t_{\zeta_{En}}$, (Eqs. 17 and 18). This requirement refers to the need of integrating a protein quantity over time to trigger some targets [15].

We find qualitative agreement with experimental profiles of Eya in numerically simulated profiles for both large and 3-node GRN, see Fig. 6. Note that comparison with experiments in model for the 3-node GRN is done with CiA, thus only OC and IOC should be considered.

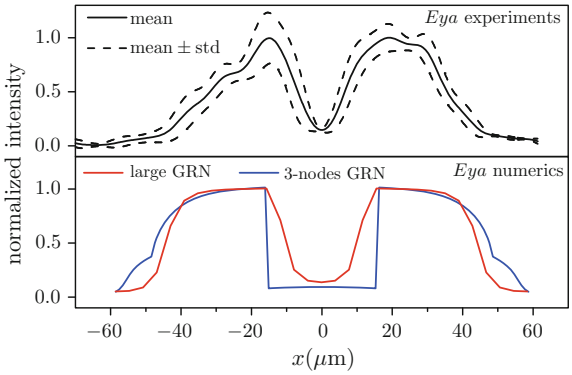

Fig. 6 Comparison of experimental profiles of Eya with numerical results for Eya profile in the model for the large GRN, and for CiA profile in the model for the 3-node GRN. Upper panel: Experimental mean profile (N = 8, solid line) with standard deviation (dashed lines). Bottom panel: Simulation of Eya and CiA concentration profiles corresponding to the numerical solution of the steady-state of Eqs. 11 and 16, respectively

4 GRN Constraints to Morphological Evolution

As we have mentioned during this chapter, the specification of cell types in space, and the determination of the size of the resulting tissues and organs during development, requires the organization and coupling of multiple molecular species both outside and inside cells. This complex process leads to the formation of organs of specific size and shape. Indeed, for a given organ and species, size and shape must be robustly resolved. This rises the following question: What makes organs of different size an shape among species? In principle, different genetic wiring could be responsible for such changes, however, from an evolutionary perspective, it would be more productive to fix genetic interactions and just tune values of biochemical interaction rates.

In previous sections, we already discussed that modification of some parameter values that imply changes in interaction rates were responsible for changes in OC and IOC size in our mathematical model. These results suggest that there might be a biochemical regulation of organ size in the ocellar complex for a fixed regulatory network.

The large network model presented in Sect. 3.1 contains far too many parameters to perform a fine-tuned analysis on every parameter. However, in a previous work [3], we performed a parameter sensitivity analysis from which we obtained two important results. The first one is the identification of a subset of parameters, which notably influence size of both OC and IOC. The second one is the finding that randomly chosen parameters provide non-random but patterned size distributions [3]. Parameters were chosen among specific ranges resolved in the sensitivity analysis. Interestingly, we find the same size distributions in the 3-node network model, thus implying that the parameters responsible for such distributions are contained within the set of parameters of this simplified model, see Fig. 7a and [1].

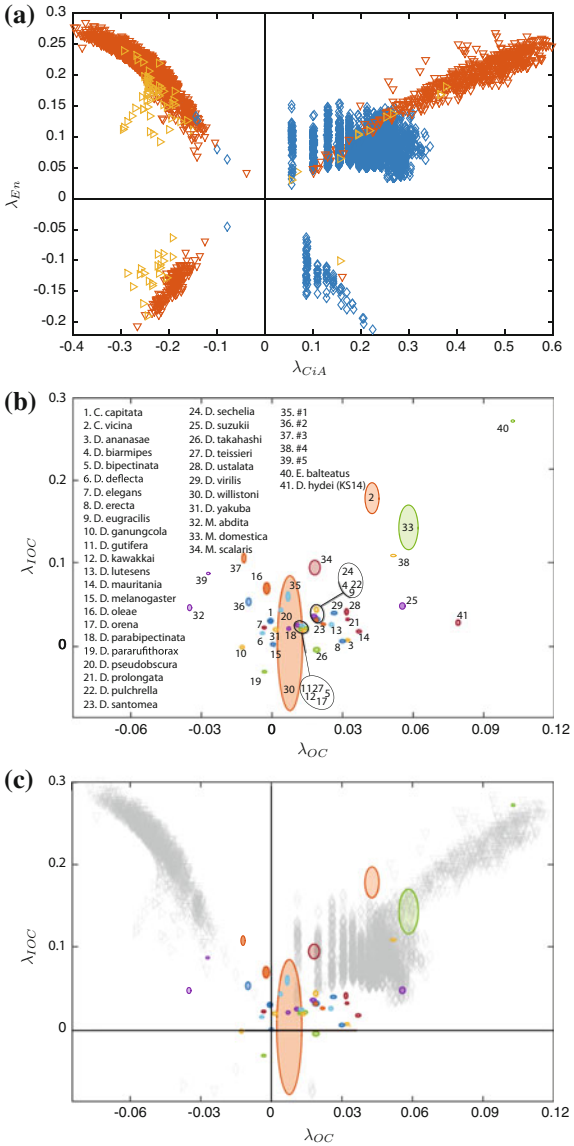

Fig. 7 Comparison of predicted and measured phenotypic space. **a** Distribution of the phenotypic space defined by variations in simulated En profiles against variations in the simulated CiA profiles, to a profile marked as control. Different colors identify different parameter ranges for complementary distance in the parameter sensitivity analysis (see details in Fig. 8 and [1]): $1 - \lambda = 0.8$ (good, blue), $1 - \lambda = 0.6$ (medium, red), and $1 - \lambda = 0.4$ (bad, yellow). **b** Size distribution of IOC against OC for a screening of 41 fly species. The ellipses defining each fly in the phenotypic space are centered in the average size value, and their axes show the standard deviation from the mean. The colors of the ellipses show proportional opacity to the number of samples, varying from N = 2 to N = 14. **c** Overlap between the phenotypic spaces for simulated and measured fly species. Modified from [1]. Licensed under CC BY 4.0

This second result would imply that ocellar size variation (ocellar width and interocellar distance) should be restricted to the specific regions of the solutions space predicted by the model. To try to validate this point, we measured the ocellar width and interocellar distance in a collection of fly species in order to overlay the experimental distribution with the numerical one. The number of measured fly species is sufficiently large to partially match with the numerical size distribution. We found a beautiful qualitative agreement between experimental and numerical results, see Fig. 7b, c. Interestingly we find a quantitative positive size limit for small IOC. This may reflect that the functional behavior for two very close ocelli is not very different from one single fused ocellus, thus ocelli that are too close might be of very limited functional value and therefore not evolutionary selected. We have to note, though, that the sample of fly species is limited in size and biased towards species closely related to *Drosophila melanogaster*, our genetic model. A study including a broader sample and a larger number of species is necessary to further support that the structure of the GRN network we have defined indeed constrains the morphological evolvability of the ocellar complex along the predicted directions.

Once we find the agreement between the experimental and numerical size distributions, we wonder whether we could identify a subset of parameters in the 3-node-network model as responsible of the size variation. To analyze this, we first perform a parameter normalization such that we end with non-dimensional equations. One of the advantages of this process is that we reduce the number of parameters. We choose the degradation rate β_{PtcHh} as normalization rate, thus the values of the non-dimensional parameters are relative to the degradation rate of PtcHh. The non-dimensional version of Eqs. 15–17 reads:

$$\partial_\tau P = (k_{MP}\, M(x) + k_{CP}\, C - k_{EP}\, E)\, \Theta\left(E^{crit} - E\right) - P \tag{19}$$

$$\partial_\tau C = \frac{\frac{k_{PC}}{1+k_{EC}\, E}\, (\varphi_1\, P)^{n_C}}{k_{m_C}^{n_C} + (\varphi_1\, P)^{n_C}} - k_C\, C \tag{20}$$

$$\partial_\tau E = \frac{k_{CE}\, (\varphi_2\, C)^{n_E}}{k_{m_E}^{n_E} + (\varphi_2\, C)^{n_E}} + k_{EE}\, E\, Dl(\zeta_E, \zeta_\tau, \tau_{\zeta_E}) - k_E\, E\,, \tag{21}$$

with normalized parameters obtained by dividing Eqs. 15–17 by β_{PtcHh} and then by $\alpha_0 = \alpha_{hh}/\beta_{PtcHh}$, thus $\tau = t\, \beta_{PtcHh}$, $P = PtcHh/\alpha_0$, $C = CiA/\alpha_0$, $E = En/\alpha_0$, $k_{MP} = \alpha_{Hh-PtcHh}/\beta_{PtcHh}$, $k_{CP} = \alpha_{CiA-PtcHh}/\beta_{PtcHh}$, $k_{CE} = \gamma_{CiA-En}/(\alpha_0\, \beta_{PtcHh})$, $k_{EP} = \alpha_{En-PtcHh}/\beta_{PtcHh}$, $k_{PC} = \gamma_{PtcHh-CiA}/(\alpha_0\, \beta_{PtcHh})$, $k_{EE} = \alpha_{En-En}/\beta_{PtcHh}$, $k_{EC} = \phi_{En-CiA}\, \alpha_0$, $\varphi_1 = \alpha_0\, \alpha_{PtcHh-CiA}$, $\varphi_2 = \alpha_0\, \alpha_{CiA-En}$. Critical concentration for E reads $E^{crit} = (k_{MP}\, M(x) + k_{CP}\, C)/k_{EP}$, $k_C = \beta_{CiA}/\beta_{PtcHh}$, $k_E = \beta_{En}/\beta_{PtcHh}$. The function $M(x)$ is the steady-state solution of the reaction-diffusion equation for the morphogen M that reads:

$$\partial_\tau M = d\, \partial_x^2 M - k_M\, M + \delta(x)\,, \tag{22}$$

with $M = Hh/\alpha_0, d = D/\beta_{PtcHh}, k_M = \beta_{Hh}/\beta_{PtcHh}$ and $\delta(x)$ as referred in Eq. 14.

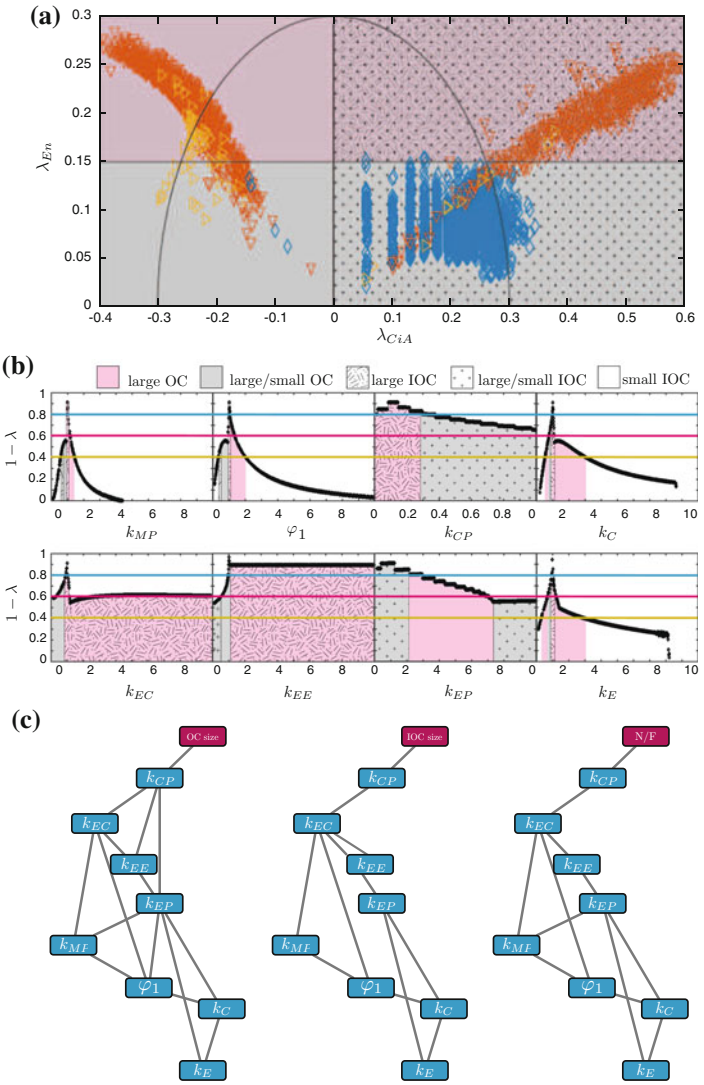

Fig. 8 Bayesian network (BN) analysis. **a** Classification of the phenotypic subspace (with $\lambda_{En} > 0$) according to the distance of the OC (λ_{CiA}) and IOC (λ_{En}) lengths to the control. Horizontal line at ($\lambda_{En} = 0.15$) delimits zones in the IOC size morphological subdivision. The phenotypes within the semicircle are considered similar (near, N) to the control value, while those outside the semi-circumference (centered at ($\lambda_{CiA} = 0$, $\lambda_{En} = 0$) and radius of 0.3) are considered less so (far, F). **b** Distribution of complementary distance ($1 - \lambda$) between control pattern and the one obtained when varying parameters in a two orders of magnitude range. Thresholds for a complementary distance $1 - \lambda = 0.8$ ('good', blue), $1 - \lambda = 0.6$ ('medium', red) and $1 - \lambda = 0.4$ ('bad', yellow) are indicated. Colors and textures link different parameter regimes, shown in **b**, and regions in the phenotypic space in **a**, for parameters chosen by the BNs in **c**. **c** Bayesian networks for the three phenotypic classes: large/small OC (left), large/small IOC (middle), and ocellar regions near/far from the control N/F (right). These networks show eight parameters with the greatest influence to define regions in the phenotypic space. Panels **a**, **c** modified from [1]. Licensed under CC BY 4.0

Then, we applied a machine learning method, Bayesian networks (BNs), to analyze the significance of the parameters in the specification of the OC and IOC size. BNs are acyclic, directed graphs connecting series of variables linked by their conditional probabilities [19]. We use BNs to compute the probability that a given set of values for OC and IOC size falls within a given region in the size distribution space considering the total number of parameters in the model. To perform this analysis, we first define three distributions of OC and IOC according to their location within the phenotypic space, see Fig. 8a. We thus define euclidean distances λ_{En} and λ_{CiA}, that relates to the IOC and OC size, respectively. These distances are measured from each OC-IOC configuration to a control value we choose for normalization, and that corresponds to the measures of the fruit fly *Drosophila melanogaster*. We then distinguish between configurations with large IOC ($\lambda_{En} \geq 0.15$) and small IOC ($\lambda_{En} < 0.15$), and large OC ($\lambda_{CiA} \geq 0$) and small OC ($\lambda_{CiA} < 0$), see Fig. 8a where only positive values for λ_{En} are shown; (*nota bene:* we just found a small number of configurations with negative λ_{En}, which could imply that the system self-constrains to avoid configurations with two ocelli very close to each other. From an evolutionary and developmental perspective this might imply that there is a limit in the closeness of two developing ocelli, as the efficiency of their functionality might be similar then to develop only one large ocellus, which probably reduces cost from a thermodynamic perspective). Figure 8b shows the sensitivity to the change in the ocellar concentration pattern when modifying parameters around the control. We also marked the parametric regions for OC and IOC sizes as in Fig. 8a. The application of the BNs method reported a ranked subset of coupled parameters to produce a specific size distribution of OC and IOC among the three different categories defined above, where these categories indicate whether (i) the OC is large or small, (ii) the IOC is large or small and (iii) the set (OC, IOC) is near or far from the reference set of OC and IOC size that we match with the experimental case of the fruit fly *Drosophila melanogaster*, see details in [1] and Fig. 8.

5 Oscillations in GRN for the Formation of the Ocellar Complex

Oscillatory behaviors have been observed and modeled at different levels of cellular organization [20]. These oscillations often arise due to the negative feedbacks between regulatory proteins and, in general, they are represented by limit cycles. Some oscillatory processes have been already modeled without their experimental evidence existing even. Recently, there is a tendency to seek and attribute a meaning to biological oscillations, although there is not unanimous agreement about its importance. Possibly, the oscillations can emerge so that the systems must adapt to persistent stimuli and, in many cases, so one might obtain important additional information about processes that lead to evolutionary selection. It is interesting, therefore,

to determine if the oscillations are in fact a hallmark of signaling pathways, allowing to the cells to organize and coordinate processes at intracellular and intercellular levels [13, 32, 38].

5.1 Analysis of Oscillations

We discussed in Ref. [4] that the network topology of both the large and the 3-node network models, introduced in Sects. 3.1 and 3.2, respectively, define network topologies that can lead to oscillatory behaviors in the levels of concentration of the nodes that form the network. To demonstrate this, we performed a Boolean networks analysis [4]. The presence of En as a repressor of the Hh signaling pathway establishes a negative feedback within the network that might be able to change the system dynamics causing oscillations in the concentration of genetic species. In principle, though our analysis with Boolean networks reveals oscillatory behaviors, the actual network can be biochemically regulated such that the concentration of the different genetic species reach a steady state or show oscillations. For simplicity, we further analyze the scope of the 3-node network model in an oscillatory regime.

The 3-node network is modelled by the set of equations normalized (Eqs. 19–22). The initial conditions for each variable and the values for all the parameters used in the simulations are found, respectively, in Tables 1 and 2. Some results that derive from the oscillatory behavior studied show that:

(i) The model shows parameter dependent spatiotemporal oscillations (Fig. 9). In all cases, the oscillatory states are represented by limit cycles with period-1 (one maximum in a cycle).

(ii) An increase in the rate constant which characterizes the activation of P on C (φ_1) expands the oscillatory region, see Fig. 10, while an increase in the rate constant which characterizes the repression of E on C (k_{EC}) reduces the oscillatory region. Figure 10 shows bifurcation diagrams for spatial dependent P concentration. The profile of each bifurcation diagram shows an oscillatory region between two steady regions. Points in the oscillatory region indicates maximal, times averages of, and minimal amplitudes of oscillation.

(iii) On the other hand, the oscillation in concentration of a single variable (P) is found in phase difference for different positions that oscillate with the same period (Fig. 11a). We also observe a phase difference among local oscillations of the concentrations of the different variables (P, E and C), see Fig. 11b.

Table 1 Initial concentration of the variables in the 3-node network model

Variable	Description	Initial condition
P	P concentration	10
C	C concentration	0
E	E concentration	0.1

Table 2 Parameter values

Parameter	Description	Value
d	Hh effective diffusion coefficient	$0.5\,\mu m^2$
k_M	Hh effective degradation rate	0.01
α_0	Hh production rate	$1\,\mu M$
k_{MP}	Association rate for PtcHh complex formation	1
φ_1	PtcHh activating CiA rate	1
φ_2	CiA activating En rate	1
k_{CP}	CiA activating PtcHh rate	0.1
k_{EP}	En repressing PtcHh rate	1
k_{EC}	En repressing CiA rate	0.99
k_{EE}	En translation rate	1
Dl	En self-activation switch	1-ON, 0-OFF
ζ_{En}	En threshold for Dl activation	250
ζ_t	Time interval with En over ζ_{En} for Dl activation	1500
k_{PC}	Maximum CiA production rate	10000
k_{CE}	Maximum En activation by CiA	10000
k_C	CiA degradation rate	1
k_E	En degradation rate	1
k_{m_C}	CiA half-maximal activation concentration	2000
k_{m_E}	En half-maximal transcriptional activation	90
n_C	Hill coefficient for CiA transcription	2
n_E	Hill coefficient for En transcription	4

(iv) The period of oscillations in concentrations first increases, then passes through a maximum value and, finally, decreases as the morphogen concentration increases (or distance to the morphogen source decreases). The amplitude of oscillations shows a similar behavior, see Fig. 11c, d.

5.2 Periodic Perturbation of the Oscillatory Kinetics Observed in the Model

In the next step, we carry out a study of perturbations. The motivation for this study is the assumption that the actual GRN is larger and more complicated than the one modeled. We consider that in a larger network there may be unknown motifs which also present oscillatory dynamics. These unknown motifs can, in principle, oscillate with different frequencies to those in the 3-node network, to which may interact with. In this case, the 3-node network can show more complex dynamics.

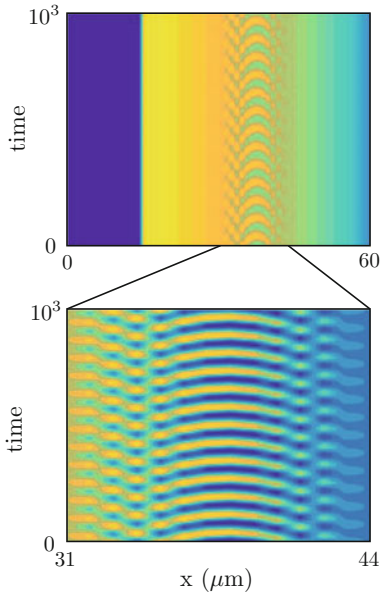

Fig. 9 Spatiotemporal dynamic of C. In this scenario E is not self-regulated (Dl = 0), and the OC region is defined by C levels in an oscillatory regime. Parameter values in Table 2

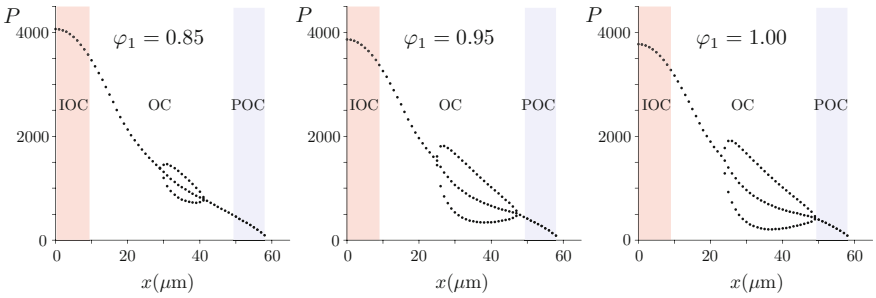

Fig. 10 Bifurcation diagrams for spatial dependent P concentration. The diagrams show an oscillatory region between two steady regions. The width of the oscillatory region expands for increasing values of φ_1

In this sense, one of the most studied mechanisms in an oscillatory system is the coupling between an internal autonomous oscillation and an external periodic perturbation. In general, interaction between external and internal dynamics produces synchronization, although, in some cases, this does not happen and new complex dynamic can appear, such as the quasiperiodic and chaotic behaviors. It is interesting, therefore, to obtain additional information about the effect that periodic perturbations has on intracellular kinetic oscillations in order to determine if these oscillations are a hallmark of cellular signaling pathways.

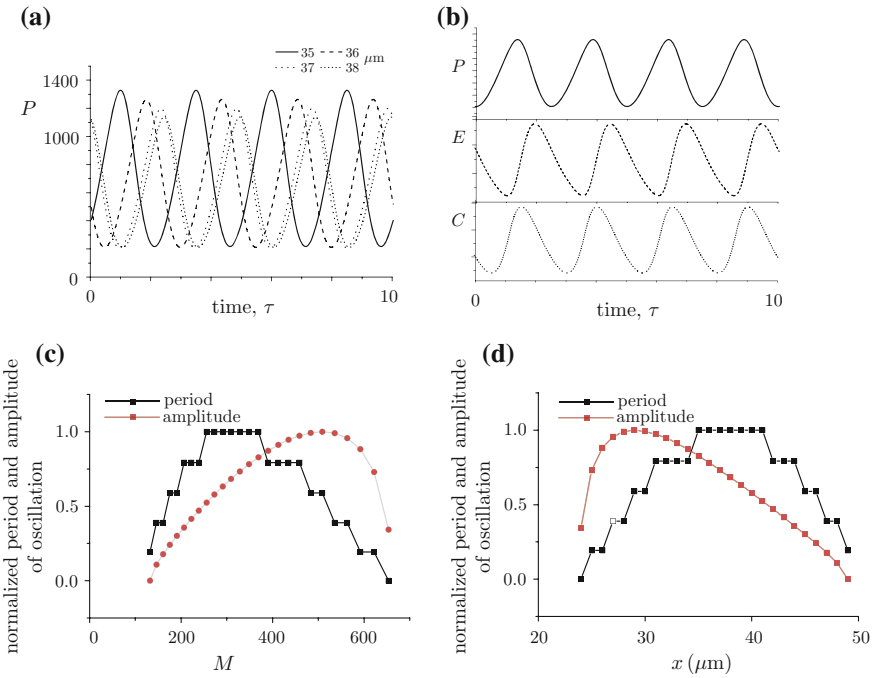

Fig. 11 **a** Phase differences in the oscillation of P concentration at different positions. **b** Local phase difference in the oscillation of the concentrations of variables P, E and C ($x = 35\,\mu\text{m}$). **c**, **d** Variation of the oscillation period and amplitude of the normalized P concentration as a function of M **c** and position **d**

From Eqs. 19–21 of the 3-node network model, for a given position and stationary morphogen concentration, we analyze the response that periodic perturbations have on a natural state which oscillates with period-1 and f_0 frequency.

In order to do this, we apply a perturbation on the rate constant of the activation process of P on C, φ_1, such that the perturbed parameter φ^* reads

$$\varphi_1^* = \varphi_1(1 + A\ \sin(2\pi\ f\ t))\,, \tag{23}$$

where A and f are normalized amplitude and frequency of perturbation (f is different from the natural, not forced, frequency f_0).

Some representative cases are shown in Fig. 12. This shows forced temporary oscillations of C (down) and E (up) along with their corresponding Poincaré maps, next maxima maps and Fourier spectra. Period-n (Pn) indicates oscillations with n maxima in each cycle (see Fig. 12b for n = 2, and Fig. 12c for n = 1). A curve of n loops corresponds to Pn oscillations in the Poincaré map. In next maxima map, n points indicate a Pn oscillation. Fourier spectra are discrete, appearing one fundamental frequency and its harmonics. In these cases, the system responds with

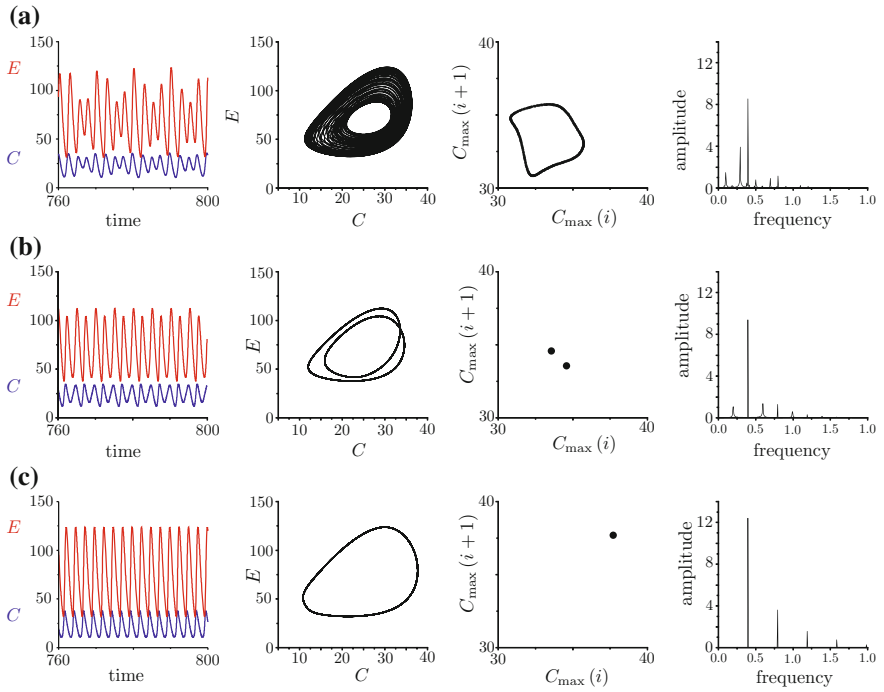

Fig. 12 Forced oscillations for $A = 0.4$. Temporary series show for **a** $f = (3/4)\,f_0$, quasiperiodic oscillations; **b** $f = (3/2)\,f_0$, P2 oscillations; **c** $f = 3f_0$, P1 oscillations

the natural frequency. Quasiperiodic oscillations can be also observed (see Fig. 12a): Poincaré map shows the typical toroidal shape; next maxima map represents one closed curve; and Fourier spectrum is discrete with several fundamental frequencies.

We can conclude that:

(a) Forced kinetics are mainly periodic or quasiperiodic. In the periodic kinetics the system oscillates with the natural frequency f_0.

(b) There is no transition to periodic oscillations with the external frequency nor even to large perturbation amplitudes. In this case, the perturbation is relatively inefficient.

(c) We show an amplification capability that the perturbations have on the oscillations [44].

(d) Our results agree with those predicted by other models related to gene expressions and proteins [45, 46].

6 Summary and Perspectives

The study of the coupling between chemical patterns and gene regulatory networks by a joint workforce of theoreticians and experimentalists is an emerging research area within the fields of Developmental Biology, Regeneration and Cancer. In this chapter, we followed this approach in the study of the ocellar complex integrating approaches from developmental genetics, evolution and systems dynamics. We found that the ocellar complex pattern is driven by the morphogen *hedgehog* (Hh), which convey cells with positional information in a *french flag model* fashion, where different morphogen concentration thresholds define boundaries of cellular differentiation. These boundaries are set by the coupling of the extracellular morphogen to a complex intracellular gene regulatory network, which we modeled in a simplified one-dimensional system of partial and ordinary differential equations. From this model, we found that quantitative changes in parameter values seem sufficient to explain the quantitative morphological variation found in nature, in the size of the ocellar complex constitutive elements among different fly species, without the need of gene network rewiring. Our analysis further identifies likely candidate processes to be responsible for ocellar morphological evolution. The specific wiring of the gene regulatory network contains a negative feedback, the topology of which shows oscillatory behaviors. In the models presented here, we observed parameter-dependent spatio-temporal oscillations in the ocellus region. These self-sustained oscillations are represented in the form of limit cycles. We studied the dynamics of such oscillations coupled to a second oscillator in the form of a harmonic perturbation to show different *in silico* oscillatory states, which range in complexity from P1 to quasiperiodic states. An experimental analysis for validating both autonomous and forced oscillations has not been explored yet.

Acknowledgements Grants BFU2012-34324 and BFU2015-66040-P (MINECO, Spain, co-funded by Feder) to FC. We thank M Sánchez-Aragón and MA Domínguez-Cejudo for the data in Fig. 6. DAH acknowledges S. Roldán and E. Roldán of the Nota Bene group at MPIPKS for their Iberian support and discussions. MCL acknowledges Junta de Andalucía (Spain) by partially funding her research group (FQM-122).

References

1. Aguilar-Hidalgo, D., Becerra-Alonso, D., García-Morales, D., Casares, F.: Toward a study of gene regulatory constraints to morphological evolution of the Drosophila ocellar region. Dev. Genes Evol. **226**(3), 221–233 (2016)
2. Aguilar-Hidalgo, D., Córdoba, A., Lemos, M.C.: Complex networks evolutionary dynamics using genetic algorithms. Int. J. Bifurc. Chaos **22**(7), 1250156 (2012)
3. Aguilar-Hidalgo, D., Domínguez-Cejudo, M.A., Amore, G., Brockmann, A., Lemos, M.C., Córdoba, A., Casares, F.: A Hh-driven gene network controls specification, pattern and size of the Drosophila simple eyes. Development **140**(1), 82–92 (2013)
4. Aguilar-Hidalgo, D., Lemos, M.C., Córdoba, A.: Core regulatory network motif underlies the ocellar complex patterning in Drosophila melanogaster. Physica D **295–296**, 91–102 (2015)

5. Aguilar-Hidalgo, D., Lemos, M.C., Córdoba, A.: Evolutionary dynamics in gene networks and inference algorithms. Computer **3**(1), 99–113 (2015)
6. Alexandre, C., Jacinto, A., Ingham, P.W.: Transcriptional activation of hedgehog target genes in Drosophila is mediated directly by the cubitus interruptus protein, a member of the GLI family of zinc finger DNA-binding proteins. Gene Dev. **10**(16), 2003–2013 (1996)
7. Alon, U.: An Introduction to Systems Biology: Design Principles of Biological Circuits. Chapman & Hall/CRC; Mathematical and Computational Biology. Taylor & Francis, Boca Raton, Florida, USA (2007)
8. Arnone, M.I., Davidson, E.H.: The hardwiring of development: organization and function of genomic regulatory systems. Development **124**(10), 1851–1864 (1997)
9. Averbukh, I., Ben-Zvi, D., Mishra, S., Barkai, N.: Scaling morphogen gradients during tissue growth by a cell division rule. Development **141**(10), 2150–2156 (2014)
10. Blanco, J., Pauli, T., Seimiya, M., Udolph, G., Gehring, W.J.: Genetic interactions of eyes absent, twin of eyeless and orthodenticle regulate sine oculis expression during ocellar development in Drosophila. Dev. Biol. **344**(2), 1088–1099 (2010)
11. Blanco, J., Seimiya, M., Pauli, T., Reichert, H., Gehring, W.J.: Wingless and Hedgehog signaling pathways regulate orthodenticle and eyes absent during ocelli development in Drosophila. Dev. Biol. **329**(1), 104–115 (2009)
12. Brockmann, A., Domínguez-Cejudo, M.A., Amore, G., Casares, F.: Regulation of ocellar specification and size by twin of eyeless and homothorax. Dev. Dyn. **240**(1), 75–85 (2011)
13. Cheong, R., Levchenko, A.: Oscillatory signaling processes: the how, the why and the where. Curr. Opin. Genet. Dev. **20**, 665–669 (2010)
14. Crombach, A., Wotton, K.R., Cicin-Sain, D., Ashyraliyev, M., Jaeger, J.: Efficient reverse-engineering of a developmental gene regulatory network. PLoS Comput. Biol. **8**(7), e1002589 (2012)
15. Dessaud, E., Ribes, V., Balaskas, N., Yang, L.L., Pierani, A., Kicheva, A., Novitch, B.G., Briscoe, J., Sasai, N.: Dynamic assignment and maintenance of positional identity in the ventral neural tube by the morphogen sonic hedgehog. PLoS Biol. **8**(6), e1000382 (2010)
16. Dillon, R., Othmer, H.G.: A mathematical model for outgrowth and spatial patterning of the vertebrate limb bud. J. Theor. Biol. **197**(3), 295–330 (1999)
17. Domínguez-Cejudo, M.A., Casares, F.: Anteroposterior patterning of Drosophila ocelli requires an anti-repressor mechanism within the hh pathway mediated by the Six3 gene Optix. Development **142**(16), 2801–2809 (2015)
18. Fried, P., Sánchez-Aragón, M., Aguilar-Hidalgo, D., Lehtinen, B., Casares, F., Iber, D.: A model of the spatio-temporal dynamics of drosophila eye disc development. PLoS Comput. Biol. **12**(9), e1005052 (2016)
19. Friedman, N., Goldszmidt, M., Lee, T.J.: Bayesian network classification with continuous attributes: getting the best of both discretization and parametric fitting. In: J.W. Shavlik (ed.) Proceedings of the International Conference on Machine Learning, ICML, pp. 179–187. Morgan Kaufmann, San Francisco, CA, USA (1998)
20. Goldbeter, A.: Biochemical Oscillations and Cellular Rhythms. The Molecular Bases of Periodic and Chaotic Behaviour. Cambridge University Press, Cambridge, UK (1996)
21. Gregor, T., Bialek, W., de Ruyter van Steveninck, R.R., Tank, D.W., Wieschaus, E.F.,: Diffusion and scaling during early embryonic pattern formation. P. Natl. Acad. Sci. USA **102**(51), 18403–18407 (2005)
22. Ingham, P.W.: Signalling by hedgehog family proteins in Drosophila and vertebrate development. Curr. Opin. Genet. Dev. **5**(4), 492–498 (1995)
23. Jaeger, J., Surkova, S., Blagov, M., Janssens, H., Kosman, D., Kozlov, K.N., Manu, Myasnikova, E., Vanario-Alonso, C.E., Samsonova, M., Sharp, D.H., Reinitz, J.: Dynamic control of positional information in the early drosophila embryo. Nature **430**, 368–371 (2004)
24. Jürgens, G., Hartenstein, V.: The terminal regions of the body pattern. In: M. Bate, A. Martinez Arias (eds.) The Development of Drosophila Melanogaster, vol. I. Cold Spring Harbor Laboratory Press, Long Island, New York, USA (1993)

25. Koch, A.J., Meinhardt, H.: Biological pattern formation: from basic mechanisms to complex structures. Rev. Mod. Phys. **66**, 1481–1507 (1994)
26. Krapp, H.G.: Ocelli. Curr. Biol. **19**(11), R435–R437 (2009)
27. Lam, K.Y., Westrick, Z.M., Müller, C.L., Christiaen, L., Bonneau, R.: Fused regression for multi-source gene regulatory network inference. PLoS Comput. Biol. **12**(12), e1005157 (2016)
28. Lawrence, P.A., Struhl, G.: Morphogens, compartments, and pattern: lessons from Drosophila? Cell **85**(7), 951–961 (1996)
29. Ma, C., Moses, K.: Wingless and patched are negative regulators of the morphogenetic furrow and can affect tissue polarity in the developing Drosophila compound eye. Development **121**(8), 2279–2289 (1995)
30. Mizunami, M.: Functional diversity of neural organization in insect ocellar systems. Vision Res. **35**(4), 443–452 (1995)
31. Ortega-Hernández, J.: Homology of head sclerites in Burgess Shale euarthropods. Curr. Biol. **25**(12), 1625–1631 (2015)
32. Pigolotti, S., Krishna, S., Jensen, M.H.: Oscillation patterns in negative feedback loops. P. Natl. Acad. Sci. USA **104**(16), 6533–6537 (2007)
33. Romanova-Michaelides, M., Aguilar-Hidalgo, D., Jülicher, F., González-Gaitán, M.: The wing and the eye: a parsimonious theory for scaling and growth control? WIREs Dev. Biol. **4**(6), 591–608 (2015)
34. Royet, J., Finkelstein, R.: Pattern formation in Drosophila head development: the role of the orthodenticle homeobox gene. Development **121**(11), 3561–3572 (1995)
35. Royet, J., Finkelstein, R.: Establishing primordia in the Drosophila eye-antennal imaginal disc: the roles of decapentaplegic, wingless and hedgehog. Development **124**(23), 4793–4800 (1997)
36. Szederkényi, G., Banga, J.R., Alonso, A.A.: Inference of complex biological networks: distinguishability issues and optimization-based solutions. BMC Syst. Biol. **5**(1), 177 (2011)
37. Thompson, D.A.W.: On Growth and Form. The Complete Revised Edition. Dover Publications Inc, New York, USA (1992)
38. Tiana, G., Krishna, S., Pigolotti, S., Jensen, M.H., Sneppen, K.: Oscillation and temporal signalling in cells. Phys. Biol. **4**, R1–R17 (2007)
39. Treisman, J.E., Rubin, G.M.: Wingless inhibits morphogenetic furrow movement in the Drosophila eye disc. Development **121**(11), 3519–3527 (1995)
40. Turing, A.M.: The chemical basis of morphogenesis. Philos. T. R. Soc. Lond. **237**(641), 37–72 (1952)
41. Wartlick, O., Mumcu, P., Jülicher, F., González-Gaitán, M.: Understanding morphogenetic growth control - lessons from flies. Nat. Rev. Mol. Cell Bio. **12**(9), 594–604 (2011)
42. Werner, S., Stückemann, T., Beirán Amigo, M., Rink, J.C., Jülicher, F., Friedrich, B.M.: Scaling and regeneration of self-organized patterns. Phys. Rev. Lett. **114**(13), 138101 (2015)
43. Wolpert, L.: Positional information and the spatial pattern of cellular differentiation. J. Theor. Biol. **25**(1), 1–47 (1969)
44. Zhdanov, V.P.: Amplification of kinetic oscillations in gene expression. JETP Lett. **88**(4), 281–285 (2008)
45. Zhdanov, V.P.: Periodic perturbation of the bistable kinetics of gene expression. Physica A **390**, 57–64 (2011)
46. Zhdanov, V.P.: Periodic perturbation of genetic oscillations. Chaos Soliton Fract. **45**, 577–587 (2012)

Computation of Invariant Curves in the Analysis of Periodically Forced Neural Oscillators

Alberto Pérez-Cervera, Gemma Huguet and Tere M-Seara

Abstract Background oscillations, reflecting the excitability of neurons, are ubiquitous in the brain. Some studies have conjectured that when spikes sent by one population reach the other population in the peaks of excitability, then information transmission between two oscillating neuronal groups is more effective. In this context, phase locking relationships between oscillating neuronal populations may have implications in neuronal communication as they assure synchronous activity between brain areas. To study this relationship, we consider a population rate model and perturb it with a time-dependent input. We use the stroboscopic map and apply powerful computational methods to compute the invariant objects and their bifurcations as the perturbation parameters (frequency and amplitude) are varied. The analysis performed shows the relationship between the appearance of synchronous and asynchronous regimes and the invariant objects of the stroboscopic map.

Keywords Synchronization · Phase locking · Stroboscopic map · Invariant curves · Rotation number

1 Introduction

Since it was first reported in 1929 by Hans Berger [2], neural oscillatory activity has been a topic of great interest and debate in neuroscience. Although its role is not fully understood, electroencephalographic patterns evidence its importance in brain function. In particular, oscillations have been linked to many different processes as memory or perception [4]. Although oscillatory behaviour can occur across different

A. Pérez-Cervera (✉) · G. Huguet · T. M-Seara
Dept. Matemàtica Aplicada, Universitat Politècnica de Catalunya Avda.,
Diagonal 647 (ETSEIB), E-08028 Barcelona, Spain
e-mail: alberto.perez@upc.edu

G. Huguet
e-mail: gemma.huguet@upc.edu

T. M-Seara
e-mail: tere.m-seara@upc.edu

J. F. R. Archilla et al. (eds.), *Nonlinear Systems, Vol. 2*, Understanding
Complex Systems, https://doi.org/10.1007/978-3-319-72218-4_3

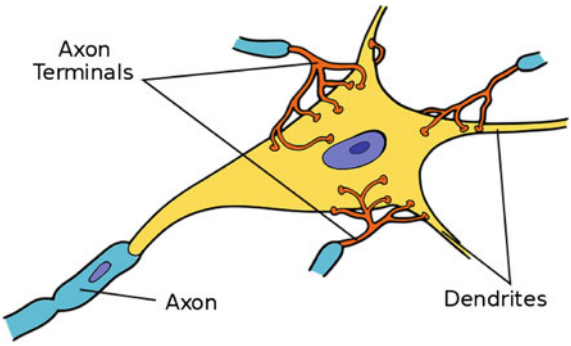

Fig. 1 Schematic of a neuron with different synaptic connections. It can be seen how axon terminals from neighbouring neurons contact the dendrites of the receiving neuron

brain scales, this work will focus on oscillations generated by neuronal ensembles or populations.

Neurons are the fundamental cells within the brain, and they basically communicate through electrical impulses [6]. Neurons integrate inputs from neighbouring neurons across dendrites. When these inputs cause the neuron membrane potential to reach a certain critical value or threshold, the neuron will respond with a characteristic voltage change of large amplitude and short time duration ($\approx$1 ms) known as action potential or spike. This action potential then travels along the axon of the neuron to the axon terminal, where its effect will be felt by the neighbouring neurons (Fig. 1). Neurons can be excitatory or inhibitory, depending on the effect of the connection (synapse) on the receiving neuron: inputs from an excitatory (inhibitory) neuron depolarize (hyperpolarize) the membrane potential of the receiving neuron.

In this paper, we explore the oscillatory activity emerging from a neuronal network consisting of a single population of excitatory neurons and a single population of inhibitory neurons (E-I network). Under the appropriate stimulus, the firing of the excitatory population activates the inhibitory population that, on its turn, suppresses the excitatory activity. Once the inhibitory effect has vanished, if the stimulus remains, the excitatory neurons will fire again generating an oscillatory pattern. The excitability of the excitatory population is not the same for all the phases of the cycle due to the inhibitory action. Indeed, when the excitatory population receives an external input at the phase in which the inhibition is not present, the excitatory cells can respond effectively, while if the inhibition is present, the input might be ignored (see Fig. 2). This mechanism, known as communication through coherence, has been invoked to explain neural communication between brain areas [7]. In this context, two neuronal groups with underlying oscillatory activity communicate much effectively when they are properly phase-locked so that the windows for inputs and outputs are open at the same times. Although the functional role of the brain oscillations is still unknown, a growing number of studies have recently suggested that in several cognitive tasks (such as sensory perception, working memory, and attention), synchronized background oscillations may coordinate computations involving different brain areas [15].

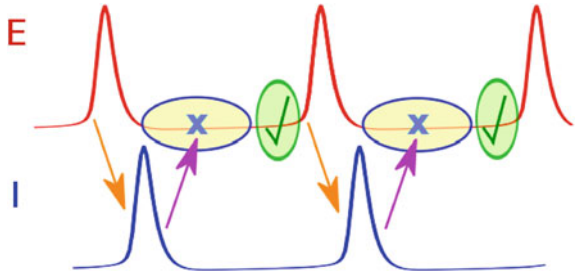

Fig. 2 Oscillations arise from the interaction between the inhibition and the excitation. We illustrate how different phases of the oscillation may have different excitability properties due to the inhibition as suggested in [18]

A simplified framework for studying this situation is to consider the effect of an external oscillatory input onto a network model consisting of excitatory and inhibitory cells showing oscillations. For such network we consider the simplest canonical model describing the mean firing rates of the excitatory and inhibitory populations: the Wilson–Cowan equations [20]. As the parameters of this model can be chosen so that the system shows oscillations we can simulate the framework of interest.

In particular, we focus on oscillations of the Wilson–Cowan model arising from a Hopf bifurcation. The periodic forcing of such bifurcation has been studied in classical papers [9], and recently, in the neuroscience context [19]. In this work, we aim to understand the different mechanisms which give rise to synchronous activity between the *E*-*I* network and the external T'-periodic input. As we study a periodic perturbation, we consider the stroboscopic map (i.e. the time-T' map of the flow) and identify an attracting invariant curve of the map, where the dynamics on it can be understood by means of the rotation number. The rotation number indicates the relationship between the period of the forced oscillator and the external forcing; rational values of this magnitude correspond to synchronous regions while irrational values correspond to asynchronous regions. Thus, assuming the existence of an invariant curve, we compute the rotation number as the amplitude and the frequency of the external periodic input are varied and identify the synchronous solutions. We also identify regions where this computation fails, which correspond to the breakdown of the invariant curve. To provide a full understanding of the dynamics beyond the breakdown of the invariant curve, we compute the fixed points of the map as well as their bifurcations. Bifurcations of the fixed points can be related to the breakdown of the invariant curve. Thus, we apply powerful computational methods [11] to compute the invariant curve and its internal dynamics, which provide a framework that enlarges the comprehension of the dynamics generated by the periodic forcing.

2 Mathematical Model

A neuronal population can be modelled as a neuronal network consisting of N neurons connected through synapses. If each neuron is described by a system of n differential equations, a network of N neurons will be described by a system of $N \cdot n$ equations.

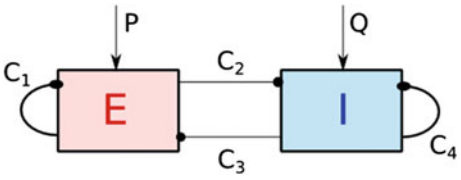

Fig. 3 Schematic of a neuronal network modelled by the mean field model (1)

This approach, although generates very accurate results, considers a high dimensional system, that requires a high computational effort to integrate it and makes the mathematical analysis difficult. As an alternative to this approach, there exist mean field models, which use a single variable to describe the mean activity of a population. These models have a reduced number of equations and are suitable for analysis. One of the most famous rate models are the Wilson–Cowan equations [20]:

$$\begin{aligned} \tau_e \frac{dE}{dt} &= -E + (1 - r_e E) S_e(c_1 E - c_2 I + P), \\ \tau_i \frac{dI}{dt} &= -I + (1 - r_i I) S_i(c_3 E - c_4 I + Q), \end{aligned} \tag{1}$$

where the variables E and I correspond to the fraction of neurons of the excitatory and the inhibitory populations respectively which are emitting an action potential at time t. The coupling constants c_i determine the strength of connexions between neuronal populations. P and Q are the (constant) external inputs which are injected to E and I populations, respectively (see Fig. 3). Coupling constants c_i are positive, whereas external currents P and Q can be either positive or negative depending whether its action is excitatory or inhibitory.

Assuming that a population k is receiving an input x, the proportion of cells which will fire as a result of this input is modelled by the response function $S_k(x)$, a sigmoidal function defined as:

$$S_k(x) = \frac{1}{1 + e^{-a_k(x-\theta_k)}}, \qquad \text{with} \quad k = e, i,$$

where the parameters θ_k and a_k are the position of the maximum slope and the value of this maximum slope, respectively.

Neurons have a refractory period r_k during which they can not respond to external inputs. The factor $(1 - r_k k)$ in Eq. (1), represents the proportion of neurons of the population k which are able to be excited. In [14] it is shown how this term only rescales the parameters on the nonlinearities $S_k(x)$ and does not change the qualitative behaviour of the system. For this reason, from now on, we will consider $r_k = 0$.

2.1 Dynamical Analysis

In this subsection we study the most important objects (critical points and limit cycles) of system (1) and their bifurcations. Nullclines of (1), when $r_e = r_i = 0$, are given by

$$\begin{aligned} E &= f_e(I, Q) = \frac{1}{c_3}[S_i^{-1}(I) + c_4 I - Q], \\ I &= g_i(E, P) = \frac{1}{c_2}[c_1 E - S_e^{-1}(E) + P]. \end{aligned} \tag{2}$$

As it can be seen in Eq. (2), P and Q translate nullclines and thus determine their intersection. Consequently, the name and position of the critical points of the system will depend on the values of P and Q (Fig. 4 left). For this reason parameters P and Q will be considered as bifurcation parameters.

Choosing the set of constants adequately, the Wilson–Cowan equations show oscillatory behaviour [20]. In particular, as it can be seen in Fig. 4 (right), oscillations in the Wilson–Cowan model reproduce the oscillatory mechanism stated in the introduction: for a strong enough input value P, the excitatory activity will increase, activating the inhibitory cells which, in its turn, will suppress the excitatory activity and in consequence, the inhibitory activity. Once the inhibitory effect has vanished, the external input P –if still present–, will activate the excitatory cells again, generating an oscillatory pattern. The following set of parameters $\mathscr{P}$ ensures the existence of oscillations for some (P, Q) stimulus values and for this reason they will be the default parameters used throughout the work:

$$\begin{aligned} \mathscr{P} = \{&c_1 = 13, c_2 = 12, a_e = 1.3, \theta_e = 4, r_e = 0, \tau_e = 1 \\ &c_3 = 6,\ c_4 = 3,\ a_i = 2,\ \theta_i = 1.5,\ r_i = 0,\ \tau_i = 1\}. \end{aligned} \tag{3}$$

As system (1) is 2-dimensional and the phase space is bounded, using Poincaré-Bendixon theorem it is enough to require that the system has a unique unstable critical point to guarantee the existence of a periodic orbit (oscillations). Such oscillations are going to appear across Hopf, Saddle-Node on Invariant Circle (SNIC bifurcation) and Homoclinic bifurcation [3, 12]. As a first step to find these bifurcations we look for bifurcations of the critical points of the system. Thus, by defining $DX(E, I, P, Q)$ the Jacobian matrix of system (1), we can look for points (E, I, P, Q) satisfying (2) and conditions $\mathrm{Tr}\, DX(E, I, P, Q) = 0$ for the Hopf bifurcation and $\mathrm{Det}\, DX(E, I, P, Q) = 0$ for the Saddle-Node bifurcation. As we are dealing with non linear equations, the computation of the bifurcation diagram (Fig. 5) requires computational methods for continuation of curves [17].

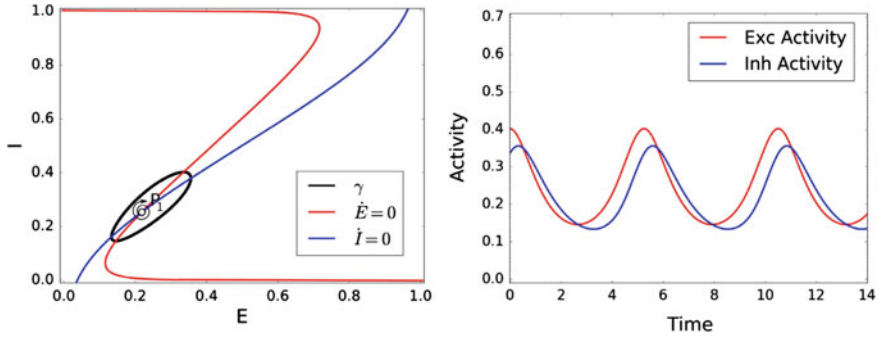

Fig. 4 Left: Nullclines and phase space for the set of parameters $\mathscr{P}$ given in (3) and $(P, Q) = (2.5, 0)$. There exists a limit cycle γ and an unstable focus P_1. Right: Dynamics for system (1) over the limit cycle γ. The oscillations arise from the interactions between the excitatory inhibitory populations

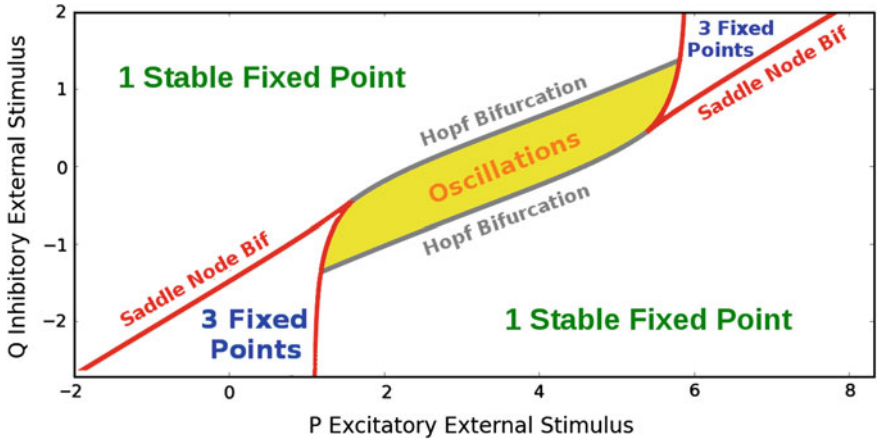

Fig. 5 Bifurcation diagram for the Wilson–Cowan system (1) as a function of external stimulii P and Q. Parameters for system (1) are given by the set $\mathscr{P}$ in (3)

3 Non Autonomous Perturbation

In this section we will study the effects of a T'-periodic non-autonomous perturbation onto the Wilson–Cowan equations (1). Concretely we will study the following model:

$$\begin{aligned} \tau_e \frac{dE}{dt} &= -E + S_e(c_1 E - c_2 I + P + Ap(t)), \\ \tau_i \frac{dI}{dt} &= -I + S_i(c_3 E - c_4 I + Q), \end{aligned} \tag{4}$$

where A is the amplitude of the perturbation and $p(t)$ is the T'-periodic function:

$$p(t) = 1 + \cos(\frac{2\pi t}{T'}),$$

modelling the activity of an external excitatory population.

3.1 The Stroboscopic Map

The stroboscopic map is the most natural approach when considering the study of T'-periodic perturbations. It is defined by

$$\begin{aligned} F_A : \mathbb{R}^2 &\to \mathbb{R}^2, \\ x &\to F_A(x) = \phi_A(t_0 + T'; t_0, x), \end{aligned} \tag{5}$$

where $\phi_A(t; t_0, x)$ is the solution of (4) such that $\phi_A(t_0; t_0, x) = x$.

As it is well known, the fixed points and invariant curves of the stroboscopic map (5) correspond to periodic and quasiperiodic solutions of system (4) respectively. For instance, if $\gamma(t) = \phi_A(t; t_0, x)$ is a solution of system (4) and $[F_A(x)]^q = x$, then by definition $\phi_A(t_0 + qT'; t_0, x) = x$ and therefore $\gamma(t)$ is periodic of period qT'. Analogously, if $\gamma(t) = \phi_A(t; t_0, x)$ is a periodic orbit of period T of (4) with $\frac{T'}{T} = \frac{p}{q}$, $p, q \in \mathbb{N}$, then

$$[F_A(x)]^q = \phi_A(t_0 + qT'; t_0, x) = \phi_A(t_0 + pT; t_0, x) = x, \tag{6}$$

that is, fixed points x for the map $[F_A(x)]^q$ will correspond to periodic orbits of the system (4). In the neuroscience context, relationship (6) indicates that a *p:q* phase locking state has been established between the population and the perturbation. In the Wilson–Cowan model this means that the neuronal population variables E and I have completed p revolutions in the same time that the perturbation $p(t)$ has completed q revolutions. By contrast, if $\gamma(t) = \phi_A(t; t_0, x)$ is periodic of period T but $\frac{T'}{T} \notin \mathbb{Q}$, then $[F_A(x)]^n \neq x \ \forall \ n \in \mathbb{N}$ and $[F_A(x)]^n$ fills densely $\Gamma_A = \{\overline{\phi_A(t_0 + nT'; t_0, x), n \in \mathbb{N}}\}$ which is an invariant curve for $F_A(x)$. So, depending on the amplitude A and the period T' of the perturbation, the system in (4) can display either a *p:q* synchronous regime synchronous regime or an asynchronous regime.

3.2 Computing the Rotation Number in the Perturbed Framework

In this section we will explain how to compute the rotation number. Consider the set of parameters $\mathscr{P}$ defined in (3), and let $(P, Q) = (2.5, 0)$. As bifurcation diagram on

Fig. 5 shows, for this set of parameters the unperturbed Wilson–Cowan equations (1) display an unstable focus P_1 and an attracting limit cycle γ of period $T \approx 5.26$.

When $A = 0$ the phase portrait described by the stroboscopic map (5) is the same as the one generated by the unperturbed system (1). In particular, $F_0(P_1) = P_1$ and $F_0(\gamma) \subseteq \gamma$, $\forall\ T'$, that is, P_1 and γ are an unstable fixed point and an attracting invariant curve for the map (5), respectively. When applying a T'-periodic continuous perturbation, as both objects P_1 and γ are normally hyperbolic, they will continue existing for weak enough perturbations, and they can be studied as invariant objects for the stroboscopic map F_A when $A \neq 0$. In particular, while the unstable focus $P_1 = P_1(A)$ will remain an unstable fixed point for the stroboscopic map F_A, the attracting limit cycle γ will become an attracting invariant curve Γ_A. Over the invariant curve Γ_A we can define and compute the rotation number.

The rotation number is defined for any continuous orientation preserving map of the circle

$$\begin{aligned} f : \mathbb{T} &\to \mathbb{T} \\ \theta &\mapsto f(\theta) \end{aligned}$$

as

$$\rho = \lim_{n\to\infty} \frac{\theta_n - \theta_0}{n}, \qquad \theta_n = f^n(\theta_0). \tag{7}$$

As it is well known, ρ exists and is independent of the point θ_0 [1]. Moreover, if $\rho = \frac{p}{q} \in \mathbb{Q}$, the map f has, at least, one periodic point θ^* of period q. On the other hand, under some regularity assumptions, if $q \in \mathbb{R} \setminus \mathbb{Q}$, the map f is conjugated to a rotation of angle ρ and the orbit of every point θ fill densely $\mathbb{T}$.

In our case, one can take $f := f_A = F_{A|_{\Gamma_A}}$ and compute the rotation number as follows: given a point $x \in \Gamma_A$, define the angle θ between the line from $P_1(A)$ to x and the positive E-axis. Then, given a point $x_0 \in \Gamma_A$ for $x_n = f_n^A(x_0)$, one can compute the rotation number in (7).

When computing ρ numerically, usually the limit to infinity is substituted by a large enough number of iterations but the convergence to ρ is very slow. We used the methods presented in [16], which refine the computation of rotation numbers saving computational effort and accelerating the convergence of the method.

Recall that if $\rho = \frac{p}{q}$ with $p, q \in \mathbb{N}$ there exists a θ^* such that $f_A^q(\theta^*) = \theta^*$, and the corresponding point x^* is a q-periodic orbit of F_A, which turns p times around the invariant curve Γ_A. This indicates the appearance of a given $p{:}q$ phase locking regime in system (4).

In Fig. 6 we show the computation of the rotation number for some amplitude values A and varying T'. We observe the classical Devil's Staircase function [1]. The function shows intervals on the x-axis (showing the ratio $\frac{T'}{T}$) for which the rotation number $\rho(T')$ is constant (there exists a solution of (4) which is phase-locked to the periodic perturbation). For small positive amplitudes, the largest intervals correspond to the phase locked states 1:1 ($\rho = 1$) and 1:2 ($\rho = \frac{1}{2}$) (Fig. 6 top). The phase-locked intervals widen as the amplitude is increased (Fig. 6 bottom). The rotation number displays a discontinuity at some values of T' jumping suddenly to $\rho = 1$ as the

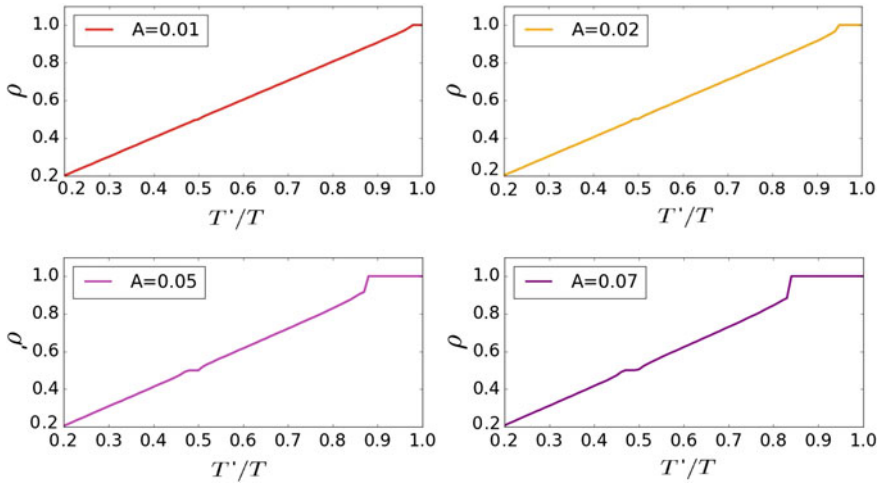

Fig. 6 Rotation number computed for different amplitudes in the perturbed Wilson–Cowan model (4). Parameters used were the set $\mathscr{P}$ in (3), and $(P, Q) = (2.5, 0)$

amplitude is increased. As the rotation number is defined over the invariant curve Γ_A, this discontinuity may indicate a bifurcation or the breakdown of the invariant curve appearing for non-weak amplitudes that we will investigate in the next sections.

3.3 Bifurcation Analysis

In order to understand the dynamics that occur in system (4) depending on the period T' and the amplitude A of the perturbation, we will begin by computing bifurcations for the fixed points of the stroboscopic map (5).

Given a map depending in one parameter $\alpha \in \mathbb{R}$:

$$\begin{aligned} F : \mathbb{R}^n \times \mathbb{R} &\to \mathbb{R}^n \\ (x, \alpha) &\to F(x, \alpha). \end{aligned} \tag{8}$$

If there exists (x_0, α_0) such that

1. $F(x_0, \alpha_0) = x_0$
2. $DF(x_0, \alpha_0)$ has eigenvalues λ with $|\lambda| \neq 1$,

then x_0 is called a hyperbolic fixed point and it is known that for $\alpha \simeq \alpha_0$, there exists x_α fixed point of $F(x_\alpha, \alpha)$ of the same topological type of x_0. Otherwise, when (2) fails we call α_0 a bifurcation value.

Thus, bifurcation values of the map F must satisfy being fixed points of the map (8) and also a bifurcation condition Φ_{BIF}. Mathematically,

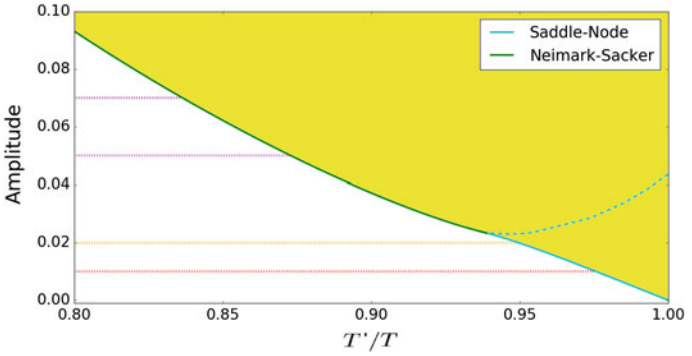

Fig. 7 Bifurcation diagram for the stroboscopic map F_A of the perturbed Wilson–Cowan system (4). Parameters used were the set $\mathscr{P}$ and $(P, Q) = (2.5, 0)$. Two bifurcations were found: Neimark-Sacker (green curve) and Saddle-Node (cyan curve). The solid line corresponds to a SN between a saddle and a stable node whereas the dashed line corresponds to a SN between a saddle and an unstable node. Constant amplitudes, for which rotation numbers in Fig. 6 were computed, were drawn respecting the same color code. Inside the yellow area there exists a stable fixed point for the map F_A corresponding to a 1:1 phase locking relationship

$$G(x, \alpha) = \begin{cases} F(x, \alpha) - x = 0 \\ \Phi_{BIF}(x, \alpha) = 0. \end{cases} \tag{9}$$

We look for bifurcations of the fixed points of the map defined in (6) for $q = 1$. We found two bifurcations of fixed points (see Fig. 7): Saddle-Node (*SN*) and Neimark-Sacker (*NS*). At it is well known, a SN bifurcation occurs when one of the real eigenvalues for the fixed point equals one, whereas a NS bifurcation occurs when a fixed point has a pair of complex eigenvalues whose modulus equals one. In a 2D system the conditions which must be satisfied at these bifurcation values are written as

$$\Phi_{SN} = det(DF - Id) = 0,$$
$$\Phi_{NS} = Tr(DF) - 1 = 0,$$

where we denote by DF the Jacobian matrix of the map F evaluated at the fixed point, whose computation requires the integration of a second order variational system [17].

Computations depicted in Fig. 7 also enlight the rotation number results shown in Fig. 6. One guesses that discontinuities on the rotation number in Fig. 6 can be caused by the disappearance of the invariant curve (which exists for small amplitudes) across a Neimark-Sacker bifurcation. To give a complete description of the dynamics, besides the computation of the fixed points and its bifurcations we are going to compute the invariant curves to check its persistence and relate its disappearance with the discontinuities observed in the rotation number curves.

3.4 Computation of Invariant Curves

As it was observed in Sect. 3.3, the computation of invariant curves is needed to provide a full description of the dynamics generated by the perturbation in (4). The framework developed in [5] allows us to compute a parameterization of the invariant curve Γ_A issuing from the unperturbed limit cycle γ. We now briefly review the method and refer the reader to [5] for a detailed description of the method.

Given a map $F : \mathbb{R}^2 \to \mathbb{R}^2$ having an invariant curve Γ_A, we look for a parameterization $K : \mathbb{T} \to \mathbb{R}^2$ of this invariant curve by solving the following invariance equation

$$F(K(\theta)) = K(f(\theta)), \tag{10}$$

where $K(\theta)$ and the dynamics inside the curve $f(\theta)$ are both unknown. Differentiating (10) we find the invariance equation for the tangent bundle $DK(\theta)$:

$$DF(K(\theta))DK(\theta) = DK(f(\theta))Df(\theta), \tag{11}$$

and imposing the invariance of the normal (stable) bundle of $K(\theta)$, denoted by $N(\theta)$, we have the following invariance equation

$$DF(K(\theta))N(\theta) = N(f(\theta))\Lambda_N(\theta), \tag{12}$$

where $\Lambda_N(\theta)$ denotes the linearised dynamics over $N(\theta)$.

In order to express in a more compact way the invariance equations (11) and (12) we introduce the matrices $P(\theta) = \big(DK(\theta)\ N(\theta)\big)$, and $\Lambda(\theta) = \mathrm{Diag}(Df(\theta), \Lambda_N(\theta))$:

$$DF(K(\theta))P(\theta) = P(f(\theta))\Lambda(\theta). \tag{13}$$

Therefore, if we express the linear map $DF(K(\theta))$ in the basis provided by $P(\theta)$, it becomes diagonal. Taking profit of this adapted invariant frame, a Newton method is performed. As it is usual in Newton methods, we assume given the approximation for the unknowns $K(\theta), f(\theta), N(\theta)$ and $\Lambda_N(\theta)$ and we compute better approximations:

$$\bar{K}(\theta) = K(\theta) + \Delta K(\theta), \tag{14}$$
$$\bar{f}(\theta) = f(\theta) + \Delta f(\theta), \tag{15}$$
$$\bar{N}(\theta) = N(\theta) + \Delta N(\theta), \tag{16}$$
$$\bar{\Lambda}_N(\theta) = \Lambda_N(\theta) + \Delta\Lambda_N(\theta). \tag{17}$$

To determine the correction terms $\Delta K(\theta)$, $\Delta f(\theta)$, $\Delta N(\theta)$, $\Delta\Lambda_N(\theta)$, the Newton method performed is split in two substeps. In the first one, we look for corrections $\Delta K(\theta)$ and $\Delta f(\theta)$. We begin by substituting expressions (14) and (15) into the invariance equation (10), and then expanding in Taylor series around K and f respectively and neglecting quadratically small terms, we obtain

$$0 = E(\theta) + DF(K(\theta))\Delta K(\theta) - DK(f(\theta))\Delta f(\theta) - \Delta K(f(\theta)) \tag{18}$$

where $E(\theta) = F(K(\theta)) - K(f(\theta))$ is the error for the approximated solution.

Writing Eq. (18) in the adapted frame provided by $P(\theta)$, that is, writing $\Delta K(\theta) = P(\theta)\xi(\theta)$, we obtain the following cohomological equation

$$\eta(\theta) = \Lambda(\theta)\xi(\theta) - \xi(f(\theta)) - \begin{pmatrix} \Delta f(\theta) \\ 0 \end{pmatrix}$$

where $\eta(\theta) = -(P(f(\theta)))^{-1}E(\theta)$ is the error of the approximate solution in the adapted frame. $\eta(\theta)$ is a vector which has tangent and normal components, each of them having different equations

$$\begin{aligned} \eta^T(\theta) &= \Lambda_T(\theta)\xi^T(\theta) - \xi^T(f(\theta)) - \Delta f(\theta), \\ \eta^N(\theta) &= \Lambda_N(\theta)\xi^N(\theta) - \xi^N(f(\theta)), \end{aligned}$$

where unknowns ξ^T and ξ^N, can be computed separately by means of a fixed point method.

So far, we have find the corrections $\Delta K(\theta)$ and $\Delta f(\theta)$. Then one can proceed to the second substep of the Newton method. Analogously to the first substep, by substituting the Eqs. (16) and (17) in the invariance equation (12) and applying the same methodology as in the first substep one can find the new corrections for the normal bundle $\Delta N(\theta)$ and its linearised dynamics $\Delta\Lambda_N(\theta)$. See [5] for more details.

We have reviewed the principal steps of the method. Next we are going to provide some details about the computation of the initial seeds for the Newton method in our problem. For a small perturbation, one can use as initial seed the invariant curve for the unperturbed system. Having an unperturbed system which displays a limit cycle $\gamma(t)$ of period T, we can define $\theta = \frac{t}{T}$ as an angular variable which parameterizes the limit cycle $\Gamma_0(\theta) = \gamma(\theta T)$. Therefore, as initial seed for the parameterization K and the dynamics on it when A is small we will take $K_0(\theta) = \Gamma_0(\theta)$ and $f_0(\theta) = \theta + \frac{T'}{T}$.

In order to find an initial seed for the normal bundle and its dynamics, we need to compute the derivative of the limit cycle respect its normal bundle direction. For that aim we use methods in [10], which provide an analytical solution for the value of that derivative. In particular they parameterize the stable manifold $\mathscr{M}$ of the unperturbed limit cycle γ by using an angular variable θ over the limit cycle and a variable σ which moves in the transverse direction to the limit cycle. Dynamics of both variables θ and σ are given by:

$$\begin{aligned} \dot{\theta} &= 1/T, \\ \dot{\sigma} &= \lambda\sigma/T, \end{aligned} \tag{19}$$

where T and λ are the period and the characteristic exponent of the limit cycle γ respectively. By using variables θ and σ we look for a parameterization for $\mathscr{M}$ $K(\theta, \sigma)$ such that, by (19):

$$\left(\frac{1}{T}\partial_\theta + \frac{\lambda\sigma}{T}\partial_\sigma\right) K(\theta,\sigma) = X(K(\theta,\sigma)), \tag{20}$$

where X is the vector field (1). Expanding $K(\theta,\sigma)$ one gets:

$$K(\theta,\sigma) = K_0(\theta) + \sigma K_1(\theta) + \mathcal{O}(\sigma^2), \tag{21}$$

were it is clear that $K_0 = \Gamma_0$, and by using (19) it is easy to see that

$$F(K(\theta,\sigma)) = K\left(\theta + \frac{T'}{T}, \sigma e^{\frac{\lambda T'}{T}}\right), \tag{22}$$

and therefore, differentiating (22) respect to σ:

$$\frac{\partial F(K(\theta,\sigma))}{\partial\sigma}_{|_{\sigma=0}} = DF(K_0(\theta))K_1(\theta) = e^{\frac{\lambda T'}{T}} K_1(\theta), \tag{23}$$

and comparing expressions (23) and (12) it is clear that over the unperturbed limit cycle, $N(\theta) = K_1(\theta)$ and $\Lambda_N(\theta) = e^{\frac{\lambda T'}{T}}$.

In [10] is demonstrated that to obtain $K_1(\theta)$ is only necessary to compute the fundamental matrix $\Phi(t)$ ($\Phi(0) = Id$), of the variational equations on the periodic $\gamma(t)$. Then, if we denote by v the eigenvector of the monodromy matrix $\Phi(T)$ associated to the eigenvalue e^{λ}, $K_1(\theta)$ is given by $K_1(\theta) = e^{-\lambda\theta}\Phi(T\theta)v$.

In order to explain rotation number discontinuities we apply this method to compute invariant curves for system (4) which complete the bifurcation diagram analysis in Fig. 7. If we fix $\frac{T'}{T} = 0.965$ we expect to cross a SN bifurcation for an amplitude $A_{SN} \simeq 0.014$. This is exactly what Fig. 8 shows: for a value of $A = 0.01 < A_{SN}$ there exists an invariant curve whose dynamics have no crossings with the fixed points of $f(\theta) = \theta$. By contrast for $A = 0.02 > A_{SN}$ two crossings appear between $f^A(\theta)$ and $f(\theta) = \theta$ indicating the presence of two fixed points over the invariant curve. This can be seen in another way when looking at the rotation number results: for $A = 0.01$ rotation number was different from 1, whereas it was equal to 1 for $A = 0.02$ which showed fixed points.

By contrast when fixing $\frac{T'}{T} = 0.85$ a NS bifurcation is expected to be crossed at $A \simeq 0.062$. This is exactly what Fig. 9 shows: as the amplitude is increased, the invariant curve shrinks, but there are no crossings between the dynamics $f^A(\theta)$ and the line of fixed points. These results are consistent with rotation number results in Fig. 6. When looking at values of ρ at $\frac{T'}{T} = 0.85$, when $A = 0.05 < A_{NS}$ a rotation number different from one appears as it is expected in an invariant curve with no fixed points over it. By contrast, for $A = 0.07 > A_{NS}$ as there is no invariant curve, rotation number calculations do not work. Nevertheless, a value for $\rho(0.85) = 1$ was computed. This result is a consequence of having a fixed point dynamics calculated assuming that an orientation preserving map is defined. So, although the dynamics tend to a fixed point we assume that each iteration of the map gives a complete revolution before returning to the fixed point.

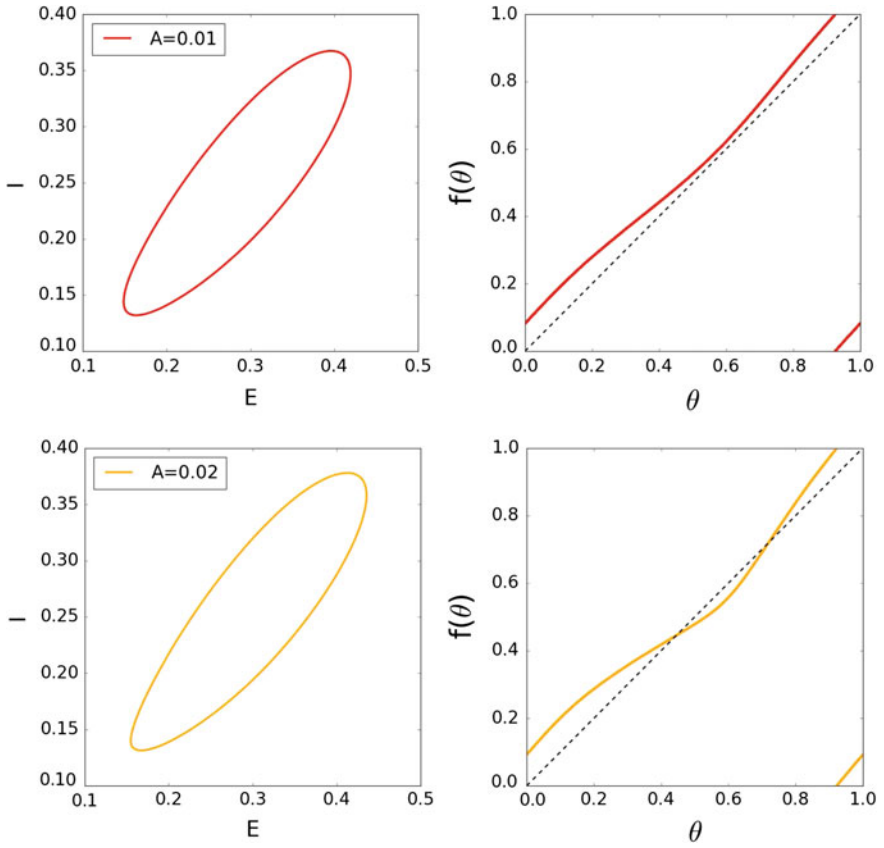

Fig. 8 (Left) Invariant curve for the stroboscopic map with different amplitudes and $\frac{T'}{T} = 0.965$. (Right) Dynamics $f(\theta)$ over the invariant curve

4 Dynamics of the Stroboscopic Map

Section 3 was devoted to the introduction of the stroboscopic map, its invariant objects and its bifurcations, providing techniques to compute all of them. In this section we aim at using all the tools provided in Sect. 3 to give a full description of the stroboscopic map dynamics for the perturbed system (4) close to the 1:1 phase-locking area by describing the evolution of all invariant objects of the system. Finally, will distinguish asynchronous from synchronous areas and study its implications for neuroscience.

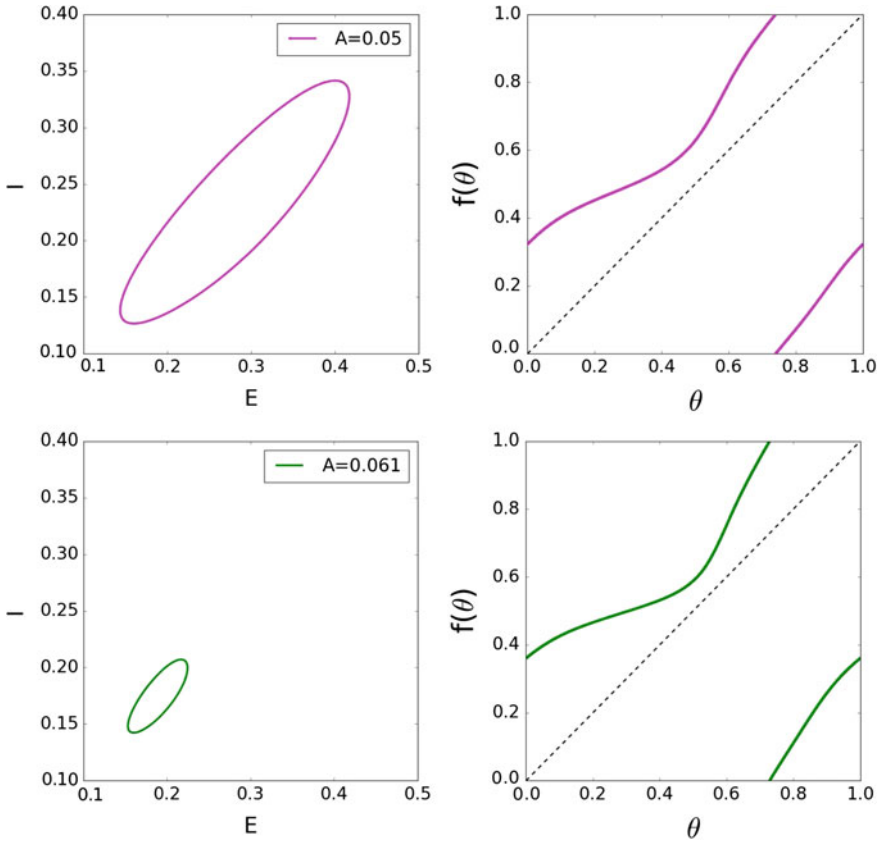

Fig. 9 (Left) Invariant curve for the stroboscopic map with different amplitudes and $\frac{T'}{T} = 0.85$. (Right) Dynamics $f(\theta)$ over the invariant curve

4.1 Phase Space Analysis

As the bifurcation analysis in Fig. 7 shows, there exist two possible bifurcations depending on the period T' and the amplitude of the perturbation: a Neimark-Sacker (NS) and a Saddle-Node (SN) bifurcation. Moreover, a Bogdanov-Takens bifurcation occurs at $(A, \frac{T'}{T}) \simeq (0.023, 0.9388)$ delimiting the NS and SN bifurcation curves. As different bifurcations will generate different dynamics, we will present phase portraits for the stroboscopic map at the crossing of both bifurcations in order to provide a description of the dynamics of the system (4) close to resonance 1:1. More precisely, we will restrict the analysis of dynamics to the range of $\frac{T'}{T}$ values that we have shown in Fig. 7, this is from 0.8 to 1 where the rotation number presented discontinuities.

For values of T' such that $0.9388 < \frac{T'}{T} < 1$, the phase portrait for system (4) can be seen in Fig. 10. In region A_1, the attracting invariant curve Γ_A generated from

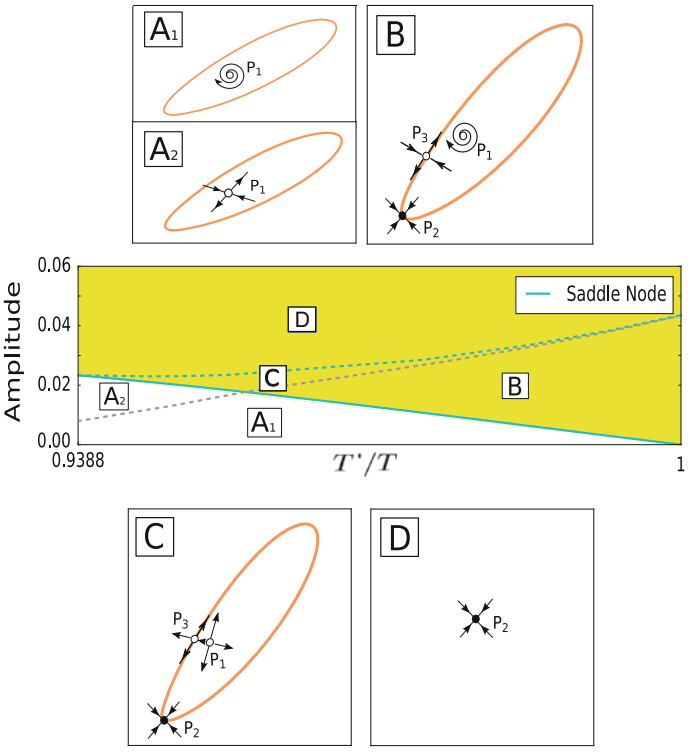

Fig. 10 Dynamics when a Saddle-Node bifurcation is crossed. Fixed points and invariant curves were computed using provided numerical methods

unperturbed limit cycle γ has no fixed points of F_A, and an unstable focus P_1 exists inside Γ_A. Once the Saddle-Node bifurcation (solid blue line) is crossed (region B), there appear two fixed points on the invariant curve Γ_A: a stable node P_2 and a saddle P_3. The invariant curve consists of the union of the saddle P_3, its unstable invariant manifolds, and the stable node P_2. When increasing the amplitude (region C), P_1 becomes an unstable node (dashed gray line). If the amplitude is increased further, P_1 will coalesce with P_3 in a unstable Saddle-Node bifurcation (dashed blue line) leaving the stable node P_2 as the unique fixed point (region D). As one may note it is possible to pass from area A_1 to area C, without passing from B. When entering in the area A_2 the unstable focus P_1 can become an unstable node before crossing the SN bifurcation.

For values of T' such that $0.8 < \frac{T'}{T} < 0.9388$, the phase portrait for system (4) can be seen in Fig. 11. The attracting invariant curve Γ_A has no fixed points of F_A, and an unstable focus P_1 exists inside Γ_A (region A). As the amplitude A is increased, this situation persists until we reach the Neimark-Sacker bifurcation (green curve), where the curve Γ_A collapses with P_1 and disappears while P_1 becomes a stable focus (region B).

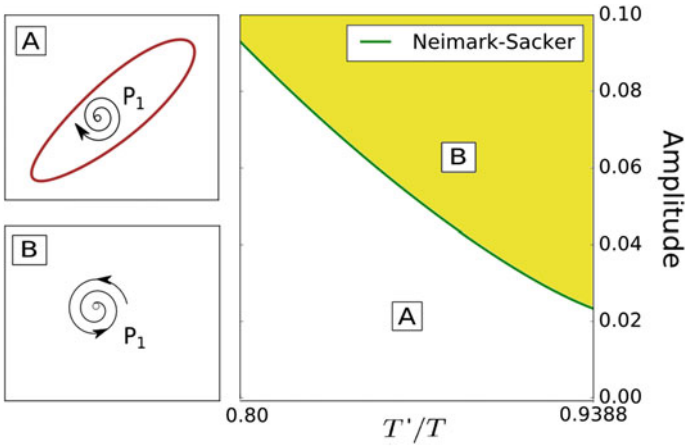

Fig. 11 Dynamics when a Neimark-Sacker bifurcation is crossed. Fixed points and invariant curves were computed using provided numerical methods

Phase space analysis performed gives a fully understanding of the dynamics for the perturbed system (4), demonstrating the presence of a fixed point for the map F_A and thus explaining discontinuities and results for rotation number. For a given amplitude, discontinuities in the rotation number are expected to appear for the exact value of $\frac{T'}{T}$ for which a NS bifurcation appears.

4.2 From Synchronous to Asynchronous Behaviour

As fixed points for the stroboscopic map correspond to periodic orbits of the system (4), the disappearance of stable fixed points across bifurcations separates the synchronous from the asynchronous regime. Computing the bifurcation curves of system (4) is the most natural way for delimiting and studying a given phase locking relationship. In Fig. 12 we show the stable solutions for a synchronous and an asynchronous state. It can be seen how the phase or time lag between the system and the perturbation is constant in the synchronous regime whereas it is not the case in the asynchronous.

As various theories suggest synchrony between oscillating activity of two neuronal populations may have very important implications in neural communication [13]. In particular, this time lag difference may underlie a possible mechanism for selection of transmitted information [8].

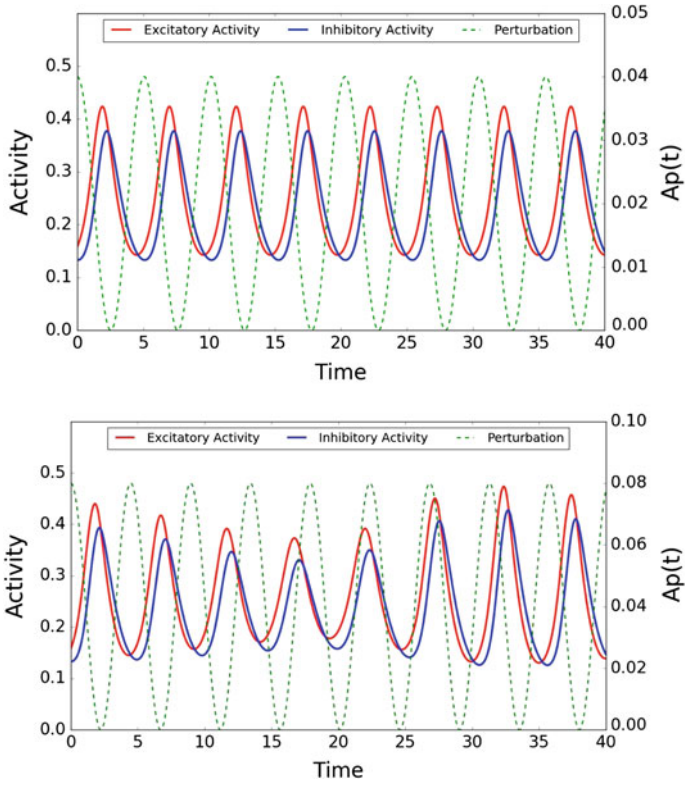

Fig. 12 (Top) Synchronous solution of system (4) for $A = 0.02$ and $\frac{T'}{T} = 0.965$. (Bottom) Asynchronous solution of system (4) for $A = 0.04$ and $\frac{T'}{T} = 0.85$

5 Summary

We have considered a periodic perturbation of the Wilson–Cowan equations and we have looked for synchronous and asynchronous regimes. In particular, we have studied phase locking relationships through the rotation number. Computations of this magnitude showed discontinuities which have been understood through the computation of the main invariant objects (fixed points and invariant curves) of the stroboscopic map close to the resonance 1:1. We have shown how powerful computational methods for invariant curves provide a further understanding of the dynamics generated by a periodic perturbation. Thus, this work aims at providing powerful tools to study interactions of brain rhythms in the brain.

Acknowledgements A.P, G.H and T.S acknowledge financial support from the Spanish MINECO-FEDER Grants MTM2012-31714, MTM2015-65715-P and the Catalan Grant 2014SGR504.

References

1. Arrowsmith, D.K., Place, C.M.: An Introduction to Dynamical Systems. Cambridge University Press, Cambridge (1990)
2. Berger, H.: Über das elektrenkephalogramm des menschen. Arch. Psychiat. Nerven. **87**(1), 527–570 (1929)
3. Borisyuk, R.M., Kirillov, A.B.: Bifurcation analysis of a neural network model. Biol. Cybern. **66**(4), 319–325 (1992)
4. Buzsáki, G., Draguhn, A.: Neuronal oscillations in cortical networks. Science **304**(5679), 1926–1929 (2004)
5. Canadell, M., Haro, A.: Parameterization method for computing quasi-periodic reducible normally hyperbolic invariant tori. In: F. Casas, V. Martínez (eds.) Advances in Differential Equations and Applications, vol. 4, pp. 85–94. Springer, Berlin (2014)
6. Dayan, P., Abbott, L.F.: Theoretical Neuroscience. Computational Modeling of Neural Systems. MIT Press, Cambridge (2001)
7. Fries, P.: A mechanism for cognitive dynamics: neuronal communication through neuronal coherence. Trends Cogn. Sci. (Regul. Ed.) **9**(10), 474–480 (2005)
8. Fries, P., Reynolds, J.H., Rorie, A.E., Desimone, R.: Modulation of oscillatory neuronal synchronization by selective visual attention. Science **291**(5508), 1560–1563 (2001)
9. Gambaudo, J.M.: Perturbation of a Hopf bifurcation by an external time-periodic forcing. J. Differ. Equ. **57**(2), 172–199 (1985)
10. Guillamon, A., Huguet, G.: A computational and geometric approach to phase resetting curves and surfaces. SIAM J. Appl. Dyn. Syst. **8**(3), 1005–1042 (2009)
11. Haro, À., Canadell, M., Figueras, J.L., Luque, A., Mondelo, J.M.: The Parameterization Method for Invariant Manifolds. Springer, Berlin (2016)
12. Hoppensteadt, F.C., Izhikevich, E.M.: Weakly connected neural networks. In: Mardsen, J.E., Sinovich, L., John, F. (eds.) Applied Mathematical Sciences, vol. 126. Springer Science & Business Media, New York (1997)
13. Niebur, E., Hsiao, S.S., Johnson, K.O.: Synchrony: a neuronal mechanism for attentional selection? Curr. Opin. Neurobiol. **12**(2), 190–194 (2002)
14. Pinto, D.J., Brumberg, J.C., Simons, D.J., Ermentrout, G.B., Traub, R.: A quantitative population model of whisker barrels: re-examining the Wilson-Cowan equations. J. Comput. Neurosci. **3**(3), 247–264 (1996)
15. Roberts, M.J., Lowet, E., Brunet, N.M., Ter Wal, M., Tiesinga, P., Fries, P., De Weerd, P.: Robust gamma coherence between macaque V1 and V2 by dynamic frequency matching. Neuron **78**(3), 523–536 (2013)
16. Seara, T.M., Villanueva, J.: On the numerical computation of Diophantine rotation numbers of analytic circle maps. Physica D **217**(2), 107–120 (2006)
17. Simó, C.: On the analytical and numerical approximation of invariant manifolds. In: Les Méthodes Modernes de la Mécanique Céleste. Modern Methods in Celestial Mechanics, vol. 1, pp. 285–329 (1990)
18. Tiesinga, P., Sejnowski, T.J.: Cortical enlightenment: are attentional gamma oscillations driven by ING or PING? Neuron **63**(6), 727–732 (2009)
19. Veltz, R., Sejnowski, T.J.: Periodic forcing of inhibition-stabilized networks: nonlinear resonances and phase-amplitude coupling. Neural. Comput. **27**(12), 2477–2509 (2015)
20. Wilson, H.R., Cowan, J.D.: Excitatory and inhibitory interactions in localized populations of model neurons. Biophys. J. **12**(1), 1–24 (1972)

Part II
Optics

Solitary Waves on Graphene Superlattices

Francisca Martin-Vergara, Francisco Rus and Francisco R. Villatoro

Abstract This chapter reviews the basic theoretical aspects of the propagation of solitary electromagnetic waves in graphene superlattices, a one atom thick sheet of graphene deposited on a superlattice, made by several periodically alternating layers of SiO_2 and h-BN. The electronic band structure of graphene and the techniques of band gap engineering are briefly presented. The analysis of the electronic properties of graphene superlattices by using both the transfer matrix method and the Kronig–Penny model are summarized. The nonlinear wave equation for the vector potential of the electromagnetic wave field is derived. This graphene superlattice equation (GSLeq) generalizes the sine-Gordon equation (sGeq). Hence, it also has kink and antikink solutions propagating at a constant speed. There is no closed-form expression for their shape. A straightforward asymptotic method is applied in order to analytically approximate its shape. The interactions of kinks and antikinks is studied by using a numerical method, the Strauss–Vázquez, which is a conservative, finite difference scheme. This numerical method is second-order accurate in both space and time, and nonlinearly stable, exactly conserving a discrete energy. Extensive numerical results for the kink–antikink interactions are presented as a function of a asymptotic parameter. For small values of this parameter, the interaction is apparently elastic, without noticeable radiation, being very similar to that expected for the sGeq. For large values of the asymptotic parameter, the inelasticity of the interaction results in the emission of wavepackets of radiation. In summary, the whole set of results suggest that the GSLeq behaves as a nearly integrable perturbation of the sGeq. Consequently, graphene superlattices can be used to study nonlinear wave phenomena with electromagnetic waves in the THz scale.

F. Martin-Vergara (✉) · F. Rus · F.R. Villatoro
Dept. Lenguajes y Ciencias de la Computación, Escuela de Ingenierías Industriales, Universidad de Málaga, Ampliación del Campus de Teatinos, 29071 Málaga, Spain
e-mail: fmarver@uma.es

F. Rus
e-mail: rusman@lcc.uma.es

F.R. Villatoro
e-mail: villa@lcc.uma.es

J. F. R. Archilla et al. (eds.), *Nonlinear Systems, Vol. 2*, Understanding Complex Systems, https://doi.org/10.1007/978-3-319-72218-4_4

Keywords Topological solitons · Kinks · Sine–Gordon equation · Nonlinear Klein–Gordon equation · Graphene superlattices · Plasmonics · THz electromagnetic waves

1 Introduction

Graphene is a two-dimensional (2D) allotrope of carbon isolated in 2004 by the research group of Andre K. Geim and Konstantin S. Novoselov [18], a breakthrough awarded with the Nobel Prize in Physics 2010. This extraordinary material has remarkable mechanical, heat conduction, and electrical conduction properties. Some researchers consider that it can be the future of electronic and optoelectronic silicon industry. However, current devices are based on semiconductors, materials with a band gap, but graphene is gapless, a semimetal. The gap is a region of forbidden energies between the maximum energy of the valence band and minimum one of the conduction band. Fortunately, a gap can be engineered in graphene, for example, by placing on top of a properly selected substrate [29]. Thanks to this design transistors and other optoelectronic devices have been developed.

The non-linear electrodynamic response of 2D electrons and holes in graphene shows higher harmonics generation [16, 17]. The most relevant application is the generation of terahertz (THz) radiation by using a graphene superlattice [20]. This structure is formed by a graphene sheet deposited on periodically alternating strips of silicon dioxide (SiO_2, or any material that does not affect the band structure of graphene) and hexagonal boron nitride (h-BN, or any other material that introduces a band gap , like silicon carbide, SiC). The h-BN (SiC) layers are located so that its hexagonal crystal lattice is under the hexagonal crystal lattice of graphene so a band gap of up to 0.053 eV (0.26 eV) appears in the band structure of graphene.

Nonlinear solitary electromagnetic waves can propagate in a graphene superlattice subjected to sinusoidal electromagnetic radiation if radiation frequency is much larger than the plasma frequency, as shown by S.V. Kryuchkov and E.I. Kukhar' [9, 12]. By using the expression for the dimensionless energy of electron in the graphene superlattice obtained in Ref. [28], the nonlinear d'Alembert equation for the amplitude of the transversal component of the vector potential of the electromagnetic wave field results in a sine-Gordon equation (sGeq) [10]. Such equation propagates both cnoidal (written in terms of Jacobi elliptic functions) and sinusoidal waves.

For strong fields, a generalization of the sine-Gordon equation has been obtained in Ref. [11], hereon referred to as Graphene Superlattice equation (GSLeq), also referred to as Kryuchkov–Kukhar equation (KKeq). This chapter presents an asymptotic approximation to the shape function of kinks and antikinks of this equation. The method uses an ansatz based on the corresponding solutions of the sGeq. The study of the interactions of kinks and antikinks require the use of numerical methods. For illustration purposes only the Strauss–Vázquez method [24] is presented. This second-order method in space and time exactly conserves a discrete analog of the energy of the GSLeq, being nonlinearly stable. This numerical method is used to

assess the validity of the asymptotic solution. Finally, some examples of kink-antikink interactions are presented.

The contents of this chapter are as follows. Section 2 briefly reviews the electronic properties of graphene, including its gapless band structure and its gap engineering when placed on a proper substrate. Ratnikov's graphene superlattice is reviewed in Sect. 3, where the corresponding dispersion relation is derived using two procedures, a Kronig–Penney model for piecewise constant band gaps and a wavefunction overlapping method for a general modulation of the band gap. Both procedures result in the same approximation to the dispersion relation for low energy electrons. It is used in Sect. 4 to obtain the graphene superlattice equation for the nonlinear propagation of electromagnetic waves. The solitary waves solutions of this equation are asymptotically approximated in Sect. 5. A conservative, finite difference, numerical method is presented in Sect. 6, where its main properties are discussed. Section 7 is devoted to a brief summary of the numerical results obtained after an extensive analysis of the interactions between kinks and antikinks of the GSLeq. Finally, Sect. 8 summarizes our chapter and includes some further research to be done in the electromagnetic propagation of nonlinear waves in graphene superlattices.

2 Graphene

Graphene is made out of carbon atoms arranged on a honeycomb lattice with a distance $\tilde{a} = 0.142\,\text{nm}$ between nearest neighbor carbon atoms. This hexagonal structure is not a Bravais lattice, but it can be understood as a triangular lattice with two atoms in the unit cell (also as two overlapping triangular sublattices). Each carbon atom has four valence electrons; in graphene, three are in sp^2 hybridized orbitals forming strong covalent bonds with neighboring atoms, and the fourth one is in a $2p_z$ orbital forming π bonds. The electronic properties of graphene at low energies depend only on these π electrons that move freely on the lattice. Let us briefly review the band structure of graphene, the Dirac equation description for the carriers, and the basis of band gap engineering [2].

2.1 Gapless Graphene

The electronic band structure of graphene was first determined in 1947 by Philip R. Wallace [25] in order to understand graphite. The standard method to calculate the band structure of a solid is the use of the single electron approximation introduced in 1928 by Felix Bloch. Wallace used a further simplification, the tight-binding approximation (TBA), also referred to as linear combination of atomic orbitals (LCAO), developed by Gregory H. Wannier en 1937. In the TBA, the electrons are localized around the atoms of the lattice and electronic conduction results from the hopping of the electrons both to nearest (nn) and next nearest neighbor (nnn) atoms. In graphene,

electrons hop in the same sublattice (to nnn atoms) with hopping energy $E_{t'} \approx 0.3$ eV, which it is smaller than the $E_t \approx 3$ eV for hopping to a nn atom (between different sublattices). This process is described by a 2×2 Hamiltonian matrix $\mathrm{H}_{IJ}(\mathbf{p})$, where $I, J \in \{A, B\}$ are the labels of the two sublattices, and $\mathbf{p}$ is the momentum of the electrons. In graphene, both sublattices are identical, so $\mathrm{H}_{AA}(\mathbf{p}) = \mathrm{H}_{BB}(\mathbf{p})$; additionally, the complex conjugate equality $\mathrm{H}_{AB}(\mathbf{p}) = \mathrm{H}_{BA}(\mathbf{p})^*$ holds by symmetry. After taking the Fourier transform of the Hamiltonian matrix $\mathrm{H}_{IJ}(\mathbf{k})$ and applying the Bloch theorem, the final result is given by [25]

$$E_{\pm}(\mathbf{k}) = \pm E_t \sqrt{3 + f(\mathbf{k})} - E_{t'} f(\mathbf{k}) , \tag{1}$$

$$f(\mathbf{k}) = 2\cos\left(\sqrt{3}\, k_y\, \tilde{a}\right) + 4\cos\left(\frac{\sqrt{3}}{2} k_y\, \tilde{a}\right) \cos\left(\frac{3}{2} k_x\, \tilde{a}\right) ,$$

where the plus sign applies to the band above the Fermi level, the conduction (π^*) band for electrons, and the minus sign to that below the Fermi level, the valence (π) band for holes. Figure 1 shows these two bands [2].

The key feature of the graphene band structure is the appearance of Dirac points where the π and π^* bands touch each other in a double cone structure, referred to as Dirac cones. Figure 1 shows a zoom of one of the six Dirac cones. Strictly, only two of the Dirac points must be shown. The carbon lattice in the coordinate space is transformed into the reciprocal lattice in momentum coordinates. Correspondingly, the position of the two identical carbon atoms in the unit cell transform into two momentum points K and K' at the corners of the so-called Brillouin zone. The two bands with energy closer to the Fermi level cross exactly at these points since $\mathrm{H}_{AA}(\mathbf{k}) = \mathrm{H}_{BB}(\mathbf{k})$, hence the Dirac points are located at K and K'. The energy dispersion relation (1) for low energy electrons (less than ≈ 1 eV around the Fermi energy) is approximately linear (cone shaped). Concretely, it is given by

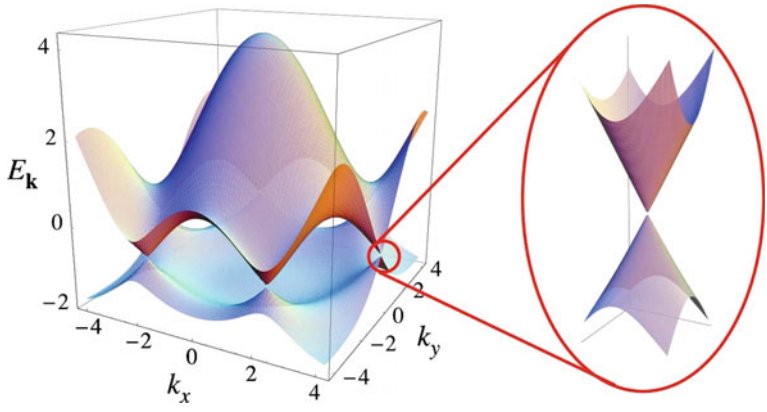

Fig. 1 Energy spectrum of the graphene calculated from its dispersion relation. Reproduced with permission from [2]. Copyright (2009) by the American Physical Society

$$E_{\pm}(\mathbf{k}) \approx \pm\hbar\, \upsilon_F(x)\, |\mathbf{k}|, \tag{2}$$

where $\mathbf{k}$ is the momentum measured relatively to either K or K' Dirac points, and the $\pm$ sign corresponds to the conduction and valence bands, respectively. This linear dispersion relation differs from the parabolic dispersion usual in solid-state physics, where the energy $E(\mathbf{k}) = |\mathbf{k}|^2/(2\,m^*)$, with m^* the effective electron mass. In such a case, the speed $\upsilon = k/m^* = \sqrt{2\,E/m^*}$ changes substantially with energy. Instead, the linear dispersion relation (2) corresponds to massless quasiparticles propagating with the Fermi speed $\upsilon_F(x)$ in graphene. This fact explains its very high electrical and thermal conductivities.

The energy dispersion (2) resembles the energy of ultra-relativistic particles, like massless neutrinos. In fact, the quasiparticles in graphene behave as massless, chiral, Dirac fermions, as discovered by Wallace [25]. They mimick the physics of quantum electrodynamics for massless fermions, except that they move with Fermi speed $\upsilon_F = 3\,E_t\,\tilde{a}/2 \simeq 1 \times 10^6$ m/s, i.e. 300 times smaller than the speed of light in vacuum. The appearance of the Dirac equation in graphene electronics can be explained as illustrated in Fig. 2 [4, 6]. The low energy quasiparticles have a momentum localized around a Dirac point, hence they have a (valley) pseudospin ξ, given by $\xi = +1$ for the K point (sublattice A) and $\xi = -1$ for the K' point (sublattice B). They also have a chirality η defined by the normalized projection of this pseudospin onto the momentum, given by $\eta = +1$ $(= -1)$ for the conduction band, $E > E_F$, in the K (K') point and $\eta = -1$ $(= +1)$ for the valence band, $E < E_F$, in the K (K') one; i.e. electrons (holes) are right- (left-)handed near K point and left- (right-)handed near K' one. Since the origin of the Dirac cones is the crossing of two bands associated to the π electrons, when a quasiparticle cross the Fermi level it cannot leave the original band, so it cannot change its chirality. Accordingly, a helicity (or absolute chirality) can be defined and fixed for each quasiparticle: they are right-handed for $\eta = +1$ and left-handed for $\eta = -1$. In analogy with massless neutrinos, graphene quasiparticles have one-half pseudospin and fixed helicity, being governed by the massless Dirac equation. And their wavefunction has four components labelled by (ξ, η), grouped into two pseudospinors labelled by ξ.

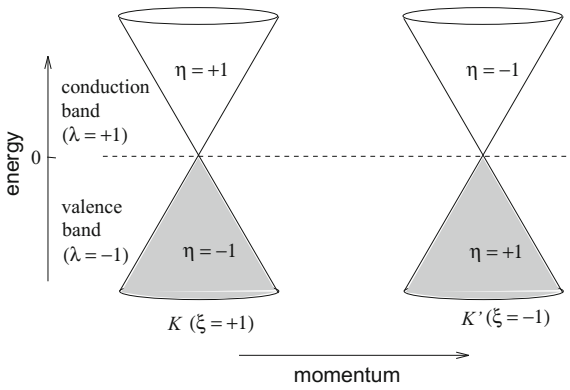

Fig. 2 Relation between band index $\lambda = \xi\,\eta$, pseudospin ξ, and chirality η in graphene. Reproduced with permission from [6]. Copyright (2011) by the American Physical Society

The electronic structure for low momentum quasiparticles is governed by the Dirac equation $\mathrm{H}(\mathbf{p})\,\Psi(\mathbf{x}) = E\,\Psi(\mathbf{x})$, with Hamiltonian

$$\mathrm{H}(\mathbf{p}) = \upsilon_F\,\mathbf{p}\cdot\sigma = \upsilon_F\,(p_x\,\sigma_x + p_y\,\sigma_y)\,,$$

where $\mathbf{p} = -\mathrm{i}\,\hbar\,\nabla$ is the momentum operator ($p_i = -\mathrm{i}\,\hbar\,\partial_i$), and σ_i are the Pauli matrices

$$\sigma_0 = \begin{pmatrix} 1 & 0 \\ 0 & 1 \end{pmatrix}, \quad \sigma_x = \begin{pmatrix} 0 & 1 \\ 1 & 0 \end{pmatrix}, \quad \sigma_y = \begin{pmatrix} 0 & -\mathrm{i} \\ \mathrm{i} & 0 \end{pmatrix}, \quad \sigma_z = \begin{pmatrix} 1 & 0 \\ 0 & -1 \end{pmatrix}.$$

Hence the Dirac-like Hamiltonian is given by

$$\mathrm{H} = \begin{pmatrix} 0 & -\mathrm{i}\,\hbar\,\upsilon_F\,(\partial_x - \mathrm{i}\,\partial_y) \\ \mathrm{i}\,\hbar\,\upsilon_F\,(\partial_x + \mathrm{i}\,\partial_y) & 0 \end{pmatrix}. \tag{3}$$

In momentum space, the two-component pseudospinors for the momentum around K and K' are given by the $\Psi_{\pm,K}(\mathbf{k})$ and $\Psi_{\pm,K'}(\mathbf{k})$, respectively, where the $\pm$ signs correspond to the eigenenergies $E = \pm\upsilon_F\,|\mathbf{k}|$.

2.2 Gapped Graphene

Graphene is gapless, but, fortunately, there are several routes to induce and control the appearance of a gap in graphene. The most practical is the interaction with a substrate having a honeycomb lattice in close alignment to that of the graphene. The mismatch led to a moiré pattern that breaks the symmetry between the graphene sublattices, i.e. the two carbon atoms in the unit cell, causing $\mathrm{H}_{AA}(\mathbf{k}) \neq \mathrm{H}_{BB}(\mathbf{k})$; consequently, the π and π^* bands do not cross at the K and K' points, a gap opens, and the quasiparticles adquire an effective mass. The Dirac Hamiltonian for graphene changes to $\mathrm{H} + m^*\,\upsilon_F\,\sigma_z$, with an energy spectrum at Dirac points given by

$$E_{\pm}(\mathbf{k}) \approx \pm\hbar\,\upsilon_F\,\sqrt{|\mathbf{k}|^2 + (m^*)^2}\,, \tag{4}$$

featuring a band gap of $E_g = 2\,m^*\,\upsilon_F^2$ at charge neutrality. This value is the energy required to create an electron-hole pair.

A band gap opens in graphene when properly aligned over a substrate of hexagonal boron nitride (hBN). The honeycomb lattice of hBN is isomorph of that of graphene, but with boron and nitrogen atoms occupying the A and B sublattices; in fact, hBN has a large band gap of 5.97 eV due to the different onsite energy of the B and N atoms. Graphene on hBN is three times less rough than on silicon dioxide (SiO_2), so it was originally proposed as a better substrate; moreover, for a random crystal-

lographic orientation of the graphene to this substrate no appreciable gap opening is measured [3]. However, when the hexagonal lattices of both materials are close to their orientational alignment, the natural 1.8% mismatch acts and a gap opens; ab initio calculations estimate a maximum gap of 53 meV [5]. This gap was first experimentally measured in 2012 [27]. Unfortunately, the gap measured in other experiments, even with a fine control of the angular alignment of both crystals, show a large variability and the values are usually smaller than 20 meV. The source of this intriguing conundrum has been recently explained [8]. The application of the theory of electronic many-body exchange interactions explain the observed gaps as a result of carbon atom relaxation and electron-electron interactions. Moreover, the electron-electron interactions introduce a variation of the Fermi velocity [26].

There are other routes to engineering a band gap in graphene, achieving values from about 10 meV up to 2.3 eV, as reviewed in Ref. [7]. In relation with the graphene superlattice discussed in this chapter, the most relevant is the large band gap that opens when graphene is grown epitaxially on silicon carbide (SiC), of up to 300 meV, with good parabolic energy bands [29]. Let us emphasize that other routes have also been used in the design of graphene superlattices. For example, the tunable gap up to 250 meV appearing in bi- and trilayer graphene with broken sublattice symmetry. The gap induced by periodic modulation of the electronic structure due to molecular adsorption onto a graphene sheet, with generates band gaps of up to 206 meV. And even the use of graphene nanoribbons, that result in the largest measured band gap of about 2.3 eV in a 7-hexagon width graphene nanoribbon [7].

3 Graphene Superlattices

The spatial modulation of the band gap in graphene can be attained by placing a sheet on a substrate fabricated from different dielectrics, i.e. using a graphene superlattice (GSL). Current literature presents a large number of proposals, but in this chapter only the GSL introduced in 2009 by Pavel V. Ratnikov [21] is considered. A one-dimensional (1D) graphene superlattice given by a graphene monatomic layer deposited on a strip substrate combined from SiO_2 (or any other dieletric not affecting the band structure of graphene) and hBN (or any other substrate that gaps the graphene, like SiC). The simplicity of the manufacture and control of the periodicity of Ratnikov's GSL is accompanied by the easy calculation of the band structure.

3.1 Piecewise Constant Gap Modulation

Figure 3 shows Ratnikov's GSL with a piecewise constant modulation of the parameters of the superlattice. The band structure can be calculated by using of the transfer matrix method [21]. Here, we will use a Kronig–Penney model based on Dirac equation [15]. Recently, the variation of the Fermi velocity due to electron-electron

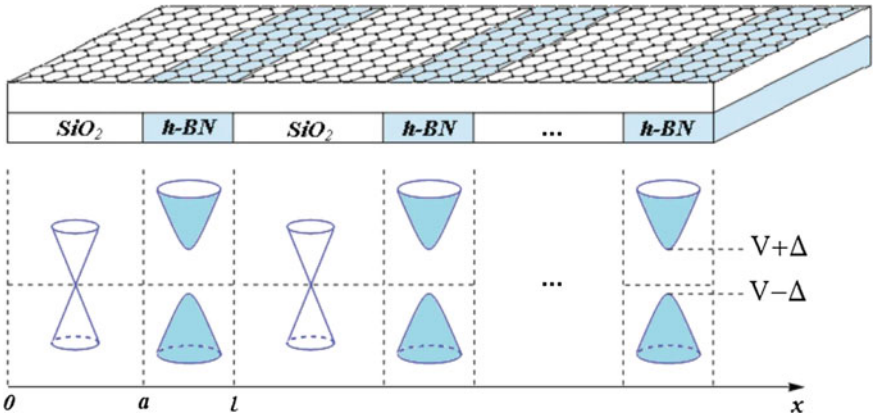

Fig. 3 Top: graphene layer on the striped substrate composed of silicon oxide and hexagonal boron nitride. Bottom: schematic diagram showing the electronic energy spectrum in graphene SL. Reproduced with permission from [15]. Copyright (2012) by the American Physical Society

interactions in graphene on hBN has been taken into account by several authors [14, 22]. We also consider it in this section.

The massless fermion quasiparticles are subjected to a position-dependent band gap and band shift in the superlattice period l. Hence, the electronic structure for low momentum quasiparticles is governed by the Dirac-like Hamiltonian

$$\begin{aligned} \mathrm{H} &= \upsilon_F(x)\,(p_x\,\sigma_x + p_y\,\sigma_y) + \Delta(x)\,\sigma_z + V(x)\,\sigma_0 \\ &= \begin{pmatrix} V(x)+\Delta(x) & -\mathrm{i}\,\hbar\,\upsilon_F(x)\,(\partial_x - \mathrm{i}\,\partial_y) \\ \mathrm{i}\,\hbar\,\upsilon_F(x)\,(\partial_x + \mathrm{i}\,\partial_y) & V(x)-\Delta(x) \end{pmatrix}, \end{aligned} \tag{5}$$

where $\Delta(x)$ is the half-width of the band gap, and $V(x)$ is the shift of the forbidden band center in the gapped graphene with respect to the Dirac point in the gapless graphene. The l-periodic functions $\Delta(x)$ and $V(x)$ are incorporated into Eq. (5) as a scalar potential and a time-like vector potential, respectively. For simplicity, it is assumed that $\Delta(x)$, $V(x)$, and $\upsilon_F(x)$ are piecewise-constant functions.

The solution of the Dirac equation $\mathrm{H}\,\Psi(x, y) = E\,\Psi(x, y)$, thanks to translation invariance in the y direction, can be separated into $\Psi(x, y) = \exp(\mathrm{i}\,k_y\,y)\,\Psi(x)$, where the two-component pseudospinor function $\Psi(x)$ satisfies the differential equation

$$\mathrm{i}\,\frac{d\Psi}{dx} = \mathrm{h}(x)\,\Psi(x)\,, \tag{6}$$

with

$$\begin{aligned} \mathrm{h}(x) &= \sigma_x^{-1}\,\sigma_y\,k_y + \sigma_x^{-1}\,\sigma_0\,\frac{V(x)-E}{\hbar\,\upsilon_F(x)} + \sigma_x^{-1}\,\sigma_z\,\frac{\Delta(x)}{\hbar\,\upsilon_F(x)} \\ &= \mathrm{i}\,\sigma_z\,k_y + \sigma_x\,\frac{V(x)-E}{\hbar\,\upsilon_F(x)} - \mathrm{i}\,\sigma_y\,\frac{\Delta(x)}{\hbar\,\upsilon_F(x)} \\ &= \begin{pmatrix} \mathrm{i}\,k_y & \dfrac{V(x)-E-\Delta(x)}{\hbar\,\upsilon_F(x)} \\ \dfrac{V(x)-E+\Delta(x)}{\hbar\,\upsilon_F(x)} & -\mathrm{i}\,k_y \end{pmatrix}. \end{aligned} \tag{7}$$

The Bloch's theorem states that the solution of the Eq. (6) in the l-period holds $\Psi(l) = \exp(\mathrm{i}\,k\,l)\,\Psi(0)$, where k is the Bloch wave vector determined by the dispersion relation of the graphene superlattice, to be calculated as follows. The formal solution of Eq. (6) is

$$\Psi(x) = \mathrm{T}(x;x_0)\,\Psi(x_0)\,, \qquad \mathrm{T}(x;x_0) = \exp\left(-\mathrm{i}\,(x-x_0)\,\mathrm{h}(x)\right)\,, \tag{8}$$

where $\mathrm{h}(x)$ is constant when both points x and x_0 belong to the same space-homogeneous region, i.e. either $\mathrm{h}(x) = \mathrm{h}(0^+)$ for $0 < x_0 < x < a$, with $\Delta(x) = V(x) = 0$, and $\upsilon_F(x) = \upsilon_{F,0a}$, or $\mathrm{h}(x) = \mathrm{h}(l^-)$ for $a < x_0 < x < l$, with $\Delta(x) = \Delta_0$, $V(x) = V_0$, and $\upsilon_F(x) = \upsilon_{F,al}$.

The solution of Eq. (6) in the l-period is given by

$$\Psi(l) = \mathbf{T}(l;0)\,\Psi(0) = \mathbf{T}(l;a)\,\mathbf{T}(a;0)\,\Psi(0)\,.$$

The exponential of the matrix $\mathrm{h}(x)$ can be easily calculated taking into account that

$$\mathrm{h}^2(x) = K^2(x)\,\sigma_0\,, \qquad K^2(x) = \frac{(V(x)-E)^2 - \Delta^2(x)}{(\hbar\,\upsilon_F(x))^2} - k_y^2\,. \tag{9}$$

Hence, all even powers of the matrix h are proportional to σ_0, while all odd powers are proportional to h itself. Therefore, a straightforward calculation shows that

$$\mathrm{T}(x;x_0) = \sigma_0\,\cos\alpha(x) - \mathrm{i}\,\mathrm{h}(x)\frac{\sin\alpha(x)}{K(x)}\,, \tag{10}$$

where $\alpha(x) = (x-x_0)\,K(x)$. In matrix form we have

$$\begin{aligned} \mathrm{T}(a;0) &= \exp(-\mathrm{i}\,a\,\mathrm{h}(0^+)) \\ &= \begin{pmatrix} \cos(k_x\,a) + \dfrac{k_y}{k_x}\sin(k_x\,a) & \mathrm{i}\,\sin(k_x\,a)\dfrac{E}{\hbar\,\upsilon_{F,0a}\,k_x} \\ \mathrm{i}\,\sin(k_x\,a)\dfrac{E}{\hbar\,\upsilon_{F,0a}\,k_x} & \cos(k_x\,a) - \dfrac{k_y}{k_x}\sin(k_x\,a) \end{pmatrix}, \end{aligned}$$

where

$$k_x = K(0^+) = \frac{1}{\hbar\, v_{F,0a}} \sqrt{E^2 - (\hbar\, v_{F,0a}\, k_y)^2}\,,$$

and, similarly,

$$\begin{aligned} \mathrm{T}(l;a) &= \exp(-\mathrm{i}\,\bar{a}\,\mathrm{h}(l^-)) \\ &= \begin{pmatrix} \cos(q_x\,\bar{a}) + \dfrac{k_y}{q_x}\sin(q_x\,\bar{a}) & -\mathrm{i}\,\sin(q_x\,\bar{a})\dfrac{V_0 - E - \Delta_0}{\hbar\, v_{F,al}\, q_x} \\ -\mathrm{i}\,\sin(q_x\,\bar{a})\dfrac{V_0 - E + \Delta_0}{\hbar\, v_{F,al}\, q_x} & \cos(q_x\,\bar{a}) - \dfrac{k_y}{q_x}\sin(q_x\,\bar{a}) \end{pmatrix}, \end{aligned}$$

where $\bar{a} = l - a$, and

$$q_x = K(l^-) = \frac{1}{\hbar\, v_{F,al}} \sqrt{(V_0 - E)^2 - \Delta_0^2 - (\hbar\, v_{F,al}\, k_y)^2}\,.$$

Note that for $(V_0 - E)^2 - \Delta_0^2 < (\hbar\, v_{F,al}\, k_y)^2$, the wave number q_x is imaginary, and in such a case usually q_x is replaced by $\mathrm{i}\,|q_x|$.

The dispersion relation for the graphene superlattice is obtained from the Bloch condition $\exp(\mathrm{i}\,k\,l)\,\Psi(0) = \mathbf{T}(l;a)\,\mathbf{T}(a;0)\,\Psi(0)$, by equating the real part of the left-hand side and the trace of the right-hand side, i.e. $2\cos(k\,l) = \mathrm{Tr}(\mathrm{T}(l;a)\,\mathrm{T}(a;0))$, resulting in

$$\begin{aligned} \cos(k\,l) &= \cos(k_x\,a)\,\cos(q_x\,\bar{a}) \\ &\quad + \frac{E\,V_0 - E^2 - v_{F,0a}\,v_{F,al}\,(\hbar\,k_y)^2}{\hbar^2\, v_{F,0a}\, v_{F,al}\, k_x\, q_x}\,\sin(k_x\,a)\,\sin(q_x\,\bar{a})\,. \end{aligned} \tag{11}$$

This dispersion relation is a transcendental equation for the energy $E(k, k_y)$ since $k_x \equiv k_x(E, k_y)$ and $q_x \equiv q_x(E, k_y)$. Its solution requires numerical methods.

The detailed analysis of the dispersion relation (11) is outside the scope of this chapter. Let us summarize the main results [1, 15, 21] in the case that the Fermi level is between the conduction and valence bands at any V_0 (valid for hBN, but not for SiC without external dc bias). When $V_0 = 0$, the conduction and valence bands are located symmetrically with respect to $E = 0$, as in the gapless graphene. As V_0 increases, these bands gradually shift up, and the gap width at the center ($k = k_y = 0$) increases until a critical value $V_0 = V_c$ is reached; then the superlattice becomes gapless with two extra Dirac points appearing in symmetric positions on the k_y-axis. Further increase of V_0 results in formation of new additional cone-like Dirac points which originate from $k_y = 0$.

In order to perform further analytical calculations, the dispersion relation (11) must be approximated by using some reasonable hypothesis. For low energy excitations, usually $a\,E \ll \hbar\, v_{F,0a}$, and $\bar{a}\,E \ll \hbar\, v_{F,al}$; in such a case $k_x \ll k_y$ and $q_x \ll k_y$, so the carriers propagate like in a periodic planar array formed by parallel nanowires;

i.e. they only move along the gapped graphene strips, but do not move between the gapless graphene strips [21, 28]. In such a case, the cosine and sine functions in Eq. (11) can be linearized yielding

$$\cos(k\,l) = 1 + \frac{a\,\bar{a}}{\hbar^2\,\upsilon_{F,0a}\,\upsilon_{F,al}}\left(E\,V_0 - E^2 - \upsilon_{F,0a}\,\upsilon_{F,al}\,(\hbar\,k_y)^2\right)\,. \tag{12}$$

The solution of this quadratic equation on the energy results in

$$E(k,k_y) = E_w \pm \sqrt{\Gamma^2 - \upsilon_{F,0a}\,\upsilon_{F,al}\,\hbar^2\,k_y^2 + \Upsilon^2\,(1-\cos(k\,l))}\,. \tag{13}$$

where

$$E_w = \frac{V_0}{2}\,,\qquad \Gamma^2 = \frac{V_0^2}{4}\,,\qquad \Upsilon^2 = \frac{\upsilon_{F,0a}\,\upsilon_{F,al}\,\hbar^2}{a\,\bar{a}}\,. \tag{14}$$

3.2 General Periodic Gap Modulation

Figure 4 shows an arbitrary periodic modulation of the band gap for the Ratnikov's GSL, as considered in Ref. [11]. The Dirac equation for the electrons in the GSL is given by

$$\left(\upsilon_F\,(p_x\,\sigma_x + p_y\,\sigma_y) + \Delta(x)\,\sigma_z\right)\,\Psi = E\,\Psi\,, \tag{15}$$

where $\Delta(x)$ is an l-periodic function, not necessarily piecewise constant; for simplicity we have taken $V(x) = 0$ and $\upsilon_F(x)$ constant. The solution of Eq. (15) can be expanded in a linear combination of two-component pseudospinors given by

$$\Psi(x,\,y) = \exp(\mathrm{i}\,k_y\,y)\,\sum_n a_n\,\psi_n(x - n\,l)\,, \tag{16}$$

whose coefficients a_n are determined by the Bloch theorem as $a_n = \exp(\mathrm{i}\,n\,k\,l)$. Let us assume that the energy E_w of the electrons at the central gapless region in the

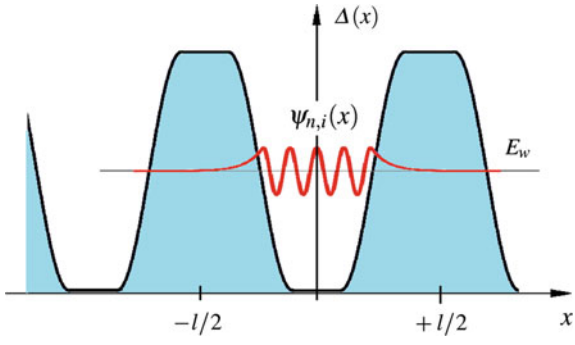

Fig. 4 Scheme of a general periodic modulation of the band gap of the graphene superlattice

potential wells behaves as if there is no superlattice, i.e. the Dirac equation reduces to $\upsilon_F\, p_x\, \sigma_x\, \psi_n = E_w\, \psi_n$. Substracting this equation to Eq. (15) results in

$$\sum_n a_n\, \hat{\mathrm{H}}\, \psi_n = (E(\mathbf{k}) - E_w) \sum_n a_n\, \psi_n\,, \tag{17}$$

where

$$\hat{\mathrm{H}} = \begin{pmatrix} \Delta(x) & -\mathrm{i}\,\hbar\,\upsilon_F\, k_y \\ \mathrm{i}\,\hbar\,\upsilon_F\, k_y & -\Delta(x) \end{pmatrix}, \qquad \psi_n = \begin{pmatrix} \psi_{n,A} \\ \psi_{n,B} \end{pmatrix}. \tag{18}$$

Since $\hat{\mathrm{H}}^2 = (\Delta^2(x) + (\hbar\,\upsilon_F\, k_y)^2)\,\sigma_0$, the multiplication of both sides of Eq. (17) by $\hat{\mathrm{H}}$ yields

$$(\Delta^2(x) + (\hbar\,\upsilon_F\, k_y)^2) \sum_n a_n\, \psi_{n,i} = (E(\mathbf{k}) - E_w)^2 \sum_n a_n\, \psi_{n,i}\,. \tag{19}$$

The dispersion relation is given by

$$\sum_n a_n\, W_n = \left((E(\mathbf{k}) - E_w)^2 - (\hbar\,\upsilon_F\, k_y)^2\right) \sum_n a_n\, S_n\,, \tag{20}$$

where

$$S_n = S_{-n} = \int_0^l \psi_{n,i}(x - n\,l)\, \psi_{n,i}(x)\, dx\,,$$

$$W_n = W_{-n} = \int_0^l \Delta^2(x)\, \psi_{n,i}(x - n\,l)\, \psi_{n,i}(x)\, dx\,.$$

The dispersion relation (20) is equivalent to Eq. (11) in the piecewise constant case.

Let us approximate the dispersion relation (20) down to the same order of Eq. (13). It is sufficient to neglect all the overlaps except those between the neighboring wavefunctions as follows

$$\sum_n a_n\, S_n = \sum_n e^{\mathrm{i}\,n\,k\,l}\, S_n = 1 + 2 \sum_{n=1}^{\infty} S_n\, \cos(n\,k\,l) \approx 1 + 2\, S_1\, \cos(k\,l)\,,$$

$$\sum_n a_n\, W_n = \sum_n e^{\mathrm{i}\,n\,k\,l}\, W_n = a_0\, W_0 + 2 \sum_{n=1}^{\infty} W_n\, \cos(n\,k\,l) \approx W_0 + 2\, W_1\, \cos(k\,l)\,.$$

Under this hypothesis, the dispersion relation (20) simplifies to

$$\begin{aligned}(E(\mathbf{k}) - E_w)^2 - (\hbar\,\upsilon_F\, k_y)^2 &\approx \frac{W_0 + 2\, W_1\, \cos(k\,l)}{1 + 2\, S_1\, \cos(k\,l)} \\ &\approx W_0 - 2\,(W_0\, S_1 - W_1)\, \cos(k\,l)\,,\end{aligned} \tag{21}$$

whose solution yields

$$E(\mathbf{k}) = E_w \pm \sqrt{\Gamma^2 + (\hbar\, \upsilon_F\, k_y)^2 + \Upsilon^2\,(1 - \cos(k\, l))}\,, \tag{22}$$

where

$$\Gamma^2 = W_0 - 2\,(W_0\, S_1 - W_1)\,, \qquad \Upsilon^2 = 2\,(W_0\, S_1 - W_1)\,. \tag{23}$$

4 Electromagnetic Waves

The graphene superlattice energy spectrum is nonadditive so there is a dependence of charge carrier motions along orthogonal directions. An electromagnetic (EM) wave normally incident on the GSL introduces an asymmetry in the charge carriers and a dc current component orthogonal to the superlattice axis emerges [13]. As a result nonlinear effects appear and the EM wave is described by a nonlinear Klein–Gordon equation first obtained by Sergey V. Kryuchkov and Egor I. Kukhar' [11].

For simplicity, let us consider that the EM field has a constant vector potential $\mathbf{A} = (A_x, 0, 0)$ along the graphene superlattice axis. An electron current density arise in the conduction band along the same axis given by

$$j_x = -e \sum_{\mathbf{p}} f(\mathbf{p}, t)\, V_x(\mathbf{p})\,, \tag{24}$$

where the electron velocity $V_x(\mathbf{p}) = \partial E(\mathbf{p})/\partial p_x = (1/\hbar)\,\partial E(\mathbf{k})/\partial k$ is calculated from either Eq. (13) or (22), and $f(\mathbf{p}, t)$ is the nonequilibrium distribution function that solves the kinetic Boltzmann equation with a term taking into account the EM field action. The collisionless regime is enough under the assumption that the characteristic scale of variation of the electromagnetic field is large in comparison with the de Broglie wavelength of the electron and with the period of the superlattice, and that the characteristic time of the variation of the EM field is much less than the free transit time of the electrons. In such a case, $f(\mathbf{p}, t) = f_0(\mathbf{p})$, the equilibrium distribution function. Hence Eq. (24) reduces to

$$j_x = -e \sum_{\mathbf{p}} f_0 \left(\mathbf{p} - \frac{e}{c}\,\mathbf{A}\right)\, V_x(\mathbf{p})\,, \tag{25}$$

where the change of variables $\mathbf{p}' = \mathbf{p} - (e/c)\,\mathbf{A}$, results in

$$j_x = -e \sum_{\mathbf{p}'} f_0(\mathbf{p}')\, V_x \left(\mathbf{p}' + \frac{e}{c}\,\mathbf{A}\right)\,. \tag{26}$$

In order to simplify the analysis, let us assume that the electron gas is nondegenerate. This condition requires low temperatures $\theta \ll \Gamma$, and that the chemical

potential μ is such that $\exp((\Gamma - \mu)/\theta) \gg 1$. Both conditions are equivalent to [11]

$$\frac{\theta\, \Gamma}{n_0\, \hbar^2\, (\upsilon_F)^2} \gg 1\,.$$

This condition holds for typical values of the GSL parameters, i.e. $n_0 = 10^{10}\ \mathrm{cm}^{-2}$, $\Gamma = 0.13$ eV, and $\upsilon_F = 10^8$ cm/s, under *low* temperatures within the range 10 K $\ll \theta \ll 10^3$ K.

For a nondegenerate electron gas, the summation over the momentum in Eq. (26) yields

$$j_x = -\frac{e\, n_0}{w_0}\, \frac{\Upsilon^2\, l}{\hbar}\, \frac{\sin\alpha}{2\sqrt{\Gamma^2 + \Upsilon^2\,(1 - \cos\alpha)}}\,, \tag{27}$$

where n_0 is the surface concentration of the charge carriers, $w_0 \approx 0.12\,\mathrm{nm}$ is the width of the graphene sheet, and $\alpha = e\, l\, A_x/(\hbar\, c)$ is the dimensionless potential of the EM field.

The nonhomogeneous wave equation for the vector potential $\mathbf{A}$, i.e.

$$\frac{\partial^2 \mathbf{A}}{\partial t^2} - c^2\, \nabla^2\, \mathbf{A} = \frac{4\,\pi}{c}\, \mathbf{j}\,, \tag{28}$$

after the substitution of Eq. (27), yields a nonlinear Klein–Gordon equation for the normalized potential α given by

$$\frac{\partial^2 \alpha}{\partial t^2} - c^2\, \frac{\partial^2 \alpha}{\partial y^2} + \frac{\omega_{pl}^2\, b^2\, \sin\alpha}{\sqrt{1 + b^2\,(1 - \cos\alpha)}} = 0\,, \tag{29}$$

where $b = \Upsilon/\Gamma$ is a geometrical parameter, and ω_{pl} is the plasma frequency given by

$$\omega_{pl}^2 = \frac{2\,\pi\, n_0\, e^2\, l^2\, \Gamma}{w_0\, \hbar^2}\,.$$

Hereafter, Eq. (29) is referred to as graphene superlattice equation.

5 Kinks and Antikinks

Equation (29) is a Klein–Gordon equation with periodic nonlinearity, in analogy to the sine-Gordon, hence it has kink and antikink solutions. In order to study these solutions by using asymptotic and numerical methods, it is convenient to start with a nondimensionalization. By making the change of variables $t' = \omega_{pl}\, b\, t$, $y' = \omega_{pl}\, b\, y/c$, and $u = \alpha$, then Eq. (29) yields

$$\frac{\partial^2 u}{\partial t^2} - \frac{\partial^2 u}{\partial y^2} + \frac{dG(u)}{du} = 0, \tag{30}$$

where the primes have been dropped and

$$\frac{dG(u)}{du} = \frac{\sin u}{\sqrt{1 + b^2\,(1 - \cos u)}}. \tag{31}$$

The nonlinear potential $G(u)$ can be written as

$$\begin{aligned} G(u) &= \frac{2}{b^2}\left(\sqrt{1 + b^2\,(1 - \cos u)} - 1\right), \\ &= \frac{2\,(1 - \cos u)}{1 + \sqrt{1 + b^2\,(1 - \cos u)}}, \end{aligned} \tag{32}$$

where the constant of integration has been selected in order that it reduces to the potential of the sGeq, i.e. $G(u) = 1 - \cos u$, for $b = 0$.

Equation (30) is Lorentz invariant (with $c = 1$). Hence, a solitary wave solution with speed v can be obtained by applying a Lorentz boost to a static solution $u(y)$, i.e. $u(y, t) = u((y - v\,t)/\sqrt{1 - v^2})$. The static solution solves the Newton's equation given by

$$\frac{d^2 u}{dy^2} = \frac{dG(u)}{du}, \tag{33}$$

which reduces to a first-order differential equation of motion given by

$$\frac{1}{2}\left(\frac{du}{dy}\right)^2 = G(u). \tag{34}$$

The static solutions with finite energy such that $u(+\infty) \neq u(-\infty)$ are called topological. Such solutions can be split into topological sectors according to their asymptotic behaviour at $y \to \pm\infty$. The potential $G(u)$ has infinite minima at $\breve{u}_n = 2\,\pi\,n$, and maxima at $\hat{u}_n = (2\,n + 1)\,\pi$, with $n \in \mathbb{Z}$.

A kink in topological sector n, also referred to as either n-kink or $(n, n + 1)$-solution, is a static solution monotonically connecting the asymptotic values $2\,\pi\,n$, and $2\,\pi\,(n + 1)$; similarly, an antikink in topological sector n, also referred to as n-antikink or $(n, n - 1)$-solution monotonically connects the asymptotic values $2\,\pi\,n$, and $2\,\pi\,(n - 1)$. The position y_0 of the kink (antikink) is that of the inflection point $\hat{u}_n$ ($\hat{u}_{n-1}$). Hence, the n-kink, or $(n, n + 1)$-solution, of Eq. (34) can be written in integral form as

$$\int_{\hat{u}_n}^{u} \frac{d\tilde{u}}{\sqrt{2\,G(\tilde{u})}} = \int_{y_0}^{y} d\tilde{y}, \qquad \breve{u}_n < u < \breve{u}_{n+1}. \tag{35}$$

It is widely known that the 0-kink of the sGeq, viz. $G(u) = 1 - \cos u$, is given by

$$\int_{\pi}^{u} \frac{d\hat{u}}{\sqrt{2\,(1-\cos\hat{u})}} = \log\tan\frac{u}{4} = y - y_0, \qquad 0 < u < 2\,\pi, \tag{36}$$

whose inversion results in

$$u_{k,0}(y) = 4\,\arctan(\exp(y - y_0)). \tag{37}$$

Consequently, the n-kink of the sGeq is given by $u_{k,n}(y) = 2\,\pi\,n + u_{k,0}(y)$, and its n-antikink by $u_{a,n}(y) = 2\,\pi\,n - u_{k,0}(y)$.

For the GSLeq, Eq. (35) reads as

$$\int_{\hat{u}_n}^{u} \frac{\sqrt{1+\sqrt{1+b^2\,(1-\cos\tilde{u})}}}{2\,\sqrt{1-\cos\tilde{u}}}\,d\tilde{u} = y - y_0, \tag{38}$$

whose left-hand side results in a cumbersome expression written in terms of the elliptic integral of the first kind and the complete elliptic integral of the third kind; apparently, its inversion function cannot be written using known analytical functions.

5.1 One Asymptotic Approximation to the 0-Kink

The 0-kink of the Kryuchkov–Kukhar equation can be formally expanded as a power series in b^2, such that the leading-order term is the 0-kink of the sGeq. Instead of using Eq. (38), it is better to use Eq. (34) since the asymptotic expansion is regular. The idea is the substitution of

$$u(y) = u_0(y) + u_1(y)\,b^2 + u_2(y)\,b^4 + \mathrm{O}(b^6), \tag{39}$$

into the ordinary differential equation

$$\frac{du}{dy} = \sqrt{\frac{4\,(1-\cos u)}{1+\sqrt{1+b^2\,(1-\cos u)}}}, \qquad u(0) = \pi, \tag{40}$$

and formally equate powers of b^2. The leading-order results in

$$\frac{du_0}{dy} = \sqrt{2\,(1-\cos u_0(y))}, \qquad u(0) = \pi, \tag{41}$$

whose solution is Eq. (37), i.e.

$$u_0(y) = 4\ \arctan(\exp(y)). \tag{42}$$

The next order yields

$$\frac{du_1(y)}{dy} - \frac{\sin u_0(y)}{\sqrt{2\,(1-\cos u_0(y))}} = \frac{1}{4\sqrt{2}}\sqrt{(1-\cos u_0(y))^3}, \qquad u_1(0) = 0, \tag{43}$$

whose solution is

$$u_1(y) = -\frac{1}{2}\ \mathrm{sech}(y)\ \tanh(y). \tag{44}$$

Iterating this procedure by means of using a computer algebra software like Wolfram Mathematica, the result is

$$\begin{aligned} u(y) = {} & 4\ \arctan(\exp(y)) \\ & - \frac{b^2}{2}\ \mathrm{sech}(y)\ \tanh(y) \\ & + \frac{7\,b^4}{96}\ (5 + \cosh(2\,y))\ \mathrm{sech}^3(y)\ \tanh(y) \\ & - \frac{b^6}{2560}\ (1003 + 276\ \cosh(2\,y) + 41\ \cosh(4\,y))\ \mathrm{sech}^5(y)\ \tanh(y) \\ & + \frac{b^8}{20643840}\ \mathrm{sech}^8(y)\ (8979355\ \sinh(y) + 1077279\ \sinh(3\,y) \\ & + 376019\ \sinh(5\,y) + 46159\ \sinh(7\,y)) + \mathrm{O}(b^{10}). \end{aligned} \tag{45}$$

Note that high-order terms can be easily calculated if required.

5.2 Another Asymptotic Approximation to the 0-Kink

Inspired by the 0-kink of the sGeq, let us introduce the ansatz

$$u(y) = 4\ \arctan(\exp(v(y))), \tag{46}$$

into Eq. (40) in order to obtain

$$\frac{dv}{dy} = \sqrt{\frac{2}{1+\sqrt{1+2\,b^2\ \mathrm{sech}^2(v)}}}, \qquad v(0) = 0, \tag{47}$$

where the identity

$$\cos(4\ \arctan(z)) = \frac{z^4 - 6\,z^2 + 1}{(z^2+1)^2},$$

has been used.

Another asymptotic expansion for the 0-kink of the GSLeq can be obtained by introducing into Eq. (47) the expansion of $v(y)$ in powers series of b^2 given by

$$v(y) = v_0(y) + v_1(y)\,b^2 + v_2(y)\,b^4 + \mathrm{O}((b^6). \tag{48}$$

The leading-order results in

$$\frac{dv_0(y)}{dy} = 1, \qquad v(0) = 0, \tag{49}$$

whose solution is $v_0(y) = y$, as expected. The next order yields

$$\frac{dv_1(y)}{dy} = \frac{1}{4}\ \mathrm{sech}^2(v_0(y)), \qquad v_1(0) = 0, \tag{50}$$

whose solution is

$$v_1(y) = -\frac{1}{4}\ \tanh(y). \tag{51}$$

Iterating this procedure, the result is

$$\begin{aligned} v(y) = y &- \frac{b^2}{4}\ \tanh(y) + \frac{b^4}{96}\ \left(10 + 11\ \mathrm{sech}^2(y)\right)\ \tanh(y) \\ &- \frac{b^6}{1920}\ \left(168 + 104\ \mathrm{sech}^2(y) + 223\ \mathrm{sech}^4(y)\right)\ \tanh(y) \\ &+ \frac{b^8}{215040}\ (20592 + 12760\ \mathrm{sech}^2(y) + 8254\ \mathrm{sech}^4(y) \\ &\qquad + 33469\ \mathrm{sech}^6(y))\ \tanh(y) + \mathrm{O}(b^{10}), \end{aligned} \tag{52}$$

to be introduced into Eq. (46) in order to obtain the 0-kink of the Kryuchkov–Kukhar equation.

Figure 5 shows the kink solution approximated by the asymptotic analysis using Eqs. (46) and (52) for $b = 0, 0.25, 0.50, 0.75$, and 1.00; note that, due to the limited graphical resolution, the plots of the asymptotic solution (45) effectively coincide with those shown in this figure. The left plot in Fig. 5 uses the normalized coordinate y' (where the omitted primes are recovered) given by $y' = \omega_{pl}\,b\,y/c$; the parameter b does not influences the solution up to the graphical resolution. In order to highlight the difference, it is necessary to return to the non-normalized y coordinate; the axis of the right plot in Fig. 5 uses the coordinate y'/b (in fact $c\,y'/(\omega_{pl}\,b)$ with $c = 1$ and

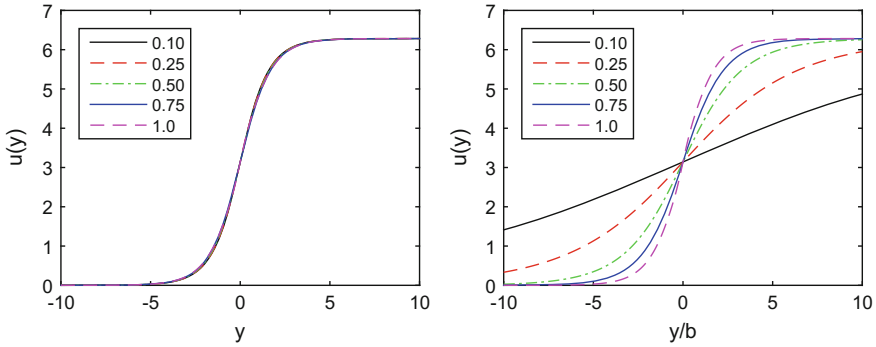

Fig. 5 Kink asymptotic solution calculated using Eqs. (46) and (52) for $b = 0.10, 0.25, 0.50, 0.75,$ and 1.0. See the main text for further explanation

$\omega_{pl} = 1$). The plots show that the solution sharpens as the geometrical parameter grows, starting with the widest one for $b = 0$, the kink of the sGeq.

6 Numerical Method

The analysis of the kink-antikink interaction in the SGLeq requires the use of numerical methods. The initial value problem for Eq. (30) with given initial conditions $u(x, 0)$, and $\partial u(x, 0)/\partial t$, using the nonlinear potential (31), can be solved numerically by either finite difference, finite element, pseudospectral, or spectral methods. Let us consider in this chapter the widely used Strauss–Vázquez method [24], originally developed for solving nonlinear Klein–Gordon equations like Eq. (30). Let us discretize the spatial interval $y \in [-L, L]$ with a uniform mesh with nodes $y_j = -L + j\,\Delta y$, for $j = 0, 1, \ldots, M$, where $\Delta y = 2\,L/M$, and the time $t^m = m\,\Delta t$, for $m = 0, 1, \ldots$, using a fixed time step Δt. The numerical solution $u_j^m \approx u(y_j, t^m)$ is obtained by the Strauss–Vázquez method given by

$$\frac{u_j^{m+1} - 2u_j^m + u_j^{m-1}}{\Delta t^2} - \frac{u_{j+1}^m - 2u_j^m + u_{j-1}^m}{\Delta y^2} + \frac{G(u_j^{m+1}) - G(u_j^{m-1})}{u_j^{m+1} - u_j^{m-1}} = 0\,. \quad (53)$$

This finite difference scheme is second-order in space and time, being nonlinearly stable since it exactly conserves a discrete energy. The analytical energy conserved by Eq. (30) is given by

$$E(u) = \int \left(\frac{1}{2} \left(\frac{\partial u}{\partial t} \right)^2 + \frac{1}{2} \left(\frac{\partial u}{\partial y} \right)^2 + G(u) \right) dy\,, \quad (54)$$

where each term in the integrand is bounded by $E(u)$ for $G(u) \geq 0$. After multiplying of Eq. (53) by $(u_j^{m+1} - u_j^{m-1})/2$ results that the following discrete energy

$$E^m = \frac{\Delta y}{2} \sum_j \left(\frac{u_j^{m+1} - u_j^m}{\Delta t} \right)^2 + \frac{\Delta y}{2} \sum_j \left(\frac{u_{j+1}^{m+1} - u_j^{m+1}}{\Delta y} \right)^2 \left(\frac{u_{j+1}^m - u_j^m}{\Delta y} \right)^2 + \Delta y \sum_j \frac{G(u_j^{m+1}) + G(u_j^m)}{2}, \tag{55}$$

is conserved; concretely, $E^m = E^{m-1}$. Hence, the scheme is nonlinearly stable, $E^m = E^0$, for $m = 1, 2, \ldots$. For the numerical validation of the method the conservation of the discrete momentum [19] given by

$$P^m = -\Delta y \sum_j \left(\frac{u_{j+1}^{m+1} - u_{j-1}^{m+1}}{2\,\Delta y} \right) \left(\frac{u_j^{m+1} - u_j^m}{\Delta t} \right), \tag{56}$$

has also been considered. The linear stability condition for the method (53), for $G(u) = 0$, is given by

$$\left(\frac{\Delta t}{\Delta y} \right)^2 < 1 + \frac{\Delta t^2}{4}.$$

which holds under the CFL condition, $\Delta t / \Delta y < 1$.

The numerical method (53) is implicit, so a nonlinear system of equations must be numerically solved at each time step; we use Newton's method with a relative error in infinity norm small than 10^{-12} as stopping condition. This Newton's tolerance influences the conservation properties of the energy and momentum. Figure 6 shows the conservation of the energy E^m and momentum P^m invariants for $b = 0.9$, with a kink–antikink solution, both with $v = 0.5$, as initial condition, $\Delta y = 0.005$, and

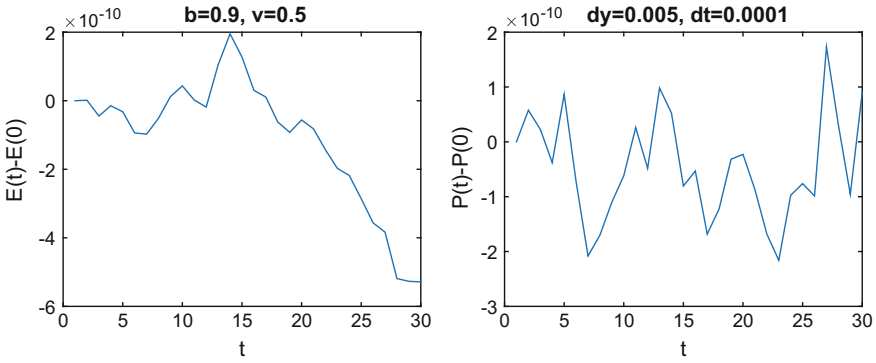

Fig. 6 Conservation of the discrete energy ($E^m - E^0$ in the left plot) and momentum ($P^m - P^0$ in the right one) for a kink–antikink solution of Eq. (30) with $v = 0.5$, $b = 0.9$, $\Delta y = 0.005$, and $\Delta t = 0.0001$

$\Delta t = 0.0001$. Both energy and momentum are well conserved, with an accuracy of the order of $O(10^{-10})$. Similar results are obtained for other values of b, including $b = 0$, cf. the sGeq.

7 Results for the Kink-Antikink Interaction

The interaction of kink and antikink for the sGeq results in the exact kink-antikink solution. The GSLeq is nonintegrable, so the corresponding solution should be obtained by means of either asymptotic or numerical methods. In the second case, the initial condition to be used is $u_{ka,n}(y) = u_{k,n}(y - y_0) + u_{a,n}(y + y_0)$, where the asymptotic approximation $u_{k,0}(y)$ for the 0-kink of the GSLeq given by Eqs. (46) and (42) is used. This solution is a good approximation when the kink and antikink are well separated.

Figure 7 shows two three-dimensional views of the interaction of a kink and an antikink for $b = 0.5$, and Fig. 8 shows snapshots of this interaction at times $t = 0, 50, 80, 120, 150$, and 180. Our numerical simulations indicate that there is no noticeable

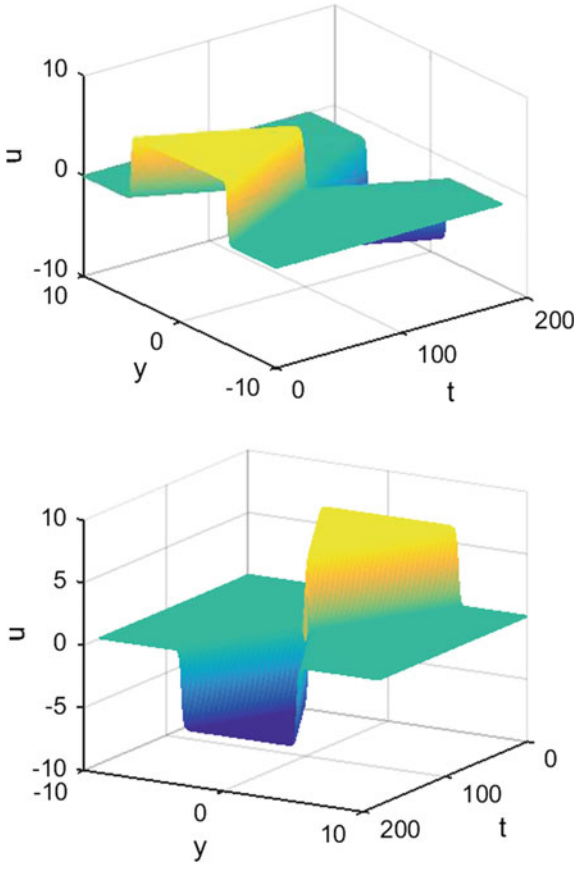

Fig. 7 Three-dimensional plots of the collision between a kink and a antikink of the GSLeq for $v = 0.5$, Δy=0.1, Δt=0.01, and b=0.5. The top and bottom plots are the same but from different views

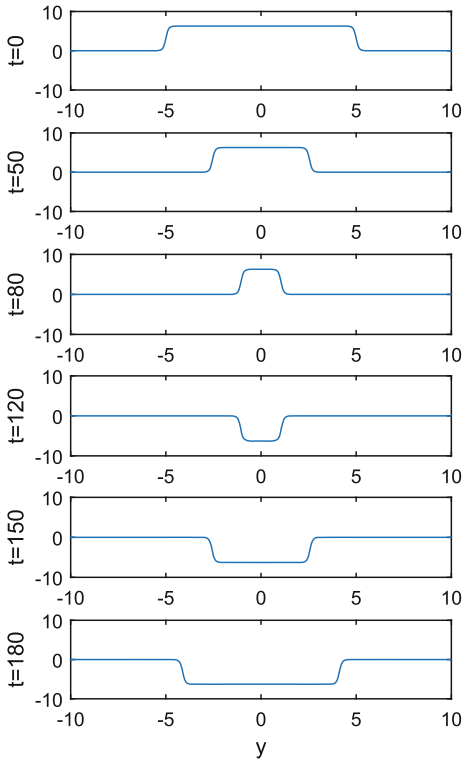

Fig. 8 Snapshots of the interaction between a kink and a antikink of the GSLeq for $v = 0.5$, $\Delta y = 0.1$, $\Delta t = 0.01$, and $b = 0.5$

difference between the solution in the cases with $b \in [0, 1)$ up to the graphical resolution of these figures. The interaction proceeds as follows. The kink moves from the left to the right approaching the antikink that moves from the right to the left. The plots show no visible radiation before, during, or after the interaction. During the collision the amplitude of the solution decreases down to zero, transforming the kink-antikink solution with positive amplitude into a antikink-kink solution with negative amplitude. In this process the kink (antikink) transforms into an antikink (kink) with opposite velocity. The collision is not exactly elastic for $b > 0$, as it is for $b = 0$ (sGeq). Very small radiation wavepackets are generated at the interaction region.

Figure 9 shows a vertical axis zoom of the same snapshots shown in Fig. 8 in order to illustrate the inelastic interaction between the kink and the antikink for $b > 0$. The radiation wavepackets emitted by the collision kink and the antikink are symmetrical in shape with respect to the interaction point; they have the same amplitude and speed, but opposite in direction of propagation. They also move faster than the speed of the kink and the antikink. The wavepackets are not self-similar, as in other nonlinear evolution equations [23]. Asymptotic methods can be applied to study in the detail the shape and characteristics of the radiation generated in the collision, but a detailed analysis is outside the scope of the chapter. Our results also

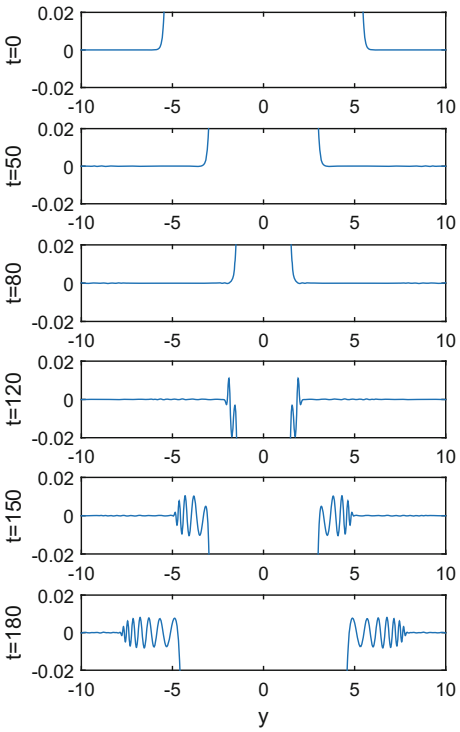

Fig. 9 Zooms in the vertical axis of the plots shown in Fig. 8. The parameters of the simulation are exactly the same

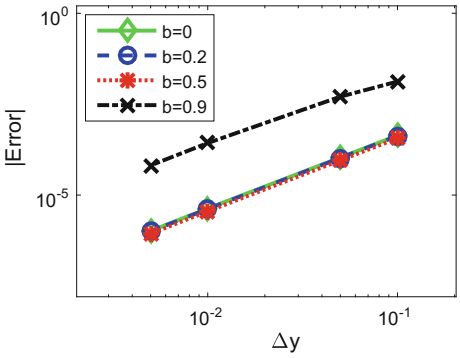

Fig. 10 Error difference between the asymptotic approximation for $\Delta t = 0.0001$, and the numerical solution as function of $\Delta y = 0.1$, 0.05, 0.01, and 0.005, and $b = 0$, 0.2, 0.5, and 0.9, for the kink-antikink collision with $v = 0.5$ at $t = 30$

indicate that no critical velocity is observed in the inelastic interaction of GSLeq; the existence of a critical speed occurs in the ϕ^4 Klein–Gordon equation, where over this velocity the kink-antikink pair annihilates.

Figure 10 shows the errors between the kink-antikink solution for $\Delta y = 0.0001$, taken as a good approximation to the exact solution, and the numerical solution for $\Delta y = 0.1$, 0.05, 0.01, and 0.005, both evaluated at $t = 30$ for $v = 0.5$. Fitting the data in Fig. 10 by a line shows that the slope is approximately equal to 2, as expected by the second-order accuracy of Strauss–Vázquez method.

Table 1 Error between asymptotic approximation and numerical solutions for $t \in [0, 30]$ for a kink-antikink solution, both with velocity $v = 0.5$, as a function of Δy and Δt, for $b = 0, 0.2, 0.5$, and 0.9. See the main text for further explanation

		Δy				
b	Δt	0.1	0.05	0.01	0.005	0.001
0	0.01	1.95×10^{-2}	4.86×10^{-3}	1.57×10^{-4}	*	*
	0.001	1.95×10^{-2}	4.71×10^{-3}	1.94×10^{-4}	4.82×10^{-5}	1.57×10^{-6}
	0.0001	1.95×10^{-2}	4.90×10^{-3}	1.94×10^{-4}	4.85×10^{-5}	1.95×10^{-6}
0.2	0.01	1.89×10^{-2}	4.71×10^{-3}	1.46×10^{-4}	*	*
	0.001	1.89×10^{-2}	4.71×10^{-3}	1.88×10^{-4}	4.63×10^{-5}	1.14×10^{-6}
	0.0001	1.89×10^{-2}	4.71×10^{-3}	1.88×10^{-4}	4.67×10^{-5}	1.55×10^{-6}
0.5	0.01	1.41×10^{-2}	1.87×10^{-3}	6.70×10^{-5}	*	*
	0.001	1.42×10^{-2}	1.87×10^{-3}	6.48×10^{-5}	6.67×10^{-5}	6.73×10^{-5}
	0.0001	1.42×10^{-2}	1.90×10^{-3}	6.48×10^{-5}	6.66×10^{-5}	6.73×10^{-5}
0.9	0.01	2.05×10^{-2}	1.57×10^{-2}	1.54×10^{-2}	*	*
	0.001	2.05×10^{-2}	1.57×10^{-2}	1.54×10^{-2}	1.54×10^{-2}	1.54×10^{-2}
	0.0001	2.05×10^{-2}	1.57×10^{-2}	1.54×10^{-2}	1.54×10^{-2}	1.54×10^{-2}

Table 1 shows the error between the asymptotic approximation given by Eqs. (46) and (52), and the numerical solution at $t = 30$ for a kink-antikink solution with velocity $v = 0.5$. Several grid sizes, $\Delta y = 0.1$, 0.05, 0.01, 0.005, and 0.001, and time steps, $\Delta t = 0.01, 0.001$, and 0.0001, for $b = 0, 0.2, 0.5$, and 0.9 have been used in Table 1; the asterisks are combinations of the grid size and time step that do not hold the CFL condition, so the corresponding simulations have not been executed. The solution is dominated by the error in the spatial discretization, as shown in Table 1, being practically independent of the time step. For low values of b, the error decreases as Δy does. For large values of b, the accuracy of the asymptotic solution decreases and the error becomes independent of Δy. The low error of the asymptotic approximation for $b \leq 5$ validates the asymptotic solution.

8 Summary

The nonlinear propagation of electromagnetic waves in Ratnikov's graphene superlattice under the incidence of normal irradiation has been studied. These superlattices are made by depositing a sheet of graphene on a periodically alternating layers of SiO_2 and h-BN (or SiC). The superlattice electronic spectrum is calculated by two methods and approximated for low energy carriers. An external electromagnetic wave introduces an asymmetry in the charge carriers and an electric field orthogonal to the superlattice axis emerges. A nonlinear Klein–Gordon equation similar to the sine-Gordon equation describes the propagation of this electromagnetic waves. This equation has kink and antikink solutions with no known closed-form expression. An analytical asymptotic approximation and a conservative, finite difference numerical scheme are presented. Extensive numerical results for the kink–antikink interactions

show that the interaction is nearly elastic, but radiation appears for large values of the geometrical parameter of the superlattice. The whole set of results suggests that graphene superlattices are useful devices to study nonlinear wave phenomena with electromagnetic waves in the THz scale.

Further research is in progress. The nearly integrability of the graphene superlattice equation suggests that perturbation methods based on the inverse scattering transform for the sine Gordon equation can be successfully used to approximate kink, antikink and kink-antikink solutions. Also direct perturbations based on multiple scales will be considered. In order to recommend the best method for the numerical solution of the graphene superlattice equation, a comparison with other finite difference, finite element, pseudospectral, and spectral methods is required.

Acknowledgements The authors acknowledge financial support from project TIN2014-56494-C4-1-P from Programa Estatal de Fomento de la Investigación Científica y Técnica de Excelencia del Ministerio de Ciencia e Innovación (MICINN) of Spain.

References

1. Barbier, M., Vasilopoulos, P., Peeters, F.M.: Extra dirac points in the energy spectrum for superlattices on single-layer graphene. Phys. Rev. B **81**, 075438 (2010)
2. Castro Neto, A.H., Guinea, F., Peres, N.M.R., Novoselov, K.S., Geim, A.K.: Influence of the constant electric field on the mutual rectification of the electromagnetic waves in graphene superlattice. Rev. Mod. Phys. **81**, 109–162 (2009)
3. Dean, C.R., Young, A.F., Meric, I., Lee, C., Wang, L., Sorgenfrei, S., Watanabe, K., Taniguchi, T., Kim, P., Shepard, K.L., Hone, J.: Boron nitride substrates for high-quality graphene electronics. Nat. Nanotechnol. **5**, 722–726 (2010)
4. Geim, A.K., MacDonald, A.H.: Graphene: exploring carbon flatland. Phys. Today **60**, 35–41 (2007)
5. Giovannetti, G., Khomyakov, P.A., Brocks, G., Kelly, P.J., Van den Brink, J.: Substrate-induced band gap in graphene on hexagonal boron nitride: ab initio density functional calculations. Phys. Rev. B **76**, 073103 (2007)
6. Goerbig, M.O.: Electronic properties of graphene in a strong magnetic field. Rev. Mod. Phys. **83**, 1193–1243 (2011)
7. Jørgensen, J.H., Čabo, A.G., Balog, R., Kyhl, L., Groves, M.N., Cassidy, A.M., Bruix, A., Bianchi, M., Dendzik, M., Arman, M.A., Lammich, L., Pascual, J.I., Knudsen, J., Hammer, B., Hofmann, P., Hornekaer, L.: Symmetry-driven band gap engineering in hydrogen functionalized graphene. ACS Nano **10**, 10798–10807 (2016)
8. Jung, J., DaSilva, A.M., MacDonald, A.H., Adam, S.: Origin of band gaps in graphene on hexagonal boron nitride. Nat. Commun. **6**, 6308 (2015)
9. Kryuchkov, S.V., Kukhar', E.I.: Influence of the constant electric field on the mutual rectification of the electromagnetic waves in graphene superlattice. Physica E **46**, 25–29 (2012)
10. Kryuchkov, S.V., Kukhar', E.I.: Mutual rectification of cnoidal and sinusoidal electromagnetic waves with orthogonal polarization planes in a graphene-based superlattice. Opt. Spectrosc. **112**, 914–919 (2012)
11. Kryuchkov, S.V., Kukhar', E.I.: The solitary electromagnetic waves in the graphene superlattice. Physica B **408**, 188–192 (2012)
12. Kryuchkov, S.V., Kukhar', E.I.: Alternating current-driven graphene superlattices: kinks, dissipative solitons, dynamic chaotization. Chaos **25**, 073116 (2015)

13. Kryuchkov, S.V., Kukhar', E.I., Yakovenko, V.A.: Effect of the mutual rectification of two electromagnetic waves with perpendicular polarization planes in a superlattice based on graphene. Bull. Russ. Acad. Sci. Phys. **74**, 1679–1681 (2010)
14. Lima, J.R.F., Moraes, F.: Indirect band gap in graphene from modulation of the fermi velocity. Solid State Commun. **201**, 82–87 (2014)
15. Maksimova, G.M., Azarova, E.S., Telezhnikov, A.V., Burdov, V.A.: Graphene superlattice with periodically modulated dirac gap. Phys. Rev. B **86**, 205422 (2012)
16. Mikhailov, S.A.: Non-linear electromagnetic response of graphene. Eur. Phys. Lett. **79**, 27002 (2007)
17. Mikhailov, S.A., Ziegler, K.: Nonlinear electromagnetic response of graphene: frequency multiplication and the self-consistent-field effects. J. Phys.-Condens. Matter **20**, 384204 (2008)
18. Novoselov, K.S., Geim, A.K., Morozov, S.V., Jiang, D., Zhang, Y., Dubonos, S.V., Grigorieva, I.V., Firsov, A.A.: Electric field effect in atomically thin carbon films. Science **306**, 666–669 (2004)
19. Pascual, P.J., Vázquez, L.: Sine–Gordon solitons underweak stochastic perturbations. Phys. Rev. B **32**, 8305 (1985)
20. Ratnikov, P.V.: Nonlinear electromagnetic response of graphene: frequency multiplication and the self-consistent-field effects. JETP Lett. **90**, 469–474 (2009)
21. Ratnikov, P.V.: Superlattice based on graphene on a strip substrate. JETP Lett. **90**, 469–474 (2009)
22. Ratnikov, P.V., Silin, A.P.: Novel type of superlattices based on gapless graphene with the alternating fermi velocity. JETP Lett. **100**, 311–318 (2014)
23. Rus, F., Villatoro, F.R.: Self-similar radiation from numerical rosenauhyman compactons. J. Comput. Phys. **227**, 440–454 (2007)
24. Strauss, W., Vázquez, L.: Numerical solution of a nonlinear Klein–Gordon equation. J. Comput. Phys. **28**, 271–278 (1978)
25. Wallace, P.R.: The band theory of graphite. Phys. Rev. **71**, 622–634 (1947)
26. Wallbank, J.R., Mucha-Kruczyński, M., Chen, X., Fal'ko, V.I.: Moiré superlattice effects in graphene/boron-nitride van der Waals heterostructures. Ann. Phys.-Berl. **527**, 359–376 (2015)
27. Yankowitz, M., Xue, J., Cormode, D., Sanchez-Yamagishi, J.D., Watanabe, K., Taniguchi, T., Jarillo-Herrero, P., Jacquod, P., LeRoy, B.J.: Emergence of superlattice dirac points in graphene on hexagonal boron nitride. Nat. Phys. **8**, 382–386 (2012)
28. Zav'ialov, D.V., Konchenkov, V.I., Kruchkov, S.V.: Transverse current rectification in a graphene-based superlattice. Semiconductors **46**, 109–116 (2012)
29. Zhou, S.Y., Gweon, G.H., Fedorov, A.V., First, P.N., de Heer, W.A., Lee, D.H., Guinea, F., Castro Neto, A.H., Lanzara, A.: Substrate-induced bandgap opening in epitaxial graphene. Nat. Mater. **6**, 770–775 (2007)

Nonlinear Vortex Light Beams Supported and Stabilized by Dissipation

Miguel A. Porras, Carlos Ruiz-Jiménez and Márcio Carvalho

Abstract We describe nonlinear Bessel vortex beams as localized and stationary solutions with embedded vorticity to the nonlinear Schrödinger equation with a dissipative term that accounts for the multi-photon absorption processes taking place at high enough powers in common optical media. In these beams, power and orbital angular momentum are permanently transferred to matter in the inner, nonlinear rings, at the same time that they are refueled by spiral inward currents of energy and angular momentum coming from the outer linear rings, acting as an intrinsic reservoir. Unlike vortex solitons and dissipative vortex solitons, the existence of these vortex beams does not critically depend on the precise form of the dispersive nonlinearities, as Kerr self-focusing or self-defocusing, and do not require a balancing gain. It has been shown that these beams play an important role in "tubular" filamentation experiments with powerful, vortex-carrying Bessel beams, where they act as attractors in the beam propagation dynamics. Nonlinear Bessel vortex beams provide indeed a new solution to the question of the stable propagation of ring-shaped vortex light beams in homogeneous self-focusing Kerr media. A stability analysis demonstrates that there exist nonlinear Bessel vortex beams with single or multiple vorticity that are stable against azimuthal breakup and collapse, and that the mechanism that renders these vortexes stable is dissipation. The stability properties of nonlinear Bessel vortex beams explain the experimental observations in the tubular filamentation experiments.

M. A. Porras (✉)
Grupo de Sistemas Complejos, ETSI de Minas y Energía, Universidad Politécnica de Madrid, Rios Rosas 21, 28003 Madrid, Spain
e-mail: miguelangel.porras@upm.es

C. Ruiz-Jiménez · M. Carvalho
Grupo de Sistemas Complejos, ETSI Agronómica, Alimentaria y de Biosistemas, Universidad Politécnica de Madrid, Ciudad Universitaria s/n, 28040 Madrid, Spain
e-mail: Carlos.Ruiz.Jimenez@gmail.com

M. Carvalho
e-mail: marciocarvalho78@gmail.com

J. F. R. Archilla et al. (eds.), *Nonlinear Systems, Vol. 2*, Understanding Complex Systems, https://doi.org/10.1007/978-3-319-72218-4_5

Keywords Nonlinear optics · Optical Kerr effect · Self-action effects · Vortex solitons · Vortex stability · Symmetry breaking · Bessel beams · Multi-photon absorption · Filamentation

1 Introduction

Self-trapping of optical beams in nonlinear media has been one of the main subjects studied in nonlinear optics [27, 30]. There is a particularly strong and sustained interest in self-trapped beams with embedded vorticity, tubular beams or vortex solitons, carrying orbital angular momentum, [12] first introduced theoretically in [23, 24], and in the problem of achieving the stability of these vortex-carrying structures [12, 21]. Their applications have provided new fields of research in information encoding, quantum entanglement, all-optical data-processing [20], optical trapping [10, 11], and several forms of angular momentum transmission from light to matter, e.g., to micro- and nano-particles, Bose–Einstein condensates or atoms [4, 29, 53].

A major issue with multidimensional solitons is their stability [25]. The ubiquitous self-focusing cubic nonlinearity gives rise to critical collapse in two dimensions [6, 17, 52], which destabilizes the solitons families. Vortex solitons are particularly prone to the instability initiated by azimuthal perturbations, which breaks their cylindrical symmetry, splitting it into fragments [12, 21]. Stabilization of vortex solitons was shown to be possible with specifically designed or "tailored" nonlinearities, such as cubic and quintic ones with opposite signs [34, 44], or nonlocal nonlinearities [55]. Nonetheless, real-world applications involve a detailed pursuit for materials, such as liquid CS_2 (in the case of the cubic-quintic nonlinearity) [16], or lead-doped glass (for the thermal nonlocal nonlinearity case) [45]. A comparable issue is the search for stable vortex solitons in dissipative systems, frequently modeled by complex Ginzburg–Landau equations with cubic and quintic nonlinearities, which support stable dissipative solitons and vortex solitons [2, 5, 22, 26, 31].

In this chapter we shall consider a homogeneous, nonlinear self-focusing Kerr media, and approach the problem of achieving stationary and stable propagation of vortex beams from a different perspective, reporting the existence of stable vortex beams in standard optical materials [40, 43]. In the context of the research on the phenomenon of filamentation induced by powerful laser pulses [9, 51], Ref. [41] reported the existence of light beams that can propagate with unchanged transversal intensity pattern, including any attenuation, in self-focusing Kerr media while their power is being continuously dissipated into matter via multi-photon absorption, eventually ionizing the medium. Multi-photon absorption of different orders takes place in air, water, silica, and other ordinary dielectric media. It occurs as a collapse-arresting mechanism that plays an essential role in filamentation [8, 9, 18, 36, 38, 49]. These light beams, originally called "nonlinear unbalanced Bessel beams", are characterized by their conical geometry and the capability of transporting infinite power. They then possess an intrinsic power reservoir that in these beams flows permanently from the outer rings, where the beam is linear Bessel-like, towards the nonlinear central

lobes, where most of the power losses due to multi-photon absorption take place, replenishing them. A fundamental difference from complex Ginzburg–Landau-based models is the absence of any gain term in order to balance out the nonlinear losses, and yet, that the propagation persists. Physically realizable versions of these nonlinear Bessel beams with finite amount of power have been shown to play a crucial role in various experiments [35–37], particularly in the filamentation induced by ultrashort pulsed (linear) Bessel beams [37, 38], where the nonlinear Bessel beams act as attractors in the nonlinear propagation [42].

It has recently been shown [19, 40] that the above nonlinear Bessel beam is only the fundamental member of an infinite family of vorticity-carrying nonlinear Bessel beams with arbitrary integer topological charge s. Throughout this chapter we will refer to these beams as nonlinear Bessel vortex beams (nonlinear BVBs). In them, both angular momentum and power move permanently in a spiral towards the core of the beam, from the outer reservoirs towards the inner, more intense rings surrounding the vortex, where they are transferred to matter. Multiphoton absorption, or coincident absorption of M photons of angular momentum $\hbar s$, can be used efficiently as a procedure of optical pump of angular momentum [29, 53]. Differently from other vortex-carrying beams, as standard vortex solitons, they may exist in common transparent dielectric as optical glasses, liquid and gases at high enough powers. Nonlinear BVBs have subsequently been realized in experiments, and have been employed for laser-powered material processing [54].

In the first part of this chapter we review the properties of nonlinear BVBs, their structure and the refilling mechanism that allows the stationary propagation with dissipation. By means of numerical simulations, we also show that nonlinear BVBs are attractors of the dynamics of linear Bessel beams. For each ideal (infinite power), linear BVB introduced in the nonlinear medium, there is a specific, ideal, nonlinear BVB that governs the dynamics: the one conserving the value of the vorticity (topological charge), the cone angle and the linear beam's inward power flux [40].

Observed in experiments of filamentation with vortex-carrying Bessel beams, three different propagation regimes in the so-called Bessel zone after the generating axicon have been reported to exist [54]. Under certain conditions, usually associated with large cone angles, a steady or tubular filamentation regime is observed, which is identified as a nonlinear BVB. Under other conditions, however, azimuthal breakup takes place, and rotating filaments, or non-rotating, disordered filaments have been observed [19, 54].

These observations suggest that stable nonlinear BVBs may exist. In the second part of this chapter we review our research on the stability properties of nonlinear BVBs and demonstrate that there indeed exist nonlinear BVBs of any topological charge presenting complete stability against azimuthal breakup and collapse alike in self-focusing Kerr media with nonlinear absorption [43]. Also, a standard analysis of the linearized equations for small perturbations predict stability, subsequently verified directly in numerical simulations of the propagation of randomly perturbed nonlinear BVBs. The linear-stability analysis is also used to demonstrate that the stability is imposed by the nonlinear absorption effect. Its stabilizing action was previously pointed out for zero-vorticity beams affected by radial and temporal per-

turbations [37, 42] and light bullets [39], but not for nonlinear BVBs under azimuthal breaking. In the stability analysis we give priority to the most destabilizing cubic self-focusing, since this nonlinearity cannot by itself support any stable 2D patterns. Yet, analog results are easily obtained for more general nonlinearities, as their particularities (such as the order of the multi-photon absorption or the form of the Kerr nonlinearity) do not critically affect the existence of nonlinear BVBs [19, 40, 41].

The study carried out for the stable case using the previously explained linear analysis and later diagnostic numerical simulations of the nonlinear propagation allow us to propose a common explanation for the experimentally observed phenomena [54].Tubular, rotary and speckle-like dynamical regimes in the Bessel region are detected after the axicon [54]; and in all the three cases, there exists an attracting nonlinear BVB that determines the dynamics: as in the ideal case, it is the nonlinear BVB with equal topological charge, cone angle, and inward power flux as the linear Bessel beam that would form in the zone of the axicon's focus, centered in the Bessel zone, under linear conditions of propagation. This fact is confirmed by the numerical observation that the dynamics in the Bessel zone develops as would do the instability, if any, of that specific nonlinear BVB. If the stability analysis gives out a stable dynamic regime for the attracting BVB, then a tubular regime is observed; the same applies if its instability is not strong enough to arise over the Bessel distance. Otherwise, the azimuthal symmetry breaking leading to rotary or speckle-like regimes perceived in the Bessel zone closely mimics the one observed in the development of the instability of the nonlinear BVB, which acts in this case as an unstable, chaotic attractor.

2 On the Dynamics of Bessel Vortex Beams in Self-focusing Media with Multiphoton Absorption

To illustrate how nonlinear BVBs arise spontaneously in optical media, we first analyze the propagation of high-order (vortex-carrying) Bessel beams [14, 15], or linear Bessel vortex beams (linear BVBs for short), at sufficiently high intensities, typically of the order of TW/cm^2, in a (linearly) transparent dielectric. We assume that the propagation is suitably modeled by the nonlinear Schrödinger equation (NLSE) with cubic, and possibly quintic, dispersive nonlinearities, and a dissipative term that accounts for nonlinear power losses associated with multi-photon absorption processes at these high intensities. For the light beam $E = A\exp[-i(\omega t - kz)]$ of angular frequency ω and linear propagation constant $k = (\omega/c)n$, n and c being the linear refractive index and the speed of light in vacuum, respectively, and of complex envelope A, this NLSE reads as

$$\frac{\partial A}{\partial z} = \frac{i}{2k}\Delta_\perp A + if(|A|^2)A - \frac{\beta^{(M)}}{2}|A|^{2M-2}A\,, \tag{1}$$

where $\Delta_\perp = \partial_r^2 + (1/r)\partial_r + (1/r^2)\partial_\varphi^2$ is the transversal Laplace operator, (r, φ) are polar coordinates in the transversal plane, $\beta^{(M)} > 0$ is the M-photon absorption coefficient, and the term $f(u) \equiv k(n_2 u + n_4 u^2)/n$, n_2 and n_4 being nonlinear refractive indexes, includes dispersive nonlinearities (cubic and quintic in this case). The multiphoton number M is given by the light wavelength and the medium chosen [9]. As an example, in air M values go from 3 to 8 for a wavelength spanning 248–800 nm [38, 49].

Linear Bessel beams are, in the paraxial form implicit in Eq. (1), the solutions $A(r, \varphi, z) \propto J_s(\sqrt{2k|\delta|}r)e^{is\varphi}e^{i\delta z}$ of Eq. (1) when all nonlinear terms are neglected, where $\delta = -k\theta^2/2 < 0$ is the shortening of the axial component of the wave vector because of the conical structure, $\theta = \sqrt{2|\delta|/k}$ is the cone angle of the Bessel beam, and $s = \pm 1, \pm 2 \ldots$ is the topological charge of the vortex at $r = 0$. To facilitate the study of the nonlinear propagation of a linear BVB of given cone angle, we introduce dimensionless variables

$$\rho \equiv k\theta r = \sqrt{2k|\delta|}r, \quad \zeta \equiv |\delta| z, \quad \tilde{A} \equiv \left(\frac{\beta^{(M)}}{2|\delta|}\right)^{\frac{1}{2M-2}} A\,, \tag{2}$$

with which Eq. (1) rewrites as

$$\frac{\partial \tilde{A}}{\partial \zeta} = i\Delta_\perp \tilde{A} + i\tilde{f}(|\tilde{A}|^2)\tilde{A} - |\tilde{A}|^{2M-2}\tilde{A}\,, \tag{3}$$

where the transversal Laplace operator is now $\Delta_\perp \equiv \partial_\rho^2 + (1/\rho)\partial_\rho + (1/\rho^2)\partial_\varphi^2$, and $\tilde{f}(u) \equiv \alpha_2 u + \alpha_4 u^2$, with

$$\alpha_2 \equiv \frac{kn_2}{n|\delta|}\left(\frac{2|\delta|}{\beta^{(M)}}\right)^{\frac{1}{M-1}}, \quad \alpha_4 \equiv \frac{kn_4}{n|\delta|}\left(\frac{2|\delta|}{\beta^{(M)}}\right)^{\frac{2}{M-1}}, \tag{4}$$

are given by the medium characteristics for a fixed value of the cone angle and the light wavelength. In water at 527 nm, for example, with the values $n = 1.33$, $n_2 = 2.7 \times 10^{-16}\,\mathrm{cm}^2/\mathrm{W}$, $n_4 \simeq 0$, $M = 4$ and $\beta^{(4)} = 2.4 \times 10^{-36}\,\mathrm{cm}^5/\mathrm{W}^3$ [37], and with typical cone angles $\theta = 3°, 2°, 1°, 0.5°$, we get respectively $\alpha_2 \simeq 0.76, 1.31, 3.30, 8.31$, and we can assume $\alpha_4 \simeq 0$. Similar values are obtained for other media at other wavelengths, and are therefore considered below. In these dimensionless variables, the linear BVB solution of Eq. (3) without nonlinear terms is written as $b_0 J_s(\rho)\exp(is\varphi)\exp(-i\zeta)$, where b_0 determines its amplitude.

The existence of nonlinear BVBs is suggested by the following numerical simulations. Solving the NLSE in Eq. (3) with the linear BVB $\tilde{A}(\rho, \varphi, 0) = b_0 J_s(\rho)e^{is\varphi}$ as initial condition at the entrance plane $\zeta = 0$ of the medium, we observe that it is not completely absorbed, as would occur to a plane wave or to a Gaussian beam; on

the contrary, it transforms spontaneously into a nondiffracting and non-attenuating beam. This fact was originally predicted and observed for the fundamental (vortex-less) Bessel beams a decade ago [37, 41], but this phenomenon is seen here to occur also with BVBs [19, 40]. In Fig. 1a–d, the radial profiles of intensity are represented at different propagation distances. For simplicity, a medium with negligible Kerr nonlinearity ($\alpha_j = 0$) is first considered. Once the propagating beam passes through a stage of strong absorption, a final steady state with a vortex is reached. This non-diffracting and non-attenuating final beam does not require Kerr non-linearities for its stationarity, as vortex solitons. The beam maintains its radial profile despite it is experiencing nonlinear losses per unit length given by

$$N(\infty) = 2\pi \int_0^\infty d\rho \rho |\tilde{A}|^{2M} . \tag{5}$$

As seen in Fig. 1e, these losses reach a positive constant value in the final steady regime. In Fig. 1a–d, we observe that the transformation into the final state starts in the central lobes and spreads conically along the cone $z = r/\theta$ (or $\zeta = \rho/2$ in our dimensionless variables) on propagation. The formation of a stationary state with similar characteristics also takes place in self-focusing and self-defocusing media, $\alpha_2 > 0$ and $\alpha_2 < 0$, as seen more concisely in Fig. 2a, b, with the only significant difference that central lobes of the final beam state are compressed or widened by the action for the respective Kerr nonlinearities. In all cases, the final beam state is a nonlinear BVB, whose intensity profile is depicted in the example of Fig. 1 by dashed lines, and whose properties will be studied in the next section.

3 Nonlinear BVBs Supported by Nonlinear Losses

As described in Refs. [19, 40], we search for nonlinear stationary solutions of the NLSE (1) whose intensity profile does not depend on the propagation coordinate z of the form

$$A(r, \varphi, z) = a(r) \mathrm{e}^{i\phi(r)} \mathrm{e}^{is\varphi} \mathrm{e}^{i\delta z} , \tag{6}$$

where $\phi(r)$ and $a(r) > 0$ are the radial phase and amplitude profiles to be determined, and δ is a constant. We do not initially assume that this constant is negative. In dimensionless variables the above Ansatz is

$$\tilde{A}(\rho, \phi, \zeta) = \tilde{a}(\rho) \mathrm{e}^{i\phi(\rho)} \mathrm{e}^{is\varphi} \mathrm{e}^{i\,\mathrm{sgn}(\delta)\zeta} , \tag{7}$$

where $\mathrm{sgn}(\delta)$ is the sign of δ. Substituting Eq. (7) in the NLSE (3) and separating real and imaginary parts we obtain the following ordinary differential equations for the amplitude and phase:

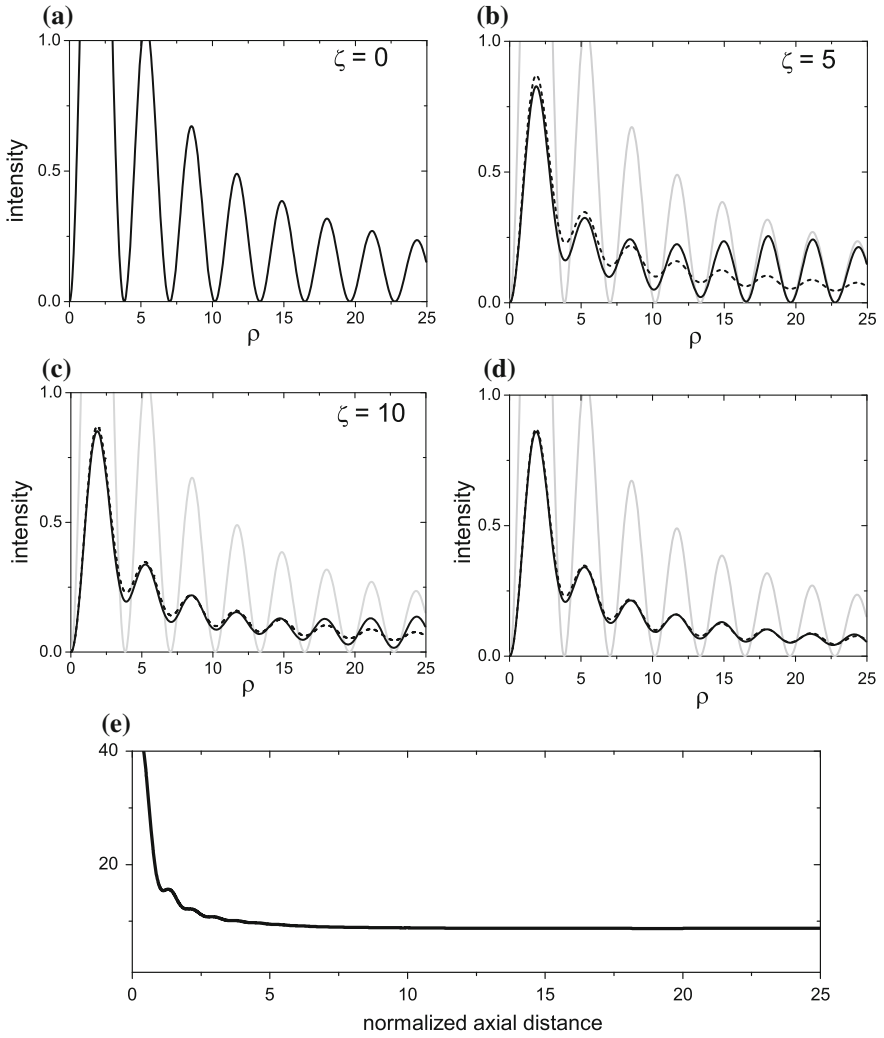

Fig. 1 **a**–**d** Radial intensity profiles at different propagation distances ζ when a linear BVB with topological charge $s = 1$ and amplitude parameter $b_0 = 3$ is introduced into a medium with four-photon absorption ($M = 4$) with negligible Kerr nonlinearity ($\alpha_2 = 0, \alpha_4 = 0$). The gray lines represent the initial linear BVB and the dashed lines the final nonlinear vortex beam with equal cone angle, topological charge and $b_0 = 1.6$. **e** Nonlinear power losses per unit length in Eq. (5) as a function of distance ζ. A previous version of this figure was published by the authors in [40]

$$\frac{d^2\tilde{a}}{d\rho^2} + \frac{1}{\rho}\frac{d\tilde{a}}{d\rho} - \left(\frac{d\phi}{d\rho}\right)^2 \tilde{a} + \tilde{f}(\tilde{a}^2)\tilde{a} - \mathrm{sgn}(\delta)\tilde{a} - \frac{s^2}{\rho^2}\tilde{a} = 0\,, \tag{8}$$

$$\frac{d^2\phi}{d\rho^2} + \frac{1}{\rho}\frac{d\phi}{d\rho} + 2\frac{d\phi}{d\rho}\frac{d\tilde{a}}{d\rho}\frac{1}{\tilde{a}} + \tilde{a}^{2M-2} = 0\,. \tag{9}$$

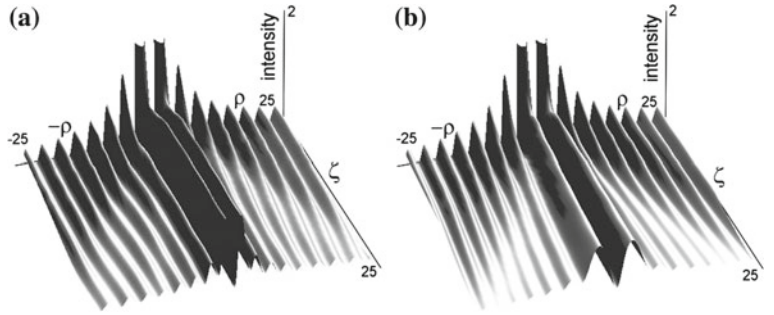

Fig. 2 Nonlinear dynamics of the intensity profile of the same linear BVB as in Fig. 1 introduced in **a** a saturable self-focusing medium with $\alpha_2 = 2$, $\alpha_4 = -1$ and in **b** a saturable self-defocusing medium with $\alpha_2 = -2$, $\alpha_4 = 1$ with four photon absorption. A previous version of this figure was published by the authors in [40]

Physically valid solutions must obey the boundary condition of localization, i.e., $\tilde{a}(\rho) \to 0$ as $\rho \to \infty$. In addition, around the vortex the amplitude is very small, and therefore the nonlinear effects are negligible; we then will demand the boundary condition $a(\rho) \simeq b_0 J_s(\rho)$ about the vortex, or, in other words, that the beam behaves as a linear BVB of a certain amplitude b_0. Since $J_s(\rho) \simeq \rho^{|s|}/(2^{|s|}|s|!)$ for $\rho \to 0$ [33], we can also write this boundary condition as

$$\tilde{a}(\rho) \simeq \frac{b_0}{2^{|s|}|s|!}\rho^{|s|} \quad \text{for} \quad \rho \to 0. \tag{10}$$

In absence of dissipation, this problem has solution with $\mathrm{sgn}(\delta) = 1$ for a discrete spectrum of values of b_0, which constitute the family of vortex solitons [12] characterized by strongly localized transversal profiles around the vortex, and with $\mathrm{sgn}(\delta) = -1$ for continuous values of b_0 from 0 to ∞, which are called nonlinear Bessel beams in transparent media. In this case, only the amplitude equation (8) is usually written because a constant phase satisfies Eq. (9) [12]. When absorption is included, there exists no solution with $\mathrm{sgn}(\delta) = +1$, i.e., the vortex solitons family does not survive dissipation effects [50]. However, with $\mathrm{sgn}(\delta) = -1$, solutions to this problem still exist with a continuous spectrum of values of b_0 up to a maximum value, $b_{0,\max}$, which constitute the family of nonlinear BVBs in Kerr nonlinear media with nonlinear absorption [19, 40].

Some cases of intensity radial profiles $\tilde{a}^2(\rho)$ are shown in Fig. 3 (solid curves) and are compared to the linear BVB with the same vortex core (same b_0). At low amplitude (small b_0), the nonlinear BVB has a linear behaviour at any radius ρ. When b_0 increases up to $b_{0,\max}$, it decreases gradually the contrast of the rings, and the rings near the center are narrower (broader) in self-focusing (self-defocusing) media. In all cases, the outer rings at $\rho \to \infty$ decay in amplitude as $\rho^{-1/2}$ and oscillate at the same radial frequency as those of the linear BVB. In self-focusing or self-defocusing

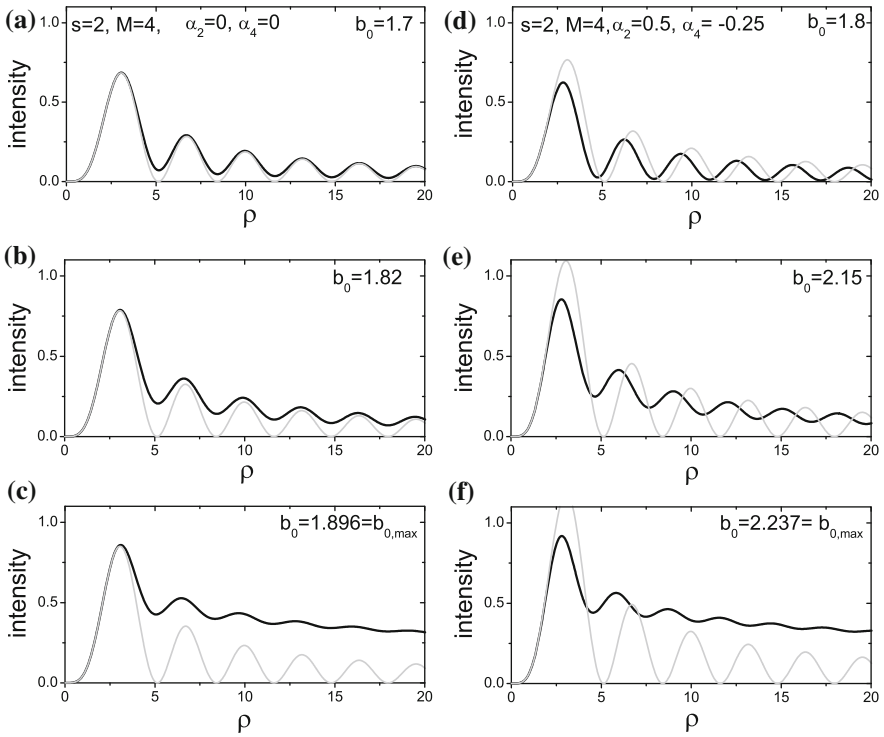

Fig. 3 For $\alpha_2 = \alpha_4 = 0$, and $M = 4$, intensity profiles of nonlinear BVBs with $s = 2$ and **a** $b_0 = 1.7$, **b** $b_0 = 1.82$ and **c** $b_0 = 1.896$. For $\alpha_2 = 0.5$, $\alpha_4 = -0.25$ and $M = 4$, intensity profiles of nonlinear BVBs with $s = 2$ and **d** $b_0 = 1.8$, **e** $b_0 = 2.15$ and **f** $b_0 = 2.237$. The dotted curves represent linear BVBs with $s = 2$ and the same b_0 as the nonlinear BVBs. Reproduced with permission from [40]. Copyright (2014) by The Optical Society of America

media, these outer rings are therefore radially shifted with respect to those of the linear BVB in order to match the compressed or enlarged inner rings.

These examples also illustrate that typical values of b_0 corresponding to intensities where the joint effect of the self-focusing and nonlinear absorption plays an essential role are of the order of unity. For instance, with $M = 4, s = 1, \alpha_2 = 3.30$ and $\alpha_4 = 0$, values $b_0 = 1.2$ and 1.6 respectively belong to nonlinear BVBs with cone angle $\theta = 1^\circ$ and peak intensities 0.77 TW/cm^2 and 1.16 TW/cm^2 in water at 527 nm [37].

Therefore, these nonlinear BVBs can propagate without any diffraction and any attenuation while their energy and angular momentum are continuously transferred to matter nonlinearly via multiphoton absorption. As pointed out above, the existence of these beams does not critically depend on the specific dispersive nonlinearities or on the order of multiphoton absorption. Only the details of the transversal structure and the specific maximum value $b_{0,\max}$ for existence depend on the choices of s, α_2, α_4 (or other dispersive nonlinearities), and multi-photon order M.

4 Stationary Propagation of Nonlinear BVBs with Nonlinear Absorption: Energy and Angular Momentum Transfer to Matter

The energy and angular momentum transferred continuously to matter is continuously replenished from an intrinsic reservoir of energy and angular momentum, which sustains the stationary propagation. To study this mechanism, we note that integration of Eq. (9) in ρ leads to

$$-2\pi\rho\frac{d\phi}{d\rho}\tilde{a}^2 = 2\pi\int_0^\rho d\rho\rho\tilde{a}^{2M}\,, \tag{11}$$

or $-F(\rho) = N(\rho)$ for short. This relation indicates that the nonlinear power losses in any circle of radius ρ, $N(\rho)$, are replenished by an inward power flux $F(\rho)$ crossing its circumference and coming from a power reservoir at large radial distances, as is illustrated in Fig. 4. Essentially, this is the mechanism of stationarity of nonlinear BVB, which is attainable only in beams transporting infinite power —the reservoir— as conical beams, and as originally proposed in Ref. [41]. This mechanism has some peculiarities with nonlinear BVBs [40]. If we write the complex envelope of a light beam (not necessarily stationary) in the form $\tilde{A} = \tilde{a}e^{i\Phi}$, the NLSE in Eq. (3) gives the continuity equation

$$\frac{1}{2}\partial_\zeta\tilde{a}^2 + \nabla_\perp\cdot\mathbf{j} = -\tilde{a}^{2M} \tag{12}$$

for the intensity $\tilde{a}^2$, where the transversal current of the intensity is given by $\mathbf{j} = \tilde{a}^2\nabla_\perp\Phi$, and $\nabla_\perp$ is the transversal gradient. The general condition for stationarity of the intensity pattern is then

$$-\nabla_\perp\cdot\mathbf{j} = \tilde{a}^{2M}\,, \tag{13}$$

expressing in differential form, and by reason of the divergence theorem, that the nonlinear power losses in any finite region of the transversal plane are compensated by an inward power flux through its contour. Equation (9) is the same as Eq. (13) for beams with radially symmetric intensity $\tilde{a}^2$ and phase $\Phi = \phi(\rho) + s\varphi - \zeta$. For these beams $\mathbf{j} = \tilde{a}^2(d\phi/d\rho\mathbf{u}_\rho + s/\rho\mathbf{u}_\varphi)$, and Eq. (11) is obtained by integrating Eq. (13) over a circle of radius ρ.

Figure 4 shows the intensity (first column), phase (second column) and the intensity current (third column) for formerly known stationary beams and for a nonlinear BVB. For linear BVBs (and also for vortex solitons) in transparent media (first row), the intensity current $\mathbf{j} = (\tilde{a}^2 s/\rho)\mathbf{u}_\varphi$ is azimuthal and solenoidal ($\nabla_\perp\cdot\mathbf{j} = 0$). For the fundamental (vortex-less) nonlinear Bessel beam (second row), the intensity current in the transversal plane $\mathbf{j} = (\tilde{a}^2 d\phi/d\rho)\mathbf{u}_\rho$ is radial inwards with a divergence that equals the nonlinear losses density $\tilde{a}^{2M}$. For the present nonlinear BVBs (third row), the intensity current has both azimuthal and radial inwards components, resulting

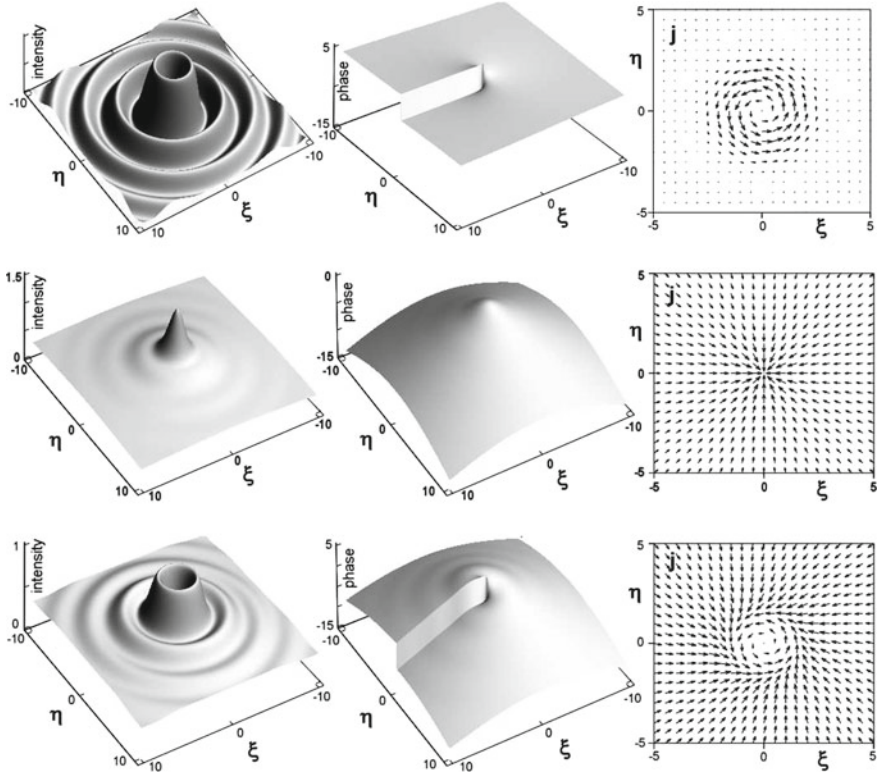

Fig. 4 Intensity profiles (first column), phase profiles (second column) and intensity current (third column) of the linear BVB with $s = 1$, and $b_0 = 1.666$ (first row), of the vortex-less ($s = 0$) nonlinear Bessel beam with $M = 4$, $\alpha_2 = \alpha_4 = 0$ and $b_0 = 1.174$ (second row) and of the nonlinear BVB with $s = 1$, $M = 4$, $\alpha_2 = \alpha_4 = 0$ and $b_0 = 1.666$ (third row). The normalized cartesian coordinates in the transversal plane are $\xi = \sqrt{2k|\delta|}x$ and $\eta = \sqrt{2k|\delta|}y$ in the transversal plane. A previous version of this figure was published by the authors in [40]

in a permanent inwards spiral transporting power from the intrinsic power reservoir towards the inner rings, where most of dissipation of energy into matter takes place.

A similar situation occurs with the angular momentum. The nonlinear BVB carries axial orbital angular momentum of density given by [12] $L = \tilde{a}^2 \partial \Phi / \partial \varphi = s\tilde{a}^2$. The angular momentum is then proportional to the topological charge s and to the intensity. As the intensity, the angular momentum density remains stationary, but is permanently flowing spirally with a current

$$s\mathbf{j} = s\tilde{a}^2 \left(\frac{d\phi}{d\rho} \mathbf{u}_\rho + \frac{s}{\rho} \mathbf{u}_\varphi \right) \tag{14}$$

proportional to the current of the intensity. The angular momentum current replenishes their losses $s\tilde{a}^{2M}$ due to the nonlinear absorption process according to the

continuity equation $-\nabla_\perp \cdot (s\mathbf{j}) = s\tilde{a}^{2M}$ for the angular momentum. Also, integration over a circle of radius ρ leads to

$$-2\pi\rho s\frac{d\phi}{d\rho}\tilde{a}^2 = 2\pi\int_0^\rho d\rho\rho s\tilde{a}^{2M}\,, \tag{15}$$

which is analogous to Eq. (11) for the energy, and expressing that the radial flux of angular momentum through any circle of radius ρ replenishes their nonlinear losses within that circle when transferred to the material medium.

5 Asymptotic Behavior at Large Distances

The asymptotic behavior of nonlinear BVBs at large radii is also determined by their non-diffracting and non-attenuating properties in media with nonlinear absorption. As will be clear in Sect. 6, this asymptotic behavior is of fundamental importance to understand the nonlinear dynamics of linear BVBs introduced in the medium. At the vortex core the nonlinear BVB behaves as the linear BVB $\tilde{A} \simeq b_0 J_s(\rho)e^{is\varphi}e^{-i\zeta}$, or what is the same [33],

$$\tilde{A} \simeq \frac{1}{2}\left[b_0 H_s^{(1)}(\rho) + b_0 H_s^{(2)}(\rho)\right]e^{is\varphi}e^{-i\zeta}\,. \tag{16}$$

The Hänkel beam $H_s^{(1)}(\rho)e^{is\varphi}e^{-i\zeta}$ carries power spirally outwards and the Hänkel beam $H_s^{(2)}(\rho)e^{is\varphi}e^{-i\zeta}$ spirally inwards. Both have the same amplitude in the linear BVB, so there is no net transport of power in the cross section [48]. In the nonlinear BVB, however, these components do not have equal amplitudes [41]. Asymptotically at large ρ the complex amplitude behaves as the "unbalanced" Bessel beam

$$\tilde{A}(\rho,\phi,\zeta) \simeq \frac{1}{2}\left[b_{\text{out}} H_s^{(1)}(\rho) + b_{\text{in}} H_s^{(2)}(\rho)\right]\mathrm{e}^{is\varphi}\mathrm{e}^{-i\zeta}, \tag{17}$$

as illustrated in the example of Fig. 5a, where the two interfering high-order Hänkel beams have different amplitudes $|b_{\text{out}}|$ and $|b_{\text{in}}|$. From the equivalent asymptotic expressions $H_s^{(1,2)}(\rho) \simeq \sqrt{2/(\pi z)}\, e^{\pm i[\rho-(\pi/2)(s-1/2)]}$ at large ρ [33], the condition that the inward radial flux $-F(\rho) = -2\pi\rho\tilde{a}^2 d\phi/d\rho = 2\pi\rho\mathrm{Im}[\tilde{A}(\partial\tilde{A}^\star/\partial\rho)]$ equals the total nonlinear power losses $N(\infty)$ leads to the relation

$$|b_{\text{in}}|^2 - |b_{\text{out}}|^2 = N(\infty)\,, \tag{18}$$

between b_{in} and b_{out}. It then follows that $|b_{\text{in}}| > |b_{\text{out}}|$ for any nonlinear BVB in a medium with dissipation. The values of these amplitudes can easily be extracted from the numerically evaluated radial profiles of intensity of nonlinear BVBs as follows. Using the same asymptotic expressions, the radial intensity at large ρ behaves as

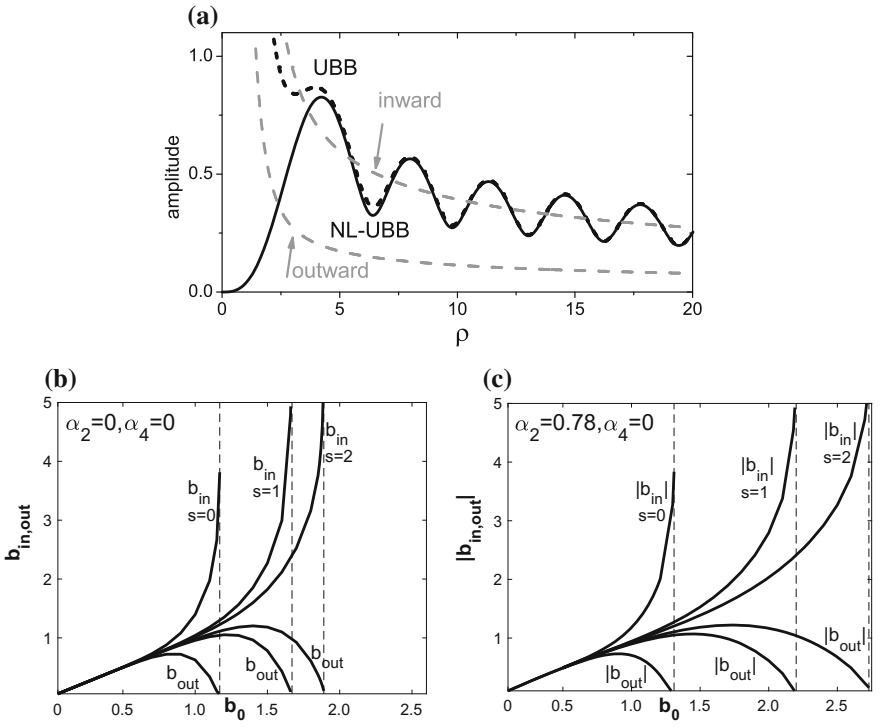

Fig. 5 **a** Amplitude of the nonlinear BVB with $M = 4$, $\alpha_2 = \alpha_4 = 0$, $l = 3$ and $b_0 = 1.9$ (solid curve), its asymptotic linear unbalanced Bessel beam (UBB) (dashed curve), and its Hänkel inward and outward components (dotted curves). **b** and **c** The values of the outward and inward amplitudes, $|b_{\text{out}}|$ and $|b_{\text{in}}|$, as functions of the amplitude b_0 of nonlinear BVBs of the indicated values of s in material media with the indicated values of α_2, α_4, and $M = 4$. The curves end at $b_{0,\max}$ for each value of the charge s, indicated as vertical dashed lines. A previous version of this figure was published by the authors in [40]

$$\tilde{a}^2 \simeq \frac{1}{2\pi\rho}\left\{|b_{\text{out}}|^2 + |b_{\text{in}}|^2 + 2|b_{\text{out}}||b_{\text{in}}|\cos\left[2\rho + \kappa\right]\right\}, \tag{19}$$

with $\kappa = -\pi s - \pi/2 + \arg(b_{\text{out}}/b_{\text{in}})$. Thus, $2\pi\rho\tilde{a}^2$ represents harmonic oscillations of contrast $C = 2|b_{\text{in}}||b_{\text{out}}|/(|b_{\text{in}}|^2 + |b_{\text{out}}|^2)$ about the central value $R = |b_{\text{in}}|^2 + |b_{\text{out}}|^2$. These properties are readily obtained from the numerically evaluated radial profiles of nonlinear BVBs, and from C and R, the amplitudes $|b_{\text{in}}|$ and $|b_{\text{out}}|$ are obtained as

$$|b_{\text{in}}|^2 = \frac{R}{2}\left(1 + \sqrt{1 - C^2}\right), \quad |b_{\text{out}}|^2 = \frac{R}{2}\left(1 - \sqrt{1 - C^2}\right). \tag{20}$$

These amplitudes are plotted as functions of b_0 in Fig. 5b, c for nonlinear BVBs of different charges in different media. It is numerically found that b_{in} and b_{out} are real

quantities in absence of dispersive nonlinearities, and also that $\arg b_{\text{in}} = -\arg b_{\text{out}}$ with dispersive nonlinearities as self-focusing or self-defocusing.

6 Propagation of Bessel Vortex Beams in Nonlinear Media Revisited: The "Selection Problem"

In the numerical simulations of propagation of linear BVBs, as in Fig. 1, we observe that one of the nonlinear BVBs studied previously is formed spontaneously, acting thus as an attractor of the nonlinear dynamics. The nonlinear BVB has always the same cone angle and topological charge as the input linear BVB. The so-called "selection problem"is the determination of the precise amplitude or intensity of the final BVB, i.e., the determination of the parameter b_0 of the final nonlinear BVB, say $b_0(\infty)$. This problem arose for the first time in Ref. [36] and remained unsolved for the vortex-less case. In the numerical simulation of Fig. 1, for example, the linear BVB with $b_0(0) = 3$ is attracted by the nonlinear BVB with $b_0(\infty) = 1.60$.

Figure 6 summarizes the results of a large number of similar numerical simulations, and unveils the law underlying the selection of the final nonlinear BVB, i.e., the value of $b_0(\infty)$. Figure 6a depicts the pairs $[b_0(0), b_0(\infty)]$ of the input linear BVB and final nonlinear BVB extracted from these simulations for $s = 0, 1$ with a particular cone angle and medium (particular values of α and M). The attracting nonlinear BVB tends to match that with the maximum amplitude that the medium can support when the intensity of the input linear BVB is extremely high. On the other side, the selected nonlinear BVB does not differ substantially from the launched beam at low enough intensities.

The solution of the selection problem arises from the evaluation of the inward and outward amplitudes, $b_{\text{in}}(\infty)$ and $b_{\text{out}}(\infty)$ of the nonlinear BVB attractor with $b_0(\infty)$, represented in Fig. 6b, c for the respective cases with $s = 0$ and $s = 1$. As seen, $|b_{\text{in}}(\infty)|$ is given by the identity function as a function of $b_0(0)$. Taking into account that for the linear BVB introduced in the medium $|b_{\text{in}}(0)| = b_0(0)$, we can then conclude that *the amplitude of the asymptotic inward Hänkel component is a conserved quantity during the nonlinear wave propagation.* In fact, the inward Hänkel beam behaves like a linear beam that carries the power from its reservoir at large radial distances, and therefore is not involved in the nonlinear absorption effects taking place in the inner rings. Thus, given the amplitude of the input linear BVB determined by $b_0(0)$, the attracting nonlinear BVB is that with $b_0(\infty)$ whose inward component equals $b_0(0)$, that is,

$$|b_{\text{in}}(\infty)| = b_0(0)\,. \tag{21}$$

Therefore, given a material medium and cone angle (M, α_2 and α_4) and a topological vorticity or charge s, graphs such as those in Fig. 5b, c for the amplitude of the inward Hänkel component can be obtained from the radial profiles of the nonlinear BVBs of

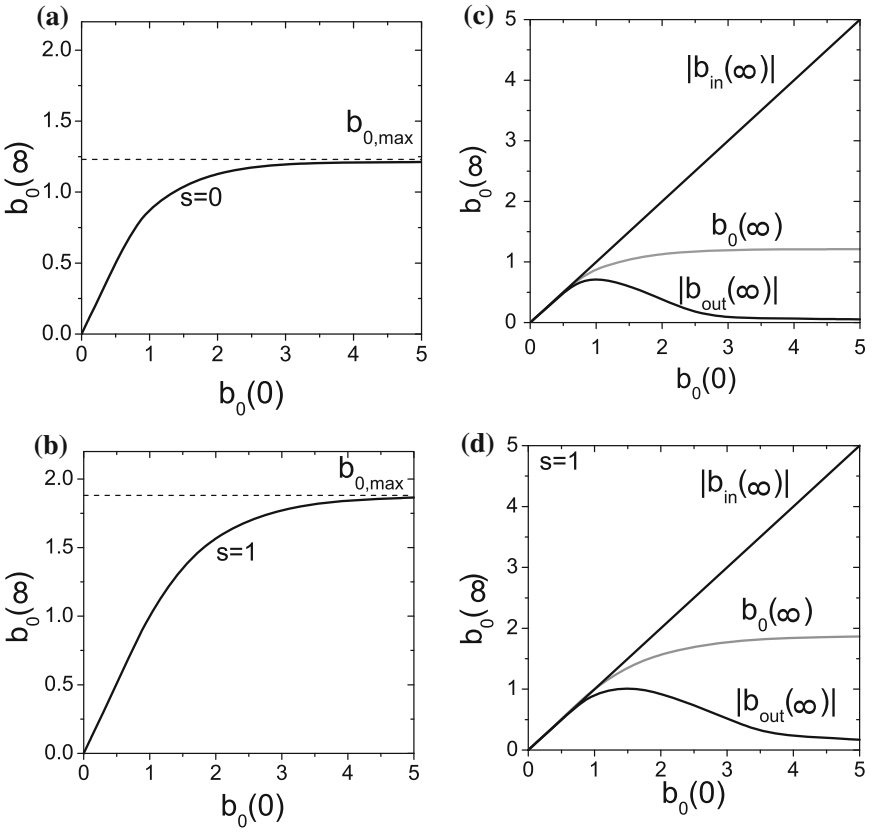

Fig. 6 **a** and **b** Values of the amplitude $b_0(\infty)$ of the attracting nonlinear BVB as a function of the amplitude $b_0(0)$ of the input linear BVB for $s = 0$ and $s = 1$ in a medium and cone angle such that $\alpha_2 = 0.5$ and $\alpha_4 = -0.25$ and $M = 4$, obtained by solving numerically the NLSE in Eq. (3). **c** and **d** For the respective cases with $s = 0$ and $s = 1$, the black curves represent the amplitudes $|b_{\text{in}}(\infty)|$ and $|b_{\text{out}}(\infty)|$ of the inward and outward Hänkel components of the attracting nonlinear BVB with the amplitude $b_0(\infty)$ (gray curves). As a function of $b_0(0)$, $|b_{\text{in}}(\infty)|$ is then found to be the identity function, i. e., $|b_{\text{in}}(\infty)| = b_0(0)$. Previous versions of figures **c** and **d** were published by the authors in [40]

different amplitudes supported by the medium. The nonlinear BVB attractor can be obtained from these graphs as one whose amplitude of the inward Hänkel component coincides with the amplitudes b_0 of the linear BVB that is launched in the medium. These conclusions are drawn here with *ideal*, linear or nonlinear BVBs, but they will be seen in Sect. 8 to hold the same in actual settings with finite-power versions of these beams.

7 Stability of Nonlinear BVBs

It is well known that vortex solitons are prone to azimuthal breaking instability in self-focusing Kerr media [12]. Only in specifically tailored media, as specific saturable, cubic-quintic nonlinearities [34, 44], or nonlocal Kerr nonlinearities [55], stable vortex solitons have been reported to exist. Stability of some nonlinear BVBs is suggested by the above simulations of the propagation of linear BVBs attracted by a specific nonlinear BVB. Also, nonlinear BVBs have been observed to be spontaneously formed in experiments under specific conditions associated with large cone angles [54], which further supports the existence of stable nonlinear BVB in media such as glasses.

In this section we perform a linear-stability analysis of the nonlinear BVBs and find there exists a subset of them that is stable against radial and azimuthal perturbations. The results from the stability analysis are corroborated by direct numerical simulations of the propagation of perturbed nonlinear BVBs. For simplicity, in this section we only consider the more destabilizing self-focusing (positive) cubic nonlinearity and dissipation, but, as the existence of nonlinear BVBs, similar results regarding stability or instability are readily seen to hold with more general dispersive nonlinearities. We will then write $\alpha \equiv \alpha_2$, and consider $\alpha_4 = 0$.

The linear-stability analysis applied to our case will be the usual one [12], where we take a nonlinear BVB plus a small perturbation as

$$\tilde{A} = \tilde{A}_s + \varepsilon \left[u_m(\rho) e^{i\kappa\zeta + im\varphi} + v_m^\star(\rho) e^{-i\kappa^\star\zeta - im\varphi} \right] e^{is\varphi - i\zeta}, \tag{22}$$

being $\tilde{A}_s = \tilde{a} e^{i\phi} e^{is\varphi - i\zeta}$ a nonlinear BVB, ε an arbitrary small amplitude of perturbations with eigenmodes $[u_m(\rho), v_m(\rho)]$ and integer winding number m. Valid solutions $u_m(\rho)$, $v_m(\rho)$ to our system must comply with the usual boundary conditions $u_m \sim \rho^{|s+m|}$ and $v_m \sim \rho^{|s-m|}$ for $\rho \to 0$, as well as vanishing for $\rho \to \infty$. Substituting the above Ansatz in Eq. (3) gives the following linearized equations:

$$\begin{pmatrix} H_+ & f \\ -f^\star & -H_-^\star \end{pmatrix} \begin{pmatrix} u_m \\ v_m \end{pmatrix} = \kappa \begin{pmatrix} u_m \\ v_m \end{pmatrix}, \tag{23}$$

where

$$f \equiv [\alpha \tilde{a}^2 + i(M-1)\tilde{a}^{2M-2}] e^{2i\phi}, \tag{24}$$

and

$$H_\pm \equiv \frac{d^2}{d\rho^2} + \frac{1}{\rho}\frac{d}{d\rho} - \frac{(s \pm m)^2}{\rho^2} + 1 + (2\alpha\tilde{a}^2 + iM\tilde{a}^{2M-2}). \tag{25}$$

If there exists an eigenvalue $\kappa_I \equiv \mathrm{Im}\{\kappa\} < 0$, then an instability will develop. In this case, it is expected to manifest itself in a weakly perturbed BVB through the breakup of the first ring (the brightest), and perhaps the secondary rings too, and the number of fragments resulting from this breakup is expected to coincide with the winding

number m of the mode with the largest growth rate. Also, several unstable modes with similar growth rate may compete, or induce different number of fragments in different rings. The analysis of Eqs. (22) and (23) for all integers $m = 0, 1, 2 \ldots$ covers all type of weak perturbations, since these equations result from introducing a nonlinear BVB plus a general perturbation, i.e., $\tilde{A} = \tilde{A}_s + \varepsilon p(\rho, \varphi, \zeta)$, into the NLSE, linearizing, expanding p in azimuthal harmonics, and solving the equations for each harmonic [12].

We solved the problem in Eq. (23) numerically, as done previously for radial perturbations ($m = 0$) to the fundamental nonlinear Bessel beam [37, 41, 42]. Weaker localization and the structured radial profile of the nonlinear BVBs make the numerical procedure used to solve Eq. (23) more difficult when compared to other cases, such as the vortex solitons in the complex Ginzburg–Landau model [2, 5, 22, 31]. We transform it into an algebraical eigenvalue problem of a $2N \times 2N$ matrix by introducing a discretization in a radial grid of step h and N points, so that the largest radius is Nh, with boundary conditions $u \sim \rho^{|s+m|}$, $v \sim \rho^{|s-m|}$ for $\rho \to 0$, and $u, v = 0$ at $\rho = Nh$. Stability or instability is inferred from the spectrum of $2N$ eigenvalues in the double limit $h \to 0$, $N \to \infty$. For fixed truncation radius Nh, no substantial difference between the eigenvalues is found provided that the nonlinear BVB profile is adequately sampled (e.g., $h = 0.1$, $N = 2000$ and $h = 0.2$, N=1000). We then focus on increasing truncation radius Nh by fixing h and increasing the number of points N, since important differences are found. In case of instability with low growth rate $|\kappa_I|$, these differences arise because the associated eigenmode u, v presents the slow exponential decay $\sim e^{\kappa_I \rho/2}$ [37], so that it is only adequately replicated by the truncated system if Nh is much larger than $2/|\kappa_I|$. In other terms, the minimum reliable growth rate obtainable from the truncated system is $|\kappa_I| \gg 2/Nh$. Specially developed routines for sparse matrices were used to calculate the eigenvalues of matrices up to 32 000 $\times$32 000 in order to increase accuracy for the minuscule growth rates involved, sampling our system with N = 16 000 points. These technical details are explained to stress that proving stability with this method requires, strictly speaking, to infer the limit $N \to \infty$.

Figure 7a, b display results for the growth rates of unstable modes of nonlinear BVBs with $s = 1$, two choices of b_0 and varying α, and Fig. 7c–f illustrate how these results are obtained. For all m, the growth rates computed with finite N behave as almost straight lines that tend to cut the horizontal axis at certain positive values of α, but this behavior is interrupted when the growth rate is comparable to the minimum reliable value $2/Nh$, as seen in Fig. 7c, d for the two modes with higher growth rate or leading to instability down to lower values of α. For high values of α, no difference is observed with increasing N, and these values are attributed to a genuine instability of the corresponding nonlinear BVB in the limit $N \to \infty$. In Fig. 7e, f we plot the detailed behavior of the growth rate in the region of small α where relevant differences with N are observed. The growth rate is seen to converge to positive values for some α, but is observed to approach zero for the smallest values of α. The insets of Fig. 7e, f indicate an approximate decay $1/N$ for the particular values of α where convergence to a positive value is not observed. Similar behavior is observed for all other relevant modes m. Up to the limit of our computational capability, we

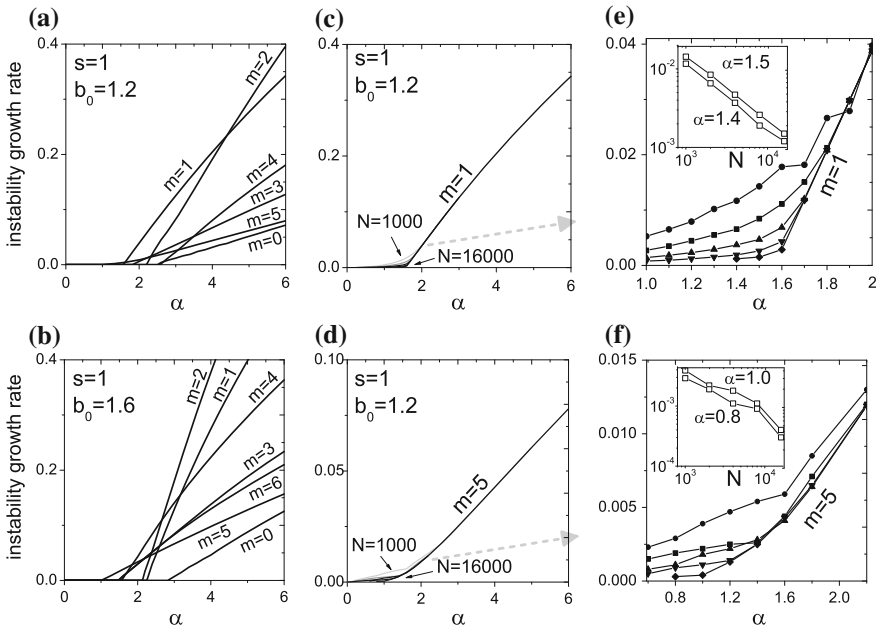

Fig. 7 **a** and **b** Growth rates of unstable perturbation modes of the indicated nonlinear BVBs. **c** and **d** The same but evaluated with $h = 0.2$, $N = 1000$, 2000, 4000, 8000 and 16000 from the lighter to the darker curves. **e** and **f** Zoom of the region where the growth rate depends appreciably on N. $N = 1000$ (circles), 2000 (squares), 4000 (up triangles), 8000 (down triangles), 16000 (rhombuses). The insets plot the growth rates as functions of N for particular values of α, suggesting a decay of the growth rate as $\sim 1/N$. A previous version of this figure was published by the authors in [43]

can then say that there exist nonlinear BVBs in Kerr media that are stable against all type of small perturbations, as shown in Fig. 7a, b; here, for $M = 4$ and $s = 1$ these are nonlinear BVBs with $\alpha \lesssim 1.1$ for $b_0 = 1.2$, and with $\alpha \lesssim 1$ for $b_0 = 1.6$.

Direct numerical simulations of the NLSE in Eq. (3) were also carried out using a split-step Fourier method. In all cases, nonlinear BVBs with an initial perturbation made up of random noise have their rings broken into fragments moving along circular trajectories if unstable. Comparing Fig. 8 with Fig. 7b, it can be verified that the number of fragments is exactly equal to the winding number m of the unstable mode with the highest instability growth rate. The higher this rate is, the earlier the BVB will break up. On a special note, a mode competition can be seen in Fig. 8b, where the internal ring splits into two parts and the external ones into four, in agreement with the existence of two almost equally unstable perturbation eigenmodes.

If stability is predicted by our model, as for $\alpha = 1$ in Fig. 7a, our simulations (ran up to $\zeta = 300$) show that the nonlinear BVB squanders the initial perturbation and keeps its structure throughout the whole propagation, as illustrated in Fig. 9a, b. For unstable nonlinear BVBs, the development of the instability into large perturbations is not generally determined by the number of rotating portions in the small-perturbation

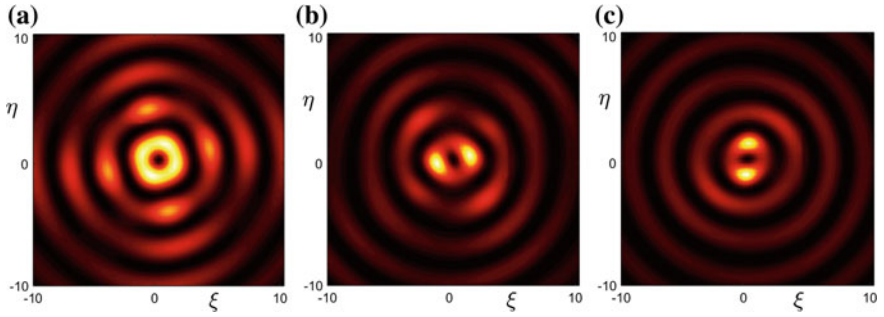

Fig. 8 For $M = 4$, $s = 1$ and $b_0 = 1.6$, the transverse intensity distributions $|\tilde{A}|^2$ of the initially perturbed vortex with **a** $\alpha = 2.2$ at $\zeta = 100$, **b** $\alpha = 2.8$ at $\zeta = 45$, and **c** $\alpha = 4$ at $\zeta = 15$. The numbers of fragments into which the unstable vortices split are exactly predicted by the linear-stability analysis. A previous version of this figure was published by the authors in [43]

regime, as known for the case of usual vortex solitons [12]. This can be readily seen in the following examples: Fig. 7a for $\alpha = 3$ predicts the single circulating fragment that indeed appears in Fig. 9c. This fragment breaks afterwards into two circulating fragments observed in Fig. 9d. Also, Fig. 7a for $\alpha = 6$ predicts the two circulating fragments that are shown in Fig. 9e. These two fragments decay at longer propagation distances into several randomly located, non-rotating splinters that emerge and wane during the propagation, as illustrated in Fig. 9f. For further purposes, we have also plotted in Fig. 9g–i the peak intensity in the course of propagation for the three perturbed nonlinear BVBs considered. For $\alpha = 3$, instability leads to quasi-periodic oscillations that are damped after the secondary splitting. For the more unstable case with $\alpha = 6$, where the filaments are non-rotating and disordered, the behavior of the peak intensity indicates an endless chaotic regime continuously fed by the reservoir.

Stable nonlinear BVBs with multiple vorticity ($|s| > 1$) have their existence demonstrated in Fig. 10, which sum up the results of the linear-stability analysis for cases $s = 2$ and $s = 3$. A similar outcome is forecasted to ensue for $s > 3$. Note that the stabilization of vortices with $s > 1$ is achieved for the first time with this setup, as previously attempts failed [1, 3, 7, 13, 28, 32, 46, 47, 56].

The mechanism behind vortex stability in the current system can be envisaged from a deeper observation of Fig. 10. In it, we also plot the instability growth rates for nonlinear BVBs in the completely transparent medium after setting all dissipative terms in the equations to zero in our model. As expected, all nonlinear BVBs are now unstable. The BVB intensity profiles obtained with and without dissipation in all cases shown in Fig. 10 are almost identical, aside that with dissipation the contrast of the radial oscillations is a bit smaller than unity. However, the beams in the medium without dissipation are unstable, and the beams in the medium with dissipation

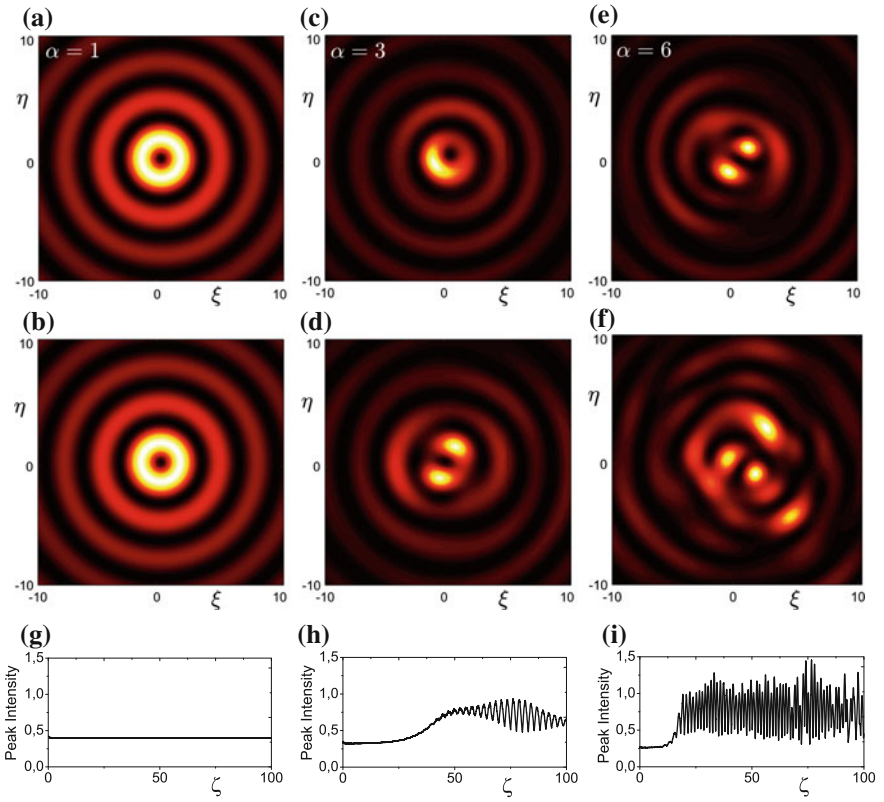

Fig. 9 For $M = 4$, $s = 1$ and $b_0 = 1.2$, the transverse intensity distributions, $|\tilde{A}|^2$, of the initially perturbed BVB with $\alpha = 1$ at propagation distances **a** $\zeta = 10$ and **b** $\zeta = 300$, with $\alpha = 3$ at propagation distances **c** $\zeta = 40$ and **d** $\zeta = 96$, and with $\alpha = 6$ at **e** $\zeta = 23$ and **f** $\zeta = 93$. The results in **a**, **b** corroborate the stability, and the results in **c**–**f** demonstrate the secondary breakup of fragments produced by the primary instability. **g**–**i** Peak intensity in the three respective cases with $\alpha = 1, 3$ and 6 as functions of the propagation distance

and with $\alpha \lesssim 1$ are stable. In this respect, we note that stabilization is reported to occur in Refs. [19, 54] when the cone angle increases (i.e., α decreases), and qualitatively explained as inefficient nonlinear wave mixing or suppressed growth of the modulation instability at these cone angles. The results presented in Fig. 10 from the linear-stability analysis quantify how using large cone angles help stabilize the system, with and without dissipation. Besides the quantification of the effect, it also demonstrates that the stabilization is never complete without taking dissipation into consideration. This means, in other words, that the mere increase of the cone angle does not produce, by itself, completely stable nonlinear BVBs without dissipation.

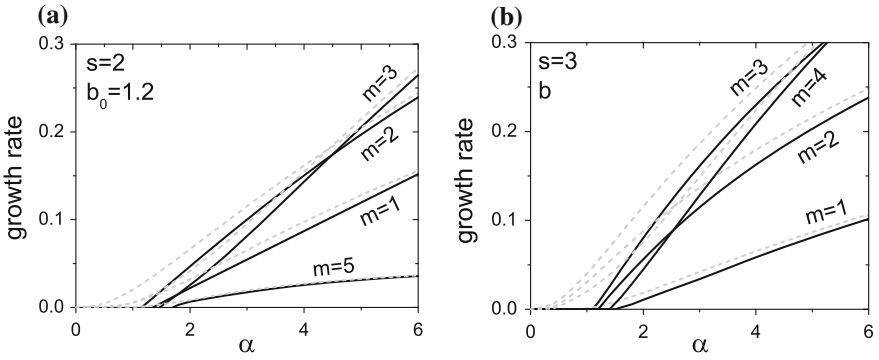

Fig. 10 For $M = 4$, growth rates of the most unstable modes of nonlinear BVBs with $s = 2$ and $s = 3$ (solid curves), and of their nonlinear BVB counterparts with the same parameters in the absence of absorption (dashed curves). A previous version of this figure was published by the authors in [43]

8 Tubular, Rotating, and Speckle-Like Dynamical Regimes of Filamentation from Axicon-Generated Nonlinear Bessel Vortex Beams

All preceding results regard to ideal, linear or nonlinear, conical beams in the sense that they transport infinite power. We now consider the experimental implications of these results in experiments that generate actual Bessel beams with finite power and their nonlinear counterparts. In most of these arrangements, a Gaussian beam with intrinsic vorticity s crosses an axicon [19, 38, 42], or equivalent device to create a conical beam [54]. The nonlinear medium is usually placed close or immediately after the axicon, so that we can model the optical field at the entrance plane of the medium by $A(r, \varphi, 0) = \sqrt{I_G}\exp(-r^2/w_0^2)\exp(-ikr\theta)\exp(is\varphi)$ [19, 54], where $\sqrt{I_G}$ and w_0 are the amplitude and width of the Gaussian beam, and θ the cone angle imprinted by the axicon. With our variables the input optical field reads as $\tilde{A}_G(\rho, \varphi, 0) = b_G\exp(-\rho^2/\rho_0^2)\exp(-i\rho)\exp(is\varphi)$, where amplitudes, transversal and axial lengths scale as specified in Eq. (2). If propagation after the axicon were linear, then a finite-power version of the linear BVB $\tilde{A}_B \simeq b_B J_s(\rho)\exp(is\varphi)$ would form at the axicon focus, with intensity $b_B^2 = \pi\rho_0 e^{-1/2}b_G^2$. The focus is placed at $\rho_0/4$ in our dimensionless axial coordinate, half of the Bessel distance $\rho_0/2$ ($w_0/2\theta$ and w_0/θ, respectively, in physical units).

With this arrangement, quasi-stationary and rotary regimes of nonlinear propagation after the axicon have been described in Ref. [19], and quasi-stationary, rotary and speckle-like (chaotic) regimes in Ref. [54]. In these studies, the quasi-stationary evolution of the system is related with the emergence of a nonlinear BVB, supposedly stable; and in Ref. [19] the rotary evolution of the system is hypothesized to be associated with either an unstable nonlinear BVB, or with nonexistence of a station-

ary state in the specific experimental configuration. In neither case the corresponding nonlinear BVB was identified, so that these conjectures were not verified.

Recent investigation for the vortex-less case ($s = 0$) [42] has shown that the dynamics of the nonlinear propagation after the axicon is determined in the Bessel zone by the fundamental ($s = 0$) nonlinear Bessel beam with amplitude $|b_{\text{in}}| = b_B$. This means that, in the vortex-less situation, the law of conservation of the amplitude of the inward Hänkel component, described in Sect. 6, holds also in actual settings with finite power, but is reinterpreted here by stating that the nonlinear BVB that acts as an attractor in the Bessel zone is that with the same cone angle and with amplitude $|b_{\text{in}}|$ equal to that of the linear Bessel beam that would emerge at the axicon focus in linear propagation. It has been further verified that if this fundamental nonlinear Bessel beam is stable, the system smoothly develops into it about the center of the Bessel zone and decays afterwards. On the other hand, if the nonlinear BVB is not stable, an unstable regime characterized by the signatures of the evolvement of the instability forms in the Bessel zone.

The same conclusion appears to be valid for the nonlinear BVB of arbitrary topological charge ($s \neq 0$), as supported by the extensive numerical simulations carried out. The dynamics in the Bessel zone is also determined by the nonlinear BVB with b_0 so that the amplitude of the inward Hänkel component is $|b_{\text{in}}| = b_B$, and its cone angle and vorticity s are the same as those from its linear counterpart. The complete agreement between the prediction obtained from the stability analysis for a specific nonlinear BVB and the observed azimuthal-symmetry-breaking dynamics in the Bessel zone demonstrates it.

Three particularly significant examples are displayed in Fig. 11. These are three illuminating Gaussian beams, respectively with $b_G = 0.0402$ (left), 0.0341 (center) and 0.030 (right), all of them with an intrinsic single vortex $s = 1$ and $\rho_0 = 400$. The Bessel amplitudes yielded under linear propagation would then be, in this order, $b_B = 1.11$, 0.94 and 0.829. These illuminating beams are chosen such that the attracting nonlinear BVBs in respective nonlinear media with $M = 4$ and $\alpha = 1$, 3 and 6, and with $|b_{\text{in}}| = b_B$, are characterized by $b_0 = 1.2$ in all three cases.

Under these conditions, Fig. 7a obtained from our analysis, and the numerical simulations of the propagation of the perturbed respective nonlinear BVBs in Fig. 9, predict instability for $\alpha = 3$ and 6, with inverse growth rates, or characteristic length of development of the instability, much shorter than the length of the Bessel zone, $\rho_0/2$. On the contrary, for $\alpha = 1$ stability is predicted in Figs. 7a and 9.

As seen in Fig. 11a, b, the stable nonlinear BVB with $\alpha = 1$ is smoothly formed about the axicon focus ($\rho_0/4 = 100$), followed by a smooth decay towards the end of the Bessel zone. The propagation thus resembles the robust propagation of the stable nonlinear BVB in Fig. 9a, b, only limited by the finite power of the reservoir, which depleted at the end of the Bessel zone. The evolution of the instability leading to the azimuthal breakup can be clearly observed in Fig. 11c, d for $\alpha = 3$ and Fig. 11e, f for $\alpha = 6$. The dynamics within the Bessel zone starts from the regime of small

perturbations predicted by our linear-stability analysis in Fig. 7a, and then proceeds to the regime of large perturbations regime seen in Fig. 9c, d for $\alpha = 3$ and Fig. 9e, f for $\alpha = 6$. At $\alpha = 3$, a rotatory regime with initially one fragment that later breaks into two is observed, as in the development of instability in Fig. 9c, d. At $\alpha = 6$, a rotatory regime with initially two fragments later breaks into randomly placed non-rotating spots, indicating a stronger instability, also as in the development of instability in Fig. 9e, f. The behavior of the peak intensity in the central part of the Bessel zone is plotted in Fig. 11g–i in the three representative examples studied. In all them, the peak intensity reproduces the dynamics also observed in the development of the instability, if any, triggered by noise of the respective nonlinear BVBs plotted in Fig. 9g–i.

When compared to the quasi-stationary and rotary regimes described numerically in [19], the similarity is remarkable. A strong parallel can also be established with the quasi-stationary, rotary and speckle-like regimes described experimentally in [54]. When subjected to the linear-stability analysis procedure, the previously mentioned representative examples admit a unified interpretation in terms of the stability or instability properties of a particular nonlinear BVB: that conserving the topological charge, the cone angle, and with amplitude b_0 satisfying the condition $|b_{\text{in}}| = b_B$. The existence and uniqueness of a single nonlinear BVB satisfying the condition $|b_{\text{in}}| = b_B$ is ensured considering that for a given M, α and s, $|b_{\text{in}}|$ is a strictly growing function of b_0 taking all values between $|b_{\text{in}}| = 0$ and $|b_{\text{in}}| = \infty$, as seen in Fig. 5b, c.

It is possible, for example, to study more in depth the experimental phenomena of the quasi-stationary, rotating and speckle-like regimes reported in Fig. 4 of [54]. Based on the values of the material constants, cone angles and three pulse energies, we can characterize the three attracting nonlinear BVBs as those determined by $M = 5$, $s = 3$, $\alpha = 14.89$, and $b_0 = 0.368$, 0.822 and 1.644. Through the stability analysis we obtain, respectively, the largest dimensionless growth rates in each case as 0.026, 0.245 and 0.784, or, multiplying by $|\delta|$, $2.48\,\text{cm}^{-1}$, $23.4\,\text{cm}^{-1}$ and $74.9\,\text{cm}^{-1}$ in physical units. The different observed behaviors can be understood when we compare the length of the Bessel zone ($\sim 0.072\,\text{cm}$), with the associated characteristic lengths of the instability development, or inverse growth rates: 0.402 cm, 0.043 cm and 0.013 cm. In the first case the instability had not yet the opportunity to develop; in the second case the rotating filaments observed correspond to the azimuthal primary break in the nonlinear BVB instability; and in the third case the random filaments observed correspond to a completely developed nonlinear BVB instability.

Lastly, the existence of truly stable nonlinear BVBs demonstrated in this work guarantees the existence of a regime of tubular-beam propagation. The only limitation on this regime comes by the limited quantity of power that can be stored in the reservoir, whose exhaustion will delimit the Bessel zone. Thus, the stable vortex tubules can be increased endlessly by incrementing the power supplied to the reservoir, for example, through the increase of ρ_0.

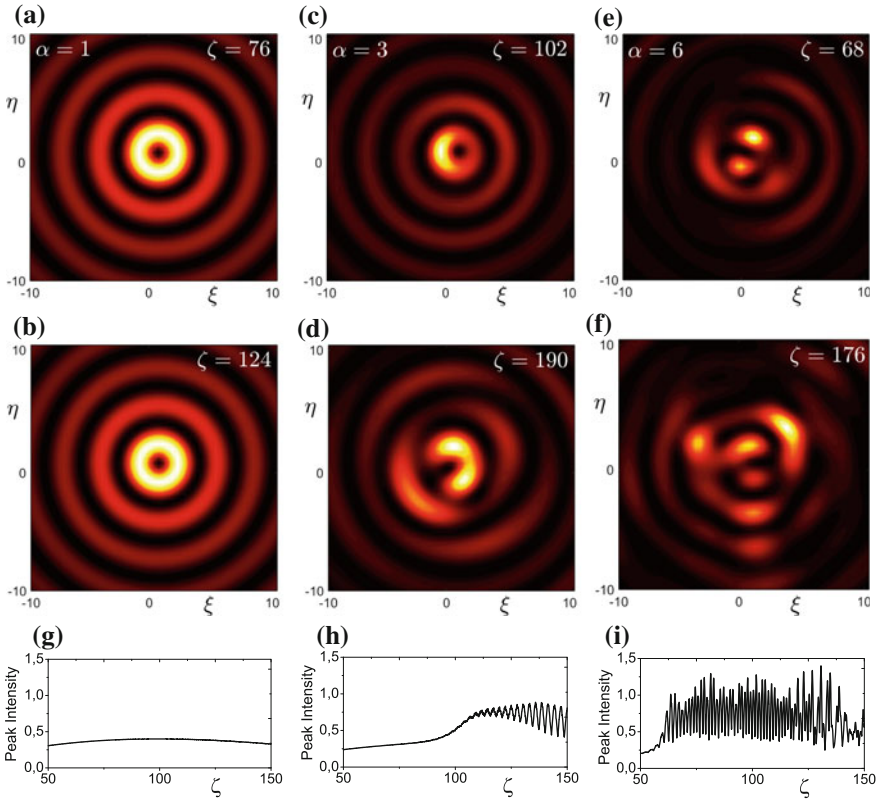

Fig. 11 Normalized intensity profiles at the propagation distances indicated in the panels for $\alpha = 1$ (left), $\alpha = 3$ (center), and $\alpha = 6$ (right), in a medium characterized by a four-photon absorption, produced by axicons illuminated by Gaussian beams with $\rho_0 = 400$ and carrying a vortex of charge $s = 1$ in their center, but with the different amplitudes $b_G = 0.0402$ (left), 0.0341 (center) and 0.030 (right). The respective linear Bessel amplitudes are $b_B = 1.11$, 0.94 and 0.829. These values are chosen such that all three nonlinear BVBs with $s = 1$ and $|b_{\text{in}}| = b_B$ in samples with the corresponding values of α and M, have the same $b_0 = 1.2$, which can be identified using the method explained in Sect. 5 or in Ref. [40]. **g–i** Peak intensity as a function of the propagation distance in the central part of the Bessel zone for the three cases. This figure is to be compared with Fig. 9 and illustrates that the dynamics in the Bessel zone duplicates that in the development of instability, if any, of each nonlinear BVB

9 Summary

In this chapter we have reviewed the properties of nonlinear BVBs, nonlinear conical beams that propagate without any change, including any attenuation, in homogeneous Kerr media with nonlinear absorption. These beams form narrow and (ideally) infinitely long tubes of light where energy and orbital angular momentum can be transmitted to matter, yet the energy and angular momentum of the nonlinear BVB

are uninterruptedly renovated by inward spiral currents arriving from a reservoir at large radius. Nonlinear BVBs emerge naturally in the propagation of linear BVBs at intensities at which multi-photon absorption are significant.

Though a linear-stability analysis we have demonstrated that nonlinear BVBs may be stable against azimuthal symmetry breaking and collapse. These stable vortices can have multiple vorticities, and do not require materials with specific nonlinearities. They can propagate robustly in usual dielectrics like water, air, or optical glasses at high enough intensities, typically tens of TW/cm^2 in gases or a fraction TW/cm^2 in condensed matter. It is then not surprising that, contrary to previous settings, these vortices have been observed before their stability is demonstrated. The proof of stability has major implications in these experiments with powerful pulsed Bessel beams and their applications. The tubular filamentation regime, for instance, is only limited by the quantity of power stored in the reservoir (and depleted at the end of the Bessel zone), and as such can be enlarged by simply increasing the amount of power of the illuminating beam.

From the stability analysis and diagnostic numerical simulations we have extracted simple basal laws that govern the propagation of powerful Bessel beams in nonlinear media, that apply both in ideal situations with infinite power and in actual experiments. We have shown that the propagation is in all cases determined by a nonlinear BVB attractor. We have identified it as the nonlinear BVB preserving the cone angle, the topological charge and the inward component of the power flux of the Bessel beam. We point out that attractors are not necessarily stable attractors, as is well-known in the field of nonlinear and chaotic dynamical systems. The tubular, rotating and speckle-like (chaotic) regimes observed in experiments are just manifestations of the stability/instability properties of the attracting nonlinear BVB. Understanding these laws is of fundamental importance for improving the applications of these powerful nonlinear Bessel beams.

Acknowledgements M.A.P. acknowledges support from Project of the Spanish Ministerio de Economía y Competitividad No. MTM2015-63914-P.

References

1. Adhikari, S.K.: Collapse of attractive Bose–Einstein condensed vortex states in a cylindrical trap. Phys. Rev. E **65**, 016703 (2001)
2. Akhmediev, N., Soto-Crespo, J.M., Grelu, P.: Spatiotemporal optical solitons in nonlinear dissipative media: from stationary light bullets to pulsating complexes. Chaos **17**, 037112 (2007)
3. Alexander, T.J., Bergé, L.: Ground states and vortices of matter-wave condensates and optical guided waves. Phys. Rev. E **65**, 026611 (2002)
4. Allen, L., Padgett, M., Babiker, M.: The orbital angular momentum of light. Progr. Opt. **39**, 291–372 (1999)
5. Aranson, I.S., Kramer, L.: The world of the complex Ginzburg–Landau equation. Rev. Mod. Phys. **74**, 99–143 (2002)

6. Bergé, L.: Wave collapse in physics: principles and applications to light and plasma waves. Phys. Rep. **303**, 259–370 (1998)
7. Carr, L.D., Clark, C.W.: Vortices in attractive Bose–Einstein condensates in two dimensions. Phys. Rev. Lett. **97**, 010403 (2006)
8. Couairon, A., Gaizauskas, E., Faccio, D., Dubietis, A., Trapani, P.D.: Nonlinear X-wave formation by femtosecond filamentation in Kerr media. Phys. Rev. E **73**, 016608 (2006)
9. Couairon, A., Mysyrowicz, A.: Femtosecond filamentation in transparent media. Phys. Rep. **441**, 47–189 (2007)
10. Curtis, J.E., Grier, D.G.: Structure of optical vortices. Phys. Rev. Lett. **90**, 133901 (2003)
11. Daly, M., Sergides, M., Chormaic, S.N.: Optical trapping and manipulation of micrometer and submicrometer particles. Laser Photonics Rev. **9**, 309–329 (2015)
12. Desyatnikov, A.S., Torner, L., Kivshar, Y.S.: Optical vortices and vortex solitons. Progr. Opt. **47**, 291–391 (2005)
13. Dodd, R.J.: Approximate solutions of the nonlinear Schrödinger equation for ground and excited states of Bose–Einstein condensates. J. Res. Natl. Inst. Stand. Technol. **101**, 545–552 (1996)
14. Durnin, J.: Exact solutions for nondiffracting beams. I. The scalar theory. J. Opt. Soc. Am. A **4**, 651–654 (1987)
15. Durnin, J., Miceli, J.J., Eberly, J.H.: Diffraction-free beams. Phys. Rev. Lett. **58**, 1499–1501 (1987)
16. Falcao-Filho, E.L., de Araujo, C.B.: Robust two-dimensional spatial solitons in liquid carbon disulfide. Phys. Rev. Lett. **110**, 013901 (2013)
17. Fibich, G.: The Nonlinear Schrödinger Equation: Singular Solutions and Optical Collapse. Springer, Heidelberg (2015)
18. Gaizauskas, E., Dubietis, A., Kudriasov, V., Sirutkaitis, V., Couairon, A., Faccio, D., Trapani, P.D.: On the role of conical waves in self-focusing and filamentation of femtosecond pulses with nonlinear losses. In: Boyd, R.W., Lukishova, S.G., Shen, Y.R. (eds.) Self-Focusing: Past and Present. Fundamentals and Prospects, Topics in Applied Physics, vol. 114, pp. 457–479. Springer, New York (2009)
19. Jukna, V., Milián, C., Xie, C., Itina, T., Dudley, J., Courvoisier, F., Couairon, A.: Filamentation with nonlinear Bessel vortices. Opt. Express **22**, 25410–25425 (2014)
20. Kivshar, Y.S., Agrawal, G.P.: Optical Solitons: From Fibers to Photonic Crystals. Academic Press, San Diego (2003)
21. Kivshar, Y.S., Pelinovsky, D.E.: Self-focusing and transverse instabilities of solitary waves. Phys. Rep. **331**, 117–195 (2000)
22. Knobloch, E.: Spatial localization in dissipative systems. Annu. Rev. Condens. Matter Phys. **6**, 325–359 (2015)
23. Kruglov, V.I., Logvin, Y.A., Volkov, V.M.: The theory of spiral laser beams in nonlinear media. J. Mod. Opt. **39**, 2277–2291 (1992)
24. Kruglov, V.I., Vlasov, R.A.: Spiral self-trapping propagation of optical beams in media with cubic nonlinearity. Phys. Lett. A **111**, 401–404 (1985)
25. Kuznetsov, E.A., Dias, F.: Bifurcations of solitons and their stability. Phys. Rep. **507**, 43–105 (2011)
26. Malomed, B.A., Crasovan, L.C., Mihalache, D.: Stability of vortex solitons in the cubic-quintic model. Physica D **161**, 187–201 (2002)
27. Malomed, B.A., Mihalache, D., Wise, F., Torner, L.: Spatiotemporal optical solitons. J. Opt. B: Quantum Semiclassical Opt. **7**, R53–R72 (2005)
28. Malomed, B.A., Lederer, F., Mazilu, D., Mihalache, D.: On stability of vortices in three-dimensional self-attractive Bose–Einstein condensates. Phys. Rev. A **361**, 336–340 (2007)
29. Masalov, A.V.: Transfer of a high angular momentum from a photon to an atom. Laser Phys. **7**, 751–754 (1997)
30. Mihalache, D.: Linear and nonlinear light bullets: recent theoretical and experimental studies. Rom. J. Phys. **57**, 352–371 (2012)

31. Mihalache, D., Mazilu, D., Lederer, F., Kartashov, Y.V., Crasovan, L.C., Torner, L., Malomed, B.A.: Stable vortex tori in the three-dimensional cubic-quintic Ginzburg–Landau equation. Phys. Rev. Lett. **97**, 073904 (2006)
32. Mihalache, D., Mazilu, D., Malomed, B.A., Lederer, F.: Vortex stability in nearly-two-dimensional Bose–Einstein condensates with attraction. Phys. Rev. A **73**, 043615 (2006)
33. Olver, W.J.: NIST Handbook of Mathematical Functions. Cambridge University Press, New York (2010)
34. Paz-Alonso, M.J., Michinel, H.: Superfluidlike motion of vortices in light condensates. Phys. Rev. Lett **94**, 093901 (2005)
35. Polesana, P., Faccio, P., Trapani, P.D., Dubietis, A., Piskarskas, A., Couairon, A., Porras, M.A.: High localization, focal depth and contrast by means of nonlinear Bessel beams. Opt. Express **13**, 6160–6167 (2005)
36. Polesana, P., Dubietis, A., Porras, M.A., Kucinskas, E., Faccio, D., Couairon, A., Trapani, P.D.: Near-field dynamics of ultrashort pulsed Bessel beams in media with Kerr nonlinearity. Phys. Rev. E **73**, 056612 (2006)
37. Polesana, P., Couairon, A., Faccio, D., Parola, A., Porras, M.A., Dubietis, A., Piskarskas, A., Trapani, P.D.: Observation of conical waves in focusing, dispersive, and dissipative Kerr media. Phys. Rev. Lett. **99**, 223902 (2007)
38. Polesana, P., Franco, M., Couairon, A., Faccio, D., Trapani, P.D.: Filamentation in Kerr media from pulsed bessel beams. Phys. Rev. A **77**, 043814 (2008)
39. Porras, M.A., Redondo, F.: On the stabilizing effect of nonlinear energy losses in light bullet propagation. J. Opt. Soc. Am. B **30**, 603–609 (2013)
40. Porras, M.A., Ruiz-Jiménez, C.: Nondiffracting and non-atenuating vortex light beams in media with nonlinear absorption of orbital angular momentum. J. Opt. Soc. Am. B **31**, 2657–2664 (2014)
41. Porras, M.A., Parola, A., Faccio, D., Dubietis, A., Trapani, P.D.: Nonlinear unbalanced Bessel beams: stationary conical waves supported by nonlinear losses. Phys. Rev. Lett. **93**, 153902 (2004)
42. Porras, M.A., Ruiz-Jiménez, C., Losada, J.C.: Underlying conservation and stability laws in nonlinear propagation of axicon-generated Bessel beams. Phys. Rev. A **92**, 063826 (2015)
43. Porras, M.A., Carvalho, M., Leblond, H., Malomed, B.A.: Stabilization of vortex beams in Kerr media by nonlinear absorption. Phys. Rev. A **94**, 053810 (2016)
44. Quiroga-Teixeiro, M., Michinel, H.: Stable azimuthal stationary state in quintic nonlinear optical media. J. Opt. Soc. Am. B **14**, 2004–2009 (1997)
45. Rotschild, C., Cohen, O., Manela, O., Segev, M.: Solitons in nonlinear media with an infinite range of nonlocality: first observation of coherent elliptic solitons and of vortex-ring solitons. Phys. Rev. Lett. **95**, 213904 (2005)
46. Saito, H., Ueda, M.: Split instability of a vortex in an attractive Bose–Einstein condensate. Phys. Rev. Lett. **89**, 190402 (2002)
47. Sakaguchi, H., Li, B., Malomed, B.A.: Creation of two-dimensional composite solitons in spin-orbit-coupled self-attractive Bose–Einstein condensates in free space. Phys. Rev. E **89**, 032920 (2014)
48. Salo, J., Fagerholm, J., Friberg, A., Salomaa, M.M.: Unified description of nondiffracting X and Y waves. Phys. Rev. E **62**, 4261–4275 (2000)
49. Schwarz, J., Rambo, P., Diels, J.C., Kolesik, M.: Ultraviolet filamentation in air. Opt. Commun. **180**, 383–390 (2000)
50. Silberberg, Y.: Solitons and two-photon absorption. Opt. Lett. **15**, 1005–1007 (1990)
51. Skupin, S., Nuter, R., Bergé, L.: Optical femtosecond filaments in condensed media. Phys. Rev. A **74**, 043813 (2006)
52. Sulem, C., Sulem, P.L.: The Nonlinear Schrödinger Equation: Self-Focusing and Wave Collapse. Springer, Berlin (1999)
53. Tabosa, J.W.R., Petrov, D.V.: Optical pumping of orbital angular momentum of light in cold Cesium atoms. Phys. Rev. E **83**, 4967–4970 (1999)

54. Xie, C., Jukna, V., Milián, C., Giust, R., Ouadghiri-Idrissi, I., Itina, T., Dudley, J.M., Couairon, A., Courvoisier, F.: Tubular filamentation for laser material processing. Sci. Rep. **5**, 8914 (2015)
55. Yakimenko, I., Zaliznyak, Y.A., Kivshar, Y.: Stable vortex solitons in nonlocal self-focusing nonlinear media. Phys. Rev. E **71**, 065603(R) (2005)
56. Zhang, Y.C., Zhou, Z.W., Malomed, B.A., Pu, H.: Stable solitons in three dimensional free space without the ground state: self-trapped Bose–Einstein condensates with spin-orbit coupling. Phys. Rev. Lett. **115**, 253902 (2015)

Spatial Solitons in Nonlinear Photonic Crystal Fibers

José R. Salgueiro and Albert Ferrando

Abstract This chapter aims to review the most relevant results on solitons in nonlinear solid-core photonic crystal fibers since their introduction about fifteen years ago. These include fundamental solitons and vortices, as well as vector systems of two fundamental, vortex or mixed components. Also other related systems as solitons in double-core photonic crystal fibers will be reviewed. The presentation will describe the mode families as well as their stability properties. The work is intended to be a comprehensive document on the field and provide a fast update to the reader as well as the necessary sources for a further detailed documentation.

Keywords Photonic crystal fibers · Spatial solitons · Vortices · Vector solitons Discrete symmetry · Nonlinear modes

1 Introduction

Photonic crystals have recently brought new possibilities to waveguiding and control of light. They are structures with a periodic variation of the dielectric function that lead to the possibility of existence of band gaps, i.e. regions of the frequency spectrum for which light is unable to propagate, analogously to the energy band gaps characteristic of the periodic atomic structures of solids [24]. Band gaps appear because of Bragg reflections produced in the periodic structure and are the key of a tight localization of light around defects in the structure. In such a way light can be forced to propagate along designed paths avoiding scattering losses even for strong bends in contrast to the case of conventional waveguides. The application of this

J.R. Salgueiro (✉)
Departamento de Física Aplicada, Universidade de Vigo, Escola de Enxeñaría Aeronáutica e do Espazo, Campus As Lagoas s/n, 32004 Ourense, Spain
e-mail: jrs@uvigo.es

A. Ferrando
Departament d'Òptica, Interdisciplinary Modeling Group InterTech, Universitat de València, Dr. Moliner 50, 46100 Burjassot (València), Spain
e-mail: albert.ferrando@uv.es

J. F. R. Archilla et al. (eds.), *Nonlinear Systems, Vol. 2*, Understanding Complex Systems, https://doi.org/10.1007/978-3-319-72218-4_6

technique to optical fibers leaded to the *Bragg fiber* [61], which was a multilayer structure presenting an air core and a cladding formed by a periodic structure made of concentric cylinders of alternate refractive indices. Light of frequency in the bandgap keeps inside the core as it cannot propagate through the cladding.

More recently the *photonic crystal fiber* (PCF) was proposed. It also presents a periodic structure and is formed by an array of air holes which run parallel to the fiber axis with a central defect. This defect can be an air hole of a different diameter than the rest (*hollow core* fibers) or the absence of such an air hole (*solid core* fibers). This type of fibers reached a great interest as very intriguing and useful properties were found [28, 43]. Among them we can mention the strong monomode character of the fiber despite of the light frequency even for large values of the core radius, the possibility of designing the zero-dispersion point adjusting the geometrical parameters, or the capability of actuate on their birefringence properties also establishing the proper geometrical parameters. Since their introduction, PCFs have gone through successive improvements in their fabrication processes and have reached an increased number of functionalities [44, 45] to become key components of a number of today's technologies as frequency comb systems [57] or high power fiber lasers [62].

Very interesting applications arise when considering nonlinear materials. Particularly in the case of solid-core PCFs, since light is strongly localized inside the core, the observation of nonlinear effects is possible at relative low powers. In such a way PCFs are the basis of, for instance, supercontinuum generation systems [43, 56] which can now operate with fs pulses of few nanojoules (nJ), in contrast to the milijoule (mJ) typical pulse energy necessary when conventional fibers are used. A selective filling of the holes of the fiber with a liquid, which can even show a nonlinear behavior, creating infiltrated PCFs, also brings new possibilities and applications as properties can be easily tuned by the type of liquid and the geometrical distribution of filled holes [3, 42, 58].

Self-trapping nonlinear mechanism as the optical Kerr effect, linked to the third order susceptibility, contribute to the localization allowing the existence of modes in the form of spatial solitons. In such a case, the PCF matrix has proved to be determinant for the stability properties of those nonlinear modes. In fact, it was demonstrated the existence of stable fundamental solitons [15] which are known to be unstable in homogeneous Kerr media, where they suffer from spreading or collapse upon propagation. Also, concerning optical vortices—higher order states with a phase dislocation at its center around which phase changes linearly as $2l\theta$, being θ the azimuthal angle and l the winding number or vorticity—the PCF lattice also contributes to enhance their stability. Unlike homogeneous Kerr media where those states break-up due to the azimuthal instability into a number of fundamental solitons that fly off the main ring and subsequently they collapse, in PCFs non-collapsing states do exist under a power threshold and, additionally, the distance at which states do break up can be also made quite long [16, 50]. This effect of stabilization by a periodic medium was also observed in other systems as for instance in square lattices [2, 59].

The discrete symmetry characterizing PCFs conditions the shape of the modes they are able to support. For linear systems—or nonlinear at low power—modes

must belong to the symmetry group characterizing the PCF structure. For instance, in the common case of a hexagonal-lattice PCF this group is $\mathscr{C}_{6v}$ which implies the invariance under rotations of $\pi/3$ radians plus reflections respect to the cartesian coordinate axes. However, for moderately high power, when nonlinear effects dominate, modes with less symmetry belonging to a subgroup of the lattice symmetry group are possible. Even, for very high power, completely asymmetric solutions may arise. Nonlinear systems with discrete symmetry are of great interest due to the enhanced stability properties they present respect to their homogeneous counterparts [18, 38]. PCFs, as discrete systems, also share the properties mentioned above and limitations in the mode spectrum do arise. For instance, cluster-like solutions are restricted to those with some particular numbers of clusters (three or six for a hexagonal lattice) or vortex solutions are restricted to those with vorticity $l \leq 2$ [17].

Additionally, there are other guiding nonlinear systems that present similarities with PCFs due to the discrete rotational symmetry of their structures. Because of their equivalent rotational properties, the symmetry analysis of their nonlinear mode spectrum can be performed in the same way as in PCFs. Thus, most of the main results obtained for PCF modes can be straightforwardly translated to other similar nonlinear waveguides with the same symmetry properties. An example is provided by Bessel lattices in which higher-order Bessel beams are able to optically induce an azimuthal modulation of the refractive index [25]. This modulation permits the implementation of a rotational discrete symmetry of even order at will. In this case, the same classification scheme found for PCFs applies and the set of potential nonlinear solutions follows identical rules. Another example is provided by a system of two-dimensional coupled nonlinear waveguide arrays [7–9, 30, 31, 35, 36, 55]. When the geometry of the waveguide array implements a discrete rotational symmetry, the classification of nonlinear modes follows the same symmetry rules that will be described here for spatial solitons in PCFs. The classification of soliton solutions in circular arrays of nonlinear waveguides provides an excellent example of this feature [8].

More complex systems based on the nonlinear PCF were proposed and studied with the aim of enhancing the stability properties of the optical modes. For instance, vector systems of two or more mutually incoherent components interacting via the nonlinearity. For the case of a Kerr-type nonlinearity two-component fundamental modes stable in a particular region of the domain were found [51]. The PCF plays an important role in the stability of such modes as they are known to be unstable in homogeneous media [33]. Also vector modes with vortex components were found fully stable [47] or with enhanced stability respect to the scalar counterpart.

Finally, other interesting related systems are multi-core PCFs where two or more close defects are introduced into the periodic matrix creating devices similar to directional couplers [6, 29]. This multicore arrangement produces a decrease in the symmetry of the lattice and consequently restricts the modal solutions allowed to exist. For example in dual-core PCFs with a hexagonal lattice, two close defects are present and so the original $\mathscr{C}_{6v}$ symmetry is reduced to $\mathscr{C}_{2v}$ at moderate power. For higher power, however, more asymmetric solutions may exist, breaking the global and even the local symmetry of each core. Optical modes containing fundamental

states in each of the cores have been found [51] as well as states combining two vortices or fundamental states and vortices [54].

In the following sections we will review the main results on nonlinear solid core PCFs as concerns the existence and stability of fundamental modes and first order vortices. Next section is devoted to the classification of solutions according to their symmetry properties. In Sect. 3 we deal with the fundamental solitons and vortices in PCFs. Next, Sect. 4 will describe and analyze vector systems with two fundamental soliton components, as well as those containing vortices in one or both components. Finally, in Sect. 5 the dual-core system is reviewed, also in the case of presenting fundamental fields in both cores as well as in the case where at least one of the cores contains a vortex.

2 Optical Modes with Discrete Symmetry

The optical modes of a fiber made, partially or totally, of a nonlinear material in the scalar approximation are given by the eigenfunctions of the nonlinear Helmholtz operator in the two transverse dimensions $(\tilde{x}, \tilde{y})$. It is assumed that both the fiber refractive and nonlinear indices are invariant along the axial direction $\tilde{z}$. Because of the axial invariance, the eigenfunctions of the linear Helmholtz operator also have to be eigenfunctions of the axial translational operator. When the nonlinearity depends on the modulus of the electric field exclusively this condition is also fulfilled by the whole nonlinear non-paraxial Helmholtz operator. Axial translational symmetry requires that modes have to present the form $E(\tilde{x}, \tilde{y}, \tilde{z}) = \phi(\tilde{x}, \tilde{y}) \exp\left(i\tilde{\beta}\tilde{z}\right)$, where $\tilde{\beta}$ is the propagation constant or effective index describing the evolution of the wave along the fiber axis. In this way, the amplitudes of the optical modes of a nonlinear fiber must fulfill the following nonlinear eigenvalue differential equation:

$$\left\{\tilde{\nabla}^2 + k^2\left[\varepsilon\left(\tilde{x}, \tilde{y}\right) + \varepsilon_{NL}\left(|\phi|\right)\right]\right\}\phi\left(\tilde{x}, \tilde{y}\right) = \tilde{\beta}^2\phi\left(\tilde{x}, \tilde{y}\right), \tag{1}$$

where $\tilde{\nabla} = (\partial/\partial\tilde{x}, \partial/\partial\tilde{y})$ is the transverse Laplace operator, k is the wavenumber related to the frequency ω as $k = \omega/c$, c being the vacuum speed of light, $\varepsilon\left(\tilde{x}, \tilde{y}\right)$ is the linear dielectric function and $\varepsilon_{NL}\left(|\phi|\right)$ its nonlinear counterpart which, as mentioned, depends exclusively on the modulus of the field. For the current symmetry analysis, the nonlinear dielectric function ε_{NL} can include different types of nonlinearities provided they depend on $|\phi|$. For example, for the standard case of a Kerr nonlinearity $\varepsilon_{NL}\left(|\phi|\right) = \gamma_2|\phi|^2$, where γ_2 is the nonlinear parameter of the Kerr medium, related to the standard nonlinear index n_2 by the simple relation $\gamma_2 \approx c\varepsilon_0\varepsilon n_2$, where ε_0 is the vacuum permittivity and ε is the linear dielectric constant of the material. In general, both γ_2 and n_2 can depend on the transverse coordinates $(\tilde{x}, \tilde{y})$, thus indicating that the distribution of nonlinear material in the fiber can be transversally inhomogeneous, although it has to be $\tilde{z}$-independent to ensure axial translation invariance.

In the paraxial approximation, the 3D non-paraxial Helmholtz equation is reduced by means of a decomposition in a fast and slow varying functions on the axial coordinate. That is, we write E as $E(\tilde{x}, \tilde{y}, \tilde{z}) = \tilde{U}(\tilde{x}, \tilde{y}, \tilde{z}) \exp(-ik_0 n_a \tilde{z})$—$n_a$ is an arbitrary reference index that we take as that of the material in the holes—in such a way the axial second derivative of the envelope $\tilde{U}$ is neglected in the 3D Helmholtz equation, giving rise to a Schrödinger-like equation for the function $\tilde{U}$. We consider a Kerr nonlinearity and a PCF structure made of two materials, one of index n_a in the holes and other of index n_s for the rest of the structure (the substrate). We normalize the original spatial coordinates and the field $\tilde{U}$ as $x = k(2\delta)^{1/2}\tilde{x}$, $y = k(2\delta)^{1/2}\tilde{y}$, $z = k\delta\tilde{z}$, and $U(x, y, z) = (\gamma/\delta)^{1/2}\tilde{U}(\tilde{x}, \tilde{y}, \tilde{z})$, where $k = k_0 n_a$ is the wavenumber in the holes and $\delta = n_s - n_a$ is the PCF index contrast. In this way, we obtain the paraxial equation in its canonical dimensionless form:

$$i\frac{\partial U}{\partial z} = \nabla^2 U + \left[1 + W(x, y)\left(1 + |U|^2\right)\right] U, \tag{2}$$

where $W(x, y)$ describes the PCF structure taking value 1 in the substrate and 0 in the holes. For the calculation of modes we require the solutions to be of the form $U(x, y, z) = u(x, y) \exp(-i\beta z)$, where β is the paraxial propagation constant. The relation with the non-paraxial propagation constant in Eq. (1) is simply $\tilde{\beta} = k(1 + \beta\delta)$. The eigenvalue equation for modes is:

$$\nabla^2 u + \left[1 + W(1 + u^2)\right] u = \beta u. \tag{3}$$

The field $u(x, y)$ describing the profile of the mode is in general a complex function as modes may include a transversal phase distribution. It is the case of the vortex states showing a phase dislocation at the center of the fiber core and presenting a linear distribution of phase $\exp(il\theta)$, where l is an integer number and θ the azimuthal coordinate. Equation (3) is solved for the different systems considered in the subsequent sections using numerical methods as those described in Ref. [53], and the solutions obtained can be classified by means of their propagation constant β and their power flux in the axial direction $\hat{z}$,

$$P = \int_A |u|^2 dx\, dy, \tag{4}$$

where A stands for the transversal plane of the PCF.

2.1 Linear System

The classification of solutions of the non-paraxial eigenvalue Eq. (1) or, equivalently, of its paraxial counterpart [Eq. (3)] in terms of rotational discrete symmetries, typical for a PCF, is standard in the linear case. If the linear refractive index presents a

rotational symmetry of order N, so that, $\varepsilon(\mathbf{x}_t) = \varepsilon[R(\theta_N)\mathbf{x}_t]$, where $\mathbf{x}_t = (x, y)^\top$ and $R(\theta_N)$ is the 2D matrix rotation of angle $\theta_N = 2\pi/N$, then the solutions of the linear eigenvalue equation [Eq. (1)] have to be eigenfunctions of the discrete rotation operator as well. In terms of the structure function W in the paraxial equation [Eq. (3)] the invariance requirement is the same: $W(\mathbf{x}_t) = W[R(\theta_N)\mathbf{x}_t]$. From now on, we will refer to the symmetry properties of the non-paraxial equation [Eq. (1)] and the field ϕ but all properties apply analogously to its paraxial counterpart [Eq. (3)].

Let us define the rotation operator acting on the field amplitude ϕ as $G_N \in \mathscr{C}_N$, being $\mathscr{C}_N$ the point group of finite rotations of Nth order. Thus, by definition, taking into account that ϕ is a scalar (and not a vector) field, it is transformed as:

$$G_N \phi[\mathbf{x}_t] = \phi[R(\theta_N)\mathbf{x}_t]. \tag{5}$$

The eigenfunctions of this operator have to fulfill the eigenvalue condition,

$$G_N \phi[\mathbf{x}_t] = \eta \phi[\mathbf{x}_t], \tag{6}$$

where ε is the group operator eigenvalue, which in principle is complex. Since the discrete rotation operator is cyclic, so that the application of N consecutive discrete rotations of N order leave the function unaltered, this implies that the complex eigenvalue η fulfills the condition $\eta^N = 1$. Thus the eigenvalue is a root of unity of order N. All the root of unity can be classified according to a discrete number m and represented by pure phase complex numbers:

$$\eta_m = \exp\left(i\frac{2\pi}{N}m\right), \tag{7}$$

where $m = -N/2, \ldots, +(N/2-1)$ if N is even and $m = -(N-1)/2, \ldots, +(N-1)/2$, if N is odd. The group operator commutes with the linear differential operator in Eq. (1)—let us refer to it as L_0—since the Laplace operator is invariant under *any* rotation and, by hypothesis, $\varepsilon(\mathbf{x}_t)$ is invariant, so that $[L_0, G_N] = 0$ for all the elements of the discrete rotation group. This ensures that the eigenstates of L_0 have to be simultaneously eigenstates of G_N as well, and so the PCF linear modes admit a classification in terms of the discrete number m:

$$L_0 \left|\tilde{\beta}_n^2; m\right\rangle = \tilde{\beta}_n^2 \left|\tilde{\beta}_n^2; m\right\rangle \quad \text{and} \quad \hat{G}_N \left|\tilde{\beta}_n^2; m\right\rangle = \exp\left(i\frac{2\pi}{N}m\right)\left|\tilde{\beta}_n^2; m\right\rangle. \tag{8}$$

In systems with discrete rotational symmetry modes cannot be eigenstates of the orbital angular momentum (OAM) operator $\hat{L}_z$. However, they are instead eigenstates of the discrete rotation operator $\hat{G}_N$. The number m plays the role of l, the eigenvalue of the OAM operator, for these states. It can be proved that the number m can be interpreted as a *pseudomomentum*, or Bloch momentum, for Bloch waves in the angular coordinate [10]. Consequently it is natural to refer to it as the orbital angular pseudomomentum (OAPM) of a given mode. Unlike l, OAPM is conserved during

propagation since it is a "good quantum number", i.e., $\left[L_0, \hat{G}_N\right] = 0$. For example, for a typical hexagonal PCF, for which $N = 6$, all eigenfunctions in the scalar approximation can be labelled using two numbers, the OAPM $m = 0, \pm 1, \pm 2, 3$ and $n_r = 0, 1, 2, \ldots$, the *radial quantum number* that gives the number or radial nodes of the corresponding eigenfunction ϕ_{m,n_r}. In Fig. 1 we provide a representation of the characteristic spectrum of modes for an hexagonal PCF in the scalar approx-

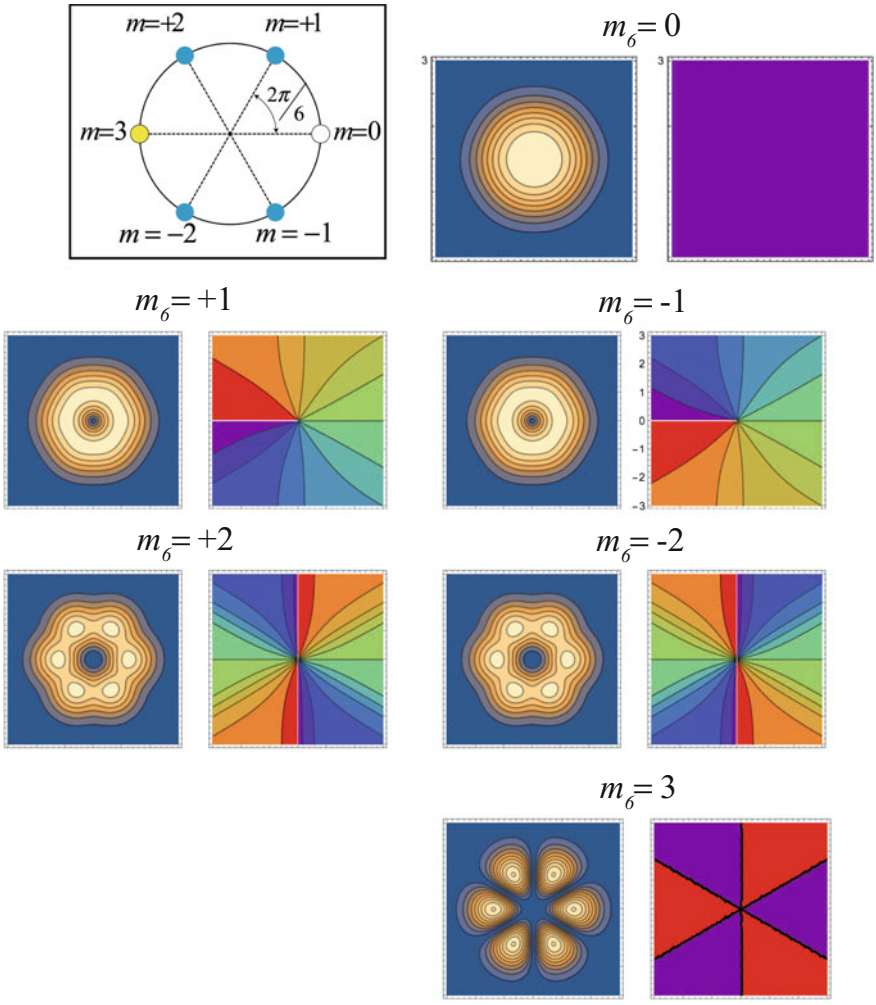

Fig. 1 Typical amplitude (left pictures) and phase (right pictures) of modes with highest effective index according to their OAPM for an hexagonal PCF. Modes with $m_6 = 0$ and $m_6 = 3$ are singlets, modes with $|m_6| = 1, 2$ form degenerate doublets (the group order has been included explicitly as a subindex). Inset upper left: roots of unity for $N = 6$, classifying the modes of the hexagonal PDF in terms of the OAPM m

imation according to this classification. In the mathematical language of discrete group theory, the OAPM m is univocally connected to the so-called character of a representation that classifies the six representations of the point group $\mathscr{C}_6$, and includes all discrete rotations of 6th order [22]. In this way, each solution with a given m belongs to the corresponding representation of the group $\mathscr{C}_6$ labelled by m. The interpretation of m as the OAPM of an angular Bloch mode makes it, however, easier to interpret physically. The commutation relation $\left[L_0, \hat{G}_N\right] = 0$ guarantees that if a solution belongs to a given representation, i.e. it has a well defined OAPM m, propagation will not modify its OAPM. Thus, the solution will remain in this representation indefinitely as the symmetry is not broken [10].

Along with discrete rotational symmetries, PCFs can enjoy mirror symmetries. Mirror symmetries are reflection symmetries, so that the structure remains unchanged after a reflection with respect to a given axis. For example, the hexagonal PCF with round holes, besides being invariant under $\pi/3$ rotations, is invariant under reflections with respect to the x and y axes. Mathematically, for the hexagonal PCF this means that $\varepsilon(-x, y) = \varepsilon(x, -y) = \varepsilon(x, y)$. In general, we would write $\varepsilon(\mathbf{x}_t) = \varepsilon(R_\alpha \mathbf{x}_t)$, where R_α represents a mirror reflection with respect to the axis r_α. This fact has further restrictions on PCF modes. When we include mirror symmetry and rotational symmetry together, PCF modes must lie in the representations of the group $\mathscr{C}_{6v}$ instead of just $\mathscr{C}_6$. This fact means that modes, besides being eigenmodes of the discrete rotation operator as in Eq. (8) have to be eigenmodes of the mirror reflection operator: $\hat{R}_\alpha \phi[\mathbf{x}_t] = \phi[R_\alpha \mathbf{x}_t] = \sigma_\alpha \phi[\mathbf{x}_t]$. Since two consecutive reflections with respect the same symmetry axis leave the function unaltered we have $\sigma_\alpha^2 = 1$, which implies that the only allowed eigenvalues for the mirror operator are $\sigma_\alpha = \pm 1$. Since R_α is a symmetry of L_0, so that $[L_0, R_\alpha] = 0$, their eigenvalues σ_α are also used to classify PCF modes together with the OAPM m. In general, for a PCF with extended symmetry $\mathscr{C}_{Nv}$ including mirror reflections, we will have, complementing Eq. (8),

$$L_0 \left|\tilde{\beta}_n^2; m, \sigma_\alpha\right\rangle = \tilde{\beta}_n^2 \left|\tilde{\beta}_n^2; m, \sigma_\alpha\right\rangle. \tag{9}$$

For example, for the case of the hexagonal PCF whose modes are represented in Fig. 1, the singlet mode with $m = 3$ is also an eigenmode of the reflection operators $\hat{R}_x$ and $\hat{R}_y$ with eigenvalues $\sigma_x = +1$ and $\sigma_y = -1$, respectively. This property is immediately obtained by direct observation of its phase. In the case of singlets, modes have to be eigenmodes of the reflection operator themselves. In the case of doublets, mirror symmetry transform modes among themselves but preserving the representation [22]. For example, for the hexagonal PCF $\hat{R}_{x,y} \left|\tilde{\beta}_n^2; m = +|m|\right\rangle = \left|\tilde{\beta}_n^2; m = -|m|\right\rangle$.

2.2 Nonlinear System

The classification of modes in the linear case is standard and is based on the same principles as that of electrons in electronic crystals. However, the situation changes when we consider the nonlinear term in the eigenmode Eq. (1) or (3). According to Eq. (1), a nonlinear solution ϕ_{nl} can be considered as an eigenmode of the opera-

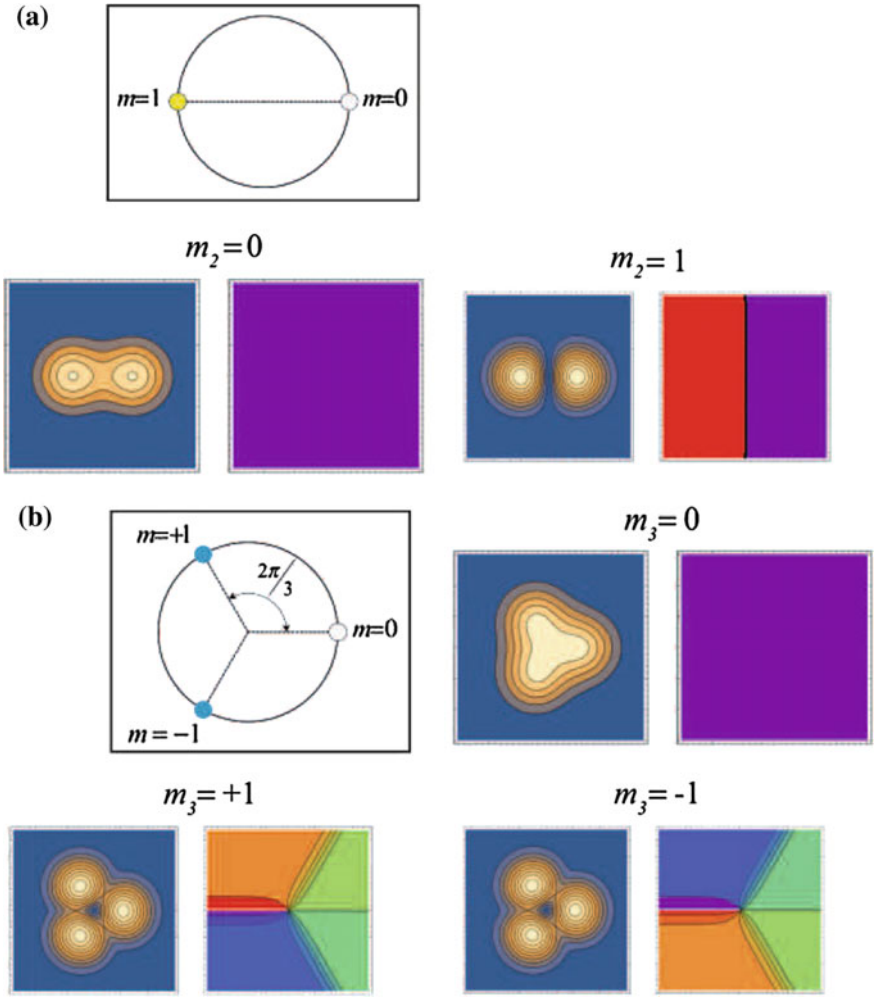

Fig. 2 Characteristic form for the amplitude (left pictures) and phase (right pictures) of stationary nonlinear modes of a system with discrete rotational symmetry of order $N = 6$ but owning lower order symmetry ($N = 2, 3$). **(a)** The two single-dimensional representations of $\mathscr{C}_2$ with $m_2 = 0, 1$. **(b)** The one single-dimensional representation of $\mathscr{C}_3$ (with $m_3 = 0$) and the one two-dimensional (with $m_3 = \pm 1$) representations of $\mathscr{C}_3$. Roots of unity are also shown for each case

tor $L(\phi_{\rm nl}) = L_0 + k^2\varepsilon_{NL}(|\phi_{\rm nl}|)$ generated by itself. This implies that a solution $\phi_{\rm nl}$ appears self-consistently—and *simultaneously*—as generating a nonlinear modulation of the refractive index through the term $\varepsilon_{NL}(|\phi_{\rm nl}|)$ and as an eigenmode of the full operator $L(\phi_{\rm nl})$ generated by itself. This two-fold role requires a compatibility between the symmetry of the solution and that of the medium [20]. The main result is that for a given order N of the discrete rotational symmetry of the system, for example that of the structural function W in Eq. (3), the solutions can only belong to a representation of the original group $\mathscr{C}_N$ or to some of its subgroups. Interestingly enough, the subgroups of a given point group $\mathscr{C}_N$ can be easily determined by decomposing its order N in prime factors. So that, the $\mathscr{C}_6$ group associated to an hexagonal PCF has $\mathscr{C}_3$ and $\mathscr{C}_2$ as nontrivial subgroups since $6 = 3 \times 2$. On the contrary, for example, $\mathscr{C}_5$ has no nontrivial subgroup since 5 is only divisible by 1. For this argument, the identity group (no rotational symmetry at all) is obviously a subgroup of all point groups. In this way, we expect the nonlinear modes of the Eq. (1) or (3) to be classified according to the representations of the original symmetry group $\mathscr{C}_6$, as in the linear case in Fig. 1. But also we expect nonlinear modes to exist with lower symmetry corresponding to the subgroups $\mathscr{C}_3$ and $\mathscr{C}_2$, as in Fig. 2. According to the roots of unity for $N = 2$ and $N = 3$, the allowed values for the OAPM in both cases are $m_2 = 0, 1$ and $m_3 = 0, \pm 1$ (for the sake of clarity we indicate the order of the group as a subindex of the OAPM).

When mirror reflections are included in the nonlinear analysis, the previous arguments also remain. For example, if we consider $\mathscr{C}_{6v}$ instead of the pure point group $\mathscr{C}_6$ we can obtain solutions belonging to the representations of the subgroups $\mathscr{C}_{3v}$ and $\mathscr{C}_{2v}$.

3 Nonlinear Modes in Solid-Core Photonic Crystal Fibers

Solid-core PCFs are fibers whose transverse structure is given by a 2D periodic distribution of holes in a dielectric medium (usually silica), which extend along the entire fiber length [see Fig. 3a]. This periodic modulation of the linear dielectric constant is most times hexagonal. It can be also square but the PCF fabrication process makes the hexagonal geometry easier to produce. So, a solid-core PCF can be considered a particular case of a 2D photonic crystal with an important peculiarity, which is the presence of a defect, in this case the absence of the central hole at the fiber symmetry axis. The central defect, or PCF core, is the region where light can be localized in the transverse plane. The surrounding periodic lattice is known as the PCF cladding, following standard fiber optics terminology and is characterized by the lattice period (or pitch) Λ and the hole radius a [see Fig. 3b]. So that, PCF linear guided modes are mostly confined in the solid core region and present the rotational symmetry dictated by the 2D structure of the photonic crystal cladding. For an hexagonal lattice, this symmetry is $\mathscr{C}_6$ since the core center is located at the symmetry axis of finite rotations. Thus, all linear PCF modes have to classify according to the representations of this group and they, in fact, present the symmetry features of modes in

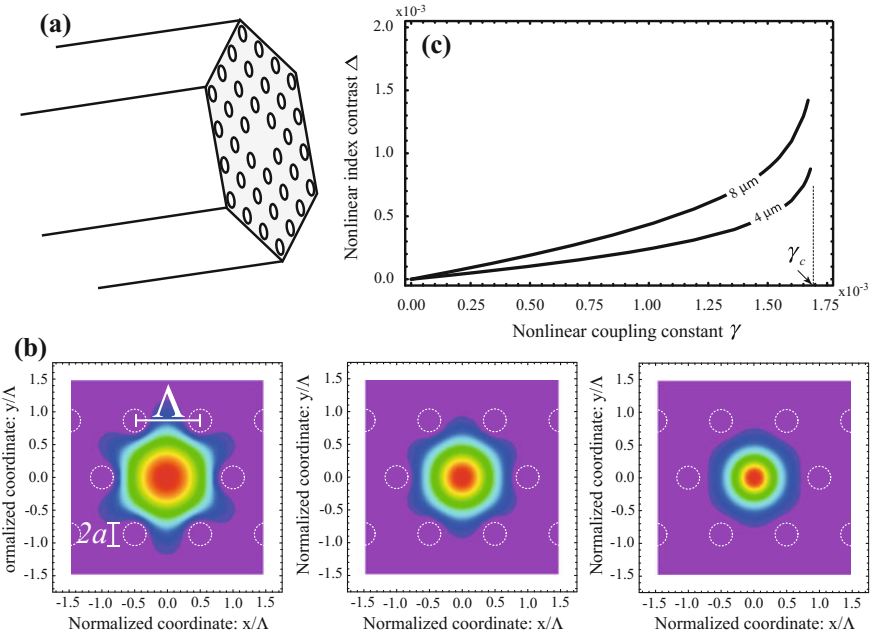

Fig. 3 **a** Typical structure for a solid-core PCF. **b** Three examples of the family of fundamental solitons of a nonlinear (Kerr) PCF for three increasing values of power ($\Lambda = 23\,\mu$m and $a = 4\,\mu$m). **c** Nonlinear effective index contrast (Δ) vs normalized power (γ) of two families of fundamental solitons corresponding to a hole radius of $a = 4\,\mu$m and $a = 8\,\mu$m

Fig. 1. Numerical modeling of a realistic solid-core PCF showed that this structure supported a fundamental mode belonging to the $m = 0$ representation of $\mathscr{C}_6$ [13] as well as higher order modes of vortex type belonging to the $|m| = 1$ representation of that group [12]. Those calculations are performed by solving the full-vector Maxwell's equation, so that they include the two polarization degrees of freedom for every mode. In order to compare to our previous mode classification, valid for a scalar field, we have to duplicate the dimension of every representation. Thus, the fundamental mode with $m = 0$, as well as the other scalar singlet with $m = 3$, have to appear as a polarization doublet whereas the eigenmodes with $|m| = 1, 2$ must form degenerate quadruplets. Indeed, the full-vector calculation in Ref. [12] shows a polarization doublet for the fundamental mode and an *almost* degenerate quadruplet for the vortex-like solutions with $|m| = 1$. Fourth-fold degeneracy is broken by polarization mixing terms inherent to a full-vector description, absent in the scalar case. This breaking is small and not relevant unless an accurate determination of the propagation constant is required, such as in the calculation of the group velocity dispersion of the mode [11, 12].

3.1 Fundamental Modes

Spatial solitons in the fundamental representation of $\mathscr{C}_6$ were found to exist in PCFs by assuming a nonlinear response of the Kerr type in the dielectric [15]. These nonlinear modes are characterized by an OAPM $m_6 = 0$ as the fundamental mode of a linear PCF. The main difference, as in any nonlinear soliton solution, comes from the fact that both its propagation constant and shape change with power. This is in clear contrast with a purely linear solution, for which a modification in power only produces a global rescaling of the mode by a constant factor, but it leaves its shape unaltered. A family of fundamental spatial solitons of a Kerr PCF—parametrized by power—is thus obtained, as shown in Fig. 3b. In Fig. 3c it is represented the nonlinear effective index contrast Δ—defined as the difference between the effective refractive index of the nonlinear fundamental mode with respect to its linear counterpart—in terms of the normalized power of the solution. Normalized power is obtained dividing power by a characteristic area of the mode A_0, $\gamma = Pn_2/A_0$, n_2 being the nonlinear refractive index. The nonlinear index [Fig. 3c] contrast is a monotonically increasing function of the power, as expected for a bright soliton in a self-focusing Kerr medium, and it branches out from a linear solution, which is always existing. Higher powers correspond to more localized solutions, as clearly seen in Fig. 3b. These solutions are stable below a critical power value γ_c. Above this value, the soliton experiences an instability similar to that of the Townes' soliton in an homogenous medium [15]. Fundamental spatial solitons were found experimentally in related nonlinear systems, such as optically induced square lattices with no defect [19]. Analogously to what happens in PCFs, they belong to the $m_4 = 0$ fundamental representation of $\mathscr{C}_4$.

3.2 Vortex Modes

More complicated phase structures owning nonzero OAPM have been also found in periodic lattices. Prediction of these vortex soliton states was made in the framework of the discrete nonlinear Schrödinger equation [34] as well as in the continuous nonlinear Schrödinger equation [60]. In optically-induced square lattices with no defect, optical vortices have been experimentally demonstrated [18, 37]. Since the order of symmetry of the square lattice is $N = 4$, symmetry requirements determine that vortex solutions with fourth-fold symmetry can only have an OAPM of $m_4 = \pm 1$. In a PCF, which can be considered as a photonic lattice with a defect, prediction of vortex solutions localized at the fiber core was reported a bit later [16]. Our previous symmetry analysis in Sect. 2 states that for a hexagonal PCF nonlinear solutions can exist realizing the full symmetry of the system ($N = 6$) or that of its subgroups ($N = 3$, $N = 2$ or $N = 1$). Vortex solutions realizing the full symmetry can only exist in representations defined by an OAPM of $m_6 = \pm 1, \pm 2$. In Fig. 4 (pictures c, d) the amplitude (modulus) and phase of such vortex solutions are represented. The amplitude clearly exhibits the $N = 6$ symmetry of the PCF cladding. The profile of

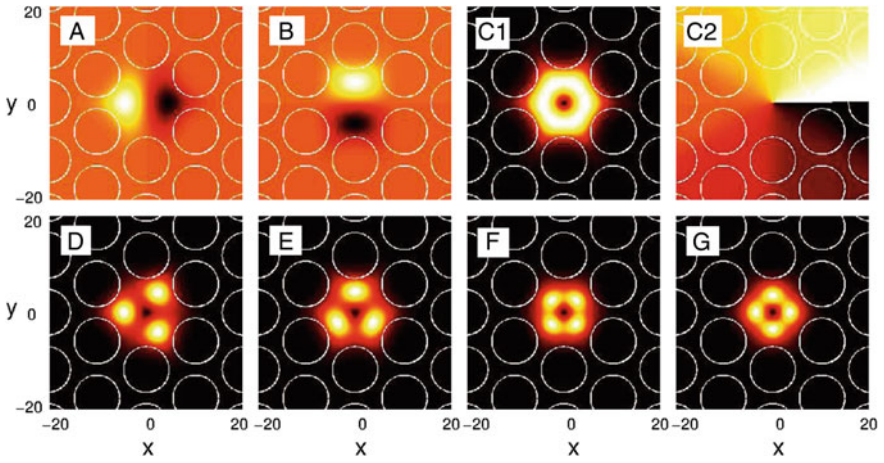

Fig. 4 Examples of nonlinear modes of the PCF with different symmetry. Images A, B: amplitude of two nodal solutions of symmetry $N = 2$. Images C1, C2: modulus and phase of a full symmetric vortex ($N = 6$ symmetry). Images D, E: two cluster-vortex solutions with symmetry $N = 3$ (modulus). Images F, G: cluster-vortex solutions of symmetry $N = 1$ (modulus). Labelling letters correspond to points in Fig. 6

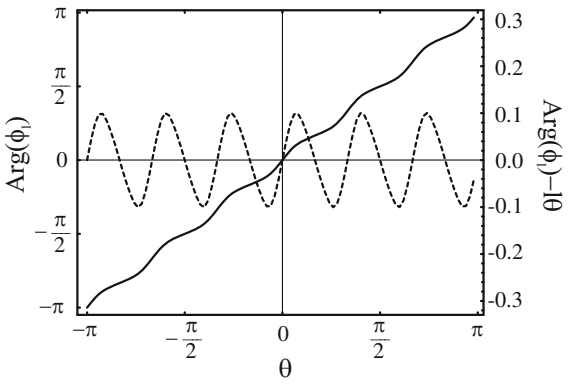

Fig. 5 Phase profile of a vortex soliton solution with OAPM $m_6 = +1$ at a fixed radius. Reprinted with permission from [16]. Copyright (2004) by the Optical Society of America

the phase evaluated along a circle of fixed radius centered at the origin (Fig. 5) shows the typical 2π slope of an optical vortex—indicating that the solution has an OAPM of $m_6 = +1$—along with a slight modulation. When the linear phase dependence is subtracted from the total phase, we can clearly appreciate the additional $N = 6$ modulation introduced by the discrete rotational symmetry.

Nonlinear soliton PCF modes having lower symmetry, in this case of order $N = 2$, have been also found [14]. These solutions present nodal lines, characteristic of solutions in the representation of the $\mathscr{C}_2$ rotation group as showed previously in Fig. 2. Two examples of these nodal solitons—or dipole solitons as they are also known—are represented in Fig. 4 (images a and b). Their amplitude is clearly invariant under

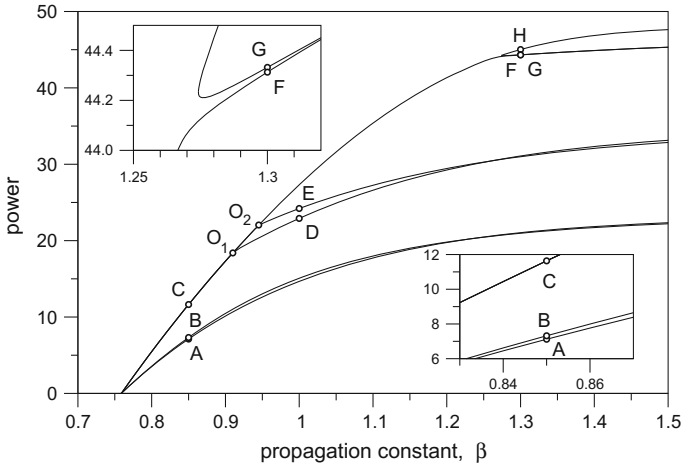

Fig. 6 Power versus propagation constant for different nonlinear mode families of the PCF. O_1 and O_2 are bifurcation points. Labelling letters correspond to examples in Fig. 4. Insets are two zoomed areas of the main plot for a better clarity. Parameters: $\Lambda = 10$, $a = 4$, $n_a = 0$, $n_s = 1$. Reprinted with permission from [50]. Copyright (2009) by Springer

$N = 2$ rotations. Their phase indicated that both solutions have an OAPM of $m_2 = 1$ since their phase change π radians under a 180° rotation. Both modes are, however, non-degenerate. The explanation can be also given in terms of symmetry. These two modes present different symmetry properties under mirror reflections $\hat{R}_x$ and $\hat{R}_y$. The one labelled A is $|m_2 = 1; \sigma_x = +1, \sigma_y = -1\rangle$ whereas the one labelled B is $|m_2 = 1; \sigma_x = -1, \sigma_y = +1\rangle$.

In Fig. 6 it is plotted the dependence of the propagation constant (horizontal axis) to the power (vertical axis) for different vortex-mode families. Nodal solitons are described by lines containing points A and B whereas vortex solitons correspond to line containing point C. In the linear case, at zero power, all three solutions are degenerate and superposition principle holds. This means that linear nodal solutions can be obtained simply by linearly combining vortex solutions and vice versa. However, when nonlinearity is switched on (power increases) this argument no longer holds. Nodal soliton and vortex soliton solutions now belong to representations of the different groups $\mathscr{C}_2$ and $\mathscr{C}_6$ respectively, and so they are no longer degenerate. The splitting becomes more obvious as we increase the power. In this sense, one can see that nonlinearity breaks the original symmetry of the system $\mathscr{C}_6$ into that of its subgroup $\mathscr{C}_2$. As power is increased we can also appreciate (Fig. 6) the gap generated between the two nodal solutions with the same OAPM ($m_2 = 1$). This gap indicates that the different behavior under the reflection symmetries $\hat{R}_x$ and $\hat{R}_y$ puts these solutions in two different representations of the group $\mathscr{C}_{2v}$ (discrete $\pi-$rotations plus mirror reflections) and thus they cannot appear degenerated. At large power, however, the gap closses again because both modes become more localized and stop feeling the effects of the PCF structure.

In the same way, vortex soliton solutions owning discrete rotational symmetry of order $N = 3$ can be found in a hexagonal PCF, as shown in Fig. 4e, f [54]. Unlike dipole solitons, tripole-shaped vortices cannot be obtained as a linear combination of the $\mathscr{C}_6$ symmetric vortex and anti-vortex linear solutions with $m_6 = \pm 1$. So they do not branch out from a linear solution but they appear above a certain power threshold, bifurcating from the $\mathscr{C}_6$ branch (Fig. 6). The two solutions in Fig. 4e, f are non-degenerated despite they have identical OAPM ($m_3 = +1$) and so they bifurcate at different points O_1 and O_2. Here, the breaking of the degeneracy is due to the particular form of the amplitude profiles, which present a different distribution of the intensity maxima respect to the hexagonal lattice of the cladding.

Finally, for high enough power fully asymmetric solutions may appear which belong to the trivial subgroup $\mathscr{C}_1$. They appear as solutions in the form of quadrupoles [Fig. 4g, h] and branch from the vortex with $\mathscr{C}_1$ symmetry at a *pseudobifurcation* [1, 21]. Both types of quadrupoles are not either degenerated due to the different distribution of amplitude respect to the PCF structure and they join to the symmetric vortex branch.

The PCF structure introduces an increase of stability in vortex modes. In homogeneous media they are known to suffer from the collapsing instability for large power or at least the azimuthal instability which breaks the mode into a number

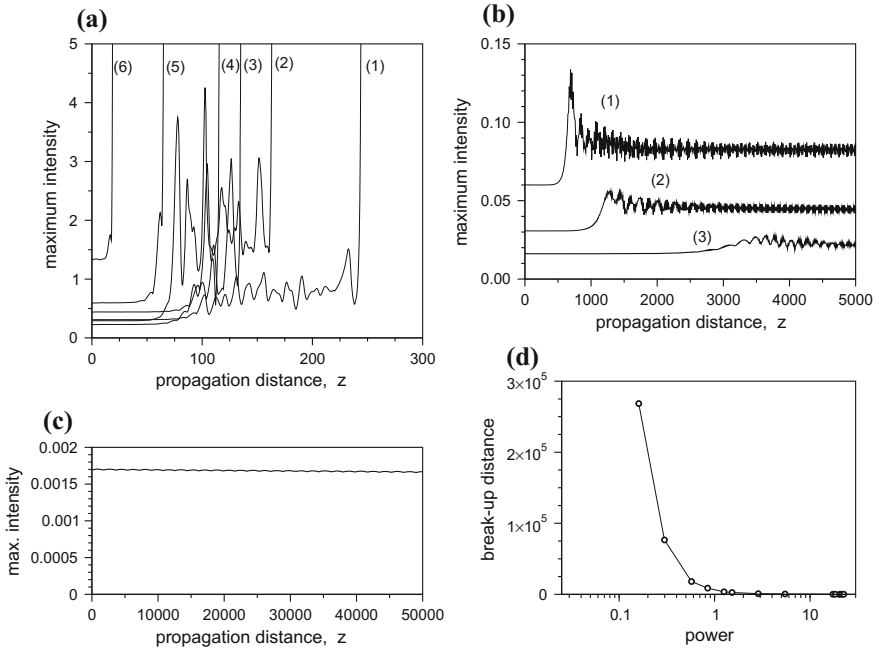

Fig. 7 **a–c** Maximum intensity versus propagation distance for different vortex modes showing break up and collapse **(a)**, only break up **(b)** and virtual stability **(c)**. **d** Breaking distance versus power for a vortex soliton. Reprinted with permission from [50]. Copyright (2009) by Springer

of fundamental solitons which may also collapse afterwards. The PCF is able to suppress collapse and to partially suppress the azimuthal instability [16, 50], rising the propagation distance up to that at which the modes may survive before breaking up. In Fig. 7 the two different scenarios are shown: break up and further collapse [Fig. 7a] and break up with the fundamental solitons kept oscillating inside the core [Fig. 7b]. In this latter case, the surviving distance is larger as mode power is lower. For low powers this distance may reach large values making the modes virtually stable [Fig. 7c, d].

4 Vector Solitons in PCF

Vector solitons constitute another interesting system which extend the possibilities and applications of the single (or scalar) solitons. It is composed of two or more beams which propagate colinearly and interact incoherently via the nonlinear terms [27]. This incoherent interaction is usually achieved using beams with orthogonal mutual polarizations or presenting different frequency. The modelling can be carried out using a equation similar to Eq. (3) for each of the components with added terms to account for cross coupling among components. Considering a two-component system and naming as $u(x, y)$ and $v(x, y)$ the field envelopes of such components and β_1 and β_2 their respective propagation constants, we will use the following model of two coupled equations:

$$\nabla^2 u + n_a u + W(x, y)\left(\delta + u^2 + \mu v^2\right) = \beta_1 u \tag{10}$$

$$\nabla^2 v + n_a v + W(x, y)\left(\delta + v^2 + \mu u^2\right) = \beta_2 v. \tag{11}$$

where, as was stated above, $\delta = n_s - n_a$ is the difference between the indices in the substrate and the holes and W(x,y) describes the PCF network with the central defect. The parameter μ is the coupling coefficient and accounts for the interaction between both components. Every beam is consequently influenced by its own's power (self modulation term) as well as by the other's power (cross modulation term). The scenario can be initially described as one intense beam which creates a waveguide and the other low-power beam is forced to propagate as the optical mode of such waveguide. The description under these circumstances would be made dropping the cross-modulation term in Eq. (10) and the sef-modulation term in Eq. (11). However, if the second beam is also intense enough, it modifies the waveguide itself creating the bounded two-component system which should be described using all the terms.

Typical values for the coupling parameter depend on the mechanism responsible for the nonlinearity and the material anisotropy [27]. For instance, for a nonlinearity derived from molecular orientation $\mu \leq 7$, while for nonresonant Kerr-type nonlinearities $\mu \geq 2/3$. Relevant cases are $\mu = 2/3$ for beams with orthogonal polarization and $\mu = 2$ for beams of different frequency.

The existence of the external potential of the PCF makes the system non-rescalable in contrast to the case of nonlinear homogeneous media, where one of the propagation constants as well as the parameter δ could be dropped from the equations by means of a proper rescaling of the coordinates and fields [33]. In the present case the index difference δ has to be maintained in the model (in contrast to the scalar case) and a rescaling of such parameter would allow dropping one of the propagation constants. Anyway, the study will be made in terms of one of the propagation constants, say β_2, assigning a fixed value to the other one, and assuming that such a restriction will not introduce important changes or loss of generality.

4.1 Fundamental Vector Solitons

The simplest case is that of considering two coupled fundamental beams [51]. If power of one of the beams approaches zero we have the scalar case studied in the previous sections. In Fig. 8a we show the power curves, calculated using the expression (4), of both solutions, one for $v = 0$ (labelled P_1), which is an horizontal line as propagation constant remains at a fixed value, and the other for $u = 0$ (labelled P_2) which describes the scalar family parametrized by β_2. For both nonvanishing components there is a family of vector solitons (P_{total}) which bifurcates from the scalar solitons at points O_1 and O_2. This means the vector solution exists only for values of β_2 between such bifurcation points. Close to point O_1 component v dominates and component u is close to zero while close to point O_2 the opposite situation

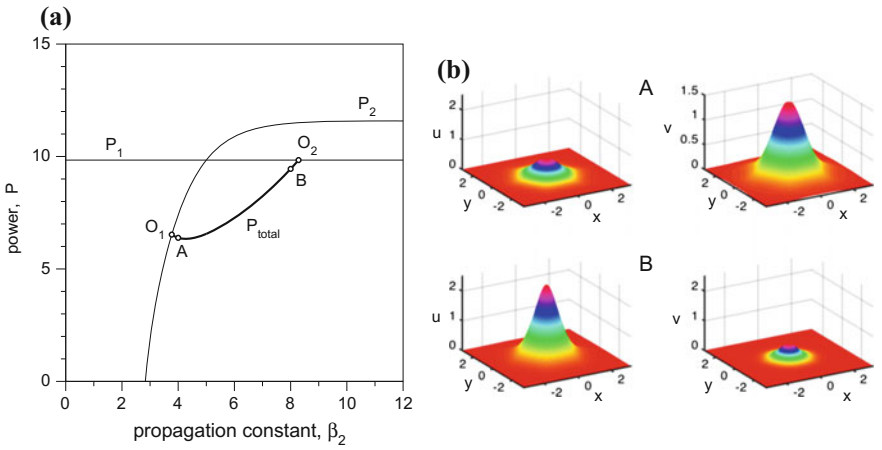

Fig. 8 **a** Power versus β_2 for scalar solitons (P_1 and P_2) and for vector solitons (P_{total}). Points A and B represent the examples showed in **b** as well as in Fig. 9. O_1 and O_2 are the bifurcation points. Parameters: $\Lambda = 2$, $a = 0.75$, $n_a = 1$, $\delta = 3$, $\mu = 2.0$, $\beta_1 = 5$ and $\beta_2 = 4$ (mode A) and $\beta_2 = 8$ (mode B)

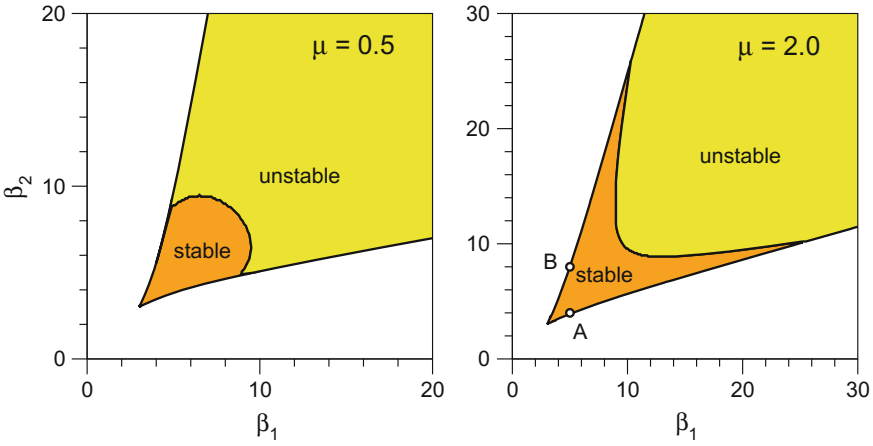

Fig. 9 Existence domain of vector solitons (shaded region) in the plane (β_1, β_2) for two cases of coupling, respectively smaller ($\mu = 0.5$) and larger ($\mu = 2.0$) than unity. The stability regions are also indicated in the plots. Points labelled A and B correspond to the examples in Fig. 8. Reprinted with permission from [51]. Copyright (2005) by Wiley-VCH Verlag GmbH & Co. KGaA

takes place [see labelled A and B in Fig. 8b]. Also, curve P_{total} describing the vector solitons is under curves P_1 and P_2 (power smaller than the components) for $\mu > 1$ whereas it is over them (power larger than individual components) for $\mu < 1$.

Letting β_1 change it is possible to build the existence domain for vector solitons in the plane (β_1,β_2) as shown in Fig. 9. Shaded area corresponds to the existence of the vector soliton solutions and the limiting lines constitute the points where one of the components vanishes and so they can be termed *bifurcation lines*.

The stability of the vector solitons can be studied by the matrix stability criterion [39, 40, 51]. The method consists in evaluating the number and sign of the eigenvalues of the matrix Schrödinger operators. Those eigenvalues can be obtained by numerical computation of a linearized spectral problem. Additionally, a simplification of the problem is possible in the neighborhood of the bifurcation points, i.e. close to the limiting lines shown in Fig. 9. Computations can be carried out analytically using perturbation series expansions [39, 41, 60].

According to the generalized matrix stability criterion the boundaries between zones where solutions are stable and those where they are unstable fulfill the condition $det(D) = 0$, were D is the matrix of derivatives $D_{ij} = \partial P_i / \partial \beta_j$, P_i and β_j being the power and propagation constant of the components i and j respectively. Those indices take values 1 (referring to component u) and 2 (referring to component v). According to this, the result shown in Fig. 9 is obtained after applying the above criterion to the numerically calculated solutions. The stability condition allows determining the boundary line separating the regions of different shading colour. A set of few simulations using a standard beam propagation method (BPM) applied to solutions of both regions allowed determining that solutions belonging to

the region close to the apex (dark colour shading) are stable while those in the light colour shading are unstable. The boundary changes curvature depending whether the coupling parameter is smaller or larger than unity. Besides, in the case $\mu > 1$, the boundary line approaches asymptotically to the bifurcation curves, as can be analytically demonstrated [51]. The stability criterion, able to provide a result on the stability in terms of the slopes of the power curves, is somehow analogous to the Vakhitov-Kolokolov criterion useful for determining the stability of the scalar fundamental solitons [27].

4.2 Vortex Vector Solitons

Another case of vectorial system takes place when at least one of the components is a vortex. In such a case, the fields $u(x, y)$ and $v(x, y)$ describing both components are complex numbers as happened in Sect. 3 for the scalar case. Two different cases may be considered: a combination of a fundamental soliton with a vortex or the combination of two vortices. A related, though different, case would be the combination of two scalar first order solitons (dipoles) which is a system lacking angular momentum and does not require a complex field to be described.

Vortex vectorial systems, fundamental-vortex as well as double-vortex, have proved to be more stable than single-component vortices in homogeneous nonlinear media [48]. Besides, taking into account that the PCF matrix also increased stability of fundamental scalar and vortex solitons, as was demonstrated above, one may wonder about the stability of vortex vectorial states in the PCF matrix, as it concerns the azimuthal instability as well as the collapsing instability. In the following the main general families of vector-vortex solutions are described and classified and their stability properties analyzed.

In Fig. 10 it is shown a simplified power diagram with the basic solution types. The complete diagram should contain additional lines representing variants of those families with slightly different configuration as will be described below. The study is made in terms of the propagation constant of the second component (β_2), keeping β_1 fixed ($\beta_1 = 1$). Thin dashed lines represent the scalar solutions from which vector ones bifurcate. Those corresponding to a single component soliton (first component) present a constant power (horizontal lines) since β_1 remains fixed. The ones with the soliton at the second component are basically the same already classified and presented in Fig. 6, i.e. single dipoles (SD) and single vortices with doughnut shape (SV) or tripole shape (ST).

The rest of the lines constitute vector modes bifurcating from the scalar ones at two bifurcation points, at which one of the respective components vanishes. Consequently those modes exist for a particular range of values of β_2. In the figure they are plotted families of solutions without vorticity (thick dashed lines) in the form of combinations of a fundamental state and a dipole (FD), as well as combinations of two dipole states (DD). Continuous lines correspond to solutions showing vorticity. Thin continuous lines describe combinations of a fundamental soliton and a vortex with a doughnut

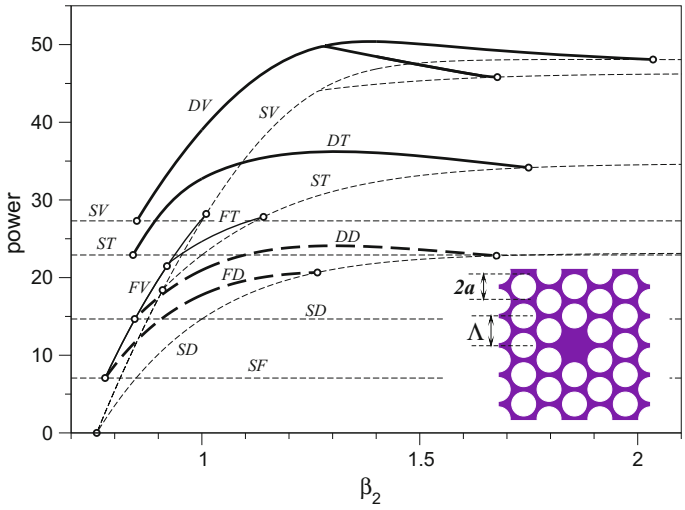

Fig. 10 Simplified power diagram for vector vortex solitons, showing power versus propagation constant β_2. Thin dashed lines represent the scalar solutions in the form of single dipoles (SD), fundamental solitons (SF) and vortices with a doughnut shape (SV) as well as with a tripole shape (ST). Thick dashed lines correspond to first order modes without vorticity: fundamental-dipole (FD) and double-dipole (DD) modes. Thin continuous lines correspond to combinations of a fundamental soliton and a vortex with doughnut shape (FV) or tripole shape (FT). Thick continuous lines are double-vortex families with doughnut (DV) and tripole (DT) shape. Inset: detail of the PCF structure (transversal plane). Parameters: $\Lambda = 10$, $r = a = 4$, $n_a = 0$, $\delta = 1.0$, $\mu = 0.4$ and $\beta_1 = 1$. Reprinted with permission from [47]. Copyright (2016) by IOP Publishing

shape (FV) or tripole shape (FT). On the other hand thick continuous lines represent the double-vortex modes with a doughnut shape (DV) or tripole shape (DT).

There exist different families of the same type which are not shown in the simplified diagram of Fig. 10. For instance, the double-dipole modes may have two similar components with the lobes facing inter-hole spaces, similar to those shown in Fig. 4a (the family actually shown in Fig. 10), or two components with lobes facing holes of the PCF, as those shown in Fig. 4b. Also, there exists a state with one different type of dipole at each component. In such a case, the family presents a higher power and the second bifurcation point is suppressed, existing for an unlimitted value of β_2, although power saturates al large β_2 [47]. On the other hand there exist two different families of fundamental-dipole (FD) modes which lack angular momentum and are real-valued fields presenting the shape shown in Fig. 11 (cases a and b).

Concerning fundamental-vortex solitons, in Fig. 11c, d, e some examples are presented. Family c is a $\mathscr{C}_{6v}$-symmetric state while families d and e present a reduced symmetry of the subgroup $\mathscr{C}_3$ and so they bifurcate from the FV family at a higher power.

Next, the double-vortex family (DV), when power rises, goes through a pseudobifurcation as happened in the scalar case, ensuing a symmetry breaking and originating

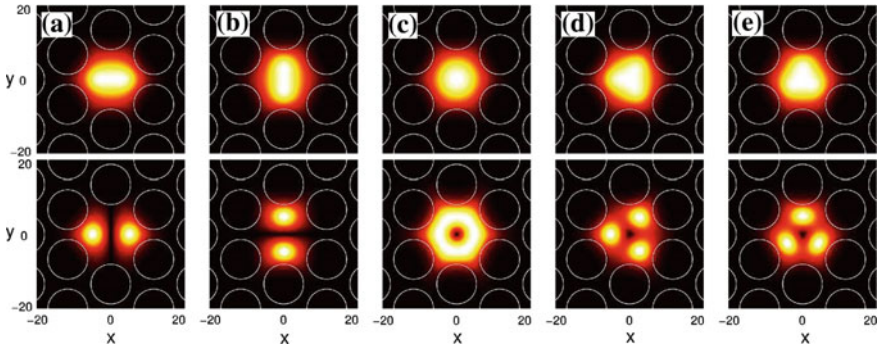

Fig. 11 Examples of vector modes combining a fundamental soliton at the first component with a dipole (cases **a**, **b**), doughnut-shaped vortex (**c**) or tripole-shaped vortex (**d**, **e**). Top images correspond to the first component, bottom images are the second component. Reprinted with permission from [47]. Copyright (2016) by IOP Publishing

asymmetric solutions with a quadrupole shape which belong to the trivial subgroup $\mathscr{C}_1$. Additionally, there also exist double-vortex modes with a tripole shape (DT) presenting the symmetry of the subgroup $\mathscr{C}_3$. These tripoles may present the lobes located at the same place for both components or out of place, being one component rotated a multiple of $\pi/3$ respect to the other. This second possibility may only take place for a weak coupling (low value of μ) and the state bifurcates from the doughnut DV families instead from the scalar ST ones as happens for the states with both components in place. A more detailed discussion is found in Ref. [47].

An interesting thing is the stability of the different vector solutions. Unlike the double-fundamental modes studied in Sect. 4.1 it is not possible to apply the Vakhitov-Kolokolov criterion as such criterion is only valid when considering fundamental states (see Chap. 2 in Ref. [27]). Because of that we studied stability numerically by direct simulation using a BPM algorithm. As for the case of scalar modes, there are three different scenarios depending on the family considered as well as power or propagation constant of the modes: full stability, decay due to the azimuthal instability and collapse. In order to quantify the stability degree in the two latter cases, different states were propagated and the maximum amplitude recorded at each propagation step. By means of a further analysis it is possible to evaluate the break-up and collapsing distances by examining the points at which maximum amplitude changes by a fraction of the initial value. For the case of azimuthal break-up we chose a fraction of 0.05 (5%) while for detecting collapse we chose a fraction of 100.

Double-dipole states proved to be strongly unstable so we will focus on the rest of modes. For FD, FV and FT, however, depending on the propagation constant β_2 all three scenarios are possible. In Fig. 12a it is plotted the maximum amplitude versus propagation constant for different instability cases: for FD modes, a break-up case (A_1) and a collapsing case (A_2). For FV states, a direct collapse (A_5) and two azimuthal decays, one maintained indefinitely (A_3) and another one followed by a collapse (A_4). On the other hand, in Figs. 12b, c the decay and collapse distances

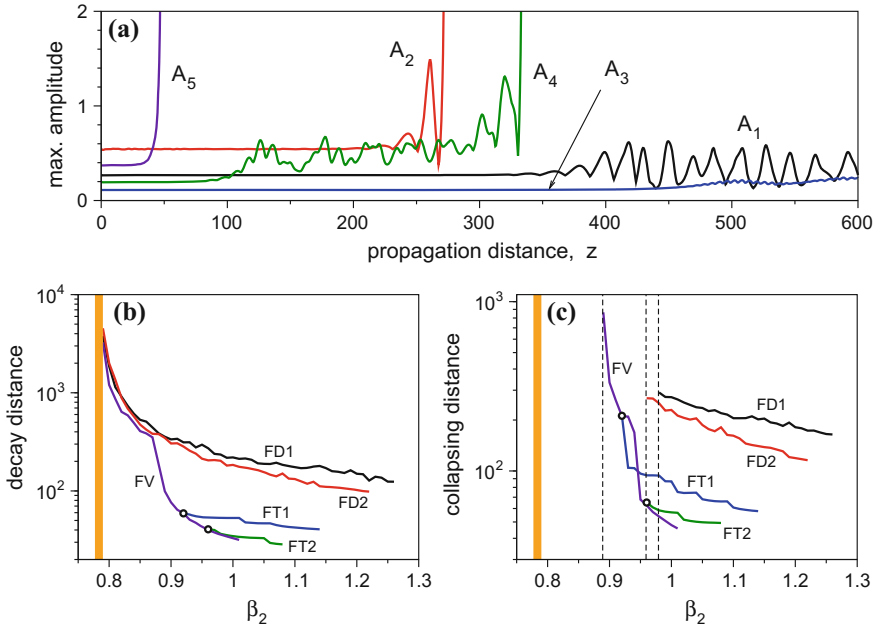

Fig. 12 **a** Maximum amplitude of the second component (dipole or vortex) for two FD (A_1 and A_2), and three FV modes (A_3–A_5). **b** Azimuthal break up distance for FD, FV and FT families in terms of β_2. **c** Collapsing distance for FD, FV and FT families versus β_2. Shaded area mark the full stability region. Vertical dashed lines represent the collapsing thresholds. Circular points stand for the bifurcation points. Reprinted with permission from [47]. Copyright (2016) by IOP Publishing

are plotted versus propagation constant. For any of those families a small band of stability exists (shaded region). Also there exists an interval where modes break-up but do not collapse (β_2 on the left of the vertical dashed lines). For larger values of β_2 modes do collapse.

Concerning double-vortex solutions it is not possible to find full stable states in contrast to what happened in the case of FV modes. Nevertheless, stability changes quite a lot with the value of the propagation constant as it dramatically increases at low values of β_2. At this point an important issue arises. Both components may present the same vorticity sign or opposite sign, these latter being the so called hidden vorticity (HV) modes. The stability properties are strongly dependent on this property in such a way that HV modes reach a high maximum of stability for a particular value of β_2 close to the low limit. The stronger stability of HV solutions was already observed in other systems as nematic media [23] or in the context of Bose-Einstein condensates [5]. Finally, a comparison of the stability properties among the different double-vortex families shows that no big differences exist. This means that the PCF matrix has a marginal influence on the stability of these kind of states as already was demonstrated for other discrete-symmetric systems like waveguide arrays [8, 34].

5 Nonlinear Dual-Core PCF

An interesting system, easy to implement in a PCF matrix and with very interesting properties and applications is the multi-core PCF, i.e. a PCF structure with a number of close defects. This system constitutes a set of coupled waveguides, and a proper design can lead to devices useful to perform operations like broadband directional coupling or polarization splitting [26, 29, 46, 63]. The most simple case, when only two close defects are considered, resembles the two-waveguide nonlinear directional coupler [1]. The modes of the system are, however, conditioned by the discrete symmetry of the PCF. Again, the system may have different stability properties depending on the power and type of the light beams launched into the system. In this section we review the most relevant results of the nonlinear dual-core PCF describing the different types of modes and their stability properties.

5.1 Fundamental Solitons in Dual-Core PCF

For a linear system, when a fundamental beam is launched into one of the cores, a beating between both cores takes place as is usual in a directional coupler, in such a way that light periodically passes from one core to each other. A complete power transfer takes place if the coupler is symmetric, i.e. made of two identical waveguides, as is the present case. Nonlinear regime brings new and useful properties coming from a different modal structure respect to the linear counterpart [4, 49].

To describe the dual-core system we use the same model as for the single core [Eq. (3)] but now the function $W(x, y)$ describes the PCF matrix with both defects (value one in the substrate and zero in the holes). The numerical solution leads to the different modes which come as families parametrized by the propagation constant β, and are characterized by the power given by Eq. (4). Three different types of fundamental modes, i.e. with a single hump at each core, are found. On one hand the usual symmetric and antisymmetric modes, also characteristic of linear couplers (Fig. 13, cases a and b). In Fig. 14 we show the power diagram for such modes. Power curves start at points on the horizontal axis, at values corresponding to the propagation constant of the linear modes (the symmetric mode is the fundamental), and power rises with the propagation constant in a similar fashion as happened for the single core PCF. At a particular power threshold there appears a new mode, an asymmetric one (Fig. 13, case c) bifurcating from the symmetric mode at point O_1 (Fig. 14). This mode exists because of the nonlinearity, as it requires a symmetry breaking in the dual-core PCF structure, and is the key of its switching properties.

Considering the system nonlinear and launching a fundamental beam into one of the cores, transference of the power to the second core is suppressed if the launched beam has a power over a specific threshold. The explanation for this fact relies in the fact that over the bifurcation point the symmetric mode turns into unstable, appearing the new asymmetric mode which is however stable.

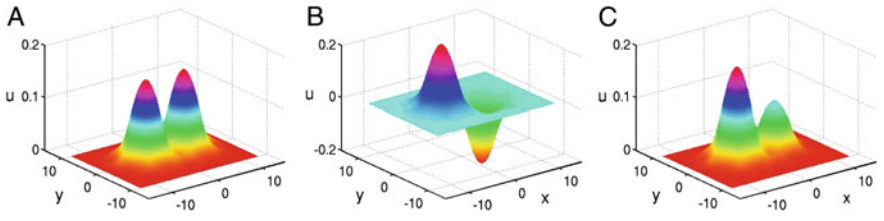

Fig. 13 Examples of the modes symmetric (left), antisymmetric (center) and asymmetric (right) of the nonlinear dual-core coupler ($\beta = 3.95$). Images show the amplitude profile of the modes. Labels A, B and C correspond to points in Fig. 14. Parameters: $\Lambda = 2$, $a = 0.75$, $n_a = 0$, $\delta = 5$

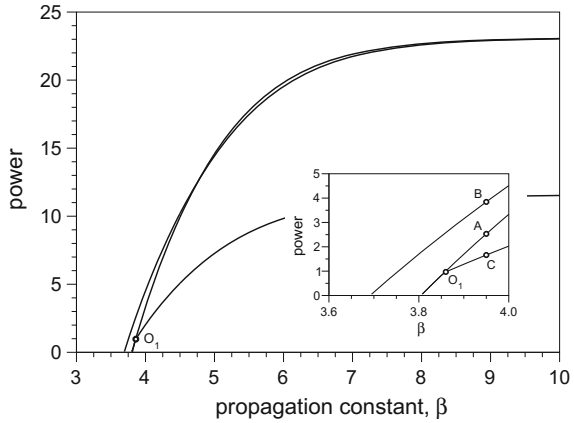

Fig. 14 Power diagram for the symmetric (A), antisymmetric (B) and asymmetric (C) modes of the dual-core PCF coupler. O_1 is the bifurcation point for the asymmetric mode. Inset: enlargement of the power diagram close to the bifurcation point. Labels mark points corresponding to the examples shown in Fig. 13. Reprinted with permission from [49]. Copyright (2005) by the Optical Society of America

In Fig. 15 we present the switching curve of the coupler. It was built carrying out a set of numerical simulations using the standard beam propagation method. First, the system is simulated as linear. A fundamental mode of the linear single-core PCF is launched into one of the cores and the distance where the whole power is transferred to the second core (beat length) was evaluated. For the particular parameters taken for our system it was $z_b = 21.23$. Then simulations are carried out in a nonlinear regime, launching beams of different power P_{in} into one of the cores and letting them propagate for the beat distance z_b. At that point, output power (P_{out}) at the excited core is evaluated for every beam. The fraction of light remaining in the excited core P_{out}/P_{in} is plotted against input power in Fig. 15. We see the curve raises from almost zero to one at the point where P_{in} overpasses the power threshold. This means that power goes from a total transfer to the second core to completely remain in the first one. Besides, the large slope of the curve means the change of state takes place sharply and this means a fast change of the status at the triggering point.

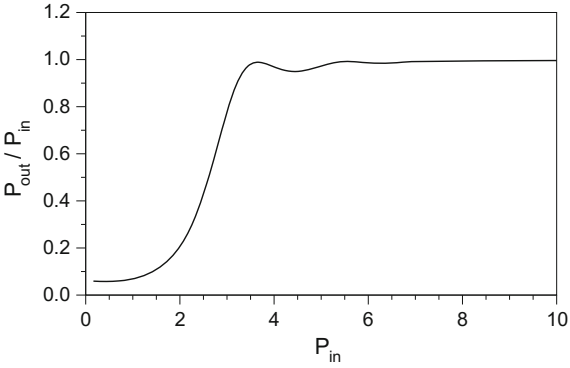

Fig. 15 Switching curve: ratio of output power to input power for the excited waveguide of a beat length z_b. Reprinted with permission from [49]. Copyright (2005) by the Optical Society of America

5.2 *Vortices in Dual-Core PCF*

Now we turn to consider solutions with phase dislocations centered on one or both defects of the dual-core PCF matrix [54]. As happened with the single-core PCF this brings additional complexity to the system modeling as now we have to consider complex-evaluated fields. The model is the same as the one described in Sect. 3.2 but now the symmetry properties of the solutions to seek are different. In fact, the original symmetry of the single-core PCF described by the group $\mathscr{C}_{6v}$ is reduced to that of the group $\mathscr{C}_{2v}$, and so the solutions must remain invariant under rotations of π radians or reflections respect to the coordinate axes. Nevertheless, this symmetry can be broken by the nonlinear effect if power is large enough (trivial subgroup $\mathscr{C}_1$). Taken this into account we were able to find different types of symmetric and asymmetric solutions containing vortices in one or both cores. Besides, as in the case of the single-core PCF, there are also first-order solutions without any angular momentum, which in this case present the form of symmetric or asymmetric dipoles.

We have classified the different solutions in four main types for convenience. In Fig. 16 we show a simplified power diagram showing them. There exist first order solutions exempt of any vorticity with the shape of double-dipoles (dashed curve in Fig. 16) that we label as *DD*. Such line is actually made of four close-together lines since four different types of double-dipoles exist [see Fig. 17a–d]. We name solutions in Figs. 17a, b as *bounding* (*b*) and *antibounding* (*a*) regarding the molecular orbital theory, since they are respectively characterized by a high and a low field density in the inter-core region. The other two families of solutions [Fig. 17c, d] are named *parallel* (*p*) and *crossed* (*x*) because they present both dipoles with same and opposite sign distribution respectively.

For large enough power asymmetric dipoles appear (unbalanced power of both cores) as a consequence of a spontaneous symmetry breaking (SSB). We label these solutions as *AD*. Two types of such solutions were found [Fig. 17e, f] showing respectively a dipole with lobes facing inter-hole spaces or facing holes of the PCF respec-

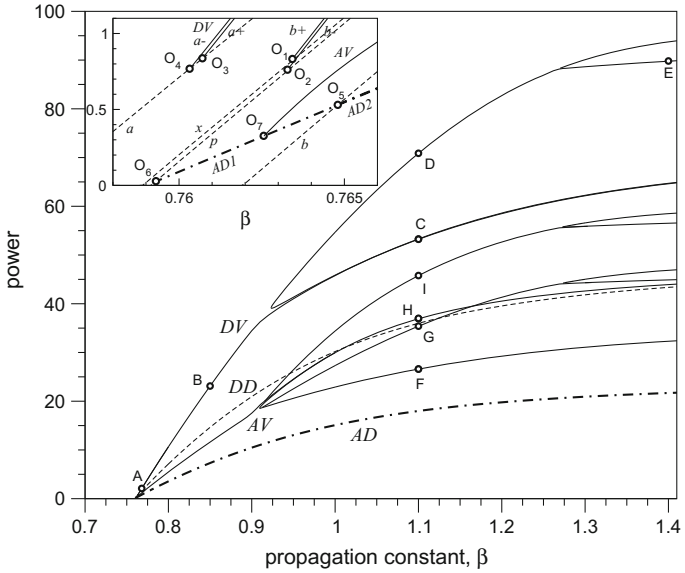

Fig. 16 Power versus propagation constant for the different general families of vortex solutions of the dual core PCF. Dashed lines are the double dipole families (DD) and dotted-dashed line corresponds to the asymmetric dipoles (AD). Continuous lines are the vortex-families, double vortex (DV) and asymmetric vortices (AV). Labelled points with upright capital letters correspond to examples in Figs. 17–19. Inset: zoomed low power region. O_1–O_4 are the bifurcation points for the double-vortices (DV). O_5 and O_6 are the bifurcation points for both asymmetric dipole families (AD1 and AD2). O_7 is the bifurcation point for the asymmetric-vortices (AV). Italic small letters label the different curves identifying the corresponding family. Parameters: $\Lambda = 10, a = 4, n_a = 0$

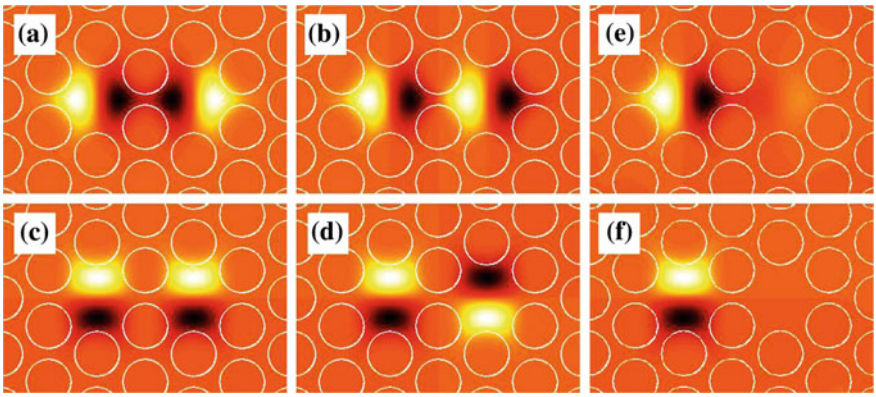

Fig. 17 **a–d** Different types of double-dipoles (DD) in the dual-core PCF: bounding **(a)**, antibounding **(b)**, parallel **(c)** and crossed **(d)**. **d–f** Examples of asymmetric dipoles (AD). Reprinted with permission from [54]. Copyright (2009) by the Optical Society of America

tively. These solutions bifurcate from two of the *DD* solutions as shown in the zoomed power diagram shown as an inset in Fig. 16 (curves labelled *AD1* and *AD2*).

A second main family of solutions is that of the symmetric double-vortex modes. These solutions present a vortex field at each of the cores that may show different amplitude and phase distribution. These solutions are purely nonlinear as double dipoles are non-degenerated (even in the linear regime) due to the symmetry reduction induced by the double-core structure in contrast to the case of a single-core PCF. Consequently they cannot be combined to form a stationary state. In a nonlinear regime, however, an asymmetric combination of a *bounding* or *antibounding* double-dipole with a *parallel* or *crossed* double-dipole, respectively as real and imaginary part of the field amplitude, is possible to form such kind of solutions.

At moderate power, there exist symmetric vortices with the shape of a double-vortex with a doughnut shape (curve labelled *DV* in Fig. 16). We found four different types of such solutions (there are actually four close-together curves as shown in the inset of Fig. 16). They can be of *bounding* or *antibounding* type depending whether they are formed by a *b* or *a* double-dipole and also both cores can present the same (+) or opposite (-) vorticity depending on the phase structure. Then we name those solutions as $b+$, $b-$, $a+$ and $a-$. They bifurcate from the *DD* families as shown in Fig. 16 (inset).

At higher power, as happened in single core PCF, solutions with field distribution in the form of double-tripoles or even double-quadrupoles appear. Some examples of possible solutions are shown in Fig. 18. They are two types of double-tripoles and two of double-quadrupoles which are $\mathscr{C}_{2v}$-symmetric. Any other combinations are not allowed at moderate power due to the reduced symmetry of the dual-core PCF. Interestingly, the point at which double-tripoles arise is a pseudobifurcation [21] point as the emergent solutions are actually asymmetric. The case of the double-quadrupole modes is similar but, as in the case of the single-core PCF, they appear at larger power because the quadrupole itself does not present the symmetry of the PCF matrix.

Finally there is a main family of solutions that we name as asymmetric vortices (labelled AV in Fig. 16) and can be of two different types: single-vortex modes (SV), i.e. modes with negligible power in one of the cores [see examples in Fig. 19 (cases F1, F2 and G)], and vortex-fundamental modes (VF) or combinations of a vortex in one of the cores and a fundamental field in the other [examples are in Fig. 19 (cases H1, H2 and I)]. At low power it describes a SV mode which bifurcate from one of the asymmetric dipole families (Fig. 16, inset). At a specific power threshold it goes through a complicated pseudobifurcation where different vortex-fundamental [including doughnut (VF) and tripole (TF) shaped ones] as well as single-tripole (ST) families originate (see Ref. [54] for a detailed description). For even larger power, the SV and VF families (doughnut shaped) originate modes with quadrupole shape: single quadrupoles and quadrupole-fundamental states.

An interesting point is the fact that the existence of symmetric DVs and SVs solutions suggests the existence of asymmetric DVs that could be generated from the symmetric DV via spontaneous symmetry breaking (bifurcation). However, it is not posible to find such solutions and this is again explained because of the reduced

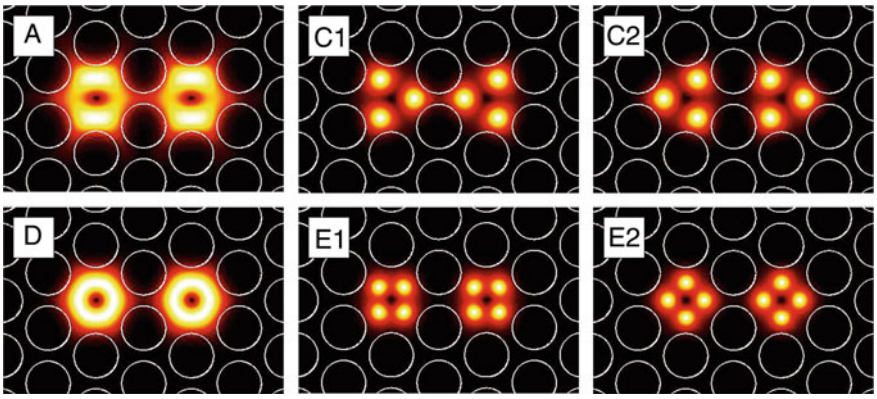

Fig. 18 Different shaped examples of DVs in the dual-core PCF: double-vortices (images labelled A, D), two types of double-tripoles (images C1 and C2) and two types of double-quadrupoles (images E1 and E2). Letters correspond to points in Fig. 16. Reprinted from [54]. Copyright (2009) by the Optical Society of America

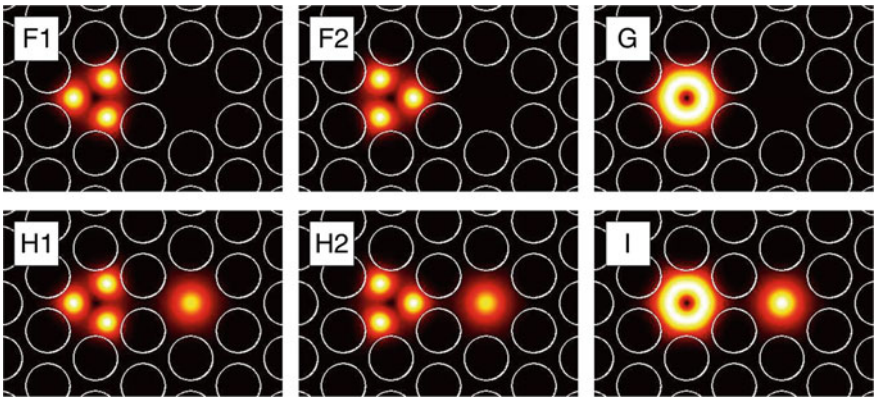

Fig. 19 Different examples of single vortices (image G), including single tripoles (images F1 and F2), and combinations of a vortex (including tripole-shaped) and a fundamental state (images H1, H2 and I) in the dual-core PCF. Letters correspond to points in Fig. 16. Reprinted from [54]. Copyright (2009) by the Optical Society of America

symmetry of the dual-core PCF, producing DD modes which are nondegenerated. In fact, the existence of a stationary vortex requires a specific power ratio between the real and the imaginary part. On the other hand, an asymmetric mode also requires a particular ratio between power carried by each core and both conditions cannot be satisfied simultaneously to form an asymmetric DV stationary solution. The only possibility is a combination of a vortex in one of the cores and a field without phase structure in the other one.

The stability of the different families of stationary states can be studied by numerical simulations using the standard beam propagation method [32, 52, 54]. The states

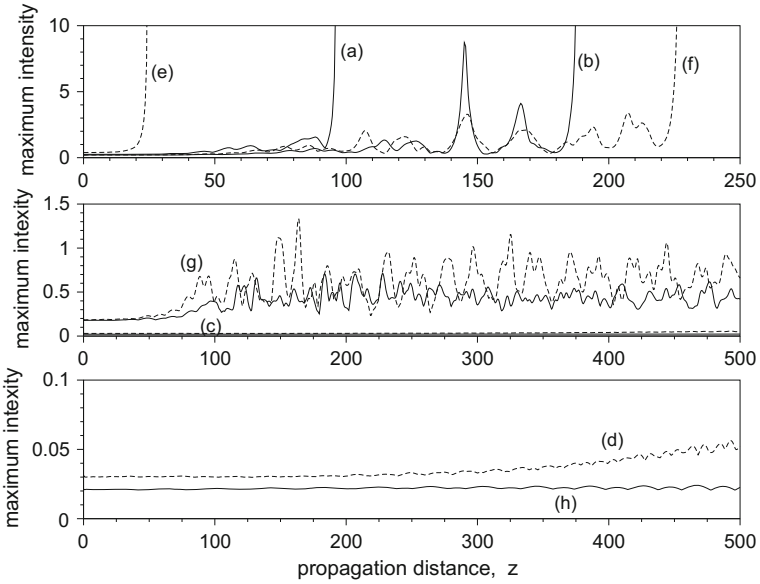

Fig. 20 Intensity at the maximum for different families of DVs (continuous lines) and SVs (dashed lines). DVs correspond to powers P = 34.4 (**a**), P = 30.1 (**b**), P = 27.9 (**c**), P = 5.8 (**d**). SVs correspond to P = 27.3 (**e**), P = 15.8 (**f**), P = 15.1 (**g**) and P = 2.76 (**h**). Reprinted from [54]. Copyright (2009) by the Optical Society of America

are basically unstable and the results show the existence of two different scenarios. Modes characterized by a power over a threshold undergo collapse after a particular propagation distance. The larger the power the shorter the distance to which they collapse as it can be seen in Fig. 20 [cases a, b, e and f corresponding to DV and SV states]. Interestingly, the collapse distance depends on the power or propagation constant and not so much on the type of family considered. In fact, families with power distribution in both cores (DV and VF) present a collapse threshold about $P \sim 30$ while those families with power mainly in one of the cores (like SV or ST) present a threshold around $P \sim 15.75$. At any of the former cases $\beta \sim 0.88$. This is approximately the point at which tripole solutions originate and consequently such tripole solutions are unstable and do collapse.

The second scenario takes place under the above mentioned collapsing threshold. Modes do not collapse but after some propagation distance they develop the azimuthal instability. This means the phase structure is destroyed and the vortices break into fundamental solitons which remain spinning inside the core. Again, the break-up distance depends on power in such a way that the larger the power is the shorter the distance at which modes decay [see Fig. 20 cases c, d, g and h]. At low power, close to the linear limit, modes may propagate for a quite long distance before decaying.

6 Conclusions

The main results on nonlinear solid-core photonic crystal fibers were reviewed as it concerns mode classification and their stability properties. The study includes a discussion on discrete symmetry systems and the use of such symmetries to predict and classify the different solution families, in a linear as well as a nonlinear regime. The first considered system was a single core PCF and it was demonstrated that fundamental modes as well as vortex modes can be found stable (fundamental modes) or virtually stable (vortices) in contrast to the homogeneous media case. Next, a vector two-component system was studied. In this case, systems of two fundamental components or a fundamental component and a vortex are found to be fully stable under certain power conditions. Double-vortex systems, though not fully stable, also improve their stability respect to their scalar counterparts. Finally the case of a dual-core PCF is studied, revealing the effects that a reduction of the symmetry has on the solutions and demonstrating that an efficient switching operation is posible using this structure which constitutes a directional coupler.

Acknowledgements This work was supported by the MINECO (Government of Spain) under Grants TEC2014-53727-C2-1-R and FIS2014-61984-EXP, as well as by Xunta de Galicia under grant GPC2015/019.

References

1. Akhmediev, N.N., Ankiewicz, A.: Solitons: Nonlinear Pulses and Beams. Chapman and Hall, Cornwall (1997)
2. Baizakov, B.B., Malomed, B.A., Salerno, M.: Multidimensional solitons in periodic potentials. Europhys. Lett. **63**(5), 642 (2003)
3. Bennet, F., Farnell, J.: Waveguide arrays in selectively infiltrated photonic crystal fibres. Opt. Commun. **283**(20), 4069–4073 (2010)
4. Betlej, A., Suntsov, S., Makris, K.G., Jankovic, L., Christodoulides, D.N., Stegeman, G.I., Fini, J., Bise, R.T., DiGiovanni, D.J.: All-optical switching and multifrequency generation in a dual-core photonic crystal fiber. Opt. Lett. **31**(10), 1480–1482 (2006)
5. Brtka, M., Gammal, A., Malomed, B.A.: Hidden vorticity in binary Bose-Einstein condensates. Phys. Rev. A **82**, 053,610 (2010)
6. Chen, M.Y., Zhou, J.: Mode converter based on mode coupling in an asymmetric dual-core photonic crystal fibre. Abbreviation Title J. Opt. A: Pure Appl. Opt. **10**(11), 115,304 (2008)
7. Christodoulides, D.N., Eugenieva, E.D.: Blocking and routing discrete solitons in two-dimensional networks of nonlinear waveguide arrays. Phys. Rev. Lett. **87**(23), 233,901 (2001)
8. Desyatnikov, A.S., Dennis, M.R., Ferrando, A.: All-optical discrete vortex switch. Phys. Rev. A **83**, 063,822 (2011)
9. Diebel, F., Leykam, D., Boguslawski, M., Rose, P., Denz, C., Desyatnikov, A.S.: All-optical switching in optically induced nonlinear waveguide couplers. Appl. Phys. Lett. **104**(26), 261,111 (2014)
10. Ferrando, A.: Discrete-symmetry vortices as angular Bloch modesloch modes. Phys. Rev. E **72**(3), 036,612 (2005)

11. Ferrando, A., Silvestre, E., Andrés, P., Miret, J.J., Andrés, M.V.: Designing the properties of dispersion-flattened photonic crystal fibers. Opt. Express **9**(13), 687 (2001)
12. Ferrando, A., Silvestre, E., Miret, J.J., Andrés, P.: Vector description of high-order modes in photonic crystal fibers. J. Opt. Soc. Am. **17**, 1333–1340 (2000)
13. Ferrando, A., Silvestre, E., Miret, J.J., Andrés, P., Andrés, M.V.: Full-vector analysis of a realistic photonic crystal fiber. Opt. Lett. **24**(5), 276 (1999)
14. Ferrando, A., Zacarés, M., Andrés, P., Fernández de Córdoba, P., Monsoriu, J.A.: Nodal solitons and the nonlinear breaking of discrete symmetry. Opt. Express **13**(4), 1072 (2005)
15. Ferrando, A., Zacarés, M., Fernández de Córdoba, P., Binosi, D., Monsoriu, J.A.: Spatial soliton formation in photonic crystal fibers. Opt. Express **11**(5), 452–459 (2003)
16. Ferrando, A., Zacarés, M., Fernández de Córdoba, P., Binosi, D., Monsoriu, J.A.: Vortex solitons in photonic crystal fibers. Opt. Express **12**(5), 817–822 (2004)
17. Ferrando, A., Zacarés, M., García-March, M.A.: Vorticity cutoff in nonlinear photonic crystals. Phys. Rev. Lett. **95**, 043,901 (2005)
18. Fleischer, J.W., Bartal, G., Cohen, O., Manela, O., Segev, M., Hudock, J., Christodoulides, D.N.: Observation of vortex-ring "discrete" solitons in 2D photonic lattices. Phys. Rev. Lett. **92**, 123,904 (2004)
19. Fleischer, J.W., Segev, M., Efremidis, N.K., Christodoulides, D.N.: Observation of two-dimensional discrete solitons in optically induced nonlinear photonic lattices. Nature **422**(6928), 147–150 (2003)
20. García-March, M.A., Ferrando, A., Zacarés, M., Vijande, J., Carr, L.D.: Angular pseudo-momentum theory for the generalized nonlinear Schrödinger equation in discrete rotational symmetry media. Physica D **238**(15), 1432–1438 (2009)
21. Gubeskys, A., Malomed, B.A.: Spontaneous soliton symmetry breaking in two-dimensional coupled Bose-Einstein condensates supported by optical lattices. Phys. Rev. A **76**, 043,623 (2007)
22. Hamermesh, M.: Group Theory and its Application to Physical Problems. Addison-Wesley, Reading, Massachusetts (1964)
23. Izdebskaya, Y.V., Rebling, J., Desyatnikov, A.S., Kivshar, Y.S.: Observation of vector solitons with hidden vorticity. Opt. Lett. **37**(5), 767–769 (2012)
24. Joannopoulos, J.D., Johnson, S.G., Winn, J.N., Meade, R.D.: Photonic Crystals: Molding the Flow of Light, 2nd edn. Princeton University Press, Princeton (2008)
25. Kartashov, Y.V., Ferrando, A., Egorov, A.A., Torner, L.: Soliton topology versus discrete symmetry in optical lattices. Phys. Rev. Lett **95**(12), 123,902 (2005)
26. Kim, H., Kim, J., Paek, U.C., Lee, B.H., Kim, K.T.: Tunable photonic crystal fiber coupler based on a side-polishing technique. Opt. Lett. **29**(11), 1194–1196 (2004)
27. Kivshar, Y.S., Agrawal, G.P.: Optical Solitons: From Fibers to Photonic Crystals. Academic Press, San Diego (2003)
28. Knight, J.C.: Photonic crystal fibres. Nature **424**, 847–851 (2003)
29. Lagsgaard, J., Bang, O., Bjarklev, A.: Photonic crystal fiber design for broadband directional coupling. Opt. Lett. **29**(21), 2473–2475 (2004)
30. Lederer, F., Stegeman, G.I., Christodoulides, D.N., Assanto, G., Segev, M., Silberberg, Y.: Discrete solitons in optics. Phys. Rep. **463**(1–3), 1–126 (2008)
31. Leykam, D., Malomed, B., Desyatnikov, A.S.: Composite vortices in nonlinear circular waveguide arrays. J. Opt. B: Quantum Semiclassical Opt. **15**(4), 044,016 (2013)
32. Li, P., Zhao, J., Liu, S., Gan, X., Peng, T., Jiao, X.: Dynamic behaviors of optical vortices in dual-core photonic crystal fibers. Opt. Commun. **285**(9), 2355–2359 (2012)
33. Malmberg, J.N., Carlsson, A.H., Anderson, D., Lisak, M., Ostrovskaya, E.A., Kivshar, Y.S.: Vector solitons in $(2 + 1)$ dimensions. Opt. Lett. **25**(9), 643–645 (2000)
34. Malomed, B.A., Kevrekidis, P.G.: Discrete vortex solitons. Phys. Rev. E **64**, 026,601 (2001)
35. Minardi, S., Eilenberger, F., Kartashov, Y.V., Szameit, A., Röpke, U., Kobelke, J., Schuster, K., Bartelt, H., Nolte, S., Torner, L., Lederer, F., Tünnermann, A., Pertsch, T.: Three-dimensional light bullets in arrays of waveguides. Phys. Rev. Lett. **105**(26), 263,901 (2010)

36. Mingaleev, S.F., Kivshar, Y.S., Sammut, R.A.: Long-range interaction and nonlinear localized modes in photonic crystal waveguides. Phys. Rev. E **62**(4), 5777–5782 (2000)
37. Neshev, D.N., Alexander, T.J., Ostrovskaya, E.A., Kivshar, Y.S.: Observation of discrete vortex solitons in optically induced photonic lattices. Phys. Rev. Lett. **92**(12), 123,903 (2004)
38. Ostrovskaya, E.A., Kivshar, Y.S.: Matter-wave gap vortices in optical lattices. Phys. Rev. Lett. **93**, 160,405 (2004)
39. Pelinovsky, D.E.: Inertia law for spectral stability of solitary waves in coupled nonlinear Schrödinger equations. Proc. R. Soc. Lond. Ser. A **461**, 783–812 (2005)
40. Pelinovsky, D.E., Kivshar, Y.S.: Stability criterion for multicomponent solitary waves. Phys. Rev. E **62**, 8668–8676 (2000)
41. Pelinovsky, D.E., Yang, J.: Internal oscillations and radiation damping vector solitons. Stud. Appl. Math. **105**, 245–267 (2000)
42. Rosberg, C.R., Bennet, F.H., Neshev, D.N., Rasmussen, P.D., Bang, O., Krolikowski, W., Bjarklev, A., Kivshar, Y.S.: Tunable diffraction and self-defocusing in liquid-filled photonic crystal fibers. Opt. Express **15**(19), 12145–12150 (2007)
43. Russell, P.: Photonic crystal fibers. Science **299**, 358–362 (2003)
44. Russell, P.: Photonic crystal fibers: A historical account. IEEE LEOS Newsl. **21**, 11–15 (2007)
45. Russell, P.S.: Photonic-crystal fibers. J. Lightwave Technol. **24**(12), 4729–4749 (2006)
46. Saitoh, K., Sato, Y., Koshiba, M.: Coupling characteristics of dual-core photonic crystal fiber couplers. Opt. Express **11**(24), 3188–3195 (2003)
47. Salgueiro, J.R.: Vector–vortex solitons in nonlinear photonic crystal fibers. J. Opt. **18**(7), 074,004 (2016)
48. Salgueiro, J.R., Kivshar, Y.S.: Single- and double-vortex vector solitons in self-focusing nonlinear media. Phys. Rev. E **70**, 056,613 (2004)
49. Salgueiro, J.R., Kivshar, Y.S.: Nonlinear dual-core photonic crystal fiber couplers. Opt. Lett. **30**(14), 1858–1860 (2005)
50. Salgueiro, J.R., Kivshar, Y.S.: Optical vortex solitons and soliton clusters in photonic crystal fibres. Eur. Phys. J.-Spec. Top. **173**, 281–288 (2009)
51. Salgueiro, J.R., Kivshar, Y.S., Pelinovski, D.E., Simón, V., Michinel, H.: Spatial vector solitons in nonlinear photonic crystal fibers. Stud. Appl. Math. **115**, 157–171 (2005)
52. Salgueiro, J.R., Michinel, H., Ferrando, A., Kivshar, Y.S.: Switching and instabilities of optical vortices in nonlinear dual-core photonic crystal fibre couplers. J. Eur. Opt. Soc. Rapid **1**, 06,014 (2006)
53. Salgueiro, J.R., Olivieri, D., Michinel, H.: Computation of linear and nonlinear stationary states of photonic structures using modern iterative solvers. Opt. Quantum Electron. **39**, 239–260 (2007)
54. Salgueiro, J.R., Santos, F.: Nonlinear vortex modes in dual-core photonic crystal fiber couplers. J. Opt. Soc. Am. B **26**(12), 2301–2307 (2009)
55. Szameit, A., Burghoff, J., Pertsch, T., Nolte, S., Tünnermann, A., Lederer, F.: Two-dimensional soliton in cubic fs laser written waveguide arrays in fused silica. Opt. Express **14**(13), 6055 (2006)
56. Tombelaine, V., Labruyère, A., Kobelke, J., Schuster, K., Reichel, V., Leproux, P., Couderc, V., Jamier, R., Bartelt, H.: Nonlinear photonic crystal fiber with a structured multi-component glass core for four-wave mixing and supercontinuum generation. Opt. Express **17**(18), 15392–15401 (2009)
57. Udem, T., Holzwarth, R., Hansch, T.W.: Optical frequency metrology. Nature **416**(6877), 233–237 (2002)
58. Wu, D.K.C., Kuhlmey, B.T., Eggleton, B.J.: Ultrasensitive photonic crystal fiber refractive index sensor. Opt. Lett. **34**(3), 322–324 (2009)
59. Xie, P., Zhang, Z.Q., Zhang, X.: Gap solitons and soliton trains in finite-sized two-dimensional periodic and quasiperiodic photonic crystals. Phys. Rev. E **67**, 026,607 (2003)
60. Yang, J., Pelinovsky, D.E.: Stable vortex and dipole vector solitons in a saturable nonlinear medium. Phys. Rev. E **67**, 016,608 (2003)
61. Yeh, P., Yariv, A., Marom, E.: Theory of Bragg fiber. J. Opt. Soc. Am. **68**(9), 1196–1201 (1978)

62. Zervas, M.N., Codemard, C.A.: High power fiber lasers: A review. IEEE J. Sel. Top. Quantum Electron. **20**(5), 219–241 (2014)
63. Zhang, L., Yang, C.: Polarization splitter based on photonic crystal fibers. Opt. Express **11**(9), 1015–1020 (2003)

Part III
Crystals, Metamaterials and Other Condensed Matter

Nonlinear Excitations in Graphene and Other Carbon Nano-Polymorphs

Sergey V. Dmitriev, Julia A. Baimova, Elena A. Korznikova and Alexander P. Chetverikov

Abstract This review summarizes recent developments in the numerical investigations of nonlinear dynamics of graphene, carbon nanotubes, and fullerenes. Discrete breathers (DBs) or, synonymously, intrinsic localized modes are discussed together with the nonlinear delocalised vibrational modes (DVM). These nonlinear excitations are expected to considerably affect physical and mechanical properties of sp^2 carbon nanomaterials, for example, their thermal and electrical conductivity, defect nucleation and healing, etc. Our knowledge of the DB properties in carbon nanomaterials is insufficient for designing a setup for their reliable experimental observation, that is why numerical studies in this area are of crucial importance today. It is indicated that the results obtained by molecular dynamics method significantly depend on the interatomic potentials, making verification of these results by first-principle modelling indispensable. Finally, the associated challenges and prospects on the future study of nonlinear excitations in graphene and other carbon nanomaterials are discussed.

Keywords Graphene · Carbon nanotube · Fullerene · Discrete breather · Intrinsic localized mode · Delocalized vibrational mode · Molecular dynamics · ab-initio simulations

S. V. Dmitriev (✉) · J. A. Baimova · E. A. Korznikova
Institute for Metals Superplasticity Problems of RAS, 39 Khalturin St.,
450001 Ufa, Russia
e-mail: dmitriev.sergey.v@gmail.com

E. A. Korznikova
e-mail: elena.a.korznikova@gmail.com

S. V. Dmitriev
National Research Tomsk State University, 36 Lenin Ave, 634050 Tomsk, Russia

J. A. Baimova
M.N. Mikheev Institute of Metal Physics of the Ural Branch of RAS,
18 S. Kovalevskoy, 620990 Ekaterinburg, Russia
e-mail: julia.a.baimova@gmail.com

A. P. Chetverikov
Saratov State University, 83 Astrakhanskaya St., 410012 Saratov, Russia
e-mail: ChetverikovAP@info.sgu.ru

J. F. R. Archilla et al. (eds.), *Nonlinear Systems, Vol. 2*, Understanding Complex Systems, https://doi.org/10.1007/978-3-319-72218-4_7

1 Introduction

Graphene is the well-known two-dimensional (2D) crystal in the form of carbon monolayer composed of sp^2-hybridized atoms with many intriguing properties. For instance, it has lightweight, high electrical and thermal conductivity [11, 14], it is heat-resistant [9, 74, 81, 99], demonstrates highly tunable surface area [100], high mechanical strength [66] and chemical stability [4, 77, 80]. Applications in many diverse areas have been pointed out for graphene, such as photonics and optoelectronics, flexible electronics, spintronics, sensors, energy generation and storage, biomedical applications, composite materials to name a few [38, 77]. Since its successful exfoliation in 2004 the interest in graphene research has increased exponentially. In fact, graphene is closely related to other sp^2-carbon allotropes discovered earlier, such as carbon nanotubes [48] and fullerenes [65].

In the present review, nonlinear dynamics of sp^2-carbon allotropes is discussed with the emphasis on the spatially localized vibrational modes called discrete breathers (DBs) (also often termed as intrinsic localised modes, ILMs) and large-amplitude delocalized vibrational modes (DVMs).

DBs are time-periodic and spatially localized excitations which generally exist in the presence of spatial discreteness and nonlinearity [3, 17, 32, 39, 92]. Energy can be localized in a system through the excitation of a DB for much longer times compared to thermal fluctuations. Remarkably, such localised nonlinear vibrations have been also observed experimentally in various physical systems [13, 40, 82, 83]. Nevertheless, most of the results which are known for DB existence in various crystals are obtained by the atomistic simulation methods [18, 43, 44, 50, 55, 56, 84, 90, 91, 96, 98]. DBs can be pinned to the lattice or they can be mobile [28, 31, 43, 44, 57, 58, 76].

Properties of nonlinear vibrational modes should be discussed in relation to the linear phonon spectrum: DBs can have frequencies above the phonon spectrum or they can emerge within a gap, if it exists. In the latter case they are called gap DBs. DBs with frequencies above the gapless phonon spectrum have been successfully excited in graphene [33, 34, 98]. Application of homogeneous strain can produce a gap in the phonon spectrum of graphene and to make the existence of gap DBs possible [6, 33, 34, 51, 98]. Other carbon and hydrocarbon nanostructures can also support DBs. They have been found in carbon nanotubes [35, 54, 86, 90, 91], graphene nanoribbons [61, 64], and in hydrogenated graphene [8, 18, 59, 68, 89]. Fullerenes can also support long-lived nonlinear vibrational modes [84], though such modes cannot be classified as DBs, because DBs exist in the structures with translational symmetry. Examples of nonlinear excitations in carbon and hydrocarbon nanostructures are shown in Fig. 1.

Moving DBs transport relatively large portions of energy contributing to thermal conductivity. On the other hand, playing the role of scattering centers for phonons, they can reduce thermal conductivity. Furthermore, DBs can interact with the lattice

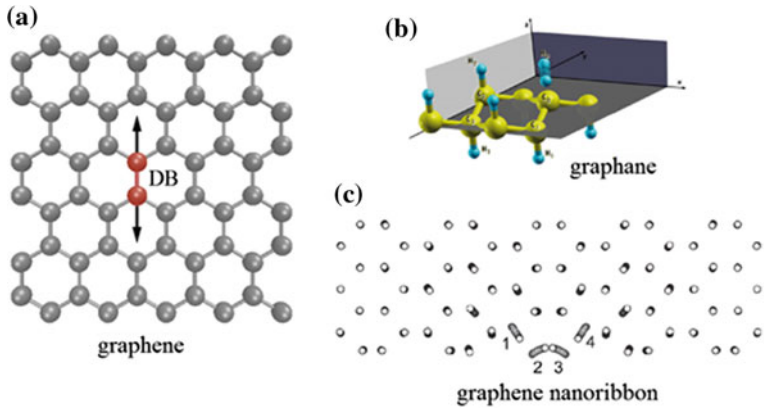

Fig. 1 Nonlinear vibrational modes in carbon nanostructures: **a** DB in unstrained graphene, **b** DB in graphane (fully hydrogenated graphene). Reproduced with permission from [18], copyright by APS. **c** DB at the edge of stretched graphene nanoribbon. Reproduced with permission from [61], copyright by EPLA

defects [28, 58, 94] or even take part in defect nucleation [91]. Thus it can be concluded that DBs can play an important role in the mechanics and physics of materials. In order to better understand the characteristics of DBs in graphene and their effect on its physical properties it is necessary to summarize the simulation data presented in the literature to date.

Numerical studies of DBs in graphene are conducted by two different methods: molecular dynamics (MD), that relies on empiric interatomic potentials, and density functional theory (DFT), which takes into account electronic structure. It was shown that the results of MD simulations are very sensitive to the choice of the interatomic potentials.

In the present review, the major progresses made in the investigations of DBs in graphene and other carbon nano-polymorphs is summarized.

2 Numerical Approaches to Simulate DBs in Carbon Nanomaterials

Most of the results on the DB properties in graphene and other carbon nano-polymorphs have been obtained to date with the use of the molecular dynamics method. Different interatomic potentials were used for the simulation of DBs by molecular dynamics: Brenner [15], standard set of interatomic potentials developed by Savin [87], Tersoff [67], AIREBO [93], LCBOP [72], and CBOP [73]. It was shown that not only stability and lifetime of DBs in graphene, but their very existence, depend on the potential used, as it will be described in Sect. 3. This is because

the interatomic potentials are typically fitted to the linear properties of solids such as their elastic moduli and phonon dispersion curves. They are also fitted to the binding energies whose values depend only on the depth of the interatomic potential but not on its profile. On the other hand, DBs are essentially nonlinear vibrational modes and their properties depend sensitively on the potential profile.

The DFT method is more accurate because it does not require the use of a phenomenological interatomic potential. The disadvantage of the method is that it is very demanding to the computational resources, especially when it is applied to a dynamical problem. Therefore, the low dimensional crystals, such as 1D carbon chains [22, 23] or 2D graphene [70, 71], are more suitable for DFT simulations. Up to date, only a few DFT studies on DBs in graphene [70, 71] and graphane [18, 19] have been done. It was shown that there is no qualitative differences between MD and DFT results for gap DB in strained graphene [51, 71]. At the same time, for DB in graphane modelled in the frame of DFT, a monotonous decrease of frequency with amplitude was observed [18], while in MD simulations a non-monotonous dependence was found [68].

Finding proper initial conditions is a very important problem in atomistic simulations of DBs in crystals. Very often DBs are excited by applying initial deviations to a few atoms. This method works well for highly localized DBs, e.g., for DB in graphane localized on a single hydrogen atom or for gap DB in strained graphene localized on two carbon atoms. There exist several systematic approaches for DB excitation. One relies on the effect of modulational instability of a zone-boundary mode leading (in some cases) to the energy localization in the form of DBs [16, 50, 60, 98]. Another one starts with the investigation of DVM frequency-amplitude dependence. If frequency of DVM with increase in its amplitude leaves phonon spectrum, one can try to obtain a spatially localized mode (i.e., DB) by superimposing a bell-shape function on the DVM [12, 63].

3 Delocalized Vibrational Modes in Graphene

Chechin with co-authors have reported the four DVMs in unstrained graphene [20] with in-plane displacements of atoms, as presented in Fig. 2a–d. These modes have been found with the use of the group-theoretical approach developed in [21]. They are symmetry-dictated exact solutions to the equations of atomic motion regardless the type of interatomic potentials and regardless the mode amplitude. One more quite obvious DVM is shown in Fig. 2e. Here the two differently colored sublattices vibrate out-of-phase in the direction normal to the graphene sheet.

DVMs are interesting for at least two reasons. Firstly, they can be modulationally unstable and the modulational instability in some cases can result in spontaneous energy localization in the form of DBs [60, 98]. For instance, the DVM

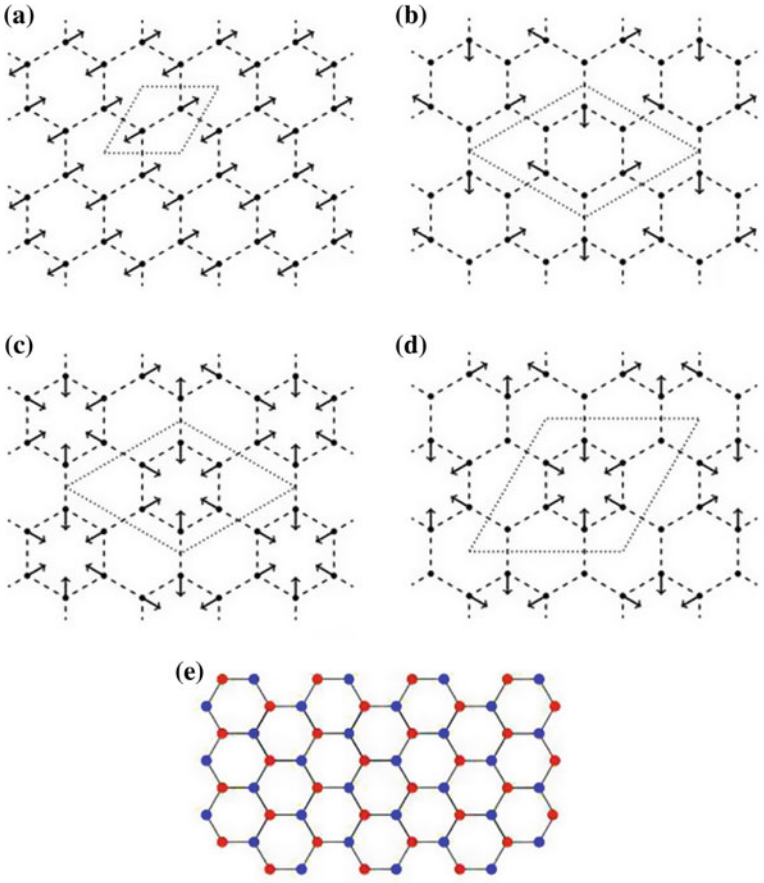

Fig. 2 **a**–**d** Four DVMs with atoms moving in plane. Dotted lines show the primitive translational cells of these dynamical structures. Reproduced with permission from [20], copyright by Institute for Metals Superplasticity Problems of RAS. **e** DVM with two sublattices (colored differently) vibrating out-of-phase in the direction normal to the graphene sheet

shown in Fig. 2a has been used in [98] for excitation of DBs as the result of modulational instability. Secondly, those DVMs whose frequency leaves phonon spectrum with increasing amplitude, can be used for setting initial conditions to excite DBs by superimposing bell-shaped functions to achieve spatially localized vibrations [12, 63].

We point out that consideration of different nonlinear excitations in crystal and their interconnection is a new trend in the study of nonlinear lattice dynamics [95].

4 Discrete Breathers in Graphene

Several types of DBs in graphene have been identified. They include the hard-type anharmonicity DBs in unstrained graphene with in-plane [33, 34, 98] and out-of-plane [12, 46, 47] atomic vibrations, as well as the soft-type anharmonicity gap DBs in strained graphene [51]. Localized defect modes in graphene have been studied in [85]. Moving wrinklon (the region where two or more wrinkles merge into one) was modelled with the Savin potential in [62].

4.1 In-Plane, Hard-Type Anharmonicity DBs in Unstrained Graphene

For the first time, DB in graphene was reported in [98] by MD simulations with the use of the Brenner interatomic potential [15]. In this work, DBs were excited through the modulational instability of the zone-boundary DVM shown in Fig. 2a, that lead to spatial energy localization in the form of DBs. Figure 3 shows the example of temporal evolution of the displacements of the two atoms in the vicinity of DB. Until 0.8 ps, the atoms vibrate following the initial mode, although the amplitude gradually increases. The vibration maintains high amplitude between 0.8 and 1.3 ps, and becomes random after 1.3 ps [98]. The frequency of the localized vibration exceeds the upper edge of the phonon band and this clearly indicates the excitation of the DB in graphene. The hard-type anharmonicity DBs in unstrained graphene were found to be unstable [33, 34].

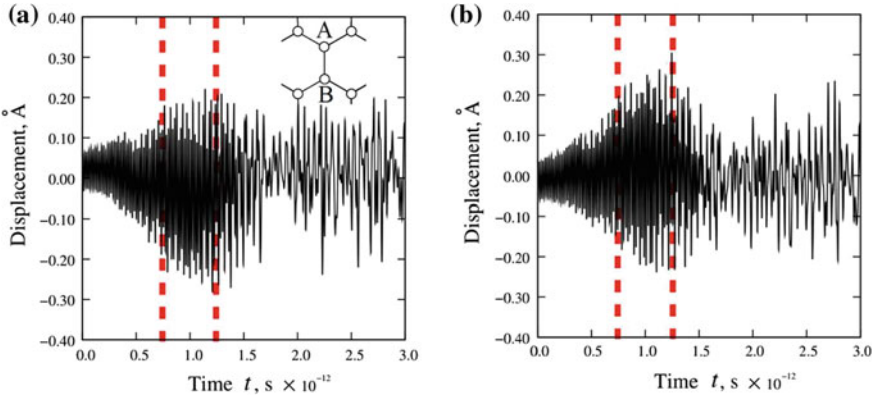

Fig. 3 Displacements as the functions of time for the atoms **a** A and **b** B [see inset in (**a**)] belonging to the energy-localized area that appeared in the graphene sheet after the development of modulational instability of the zone-boundary DVM. Reproduced with permission from [98], copyright by EPLA

Lately, even more localised modes were found in unstrained graphene. For example, in [41] the authors have found the defect nonlinear vibrational modes. The authors call these modes DBs but actually they are not DBs because they are localized on the lattice defects. The Tersoff interatomic potential used in their study supports a stable artifact defect in the form of one valence bond longer than the others. Frequencies of the defect modes lie above the phonon band and grow with the amplitude [41].

4.2 *In-Plane, Soft-Type Anharmonicity DBs in Strained Graphene*

4.2.1 Effect of Strain on Phonon DOS of Graphene

As indicated above, gap DBs can be found if there is a gap in the phonon spectrum of the structure. For graphene, a wide gap in the phonon spectrum can be induced by application of certain homogeneous elastic strain [7, 10, 30, 51]. Examples of the phonon density of states (DOS) for graphene at different strain levels are shown in Fig. 4a (for details see [51]). The whole spectrum is divided into phonons oscillating in-plane (shaded) and out-of-plane (not shaded). Note that the x (y) axis is along the zigzag (armchair) direction. It is seen that the gap in the shaded phonon spectrum is wider than that in the DOS including all frequencies. In [5] the strain map was presented with the regions where the appearance of the gap in the phonon spectrum takes place [regions 1a and 1b marked with dots and vertical hatching in Fig. 4b]. Inset in the gray area shows phonon DOS for unstrained graphene. Width of the gap

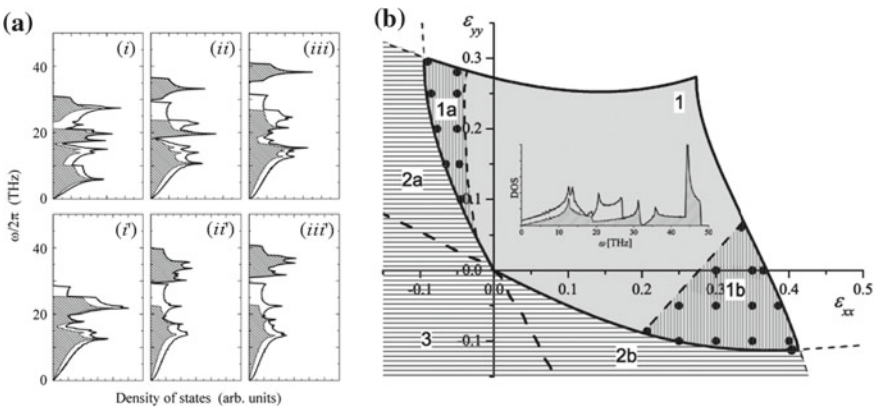

Fig. 4 **a** Effect of the elastic deformation on the phonon DOS of graphene: (i) $\varepsilon_{yy} = 0.1$, (ii) $\varepsilon_{yy} = 0$, (iii) $\varepsilon_{yy} = -0.1$, at fixed $\varepsilon_{xx} = 0.3$, $\varepsilon_{xy} = 0$; (i') $\varepsilon_{xx} = 0.2$, (ii') $\varepsilon_{xx} = -0.05$, (iii') $\varepsilon_{xx} = -0.08$, at fixed $\varepsilon_{yy} = 0.2$, $\varepsilon_{xy} = 0$. DOS for in-plane (out-of-plane) phonons are shaded (not shaded). **b** Stability range of flat graphene in the plane of strain components (ε_{xx}, ε_{yy}) for $\varepsilon_{xy} = 0$. Inset shows phonon DOS for unstrained graphene. Reproduced with permission from [5], Copyright by World Scientific

depends on the strain value. The widest gap (3.96 THz) can be found for $\varepsilon_{xx} = 0.4$ and ε_{yy} =-0.1 near the border of the stability region of flat graphene [30]. In this case graphene sheet is under tension along the zigzag direction [right bottom corner of the stability region in Fig. 4b]. Gap DBs were excited in graphene under this type of homogeneous strain [51]. For stretching along y direction quite wide gap can also be found (e.g., for ε_{xx} =-0.05 and $\varepsilon_{yy} = 0.1$), but no reports on gap DBs in graphene are known for this type of homogeneous strain.

4.2.2 Gap DBs and Their Clusters in Strained Graphene

The pioneering work on gap DBs in graphene is [51], where the existence of gap DBs was shown by MD simulations with the standard set of interatomic potentials developed by Savin [87]. Homogeneous elastic strain $\varepsilon_{xx} = 0.3$ and ε_{yy} =-0.1 was applied to graphene to open a sufficiently wide gap in the phonon spectrum. The y-components of displacements of the two atoms in the center of DB are shown in (a) as the functions of time. The stroboscopic picture of atomic motion in the vicinity of

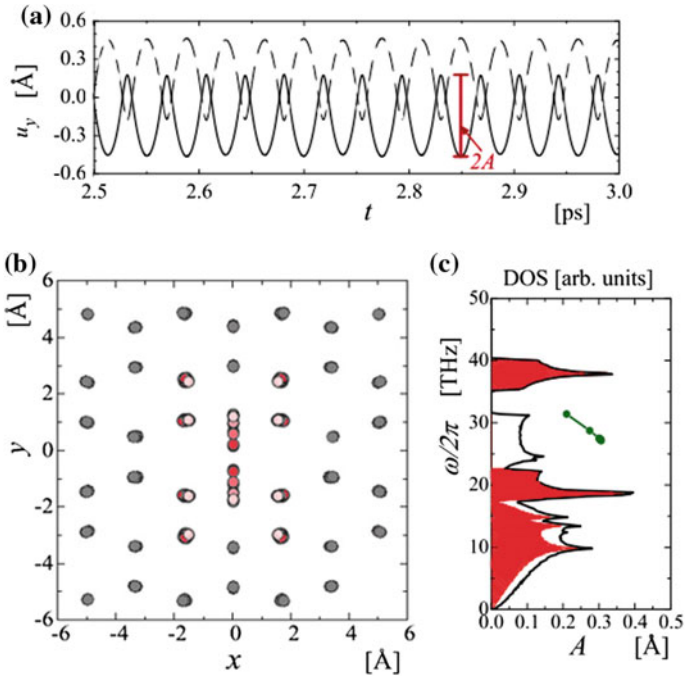

Fig. 5 **a** y-component of displacement for the two atoms in the center of DB in strained graphene as the function of time. **b** Stroboscopic picture of atomic motion in the vicinity of gap DB. **c** Phonon DOS of graphene under homogeneous strain $\varepsilon_{xx} = 0.3$, $\varepsilon_{yy} = -0.1$, $\varepsilon_{xy} = 0$. DOS for in-plane (out-of-plane) phonons are shaded (not shaded). Dots connected with the line show the dependence of DB frequency on its amplitude A

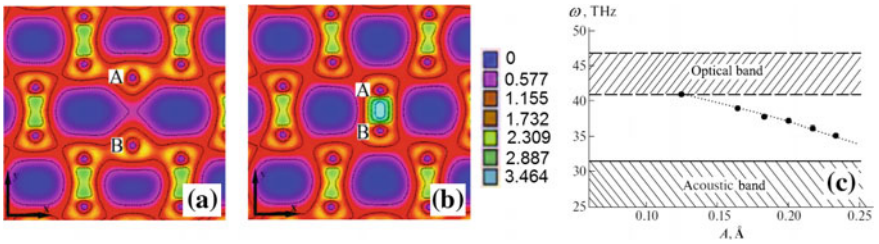

Fig. 6 Results of ab initio simulations for gap DB in strained graphene. **a**, **b** Electron density distribution in the vicinity of the DB when distance between atoms A and B is maximal and minimal, respectively. **c** Frequency of the DB as the function of amplitude

the gap DB is presented in Fig. 5b, while DOS at the considered strain level is shown in (c). As it can be seen from (c), frequency of the DB ranges from 27 to 32 THz and lies within the phonon DOS decreasing with increasing amplitude (dots connected with the line). On the other hand, DB frequency lies in the gap of shaded DOS. DB lifetime is large because the DB with in-plane oscillations does not interact with the out-of-plane phonon modes even though it has frequencies of these modes. In the work [51], DB was excited by initial shift of just two atoms connected by valence bond along the armchair (y) direction.

Gap DBs in strained graphene have been also studied with the use of the DFT approach [69–71]. In Fig. 6a,b the electron density distribution in the vicinity of the DB is shown when distance between atoms A and B is maximal and minimal, respectively. In (c) the dependence of DB frequency as the function of its amplitude is presented. This dependence is in qualitative agreement with the result of MD simulations [51] shown in Fig. 5c. Both methods predict soft type anharmonicity DB with frequency decreasing with increasing amplitude.

Interestingly, ab initio results for DB in graphane (fully hydrogenated graphene) [18] agree qualitatively with the MD results [68] only for small DB amplitudes. First principle method predicts monotonic decrease of the DB frequency with its amplitude, while MD produces a non-monotonic dependence.

Clusters of gap DBs in strained graphene also should be mentioned [6]. Different clusters of DBs including two, three, and four DBs were considered [see Fig. 7a]. It was shown that DB clusters can have very long lifetime of hundreds and thousands of oscillation periods. DBs in the clusters can exchange by their energy which is very important because they can localize a larger amount of energy than single DB. As an example, in Fig. 7b,c time evolution of amplitudes and frequencies of two DBs composing DB cluster B is presented. Time is normalized by the DB oscillation period Θ. DB amplitude slowly decreases and frequency increases with time because of the energy radiation in the form of the small-amplitude phonons. Till $t/\Theta = 660$ a quasi-periodic energy exchange between DBs can be seen. At this time a burst of energy is emitted by the DB cluster because its frequency crosses the upper edge of the out-of-plane phonon DOS. DBs survive till $t/\Theta = 1200$.

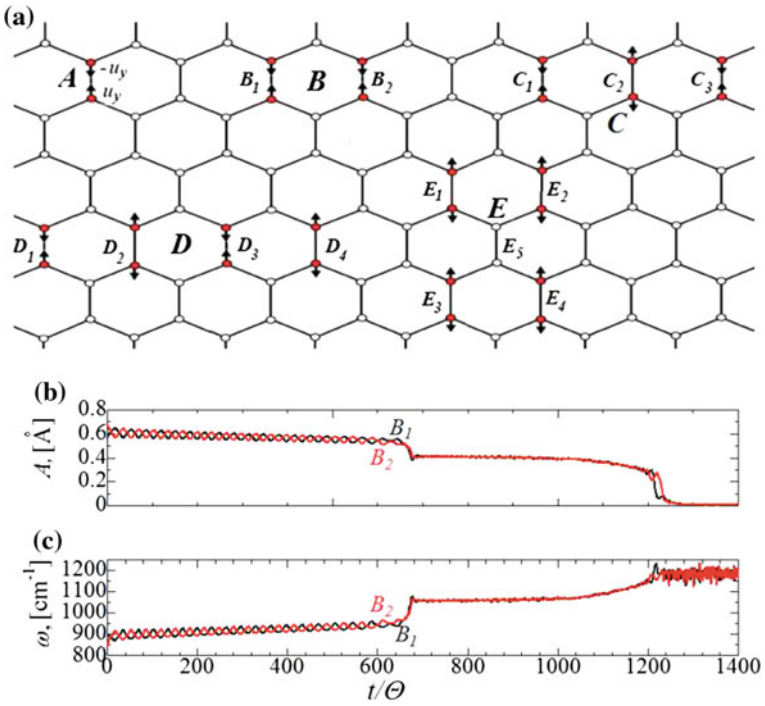

Fig. 7 **a** Clusters of gap DBs in graphene under strain $\varepsilon_{xx} = 0.3$, $\varepsilon_{yy} = -0.1$, $\varepsilon_{xy} = 0$. Arrows show the direction of initial displacement for the atoms applied to excite the DB clusters. **b**, **c** Dependence of DB amplitudes and frequencies on dimensionless time in the cluster B that includes two DBs. Here Θ is the DB oscillation period. Reproduced with permission from [6], copyright by EPLA

4.2.3 Gap DBs at the Edge of Strained Graphene Nanoribbon

Strained graphene nanoribbons with the edges parallel to the armchair direction support gap DBs localized at the edges [61, 64]. Stroboscopic picture of the atomic motion for such DB is presented in Fig. 1c. DB is mainly localized on four carbon atoms. Its frequency lies in the gap induced by the nanoribbon stretching and decreases with increasing amplitude. This modelling was done with the use of the Savin interatomic potential [87].

4.2.4 Gap DB Assisted Energy Transport in Ac Driven Graphene

Energy transport assisted by gap DBs excited in strained graphene by ac driving of a zigzag atomic row has been studied recently [37]. The simulation setup based on the Savin interatomic potential [87] is presented in Fig. 8a. Atomic rows parallel to the x axis are numbered by the index n. For driven atomic rows displacements of the atoms change in time according to the harmonic law

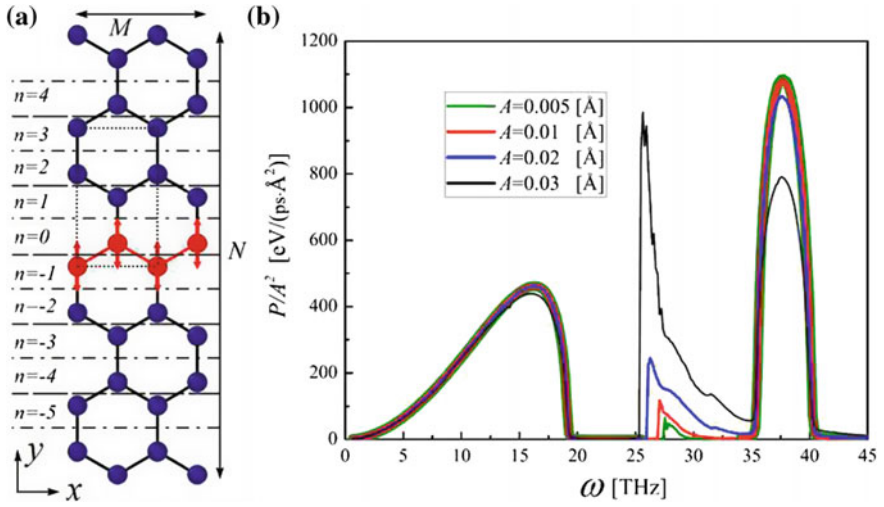

Fig. 8 **a** Simulation setup for investigation of the energy transport in strained graphene assisted by the gap DB excited by the ac driving of the zigzag atomic row. **b** Normalized power of the energy source as a function of the driving frequency ω for different driving amplitudes A. Both graphs reproduced with permission from [37], copyright by APS

$$\Delta y_0(t) = \Delta y_{-1}(t) = A\sin(2\pi\omega t), \tag{1}$$

where Δy represents the displacement of atoms from their equilibrium positions in y direction, A is the amplitude in Angstrom and ω is the frequency in THz. The problem is quasi-one-dimensional since atoms move only along y axis. The driven zigzag atomic row can be regarded as the energy source from which the energy can be given or not given to the lattice depending on the parameters of driving (A and ω). In Fig. 8b the power of the energy source P normalized to the squared driving amplitude is given as a function of the driving frequency for different driving amplitudes.

It can be seen that, as expected, power is nonzero in the acoustic band, $0 < \omega < 19$ THz, and in the optic band, $35 < \omega < 40$ THz. This is because driving at these frequencies produces phonons that carry energy along the crystal. It is also important to note that for small driving amplitudes, $A < 0.02$Å, normalized power of the source is amplitude independent. This is because the energy density of a linear phonon with frequency ω and amplitude A is proportional to $\omega^2 A^2$. For larger driving amplitudes the nonlinearity comes into play and this scaling does not work anymore. The most interesting is the appearance of non-zero power region within the gap of phonon DOS, $19 < \omega < 35$ THz, induced by the homogeneous strain $\varepsilon_{xx} = 0.3, \varepsilon_{yy} = -0.1$, $\varepsilon_{xy} = 0$ applied to graphene sheet. Phonons with such frequencies do not exist and to clarify the mechanism of energy transfer within this frequency range the time evolution of the displacements of atoms is shown in Fig. 9. In (a) the driven atom $n = 0$ vibrating with the prescribed amplitude $A = 0.01$Å and frequency $\omega = 26.7$ THz is shown. Note that this frequency is within the gap of phonon DOS. Then shown are displacements of the atoms (b) $n = 1$ *and* 2, (c) $n = 3$ *and* 4, (d) $n = 5$ *and* 6, (e)

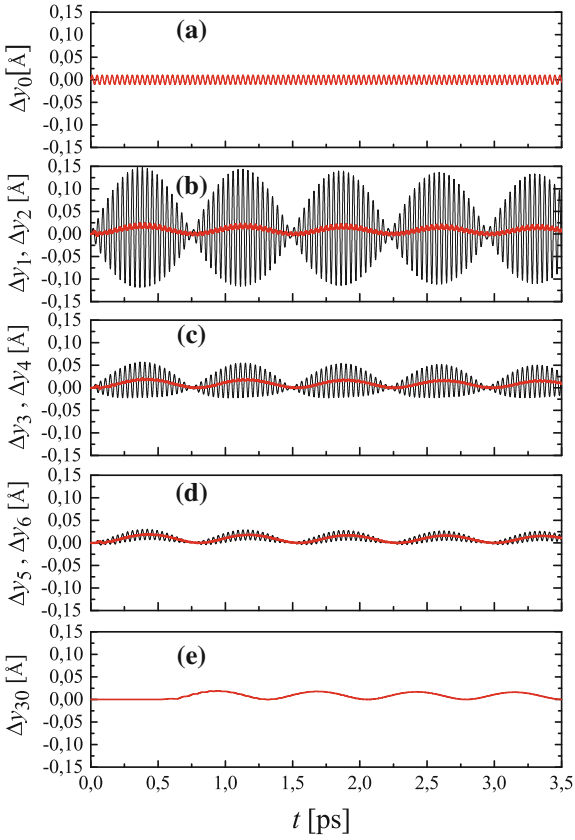

Fig. 9 Time evolution of y displacements for **a** driven atom, $n = 0$, **b** atoms $n = 1$ and 2, **c** atoms $n = 3$ and 4, **d** atoms $n = 5$ and 6, **e** atom $n = 30$. Driving amplitude is $A = 0.01$Å and frequency is $\omega = 26.7$ THz, which is within the gap of phonon DOS. Curves for odd (even) atoms are shown in black (red). Reproduced with permission from [37], copyright by APS

$n = 30$. Black (red) lines show the displacements for the odd (even) atoms. It can be clearly seen that a DB is excited on the atom with $n = 1$ whose amplitude varies quasi-periodically from zero up to a relatively large value of 0.15 Å. Other atoms have much smaller maximal amplitudes. In response to the DB amplitude variation, due to the anharmonicity effect, a low-frequency phonon is excited at the frequency of DB amplitude modulation. This can be seen in (e) where the displacement of the atom relatively far away from the DB ($n = 30$) is presented.

It can be concluded that in the case of driving frequency within the phonon gap the energy is transported by the phonons excited by the DB having quasi-periodically varying amplitude. The phonon frequency is relatively low because it is equal to the period of DB amplitude modulation. The effect of energy transfer to the lattice driven at frequencies outside the phonon band is known as supratransmission [42, 49, 52]. The well-accepted belief is that the supratransmission effect can be observed only if the driving amplitude is above a threshold value and that the energy carriers are moving DBs. In contrast to this, in the study [37] it was found that the supratransmission takes place even at small driving amplitudes and that the energy is transported by the low-frequency phonons excited by the standing DB with varying in time amplitude.

4.3 Out-of-Plane DBs in Unstrained Graphene

Very recently, in the works by Hizhnyakov et al. [46, 47], it has been shown that graphene modelled with the AIREBO potential supports DBs with the atomic displacements normal to the graphene plane. For excitation of such breathers lateral displacements were applied to a few carbon atoms. It was shown that the transverse DBs have frequencies inside the phonon band but they survive for a very long time because their frequencies are above the out-of-plane phonon frequencies and they weakly interact with the in-plane phonons.

In the work [12] the attempt to excite transverse DBs in unstrained graphene has been made with the use of the Savin and AIREBO potentials. A systematic approach for excitation of DBs was employed. This approach begins with the analysis of the amplitude-frequency dependence of the transverse DVM shown in Fig. 2e. The result is presented in Fig. 10 by open circles for the Savin potential and by filled squares for the AIREBO potential. Strikingly, the results are qualitatively different. In the case of Savin potential the DVM shows the soft-type anharmonicity since its frequency bifurcates from the upper edge of the out-of-plane phonon DOS (shown by the horizontal dashed line) and decreases with increasing amplitude. There is no chance to get a transverse localized vibrational mode by applying a bell-shaped function upon this DVM because its frequency is within the out-of-plane phonon DOS. On the other hand, for the AIREBO potential the DVM frequency bifurcates from the upper edge of the out-of-plane phonon DOS (shown by the horizontal dotted line) and increases with increasing amplitude. One can try to get a localized vibrational mode by applying a bell-shaped function upon this DVM. In [12] three different

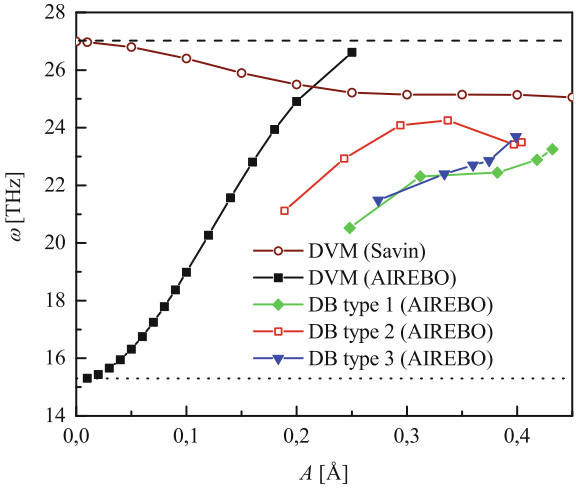

Fig. 10 Frequency as the function of amplitude for DVM modelled with the Savin potential (open circles) and AIREBO potential (filled squares) as well as for the three types of transverse DBs modelled with the AIREBO potential. Reproduced from [12] with kind permission of The European Physical Journal (EPJ). Copyright by Springer

transverse DBs were excited by choosing three different positions for the center of the bell-shaped function, see Fig. 11. The DBs of type I, II, and III are centered on (a) an atom, (b) at the center of a hexagon, and (c) at the center of a valence bond, respectively.

In Fig. 12 the displacements normal to the graphene sheet are shown as the functions of time for the transverse DBs of type (a) I, (b) II, and (c) III. For each case, shown are the atoms having the largest, second largest, and third largest vibration amplitudes.

From the results of the studies [12, 46, 47] it can be concluded that different interatomic potentials can give qualitatively different results. Thus, the AIREBO potential supports transverse DBs in graphene, while the Savin potential does not. It is also worth pointing out that application of bell-shaped functions on DVMs, whose frequencies at large amplitudes lie outside the phonon band, is a convenient and systematic method of excitation of DBs.

Existence and stability of transverse DBs have been analyzed in frame of the 1D Fermi-Pasta-Ulam model placed in 3D space [53].

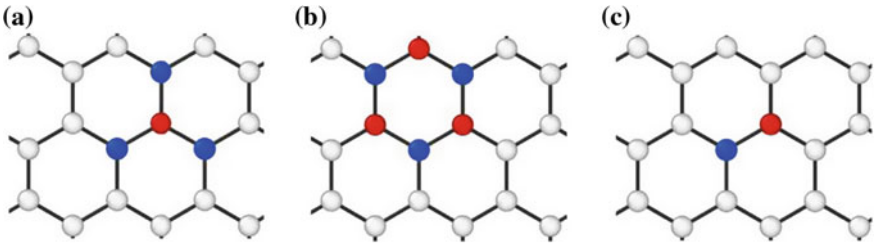

Fig. 11 Three different locations of the bell-shaped function center used to obtain the transverse DBs localized on **a** atom (type I), **b** center of a hexagon (type II), and **c** center of a valence bond (type III). Reproduced from [12] with kind permission of The European Physical Journal (EPJ). Copyright by Springer

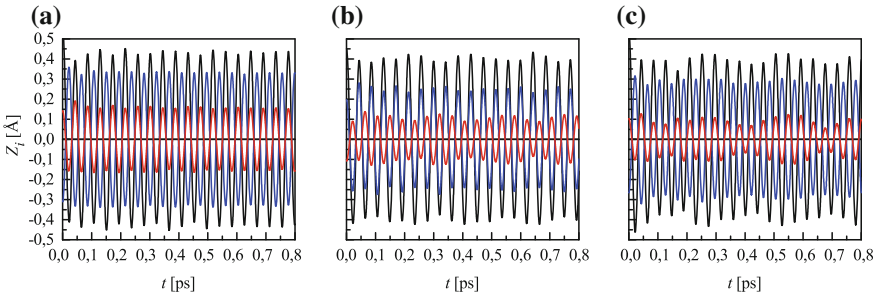

Fig. 12 Displacements normal to the graphene sheet as the functions of time for the transverse DBs of type **a** I, **b** II, and **c** III. The three curves show for each case the atoms having largest, second largest, and the third largest vibration amplitudes. Reproduced from [12] with kind permission of The European Physical Journal (EPJ). Copyright by Springer

5 Nonlinear Excitations in Other Carbon Nanopolymorphs

Firstly we discuss DBs in diamond, which is 3D crystalline carbon polymorph. DBs in Si and Ge modelled with the Tersoff potential have been reported long ago in the work [96] and confirmed later by Hizhnyakov et al. [47]. Covalent crystals Si and Ge have the same crystal lattice with diamond but the first attempt to find DBs in diamond using the Tersoff potential failed [96]. However, DBs in diamond were successfully excited employing the more advanced LCBOP potential which describes the bond orientation and switching-off effects more accurately [45, 47]. According to the results obtained in Refs. [45, 47], DBs in diamond have frequencies above the top of the phonon spectrum in the range from approximately 40 to 42.5 THz.

In the recent work [75] standing DBs and DB clusters (double and triple) were studied in diamond using the AIREBO interatomic potential, see Fig. 13a. Single DB can be excited by applying initial shifts to a pair of nearest atoms along the valence bond in the opposite directions. DB is highly localized on this pair of atoms oscillating out-of-phase, while the neighboring atoms oscillate with one order of magnitude lower amplitudes. DB frequency is above the top of the phonon spectrum and increases with the oscillation amplitude. Two different mechanisms of energy exchange between DBs in the DB clusters were revealed. In the cluster of two DBs the quasi-periodic energy exchange between DBs takes place when they oscillate with a phase shift, as shown in Fig. 13c by plotting DB kinetic energy averaged over DB oscillation period as the function of time. For comparison, in (b) the in-phase DBs do not show energy exchange. Another mechanism of energy exchange between DBs was detected in the clusters of three DBs, as shown in (d,e,f). Here at about 1.3 ps one of DBs (B1) ceases to exist giving most of its energy to DBs B2 and B3.

We now turn to the discussion of DBs in carbon nanotubes [35, 54, 86, 90, 91].

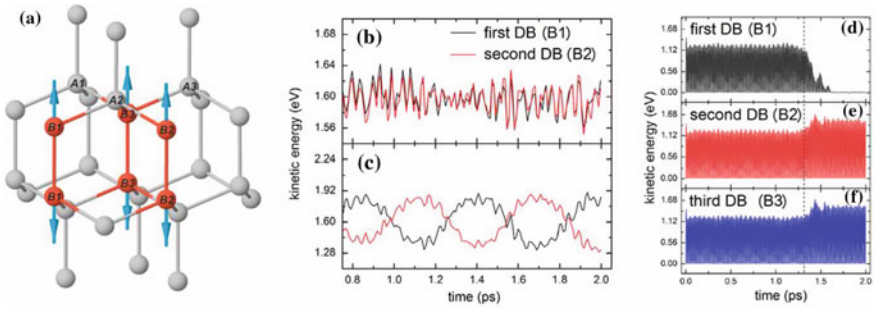

Fig. 13 **a** DB clusters in diamond. **b**, **c** Kinetic energy averaged over DB oscillation period as the function of time for the cluster of two DBs. In (**b**) the two DBs vibrate in-phase and no energy exchange between them takes place. In (**c**) there is a phase shift between two DBs and a quasi-periodic energy exchange between them can be clearly seen. **d**, **e**, **f** Same as in (**b**, **c**) but for the cluster of three DBs. At about 1.3 ps one of DBs (B1) ceases to exist giving most of its energy to the two other DBs. Reproduced with permission from [75], copyright by Elsevier

In the work [54], where the Brenner potential was used, DBs were found in the (12, 0), (10, 0), and (8, 0) zigzag carbon nanotubes but not in (7, 7), (6, 6), and (5, 5) armchair nanotubes. In the later work [90] it was shown that DBs exist in carbon nanotubes with a chiral angle less than or equal to 30^o but they do not exist in nanotubes with a chiral angle greater than or equal to 41^o. Doi and Nakatani, using the Brenner potential, have demonstrated that DBs in zigzag and armchair carbon nanotubes have frequencies above the phonon spectrum and they are unstable [35].

A very important discovery has been made in the work by Shimada et al. [91] where it was demonstrated that a DB can trigger formation of the 5-7-5-7 defect (Stone-Wales defect) in carbon nanotube under tension. This work suggests that DBs can contribute to structure evolution in crystalline solids. The Stone-Wales defect has also been investigated in fullerenes [78, 79] and graphene [9].

Nonlinear twisting mode has been identified in carbon nanotube by Savin and Kivshar [85].

Nonlinear low-frequency vibrational modes of carbon nanoscrolls have been analysed in [88]. In particular, the anomalously high coefficient of radial thermal expansion (two orders of magnitude higher than in diamond) has been explained.

The nonlinear dynamics of nanoclusters composed of C_{60} fullerene molecules has been analyzed [84]. It has been shown that such nanostructures support long-lived highly localized nonlinear vibrational modes, which resemble discrete breathers in simple nonlinear lattices. In these localized modes, the vibrational energy density is localized at a single C_{60} molecule. The lifetime of such nonlinear excitations at room temperature exceeds tens of picoseconds. That is why the C_{60} nanoclusters demonstrate anomalously slow thermal relaxation when the temperature gradient decays in accord with a power law, thus violating the Cattaneo-Vernotte law of thermal conductivity.

DFT simulations of the structure and stability of 1D carbon chains have been addressed in [22, 23]. The carbon chain (carbyne) can exist in two different modifications: cumulene with double chemical bonds between its atoms, and polyyne with alternation of single and triple bonds. It was found that above 11.2% tensile strain softening of the zone-boundary mode atomic vibrations takes place. Freezing of this soft mode leads to displacive structural phase transition.

6 Summary and Future Challenges

Graphene is a very important material in nanoscience today because of its unusual and promising properties for applications. In the present review, the nonlinear dynamics of graphene and other carbon nanostructures have been discussed.

DBs in different crystals can localize energy of order of 1 eV, in some cases they can move along crystal lattice [28, 31, 43, 57, 58], can interact with each other [57] and with lattice defects [28, 58, 94]. DBs can help to overcome potential barriers for defect migration [1, 36] or formation [91]. DBs and other nonlinear excitations can contribute to the transport of electric charge [2, 24–27] and energy [29, 31] and to

affect thermal conductivity [97]. In view of this, it is evident that nonlinear excitations in carbon nanomaterials can play important role in various processes and thus require further investigations: theoretical, numerical and experimental. The following key points are suggested for future studies of DBs in carbon nanomaterials.

Most of the studies on DBs in graphene are based on MD simulations, which are strongly dependent on the interatomic potential used. Careful DFT simulations of DBs and DB clusters in graphene at zero and finite temperatures are urgently needed to check the validity of MD results. Simultaneously, more MD simulations should be conducted in order to improve the accuracy of the interatomic potentials and to achieve a better agreement with DFT results.

To date, the effect of DBs on electronic, thermal, mechanical and other physical properties of graphene and other carbon nanostructures is not clear. Such studies can provide insight into, for example, the interplay between DBs and lattice defects or into defect nucleation mechanisms, energy transport in carbon nanostructures.

Probably the most important unsolved issue is experimental observation of DBs in carbon nanomaterials. Learning more about DB properties will help to design experimental setup for direct or indirect detection of DBs.

Acknowledgements S.V.D. would like to thank financial support from the Russian Science Foundation, grant no. 14-13-00982. E.A.K., and A.P.Ch. would like to thank financial support from the Russian Science Foundation, grant no. 16-12-10175.
J.A.B. acknowledges financial support from the Scholarship of the President of the Russian Federation for young scientists and PhD students SP-4037.2015.1.

References

1. Archilla, J.F.R., Coelho, S.M.M., Auret, F.D., Dubinko, V.I., Hizhnyakov, V.: Long range annealing of defects in germanium by low energy plasma ions. Phys. D **297**, 56–61 (2015)
2. Archilla, J.F.R., Russell, F.M.: On the charge of quodons. Lett. Mater. **6**, 3–8 (2016)
3. Aubry, S.: Breathers in nonlinear lattices: existence, linear stability and quantization. Phys. D **103**, 201–250 (1997)
4. Bahadir, E.B., Sezginturk, M.K.: Applications of graphene in electrochemical sensing and biosensing. Trends Anal. Chem. **76**, 1–14 (2016)
5. Baimova, J.: Property control by elastic strain engineering: application to graphene. J. Micromech. Mol. Phys. **2**, 1750001 (2016)
6. Baimova, J.A., Dmitriev, S.V., Zhou, K.: Discrete breather clusters in strained graphene. Europhys. Lett. **100**, 36005 (2012)
7. Baimova, J.A., Dmitriev, S.V., Zhou, K., Savin, A.V.: Unidirectional ripples in strained graphene nanoribbons with clamped edges at zero and finite temperatures. Phys. Rev. B **86**, 035427 (2012)
8. Baimova, J.A., Korznikova, E.A., Lobzenko, I.P., Dmitriev, S.V.: Discrete breathers in carbon and hydrocarbon nanostructures. Rev. Adv. Mater. Sci. **42**, 68–82 (2015)
9. Baimova, J.A., Liu, B., Dmitriev, S.V., Zhou, K., Nazarov, A.A.: Effect of Stone-Thrower-Wales defect on structural stability of graphene at zero and finite temperatures. Europhys. Lett. **103**, 46001 (2013)
10. Baimova, Y.A., Dmitriev, S.V., Savin, A.V., Kivshar, Y.S.: Velocities of sound and the densities of phonon states in a uniformly strained flat graphene sheet. Phys. Solid State **54**, 866–874 (2012)

11. Balandin, A.A., Ghosh, S., Bao, W., Calizo, I., Teweldebrhan, D., Miao, F., Lau, C.N.: Superior thermal conductivity of single-layer graphene. Nano Lett. **8**, 902–907 (2008)
12. Barani, E., Lobzenko, I.P., Korznikova, E.A., Soboleva, E.G., Dmitriev, S.V., Zhou, K., Marjaneh, A.M.: Transverse discrete breathers in unstrained graphene. Eur. Phys. J. B **90**, 38 (2017)
13. Binder, P., Abraimov, D., Ustinov, A.V., Flach, S., Zolotaryuk, Y.: Observation of breathers in Josephson ladders. Phys. Rev. Lett. **84**, 745–748 (2000)
14. Bolotin, K.I., Sikes, K.J., Jiang, Z., Klima, M., Fudenberg, G., Hone, J., Kim, P., Stormer, H.L.: Ultrahigh electron mobility in suspended graphene. Solid State Commun. **146**, 351–355 (2008)
15. Brenner, D.W.: Empirical potential for hydrocarbons for use in simulating the chemical vapor deposition of diamond films. Phys. Rev. B **42**, 9458 (1990)
16. Burlakov, V.M., Kiselev, S.A., Rupasov, V.I.: Localized excitations of uniform anharmonic lattices. JETP Lett. **51**, 544–547 (1990)
17. Campbell, D.K., Flach, S., Kivshar, Y.S.: Localizing energy through nonlinearity and discreteness. Phys. Today **57**, 43 (2004)
18. Chechin, G.M., Dmitriev, S.V., Lobzenko, I.P., Ryabov, D.S.: Properties of discrete breathers in graphane from ab initio simulations. Phys. Rev. B **90**, 045432 (2014)
19. Chechin, G.M., Lobzenko, I.P.: Ab initio refining of quasibreathers in graphane. Lett. Mater. **4**, 226–229 (2014)
20. Chechin, G.M., Ryabov, D.S., Shcherbinin, S.A.: Nonlinear vibrational modes in graphene: group-theoretical results. Lett. Mater. **6**, 9–15 (2016)
21. Chechin, G.M., Sakhnenko, V.P.: Interactions between normal modes in nonlinear dynamical systems with discrete symmetry. Exact results. Phys. D **117**, 43–76 (1998)
22. Chechin, G.M., Sizintsev, D.A., Usoltsev, O.A.: Properties of pi-mode vibrations in strained carbon chains. Lett. Mater. **6**, 146–151 (2016)
23. Chechin, G.M., Usoltsev, O.A., Sizintsev, D.A.: On stability of nonlinear atomic vibrations in strained carbon chains. Lett. Mater. **6**, 309–316 (2016)
24. Chetverikov, A.P., Ebeling, W., Lakhno, V.D., Shigaev, A.S., Velarde, M.G.: On the possibility that local mechanical forcing permits directionally-controlled long-range electron transfer along dna-like molecular wires with no need of an external electric field: mechanical control of electrons. Eur. Phys. J. B **89**, 101 (2016)
25. Chetverikov, A.P., Ebeling, W., Velarde, M.G.: On the temperature dependence of fast electron transport in crystal lattices. Eur. Phys. J. B **88**, 202 (2015)
26. Chetverikov, A.P., Ebeling, W., Velarde, M.G.: Long-range electron transport donor-acceptor in nonlinear lattices. Entropy **18**, 92 (2016)
27. Chetverikov, A.P., Ebeling, W., Velarde, M.G.: Soliton assisted control of source to drain electron transport along natural channels crystallographic axes in two-dimensional triangular crystal lattices. Eur. Phys. J. B **89**, 196 (2016)
28. Cuevas, J., Archilla, J.F.R., Sanchez-Rey, B., Romero, F.R.: Interaction of moving discrete breathers with vacancies. Phys. D **216**, 115–120 (2006)
29. Dmitriev, S.V.: Discrete breathers in crystals: energy localization and transport. J. Micromech. Mol. Phys. **1**, 1630001 (2016)
30. Dmitriev, S.V., Baimova, J.A., Savin, A.V., Kivshar, YuS: Ultimate strength, ripples, sound velocities, and density of phonon states of strained graphene. Comput. Mater. Sci. **53**, 194–203 (2012)
31. Dmitriev, S.V., Chetverikov, A.P., Velarde, M.G.: Discrete breathers in 2D and 3D crystals. Phys. Status Solidi B **252**, 1682–1686 (2015)
32. Dmitriev, S.V., Korznikova, E.A., Baimova, J.A., Velarde, M.G.: Discrete breathers in crystals. Phys. Usp. **59**, 446–461 (2016)
33. Doi, Y., Nakatani, A.: Structure and stability of nonlinear vibration mode in graphene sheet. In: Procedia Engineering, Proceedings of the 11th International Conference On The Mechanical Behavior Of Materials (ICM11), vol. 10, pp. 3393–3398 (2011). Como, Italy (2011)

34. Doi, Y., Nakatani, A.: Numerical study on unstable perturbation of intrinsic localized modes in graphene. J. Solid. Mech. Mater. Eng. **6**, 71–80 (2012)
35. Doi, Y., Nakatani, A.: Structure and stability of discrete breather in zigzag and armchair carbon nanotubes. Lett. Mater. **6**, 49–53 (2016)
36. Dubinko, V.I., Archilla, J.F.R., Dmitriev, S.V., Hizhnyakov, V.: Rate theory of acceleration of defect annealing driven by discrete breathers. In: J.F.R. Archilla, N. Jiménez, V.J. Sánchez-Morcillo, L.M. García-Raffi (eds.) Quodons in Mica: Nonlinear Localized Travelling Excitations in Crystals, Springer Series in Materials Science, vol. 221, pp. 381–398 (2015)
37. Evazzade, I., Lobzenko, I.P., Korznikova, E.A., Ovidko, I.A., Roknabadi, M.R., Dmitriev, S.V.: Energy transfer in strained graphene assisted by discrete breathers excited by external ac driving. Phys. Rev. B **95**, 035423 (2017)
38. Ferrari, A.C., et al.: Science and technology roadmap for graphene, related two-dimensional crystals and hybrid systems. Nanoscale **7**, 4598–4810 (2015)
39. Flach, S., Willis, C.R.: Discrete breathers. Phys. Rep. **295**, 181–264 (1998)
40. Flach, S., Willis, C.R.: Discrete breathers in nonlinear lattices: Experimental detection in a Josephson array. Phys. Rep. **467**, 1–116 (1998)
41. Fraile, A., Koukaras, E.N., Papagelis, K., Lazarides, N., Tsironis, G.P.: Long-lived discrete breathers in free-standing graphene. Chaos Soliton Fract. **87**, 262–267 (2016)
42. Geniet, F., Leon, J.: Energy transmission in the forbidden band gap of a nonlinear chain. Phys. Rev. Lett. **89**, 134102 (2002)
43. Haas, M., Hizhnyakov, V., Shelkan, A., Klopov, M., Sievers, A.J.: Prediction of high-frequency intrinsic localized modes in Ni and Nb. Phys. Rev. B **84**, 144303 (2011)
44. Hizhnyakov, V., Haas, M., Shelkan, A., Klopov, M.: Theory and molecular dynamics simulations of intrinsic localized modes and defect formation in solids. Phys. Scr. **89**, 044003 (2014)
45. Hizhnyakov, V., Haas, M., Shelkan, A., Klopov, M.: Standing and moving discrete breathers with frequencies above the phonon spectrum. In: J.F.R. Archilla, N. Jiménez, V.J. Sánchez-Morcillo, L.M. García-Raffi (eds.) Quodons In Mica: Nonlinear Localized Travelling Excitations In Crystals, Springer Series in Materials Science, vol. 221, pp. 229–245 (2015)
46. Hizhnyakov, V., Klopov, M., Shelkan, A.: Transverse intrinsic localized modes in monatomic chain and in graphene. Phys. Lett. A **380**, 1075 (2016)
47. Hizhnyakov, V., Shelkan, A., Haas, M., Klopov, M.: Discrete breathers above phonon spectrum. Lett. Mater. **6**, 61–72 (2016)
48. Iijima, S.: Helical microtubules of graphitic carbon. Nature **354**, 56–58 (1991)
49. Kevrekidis, P.G., Dmitriev, S.V., Takeno, S., Bishop, A.R., Aifantis, E.C.: Rich example of geometrically induced nonlinearity: From rotobreathers and kinks to moving localized modes and resonant energy transfer. Phys. Rev. E **70**, 066627 (2004)
50. Khadeeva, L.Z., Dmitriev, S.V.: Discrete breathers in crystals with NaCl structure. Phys. Rev. B **81**, 214306 (2010)
51. Khadeeva, L.Z., Dmitriev, S.V., Kivshar, Y.S.: Discrete breathers in deformed graphene. JETP Lett. **94**, 539–543 (2011)
52. Khomeriki, R., Lepri, S., Ruffo, S.: Nonlinear supratransmission and bistability in the Fermi-Pasta-Ulam model. Phys. Rev. E **70**, 066626 (2004)
53. Kimura, M., Mitani, A., Doi, S.: Existence and stability of intrinsic localized modes in a finite FPU chain placed in three-dimensional space. Lett. Mater. **6**, 22–26 (2016)
54. Kinoshita, Y., Yamayose, Y., Doi, Y., Nakatani, A., Kitamura, T.: Selective excitations of intrinsic localized modes of atomic scales in carbon nanotubes. Phys. D **77**, 024307 (2008)
55. Kiselev, S.A., Sievers, A.J.: Generation of intrinsic vibrational gap modes in three-dimensional ionic crystals. Phys. Rev. B **55**, 5755 (1997)
56. Kistanov, A.A., Baimova, Y.A., Dmitriev, S.V.: A molecular dynamics study of [111]-polarized gap discrete breathers in a crystal with NaCl-type structure. Tech. Phys. Lett. **38**, 676 (2012)
57. Kistanov, A.A., Dmitriev, S.V., Chetverikov, A.P., Velarde, M.G.: Head-on and head-off collisions of discrete breathers in two-dimensional anharmonic crystal lattices. Eur. Phys. J. B **87**, 211 (2014)

58. Kistanov, A.A., Dmitriev, S.V., Semenov, A.S., Dubinko, V.I., Terentev, D.A.: Interaction of propagating discrete breathers with a vacancy in a two-dimensional crystal. Tech. Phys. Lett. **40**, 657 (2014)
59. Kopidakis, G., Aubry, S.: Discrete breathers in realistic models: hydrocarbon structures. Phys. B **296**, 237–250 (2001)
60. Korznikova, E.A., Bachurin, D.V., Fomin, SYu., Chetverikov, A.P., Dmitriev, S.V.: Instability of vibrational modes in hexagonal lattice. Eur. Phys. J. B **90**, 23 (2017)
61. Korznikova, E.A., Baimova, J.A., Dmitriev, S.V.: Effect of strain on gap discrete breathers at the edge of armchair graphene nanoribbons. Europhys. Lett. **102**, 60004 (2013)
62. Korznikova, E.A., Dmitriev, S.V.: Moving wrinklon in graphene nanoribbons. J. Phys. D Appl. Phys. **47**, 345307 (2014)
63. Korznikova, E.A., Fomin, SYu., Soboleva, E.G., Dmitriev, S.V.: Highly symmetric discrete breather in a two-dimensional Morse crystal. JETP Lett. **103**, 277–281 (2016)
64. Korznikova, E.A., Savin, A.V., Baimova, Y.A., Dmitriev, S.V., Mulyukov, R.R.: Discrete breather on the edge of the graphene sheet with the armchair orientation. JETP Lett. **99**, 222–226 (2012)
65. Kroto, H.W., Heath, J.R., Obrien, S.C., Curl, R.F., Smalley, R.E.: C60: Buckminsterfullerene. Nature **318**, 162–163 (1985)
66. Lee, C., Wei, X., Kysar, J.W., Hone, J.: Measurement of the elastic properties and intrinsic strength of monolayer graphene. Science **321**, 385–388 (2008)
67. Lindsay, L., Broido, D.A.: Optimized Tersoff and Brenner empirical potential parameters for lattice dynamics and phonon thermal transport in carbon nanotubes and graphene. Phys. Rev. B **81**, 205441 (2010)
68. Liu, B., Baimova, J.A., Zhou, K., Dmitriev, S.V., Wang, X., Zhu, H.: Discrete breathers in hydrogenated graphene. J. Phys. D: Appl. Phys. **46**, 305302 (2013)
69. Lobzenko, I., Dmitriev, S., Baimova, J., Dzhelauhova, G.: Numerical studies of discrete quasibreathers in graphene in the framework of density functional theory. Mater. Sci. Forum **845**, 215–218 (2016)
70. Lobzenko, I.P.: Discrete breathers properties obtained from ab-initio calculations in graphene and graphane. Lett. Mater. **6**, 73–76 (2016)
71. Lobzenko, I.P., Chechin, G.M., Bezuglova, G.S., Baimova, YuA., Korznikova, E.A., Dmitriev, S.V.: Ab initio simulation of gap discrete breathers in strained graphene. Phys. Solid State **58**, 633–639 (2016)
72. Los, J.H., Fasolino, A.: Intrinsic long-range bond-order potential for carbon: performance in Monte Carlo simulations of graphitization. Phys. Rev. B **68**, 024–107 (2003)
73. Los, J.H., Ghiringhelli, L.M., Meijer, E.J., Fasolino, A.: Improved long-range reactive bond-order potential for carbon I. Construction. Phys. Rev. B **72**, 214102 (2005)
74. Los, J.H., Zakharchenko, K.V., Katsnelson, M.I., Fasolino, A.: Melting temperature of graphene. Phys. Rev. B **91**, 045415 (2015)
75. Murzaev, R.T., Bachurin, D.V., Korznikova, E.A., Dmitriev, S.V.: Localized vibrational modes in diamond. Phys. Lett. A **381**, 1003–1008 (2017)
76. Murzaev, R.T., Kistanov, A.A., Dubinko, V.I., Terentyev, D.A., Dmitriev, S.V.: Moving discrete breathers in bcc metals V, Fe and W. Comput. Mater. Sci. **98**, 88 (2015)
77. Novoselov, K.S., Fal'ko, V.I., Colombo, L., Gellert, P.R., Schwab, M.G., Kim, K.: A roadmap for graphene. Nature **490**, 192–200 (2012)
78. Podlivaev, A.I., Katin, K.P.: On the dependence of the lifetime of an atomic cluster on the intensity of its heat exchange with the environment. JETP Lett. **92**, 52–56 (2010)
79. Podlivaev, A.I., Katin, K.P., Lobanov, D.A., Openov, L.A.: Specific features of the stone-wales transformation in the C20 and C36 fullerenes. Phys. Solid State **53**, 215–220 (2011)
80. Raccichini, R., Varzi, A., Passerini, S., Scrosati, B.: The role of graphene for electrochemical energy storage. Nat. Mater. **14**, 271–279 (2015)
81. Reigada, R., Sarmiento, A., Lindenberg, K.: Energy relaxation in nonlinear one-dimensional lattices. Phys. Rev. E **64**, 066608 (2001)

82. Sato, M., Mukaide, T., Nakaguchi, T., Sievers, A.: Inductive intrinsic localized modes in a one-dimensional nonlinear electric transmission line. Phys. Rev. B **94**, 012223 (2016)
83. Sato, M., Sievers, A.: Experimental and numerical exploration of intrinsic localized modes in an atomic lattice. J. Biol. Phys. **35**, 57–72 (2009)
84. Savin, A.V., Kivshar, Yu.S.: Nonlinear breatherlike localized modes in C60 nanocrystals. Phys. Rev. B **85**, 125427 (2012)
85. Savin, A.V., Kivshar, Yu.S: Localized defect modes in graphene. Europhys. Lett. **82**, 66002 (2008)
86. Savin, A.V., Kivshar, Yu.S.: Discrete breathers in carbon nanotubes. Phys. Rev. B **88**, 125417 (2013)
87. Savin, A.V., Kivshar, Yu.S., Hu, B.: Suppression of thermal conductivity in graphene nanoribbons with rough edges. Phys. Rev. B **82**, 195422 (2010)
88. Savin, A.V., Korznikova, E.A., Dmitriev, S.V.: Low frequency vibrations of carbon nanoscrolls. Lett. Mater. **6**, 77–81 (2016)
89. Savin, A.V., Manevitch, L.I.: Discrete breathers in a polyethylene chain. Phys. Rev. B **67**, 144302 (2003)
90. Shimada, T., Shirasaki, D., Kinoshita, Y., Doi, Y., Nakatani, A., Kitamura, T.: Influence of nonlinear atomic interaction on excitation of intrinsic localized modes in carbon nanotubes. Phys. D **239**, 407–413 (2010)
91. Shimada, T., Shirasaki, D., Kitamura, T.: Stone-Wales transformations triggered by intrinsic localized modes in carbon nanotubes. Phys. Rev. B **81**, 035401 (2010)
92. Sievers, A.J., Page, J.B.: Unusual anharmonic local mode systems. In: Horton, G.K., Maradudin, A.A. (eds.) Dynamical Properties of Solids, vol. 7, pp. 137–255. North Holland, Amsterdam (1995)
93. Stuart, S.J., Tutein, A.B., Harrison, J.A.: A reactive potential for hydrocarbons with intermolecular interactions. J. Chem. Phys. **112**, 6472–6486 (2000)
94. Terentyev, D.A., Dubinko, A.V., Dubinko, V.I., Dmitriev, S.V., Zhurkin, E.E., Sorokin, M.V.: Interaction of discrete breathers with primary lattice defects in bcc Fe. Model. Simul. Mater. Sci. Eng. **23**, 085007 (2015)
95. Velarde, M.G., Chetverikov, A.P., Ebeling, W., Dmitriev, S.V., Lakhno, V.D.: From solitons to discrete breathers. Eur. Phys. J. B **89**, 233 (2016)
96. Voulgarakis, N.K., Hadjisavvas, G., Kelires, P.C., Tsironis, G.P.: Computational investigation of intrinsic localization in crystalline Si. Phys. Rev. B **69**, 113201 (2004)
97. Xiong, D., Zhang, J.: Discrete breathers: possible effects on heat transport. Lett. Mater. **6**, 27–30 (2016)
98. Yamayose, Y., Kinoshita, Y., Doi, Y., Nakatani, A., Kitamura, T.: Excitation of intrinsic localized modes in a graphene sheet. Europhys. Lett. **80**, 40008 (2007)
99. Zakharchenko, K.V., Fasolino, A., Los, J.H., Katsnelson, M.I.: Melting of graphene: from two to one dimension. J. Phys. Condens. Mat. **23**, 202202 (2011)
100. Zhu, Y., Murali, S., Cai, W., Li, X., Suk, J.W., Potts, J.R., Ruoff, R.S.: Graphene and graphene oxide: synthesis, properties, and applications. Adv. Mater. **22**, 3906–3924 (2010)

A Cellular Automaton Model for the Catalytic Oxidation of CO Including CO Desorption and Diffusion

Intermittent Oscillations in a Cellular Automaton Model for a Surface Reaction

Francisco Jiménez-Morales and M. Carmen Lemos

Abstract The oxidation of carbon monoxide (CO) on a catalyst surface is studied with a cellular automaton (CA) model previously introduced in [22]. We expand the model in order to include the effects of CO desorption and diffusion. Both processes are considered probabilistic with probabilities p_1 and p_2, respectively. In this chapter we will observe that CO desorption widens the range of the thermal relaxation parameter γ for which the reaction shows an oscillatory behavior. In the range ($0.009 < p_1 < 0.015$) and near the CO poisoned state ($0.30 \leq \gamma < 0.35$), the surface reaction shows intermittent oscillatory behaviors in which the regular quasi-periodic oscillations are interrupted by bursts of CO and O coverage. CO diffusion smooths that intermittent behavior with a reduction in the number of bursts and increases the time during which the reaction oscillates quasiperiodically.

Keywords Cellular automaton · Surface reaction · Oxidation of CO · Oscillatory behavior · Intermittency

1 Introduction

[1]The oxidation of CO on catalytic metal, type Pt, Pd, Rh or Ir, is probably the most studied reaction of heterogeneous catalysis. Besides its industrial applications, due to its relevance in the issues of improvement in the quality of the air in order to decrease the CO_2(gas) emitted in the atmosphere, the interest in this reaction is also

[1]This section modifies with permission content from previous publications by the authors given in Refs. [9, 22], copyright by AIP, Ref. [10], copyright by APS and Ref. [21], copyright by Elsevier.

F. Jiménez-Morales (✉) · M. C. Lemos
Departamento de Física de la Materia Condensada, Universidad de Sevilla,
Avda. Reina Mercedes S/n, 41012 Sevilla, Spain
e-mail: jimenez@us.es

M. C. Lemos
e-mail: lemos@us.es

J. F. R. Archilla et al. (eds.), *Nonlinear Systems, Vol. 2*, Understanding Complex Systems, https://doi.org/10.1007/978-3-319-72218-4_8

theoretical. Catalytic systems are systems formed by many particles which operate far from thermodynamic equilibrium. In these systems one can see a great variety of nonlinear phenomena as kinetic phase transitions, formation of spatio-temporal patterns, bistability, hysteresis, and many oscillatory and chaotic behaviors [36].

Since the beginning of the century, studies based on lattice-gas models [30], along with more detailed molecular information and realistic input energetics obtained from density functional theory combined with experiments employing surface science methods, have provided a better knowledge of some aspects of the reaction [17, 25, 27, 28, 31, 32, 34, 42]. However, a better understanding of the nonlinear phenomena which occur in the reaction and, in particular, the oscillatory behavior, is fully far from reached.

One of the early developed models which describes the catalyzed oxidation reaction of CO is the well-known model proposed by Ziff, Gulari, and Barshad (ZGB model) [44]. In the ZGB model this chemical reaction proceeds via Langmuir–Hinshelwood (LH) mechanism. Previous studies [13, 14] have established that LH is the dominant mechanism for this reaction. Hence, before the reaction can take place, both CO and O_2 molecules in the gas phase have to be adsorbed on the catalytic surface. If a CO molecule is in the neighborhood of an atomic oxygen O they react to form carbon dioxide (CO_2).

Ziff et al. [44] employed Monte Carlo simulations on a square lattice and with regard to the fraction of CO molecules in the gas phase, y_{CO}, they found three different zones: (i) poisoning of the catalyst by oxygen for $y_{CO} < y_1 = 0.389$; (ii) poisoning of the catalyst by CO for $y_{CO} > y_2 = 0.525$ and (iii) a reactive state for $y_1 < y_{CO} < y_2$. The transition at y_1 is a second-order kinetic phase transition (a continuous one at low CO pressure) whereas the transition at y_2 is of first order (a discontinuous one at high CO pressure), because the CO_2 production rate changes discontinuously. It should be noted that the continuous transition at low pressure (oxygen poisoned phase) has not been experimentally observed in real systems because oxygen does not impede the adsorption of CO [12, 15, 19].

The simplicity of the ZGB model allows the inclusion of many other physical processes such as diffusion of CO and desorption of adsorbates from the surface. Recently, CO desorption and coadsorption with O, oxygen repulsion and the existence of impurities in the gas have been incorporated [3–5]. Initial researches into the effects of CO desorption and diffusion from the catalytic surface were done by several author [1, 2, 12, 18], who found that when both effects are present the desorption is the dominant effect. It was also estimated that when the CO desorption probability p_1 is above a critical value $p_c \approx 0.039$ the system no longer exhibits a first-order kinetic phase transition, that is, carbon monoxide poisoned phase disappears.

On the other hand, most models proposed to describe oscillatory behaviors in CO oxidation involve nonlinearities of different nature. For example, there are models in which the catalyst temperature can stay at a value different from the room temperature. This is due to the reaction heats generated on the catalytic surface where the reaction taking place, can spread on this surface more quickly than the heat dissipated to the room, which results in an increase in the catalyst temperature. These oscillations are called thermokinetic —so that they can be distinguished from

the isothermal ones, in which the temperature of the surface is constant— and are produced by a strong nonlinear dependence on the reaction rate on surface temperature. These changes in temperature in a reaction can be taken into account just by means of the addition of an equation describing the time surface temperature change. Similar models have been used by us to study the influence of a periodic perturbation on the room temperature in Refs. [9, 10, 21].

The most frequently used methods to model kinetics of catalytic reactions have been the conventional kinetic equations obtained through mean-field theory by using different closure approximations, (see the paper of Dickman [11], one of the pioneering authors in the modeling of CO oxidation by mean-field approximations), and the Monte Carlo (MC) method (both the static method and the dynamic one, named kinetic Monte Carlo (KMC)) [43]. A recent review of the kinetic modeling of heterogeneous catalytic systems by KMC can be seen in [40].

Techniques of cellular automaton (CA) have also shown to be efficient tools for simulating the behavior of catalytic systems. A cellular automaton is a class of spatially and temporally discrete system, characterized by local interaction and synchronous dynamical evolution. The CA allows parallel processing without any difficulty, and this fact substantially reduces the computation time. The CA approach offers a way to follow the dynamical evolution of the surface reaction and can keep track of all the microscopic degrees of freedom. Systems with many discrete elements that interact locally, such as a chemical reaction, can be modeled using a CA [6, 7, 29, 41]. We proposed a CA to study the oscillatory behavior in the catalytic CO oxidation, including the surface temperature as a variable [9, 10, 21, 22]. The results from CA simulations showed different chaotic and quasiperiodical regimes.

In the present work we study how CO desorption and diffusion processes affect to the thermokinetic oscillations observed in [22]. The rest of the chapter is organized as follows: In Sect. 2 we review our original CA model and include in it new transition rules. In Sect. 3 we report our main results, and finally in Sect. 4 some conclusions are summarized.

2 The Model

[2]The surface of the catalyst is represented as a two-dimensional square lattice of size $L \times L$ with periodic boundary conditions. Each lattice cell can be in one of the following states: an empty site, □, a site occupied by an adsorbed oxygen O(ads) atom or a site occupied by an adsorbed carbon monoxide CO(ads) molecule, where (ads) indicates that the species is adsorbed on the surface. We consider four different physicochemical processes: (i) the adsorption of CO(gas) and O_2(gas) on the surface, (ii) the reaction of both molecules CO(ads) and O(ads) to produce CO_2(gas), (iii) the desorption of CO(ads) molecules, and (iv) the diffusion of CO(ads) molecules.

[2]This section modifies with permission content from previous publications by the authors given in Refs. [9, 22], copyright by AIP, Ref. [10], copyright by APS and Ref. [21], copyright by Elsevier.

A schematic representation of all the processes is given by the equations:

$$\mathrm{CO(gas)} + \square \longrightarrow \mathrm{CO(ads)} \tag{1}$$

$$\mathrm{O_2(gas)} + 2 \cdot \square \longrightarrow 2\mathrm{O(ads)} \tag{2}$$

$$\mathrm{CO(ads)} + \mathrm{O(ads)} \longrightarrow \mathrm{CO_2(gas)} + 2 \cdot \square \tag{3}$$

$$\mathrm{CO(ads)} \longrightarrow \mathrm{CO(gas)} + \square \tag{4}$$

$$\mathrm{CO(ads)_i} + \square_j \longrightarrow \mathrm{CO(ads)}_j + \square_i \tag{5}$$

We start by describing in a more detailed way the processes involved in the model and, subsequently, we will explain the simulations carried out with the CA.

2.1 Adsorption and Reaction Processes

The main assumption for modeling the adsorption processes (Eqs. 1, 2), is that the gas molecules of carbon monoxide CO(gas) and oxygen O_2(gas) move randomly over the surface and if there are free sites on the lattice they are adsorbed to become CO(ads) and O(ads). The carbon monoxide molecules will need only one free lattice cell whereas the oxygen molecule needs two available sites because it is also assumed that the gaseous oxygen molecule dissociates into two O(ads). The reaction process (Eq. 3) is modeled considering that if an O(ads) atom is in the neighborhood of a CO(ads) molecule the reaction occurs, the sites previously occupied are freed and a CO_2(gas) is formed.

The adsorption and reaction processes form the Langmuir–Hinshelwood (LH) mechanism. A schematic picture of the LH mechanism is shown in Fig. 1. The rate constants, k_i, for each one of three kinetic mechanisms named above ($i = 1$, adsorption of CO; $i = 2$, adsorption of O_2; $i = 3$ reaction), are chosen to follow the Arrhenius form:

$$k_i = A_i \exp\left(-\frac{E_i}{k_B T}\right), \tag{6}$$

where A_i are the pre-exponential factors which are constant for each chemical reaction, k_B is the Boltzmann constant, T denotes the absolute temperature of the surface, and E_i are the activation energies of each one of the three elemental processes. These activation energies correspond to the action of the substrate and in the model we assume that are not dependent on the coverage of the surface.

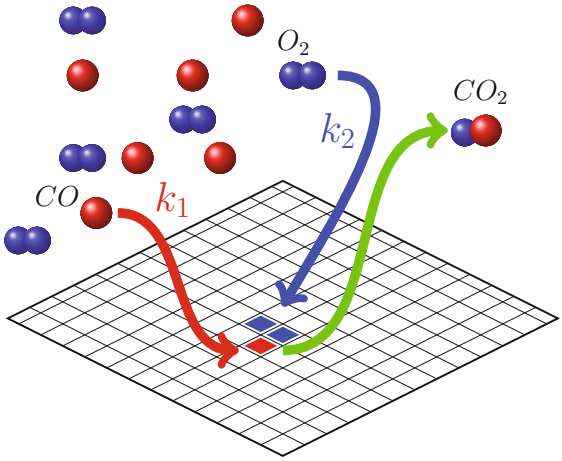

Fig. 1 The Langmuir–Hinshelwood (LH) mechanism: Gaseous molecules of CO(gas) and O_2(gas) collide randomly and are adsorbed on the surface with reaction rates k_1 and k_2, respectively. Upon adsorption the O_2(gas) molecule dissociates into two O(ads) atoms, each one residing on an adjacent surface site, and if a CO(ads) molecule is in the neighborhood, the reaction takes place and the CO_2 molecule is desorbed

2.2 CO *Desorption Process*

Equation 4 represents the CO desorption process. After the adsorption and reaction processes have taken place, the non-reacting CO(ads) molecules are allowed to be desorbed with a probability p_1, whereas the O(ads) atoms are considered immobile. This assumption is motivated by the fact that CO(ads) desorption takes place at a much lower temperature than the desorption of O(ads). The adsorption energies of O_2 are higher than those of CO. Therefore, O desorption takes place at a much higher temperature, and under most reaction conditions, the desorption of O can usually be neglected. These higher adsorption energies also indicate that the adsorbed O atoms are less mobile than the CO molecules [39].

2.3 CO *Diffusion Process*

The diffusion process of CO(ads) is represented by Eq. 5. Our diffusion algorithm is as follows:
(a) For each CO molecule adsorbed at site "i" a square box of size $r \times r$ around it is selected.
(b) If there is an empty site $\square_j$ inside that box at site "j", then the CO(ads) molecule can move to that empty place with a probability p_2.

In our diffusion process only one CO(ads) molecule is allowed to move once in each time step and the O(ads) atoms are considered immobile. Diffusion of CO(ads) molecules on a surface is a very complex process [26] that, as the CO desorption process, may depend in principle on many other parameters, such as the surface temperature, the absorbate coverage and other properties of the surface. These dependencies are not considered in our simplified model. However, we will see below that,

as in other models [18], when both diffusion and desorption processes are present the dominant effect is due to the desorption process. After the CO desorption and diffusion processes are both completed, the adsorption and reaction processes begin again.

2.4 The Effect of the Surface Temperature

The different chemical processes alter the surface temperature T of the catalyst. In our model we include the following equation to account for the variation of T:

$$\frac{dT}{dt} = -\gamma(T - T_B) + \sum_{i=1}^{5} h_i n_i \,, \tag{7}$$

where γ is the relaxation rate of T towards the room temperature T_B, h_i are related to the rates with which the reaction heats are generated in the processes (1)–(5), and n_i is the number of processes of type i that takes place per unit area (see Refs. [23, 24] for more details). The interplay among the chemical processes and the variation of the surface temperature is therefore the main mechanism that generates oscillations and thermal instabilities.

2.5 Cellular Automaton Implementation

As stated before the surface of the catalyst is discretized as a square lattice of 256 × 256 cells that can be in three different states: empty, $O(ads)$ and $CO(ads)$. To maintain the stoichiometry of the chemical reaction the lattice is also divided into non-overlapping blocks of four cells, a Margolus block, and the transition rules are applied to the whole block rather than to a single cell. The CA transition rules can be seen in Fig. 2 which shows the different initial states, the possible outcomes and their probabilities in terms of the gas concentration of carbon monoxide y_{CO} and gas concentration of oxygen $y_O = 1 - y_{CO}$. This CA approach to simulate the oxidation of carbon monoxide over a catalyst surface was originally proposed by Mai and Niessen [29]. Nevertheless, in the Mai and Niessen CA model the carbon monoxide and oxygen concentration, y_{CO} and y_O, are independent of the temperature. On the contrary in the model studied here both are functions of the surface temperature T.

A schematic graph of the CA algorithm including the effects of CO desorption and diffusion and how these processes alter the surface temperature is shown in Fig. 3.

The values of the parameters used in our simulations are the same as the ones reported by Lagos et al. [20] —for the case of small surface to volume ratio—. Hence, we assume CO adsorption and CO-O reaction as unactivated processes, O_2 adsorption being the only energetic process. We also consider that the rate of

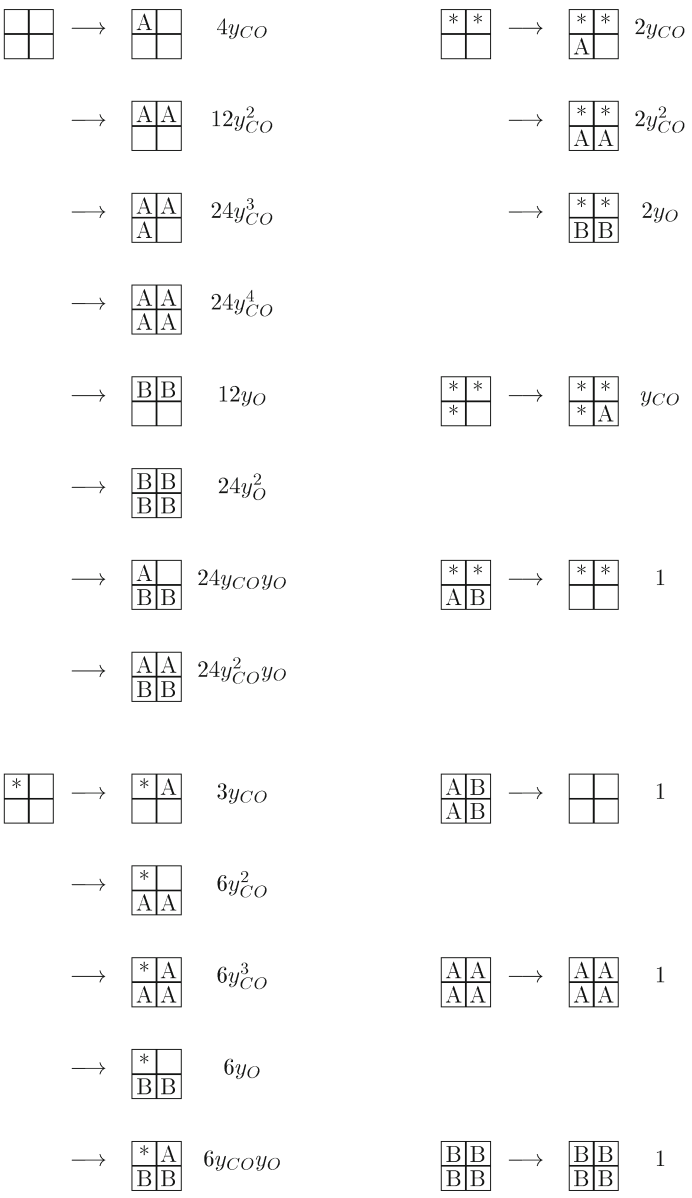

Fig. 2 Cellular automaton (CA) transition rules for the adsorption and reaction processes of the $CO + O_2$ reaction. A denotes a CO(ads) molecule, B an O(ads) oxygen atom and $\star$ any occupied site. The transition probabilities of CA depend on the initial state of the cells, on the statistical weights of the individual configurations, which are taken as classical, and on the mole fractions of the gaseous reactants, y_{CO} and y_O, where $y_O = 1 - y_{CO}$. In the model, y_{CO} is defined as $y_{CO} = k_1/(k_1 + k_2)$, where $k_i = A_i \exp[-E_i/(k_B T)]$. For each initial state, the sum of all transition probabilities is normalized to 1. Reproduced with permission from [22]. Copyright (2004) by AIP Publishing LLC

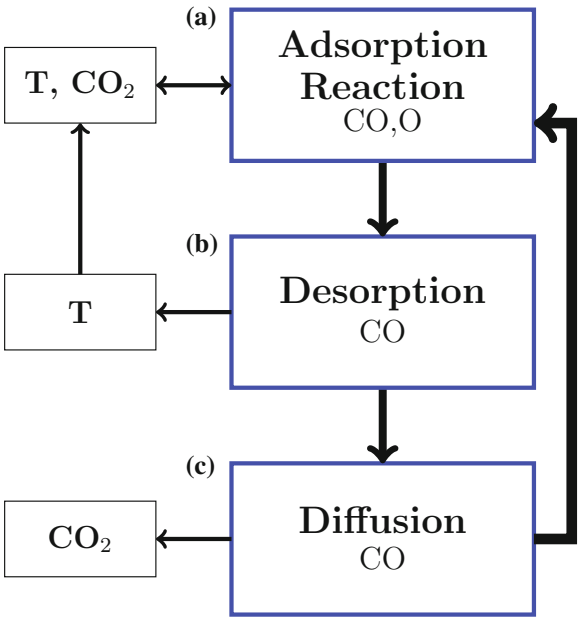

Fig. 3 The different steps of the CA model. **a** The adsorption processes, which include the production of CO_2, alter the temperature of the surface, which in turns modifies the different adsorption probabilities. **b** CO desorption process modifies the surface temperature. **c** CO diffusion process favors the production of CO_2. After CO desorption and diffusion processes are both completed, the adsorption and reaction processes begin again

reaction heat for O_2 adsorption is twice the value of that of the CO adsorption, and that the rate of reaction heat for CO_2 is negligible, both are minor simplifications. Consequently, the original CA model [22], without CO desorption nor diffusion, generates time oscillatory behavior for the following values [23, 24] of the set of parameters $\{A_i, E_i, h_i, T_B\}$: $A_1 = 5 \times 10^{-2}$ s^{-1}, $A_2 = 4 \times 10^5\, s^{-1}$, $A_3 = 1$ s^{-1}, $E_1 = 0$, $E_2/k_B = 6 \times 10^3$ K, $E_3 = 0$, $h_1 = 150\, Ks^{-1}$, $h_2 = 300\, Ks^{-1}$, $h_3 = 0$, $T_B = 300$K as environment temperature. The same set of values have been taken here and, in addition, we have assumed that the rate of reaction heat of the diffusion process is $h_5 = 0$, and that the one corresponding to CO desorption is opposite to that of CO adsorption, i.e., $h_4 = -h_1$.

3 Results

The study of the effects of CO desorption and diffusion is done in terms of the thermal relaxation parameter γ, the CO desorption probability p_1, and the CO diffusion probability p_2. Quasiperiodic behaviors in the original CA model [22] were observed in a range of values of the γ parameter: $\gamma_{min} \leq \gamma \leq \gamma_{max}$ (with $\gamma_{min} = 0.10$ and $\gamma_{max} = 0.27$). For $\gamma < \gamma_{min}$ the reaction shows an aperiodic regime and for lower γ a state poisoned by oxygen. Finally, for $\gamma > \gamma_{max}$ there is a state poisoned by CO. Now, including a probability p_1 of desorption for the CO(ads) molecules, the

poisoning of the surface with CO will happen at higher values than γ_{max}, and the range at which the quasiperiodic behavior is observed widens. From the whole set of parameters $\{\gamma, p_1, p_2\}$, we have studied some cases.

3.1 *No Diffusion* $\{\gamma = 0.30, p_1, p_2 = 0\}$

To see clearly how the CO desorption affects the oscillatory behavior of the surface reaction, we take values of the γ parameter around and slightly above the value γ_{max}. At this region if there is not desorption or p_1 is very low ($p_1 \leq 0.009$) the reaction is poisoned by CO at $T_B = 300$ K, whereas the oscillatory behaviors are found for $0.009 < p_1$.

Figure 4A shows typical Poincaré maps of the production rate of CO_2, R, versus the surface temperature for three different values of $p_1 = 0.015, 0.025$, and 0.030, with γ being equal to 0.30. For these values of p_1 the production rate R oscillates quasiperiodically, and R increases its value as p_1 grows. The desorption of CO(ads) molecules creates vacant sites inside the surface where the reaction can occur; therefore, increasing p_1 favors the reaction rate R. But a further increase of p_1, remaining $\gamma = 0.30$, as can be seen in Fig. 4B, reduces the formation of CO_2 as more CO molecules escape from the surface. Therefore there is a critical value p_c which may depend on the thermal relaxation parameter γ. Figure 4C shows the mean value of R versus p_1 for two values of γ. In this figure we can observe that for $\gamma = 0.30$ the critical value is located in the range $0.030 < p_c < 0.035$. This critical value is lower than the value of $p_c = 0.039$ obtained in Ref. [2] using Monte Carlo simulations.

Figure 5 shows the time series of T, R, n_{O}, and n_{CO} for $\gamma = 0.30$ and $p_1 = 0.025$. For this value of γ similar oscillations are observed in a broad range of the CO desorption probability $0.015 \leq p_1 \leq 0.8$ (Fig. 4). At this value of the thermal relaxation parameter, $\gamma = 0.30$, when the CO desorption probability p_1 is increased, the surface reaction goes from a CO poisoned state (if $p_1 \leq 0.009$) to a reactive state which displays quasiperiodic oscillations if $p_1 \geq 0.015$. But at the transition region between these two states, ($0.009 < p_1 < 0.015$) a new oscillatory behavior has been found.

Figure 6 shows the time series for $\gamma = 0.30$ and $p_1 = 0.011$. It can be seen that initially and during a transient time, the surface reaction oscillates in a quasiperiodic regime but, afterwards, n_{CO} grows rapidly (and n_{O} decreases) up to a high concentration value of n_{CO} (a low concentration value of n_{O}) that decays abruptly (whereas n_{O} increases). These intermittent bursts have a lower frequency than the frequencies of the quasiperiodic oscillations. Without CO desorption ($p_1 = 0$) the surface would be poisoned by CO, but now the surface recovers the reactive state.

To characterize this behavior, Fig. 7 shows the autocorrelation function $C(t) = (N-t)^{-1} \sum_{i=1}^{N} x_i x_{i+t}$ for the variables T, R, n_{CO}, and n_O. Figure 7a is for the case of quasiperiodic oscillations where it can be seen that $C(t)$ also shows oscillations that persist on time. In the case of the intermittent behavior, Fig. 7b, the autocorrelation functions of T and R show oscillations that decay in a few time steps, whereas that $C(t)$ for n_{CO} and n_O decay linearly with time.

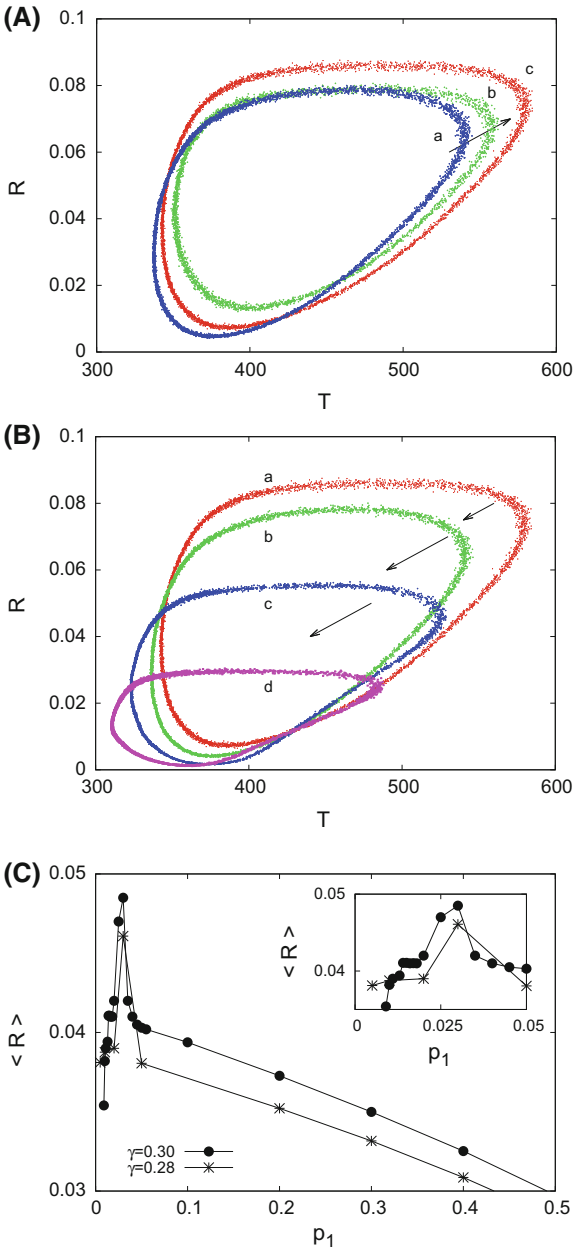

Fig. 4 The production rate of CO_2 (R) versus the surface temperature for different values of the desorption probability p_1. **A** (a) 0.015, (b) 0.025, and (c) 0.030. **B** (a) 0.030, (b) 0.035, (c) 0.500, and (d) 0.800. For **A** and **B** $\gamma = 0.30$. **C** The average production rate $\langle R \rangle$ versus p_1 for two different γ parameters (0.28 and 0.30). Introducing a small probability of desorption ($p_1 \leq 0.03$) increases the average value of R. But as p_1 is further increased the production of CO_2 diminishes linearly with p_1

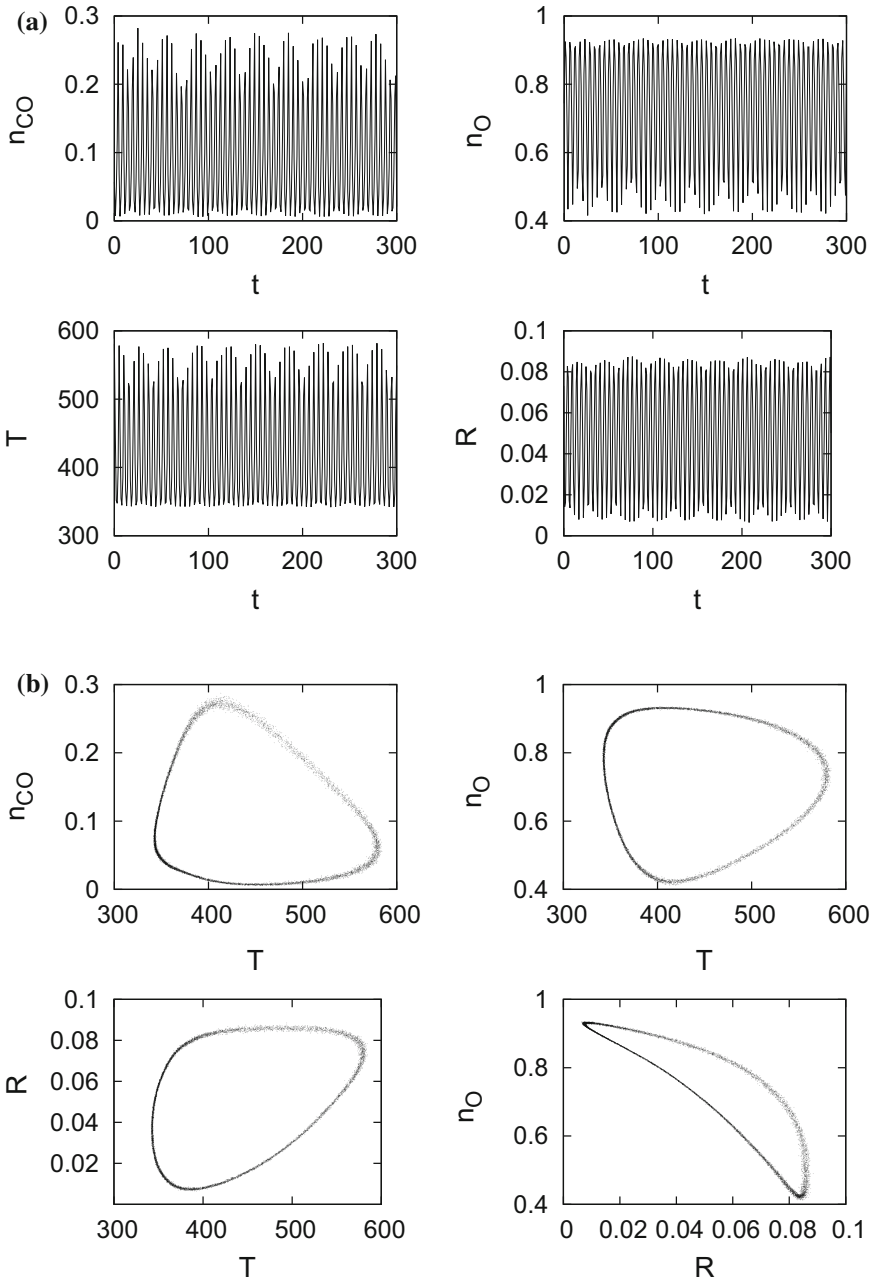

Fig. 5 Quasiperiodic oscillations for $\gamma = 0.30$ and $p_1 = 0.025$. **a** Time series of CO and O concentrations, n_{CO} and n_O, surface temperature, T, and rate of CO_2 production, R. Transient time has been discarded. **b** n_{CO} and n_O versus T, R versus T, and n_O versus R

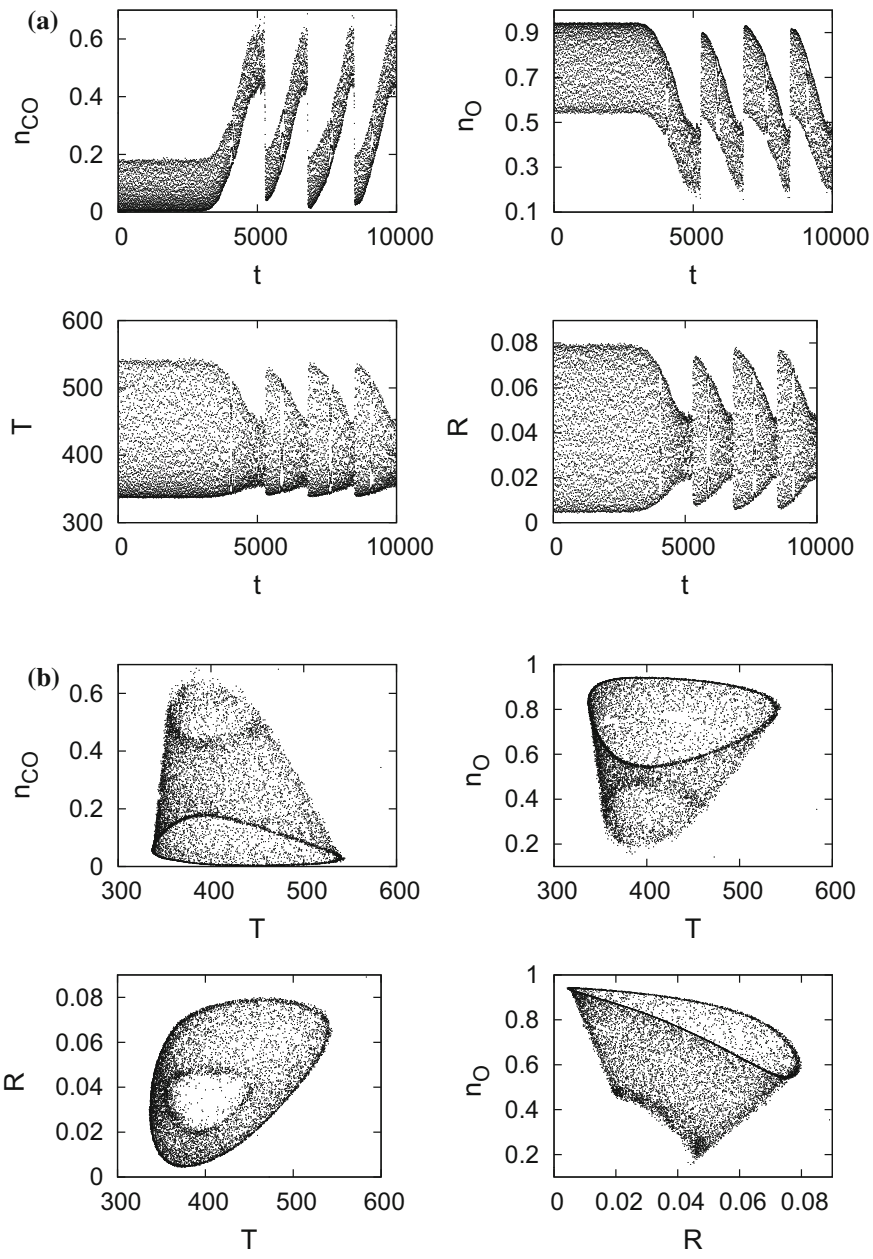

Fig. 6 Intermittent behavior for the parameters $\gamma = 0.30$ and $p_1 = 0.011$. **a** Time series of $n_{\mathrm{CO}}, n_{\mathrm{O}}$, T, and R. After a transient time oscillating in a quasiperiodic way the reaction shows an intermittent behavior. **b** n_{CO} and n_{O} versus T, R versus T, and n_{O} versus R

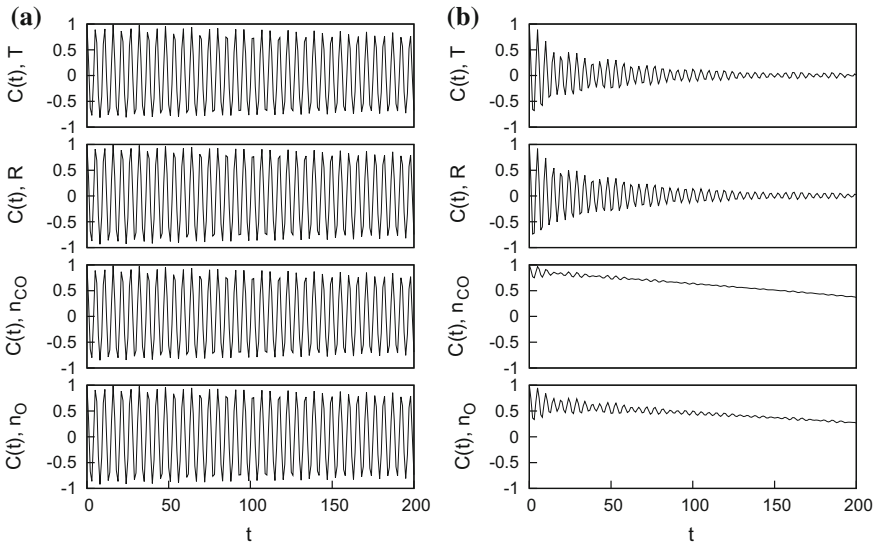

Fig. 7 Autocorrelation function $C(t)$ of T, R, n_{CO}, and n_{O} for **a** Quasiperiodic oscillation at $\gamma = 0.30$ and $p_1 = 0.025$, and **b** intermittent oscillation at $\gamma = 0.30$ and $p_1 = 0.011$

For comparison between these two behaviors, Fig. 8 shows log-log plots of the corresponding power spectrum $S(f)$ versus the frequency. For the quasiperiodic behavior, Fig. 8a, the main contributions to $S(f)$ are observed at the frequencies $f_1 = 0.21246\,\mathrm{Hz}$ and $f_2 = 0.36278\,\mathrm{Hz}$. For the intermittent behavior, Fig. 8b, the surface temperature and R power spectra, $S(f)$, shows a Lorentzian spectrum around $f = 0.20792\,\mathrm{Hz}$. For n_{CO} and n_O, the main contribution to $S(f)$ is located in the region of low frequencies where $S(f)$ shows a decaying power law of the type $1/f^2$. This intermittency can be considered to consist of two characteristic states, the regular and quasiperiodic oscillation, and the irregular bursts.

The phenomenon of intermittency is one of the mechanisms proposed for the onset of chaos. Therefore, transitions to chaos can take place according to three possible scenarios. The first is the Feigenbaum route [16], where the chaos is reached by means of bifurcations involving period doubling. Other onset to chaos is the intermittency route [33]. The name comes from the peculiar manner in which the chaos interrupts along the temporal evolution of the system: at the time series, regular behaviors (periodic basically) alternate with disordered bursts more or less short, producing an orbit that presents periods of chaos interspersed with periods of regular oscillations. A third scenario is the Ruelle–Takens–Newhouse route [35], in which the appearance of quasiperiodic behavior precedes the emergence of a strange attractor.

The results obtained from our model focus on the phenomenon of intermittency. The basic notion is that intermittency is essentially characterized by an apparently random switching back and forth between two (or perhaps more) different types of behavior. Pomeau and Manneville [33] proposed three types of intermittency

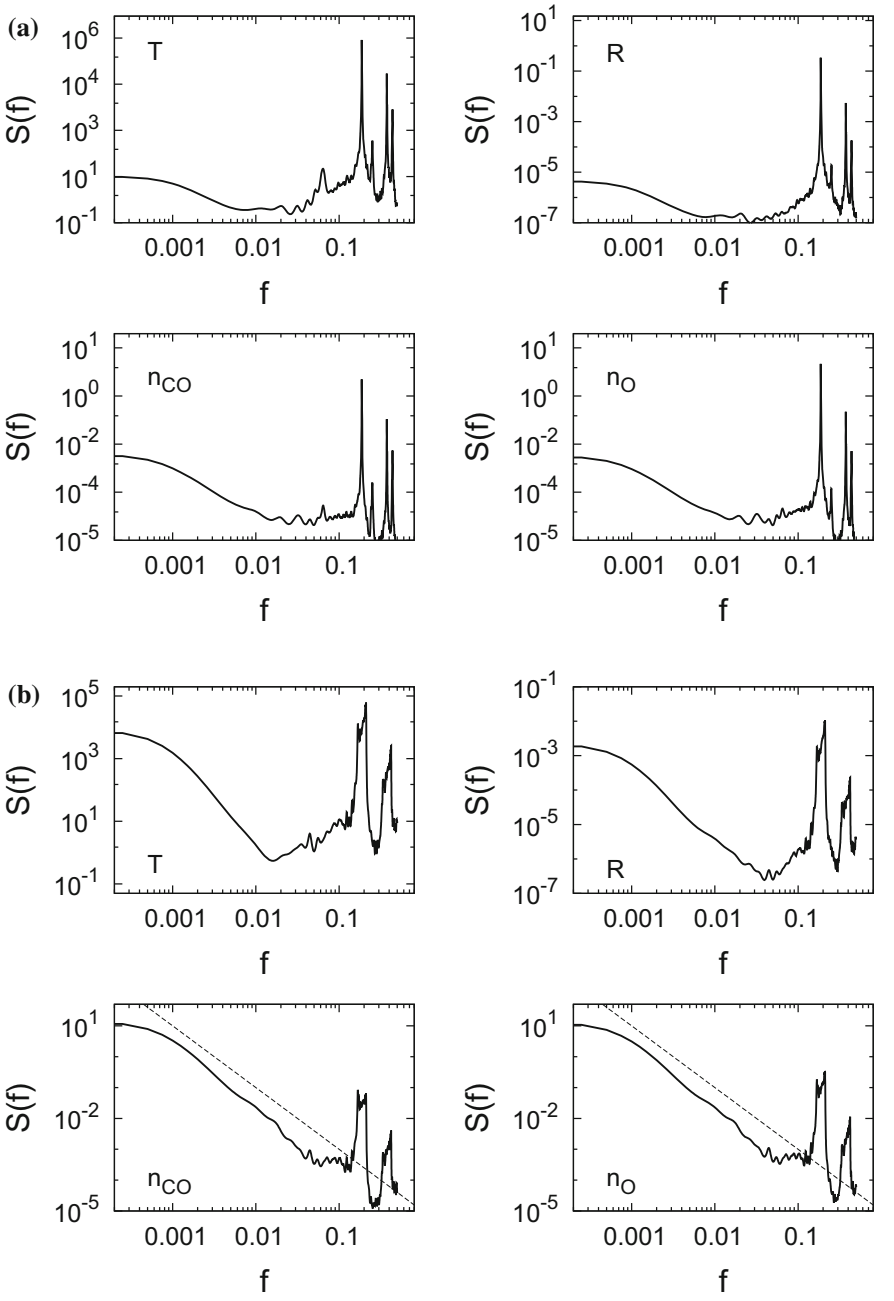

Fig. 8 Log-log plot of the power spectrum $S(f)$ of T, R, n_{CO}, and n_{O}. **a** Quasiperiodic oscillations ($\gamma = 0.30$ and $p_1 = 0.025$). **b** Intermittent behavior ($\gamma = 0.30$ and $p_1 = 0.011$). The dashed line is $1/f^2$

according to how a periodic orbit can lose its stability. These types (type I, II and III) are characterized by the changes in the Floquet multipliers [36] at the bifurcation point (the point of instability).

In type I-intermittency, the limit cycle Floquet multiplier crosses the unit circle along the real axis at the point $+1$. In this case a periodic state (a point fixed) is destroyed by a cycle fold (a saddle-node) and succeeded by chaos. The saddle-node is the bifurcation point. It is interesting to note that, during the bursts, the amplitudes of the motion are stable (on the average). Type I-intermittency has been seen particularly in systems that also show the Feigenbaum route.

In type II-intermittency, two Floquet multipliers form a complex conjugate pair crossing the unit circle. Here, the imaginary part indicates the presence of a second frequency (incommensurate) in the behavior of the system. The first frequency corresponds to the original limit cycle, which disappears at the bifurcation point. At the instability point, the limit cycle associated with the second frequency becomes unstable, and we observe burst of two-frequency behavior mixed with intervals of chaotic behavior. Thus, type II-intermittency is a type of Hopf bifurcation point. This intermittency is very difficult to observe in experimental studies.

In type III-intermittency, the limit cycle Floquet multiplier crosses the unit circle along the real axis at the point -1, and, then, a type of subcritical period-doubling bifurcation takes place. The amplitude of the subharmonic behavior (it is not stable) created at the bifurcation point grows, while the amplitude of the motion associated with the original period decreases.

Since the paper of Pomeau and Manneville, the classification of the intermittencies has been extended to other types, as for example on-off intermittency. This behavior has been observed, e.g., in coupled chaos systems [8]. The phenomenon refers to the situation where, at least, one variable of the system exhibits two different states in its time evolution. One is the "off" state where the variable remains constant, and the other is the "on" state where the variable temporarily burst out of the "off" state. One interesting result is that on-off intermittency obeys a power law $1/f^{3/2}$.

For homogeneous catalytic systems, the three routes to chaos can be experimentally identified in the well-known Belousov-Zabotinsky reaction. However, in heterogeneous catalytic systems it is more difficult to follow and analyze the emergency of chaos because, among other factors, the region of experimental parameters where the transition to chaotic behavior can take place is very small.

Slinko et al. [38] presented the result of both experimental and theoretical studies of the transition to chaos via type-I intermittency scenario in the case of CO oxidation on a zeolite-supported Pd catalyst. Their work was the first qualitative proof which showed that scenario for oscillating CO oxidation on a supported catalyst under normal pressure conditions. By using the analysis of the Fourier power spectra with CO concentrations, they could identify the route to chaos according to I-intermittency by a power law $1/f$.

From the outcomes derived from the CA model, we can say that the inclusion of CO desorption process causes the transition to chaos by means of some new type of intermittency. The exponent 2 in the power law indicates that the system dynamic shows strong correlations, but also has a random component. However, we need

to clarify what type of intermittency we have observed. We have not knowledge of any theoretical or experimental results similar to those obtained here. Only the works of Slinko et al. simulating the CO oxidation over Pd zeolite catalysts at high pressures and under isothermal conditions, presented studies of the transition to chaos according to type-I [38] or on-off [37] intermittencies.

3.2 *No Diffusion* $\{\gamma, p_1 = 0.011, p_2 = 0\}$

Taking now a fixed value of the CO desorption probability located in the intermittent region, the reactive state of the surface can be studied in terms of the thermal relaxation parameter, γ. Figure 9 plots time series of T and n_{CO} for different values of γ. Five different regimes can be observed:
(i) Poisoned state by O for $\gamma < 0.005$.
(ii) A noisy and chaotic behavior for low values of γ, in the range $0.005 \leq \gamma < 0.15$.
(iii) Regular and quasiperiodic oscillations in the range $0.15 \leq \gamma < 0.30$.
(iv) Intermittent behavior in the range $0.30 \leq \gamma < 0.35$. In this range of parameters a purely chaotic state cannot be excluded, although it has not been found yet.
(v) Poisoned state by CO for high values of $\gamma \geq 0.35$.
The poisoning of the surface by O or CO occurs at room temperature, $T_B = 300K$, while in oscillatory regimes the surface temperature fluctuates around a value greater than room temperature, that is, $T > T_B$.

The inclusion of the CO desorption effect has made the CA model much richer than the previous CA model without it [22].

3.3 *Diffusion* $\{\gamma = 0.30, p_1 = 0.012, p_2\}$

The inclusion of a diffusion probability for CO(ads) molecules, p_2, in the model does not affect quantitatively the range of the γ parameter at which the reaction shows oscillatory behaviors, but produces a small increase in the rate of CO_2 production, R. CO diffusion reduces the number of intermittent bursts. The quasiperiodic oscillations, which were only seen as a transient phenomena when CO diffusion probability was equal to zero, now are recovered as p_2 increases. Figure 10 shows the time series of the surface temperature and CO concentration for different values of the CO diffusion probability p_2. The parameter r, the radius of the neighborhood for CO diffusion process, is set to $r = 2$. For all the figures the CO desorption probability is $p_1 = 0.012$ and the thermal relaxation parameter $\gamma = 0.30$.

To grasp the shape of the attractor of the system, Fig. 11 shows time delayed pictures of the surface temperature and the production rate of CO_2. These Poincarè maps, which represent plots $T(t + 7)$ versus $T(t)$ and $R(t + 7)$ versus $R(t)$, show the evolution from intermittent oscillations to quasiperiodic one as p_2 is increased. For $p_2 = 0.05$ quasiperiodical oscillations are only observed.

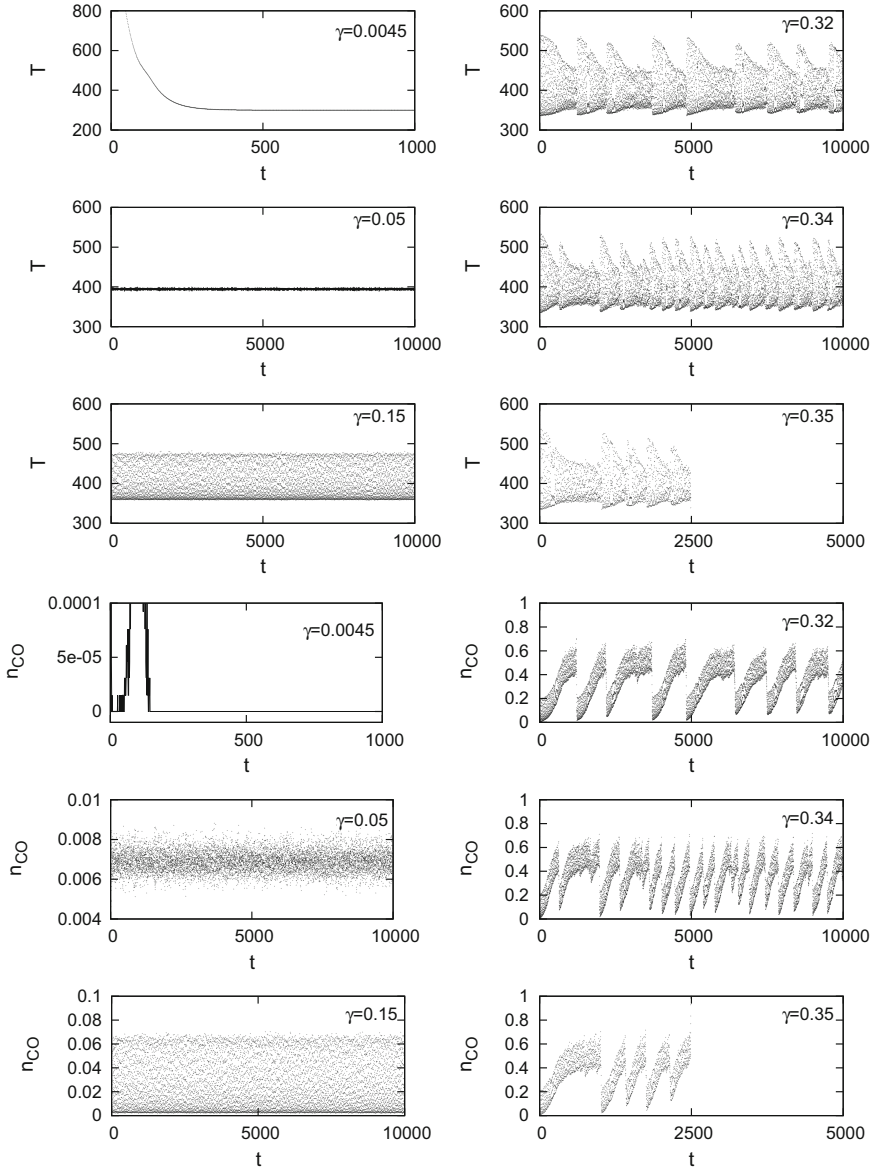

Fig. 9 Time series of the surface temperature, T, and CO concentration, n_{CO}, for different values of the γ parameter, with the CO desorption probability being fixed at the value $p_1 = 0.011$. For values of $\gamma < 0.005$ the surface is poisoned by O at $T_B = 300\,\mathrm{K}$. As γ is increased ($\gamma = 0.05$), the surface temperature oscillates around 400 K, and n_{CO} shows a chaotic behavior. For $\gamma = 0.15$ the reaction shows a regular and quasiperiodic oscillation. A further increase in γ (0.32 and 0.34) makes the reaction to oscillate intermittently until the surface is poisoned by CO at $T_B = 300\,\mathrm{K}$ for a value of $\gamma = 0.35$

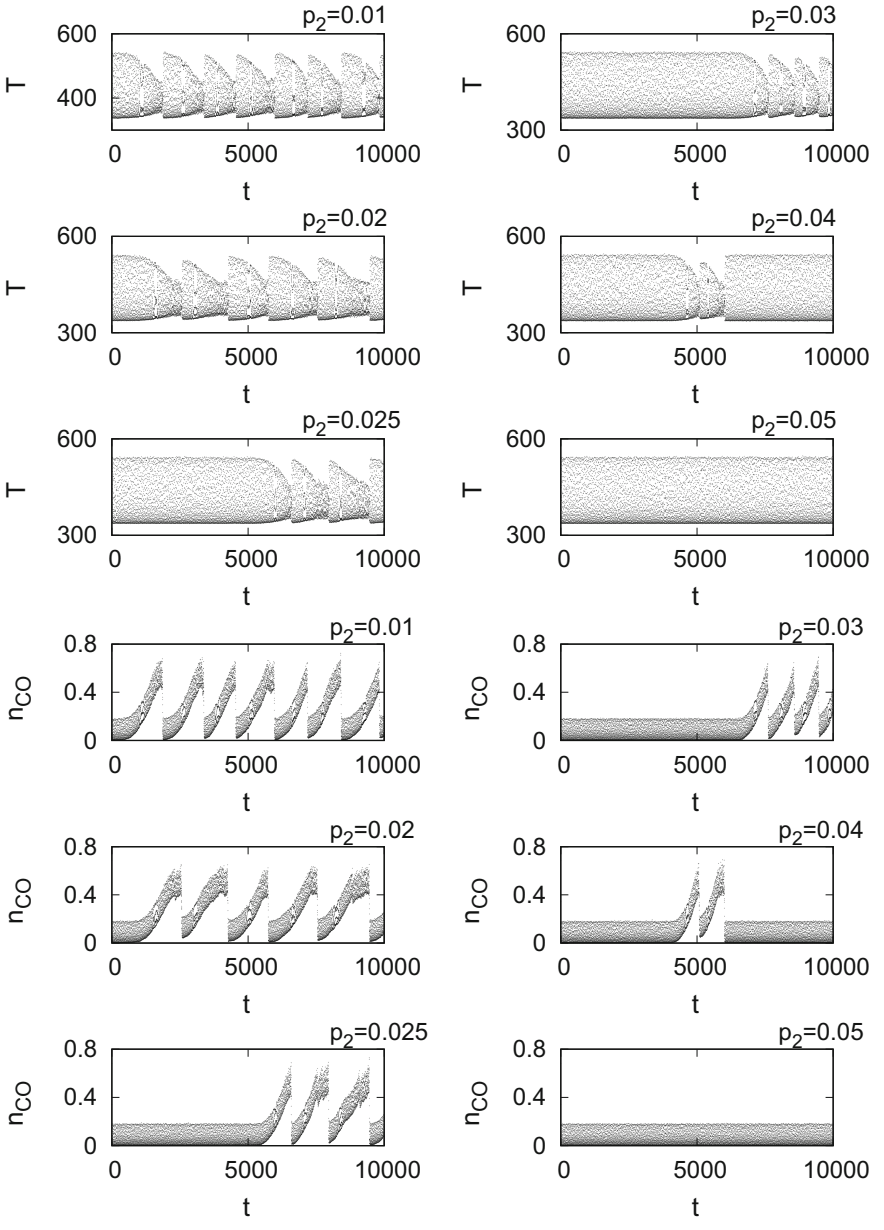

Fig. 10 Time series of T and n_{CO} for different values of the CO diffusion probability: $p_2 = 0.01, 0.02, 0.025, 0.03, 0.04$, and 0.05. The CO(ads) molecules are allowed to diffuse in a box of size 2×2 cells. The temperature relaxation parameter is $\gamma = 0.30$ and the desorption probability of CO molecules is $p_1 = 0.012$. Increasing the CO diffusion probability reduces the number of intermittent bursts until the reaction settles into the quasiperiodic regime ($p_2 = 0.05$)

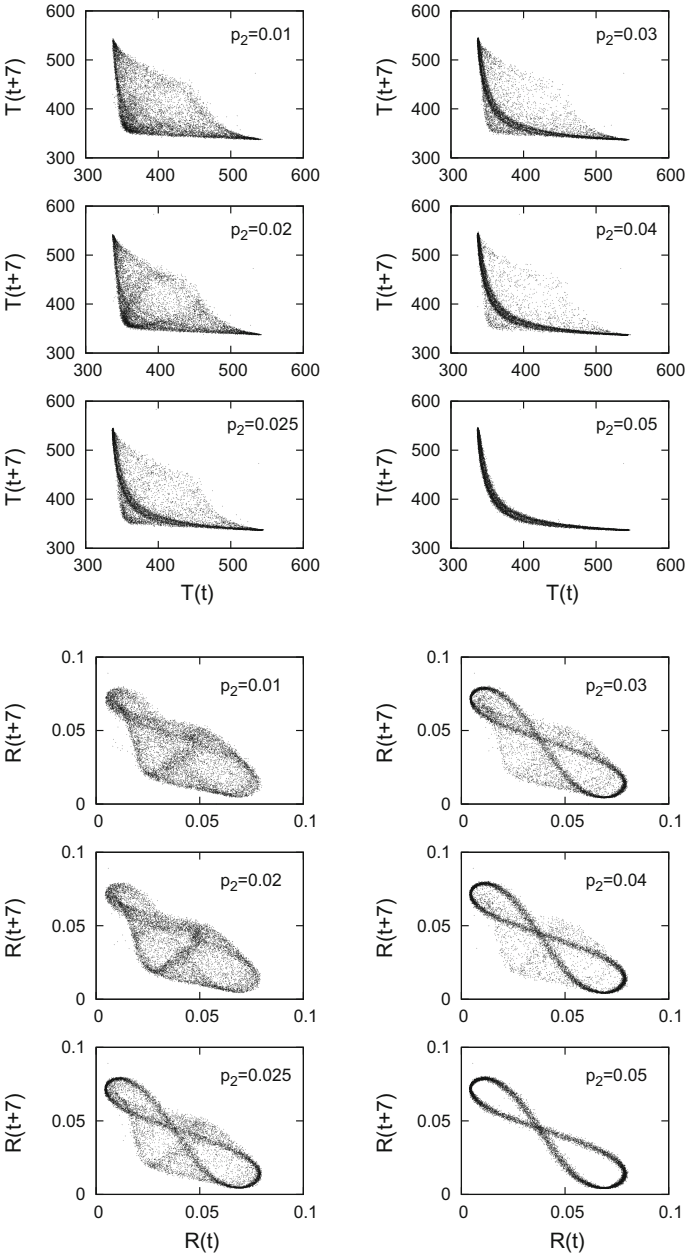

Fig. 11 Time delayed pictures of the surface temperature, T, and the production rate of CO_2, R, for different values of CO diffusion probability: $p_2 = 0.01, 0.02, 0.025, 0.03, 0.04$, and $0.05 (r = 2)$, with fixed values of the thermal relaxation parameter $\gamma = 0.30$ and CO desorption probability $p_1 = 0.012$. For low values of p_2 a noisy and intermittent attractor can be observed, and as p_2 increases the attractor is clearly defined: the behavior is quasiperiodic and the points densely populate an single and invariant closed loop

3.4 Distribution of the Adsorbed Species on the Surface

CA model allows to follow the temporal and spatial evolution of the system, a possibility that mean-field models do not offer. Thus, we can observe several spatio-temporal periodic and chaotic structures which are generated as the surface reaction takes place. Although the goal of our study is to analyze the temporal evolution of the system without stopping to observe the distribution of the adsorbed particles on the surface, in other problems the information that is extracted from the spatial structures is the key to understanding the behavior of the reaction. Therefore, to complete our study, we include snapshots of the (256×256) lattice when the system exhibits oscillatory behaviors. Figure 12 shows a set of snapshots of the surface for different values of the parameters. Each pixel in the figure represents the average value of the concentrations of CO and O, $\langle n_{\mathrm{CO}} \rangle$ and $\langle n_{\mathrm{O}} \rangle$. The color palette have been selected in order to clearly distinguish the chemical front of both chemical reactants.

Intermediate values of the concentration is colored in pink for O and red for CO. E (dark green) stands for a state with a concentration of 0.5, which means a site where CO_2 is produced. In the case of a quasiperiodic behavior, Fig. 12a, there is a homogeneous state in which any structure can be seen. As the thermal relaxation parameter γ and the CO desorption probability p_1 are increased the spatial homogeneity is lost.

3.5 Shannon Entropy

In order to characterize the different kinds of behavior that are observed as the parameters γ and p_1 are changed, we use the Shannon entropy S defined as:

$$S(p_1, \gamma) = -\sum_{i}^{N} f_i \, ln \, f_i \,, \tag{8}$$

where f_i is the frequency of a given value of the concentration of CO, and N is the number of non-void c-bins. We have taken $N = 100$. The procedure to obtain $S(p_1, \gamma)$ is as follows:
(i) The reaction is let to evolve during 1000 time steps.
(ii) Afterwards during another $t = 5000$ time steps the concentration of CO is measured.
(iii) At each time step the corresponding c-bin is increased in one unit so that at the end there will be n_i.
(iv) The frequency of each c-bin is thus given by $f_i = n_i/t$.

If the concentration has a unique value the entropy will be 0. For a periodic behavior, the value of $S(p_1, \gamma)$ will be nonzero but low. The maximum value of $S(p_1, \gamma)$ will be reached for a chaotic state in which every $f_i = 10^{-2}$.

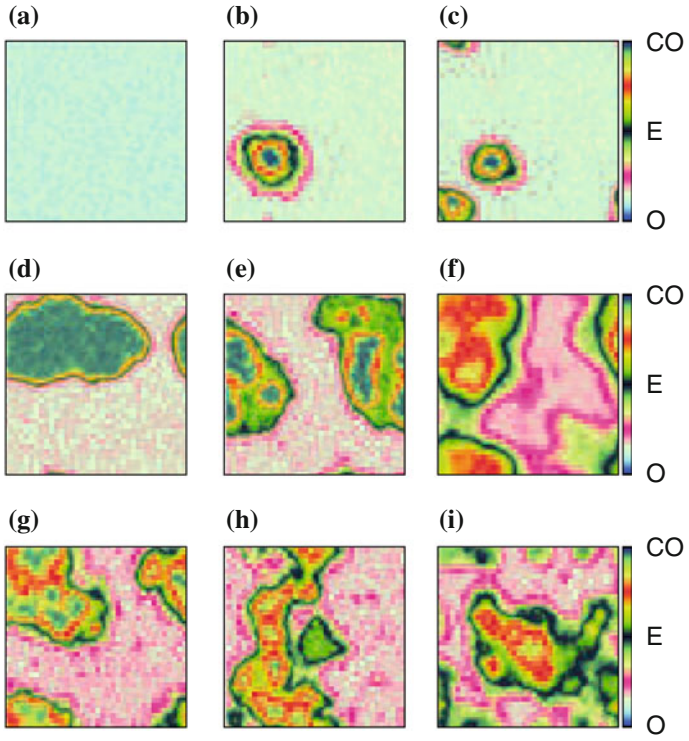

Fig. 12 Snapshots of spatial structures generated by the CA model for different values of γ, p_1, and p_2. Each pixel is an average concentrations of CO and O. E stands for a concentration of 0.5. **a** $\gamma = 0.25$, $p_1 = 0$, $p_2 = 0$. **b** $\gamma = 0.30$, $p_1 = 0.012$, $p_2 = 0$. **c** $\gamma = 0.31$, $p_1 = 0.012$, $p_2 = 0$. **d** $\gamma = 0.34$, $p_1 = 0.012$, $p_2 = 0$. **e** $\gamma = 0.31$, $p_1 = 0.013$, $p_2 = 0$. **f** $\gamma = 0.335$, $p_1 = 0.0142$, $p_2 = 0$. **g** $\gamma = 0.30$, $p_1 = 0.012$, $p_2 = 0.03$. **h** $\gamma = 0.30$, $p_1 = 0.013$, $p_2 = 0.04$. **i** $\gamma = 0.335$, $p_1 = 0.013$, $p_2 = 0.01$

Figure 13 shows the Shannon entropy for the entire set of parameters p_1 and γ. Black and white colors correspond to a periodic or fixed point behavior that occurs when the surface is poisoned either by CO or O. The colored regions blue, green and pink correspond to periodic oscillatory behaviors, while cyan color corresponds to quasiperiodic behaviors. It can be observed that the most complex region (the red one) is located at the border between the quasiperiodic region and the poisoned one.

4 Summary

We have presented here simulations of a cellular automaton (CA) model for the surface chemical reaction of CO and O that includes the effects of desorption and diffusion of adsorbed CO molecules. Each one of these processes are considered

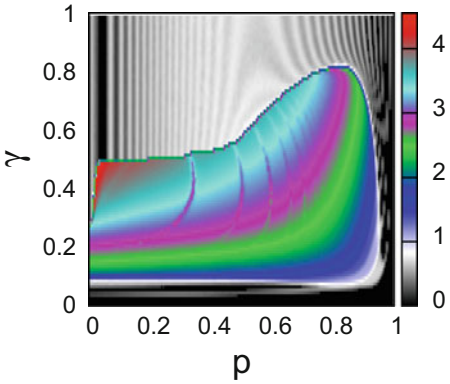

Fig. 13 Shannon entropy for the set of parameters p_1 and γ ranging both between 0 and 1. Black and white colors correspond either to a periodic state (with a single frequency) or a state where the surface is poisoned by CO or O. Blue, green and pink colors indicate periodic oscillatory behaviors, while cyan corresponds to quasiperiodic one. Intermittency region (the red one) is located at the border between the quasiperiodic region and that where the surface is poisoned by CO

probabilistic with probabilities p_1 (for CO desorption) and p_2 (for CO diffusion). The model also includes the surface temperature as a dynamic variable so that the different behaviors can be described in terms of three control parameters $\{\gamma, p_1, p_2\}$, keeping fixed the remaining parameters of the model. CO desorption widens the range of the γ parameter at which the reaction shows quasiperiodic oscillatory behaviors. The coupling between the thermal effects and CO desorption shows a new intermittent oscillatory behavior at the border between the quasiperiodic oscillatory state and the CO poisoned state in the range of parameters $0.30 \leq \gamma < 0.35$, and $0.009 < p_1 < 0.015$. The inclusion of CO diffusion only reduces the number of intermittent bursts. Intermittent behavior was already identified for oscillating CO oxidation over a zeolite-supported Pd catalyst [38].

The flexibility of the CA model allows us to take into account new effects in a simple and straightforward way. In this sense it is worth to investigate the effect of considering a long range reactivity (larger values of the diffusion parameter r), the dependence on CO desorption and diffusion processes on the surface coverage, and the assumption of CO adsorption and CO_2 as activated processes, among other topics.

Acknowledgements Junta de Andalucía partially funded the research group (FQM-122) to which the authors belong.

References

1. Albano, E.V.: Monte Carlo simulation of a bimolecular reaction of the type $A+(1/2)\,B_2 \rightarrow AB$ -the influence of A-desorption on kinetic phase transitions. Appl. Phys. A **55**(2), 226–230 (1992)
2. Brosilow, B.J., Ziff, R.M.: Effects of a desorption on the first-order transition in the A-B_2 reaction model. Phys. Rev. A **46**(8), 4534–4538 (1992)
3. Buendía, G.M., Machado, E., Rikvold, P.A.: Effect of CO desorption and coadsorption with O on the phase diagram of a Ziff–Gulari–Barshad model for the catalytic oxidation of CO. J. Chem. Phys. **131**, 184704 (2009)
4. Buendía, G.M., Rikvold, P.A.: Model for the catalytic oxidation of CO, including gas-phase impurities and CO desorption. Phys. Rev. E **88**, 012132 (2013)
5. Buendía, G.M., Rikvold, P.A.: A model for the catalytic oxidation of CO that includes CO desorption and diffusion, O repulsion and impurities in the gas phase. Physica A **424**, 217–224 (2014)
6. Chopard, B., Droz, M.: Cellular automata approach to non-equilibrium phase transitions in a surface reaction model: static and dynamic properties. J. Phys. A: Math. Gen. **21**, 205–211 (1988)
7. Chopard, B., Droz, M.: Cellular Automata Modeling of Physical Systems. Cambridge University Press, Cambridge (1998)
8. Clinton, J.: Chaos and Time-Series Analysis. Oxford University Press, Oxford (2003)
9. Córdoba, A., Lemos, M.C., Jiménez-Morales, F.: Periodical forcing for the control of chaos in a chemical reaction. J. Chem. Phys. **124**, 014707 (2006)
10. Córdoba, A., Lemos, M.C., Jiménez-Morales, F.: Stabilization from chaotic to periodical states in a model of cellular automaton for oxidation of CO. Phys. Rev. E **74**, 016208 (2006)
11. Dickman, R.: Kinetic phase transitions n a surface-reaction model: mean-field theory. Phys. Rev. A **34**(5), 4246–4250 (1986)
12. Ehsasi, M., Matloch, M., Frank, O., Block, J.H., Christmann, K., Rys, F.S., Hirschwald, W.: Steady and nonsteady rates of reaction in a heterogeneously catalyzed reaction: oxidation of CO on platinum, experiments and simulations. J. Chem. Phys. **91**(8), 4949–4960 (1989)
13. Engel, T., Ertl, G.: A molecular beam investigation of the catalytic oxidation of CO on Pd(111). J. Chem. Phys. **69**(3), 1267–1281 (1978)
14. Engel, T., Ertl, G.: Elementary steps in the catalytic oxidation of carbon monoxide on platinum metals. Adv. Catal. **28**, 1–78 (1979)
15. Ertl, G.: Oscilatory catalytic reactions at single-cristal surfaces. Adv. Catal. **37**, 213–277 (1990)
16. Feigenbaum, M.J.: Quantitative universality for a class of nonlinear transformations. J. Stat. Phys. **19**, 24–52 (1978)
17. Hess, F., Farkas, A., Seitsonen, A.P., Over, H.: First principles kinetic Monte Carlo simulations revisited: CO oxidation over RuO_2(110). J. Comput. Chem. **33**(7), 757–766 (2012)
18. Kaukonen, H.P., Nieminen, R.M.: Computer simulations studies of the catalytic oxidation of carbon monoxide on platinum metals. J. Chem. Phys. **91**(7), 4380–4386 (1989)
19. Krischer, K., Eiswirth, M., Ertl, G.: Oscillatory CO oxidation on Pt(110): modeling of temporal self-organization. J. Chem. Phys. **96**(12), 9161–9172 (1992)
20. Lagos, R.E., Sales, B.C., Suhl, H.: Theory of oscillatory oxidation of carbon monoxide over platinum. Surf. Sci. **82**, 525–539 (1979)
21. Lemos, M.C., Córdoba, A.: A cellular automaton for a surface reaction: stabilization from chaotic to periodical states. Adv. Eng. Softw. **41**(1), 32–37 (2010)
22. Lemos, M.C., Jiménez-Morales, F.: A cellular automaton for the modeling of oscillations in a surface reaction. J. Chem. Phys. **121**(7), 3206–3211 (2004)
23. Lemos, M.C., Luque, J.J., Jiménez-Morales, F.: Bistability and oscillations in a surface reaction model. Phys. Rev. E **51**(6), 5360–5364 (1995)
24. Lemos, M.C., Luque, J.J., Jiménez-Morales, F.: Influence of the interaction on oscillatory behavior in a surface reaction model. J. Chem. Phys. **109**(18), 8069–8075 (1998)
25. Liu, D.J., Evans, J.W.: Atomistic lattice-gas modeling of CO oxidation on Pd(100): temperature-programed spectroscopy and steady-state behavior. J. Chem. Phys. **124**(15), 154705 (2006)

26. Liu, D.J., Evans, J.W.: Chemical diffusion of CO in mixed CO+O adlayers and reaction front propagation in CO oxidation on Pd(100). J. Chem. Phys. **125**(5), 054709 (2006)
27. Liu, D.J., Evans, J.W.: Atomistic and multiscale modeling of CO-oxidation on Pd(100) and Rh(100): from nanoscale fluctuations to mesoscale reaction fronts. Surf. Sci. **603**(10–12), 1706–1716 (2009)
28. Liu, D.J., Evans, J.W.: Realistic multisite lattice-gas modeling and KMC simulation of catalytic surface reactions: kinetics and multiscale spatial behavior for CO-oxidation on metal (100) surfaces. Prog. Surf. Sci. **88**(4), 393–521 (2013)
29. Mai, J., Niessen, W.V.: Cellular-automaton approach to a surface reaction. Phys. Rev. A **44**(10), R6165–R6168 (1991)
30. Marro, J., Dickman, R.: Nonequilibrium phase transitions in lattice models. Cambridge University Press, Cambridge (2005)
31. Nagasaka, M., Kondoh, H., Nakai, I., Ohta, T.: CO oxidation reaction on Pt(111) studied by the dynamic Monte Carlo method including lateral interactions of adsorbates. J. Chem. Phys. **126**(4), 044704 (2007)
32. Petrova, N.V., Yakovkin, I.N.: Monte Carlo simulation of CO and O coadsorption and reaction on Pt(111). Surf. Sci. **578**(1–3), 162–173 (2005)
33. Pomeau, Y., Manneville, P.: Intermittent transition to turbulence in dissipative dynamical systems. Commun. Math. Phys. **74**, 189–197 (1980)
34. Rogal, J., Reuter, K., Scheffler, M.: CO oxidation on Pd(100) at technologically relevant pressure conditions: first-principles kinetic Monte Carlo study. Phys. Rev. B **77**(15), 155410 (2008)
35. Ruelle, D., Takens, F.: On the nature of turbulence. Commun. Math. Phys. **20**, 167–192 (1971)
36. Slin'ko, M.M., Jaeger, N.I. (eds.): Oscillating Heterogeneous Catalytic Systems. Studies in Surface Science and Catalysis, vol. 86. Elsevier, Amsterdam (1994)
37. Slin'ko, M.M., Kurkina, E.S., Liauw, M.A., Jaeger, N.I.: Mathematical modeling of complex oscillatory phenomena during CO oxidation over Pd zeolite catalysts. J. Chem. Phys. **111**(17), 8105–8114 (1999)
38. Slin'ko, M.M., Ukharskii, A.A., Peskov, N.V., Jaeger, N.I.: Identification of the intermittency-I route to chaos in oscillating CO oxidation on zeolite-supported Pd. Faraday Discuss. **120**, 179–195 (2001)
39. Somorjai, G.A., Li, Y.: Introduction to Surface Chemistry and Catalysis, 2nd edn, p. 613. Wiley, New Jersey (2010). Section 9
40. Stamatakis, M.: Kinetic modelling of heterogeneous catalytic systems. J. Phys.-Condens. Mat. **27**, 013001 (2015)
41. Toffoli, T., Margolus, N.: Cellular Automata Machines. The MIT Press, Cambridge (1987)
42. Völkening, S., Wintterlin, J.: CO oxidation on Pt(111)-scanning tunneling microscopy experiments and Monte Carlo simulations. J. Chem. Phys. **114**(14), 6382–6395 (2001)
43. Zhdanov, V.P.: Monte Carlo simulations of oscillations, chaos and pattern formation in heterogeneous catalytic reactions. Surf. Sci. Rep. **45**, 231–326 (2002)
44. Ziff, R.M., Gulari, E., Barshad, Y.: Kinetic phase transitions in an irreversible surface-reaction model. Phys. Rev. Lett. **56**, 2553–2556 (1986)

Transmission of Thermal Phonons in Superfluid Helium Through Nonlinear Meta-Interface with a Solid

Yuriy A. Kosevich, Olena Yu. Tkachenko and Eugenii S. Syrkin

Abstract The transmission of thermal phonons through the two-dimensional ultrathin layer of impurity atoms adsorbed at the interface of a solid with superfluid helium is discussed. The resonance interaction of the incident from superfluid helium phonons with the damped oscillations of the intermediate layer is analyzed. It is shown that this interaction results in the significant enhancement of the heat flux through such meta-interface compared with the heat flux through the atomically clean interface. The anharmonic phenomena in the intermediate atomic layer increase the heat flux via the nonlinear phonon transmission through the interface between superfluid helium and the solid and contribute to the dissipative properties of the interface monolayer. It is emphasized that for the parameters of the intermediate ultrathin atomic layer under consideration the enhancement of the heat flux caused by the surface phonon absorption can reach two or three orders of magnitude.

Keywords Thermal interface conductance · Interface between superfluid helium and solid · Thermal phonons · Surface phonon absorption · Nonlinear phonon transmission

Yu. A. Kosevich (✉)
Semenov Institute of Chemical Physics, Russian Academy of Sciences, ul. Kosygina 4, Moscow 119991, Russia
e-mail: yukosevich@gmail.com

O. Yu. Tkachenko
V. N. Karazin Kharkov National University, pl. Svobody 4, Kharkov 61103, Ukraine
e-mail: quantmirage@gmail.com

E. S. Syrkin
B. I. Verkin Institute of Low-Temperature Physics and Engineering, National Academy of Sciences of Ukraine, pr. Nauki 47, Kharkov 61103, Ukraine
e-mail: syrkin@ilt.kharkov.ua

J. F. R. Archilla et al. (eds.), *Nonlinear Systems, Vol. 2*, Understanding Complex Systems, https://doi.org/10.1007/978-3-319-72218-4_9

1 Introduction

P.L. Kapitza has discovered in 1941 that in the presence of a heat flux through the interface between superfluid helium and a solid the jump in temperatures between these two media is established [13]. The magnitude of the finite temperature discontinuity is proportional to the surface density of the heat flux and the corresponding coefficient, the Kapitza thermal boundary resistance, which is also called the interfacial thermal resistance or thermal boundary resistance, has the temperature dependence T^{-3}. The interfacial thermal resistance describes the ability of the interface to resist the heat flow through the boundary and the thermal resistance is finite even at atomically perfect interfaces. Later it was discovered that such temperature discontinuity takes place not only at the superfluid helium - solid interface, but at solid-solid interfaces as well [36]. Therefore the understanding of the nature and basic principles of the thermal boundary resistance at low temperature is decisive for technological applications because it is important to know how the interfaces between the materials in use influence the thermal properties of the device. For example, the knowledge of the thermal resistance of semiconductor thin films is extremely useful in creating various microelectronic and optoelectronic devices like quantum cascade lasers or light-emitting diodes [26]. Below we describe the main principles of the existing explanations of the interfacial thermal resistance.

1.1 The Interfacial Thermal Resistance

Generally, if temperatures of the two materials are different, phonons with higher energy which are incident from the hotter material, cause the energy transfer from the hotter to the cooler material. The reverse process, when the energy is transmitted through the boundary via the phonons with lower energy, also occurs. Consequently, the net heat flux Q through the interface between the two media is thought to occur as a result of the transfer of phonons across it. The two theoretical models that are widely used for the studies of the thermal properties of interfaces are the acoustic mismatch model (AMM) and the diffuse mismatch model (DMM).

The acoustic mismatch model has been elaborated by I.M. Khalatnikov [14, 15] in order to understand and describe the thermal resistance phenomenon at the superfluid helium -solid boundaries. The theory developed in [14, 15] is based on the idea that phonon transmission is equivalent to the transmission of dispersionless plane acoustic waves. Besides it is assumed in this model that the interface is perfectly flat and the contact is perfectly rigid. The transmission coefficient is obtained by solving the acoustic reflection/transmission problem at the interface between two media with different acoustic properties and respectively with mismatched acoustic impedances [acoustic mismatch model (AMM)]. The AMM was later applied to the solid-solid interfaces [27]. The AMM makes possible the qualitative explanation of the main features, including temperature dependence, of the heat exchange between superfluid helium and a solid.

The alternative diffuse mismatch model has been developed in order to describe the phonon transmission under the condition of strong scattering [36]. Original DMM assumes that phonons are scattered both elastically and diffusively at the boundary between isotropic solids. The probability of the phonon emission into the media in contact is proportional to the phonon density of states in each of the media. In other words, the mismatch of the phonon density of states controls the thermal resistance within the frame of DMM. The extension of DMM to anisotropic media and experimental demonstration of the role of anisotropy were performed in Refs. [8, 12, 32]. The influence of the phonon dispersion on the diffusive mechanism of the phonon transport across the interfaces was analyzed in Ref. [9].

The explanations of the finite temperature discontinuity at the interface within AMM and DMM have a number of similarities, but the discrepancies between them are clearly visible as well [36]. Both AMM and DMM do not account for the influence of electrons on heat transport in the system, so they can be applied only if at least one of the materials under the study is insulator, because for the metal - metal interfaces thermal energy is mainly carried by electrons and the electron scattering plays an important role in the origin of the thermal boundary resistance. Also the possible dependencies of the transmission probabilities on temperatures on the either side of the interface are considered to be negligible in these models. In the DMM, the calculation of the transmission probabilities from both media are not required, and the full information about the heat-transfer properties of the interface can be obtained in the studies of the heat flow from one material to another without exploring the inverse process. The main difference between the acoustic and diffuse mismatch models is that in the former the phonon inelastic and non-specular reflection does not exist because the interface is believed to be smooth, which allows to assume that at low temperature phonons obey the long-wave acoustic law of propagation and are reflected specularly at the interface. On the other hand, the latter model takes into account the strong diffuse scattering at imperfect interfaces at elevated temperatures.

It is well known that if the materials have very different physical properties, e.g. the electronic or acoustic properties, the energy of the incident quasiparticles will be reflected and scattered at the interface between them. The purpose of the proposed by Swartz and Pohl [36] DMM was to establish the influence of the strong diffuse scattering on the interface resistance. In the DMM, the probability of the phonon transmission is proportional to the phonon density of states in the material into which elastic wave propagates and is determined by the principle of detailed balance. Such property takes place because the important feature of the phonon scattering is that the wave vectors of outgoing and propagating across the interface phonons are independent on the wave vectors of the incident phonons - the correlations between them are destroyed by diffuse surface scattering. Therefore, in this model one can say about the mismatch between the densities of phonon states. Moreover, the change in pressure does not induce conspicuous modification of the significant difference between the phonons densities of states in liquid helium and in the solid, which makes the results of the DMM weakly dependent on pressure. Nevertheless, the value of the boundary resistance obtained within the DMM does not match on the whole the experimental data. This value also does not match the results of the AMM, and the

difference between them depends on the kind of the materials under consideration. In general, the diffuse mismatch model gives the interfacial resistance which is lower than that given by the acoustic mismatch model, and the value of the experimentally measured interfacial thermal resistance usually lies between the values given by the acoustic and diffuse mismatch models [36].

It should also be mentioned that for the simulations and modeling of the heat flow and calculations of the interfacial thermal resistance under different conditions, the molecular dynamics approach is often used for the liquid-solid boundaries, solid-solid boundaries, and the interfaces between semiconductor thin films [35]. For example, this approach allows to study the interfacial thermal transport in cases when the wave-like nature of phonons is important and no speculations about the origin of the phonon scattering are required [26].

According to the Khalatnikov theory, there are two ways for the transfer of heat through the interface between superfluid helium and a solid: by the transmission through (and emission by) the interface of thermal phonons and of thermal rotons. Here phonons and rotons are named as thermal because the respective oscillations of the helium atoms and the crystall lattice are caused by temperature-induced fluctuations, and they carry the heat energy flowing from the hotter medium to the cooler one and in the opposite direction (counterflow) [28]. At low temperature (much below the λ-point) there is almost no contribution of rotons in liquid helium to the heat flow, so the first mechanism is assumed to be the main in the Khalatnikov theory [14, 15]. Resistance to the heat transfer is explained by the strong mismatch of the longitudinal acoustic impedances of liquid helium $Z_1 = \rho_1 v_l$ and of the solid $Z_2 = \rho_2 c_l$, $Z_1 \ll Z_2$, due to which the transmission of acoustic thermal phonons across the superfluid helium - solid interface is strongly suppressed. Here $\rho_{1,2}$ and v_l, c_l are the densities and velocities of longitudinal (compression) acoustic waves in liquid helium and in the solid, respectively. The acoustic impedance has the value that depends only on the macroscopic properties of the material. It describes the ability of the material to pass or to resist the propagation of long acoustic waves. It is defined by the ratio of the sound pressure to particle velocity in a plane wave [28], in analogy with the electric impedance which is determined by Ohm's law.

The interfacial thermal resistance R relates the heat flux Q per area A (the flux per unit area) of the boundary between two media and the difference of materials temperatures ΔT at the interface:

$$R = \frac{A\Delta T}{Q} \ . \tag{1}$$

Instead of the resistance, the inverse value which is called the thermal boundary conductance is also introduced: $G = 1/R$.

The unidirectional heat flux from medium 1 to medium 2 in the acoustic mismatch model is written as:

$$Q_{1,2} = \sum_{\mathbf{k}} n(\omega, T_1)\hbar\omega(\mathbf{k})v_z^{(1)}D(\omega, \theta) \ . \tag{2}$$

Here $n(\omega, T_1)$ is a number of phonons in the energy state at temperature T_1 given by the Bose–Einstein statistics, $D(\omega, \theta)$ is the probability of phonon transmission through the interface as a function of frequency $\omega(\mathbf{k})$ and incidence angle θ, T_1 is temperature of media 1, $v_z^{(1)}$ is normal to the interface component of phonon group velocity in material 1, $v_z^{(1)} = v^{(1)} \cos\theta$, $\mathbf{k}$ is wave vector. For two materials in contact with the same temperature, the heat flux from the first medium to the second one is compensated by the counterflow from the second medium to the first one, and the net heat flux is zero. However, if there is no thermal equilibrium between the two media, the net heat flux from medium 1 to medium 2 can be found as a difference of the direct and reverse energy fluxes:

$$Q_{1\to 2} = Q_{1,2} - Q_{2,1}\,. \tag{3}$$

In the acoustic mismatch model, the phonons are considered as plane acoustic waves which transmit elastically (without change of frequency) across the interface, and the transmission probability D is defined by the ratio of the transmitted and incident acoustic phonon energies. In the case of normal phonon incidence, the energy transmission coefficient (probability) for the net heat flux through the interface can be written in terms of bulk acoustic impedances:

$$D = \frac{4Z_1 Z_2}{(Z_1 + Z_2)^2}\,. \tag{4}$$

If we have an interface between two strongly mismatched media like superfluid helium and the solid with $Z_2 \gg Z_1$, the energy transmission probability is $D = 4Z_1/Z_2 \ll 1$. In general, the transmission probability has rather complicated dependence on the incidence angle and frequency of the incident phonons. In order to find the heat flux through the boundary, the sum in (2) is taken over all wavevectors and the allowed incidence angles. The result presented by Khalatnikov is the following:

$$Q = \frac{\rho_1 v_l}{\rho_2}\frac{16\pi^5}{15}\frac{T^3 F}{(2\pi\hbar c_t)^3}\Delta T\,, \tag{5}$$

where $c_t \gg v_l$ is the velocity of transverse acoustic waves in the solid, the function F depends on the acoustic properties of the helium and the solid, and its value has the order of unity [15].

Therefore, the acoustic mismatch model allows to explain qualitatively the main features of the results observed by Kapitza and provide the quantitative numerical value of the heat flux through the liquid helium - solid boundary, and, consequently, of the interfacial thermal resistance.

1.2 Theory Modifications

However, it was discovered later that the value of the heat flux in the experiments is significantly higher (up to 2 or 3 orders of magnitude) than the value (5) predicted by the acoustic mismatch model, and the thermal resistance does not indicate a strong dependence on the pressure [36]. Therefore the additional factors are required to be taken into account to describe the experimentally observed heat transfer through the superfluid helium - solid interface. The proposals to bring together the theoretical calculations and experimental results include, for example, the account for the phonon damping, caused by the presence of defects in the near-surface area of the solid [4, 31], and for the presence of a layer of solid helium with a few-atomic thickness on the interface with the solid [30].

In the papers [40, 41], it was observed the enhancement of the heat flux due to near-surface absorption in the solid of the thermal acoustic phonons, incident from liquid helium, which is caused by resonance excitation of the damped surface Rayleigh waves at the liquid helium - metal interface. For the liquid helium - tungsten single crystal interface, it was shown that within a narrow cone of incidence angles, which is limited by a critical angle beyond which no phonon transmission into the solid is possible without taking into account some additional factors, there exist only bulk longitudinal and transverse waves with small coefficients of the acoustic energy transmission [40]. But for the range of incidence angles beyond the critical cone, the resonant absorption of the Rayleigh waves takes place and their contribution to the net energy transfer can be comparable with the contribution of bulk acoustic waves for the incidence angles below the critical value. The measured phonon transmission coefficients for the liquid helium - copper single-crystal interface were compared with the values computed within the dissipative acoustic theory, which takes into account the dissipation processes in the medium, and very good agreement between theoretical and experimental results was obtained [41]. Essentially, the method used by Zinov'eva et al. allows the studies of the surface modes as such, which made it possible to demonstrate experimentally the propagation of the Rayleigh surface waves and the pseudosurface (leaky) waves in the (001) and (111) surfaces of acoustically anisotropic copper single crystal [41]. As it was revealed in the studies of the energy transmission coefficient through the liquid helium - polycrystalline gold interface [34], the enhancement of sound absorption in the polycrystal leads to the increase in heat flux through the boundary due to the extension of the range of the allowed incidence angles up to $\pi/2$. In other words, it was shown that the enhanced scattering of sound by irregularities in the solid, which increases the acoustic (sound) attenuation in polycrystalline gold, also increases the interfacial thermal conductance between liquid helium and polycrystalline material.

Contribution of the damping of the surface Rayleigh wave by conduction electrons to the heat transfer through the liquid helium - metal interface was described by Andreev [5]. The calculations were performed in the two limits: when electron mean free path is significantly shorter and when it is much larger than the phonon wavelength. Only in the last case, the notable additional thermal flux has the same

order of magnitude as the total heat flux obtained in the Khalatnikov theory within the acoustic mismatch model. Furthermore, it was predicted that the damping of surface Rayleigh waves by electrons decreases and the Kapitza resistance correspondingly increases in the superconducting metal, in comparison with that in the same metal in normal state. All these predictions were confirmed experimentally [40]. In general, damped surface Rayleigh waves provide certain contribution to the heat flux through the liquid helium - solid interface, however this contribution does not change the order of the value of the Kapitza resistance.

In the paper [1], it was shown that surface roughness of a solid can increase the heat transfer and leads to the change in the pressure dependence of the interfacial thermal resistance. Physical conditions required for the geometrical-resonance scattering of thermal phonons in superfluid helium on the rough surface were studied in the recent paper by Ramiere et al. [33]. In this work the dependence of geometrical-resonance phonon scattering mechanisms on the surface roughness in the case of the interface of ultrahigh purity between single crystal silicon and superfluid helium were studied experimentally. It was shown that definite surface roughness values exist which are felt by incident phonons and which ensure the dominance of the geometrical-resonance scattering. It was also observed that the effect of the presence of a solid layer of helium at the interface results in the sharp drop in the Kapitza resistance at the solidification pressures. This decrease occurs due to the presence of transverse modes in the emerging surface layer of solid helium and in bulk silicon.

The heat transfer through the superfluid helium-solid interface is also affected by sound attenuation in thin surface layer in a solid, which leads to the possibility of the transmission into the solid of the thermal phonons in superfluid helium, that are incident at transcritical angles [16]. Moreover, a number of experimental [7, 37–39] and theoretical [2, 3] studies of the contribution of inelastic phonon processes to the heat flow through the superfluid helium - solid boundary were performed. In several works the direct measurements were carried out of the energy and angular distribution of the emitted by a solid phonons in superfluid helium. It was observed that the two channels exist, which were named as acoustic and background channels, of phonon transfer through the boundary with different ranges of emission angles. The acoustic channel exists in a narrow cone of incidence angles and is well described by the acoustic mismatch theory, while in the background channel almost all incidence angles are possible and phonon energy transfer through this channel is significantly higher than that through the acoustic channel. The increase in the background phonon emission from the heated solid to superfluid helium was considered to be a result of inelastic phonon processes at the interface. In the theoretical studies of the phonon transformation at such boundary, it was shown that there can be four inelastic three-phonon processes. The increase in the heat flux through the superfluid helium-solid boundary is related mainly with the inelastic process in which one phonon from the solid transforms into two phonons in the liquid. The effect of the two other processes, namely of the transformation of one phonon in the liquid into one phonon in the solid and one phonon in the liquid, and of the transformation of one phonon in the solid into one phonon in the solid and one phonon in the liquid, is significantly lower. Furthermore, it was conjectured that these inelastic phonon processes give

even greater contribution to the heat flux than elastic process in the solid heated up to 5 K. However, their influence decreases with decreasing the temperature and therefore they cannot explain the experimental values of the background radiation. All the proposed mechanisms are certainly important, but they still do not provide a satisfactory agreement between the experiment and theory.

2 Reflection and Transmission of an Elastic Wave at the Interface Between Two Media

One of the possible ways for implementing the significant phonon emission in liquid helium by the surface of a solid with an absorbed non-dissipative monolayer is to weaken the coupling of the monolayer with the solid surface [11]. But it should be noted that the used in Ref. [11] method for calculation of the heat exchange between liquid helium and the solid predicts an excessive enhancement in the heat transfer arising from the presence of the non-dissipative dynamic transition layer. This excess heat flux is related with the failure to account for the "response reaction" of liquid helium to the oscillations of the weakly-coupled interface layer [24]. More rigorous approach requires exact calculation of the energy reflection coefficient R for the longitudinal phonons, incident from liquid helium, as a function of frequency ω and angle of incidence θ. With the neglect of acoustic losses in superfluid helium, the phonon energy transmission coefficient from the helium into the solid is equal to $D(\omega, \theta) = 1 - R(\omega, \theta)$. The reflection R and transmission D coefficients take proper account for the dynamic interaction of the liquid helium with the surface layer.

In the present work, the resonance interaction of elastic waves with a dissipative homogeneous atomic monolayer, adsorbed on the liquid helium-solid interface, is studied. The interface layer is considered to have an internal dynamical degree of freedom, which is related with its weak coupling with the solid, see [6, 17, 21, 22, 24]. It is shown that the account for the dissipation in the interface monolayer considerably affects the phonon transport through the interface of the two different condensed media by means of the substantial extension of the range of transcritical angles of incidence, in which the transmission of thermal phonon energy through the liquid helium-solid interface is possible. In the absence of the dissipation, the cone of incidence angles, in which the transfer of phonon energy occurs, is limited by the small angle of total internal reflection. Such restriction is caused by large difference of sound velocities in liquid helium and in a solid, $v_l \ll c_l$, i.e. because of the strong mismatch of acoustic impedances. It is clear that substantial extension of the allowed interval of the incidence angles will result in considerable increase of the heat flux through the interface.

We consider transfer of phonons between the media 1 and 2. The liquid helium is regarded as medium 1 and we describe it as a continuous isotropic inviscid-liquid medium, the medium 2 we describe as "isotropic" model of the silicon crystal. There-

fore we introduce the scalar $\varphi^{(1)}$, $\varphi^{(2)}$ and vector $\boldsymbol{\psi}^{(2)}$ potentials, which satisfy equations of motion $\ddot{\varphi}^{(1)} = v_l^2 \Delta\varphi$, $\ddot{\varphi}^{(2)} = c_l^2 \Delta\varphi$, $\ddot{\boldsymbol{\psi}}^{(2)} = c_t^2 \Delta\boldsymbol{\psi}$, where v_l is sound velocity in helium, c_l and c_t are velocities of longitudinal and transverse acoustic waves in the solid. Then the longitudinal and transverse particle (elastic) displacements in liquid helium and in the solid can be decomposed in general as:

$$\mathbf{u}^{(1,2)} = grad\varphi^{(1,2)} + curl\boldsymbol{\psi}^{(1,2)}. \tag{6}$$

Since only longitudinal waves can propagate in superfluid helium, the vector potential $\boldsymbol{\psi}^{(1)}$ is zero, whereas both the scalar and vector potentials are nonzero in the solid:

$$\varphi^{(1)} = e^{ik_1(\cos\theta z + \sin\theta x) - i\omega t} + re^{ik_1(-\cos\theta z + \sin\theta x) - i\omega t}, \tag{7}$$

$$\psi^{(1)} = 0, \tag{8}$$

$$\varphi^{(2)} = d_l e^{ik_l(\cos\theta_l z + \sin\theta_l x) - i\omega t}, \tag{9}$$

$$\psi^{(2)} = d_t e^{ik_t(\cos\theta_t z + \sin\theta_t x) - i\omega t}. \tag{10}$$

Here r is the refection amplitude of the longitudinal (sound) wave in liquid helium which is incident on the interface, $d_{l,t}$ are the transmission amplitudes for longitudinal and transverse acoustic waves in the solid, $k_1 = \omega/v_l$, $k_{l,t} = \omega/c_{l,t}$ are bulk wavenumbers for the corresponding waves in the media 1 and 2, ω is a frequency of the incident phonons, θ and $\theta_{l,t}$ are the incidence angle in helium and propagation angles of longitudinal and transverse elastic waves in the solid, respectively; all the angles are measured from the normal to the interface between the media. The values of the reflection and transmission amplitudes give the information about the portion of the acoustic wave energy that is reflected, transmitted or absorbed due to discontinuity between the media and the presence of the dissipative adsorbed layer. In the present study, the role of the discontinuity is played by the boundary between two acoustically mismatched media.

We assume that the two-dimensional adsorbed monolayer with an internal dynamical degree of freedom is placed in the plane $z = 0$ at the interface between liquid helium ($z < 0$) and the isotropic solid ($z > 0$), and phonons are incident from the helium in the xz plane. The dynamical boundary conditions for the elastic displacements $u_i^{(1,2)}$ and bulk stresses $\sigma_{ik}^{(1,2)}$ in the media 1 and 2 are obtained by equating to zero the variation of the surface free energy, see [6, 20–22],

$$F_s = 0.5A_{ik}^{(1)}(u_i^{(s)} - u_i^{(1)})(u_k^{(s)} - u_k^{(1)}) + 0.5A_{ik}^{(2)}(u_i^{(s)} - u_i^{(2)})(u_k^{(s)} - u_k^{(2)}), \tag{11}$$

together with the bulk equations of motion $\rho^{(1,2)}\ddot{u}_i = \partial\sigma_{ik}^{(1,2)}/\partial x_k$, which results in the following set of discontinuity equations for the elastic stresses and displacements at the interface plane $z = 0$:

$$\sigma_{zz}^{(1)} - \sigma_{zz}^{(2)} = -\rho_s \frac{\partial^2}{\partial t^2} u_z^{(s)} , \tag{12}$$

$$-\sigma_{zx}^{(2)} = -\rho_s \frac{\partial^2}{\partial t^2} u_x^{(s)} , \tag{13}$$

$$\sigma_{zz}^{(1)} = A_{zz}^{(1)} \left(u_z^{(s)} - u_z^{(1)} \right) , \tag{14}$$

$$\sigma_{zz}^{(2)} = A_{zz}^{(2)} \left(u_z^{(2)} - u_z^{(s)} \right) , \tag{15}$$

$$\sigma_{zx}^{(2)} = A_{zx}^{(2)} \left(u_x^{(2)} - u_x^{(s)} \right) . \tag{16}$$

Here $u_i^{(s)}$ is the elastic displacement of the absorbed interface monolayer, ρ_s is the positive surface mass which is equal to the total mass of the absorbed atoms per unit area of the interface, $A_{ik}^{(1,2)}$ is the tensor of force constants describing the interlayer elastic interaction between the atoms of the interface monolayer and the contacting continuous media [6, 20–22]. It should be noted that $A_{ik}^{(2)}$ is in general a complex tensor which accounts for the dissipation caused by the coupling of the adsorbed monolayer with the solid [17, 23]:

$$A_{ik}^{(2)} = A'^{(2)}_{ik} - i\omega B_{ik}^{(2)} , \tag{17}$$

where $B_{ik}^{(2)}$ is a tensor of the dissipative constants of the adsorbed monolayer, similar in some sense to the viscosity tensor in bulk of a solid [25].

In terms of the vector and scalar potentials, the elastic displacements in the contacting media (1) and (2) can be written as the following:

$$u_z^{(1)} = \frac{\partial \varphi^{(1)}}{\partial z} , \tag{18}$$

$$u_z^{(2)} = \frac{\partial \varphi^{(2)}}{\partial z} + \frac{\partial \psi^{(2)}}{\partial x} , \tag{19}$$

$$u_x^{(1)} = \frac{\partial \varphi^{(1)}}{\partial x} , \tag{20}$$

$$u_x^{(2)} = \frac{\partial \varphi^{(2)}}{\partial x} - \frac{\partial \psi^{(2)}}{\partial z} . \tag{21}$$

Elastic displacements for longitudinal and transverse waves in adsorbed monolayer have the form:

$$u_z^{(s)} = u_{0z} e^{ik_1 \sin\theta x - i\omega t} , \tag{22}$$

$$u_x^{(s)} = u_{0x} e^{ik_1 \sin\theta x - i\omega t} . \tag{23}$$

Using the boundary conditions (12)–(16) and the form of the bulk displacements (18)–(21), the expressions for the reflection r and transmission $d_{l,t}$ amplitudes for longitudinal and transverse waves in Eqs. (7)–(10) and the values of the surface displacements (22) and (23), caused by the incident wave, can be obtained:

$$\begin{aligned} r = \tfrac{1}{\Delta}\Big[&\alpha\left(2\rho_2 c_t^2 k_x^2 - \rho_2 c_t^2 k_l^2 - i A_{zz}^{(2)} k_l \cos\theta_l\right)\beta_- - \alpha A_{zz}^{(2)} k_1 k_l^2 \rho_2 \times \\ &\times \left(c_l^2 - 2c_t^2 \sin^2\theta_l\right)\left(-\rho_1 k_1 v_l^2 + i A_{zz}^{(1)} \cos\theta\right) + \\ &+ \left(\omega^2 \rho_s k_x \gamma_l - 2A_{zx}^{(2)} \rho_2 c_t^2 k_x k_l \cos\theta_l\right) \times \\ &\times \left\{k_x \gamma_t \beta_- + 2A_{zz}^{(2)} \rho_2 c_t^2 k_1 k_x k_t \cos\theta_t \left(-\rho_1 k_1 v_l^2 + i A_{zz}^{(1)} \cos\theta\right)\right\}\Big], \end{aligned} \tag{24}$$

$$d_l = -\frac{i\alpha A_{zz}^{(1)} A_{zz}^{(2)} \rho_2 v_l^2 k_1^3 \cos\theta}{\Delta}, \tag{25}$$

$$d_t = -\frac{2i A_{zz}^{(1)} A_{zz}^{(2)} \rho_1 k_1^3 v_l^2 \cos\theta}{\Delta}\left(-\omega^2 \rho_s \gamma_l + 2\rho_2 A_{zx}^{(2)} c_t^2 k_l \cos\theta_l\right), \tag{26}$$

$$u_{0x} = \frac{2A_{zz}^{(1)} A_{zz}^{(2)} A_{zx}^{(2)} \rho_1 \rho_2 v_l^2 c_t^2 k_x k_t k_1^3 \cos\theta}{\Delta}\left(k_t \cos 2\theta_t - 2k_l \cos\theta_l\right), \tag{27}$$

$$\begin{aligned} u_{0z} = \frac{2i A_{zz}^{(1)} v_l^2 k_1^3 \rho_1 \cos\theta}{\Delta}\Big[&\alpha\left\{2\rho_2 c_t^2 k_x^2 - \rho_2 c_t^2 k_l^2 - i A_{zz}^{(2)} k_l \cos\theta_l\right\} + \\ &+ k_x \gamma_t \left\{\omega^2 \rho_s \gamma_l + 2A_{zx}^{(2)} \rho_2 c_t^2 k_l k_x \cos\theta_l\right\}\Big], \end{aligned} \tag{28}$$

$$\begin{aligned} \Delta = \Big[&\alpha\left(2\rho_2 c_t^2 k_x^2 - \rho_2 c_t^2 k_l^2 - i A_{zz}^{(2)} k_l \cos\theta_l\right)\beta_+ - \alpha A_{zz}^{(2)} k_1 k_l^2 \rho_2 \times \\ &\times \left(c_l^2 - 2c_t^2 \sin^2\theta_l\right)\left(\rho_1 k_1 v_l^2 + i A_{zz}^{(1)} \cos\theta\right) + \\ &+ \left(\omega^2 \rho_s k_x \gamma_l - 2A_{zx}^{(2)} \rho_2 c_t^2 k_x k_l \cos\theta_l\right) \times \\ &\times \left\{k_x \gamma_t \beta_+ + 2A_{zz}^{(2)} \rho_2 c_t^2 k_1 k_x k_t \cos\theta_t \left(\rho_1 k_1 v_l^2 + i A_{zz}^{(1)} \cos\theta\right)\right\}\Big]. \end{aligned} \tag{29}$$

Here the following notations are used to simplify the above expressions:

$$\gamma_l = \left(2\rho_2 k_l c_t^2 \cos\theta_l + i A_{zx}^{(2)}\right), \tag{30}$$

$$\gamma_t = \left(2\rho_2 k_t c_t^2 \cos\theta_t + i A_{zz}^{(2)}\right), \tag{31}$$

$$\alpha = -\omega^2 \rho_s k_t \left(k_t \rho_2 c_t^2 \cos 2\theta_t + i A_{zx}^{(2)} \cos\theta_t\right) + A_{zx}^{(2)} \rho_2 k_t^2 c_t^2 \cos 2\theta_t, \tag{32}$$

$$\beta_{\{+,-\}} = \pm A_{zz}^{(1)} \rho_1 v_l^2 k_1^2 - \rho_s \omega^2 k_1 \left(\pm \rho_1 v_l^2 k_1 + i A_{zz}^{(1)} \cos\theta\right), \tag{33}$$

$$k_x = k_1 \sin\theta = k_l \sin\theta_l = k_t \sin\theta_t. \tag{34}$$

Equation (34) reflects the conservation law of the tangential to the interface component of the phonon momentum.

We neglect the bulk dissipation of thermal phonons in superfluid helium and in the solid, and, therefore, the transmission coefficient of the acoustic energy or the transmission probability through the interface is equal to $D = 1 - R = 1 - |r|^2$, where $R = |r|^2$ is the reflection coefficient for the acoustic energy of the phonon, incident from liquid helium on the silicon surface. This is also valid when the acoustic losses in the solid are taken into account [41], but we neglect them because our calculations show that the dissipation in the adsorbed monolayer has much stronger effect on the transmission of thermal phonons through the interface.

The parameters, that are used in the expressions for the boundary conditions and which characterize the adsorbed monolayer, are expressed in terms of the macroscopic parameters of the media 1 and 2 as follows:

$$A_{zz}^{(1)} = \rho_1 v_l^2 / a \,, \tag{35}$$

$$A_{zz}^{(2)} = \sqrt{\rho_1 v_l^2 \rho_2 c_l^2}/6a(1 - i(\omega/\omega_{max})b^{(2)}) \,, \tag{36}$$

$$A_{zx}^{\prime(2)} = \sqrt{\rho_1 v_l^2 \rho_2 c_l^2}/24a(1 - i(\omega/\omega_{max})b^{(2)}) \,, \tag{37}$$

$$\rho_s = 6a\sqrt{\rho_1 \rho_2} \,, \tag{38}$$

where $b^{(2)}$ is a dimensionless reduced dissipative parameter of the 2D adsorbed monolayer, cf. Eq. (17), $\omega_{max} = v_l \pi / a$ is the maximum acoustic phonon frequency in liquid helium, $a \approx 3$Å is the interatomic spacing in liquid helium and the assumed thickness of the interface layer. The parameter $b^{(2)}$ determines the quality factor of the oscillations of the adsorbed atoms, $Q \approx \omega_{max}/(\omega b^{(2)})$, and its value can be deduced from the data on the sliding friction at incommensurate monolayer coverage of the solid surface by the corresponding atoms, see, e.g., Ref. [29]. The value of the coupling constant $A_{zz}^{(1)}$ is taken to be close to the value of the effective interparticle force constant in liquid helium. The value of the coupling constant $A_{zz}^{\prime(2)}$ (and of $A_{zx}^{\prime(2)}$) is taken larger than $A_{zz}^{(1)}$ but weaker than the effective interparticle force constant in the solid: $A_{zz}^{(1)} \ll A_{zz}^{\prime(2)} \ll \rho_2 c_l^2 / a$. Such values of the coupling constants ensure the possibility of resonance enhancement of phonon transmission through the interface with the weakly-bonded intermediate ultrathin layer [19, 21, 22], see also the discussion of resonance phonon transmission at the end of this section.

In the absence of the dissipation in the interface layer and without dissipative effects in the solid, which result in the absorption of the surface Rayleigh waves, phonon transmission through the interface can be realized only for the angles of incidence up to the critical one which is defined as $\theta_{cr} = \arcsin(v_l/c_t) \approx 0.048$ rad for transverse wave. The total phonon reflection takes place for $\theta > \theta_{cr}$ (for transcritical incidence angles) as it is described by the vector model of the solid for the interaction between phonons in liquid helium and the boundary of the solid with a

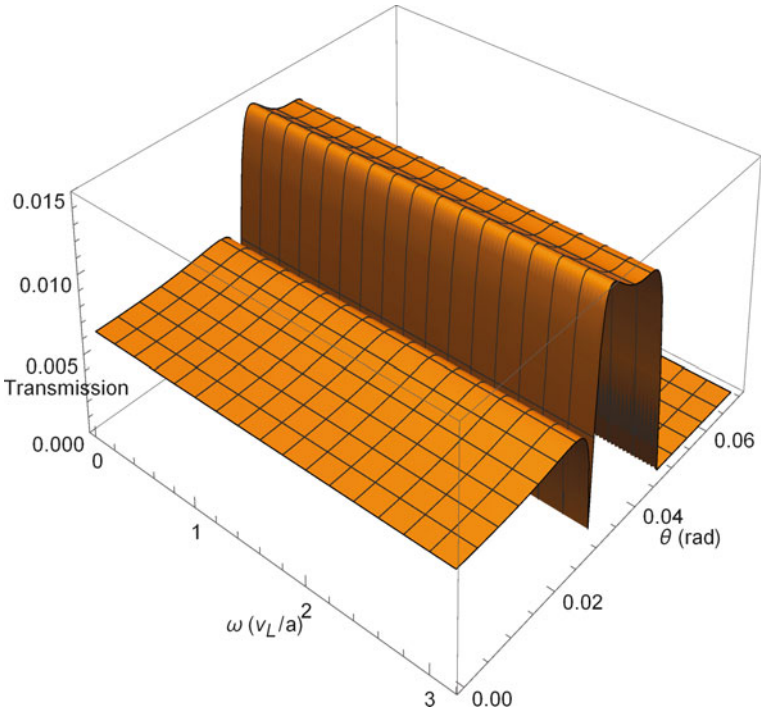

Fig. 1 Energy transmission coefficient as a function of the angle of incidence θ and frequency ω of the phonon incident from liquid helium onto an atomically clean silicon surface

dynamical non-dissipative surface layer. This effect can be clearly seen in Figs. 1 and 2, where the energy transmission coefficient as a function of the angle and frequency of an incident phonon is given for "optimal" coupling parameters described above, which realize high transmission coefficient in the presence of the dynamical interface layer. As one can see in these figures, the total reflection takes place at the liquid helium - solid interface, both with and without dynamical non-dissipative impurity monolayer, at the critical angle of incidence for longitudinal waves, with the value $\theta_l = \arcsin(v_l/c_l) \approx 0.03\,\text{rad}$.

Here liquid helium is considered to have the density $\rho_1 = 0.125\,\text{g/cm}^3$, sound (longitudinal wave) velocity $v_l = 240\,\text{m/s}$ and zero transverse wave velocity. In the isotropic silicon crystal, the longitudinal and transverse elastic wave velocities are $c_l = 8\,\text{km/s}$ and $c_t = 5\,\text{km/s}$, respectively, and the density is $\rho_2 = 2.33\,\text{g/cm}^3$. Therefore, the acoustic impedance of liquid helium is very small in comparison with the acoustic impedance of the silicon crystal, and the resonance vibration frequency $\omega_0 = \sqrt{A'^{(2)}_{zz}/\rho_s}$ of the dynamical interface monolayer is determined only by the coupling constant between the absorbed monolayer and the solid [22].

The account for the dissipation in the interface layer leads to the decrease of the reflection coefficient R for transcritical incidence angles. This results in the transfer

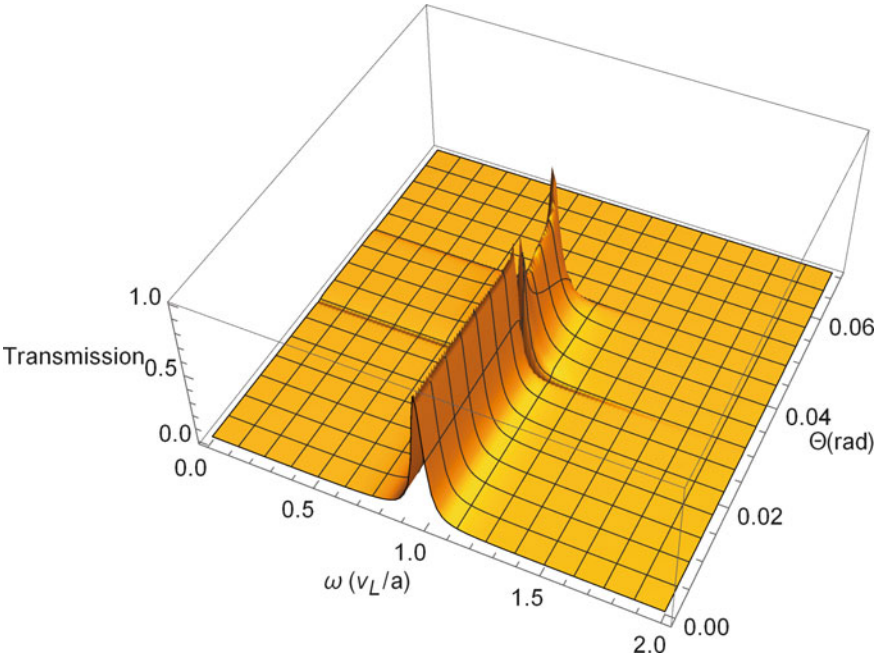

Fig. 2 Energy transmission coefficient as a function of the angle of incidence θ and frequency ω of a phonon incident from liquid helium onto a silicon surface with a dynamical non-dissipative impurity monolayer

of the energy of thermal phonons from superfluid helium into the solid, mediated by the dissipation in the interface layer. Since we can safely neglect phonon losses in superfluid helium, the transmission coefficient for the transcritical incidence angles coincides with surface absorption $A = 1 - R$.

In Fig. 3 we show the dependence of the surface absorption coefficient $A = 1 - R$ as a function of the reduced dissipative parameter $b^{(2)}$ and frequency ω for thermal phonons in superfluid helium, incident on the interface at the transcritical angle $\theta = 0.06$ rad. As one can see in this figure, there is no more phenomenon of the total wave reflection for transcritical incidence angles in the presence of interface adsorbed monolayer with the dissipative dynamics. With the increase of the dissipative parameter beyond the one that realizes the maximal surface absorption, the value of the transmission coefficient $D = A$ decreases, thus the introduction of the dissipative parameter $b^{(2)}$ larger than that in the absorption peak does not lead to further increase in the non-reflective properties of the interface. This feature is related with the property that under certain conditions the surface absorption can reach the magnitude close to unity for the transcritical incidence angle, when $A \approx 1$. This phenomenon is similar to the predicted earlier anomalous (total) absorption of bulk acoustic wave by a monolayer of the atoms with dissipative dynamics, adsorbed on a free surface of a crystal [17]. Figure 3 shows that when the dimensionless dissipative parameter $b^{(2)}$ is close to that corresponding to maximal absorption, the sharp

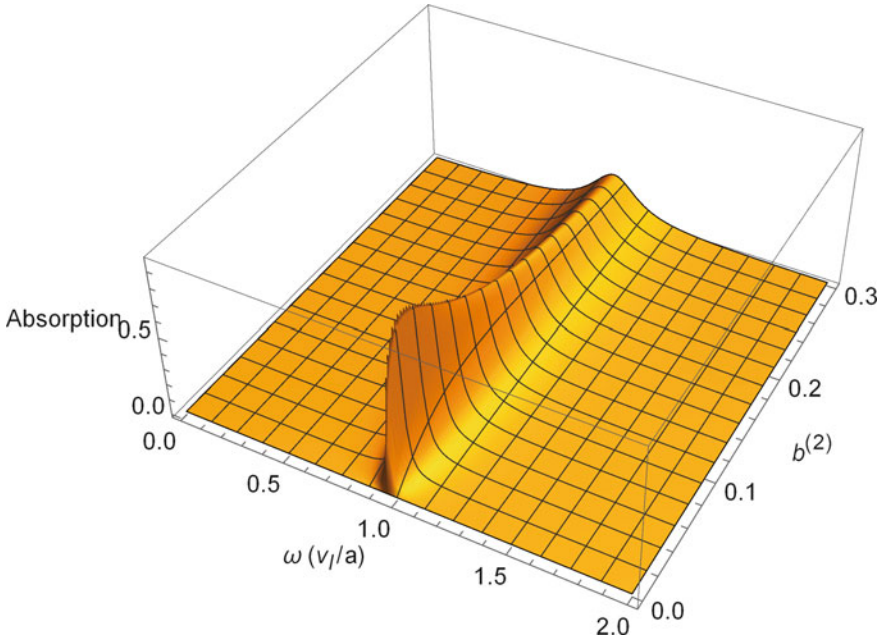

Fig. 3 Surface absorption A as a function of frequency ω and dimensionless reduced dissipative parameter $b^{(2)}$ of the dynamical adsorbed monolayer for the phonons in superfluid helium, incident on the interface at the transcritical angle $\theta = 0.06\,\text{rad}$

increase in the surface absorption at the liquid helium-solid interface is clearly seen. This feature demonstrates the high sensitivity of the heat-transfer properties of the superfluid helium - solid boundary to small variations in dissipative properties of the adsorbed monolayer. It is interesting that the changes in surface absorption occurring after the reaching by $b^{(2)}$ of the absorption peak in Fig. 3 are not so dramatic in contrast to the changes in the absorption before the peak reaching for the same interval of values of the dissipative parameter $b^{(2)}$, and the decay in surface absorption with the increase of $b^{(2)}$ beyond the peak value is moderate.

In order to realize the high transmission through the interface of two strongly mismatched media, the impedance of the thin intermediate layer for the longitudinal waves, $Z_0 = \sqrt{\rho_s A'^{(2)}_{zz}}$, must satisfy the acoustic transparency condition [21, 22]:

$$Z_0 = \sqrt{Z_1 Z_2}\,, \tag{39}$$

see also Eqs. (36) and (38). As one can see in Eq. (39), the impedance Z_0 is independent on the thickness of the interfacial layer. The acoustic transparency condition is analogous to the condition for the anti-reflective coating in optics: $n_0 = \sqrt{n_1 n_2}$, where n_0 is the refractive index of the intermediate layer, $n_{1,2}$ are the refractive indexes for the two media in contact [10].

2.1 Heat Transfer Trough the Liquid Helium-Solid Meta-interface

The net heat flux from liquid helium to the solid through the unit area is defined as

$$W = \int n\,(\hbar\omega/k_B T)\hbar\omega v_l \cos\theta\, D(\omega,\theta)\frac{d^3k}{(2\pi)^3}\,. \tag{40}$$

The thermal conductance $G(T)$ is correspondingly given by:

$$G(T) = \int \frac{\partial n\,(\hbar\omega/kT)}{\partial T}\hbar\omega v_l \cos\theta\, D(\omega,\theta)\frac{d^3k}{(2\pi)^3}\,, \tag{41}$$

where n is the Bose–Einstein distribution, $D(\omega,\theta) = 1 - |r(\omega,\theta)|^2$ is the phonon transmission coefficient through the interface between two media. The transmission coefficient has a complex dependence on the frequency and angle of incidence, and the integration over them is required. For instance, in resonance with the natural vibrations of the adsorbed non-dissipative monolayer the transmission coefficient is a function of the angle of incidence and for the normal incidence is defined only by the acoustic impedances of the two media and interface layer [22]:

$$D = \frac{4Z_1Z_2Z_0^2}{(Z_1Z_2 + Z_0^2)^2}\,. \tag{42}$$

This equation shows that the transmission coefficient indeed reaches unity, $D = 1$, under the condition (39).

The integral over the frequencies in Eq. (41) is taken up to a maximum oscillation frequency of phonons in liquid helium $\omega_{max} = v_l\pi/a$, and the integral over incidence angles is taken from zero up to $\pi/2$. In Figs. 4 and 5 we show the ratio of the conductance G_{imp} in the presence of the interface layer to the conductance G_{pure} in the case of the atomically clean liquid helium - silicon interface. Here Fig. 4 shows the ratio for the non-dissipative dynamical adsorbed monolayer, and Fig. 5 shows the ratio for the adsorbed monolayer with dissipative dynamics.

As one can see in these figures, there is a significant increase of the ratio of the conductances, by 3 orders of magnitude close to the characteristic "resonance" temperature and by 2 orders of magnitude above this temperature, in the presence of the adsorbed monolayer with dissipative dynamics, while the adsorbed monolayer without dissipative processes in it gives an increase up to one order of magnitude in the resonance. This effect characterizes the interface with the adsorbed monolayer with dissipative dynamics as the meta-interface, which has anomalously high absorption properties. Figures 4 and 5 also show that the temperature of the maximum of the conductances ratio G_{imp}/G_{pure} (the "resonance" temperature) is below 2 K, when liquid helium is superfluid, both for dissipative and non-dissipative interface layer. So, even at higher temperatures than the "resonance" one there is no quantitative coincidence

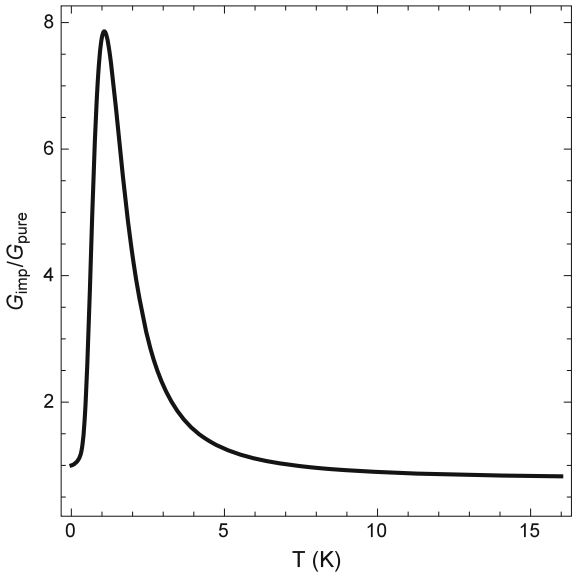

Fig. 4 Ratio of the conductances G_{imp}/G_{pure} as a function of temperature in the presence of non-dissipative dynamical adsorbed monolayer on the silicon surface

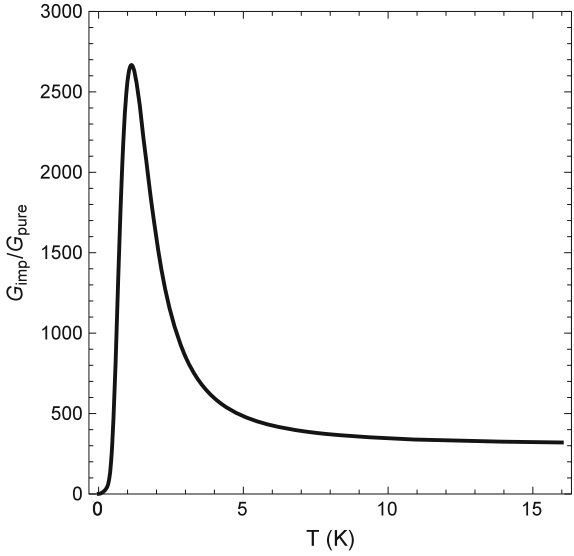

Fig. 5 Ratio of the conductances G_{imp}/G_{pure} as a function of temperature in the presence on the silicon surface of the dissipative dynamical adsorbed monolayer with $b^{(2)} = 0.05$

of the heat-transfer properties for the interfaces with dissipative dynamical adsorbed monolayer and without it. At the same time, for the non-dissipative interfacial monolayer of adsorded atoms the ratio of the conductances G_{imp}/G_{pure} is close to unity for temperatures approximately above 5 K, thus identifying the absence of the effect of the presence of the adsorbed monolayer as the media are being heated. The main factors of the strong influence of the dissipative meta-layer on the heat transfer is the

weak coupling of the monolayer with the solid, $A_{zz}^{(1)} \ll A'^{(2)}_{zz} \ll \rho_2 c_l^2/a$, in combination with the large surface mass $\rho_s > m_{He}/a^2$, where m_{He} is a mass of helium-4 atom, and the transfer of thermal phonon energy through the meta-interface at transcritical incidence angles, which is not possible in the case of absence of dissipation in the monolayer and in the solid.

It is clear that for a significant increase in the thermal phonon flux through the interface, anharmonic phenomena start to play a considerable role in vibrational dynamics of the adsorbed monolayer. Generally, the large thermally-excited mean-square fluctuations of atomic displacements $\langle u_\perp(T)^2\rangle$ and $\langle u_\parallel(T)^2\rangle$ in the weakly-coupled with a solid monolayer generate *nonlinear* phonon transmission at the multiple (second and third) harmonics - for the transmission from liquid helium to the solid, and at the sub-harmonic (one-half and one-third) frequencies - for the transmission from the solid to liquid helium [18]. These nonlinear effects can be described, respectively, by the additional cubic, $\propto (u_z^{(s)} - u_z^{(2)})^3$, and quartic, $\propto (u_z^{(s)} - u_z^{(2)})^4$, anharmonic terms in the surface free energy (5), describing the *nonlinear coupling* of the adsorbed monolayer with the solid, see also [18]. Apparently these effects, caused by the anharmonic intermediate ultrathin layer, increase the thermal phonon transfer across the interface between two media with very different vibrational spectra and strong mismatch of acoustic impedances and contribute to the dissipative properties of the interface monolayer. The presence of the dynamical anharmonic atomic layer at the meta-interface between two media with very different acoustic impedances, including the boundary between the liquid helium and a solid, also leads to the *nonreciprocity* of the transmission of thermal phonons across the interface: the heat flux through the interface with a given temperature difference depends on the *polarity* of the difference.

3 Summary

The interface thermal resistance observed by P. L. Kapitza for the superfluid helium - solid body boundary still remains the interesting subject to study. Two fundamental theories - the acoustic mismatch model and the diffuse mismatch model - do not able to provide enough qualitative and quantitative agreement with the experimental data and between each other. Therefore, this problem gives an origin for the plenty of theoretical and experimental works on the properties of the interfaces between two media in order to improve the proposed models and extend them to explore not only the interface between liquid helium and a solid, but other interfaces between different materials as well. The considerable attention in these studies is dedicated to the account of various additional factors, processes and conditions which might have influence on the dependence of the thermal boundary conductance on temperature and pressure.

We show that the dynamics of the ultrathin adsorbed monolayer with an internal degree of freedom at the superfluid helium - solid interface results in significant increase of the transmission of thermal phonons through the interface. Such

enhancement of phonon transmission occurs due to the presence of dissipation in the dynamics of the meta-interface atomic monolayer, which makes possible the transmission of the energy of thermal phonons from superfluid helium to the solid at all angles of incidence, including the transcritical incidence angles, and due to the nonlinear phonon transmission through the interface at multiple harmonics and at sub-harmonic frequencies, which contributes in turn to the dissipative properties of the adsorbed monolayer.

References

1. Adamenko, I.N., Fuks, I.M.: Roughness and thermal resistance of the boundary between a solid and liquid helium. Zh. Eksp. Teor. Fiz. **59**, 2071–2082 (1970)
2. Adamenko, I.N., Nemchenko, E.K.: Phonon transformation at the superfluid helium-solid interface. Fiz. Nizk. Temp. **39**, 975–985 (2013)
3. Adamenko, I.N., Nemchenko, E.K.: Interaction of phonons at superfluid helium-solid interfaces. Condens. Matter Phys. **17**, 13602-1–13602-9 (2014)
4. Anderson, A.C., Johnson, W.L.: The Kapitza resistance between copper and ^{3}He. J. Low Temp. Phys **7**, 1–21 (1972)
5. Andreev, A.F.: The effect of conducting electrons on the Kapitza temperature jump. Zh. Eksp. Teor. Fiz. **43**, 1535–1542 (1962)
6. Boiko, V.S., Kosevich, A.M., Kosevich, Yu.A.: Effect of reversible plasticity of superconductors on their physical properties (Review Article). Sov. J. Low Temp. Phys. **17**, 1–18 (1991)
7. Crisp, G.N., Sherlock, R.A., Wyat, A.F.G.: Energy transfer between a solid and helium by excited atoms. In: Challis, L.J., Rampton, V.M., Wyatt, A.F.G. (eds.) Phonon Scattering in Solids, pp. 21–23. Plenum Press, New York (1976)
8. Duda, J.C., Smoyer, J.L., Norris, P.M., Hopkins, P.E.: Extension of the diffuse mismatch model for thermal boundary conductance between isotropic and anisotropic materials. Appl. Phys. Lett. **95**, 031912-1–031912-3 (2009)
9. Duda, J.C., Beechem, T., Smoyer, J.L., Norris, P.M., Hopkins, P.E.: Role of dispersion on phononic thermal boundary conductance. J. Appl. Phys. **108**, 073515-1–073515-10 (2010)
10. Furman, S.A., Tikhonravov, A.V.: Basics of Optics of Multilayer Systems. Edition Frontieres, Gif-sur-Yvette (1992)
11. Gelfgat, I.M., Syrkin, E.S.: To the theory of Kapitza jump. Fiz. Nizk. Temp. **4**, 141–147 (1978)
12. Hopkins, P.E., Beechem, T., Duda, J.C., Hattar, K., Ihlefeld, J.E., Rodriguez, M.A., Piekos, E.S.: Influence of anisotropy on thermal boundary conductance at solid interfaces. Phys. Rev. B **84**, 125408-1–125408-7 (2011)
13. Kapitza, P.L.: Research of a mechanism of the heat transmission in helium-II. Zh. Eksp. Teor. Fiz. **11**, 1–31 (1941)
14. Khalatnikov, I.M.: Heat exchange between a solid body and helium II. Zh. Eksp. Teor. Fiz. **22**, 687–704 (1952)
15. Khalatnikov, I.M.: An Introduction to the Theory of Superfluidity. Westview Press, New York (2000)
16. Khalatnikov, I.M., Adamenko, I.N.: Theory of the Kapitza temperature discontinuity at a soid body-liquid helium boundary. Zh. Eksp. Teor. Fiz. **63**, 746–753 (1972)
17. Kosevich, Yu.A.: Anomalous absorption of an acoustic wave by a two-dimensional adsorbed layer on the surface of a solid. Sov. Phys. Solid State **33**, 1467–1468 (1991)
18. Kosevich, Yu.A.: Fluctuation subharmonic and multiharmonic phonon transmission and Kapitza conductance between crystals with very different vibrational spectra. Phys. Rev. B **52**, 1017–1024 (1995)

19. Kosevich, Yu.A.: Multichannel propagation and scattering of phonons and photons in low-dimension nanostructures. Phys. Uspekhi **51**, 848–859 (2008)
20. Kosevich, Yu.A., Syrkin, E.S.: Capillary phenomena and elastic waves localized near a plane crystal defect. Phys. Lett. A **122**, 178–182 (1987)
21. Kosevich, Yu.A., Syrkin, E.S.: Resonant interaction of elastic waves with a planar crystal defect. Sov. Phys. Solid State **33**, 1156–1157 (1991)
22. Kosevich, Yu.A., Syrkin, E.S.: Macroscopic dynamics of the interface between crystals and total resonance transmission of phonons. Low Temp. Phys. **20**, 517–521 (1994)
23. Kosevich, Yu.A., Syrkin, E.S.: Dissipative interaction and anomalous surface absorption of bulk phonons at a two-dimensional defect in a solid. Phys. Lett. A **251**, 378–386 (1999)
24. Kosevich, Yu.A., Syrkin, E.S., Tkachenko, O.Yu.: Transmission of quasiparticle excitations through interfaces between two media (Review Article). Fiz. Nizk. Temp. **42**, 777–786 (2016)
25. Landau, L.D., Lifshitz, E.M.: Theory of Elasticity. Pergamon Press, Oxford (1986)
26. Landry, E.S., McGaughey, A.J.H.: Effect of film thickness on the thermal resistance of confined semiconductor thin films. J. Appl. Phys. **107**, 013521-1–013521-8 (2010)
27. Little, W.A.: The transport of heat between dissimilar solids at low temperatures. Can. J. Phys. **37**, 334–349 (1959)
28. Meyer, E., Neumann, E.G.: Physical and Applied Acoustics: An Introduction. Academic Press, New York (1972)
29. Persson, B.N.J.: Sliding Friction: Physical Principles and Applications. Springer, Berlin (2000)
30. Peterson, R.E., Anderson, A.C.: The Kapitza thermal boundary resistance. J. Low Temp. Phys **11**, 639–665 (1973)
31. Pollak, G.L.: Kapitza resistance. Rev. Mod. Phys. **41**, 48–81 (1969)
32. Prasher, R.S.: Thermal boundary resistance and thermal conductivity of multiwalled carbon nanotubes. Phys. Rev. B **77**, 075424-1–075424-11 (2008)
33. Ramiere, A., Volz, S., Amrit, J.: Thermal resistance at a solid/superfluid helium interface. Nat. Mater. **15**, 512–516 (2016)
34. Shvetsov, I.N., Zinov'eva, K.N.: Propagation of sound across an interface between liquid helium and polycrystalline gold. Zh. Eksp. Teor. Fiz. **105**, 886–897 (1994)
35. Stevens, R.J., Zhigilei, L.V., Norris, P.M.: Effects of temperature and disorder on thermal boundary conductance at solid-solid interfaces: nonequilibrium molecular dynamics simulations. Int. J. Heat Mass Transf. **50**, 3977–3989 (2007)
36. Swartz, E.T., Pohl, R.O.: Thermal boundary resistance. Rev. Mod. Phys. **61**, 605–668 (1989)
37. Wyatt, A.F.G., Crisp, G.N.: Frequency of phonons emitted into liquid He by a solid. J. Phys. Colloq. **39**, C6-244–C6-245 (1978)
38. Wyatt, A.F.G., Page, G.J., Sherlock, R.A.: Angular acceptance of phonons in ^{4}He by NaF. Phys. Rev. Lett. **36**, 1184–1187 (1976)
39. Wyatt, A.F.G., Sherlock, R.A., Allum, D.R.: The temperature of phonon pulses injected into liquid ^{4} He. J. Phys. C. **15**, 1897–1916 (1982)
40. Zinov'eva, K.N.: Peculiarities of acoustic energy transmission from liquid helium to metals (Review Article). Fiz. Nizk. Temp. **23**, 485–498 (1997)
41. Zinov'eva, K.N., Narmoneva, D.A., Semenov, A.S.: Resonant acoustic modes at a liquid- ^{4}He-copper interface. Zh. Eksp. Teor. Fiz. **105**, 1280–1310 (1994)

Transport Properties of Quodons in Muscovite and Prediction of Hyper-Conductivity

F. Michael Russell

Abstract The study of intrinsic localised modes in layered crystals has been advanced by the discovery that crystals of muscovite mica can naturally record small perturbations to the lattice after the crystal has grown but is still at high temperature. This led to the discovery of two types of nonlinear lattice excitations created by energetic atomic collisions that propagate great distances in flat sheets of atoms of potassium sandwiched between mirror silicate layers. One type, called a quodon, is stable and propagates along atomic chains without lateral spreading. The second type spreads laterally in the sheet about chain directions. It has recently been shown that quodons can trap and carry a positive charge at temperatures up to at least 500 °C. As the charge is transported in absence of an applied electric field it has infinite charge mobility. This leads to the prediction of lossless transmission of electricity at elevated temperatures, called hyper-conductivity. Here, studies are reported that show quodons can couple to holes and electrons. The strength of the coupling depends on the chemical composition of the crystals. Electrons are strongly coupled to quodons in calcium-rich crystals of muscovite, sometimes called brittle-mica. In crystals with negligible Ca only holes are bound strongly. This indicates that the transport properties of muscovite can be modified by local doping. Lastly, a third type of track recording process has been found in which a gas decorates the paths of energetic mobile lattice excitations. The most probable source of the gas is argon from the decay of ^{40}K.

Keywords Quodon · Muscovite mica · Charge mobility · Hyper-conductivity

F. M. Russell (✉)
Group of Nonlinear Physics, Department of Applied Physics I,
Universidad de Sevilla, ETSII, Avda Reina Mercedes s/n, 41012 Sevilla, Spain
e-mail: mikerussell@us.es

J. F. R. Archilla et al. (eds.), *Nonlinear Systems, Vol. 2*, Understanding
Complex Systems, https://doi.org/10.1007/978-3-319-72218-4_10

1 The Study of Lines in Crystals of Muscovite

The discovery in 1963 that black lines in natural crystals of muscovite held information relating to cosmic rays led to a study of the behaviour of nonlinear lattices when subject to energetic disturbances at atomic scales. After over fifty years, sometimes working alone but progressively with collaborators, the studies led to the prediction of infinite charge mobility in muscovite and to the possibility of transporting electricity without loss at any temperature up to 500 °C. The first definitive step in this protracted study began in 1967 with the finding of *Tracks in mica caused by electron showers* [8]. Since charged leptons left tracks it was expected that positrons emitted from the decay of the radioactive isotope ^{40}K of potassium in muscovite should also leave tracks. By 1985 this had been verified and led, by 1988, to unusual properties of *Positive charge transport in layered crystalline solids* [10]. This was followed in 1989 by the *Identification and selection criteria for charged lepton tracks in mica* [9]. The observation in 1993 of tracks in mica associated with nuclear recoils from ^{40}K decay, which were inconsistent with a relativistic particle origin, indicated the possible existence of stable, highly-localised, mobile nonlinear lattice excitations later to be called quodons [19]. In an attempt to explore what kinds of excitation might occur in a chain of nonlinear interacting particles in 1995 a mechanical analogue was constructed employing dipole-dipole interactions of magnets. It demonstrated the creation of a mobile, localised, discrete-particle oscillatory excitation that propagated for over 500 particle-magnets before being extinguished by air-friction. This analogue was the means by which the experimental study of the lines in muscovite crystals linked in to the extensive body of theoretical and numerical work on solitons, kinks and breathers or bions [4]. It also introduced a connection to experimental work done by a distant relative, namely Scott-Russell, on his '*Wave of translation*' [22]. The propagation of positive charge in a layered crystal, with possible relevance to the layered high T_c superconductors, prompted a study in 1996 of *Anharmonic excitations in high T_c materials* [17]. In 1997 the first of several extensive numerical studies of the properties of chains of discrete nonlinear interacting particles began with *Moving breathers in a chain of magnetic pendulums* [20]. The fact that the potassium atoms were held in place between tightly bound silicate layers suggested on-site potentials were important. Theoretical studies of possible intrinsic localised modes in anharmonic lattices in 1D and 2D arrays of discrete particles with on-site potentials pointed to quodons behaving like breathers. This led in 1998 to *Localised moving breathers in a 2D hexagonal lattice* [5]. This prompted further study in 2001 of *Breathers in cuprate-like superconductor lattices* [21]. The reality of these elusive excitations, the quodons, was demonstrated in 2007 by *Evidence for moving breathers in a layered crystal insulator at* 300 K [18]. Measurements on long tracks of quodons, some more than 20 cm in length, showed that they created secondary quodons when scattered by crystal dislocations. These secondary quodons always started with minimal track width but, while propagating, the width jumped to that typical of the parent quodon. The reason for this was unclear. To investigate if there was sufficient energy in the nuclear recoil of ^{40}K to create *A supersonic crowdion in*

mica a study was made of the charge states in the decay of ^{40}K [1, 2]. This led by late 2015 to the realisation that quodons resulting from ^{40}K decay are always created in the presence of either a hole or an electron. This suggested that quodons might trap and carry either a hole or an electron. If it held a positive charge, or hole, then magnetite was precipitated on the track; if it was an electron then epidote was formed. However, for over 30 years there was an unexplained anomaly in the measured widths of the tracks of positrons as they slowed down. The early measurements had indicated that the width of a track progressively increased to a maximum but then rapidly decreased as the positron came to rest. The puzzle was why the track width should decrease as the positron came to rest, since it was the presence of a positive charge that triggered the recording process. This was resolved in 2015 when it was found that the end of the decoration on a track was not determined by motion of the charge but by the mechanical properties of the lattice. The precipitation of magnetite forming the decoration proceeded in the directions of lattice weakness. Since it had been found, by studying the tracks of positrons in mica, that the recording process precipitated magnetite in the presence of a positive charge, the similarity of widths of quodon and positron tracks provided, in early 2015, evidence for *Charge coupling to anharmonic lattice excitations in a layered crystal at* 800 K [13]. Exploring the consequences of this finding it was realised that the transport of charge by quodons in muscovite in absence of an applied electric potential across the crystal *indicated infinite charge mobility*, which led by April 2016 to the *Prediction of hyper-conductivity* at the Nolineal 2016 meeting. At that meeting a small group of participants decided to attempt to validate the prediction by an experiment. It is now clear that hyper-conductivity is fundamentally different from super-conductivity although both involve the unique properties of layered crystals. The background to the present work and a brief historical account is given in the book entitled **Quodons in Mica** [14, 15].

2 The Decoration on Tracks of Quodons and Charged Particles with Magnetite

The study of the properties of quodons and other non-linear lattice excitations in crystals of muscovite changed significantly during early 2015 when implications of the similarity of the extent of decoration on the tracks of quodons and slow moving positrons were re-examined [11]. The decoration with the black mineral magnetite takes the form of nanometre thick ribbons of variable width. Measurements on ^{40}K positron tracks show that the average rate of energy loss is less than 5×10^4 eV/cm or about one ionisation event per 10 micron of track length. Since the tracks are continuous the perturbation triggering the recording process must depend on electronic and not ionisation events, so is localised to less than 1 nm of the flight path. Measurements had shown that the width of positron tracks was proportional to the lattice perturbation and the decoration process magnifies this by a factor of about 10^4 thereby making the tracks visible. This lateral magnification of the initial lattice per-

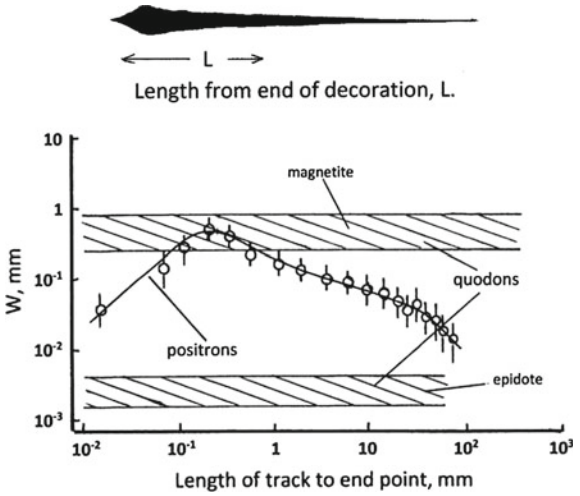

Fig. 1 Shape of typical positron track decorated with the mineral magnetite. Plot of the width of decorated tracks of positrons as they slow down compared with the average width of quodon tracks. This shows that recording process responds to quodons to the same degree as for nearly stopped positrons

turbation was found to be independent of the speed of the positrons in a given crystal. The amount of magnetite precipitated on the tracks varies from one crystal to another but the distribution along a track is, on average, the same. This is shown in Fig. 1. Was this similarity of track widths of slow moving positrons and quodons a property of the recording process or did it imply that a quodon perturbs the lattice to the same degree as a slow moving positron? When the idea of a quodon was first proposed, it was assumed that the excitation only involved relative motions of atoms within a small moving envelope [16]. Certainly, large amplitude oscillatory displacements of atoms within a quodon could create local changes in crystal potentials. Did the fact that in Fig. 1 the horizontal band of average width of decoration on quodon tracks intersected the measured width distribution curve of positrons have any significance? Might it imply that quodons could trap and carry a positive charge? If true, then it would be quite significant but there was a problem with this suggestion that hindered further study. It was known that the thickness of the ribbons of magnetite, normal to the (001)-plane, delineating tracks was approximately constant so the width of decoration should indicate the energy loss per unit length of track. The measured widths confirmed this relationship over most of the length of tracks of positrons except for the last part of less than about 0.5 mm from the supposed final rest position of a positron. The measurements indicated that in this region the extent of decoration decreased rapidly as a positron slowed to rest. This was at variance with the presumed cause of decoration, namely, the time during which a moving charge could influence a unit cell electronically to create a nucleation site. This dependence on dwell-time implied that the decoration should reach a maximum when a positron stopped and not while it was still moving. The resolution of this problem came from an unexpected direction involving chemical analyses of sheets of mica showing unusual patterns of decoration, which are now examined.

Fig. 2 Sheet used to study composition changes within a single sheet of 12 × 12 cm size and 0.5 mm thickness. The chemical analysis of the areas A, B and C is given in Table 1. The Fe content is high but there is surprisingly little variation of Fe between the different areas

In some crystals of muscovite the sensitivity of the recording process differs markedly in different regions of a sheet, as shown in Fig. 2. During the period when the recording process operates the hydrostatic pressure on a crystal should be isotropic and externally applied stresses applied to a crystal would not influence adjacent sheets inside a crystal differently. This variability of recording is unlikely to be due to a change of structure as the distribution of magnetite decoration was different in adjacent sheets cleaved from the same crystal, which showed no grain boundaries or fractures. The most probable local variable would be slight changes in the composition of a crystal. This was explored for the sheet shown in Fig. 2, which gave the results shown in Table 1.

The numbers in each column are the percentage by weight for the listed elements, the last column giving the sum-total. There are two main findings from this analysis. Firstly, all crystals showing magnetite decoration of tracks have a surprisingly high concentration of Fe. Secondly, there are only small differences in composition of the regions A, B and C. Might this point to catalytic involvement of a trace element in the recording process, such as sulphur plays in some photographic emulsions? The clear region A has lower Fe and Al and higher Si and K, these atoms being close to the K-sheets. Evidence for the reduced sensitivity of the recording process in B-type regions showing multiple 'dot-like' decorations was shown by the fading and eventual extinction of the decoration on tracks of quodons and muons as they entered such regions. When a positron is moving in the crystal the decoration follows the sequence of nucleation sites. However, when it comes to rest and annihilates it leaves a static permanent positive charge, which can trigger a lower sensitivity recording process. The ensuring accretion of magnetite strains the lattice locally so that the growth of decoration is determined by the mechanical properties of the crystal, proceeding in

Table 1 Table showing the chemical analysis of sections of a sheet showing different sensitivities for recording disturbances to the crystal. The most notable result of this analysis is that all the sheets showing decoration of tracks have about the same high concentration of Fe. The amount of Fe deposited in the decoration of tracks out of the total Fe content of muscovite ranges from less than 10^{-6} to about 10^{-4} for the most extensive decoration on fans. The regions of the first row-block correspond to the sample in Fig. 2. The last three row-blocks are for different crystals showing features of tracks decorated with magnetite. In sheets showing heavy decoration on fans, which are the tracks of laterally spreading kinks created in atomic cascades, there is significant substitution of Mg for Al (Table after Prof. J. G. Fitton from Edinburgh University)

	Sample name	SiO_2	Al_2O_3	Fe_2O_3	MgO	Na_2O	K_2O	TiO_2	MnO	LOI	$\sum$
Region B Stars & dots	Mica-01	44.89	31.73	6.45	0.85	0.10	10.353	0.275	0.077	5.00	99.73
	Mica-01	44.92	31.73	6.45	0.84	0.06	10.352	0.277	0.079	5.00	99.71
	Mica-01	44.98	31.68	6.45	0.85	0.09	10.356	0.275	0.078	5.00	99.76
Region C Quodons, etc.	Mica-02	45.54	31.16	6.44	0.93	0.08	10.489	0.269	0.075	4.89	99.88
	Mica-02	45.58	31.08	6.45	0.91	0.10	10.500	0.272	0.074	4.89	99.86
	Mica-02	45.56	31.13	6.45	0.91	0.10	10.491	0.273	0.075	4.89	99.88
Clear region Faint, good	Mica-03	45.92	31.18	6.20	0.86	0.04	10.620	0.257	0.072	4.43	99.59
	Mica-03	45.95	31.11	6.21	0.89	0.03	10.615	0.261	0.072	4.43	99.58
	Mica-03	45.95	31.13	6.20	0.89	0.06	10.616	0.264	0.073	4.43	99.62
Heavy fans	Mica-04	46.02	31.04	6.21	0.88	0.04	10.648	0.254	0.084	4.69	99.87
	Mica-04	46.04	31.02	6.21	0.89	0.02	10.658	0.257	0.082	4.69	99.87
	Mica-04	46.10	31.04	6.21	0.89	0.04	10.666	0.255	0.084	4.69	99.98
Good quodon tracks	Mica-05	46.26	29.89	6.39	1.53	n.d.	10.816	0.539	0.050	4.46	99.92
	Mica-05	46.24	29.92	6.39	1.49	n.d.	10.817	0.533	0.050	4.46	99.89
	Mica-05	46.26	29.88	6.39	1.51	n.d.	10.818	0.538	0.049	4.46	99.89
	Mica-06	45.97	30.73	6.28	1.26	n.d.	10.571	0.367	0.048	4.16	99.40
	Mica-06	45.93	30.68	6.30	1.29	n.d.	10.572	0.369	0.047	4.16	99.35
	Mica-06	46.00	30.74	6.29	1.28	n.d.	10.579	0.361	0.048	4.16	99.46

directions of lattice weakness. This is illustrated in Fig. 3. Deducting this part from the tracks showed that the rest position of a positron is at the maximum width of track. The corrected plot for the width of track of positrons as a function of distance from the stopping point is shown in Fig. 4.

This resolution of the decoration problem showed that the decoration caused by a quodon moving at near sonic speed matched that of an individual positron as it slowed to rest. Once it was realised that a quodon behaved as if it carried a positive charge it was then logical to consider how it might have trapped a charge. An analysis of the changes of charge states of potassium and daughter atoms in the several decay channels is shown in Table 2. In the dominant decay channel emitting electrons the recoil atom is positively charged. Only some of these decays will create a quodon because the component of momentum in a chain direction might be insufficient to form a quodon. In these cases, the energy is likely to be radiated as phonons leaving a stationary positive charge to trigger the magnetite recording process. This would account for the high volume-density of dots.

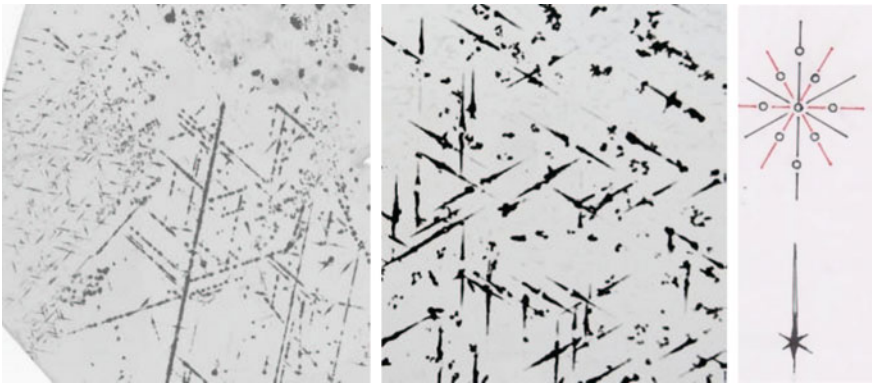

Fig. 3 The left hand side of the picture shows typical quodon tracks in the middle of the sheet, random damage spots at the upper right top and a region at the left containing many small dots of decoration; the sheet is 14 cm wide. The middle picture is an enlargement of an 8 mm wide part of the dot region. The right land side diagram shows a single dot and its relationship to the principal crystal directions. Quodons propagate in the red-line directions and the black-lines show the directions of lattice weakness. The dot region has reduced recording sensitivity but nucleation sites are provided by stationary positive charges. The two main sources of stationary positive charges are from the emission of an electron and rarely from annihilation of positrons. Precipitation on a single nucleation site proceeds in directions of lattice weakness, which are easily revealed in 'percussion figures' caused by striking a sheet with a dull point

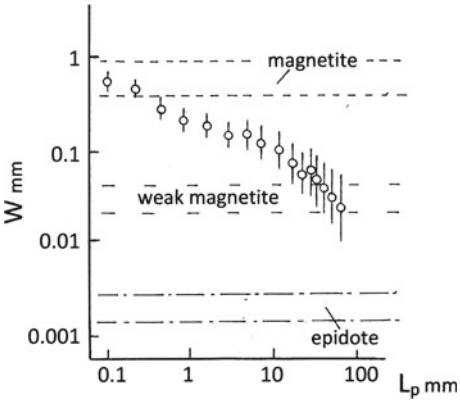

Fig. 4 Plot of the width of decoration with magnetite on tracks of positrons and quodons after allowing for the decoration due to annihilation of the positron leaving a stationary positive charge. The decoration extends mainly in the directions of lattice weakness

Until the recording processes are better understood there will continue to be some unexplained effects. For example, in many of the dots in Fig. 2 the central region is apparently not decorated and appears as a clear area. These undecorated areas might indicate significant damage to the lattice that interferes with the decoration process, perhaps by the presence of an electron. The measured thickness of the epidote ribbons shows that they extend over at least two unit cells in the direction normal to the (001)-plane. This hints at possible pathways for Fe ions to migrate slowly between adjacent K-sheets. It is very likely that such migration occurs because of the concentration of

Table 2 Table of decay channels for ^{40}K. The last row in the second column in the table shows that the dominant decay channel leaves a single positive charge on the recoiling atom as it starts to create a quodon. Reprinted with permission from [1]. Copyright (2015) by Springer

Decay	Beta-	EC1	EC1+CE[a]	EC2[b]	Beta+
Intensity	89.25%	10.55%	0.001%	0.2%	0.001%
T (keV)	1311.07	1460	1460	1504.69	483.7
Emitted charged particle	e^-	None	Shell e^-	e^- (Auger)	e^+
Recoil from	$\nu + e^-$	Gamma	Shell e^-	ν	$\nu + e^+$
Max Recoil (eV)	42	29.2(M)	49.7(M)	31.1(M)	10
Daugther	Ca^{++}	Ar^+	Ar^{++}	Ar^{++}	Ar
Max V (km/s)	14.4	12(M)	15.7(M)	12.2(M)	7
Ionization of daughter (eV)	50.6	27.7	40.8	40.8	15.8
Δq (e)	+1	0	+1	+1	−1

[a]Subset of EC1 when the gamma is delivered to a shell electron
(M) Monochromatic
[b]Direct decay to Ar ground state, with recoil from 1504.69 keV neutrino emission; 3 keV Auger e^- emitted later
EC: electron capture; CE: conversion electron; T: energy available excluding rest masses
Ionization energy of K^+ 31.6 eV

magnetite on tracks in one sheet with adjacent sheets being devoid of any decorated tracks. Accretion of magnetite on tracks to create the final widths will be a slow process relative to the creation and initial decoration of nucleation sites. Table 2 also shows that the rare emission of a positron leaves a negative charge at the site of creation of a quodon. The track of a positron can be recorded by decoration with magnetite but the negative charge on a quodon, instead of decorating with magnetite, can cause the track to be decorated with the clear mineral epidote in crystals containing some calcium. In so-called 'brittle micas' there can be up to 1% of Ca in the K sheets. Using convergent beam electron diffraction techniques, it has been shown that, contrary to magnetite decoration, the epidote delineating the quodon track is not intrusive between the silicate layers [19]. Instead, it replaces the muscovite structure to give ribbons of epidote of 3.4 nm thickness, normal to the (001)-plane, that are geometrically compatible with the surrounding muscovite. Large crystals containing significant amounts of Ca occur much less frequently than those with little Ca, such as those showing strong staining with magnetite.

3 Absence of Identifiable Electron Tracks

Although quodon tracks decorated with magnetite are associated with electron emission from ^{40}K there is no evidence for electrons leaving their paths decorated with magnetite or epidote. Nor do they leave any identifiable track decorated with another mineral. There are several contributing reasons for this absence. Electrons do not

show axial or planar channelling. When emitted they experience diffraction scattering but, in contrast to positrons, the angular distribution in the (001)-plane does not include peaks in chain directions. Instead, the probability for an electron propagating in a chain direction rapidly tends to zero. It is probable that the two recording processes are effective in proximity to the K-sheets because that is the plane of easiest cleavage. However, the progressive accretion of magnetite on the initial nucleation sites of quodon tracks arising from electron emission, leading to ribbon widths of order 1 mm, could conceal any short-range electron tracks emerging from the K-decay site. Despite these uncertainties the absence of evidence for tracks due to electrons in crystals of low Ca content suggests that they are less likely to be transported in the K-sheets than holes.

4 Migration of Argon from ^{40}K Decay

Surprisingly, a third decoration process has been found. Table 2 shows that about 10% of the decays of ^{40}K leave Argon. For many years this fact was ignored; being a noble element perhaps it migrated out of the crystals. When examining sheets of muscovite visually it often helps to observe them at near grazing angle against a white background. Sometimes the magnetite ribbons are close to a cleaved face and then appear brightly coloured because of interference of the reflected light. It was under such conditions that the sheet shown in Fig. 5 was observed. It shows regions where the lattice has been cleaved by a transparent intrusion, compatible with migration

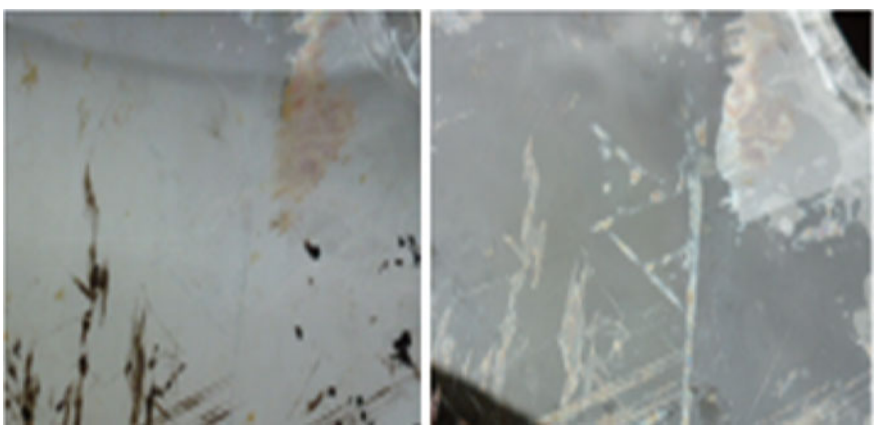

Fig. 5 Pictures of the same sheet, the left by transmission and the right by reflection. The pictures show that there is distortion of the crystal structure both in the vicinity of magnetite ribbons and elsewhere where nucleation sites have been generated. The magnetite ribbons are built from unit cells of magnetite that are intrusive between the silicate layers. That leaves voids of small volume at the edges of the ribbons. At high temperature argon atoms could migrate to those voids. Later uplift to the Earth's surface would reduce the hydrostatic pressure causing distortion of the crystal structure

of argon. The intrusive magnetite decoration forces the silicate layers apart, thereby creating small volume voids at the edges of the magnetite ribbons. These would be suitable spaces for mobile argon atoms to accumulate. Later, the argon in these voids that is initially under high pressure would cause the silicate layers to be forced apart as the hydrostatic pressure on crystals is reduced by their uplift to the Earth's surface. This accounts for the visible distortion of the sheets near ribbons as seen by reflection, which is too large to be attributed to the distortion due only to the ribbons.

5 Creation of Secondary Quodons

A notable property of quodons with track widths indicative of a positive charge is their ability to create secondary quodons. The distance between successive secondary quodon tracks is random, consistent with scattering at dislocations. It is assumed that since quodons can propagate more than 10^9 atoms in a crystal at high temperature they are not scattered by point defects such as interstitials, atomic substitutions or vacancies. Usually, at a scattering event there is no change in width of their track, indicating that the charge is not lost. However, the secondary quodons usually are created with no charge, as evidenced by the minimal decoration of their tracks, as seen in Fig. 6. It is consistent with the trigger mechanism for precipitation of magnetite that the minimal decoration sections arise from local variation of the crystal potentials due to the large amplitude of atomic movements within a quodon. After travelling random distances from their point of creation a sudden increase in their track width indicates capture of a charge. This property of creating secondary quodons limits the type of excitation that constitutes a quodon. The large number, of up to about 100, secondary quodons generated by a primary quodon of maximum available energy of 42 eV points to a minimum energy for creation of a quodon of about 0.4 eV. Crowdions are a possible candidate for quodons but require about 27 eV for their creation. Assuming the nuclear recoil motion following decay of ^{40}K is in random directions then 2% (as calculated by the author) of the observed tracks could be due to crowdions. Lastly, the secondary excitations do not show the properties exhibited by kink-like excitations that create the fan-shaped patterns associated with atomic cascades [12]. The oscillatory nature of the internal motions of atoms in a quodon can transfer momentum to a secondary quodon in either the forward or backward direction. The secondary quodons are all connected to the primary track by weakly decorated tracks consistent with no trapped positive charge. The distance travelled before a charge is trapped is variable. Figure 6 shows secondary quodons arising from a primary quodon moving horizontally. This is consistent with the inability to subdivide the single charge on the primary quodon, so a secondary quodon is created neutral. It is interesting that a very small minority of quodon tracks lie in directions of chains with atomic spacing of 0.9 nm but the majority move in chain directions with 0.54 nm spacing.

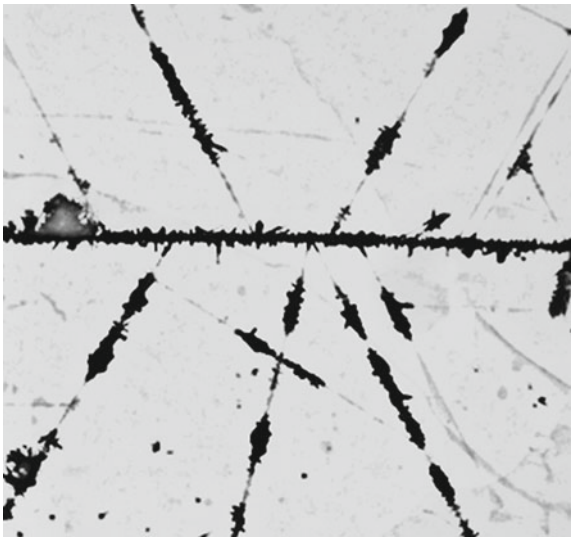

Fig. 6 Photograph of secondary quodons created by scattering of a primary quodon. The primary is moving horizontally. Since the charge on a quodon cannot be subdivided the secondary quodons are created without a charge but may trap one in flight

6 Re-examination of the Ejection Experiment

The experiment reported in 2007, designed to detect the ejection of atoms from a crystal by inelastic scattering of quodons at a crystal face, assumed that quodons were overall charge-neutral [18]. It is well known that atoms evaporated from a surface are usually neutral. However, the potassium sheets consist of cations and thus there was uncertainty about the ionisation state of ejected atoms so it was decided to introduce a region between the crystal and the detector to create a plasma through which ejected particles must travel to reach the detector. This would increase the probability for ionising ejected atoms that could then trigger the charge-sensitive channel- plate detector. The experimental arrangement is shown in diagrammatic form in Fig. 7.

A low activity source (1) of alpha particles from ^{241}Am irradiated one edge of a crystal of muscovite mica (3). This source and the crystal were held in a Faraday cage that is connected to the detector (4), also in a Faraday cage, via a voltage source. The purpose of the voltage source was to attract and focus positive ions to the detector and discriminate against electrons from field emission or other sources. Some positive ions from the low intensity plasma were detected and formed the background count-rate of the detector. It was also observed that UV radiation from an ionisation vacuum gauge contributed to the background count-rate. This effect was eliminated by introducing a multiple plate light-baffle between the gauge and the target chamber. The experiment looked for changes in the count-rate that could be attributed to effects arising from the alpha irradiation of the remote front edge of the crystal.

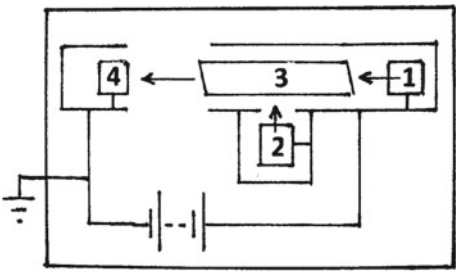

Fig. 7 Arrangement of the experiment for demonstrating ejection of ions from a remote crystal edge with the alpha source at position (1). To investigate the relationship between the alpha flux hitting the crystal and the detected count-rate the source was moved to position (2) where it could be rotated below a small hole in the metal plate supporting the crystal

By chance the supply of argon gas to the vacuum system to create a plasma ceased during a detection run. Fortunately, the vacuum pressure gauge readings were studiously recorded at the start and end of each run along with other parameters. The fact that the detector continued to record the arrival of charged atoms when the pressure was far too low to support a plasma went unnoticed. That is, the ejected particles must have had a positive charge when ejected. Only later, after the evidence from track-width data for quodons carrying charge was recognised, was the implication of the earlier experiment data appreciated. It showed that irradiation of one edge of a crystal caused ionised atoms to be ejected from a remote edge that was in a principal crystal direction from the irradiated edge.

Of course, there might be other ways for ions to leave a remote edge other than via quodon scattering. What was needed was evidence that the count-rate of ejected ions was proportional to the number of alphas irradiating the crystal with all other variables fixed. In particular, the geometry of the crystal holder, the detector and the alpha particle source had to remain unchanged. This would eliminate changes in the electric potential field distribution between the crystal edge and the detector. To this end the experiment was modified by moving the alpha source away from position (1) to position (2), still within the Faraday cage. The alpha source was mounted on the end of a metal rod that was inside a fixed metal tube, thereby causing no changes in geometry as the rod was rotated. The flux of alphas hitting the crystal then could be varied by rotating the rod holding the source under a hole in the metal support for the crystal. In this way, the flux could be varied from zero to a maximum value without changing any other parameter affecting the experiment. A sketch of the source arrangement and a plot of the measured count-rate as a function of the angle of rotation of the source is shown in Fig. 8 for one complete rotation.

There were three possible origins of charge on the ejected ions. One was the two positive charges of the alphas as they penetrated the crystal. The second source was the local ionization of the crystal by the alphas creating atomic cascades. The third source was the residual positive charge that was distributed through the crystal arising from the annihilation of the positrons from ^{40}K decay. The distance from the point of

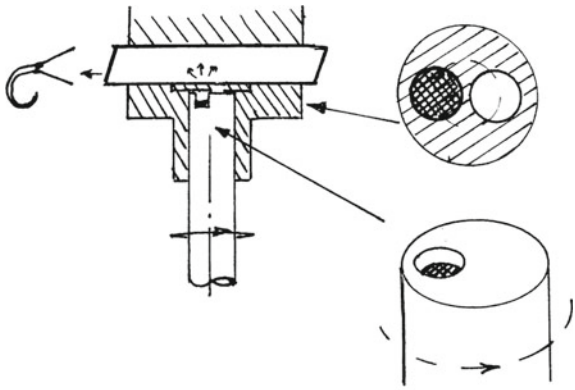

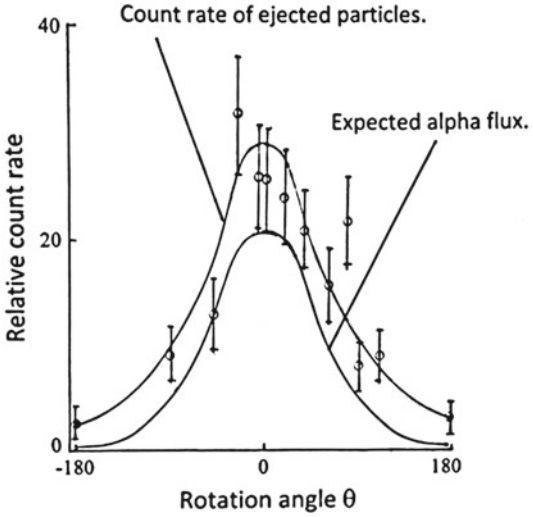

Fig. 8 Drawing showing the construction of the enclosed alpha source that can be rotated within a Faraday cage to vary the flux of alphas irradiating the crystal. The plot shows the number of charged particles detected in regular 7 min intervals vrs the rotation angle and the expected variation from the geometry. The background count rate was 3 in the same time interval

entry to the crystal of the alphas to the crystal edge was about 3 mm. This exceeds by about three orders of magnitude the range of alphas in the crystal and of the zone of ionisation created by atomic cascades. The detection of charged particles leaving the crystal showed that charge must have moved through the crystal of muscovite. As muscovite is an excellent electrical insulator the charge must have been transported through the crystal by some kind of mobile anharmonic lattice excitation. The energy and momentum needed to eject particles from the crystal could only come from the scattering of the alphas in the crystal. This result, combined with the evidence from widths of tracks of positrons and quodons in muscovite crystals, points to the current being carried by quodons.

7 Long Range Transport of Charge at Elevated Temperatures

The great lengths of the tracks of quodons decorated with magnetite or epidote, typically exceeding 10 cm, showed the tight binding of holes and electrons, respectively, to the an-harmonic lattice excitations forming quodons. This is remarkable as the tracks are formed when the crystals are at temperatures exceeding 500 °C [3]. Moreover, the crystals are formed under natural conditions and thus contain many defects, such as interstitials, vacancies, atomic substitutions, radioactive decay products, ionisation from cosmic ray particles and dislocations. It is apparent that quodons are remarkably stable entities. Their recorded tracks show that they exist in the layered structure of muscovite, in crystals containing a high concentration of Fe and variable amounts of Ca. However, the crystals used in the ejection and charge transport experiments contained only modest amounts of Fe and no detectable Ca. Hence, the recording process was not functional. This suggests that it is mainly the layered structure that allows the existence of quodons. In each of the experiments there was evidence for the transport of charge through crystals of muscovite in the absence of an applied electric field across the crystal. This is indicative of infinite charge mobility at temperatures above ambient.

8 The Influence of Chemical Doping on the Recording Process

The first indication of useful information in the 'staining' seen in muscovite crystals were the long black lines that lay in random directions. Within the realm of known physics at that time, in 1963, muons were the most likely cause. Conclusive evidence for muons came only slowly. Measurements showed that they deviated slightly in a random way from straight paths, which was consistent with scattering. If they were the tracks of muons then they must be relativistic. With this assumption it was then possible to determine their energy spectrum. It was found to be similar to the known spectrum found from measurements made in underground particle detectors. Muons can be either negatively charged or positively for anti-muons. If positively charged then they should experience channelling in a crystal. When channelling was taken into account the corrected energy spectrum was consistent with the known spectrum. This was the first indication that the recording process precipitating magnetite responded to a moving positive charge. This was later confirmed by studying the decay products of ^{40}K. If the magnetite tracks were of electrons then the duration of the recording phase would be about 10^5 times shorter, because of the ratio of emitted electrons to positrons, indicating a recording period of order hours to days instead of hundreds of years. On the basis that geological processes are usually slow – except for earthquakes – the longer timescale was the more probable. This conclusion was later shown to be correct by observation of the unique diffraction scattering pattern of positrons in muscovite.

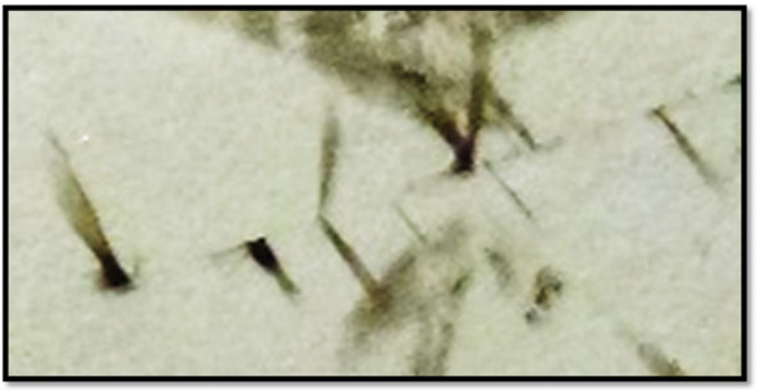

Fig. 9 Micrograph of muon tracks in muscovite showing fan-shaped decorations of lattice excitations created by nuclear scattering of the muons. These energetic scattering events create atomic cascades from which mobile nonlinear lattice excitations emerge. The quasi-2-dimensional structure of muscovite enhances the range of propagation of the excitations far beyond the range of typical discrete-particle shock-waves observed in molecular dynamic modelling studies of 3-D crystals. The portion of the sheet shown is 12 mm wide

There were three early indicators of possible stable lattice excitations capable of propagating great distances in muscovite crystals. In order of finding, firstly, in 1965, there were the fan-shaped patterns associated with nuclear scattering of muons. These are seen branching off from muon tracks in the micrograph shown in Fig. 9. Their range is typically 1 mm. Molecular dynamic studies of nuclear scattering events have given clear evidence for super-sonic discrete-particle shock waves in uniform crystals. An example is shown in Fig. 10.

Secondly, found in 1974, was the contiguous array of magnetite decorated tracks lying in atomic chain directions with a single track of a relativistic muon that is not in a chain direction. This is shown in Fig. 11. Either the muon intersected the contiguous array of unknown origin or, more probably, the array was created subsequent to a nuclear scattering of the muon dumping energy and momentum into the lattice.

The third indicator, in 1991, was the observation of clear tracks originating from the sites of ^{40}K decays that had emitted positrons in the opposite direction to the clear tracks. The material forming the clear tracks was identified as the mineral epidote [19]. This was the pivotal finding in defining a quodon because it identified a source of mobile lattice excitations that occurred throughout mica crystals. The physical properties of the source, the decay of ^{40}K, was well understood. It showed that the type of excitation that led to the fan-shaped patterns seen in Fig. 9 were fundamentally different from quodons. Although a supersonic discrete-kink like excitation describes some of the features of fans a detailed understanding of the excitation has yet to be achieved.

The quodons resulting from positron emission are created in the presence of a negative charge on the recoiling argon atom. A significant difference between tracks

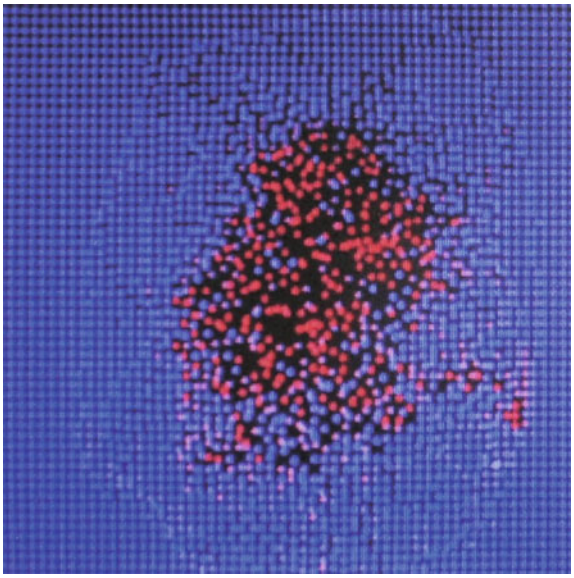

Fig. 10 Molecular dynamic study of a 5 keV impact to an atom in a crystal of gold. The figure shows a 2-atom thick slice through the atomic cascade, which stops obscuration of the shock-waves by the surrounding atoms in the crystal. The discrete-particle nature of the shock-waves, seen as irregular rings around the chaotic core, shows that only two adjacent atoms in a chain in the direction of energy propagation are involved in the lattice perturbation. These shock-waves are laterally dispersive in most uniform materials but in a quasi-2-dimensional layered crystal they are restricted in the direction normal to the layers. This enables the disturbance to propagate further in the layers, accounting in part for the large range of the fans. Reproduced from [6] after Ref. [7].

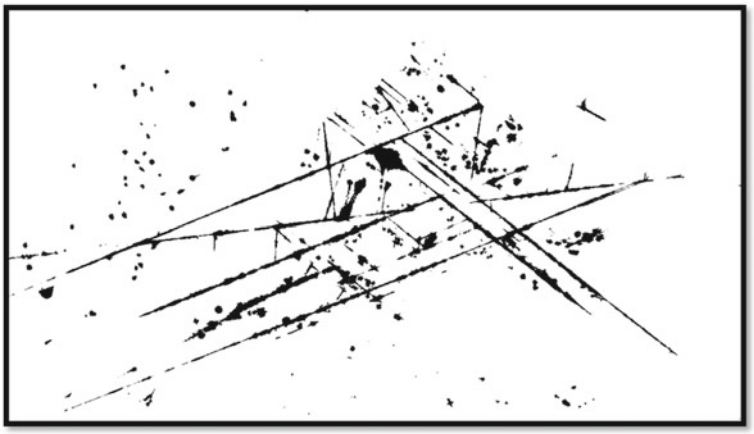

Fig. 11 This sheet shows the creation of multiple quodon tracks following a nuclear scattering event of a relativistic muon. The muon track lies at 8° to the horizontal and passes across the sheet. The sheet is 125 mm wide

decorated with epidote and those with magnetite is that the quodons creating epidote tracks appear unable to create secondary epidote tracks. Different epidote tracks can have different widths, which suggests that the width might be influenced by the quodon energy. However, each epidote track is of constant width. Although crystals with a high calcium content can show epidote tracks triggered by quodons and positron tracks decorated with magnetite they usually do not show quodon tracks decorated with magnetite. This suggests that in Ca-rich crystals holes are weakly bound to quodons. This might account for the absence of secondary quodon tracks decorated with magnetite arising from epidote tracks. In contrast to the creation of holes by annihilation of positrons, few free electrons are created near the K-sheets. This would reduce the probability for secondary quodons from epidote tracks capturing an electron and creating a secondary epidote track, as observed. It is unlikely that the epidote ribbons are dendritic growths in a meta-stable phase because of the apparent absence of secondary epitaxial ribbons in other crystal lattice directions. The lack of evidence for short sections of epidote tracks in magnetite decorated quodon tracks suggests that the ability of quodons to hold a negative charge is limited in crystals with low Ca content. A working hypothesis is that quodons are more tightly bound to holes than to electrons in crystals with low Ca content. Conversely, in Ca rich crystals electrons are bound more tightly than holes to quodons. The crystals used in the alpha irradiation experiments had low Ca content.

9 Polarisation and Residual Space Charge

The transport of charge by quodons in a layered crystal requires injection of sufficient energy and momentum to create quodons. This can be achieved by irradiating the surface of a cable containing suitable layered material with ions or neutral atoms. This method was used in the experiment in which ions, the alphas, were injected in the side of the crystal. Alternative methods might be found in the future. If ions are used, such as alpha particles, then charge is coupled to the material. This will cause a polarisation of the material. One result of this could lead to the build-up of voltage across the material. To estimate the possible significance of such an effect the arrangement and parameters of the ejection experiment is considered. The crystal was 7 mm wide, 1.5 mm thick and the dielectric constant of muscovite is about 8, giving a capacitance of about 1×10^{-13} F. The transport of one unit of charge by a quodon without loss by ejection causes a voltage difference of about 10^{-6} V. If 100 alphas per second impinge on the crystal and each alpha creates 10 quodons then the voltage across the crystal would increase at a rate of about 7 V/h. Each experimental run lasted about 24 h so a voltage of order 150 V might arise. However, this simple calculation assumes that no charge is removed or lost from the cable or crystal. In the ejection experiment charge was removed by the ejected particles.

In muscovite the decay of potassium leads to a distributed build-up of charge. The charge state of the daughter nucleus allows two routes: the dominant one yields a positive charge at the decay site and the minor one a positive charge by annihilation

of emitted positrons. The rate is about 5×10^5 decays per day in 1 cc of muscovite. These positive charges occur in or near the potassium sheets. However, about 90% of these decays result in emitted energetic electrons. These eventually are distributed throughout the lattice as they are not concentrated in the potassium sheets by diffraction scattering. Although this causes nulling of the overall space charge it does not change the concentration distribution of holes in or near the potassium sheets, which are within reach of quodons. Consequently, about 90% of quodons are created with a positive charge and there is a good probability for secondary quodons, which are created without charge, to capture a positive charge in flight. Quodons resulting from external irradiation might be created with a charge. If the irradiation is with energetic particles capable of causing ionisation in atomic cascades then they could trap charges of either sign. As the majority of quodons are created in collisions in cascades with energies below that needed for ionisation they are most likely to trap a positive charge from any residual reservoir during their flight. This highlights the desirability of creating a reservoir of holes or electrons by doping of the layered material.

10 Evidence for Infinite Charge Mobility in Muscovite

These findings were presented at the Nolineal16 meeting held at Seville. June 7–10, 2016. The most important point came from the re-examination of the ejection experiments. It showed that charge could be carried through a crystal at near sonic speed by quodons in absence of an applied electric potential across the crystal. That was evidence for infinite charge mobility. In principle, it is a simple step to combine the know properties of quodons – ability to propagate great distances in imperfect crystals at high temperatures and transport of charge at near sonic speed – to the near loss-free transmission of electricity. In normal electrical conductors electrons and holes move or drift at relatively slow speed. This ranges from about a millimetre/sec in copper, several meters/sec in semiconductors, to a kmetre/sec in carbon nanotubes. In muscovite with quodons the speed is about 3.5 km/s at any temperature up to 500 °C. The only other know examples of infinite charge mobility are low and high temperature superconductors. It is to be expected that the observation of infinite charge mobility in the layered crystal muscovite will be of some interest in those studying high T_c superconductors (HTSC). To differentiate the apparent ability of quodons to transmit electricity at high temperatures and without loss in a perfect crystal from HTSC the term ‘hyper-conductivity’ was introduced. Certainly, there is an overlap with HTSC in that layered crystal structures are imperative in both cases. It led to a small group of people gathered round a white-board in the Group of Applied Physics at the University of Seville. They were discussing the possibility of verifying the evidence for infinite charge mobility in muscovite by an alternative procedure to counting individual ions by making a direct measurement of charge transported through a natural crystal. The safest way to design such a test was to build upon the earlier experiments using alpha particles to provide the energy and

momentum needed for quodons and, additionally, a source of positive charges. The main unknown aspects in the design were the efficiency of creation of quodons and their efficiency of capture of a positive charge. This would determine the likely magnitude of any current that might pass through a crystal. The only way forward was to use the most sensitive current meter available at the University, which was a Keithley pico-amp meter. Although muscovite is a common mineral, and huge amounts are mined each year, small crystals of good habit are scarce. Several crystals were obtained by FMR from National Museums and by private purchase and one was sent to the Seville group.

Conclusion

The study of black lines and patterns in natural crystal of muscovite involved delving into multiple disciplines including cosmology, geology, nuclear physics, chemistry, solid-state physics, mathematics and numerical modelling. Sometimes the study had to await new developments in technology, especially in computing, and in assimilating new discoveries, such as channelling and intrinsic localised modes. There have been occasional tantalising diversions, like estimating the rate of fusion of hydrogen isotopes by quodons in a hypothetical layered matrix loaded with hydrogen. The main objective was to understand the origin of the lines and what they showed about anharmonic lattices and the excitations that could exist and propagate in layered crystals. It was the properties of layered structures that held the greatest interest because, in contrast to natural crystals, there is no limit to the composition and structure of sequentially deposited thin films or monatomic layers. With hindsight the strong coupling between electronic charge and anharmonic excitations should have been recognised earlier. Nevertheless, it led to evidence for infinite charge mobility and the prediction of hyper-conductivity in muscovite. In particular, it has set a critical test for verification of these phenomena. If a current is observed to flow in a crystal of muscovite, which has not been previously irradiated, by creation of quodons then the current should initially be large and then decay in time towards a finite limiting value. The source of the initial burst of current is the build-up and storage of charge from decay of ^{40}K. The asymptotic current stems from any charge introduced to the crystal in the creation of quodons that might involve ionisation of the crystal. If alpha particles are used then they will each contribute two positive charges.

Acknowledgements It is a pleasure to acknowledge the unstinting support, collaboration and guidance over many years given by J.C. Eilbeck who was able to link theory with experiment. More recently I wish to thank J.F.R. Archilla for his encouragement, collaboration and discussions on several aspects of the properties of muscovite. It is with both apprehension and anticipation that I await the result of his test of the prediction of infinite charge mobility. I also wish to acknowledge the University of Sevilla for nominating me as research collaborator in 2016. Part of this work was supported by a grant from Turbon Int. Ltd. Many people have assisted me at various stages and, in particular, I wish to acknowledge the support and guidance provided by R. Witty who enabled a critically important molecular dynamic study of the muscovite unit cell to be done by D.R. Collins.

References

1. Archilla, J.F.R., Kosevich, Yu.A., Jiménez, N., Sánchez-Morcillo, V.J., García-Raffi, L.M.: A supersonic crowdion in mica. In: Archilla, J.F.R., Jiménez, N., Sánchez-Morcillo, V.J., García-Raffi, L.M. (eds.) Quodons in Mica: Nonlinear Localized Travelling Excitations in Crystals. Springer Series in Materials Science, vol. 221, pp. 69–96 (2015)
2. Archilla, J.F.R., Russell, F.M.: On the charge of quodons. Lett. Mater. **6**, 3–8 (2016)
3. Deer, W.A., Howie, R.A., Zussman, J.: Rock-Forming Minerals: Micas, vol. 3A. The Geological Society, London (2003)
4. Eilbeck, J.C.: Numerical studies of solitons. In: A.R. Bishop, T. Schneider (eds.) Solitons and Condensed Matter Physics. Springer Series in Solid-State Sciences, vol. 8, pp. 28–43. Springer, Berlin (1978)
5. Marin, J.L., Eilbeck, J.C., Russell, F.M.: Localized moving breathers in a 2-D hexagonal lattice. Phys. Lett. A **248**, 225–232 (1998)
6. Nordlund, K.: A classical molecular dynamics computer simulation of a collision cascade (2008). http://en.wikipedia.org/wiki/File:10kevau_au.gif. Accessed 24 June 2017
7. Nordlund, K., Ghaly, M., Averback, R.S., Caturla, M., Diaz de la Rubia, T., Tarus, J.: Defect production in collision cascades in elemental semiconductors and FCC metals. Phys. Rev. B **57**(13), 7556–7570 (1998)
8. Russell, F.M.: Tracks in mica caused by electron showers. Nature **216**(5118), 907–909 (1967)
9. Russell, F.M.: Identification and selection criteria for charged lepton tracks in mica. Int. J. Radiat. Appl. Instrum. D **15**, 41–44 (1988)
10. Russell, F.M.: Positive charge transport in layered crystalline solids. Phys. Lett. A **130**, 489–491 (1988)
11. Russell, F.M.: Decorated track recording mechanisms in muscovite mica. Int. J. Radiat. Appl. Instrum. D **19**, 109–113 (1991)
12. Russell, F.M.: Energy gain by discrete particle non-linear lattice excitations. In: Carretero-González, R., Cuevas, J., Frantzeskakis, D., Karachalios, N., Kevrekidis, P.G., Palmero, F. (eds.) Localized Excitations in Nonlinear Complex Systems, pp. 289–315. Springer International Publishing, Cham (2014)
13. Russell, F.M.: Charge coupling to anharmonic lattice excitations in a layered crystal at 800 K (2015). arXiv:1503.03185 cond-mat
14. Russell, F.M.: I saw a crystal. In: Archilla, J.F.R., Jiménez, N., Sánchez-Morcillo, V.J., García-Raffi, L.M. (eds.) Quodons in Mica: Nonlinear Localized Travelling Excitations in Crystals. Springer Series in Materials Science, vol. 221, pp. 475–559 (2015)
15. Russell, F.M.: Tracks in mica, 50 years later. In: Archilla, J.F.R., Jiménez, N., Sánchez-Morcillo, V.J., García-Raffi, L.M. (eds.) Quodons in Mica: Nonlinear Localized Travelling Excitations in Crystals. Springer Series in Materials Science, vol. 221, pp. 3–33 (2015)
16. Russell, F.M., Collins, D.R.: Lattice-solitons in radiation damage. Nucl. Instrum. Methods Phys. Res. B **105**, 30–34 (1995)
17. Russell, F.M., Collins, D.R.: Anharmonic excitations in high T_C materials. Phys. Letts. A **216**, 197–202 (1996)
18. Russell, F.M., Eilbeck, J.C.: Evidence for moving breathers in a layered crystal insulator at 300 K. Europhys. Lett. **78**, 10004 (2007)
19. Russell, F.M., Steeds, J.W., Vine, W.J.: Formation of epidote fossil positron tracks in mica. Optik **92**(4), 149–154 (1993)
20. Russell, F.M., Zolotaryuk, Y., Eilbeck, J.C., Dauxois, T.: Moving breathers in a chain of magnetic pendulums. Phys. Rev. B **55**, 6304–6308 (1997)
21. Russell, F.M., Marin, J.L., Eilbeck, J.C.: Breathers in cuprate superconductor lattices. Phys. Lett. A **281**, 21–25 (2001)
22. Russell, J.S.: Report on waves. In: Report of the 14th meeting of the British Association for the Advancement of Science, pp. 311–390. John Murray (1845)

Kinks in a Lattice of Repelling Particles

Experimental Study with a Chain of Coupled Pendulums

Ahmed Mehrem, Luis J. Salmerón-Contreras, Noé Jiménez, Víctor J. Sánchez-Morcillo, Rubén Picó, Luis M. García-Raffi, Juan F. R. Archilla and Yuriy A. Kosevich

Abstract A lattice of repelling particles is a good model for studying certain properties that take place at atomic scale in Solid State Physics. In this chapter

A. Mehrem · V. J. Sánchez-Morcillo · R. Picó
Instituto de Investigación para la Gestión Integrada de las Zonas Costeras, Universitat Politècnica de València, C/.Paranimfo 1, 46730 Grao de Gandia, Spain
e-mail: ahmeh@epsg.upv.es

V. J. Sánchez-Morcillo
e-mail: victorsm@upv.es

R. Picó
e-mail: rpico@upvnet.upv.es

L. J. Salmerón-Contreras · L. M. García-Raffi (✉)
Instituto Universitario de Matemática Pura y Aplicada, Universitat Politècnica de València, Camino de Vera s/n, 46022 Valencia, Spain
e-mail: luisalco@epsg.upv.es

L. M. García-Raffi
e-mail: lmgarcia@mat.upv.es

N. Jiménez
LUNAM Université, Université du Maine, CNRS, LAUM UMR 6613 Av. O. Messiaen, 72085 Le Mans, France
e-mail: noe.jimenez@univ-lemans.fr

Present Address:
N. Jiménez
Instituto de Instrumentación para Imagen Molecular, Consejo Superior de Investigaciones Científicas, Universitat Politècnica de València, Camino de Vera s/n, 46022 Valencia, Spain
e-mail: nojigon@upv.es

J. F. R. Archilla
Group of Nonlinear Physics, Department of Applied Physics I, Universidad de Sevilla, ETSII, Avda Reina Mercedes s/n, 41012 Sevilla, Spain
e-mail: archilla@us.es

Y. A. Kosevich
Semenov Institute of Chemical Physics, Russian Academy of Sciences, Kosygin Street 4, 119991 Moscow, Russia
e-mail: yukosevich@gmail.com

J. F. R. Archilla et al. (eds.), *Nonlinear Systems, Vol. 2*, Understanding Complex Systems, https://doi.org/10.1007/978-3-319-72218-4_11

we study theoretically and experimentally the generation and propagation of kinks in such kind of systems. We propose a simple experimental setup consisting in an array of pendulums, having magnets at the extreme, i.e., that form a set of coupled magnetic dipoles. We excite pulses at one boundary of the system and demonstrate the existence of transient-kinks, whose dynamics are in very good agreement with the theoretical predictions given by the α-FPU equation. The peculiarities of the experimental system allows to study a broad range of phenomena. On one hand, by the effect of the finite size of the magnets, the model captures the dynamics of different inverse power law inter-particle interactions, ranging from the monopole limit to the dipole interaction. On the other hand, we propose the use of an external substrate potential at the bottom of the lattice that mimics the substrate potential of a crystal. Thus, the results obtained in the experimental setup can be extrapolated to other systems described by this equation.

Keywords Repulsive forces · Magnetic pendula · Kinks

1 Introduction

Matter is formed by basic units, atoms, that interact via repulsive forces and form ordered states called lattices. These repulsive forces are the results of Coulomb interactions and short range repulsive forces due to the Pauli exclusion principle of many body systems [13]. Therefore, the study of such kind of systems from different points of view gives an insight to the properties of solid state physics, the part of physics that describes atoms and ions organized in ordered lattices called crystals. We are dealing with non-contact forces that provide the coupling between neighboring particles, fixed in some positions or sites by the potential of the rest of the lattice in the mean field approximation. This coupling allows the propagation of perturbations in the form of phonons, or elementary excitations of the lattice. But we are not restricted to work at atomic scale to find in nature examples of such kind of systems and coupling among entities. For example, in Ref. [24] it is presented a system of trapped interacting particles that form an ionic crystal. Such crystals – that can be considered as a particular form of condensed matter- are formed by charged particles confined by external electromagnetic potentials (Paul or other traps) [24], and interacting by means of the Coulomb repulsion. The process of crystallization requires a lowering in temperature that is achieved by laser cooling techniques. Different crystallization patterns have been observed by tuning the shape and strengths of the traps. Crystals of trapped ions have been subject of great attention as a possible configuration to perform quantum computation [23]. Crystallization of a gas of confined electrons, known as a Wigner crystal, has also been predicted and observed [8, 16].

When these systems are perturbed at their boundaries, waves propagate through them and due to the lattice periodicity strong dispersion appears when wavelengths are of the order of the lattice period. The linear dispersion relation for low amplitudes and some nonlinear characteristics of wave propagation have to be determined in

order to characterize wave propagation. For example, it has been experimentally determined in an electrically charged, micrometer-sized dust particles immersed in the sheath of a parallel plate rf discharge in helium in a rf plasma [10], where the waves are excited by transferring the momentum from a laser to the first particle in the chain. One of the effects that appear due to the nonlinearity of interparticle interactions is the generation of harmonics.

But this is not the only case of perturbation of the propagation we can study. In charged-coupled lattices of particles there is another *bestiarium* formed as a consequence of the excitation of intense compact pulses at one boundary of the system, giving rise to solitons, breathers, kinks, quodons, crowdions... All of them are solutions of the equations that govern the dynamics of the system based on the nonlinear character of the interactions and they behave as particle-like perturbations traveling along the lattice.

In recent decades, the solitary wave theory has become a very active area of research due to its importance in many branches of mathematics and physics, such as nonlinear optics, acoustics, plasmas and fluid mechanics. In particular, kinks have been extensively studied during the recent years because they transport energy at supersonic speeds [2–4]. In ionic crystals kinks are also natural carriers of electric charge [6]. One example of this kind of materials is mica muscovite. The tracks are recorded within the cation layer of potassium ions which form a two-dimensional hexagonal lattice. Some of these tracks can be explained by the passage of swift particles as positrons, pions, antimuons and protons which are secondary particles to neutrino collisions or products of radioactive decay. But there are also many tracks along the close packed directions of this lattice that cannot be produced by charged particles and are attributed to some vibrational entities called *quodons* because of their quasi one-dimensional character [1]. Their existence has also been shown experimentally in [26]. These *quodons* are triggered by the radioactive disintegration of potassium isotopes where the recoil of the nucleus in some cases has the necessary energy to start the propagation of a perturbation that travels along a lattice direction formed by a chain of potassium ions that lies in the (001)-plane [5].

Many studies have been done about kink propagation in different media [14, 18, 25]. Peyrard et al. [20] described and discussed subsonic kinks in a monoatomic chain where they showed the discreteness effects on non-topological kink soliton dynamics in nonlinear lattices. Savin et al. [28] studied moving topological solitons (kinks and antikinks) in the nonlinear Klein-Gordon chain by using the pseudo-spectral method. Pnevmatikos, Flytzanis and Remoissenet [21] studied propagation of kinks and solitons analytically and numerically in a nonlinear diatomic chain with cubic and quartic interaction potential. The book *"Waves called solitons: concepts and experiments"* by Remoissenet [25] describes examples of many simple experimental realizations of nonlinear lattices in which kinks, in particular, can be observed.

In this work we pay attention to lattices of nonlinear oscillators coupled to the nearest neighbours by repulsive interactions. Specifically, we study a 1D chain of particles periodically distributed that interacts via repulsive Coulomb-type forces. Our purpose is the experimental study of kinks in a mechanical analogue of a chain

of repulsive particles: a chain of magnetically coupled pendulums. The system is analogous to that of [27], but here, in addition to the action of gravity, a magnetic substrate potential was added, i.e., making a mechanical analogue of the Frenkel–Kontorova model. The modeling of repulsive interactions with finite-size magnetic dipoles allows the experimental study of different functions for the repulsive interaction. We study the excitation and propagation of kinks with and without the substrate potential, and compare the experimental results with analytical and numerical ones. Good agreement was obtained, showing that it is possible to build up and measure certain properties in simple macroscopic analogues of microscopic systems.The theoretical results are based in the work [12] and the experimental results have been obtained from the work [17].

2 The Physical Model

Our theoretical model consists of an infinite chain of identical particles with mass m aligned along the x-axis. Each particle interacts with its nearest neighbors via a repulsive potential, V_{int}. In the absence of perturbations, every mass has a fixed equilibrium position being the interparticle distance a. An external potential, V_{ext}, can be added to the lattice. In condensed matter, this external potential comes from the action of the other atoms or ions in the crystal. These extra forces can be provided by a periodic on-site potential and/or forces keeping the boundary particles at fixed positions. Then, the equation of motion is written as

$$M\ddot{u}_n = V'_{\text{int}}\left(u_{n+1} - u_n\right) - V'_{\text{int}}\left(u_n - u_{n-1}\right) - V'_{\text{ext}}\,, \tag{1}$$

where u_n represents the displacement of the n-th particle measured with respect to its equilibrium position as shown in Fig. 1, M is the mass of the particle and V'_i is the derivative of the potential V_i. Therefore, the rhs of the equation is the sum of the forces on the particle n by the nearest neighbors at $n+1$ and $n-1$ and by a substrate potential which can be produced by the rest of the lattice or an external cause. In the limit of small displacements, the interaction force between particles can be approximated linearly with respect to the distance, r, i.e., $V'(r) = \kappa r$ where κ is

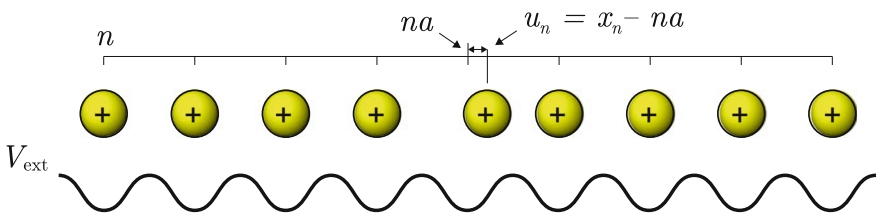

Fig. 1 The lattice of repelling coupled particles. The lattice constant is a. An external force applied in the boundaries is necessary to keep the system stable

a constant. In this limit, Eq. (1) represents a system of coupled harmonic oscillators. However, in general the potentials in physical systems are anharmonic. Chains of nonlinearly coupled oscillators with different types of anharmonic potentials have been extensively studied in the past, e.g., the celebrated cases of the α-FPU lattice, where $V'_{\text{int}}(r) = \kappa_1 r + \kappa_2 r^2$ (cubic potential), the β-FPU lattice where $V'_{\text{int}}(r) = \kappa_1 r + \kappa_3 r^3$ (quartic potential), the Toda lattice, with $V'_{\text{int}}(r) = \exp(-r) - 1$ or the granular lattice, with $V'_{\text{int}}(r) = \kappa r^{3/2}$.

In this work, we consider interparticle forces that decrease with an inverse-power law of the distance. The equation of motion for the particle n is then written in the form:

$$\ddot{u}_n = -\frac{1}{(1 + u_{n+1} - u_n)^\alpha} + \frac{1}{(1 + u_n - u_{n-1})^\alpha} - V'_{\text{ext}}\,, \tag{2}$$

The particular value of the exponent α bring us different types of interactions: $\alpha = 2$ corresponding to repulsive monopoles as in the case of electrically charged particles, e.g. in ion coulomb crystals [24] or dusty plasma crystals [19], $\alpha = 4$ corresponding to repulsive dipoles, e.g., in the interaction between distant magnetic dipoles [27], or in general any other non-integer power [18]. In the following, we present a system allowing to model different values of the exponent of the power-law, α.

3 The Lattice of Repelling Magnets

First, consider two magnetic dipoles, with magnetic moments $\mathbf{m}_1$ and $\mathbf{m}_2$. The interaction potential energy between them is given by the exact relation [11]:

$$V_{\text{int}} = \frac{\mu_0}{4\pi}\left(\frac{\mathbf{m}_1 \cdot \mathbf{m}_2}{r^3} - 3\frac{(\mathbf{m}_1 \cdot \mathbf{r}_{12})\,(\mathbf{m}_2 \cdot \mathbf{r}_{12})}{r^5}\right), \tag{3}$$

where $\mathbf{r}_{12}$ is the vector joining the centers of the dipoles, i.e., from the magnet 1 to the 2, and $r = |\mathbf{r}_{12}|$. This relation implies that, in general, the force depends on the angle between the dipoles. In the particular case when the dipole moments are equal in magnitude, parallel to each other and perpendicular to $\mathbf{r}$ (dipoles in the same plane), the force on the second magnet takes the simpler form

$$\mathbf{F}_{1,2} = -\nabla_2 V_{\text{int}} = \frac{3\mu_0}{4\pi}\frac{m^2}{r^4}\hat{r}_{12}, \tag{4}$$

where $m = |\mathbf{m}_1| = |\mathbf{m}_2|$, μ_0 is the permeability of the medium and $\hat{r}_{12}$ is the unitary vector in the direction from the center of magnet 1 to the center of magnet 2. The force on the first magnet is just the opposite. In the chain of magnetic dipoles, this is the force between two neighboring oscillators at equilibrium positions, i.e., with $r = a$.

In the case of the perturbed chain the distance between centers of nearest neighbors becomes a dynamic variable, $r_n(t)$. Assuming small displacements, i.e., a small angle between the dipole moments, we can use $r_{n+1}(t) = a + u_{n+1} - u_n$ in Eq. (4) to describe the interaction between two neighboring oscillators. The modulus of the force on the $n+1$ magnet due to the n magnet is

$$F_{n,n+1} = \frac{3\mu_0 m^2}{4\pi} \frac{1}{(a + u_{n+1} - u_n)^4} \,. \tag{5}$$

This equation for the small-angle forces is a crude approximation and exact expressions can be found in Ref. [27]. However, since our aim is to obtain simple analytical expressions based on the FPU equation, Eq. (9), we will keep this degree of accuracy. The validity of this approximation to describe our setup will be tested in the next sections when the predictions are compared with the experimental results. Comparing with the equation of motion shown in Eq. (2), we identify $\alpha = 4$.

The above expressions for the forces between magnetic dipoles are valid for loop currents or magnets of negligible dimensions. Expressions for finite size magnets can be found in the literature [7] and are in general lengthy and cumbersome. Gilbert's model for the magnetic field of magnets used here results in approximate but simple expressions for the forces [9]. For cylindrical magnets of length h with their magnetic moments parallel and their axis perpendicular to the line joining the centers, the force on magnet 2 due to the adjacent magnet 1 is expressed as

$$\mathbf{F}_{1,2} = \frac{\mu_0 m^2}{2\pi h^2} \left(\frac{1}{r^2} - \frac{r}{\left(r^2 + h^2\right)^{3/2}} \right) \hat{r}_{12} \,, \tag{6}$$

where the magnetic moment is $m = \pi h R^2 \mathrm{M}$, being M the magnetization and R the radius of the cylindrical magnet.

In the limit $h \ll r$, Eq. (6) reduces to Eq. (4), i.e. magnets with small dimensions compared to their separation interact via dipolar forces, i.e., $\alpha = 4$. In the opposite limit $h \gg r$, the interaction law approaches to a Coulomb-type force, i.e., $\alpha = 2$ for parallel magnets close to each other. In general, the interaction law of magnets can be approached well by an inverse-law with any given exponent that ranges between monopole and dipole cases. Therefore, the chain of repelling magnets allows the modeling of different physical situations just by adequately choosing the geometry of the system.

Thus, we built a chain of coupled magnets as a mechanical analogue of our lattice of particles coupled by repulsive forces. The experimental setup is shown in Fig. 2. An analogue experimental system was presented by M. Russell [27]. The chain consists of 53 identical cylindrical neodymium magnets (Webcraft GmbH, DE, magnet type N45), with mass $M = 2$ g, arranged in a one-dimensional periodic lattice. The radius and length of the magnets was $R = 2.5$ mm and $h = 14$ mm, respectively. The magnets were oriented with the closest poles being those of the same polarity, therefore producing a force that is repulsive. The value of the magnetization

was $\mathrm{M} = 1.07 \times 10^6$ A/m. The magnets were attached to a rigid bar which allows the rotation in the sagittal plane around a fixed T-shaped support, being each magnet actually a pendulum as shown in Fig. 2b. The length of the vertical bars was $L = 100$ mm, and the lattice constant, i.e., the distance between supports (and therefore the distance between magnets at equilibrium) was $a = 20$ mm. The support was specially designed to minimize the effects of friction by using additional pairs of concentric rings magnets which keep the oscillators levitating on air, with just one contact point, as shown in Fig. 2c. This system allows the minimization of the friction: strong torque forces appear at the bearings of the pendulums due to non perfect alignment. Using the quasi-levitation system the chain remains aligned to one single axis, the losses are negligible and, therefore, the experimental setup can be considered quasi-conservative.

The effect of each pendulum is to introduce an additional external force to the dynamics of the chain, corresponding to $-V'_{\mathrm{ext}}$ in Eq. (2).The restoring potential due to gravity is $V_{\mathrm{ext}} = MgL(1 - \cos\theta_n)$, being θ_n the angle formed by a magnet with respect to its vertical equilibrium position and $u_n = L\sin(\theta_n)$ is the horizontal displacement variable. For small θ_n, $u_n \simeq L\theta_n$ and the potential becomes $V_{\mathrm{ext}} \simeq \frac{1}{2}MgL\theta_n^2 = \frac{1}{2}M\Omega_0^2 u_n^2$ with $\Omega_0 = \sqrt{g/L}$ the frequency of small oscillations. The force on the pendulum n is then approximated by a linear force $F_{\mathrm{ext}}(u_n) = -V'_{\mathrm{ext}}(u_n) = -M\Omega_0^2 u_n$. For small oscillations, the interaction potential between two magnets at $n+1$ and n becomes also harmonic $V_{\mathrm{int}}(u_{n+1} - u_n) = \frac{1}{2}\kappa(u_{n+1} - u_n)^2$ for some coupling constant κ.

All magnets oscillate freely except the outermost boundary magnets. The last magnet was fixed, and the first one was attached to the excitation system. The driving

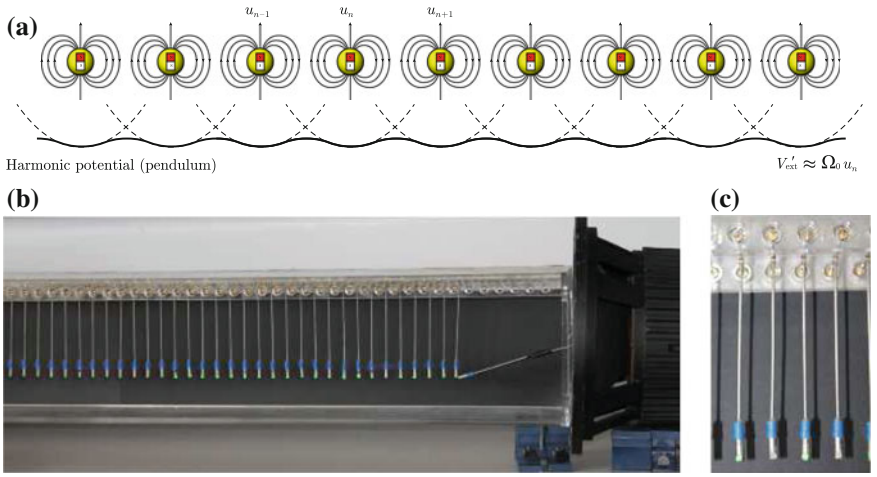

Fig. 2 **a** Scheme of the lattice of coupled particles with the harmonic restoring force. **b** The experimental setup: an array of pendulums, having magnets at the extreme, that form a set of coupled magnetic dipoles. **c** A detail of the concentric rings magnets which keep the oscillators levitating on air with only one contact point. Reproduced from [17]. Licensed under CC-BY-NC-ND

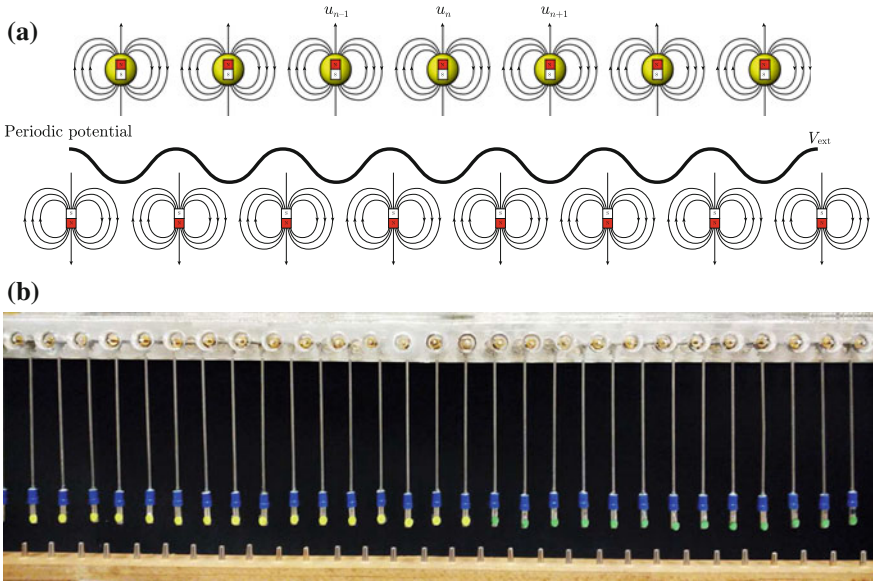

Fig. 3 **a** The scheme of the chain with added periodic substrate. The force between chain magnets and substrate magnets is repulsive. **b** The experimental setup showing on the top the moving-pendulum magnets and in the bottom the fixed-substrate magnets. Reproduced from [17]. Licensed under CC-BY-NC-ND

system consisted of a electrodynamic loudspeaker (Fostex-L363) connected to an audio amplifier (Europower EPS2500) excited by an arbitrary function generator (Tektronix AFG-2021). The first magnet was fixed to the loudspeaker's diaphragm as shown in Fig. 2, and it was forced with different pulsed excitations using a specific waveform with variable amplitude. The motion of the chain was recorded by using a GoPro-Hero3 camera. The camera was placed at proper distance from the chain in order to track the motion of a certain number of magnets. In this work, 18 magnets were recorded simultaneously. Then, each pendulum was optically tracked using image post-processing techniques. We considered the traveling wave regime, by ignoring the reflected wave using a temporal window in the analysis of the recorded video. The duration of each record was about 3.5 s and the camera resolution was set to 960p at a frame rate of 100 frames per second, i.e., a sampling frequency of 100 Hz for the measured displacement waveforms. Videos were post-processed with Matlab using standard image tracking techniques to detect the movement of the magnets obtaining finally a waveform for the position of each magnet.

In this system we have studied the propagation of kinks under two different configurations:

1. **Harmonic substrate potential**: In the first configuration, a weak harmonic potential is introduced due to the restoring force of the pendulum as shown in Fig. 2a. The length of the pendulums was designed to present a small resonating fre-

quency and, therefore, V'_{ext} is extremely weak if compared to the repulsive forces between magnets. However, the existence of the pendulum introduces a restoring force and the unique stable state corresponds to $u_n = 0$. As we will show, this has implications in the formation of kinks.

2. **Periodic substrate potential**: In the second case, a set of fixed magnets were added at the bottom of the chain, as shown in Fig. 3, being each fixed magnet at a distance of 15 mm to the chain and with the polarity vertically inverted with respect to the moving-magnets. The dimensions of the fixed NdFeB magnets were $R_{\text{fix}} = 4$ and $h_{\text{fix}} = 12.5$ mm with same magnetization as the moving ones (Webcraft GmbH, DE, magnet type S-04-13-N). All magnets were placed on non-magnetic support to prevent any interaction with the magnetic field produced by the system. The effect of this extra magnetic repulsive field is that, in addition to the weak restoring gravity forces, it produces strong repulsive magnetic forces, introducing a strong periodic substrate potential, V_{ext}, if compared to the repulsive forces between magnets. The inclusion of this substrate introduces periodic restoring forces with multiple stable states as $u_n = \pm n$: the oscillators can be at rest at different lattice positions. The situation is represented in Fig. 3a.

Thus, just by modifying the geometry of the system, e.g. the distance between the substrate magnets to the chain, the intensity of V'_{ext} can be modified, allowing the current experimental setup to be a mechanical analogue of different nonlinear lattices, ranging from the FPU lattices to the Frenkel–Kontorova ones.

4 Dispersion Relations

The dispersion relation of the lattice is derived for small amplitude waves. It can be obtained analytically by using the Taylor expansion of the α power law in the equation of motion Eq. (2), neglecting the nonlinear terms and assuming a solution in the form of $u_n = \exp[i(\omega t - qn)]$, where q is the wave number and ω is the angular frequency. Then, the dispersion relation is written as

$$\omega^2 = \omega_0^2 + \omega_c^2 \sin^2\left(\frac{q}{2}\right), \tag{7}$$

where ω_0 is the lower cut-off frequency, and $\omega_c = 2\,c_0$, with $c_0^2 = \kappa/M$, where κ is the coupling constant, being a measure of the stiffness of the interaction potential. If there is no substrate potential, i.e., $\omega_0 = 0$, the phonon frequencies are not bounded from below, and the dispersion relation is called *acoustic*. In this case c_0 is the sound phase and group velocity, that is, the velocity for the long-wavelenght limit $q \to 0$ and the maximum frequency becomes $\omega_c = 2\,c_0$, being therefore a *coupling frequency*. For the system of interest in this chapter, $\omega_0 \neq 0$, the phonon frequencies are bounded from below and the dispersion relation is called *optical*, the highest cut-off frequency becomes $\omega_{\text{top}} = (\omega_0^2 + \omega_c^2)^{1/2}$. Figure 4 shows the dispersion relation for the two configurations, with weak and strong substrate potential. It can be

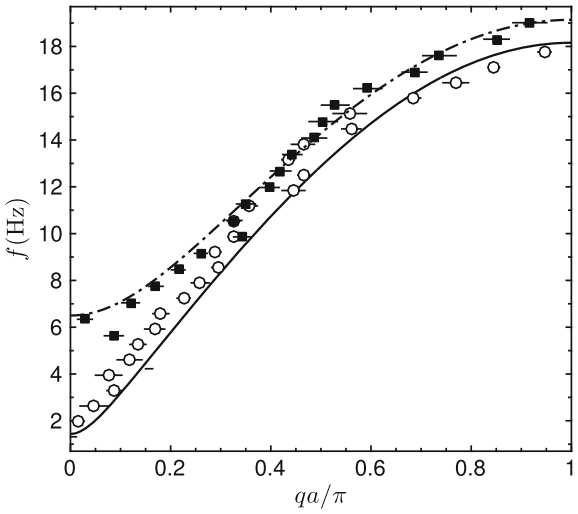

Fig. 4 Dispersion relation in case of the setup with/without substrate. (line-Dashed) Analytically presented by Eq. 7 $\omega^2 = \omega_0^2 + \omega_c^2 \sin^2(q/2)$. The frequency in Hz is given by $f = \omega/2\pi$. The experimental data with error bars (circles) for the case with weak harmonic substrate potential and (squares) for the case with stronger periodic substrate potential. Analytical results are represented by the continuous line for the weak harmonic substrate potential and $(- \cdot -)$ for the stronger periodic substrate potential. Reproduced from [17]. Licensed under CC-BY-NC-ND

observed the existence of high and low cut-off frequencies: both dispersion relations are optical. For the weak substrate potential case, the low cut-off frequency is $\omega_0 = \sqrt{g/L}$ where L is the pendulum length and the gravitational acceleration $g = 9.8\,\mathrm{m/s^2}$. In the case of the strong substrate potential, the low cut-off can be evaluated by measuring the forces of the magnetic dipoles along the axis of the chain. However, for cylindrical magnets of finite dimensions it can become cumbersome and it was estimated experimentally from the dispersion relations. In particular, in the case of the unique action of the gravity (weak substrate potential) the low cut-off frequency presented a value corresponding to $f_0 = \omega_0/2\pi = 1.6\,\mathrm{Hz}$. In the second case, with the strong substrate potential, it was increased up to 6.5 Hz. The high cut-off frequencies were respectively 18 and 19.1 Hz. In Fig. 4 we present the experimental data together with the solution given by Eq. (7) where the values ω_0 and c^2 were set to the corresponding experimental values in each case. A good agreement between the experiments and the theoretical curves is observed. Then, this system presents strong dispersion arising from the two sources, first, the lattice discreteness and, second, the substrate potential, that can be easily tuned by the modification of the geometry of the proposed setup.

5 Approximate Analytical Solution

It is well-known that the interaction of strong dispersion and nonlinearity of a system leads to the emergence of nonlinear localized traveling waves. However, Eq. (2) has no analytical solution. Therefore, we present approximate analytical solutions that capture the main dynamical features of the lattice, in particular, looking for solution of kinks. Approximate solutions can be obtained assuming a small strain $|u_{n\pm1} - u_n|$ in comparison with the lattice constant a. Under this approximation the equation of motion reduces to the well-known FPU equation. Using the FPU equation many solutions for nonlinear localized waves have been proposed in the past. Kosevich [14] obtained a model based on a FPU equation with a cubic plus quartic nonlinearity. Poggi and Ruffo [22] derived an exact solution of the FPU corresponding to Lennard-Jones interaction forces. Recently, Archilla, Kosevich et. al [3] obtained the FPU equation for a cubic plus quartic nonlinearity from the expansion of the Coulomb potential. In all these cases, the authors relied on a FPU equation to extract analytical solutions for kinks. For a weak substrate potential, Eq. (2) is a generalized form of the equation of motion presented by Archilla et al. [4]. Replacing the forces by their Taylor expansion and neglecting cubic and higher order terms, the leading equation in the general case of a inverse power law is

$$\ddot{u}_n = c_0^2 \left[(u_{n+1} - 2u_n + u_{n-1}) - \frac{1+\alpha}{2} (u_{n+1} - u_n)^2 + \frac{1+\alpha}{2} (u_n - u_{n-1})^2 \right] - \Omega_0^2 u_n, \quad (8)$$

where $c_0 = \sqrt{\alpha}$ is the normalized long wavelength phonon velocity in the absence of substrate, i.e., the speed of sound. In the case of monopolar interaction ($\alpha = 2$) it leads to

$$\ddot{u}_n = c_0^2 \left[(u_{n+1} - 2u_n + u_{n-1}) - \frac{3}{2} (u_{n+1} - u_n)^2 + \frac{3}{2} (u_n - u_{n-1})^2 \right] - \Omega_0^2 u_n, \quad (9)$$

and for dipolar interaction, $\alpha = 4$, the FPU takes the form

$$\ddot{u}_n = c_0^2 \left[(u_{n+1} - 2u_n + u_{n-1}) - \frac{5}{2} (u_{n+1} - u_n)^2 + \frac{5}{2} (u_n - u_{n-1})^2 \right] - \Omega_0^2 u_n \,. \quad (10)$$

This equations show that the nonlinearity for the case of dipolar interaction is increased, with respected to the monopolar interaction.

The on-site potential restoring force $-V'_{\text{ext}}$ is in general a nonlinear function. However, for small displacements, as considered here, it can be linearized as $-V'_{\text{ext}} = -\Omega_0^2 u_n$, where Ω_0 is the normalized frequency of oscillation of a particle due to the external potential. If the on-site potential term is neglected (no external forces acting on the chain), Eq. (9) reduces to the celebrated α-FPU equation.

Following our purpose of obtaining approximate analytical solutions that describe the main dynamical features of our system, let us neglect the weak on-site potential term. Defining the strain as $v_n = u_n - u_{n-1}$, we obtain the motion equation of the

strain for $\alpha = 2$ as

$$\ddot{v}_n = -\frac{1}{(1+v_{n-1})^2} + \frac{2}{(1+v_n)^2} - \frac{1}{(1+v_{n+1})^2}\,, \tag{11}$$

where $v_n = 0$ corresponds to an unperturbed bond. Kinks can be excited by forcing the lattice with a half-wave perturbation. That can be done producing a sinusoidal displacement of the particle at one of the boundaries during half of the period that returns to the equilibrium position after finishing the pulse. For describing a kink profile traveling to the right, the following *ansatz* is introduced [14, 15]:

$$v_n = \begin{cases} -\frac{A}{2}\left[1+\cos\left(qn-\omega t\right)\right] & \text{if} \quad -\pi < \frac{2\pi}{3}n - \omega t < \pi \\ \\ 0 & \text{otherwise.} \end{cases} \tag{12}$$

where A represents the kink strain amplitude. The displacements of the particles in the lattice corresponds to compressed bonds, so v_n is a variable that takes negative values, being its maximum value $|v_n|_{\max} = A$ corresponding to the maximal compression of a bond. Looking at Eq. (12) we realize that for such a pulsed excitation q it is not strictly speaking the wavenumber and ω the frequency, but we will adopt this terminology for being the used one in the literature.

Equation (12) with $q = 2\pi/3$ is an exact solution of the $\alpha - \beta$ FPU lattice [15]. This particular value of q is known in the literature as the *magic wavenumber*. For a given wavenumber and taking into account the relation $\lambda = 2\pi/q$ we obtain solutions where an integer value of bonds (λ) and particles ($\lambda - 1$), i.e., the kink core, are in motion. The first case is the *magic wavenumber* $\lambda = 3$ ($q = 2\pi/3$) where 2 particles are moving at a given time. The other important mode correspond to $\lambda = 2$ ($q = \pi$), referred here and beyond as the π-mode, when only one particle is moving at a given time. This mode is the limit where only one particle is moving at a given time and it corresponds to a hard-spheres potential with zero radius. This is therefore a reference mode and real systems can only approximate it at high energies.

6 Harmonic Substrate Potential

6.1 Transient Kinks

Using the weak substrate potential configuration, as shown in Fig. 2a, experimental results were obtained driving the chain at the first oscillator with a pulsed waveform excitation (half-sinusoidal wave). The obtained temporal waveforms for the displacement and the compression are shown in Fig. 5a, b for a strain amplitude $A = 0.15$. This figure shows the experimental results using the magnetic chain and the numerical simulations using Eq. (2) with an inverse power law close to the dipole iteration

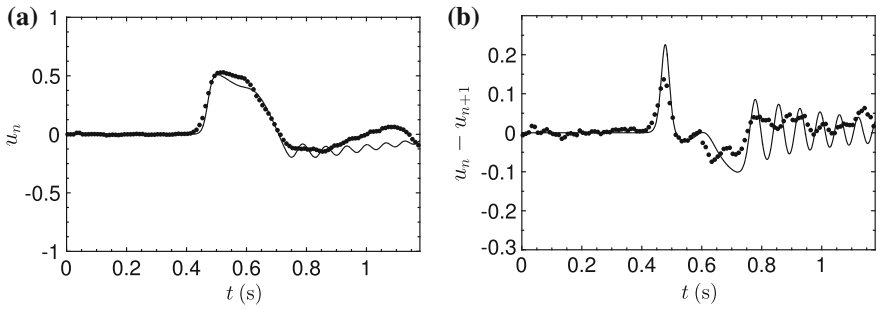

Fig. 5 **a** Kink profile in time, u_n, measured at $n = 23$. Numerical solution of Eq. (2) including the harmonic substrate (solid line), and experimental data (back dots). **b** Corresponding compression $-v_{n+1} = u_n - u_{n+1}$. Parameters $\alpha \simeq 3.6$ and approximate substrate harmonic potential with frequency $f_0 = \Omega_0/2/pi\,1.5\,\text{Hz}$

type, $\alpha = 3.6$, and a harmonic substrate potential with $f_0 = \Omega_0/2\pi = 1.5\,\text{Hz}$. The experimental data are in good agreement with the numerical simulation. It can be observed the formation of a kink at the front of the displacement wave (Fig. 5a), leading to a compression soliton as it is clearly observed in Fig. 5b. Then, after about 0.3 s, it can be seen the effect of the restoring force of the pendula: as the unique stable state is $u_n = 0$, the chain relaxes to its initial position and no exact kink can be formed. After the kink passes, a phonon tail is observed, being its arrival time given by the linear dispersion relations.

Although the kinks in a chain with a linear restoring force are not stable, the wavefront of these transient kinks obeys the analytical solution (12). The profile of the kink in space is shown in Fig. 6. Here, we show the numerical and experimental solutions, and the analytical solution of the FPU equation with $\alpha = 2$, i.e., Eq. (12). First, it can be observed that kinks can be excited in the experimental lattice for the temporal window analyzed. The experimental data are in good agreement with the numerical simulation and the analytic solution for a wavenumber $q \approx 2\pi/4$. The number of bonds in the numerical and analytical solutions can be obtained by fitting the profile to and it is $\lambda \approx 4.5$, while the number of particles in motion is $\lambda - 1 \approx 3.5$. Thus, in the experimental data, the number of bonds and number of particles in motion seem to increase from the magic wavenumber kinks $\lambda = 3$. This can be caused by the effect of the weak harmonic potential, the separation from the $\alpha - \beta$-FPU equation due to large displacements, and to the magnetic force, for which the long range interaction and the multiple neighbors interaction must be taken into account. Research on the subject is underway and will be published elsewhere [4].

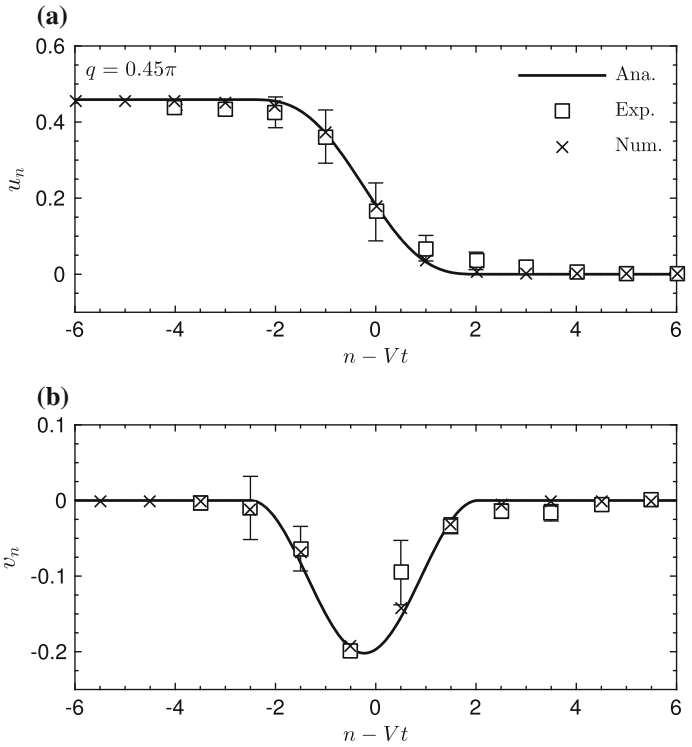

Fig. 6 **a** Kink profile in space, u_n, for pendulums ranging from $n = 23, 33$ of a chain of $N = 53$ magnets. Analytic solution using Eq. (12) $q = 2\pi/3$ (solid line), numerical simulation Eq. (2) (back dots), and experimental data (circles). **b** Corresponding strain $v_n = u_n - u_{n-1}$. Parameters $\alpha \simeq 3.6$ and approximate substrate harmonic potential with $f_0 = 1.5$ Hz. Reproduced from [17]. Licensed under CC-BY-NC-ND

6.2 *Kink Velocity*

The characterization of the kink velocity has been previously studied in Archilla et al. [2] where they used the Rotating Wave Approximation (RWA) to introduce the relation between the kink velocity V and the excitation amplitude A. When we substitute the *ansatz* of Eq. (12) into (11), we generate multiple terms with different frequencies. Following the RWA we select only terms up to the first harmonic, neglecting higher harmonics. We obtain the frequency ω as a function of the amplitude A as

$$\omega = \frac{1}{(1-A)^{3/4}} \omega_c \sin\left(\frac{q}{2}\right) , \tag{13}$$

where $\omega_c = 2c_0 = 2\sqrt{\alpha}$, and from this Eq. (13) we can calculate the kink velocity V as:

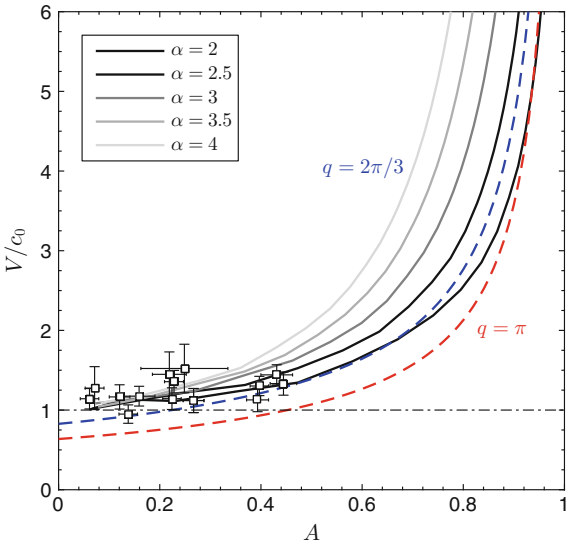

Fig. 7 Normalized kink velocity, V/c_0, versus kink amplitude, A. RWA solution $q = [\pi, 2\pi/3]$ (dashed lines), simulations of the chain for different inverse power laws (gray lines) and experimental data (markers). We tracked the pendula $n = 25, 26, 27$. Experimental data obtained with a weak harmonic potential and theoretical curves for a system without substrate as given by Eq. (14). Reproduced from [17]. Licensed under CC-BY-NC-ND

$$V = \frac{\omega}{q} = \frac{1}{(1-A)^{3/4}} \frac{2c_0}{q} \sin\left(\frac{q}{2}\right) . \tag{14}$$

Therefore, kinks are supersonic. Figure 7 shows the kink velocity V versus its amplitude A. Two cases are shown, first $q = \pi$ which means that only one particle is moving and *magic wavenumber* $q = 2\pi/3$ when two particles are in motion. The experimental results are also shown in Fig. 7 for a range of amplitudes ranging from $A = [0.07, 0.5]$. First, it can be seen that increasing the excitation amplitude makes the kink to propagate faster, being its speed always supersonic. Second, for the measured amplitude range, the experimental data for the transient kinks are compatible with the *magic wavenumber* $q = 2\pi/3$ solution and not with the π-mode as stated above. Third, the effect of the exponent of the inverse power law is to increase the sound speed in the system without substrate, which is $c_0 = \sqrt{\alpha}$. Finally, as can be clearly seen in the Taylor expansion of the FPU Eq. (8), increasing α at the particle interaction also increases the nonlinearity of the system. This leads to higher kink velocity values for the dipole interaction than for the purely Coulomb (monopole) interaction, being the family of supersonic solitons strongly dependent on the exponent of the inverse power law α.

6.3 Old Age Solution: Breathers

The kink solution is only valid for the initial transient. If the substrate potential V_{ext} introduces a linear restoring force with no periodicity in space, the unique stable

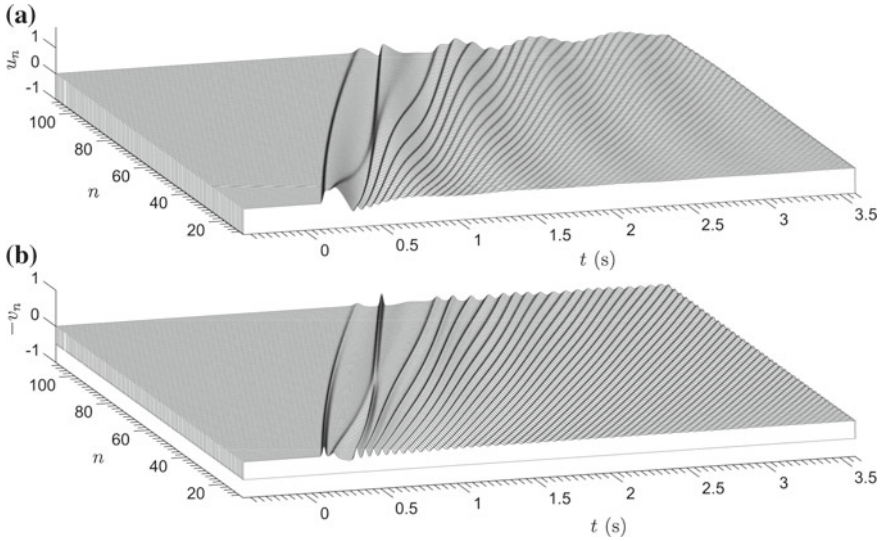

Fig. 8 Space-time profiles for transient solution. **a** Displacement and **b** compression $-v_n = u_{n-1} - u_n$ of the transient solution including a harmonic restoring force with characteristic frequency $f_0 = 1.5\,\mathrm{Hz}$

state is $u_n = 0$, and, therefore, the kink cannot be formed in the old-age solution. The transient process is shown in Fig. 8 for the displacement and for the compression $-v_n = u_{n-1} - u_n$ respectively. It can be observed that at the beginning of the chain the kink solution is similar to those obtained in the measurements. However, for longer distances the kink degenerates in other nonlinear waves. For old-age solution, we obtain other nonlinear localized excitation traveling at the kink front. The solution is shown in Fig. 9a–c for the dipole case, $\alpha = 4$. Simulations show that the nature of the dynamics of the system do not depend substantially on the exponent of the inverse power law. First, for a weak harmonic potential, similar to the effect of the pendula in the experiments, i.e. with a characteristic frequency of $f_0 = 1.5Hz$, we observe a large transient. Then, the kink disaggregates: the core of the kink transforms gradually into a breather-like localized state. The old-age solution is shown in Fig. 9a, where a stable localized nonlinear wave is observed and propagates at supersonic speed. This localized wave is internally composed of three internal solitonic oscillations that travel inside the core of the breather faster than the breather itself. Simulations show that this nonlinear localized mode is stable. Once formed, the breather composed by this three solitonic waves propagates thousand of lattice units.

The dynamics of these localized nonlinear waves is linked to the substrate potential. Figure 9b shows the space-time profile of the old-age solution for a different harmonic substrate with characteristic frequency of $f_0 = 3.5$ Hz. The transient from the kink to the breather is shortened, and also its width. Because of the shortening of the breather, its composing internal waves are more evident. Finally, the solution

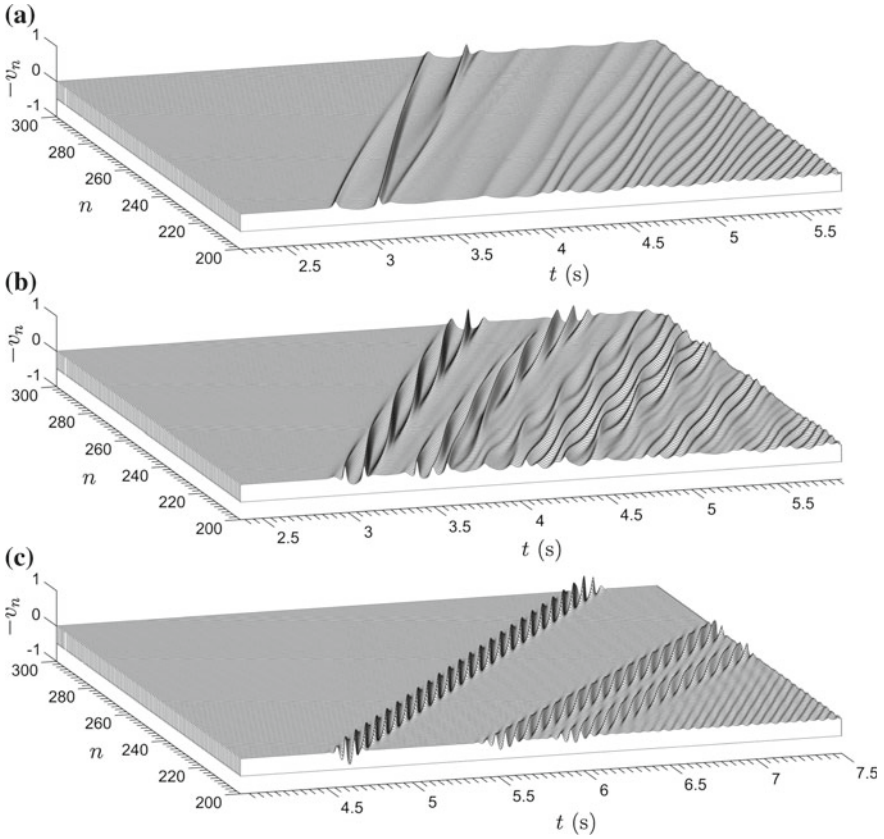

Fig. 9 Space-time profiles for the compression $-v_n = u_{n-1} - u_n$ of the old-age solution including a harmonic restoring force with characteristic frequencies of **a** $f_0 = 1.5$ Hz, **b** $f_0 = 3.5$ Hz and **c** $f_0 = 10$ Hz

including a high frequency substrate, $f_0 = 10$ Hz, is shown in Fig. 9c, where it can be observed that the breather frequency remarkably increased.

In this case, a single packet of energy propagates supersonically through the lattice. The localization also depends on the substrate potential and the strain amplitude of the localized wave, ranging from 22 lattices units for the low frequency substrate to 10 to the high frequency one. The internal dynamics shows that the core of the localized state is formed by three internal oscillations. The corresponding displacement is shown in Fig. 10a–c, where the localized waves are also clearly observed. After the wave passes, the harmonic potential force the lattice to oscillate around $u_n = 0$, therefore, no kink can be formed in the old-age solution.

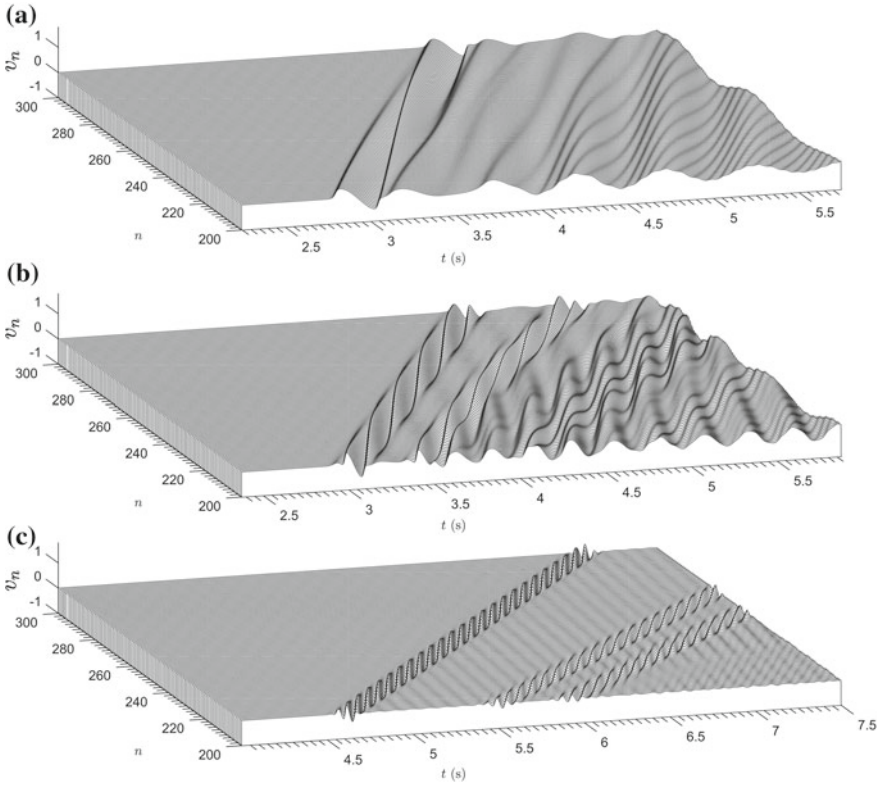

Fig. 10 Space-time profiles for the displacements v_n of the old-age solution including a harmonic restoring force with characteristic frequencies of **a** $f_0 = 1.5$ Hz, **b** $f_0 = 3.5$ Hz and **c** $f_0 = 10$ Hz

7 Periodic Substrate Potential

The experimental results previously shown were obtained including a weak on-site potential due to the gravity restoring force that brings pendulums to their equilibrium position in the chain. The smallness of this force compared to the magnetic repulsive interaction allows us to neglect the effect of the substrate potential for the transient solution observed in the experiments, i.e., the low cut-off frequency of the dispersion relation is near zero.

A more realistic model of condensed matter, with multiple stable states at $u_n = n$, can be obtained using the current experimental setup by including a strong and periodic substrate potential using the configuration shown in Fig. 3. A set of fixed magnets is placed periodically at $x = (n + 1/2)a$, being the vertical separation $h =$ 15 mm. The chain is excited under the same conditions than in the previous study. The simulated waveforms are shown in Figs. 11 and 12 for the strain and the displacement, respectively. First, it can be observed that with a periodic substrate force $V'_{\text{ext}} =$

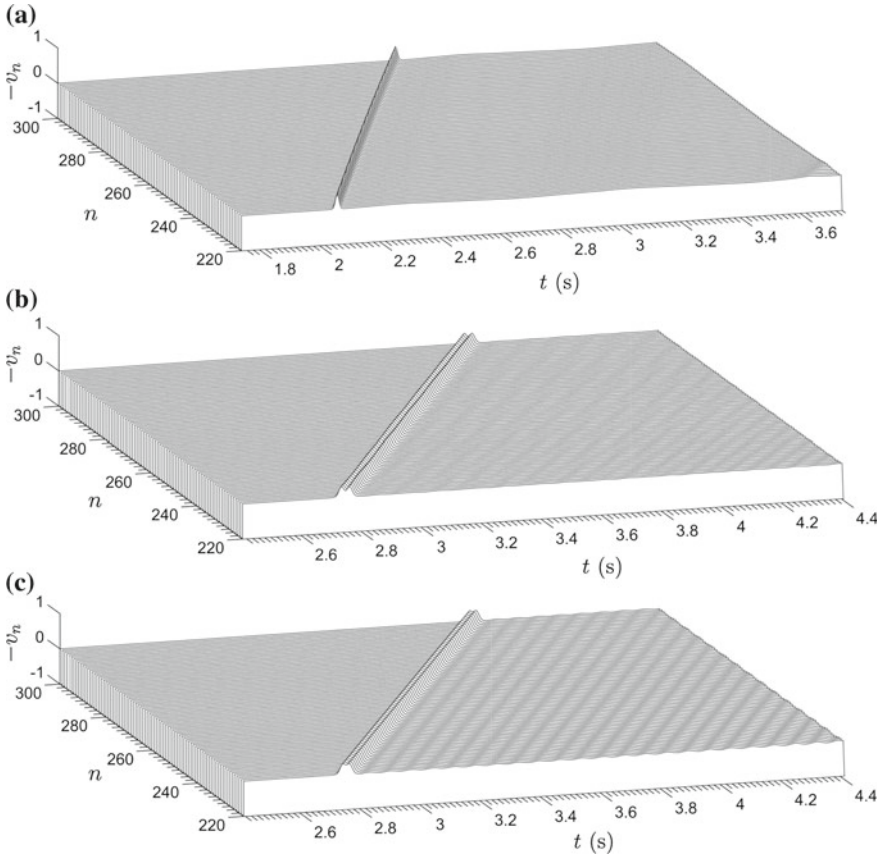

Fig. 11 Space-time profiles for the compression $-v_n = u_{n-1} - u_n$ of the old-age solution including a periodic restoring force with characteristic frequencies of **a** $f_0 = 1.5$ Hz, **b** $f_0 = 6.5$ Hz and **c** $f_0 = 10$ Hz

$\Omega_0^2 \sin 2\pi u_n$, with a characteristic frequency of $f_0 = \Omega_0/2/pi = 1.5$ Hz, a kink is formed that travels at supersonic speed, meaning at a speed both larger than the maximum group velocity of the phonons in the system with substrate, but also larger than the sound speed in the system without substrate. Behind the kink it is also observed a phonon radiation tail that oscillates at the characteristic frequency of the periodic substrate. It is worth noting here the strong differences in the dynamics of the nonlinear localized waves generated between systems using a harmonic restoring force or a periodic substrate potential, even when both small-amplitude frequency of the substrates are equal. If this frequency is increased, i.e., for stronger substrate potentials, the kinks are still observed, as shown for $f_0 = 6.5$ Hz in the space-time strain and displacement plots in Figs. 11b and 12b respectively, and in Figs. 11c and 12c for a strong substrate interaction with $f_0 = 10$ Hz. Here, the dynamics are essentially similar to the one obtained for a realistic potentials of mica muscovite in

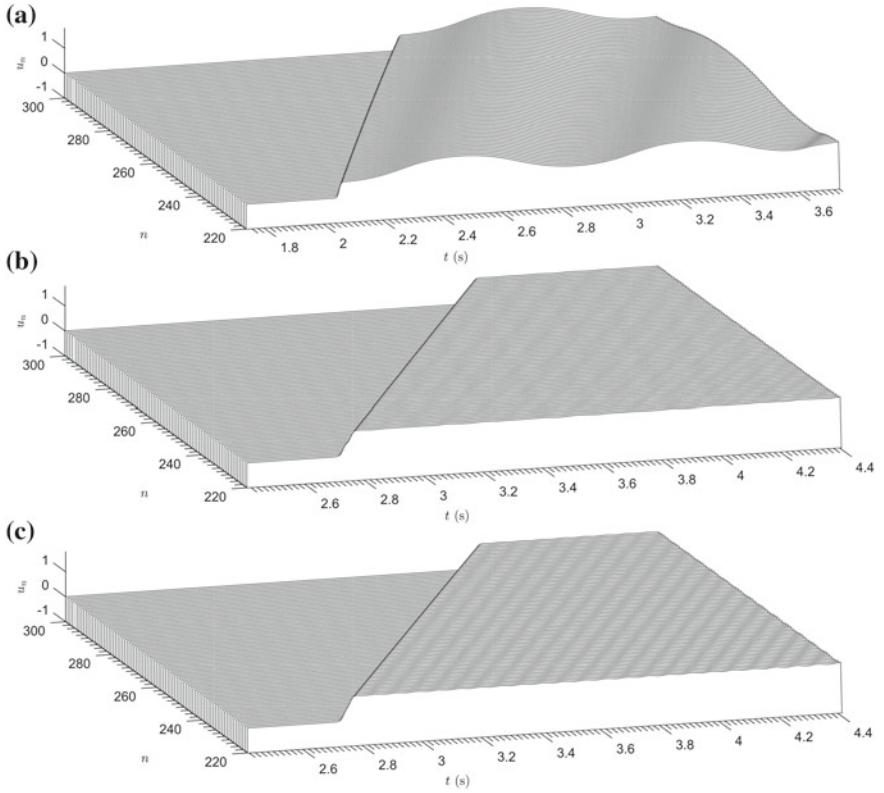

Fig. 12 Space-time profiles for the displacements u_n of the old-age solution including a periodic restoring force with characteristic frequencies of **a** $f_0 = 1.5$ Hz, **b** $f_0 = 6.5$ Hz and **c** $f_0 = 10$ Hz

Ref. [4], showing that the periodic substrate potential is a necessary factor to obtain stable kinks in latices.

8 Conclusions

Chains of particles coupled by repulsive forces allow the study of certain properties of condensed matter at a bigger scale. In particular, we have built a system of coupled pendulums that opens the possibility to perform experimental studies that at atomic scale become extremely difficult or unpractical. The study of such kind of systems have several advantages. The first one is that, after some assumptions, it is possible to approximate the corresponding equation of motion to the celebrated FPU equation, i.e., it allows us to obtain analytical approximate solutions. The second one is that

the complete equation is numerically integrable, giving a accurate approximation of the exact dynamics to guide the experiments.

In this chapter, we focus the study on kinks and localized nonlinear excitations in repulsive lattices with substrate potentials. Such type of system admits a mechanical analogue that can be studied in the laboratory and, exciting it conveniently, allows the study a broad range of nonlinear localized waves. In particular, we presented here a system consisting of a chain of repulsive oscillators coupled magnetically. The effect of the finite size of the magnets allows the modeling of different repulsive interactions, following all of them the inverse power law with the distance. Thus, just by modifying the geometry of the chain we can study repulsive interactions of monopolar (Coulomb type), dipolar or non-integer power type. Moreover, we have presented the dynamics that emerges from the different nature of the substrate potential.

If the substrate potential is purely harmonic, i.e., the restoring force is linear, as in the case of long pendulums, we show that kinks can exist only for a short time, and after a transient, supersonic breathers are formed. The dynamics of the system is deeply related with the fact that every pendulum is subjected to a restoring force, the gravity, for which the unique stable state corresponds to the displacement $u_n = 0$. The situation is completely different if we include a periodic substrate potential that allows multiple stable states in the chain. In this case, we report the generation of kinks that travel at supersonic speed through the lattice. It is worth noting here that in the chain of magnets a periodic substrate potential can be introduced simply by including a set of fixed magnets that adds repulsive periodic forces, much more intense than the corresponding to the restoring force due to gravity, i.e., that dominates the dynamics of the system.

Acknowledgements All authors acknowledge grant FIS2015-65998-C2-2-P from Ministerio de Economía y Competitividad (MINECO), Spain, which funded this research. AM gratefully acknowledge to Generalitat Valenciana (Santiago Grisolia program). LJSC gratefully acknowledge the support of PAID-01-14 at Universitat Politècnica de València. JFRA also aknowledges the (2017/FQM-280) grant from Junta de Andalucía.

References

1. Archilla, J.F.R., Jiménez, N., Sánchez-Morcillo, V.J., García-Raffi, L.M. (eds.): Quodons In Mica: Nonlinear Localized Travelling Excitations In Crystals, Springer series in materials science, vol. 221. Springer International Publishing, Cham (2015)
2. Archilla, J.F.R., Kosevich, YuA, Jiménez, N., Sánchez-Morcillo, V.J., García-Raffi, L.M.: Moving excitations in cation lattices. Ukr. J. Phys. **58**(7), 646–656 (2013)
3. Archilla, J.F.R., Kosevich, YuA, Jiménez, N., Sánchez-Morcillo, V.J., García-Raffi, L.M.: Supersonic kinks in Coulomb lattices. In: Carretero-González, R., Cuevas, J., Frantzeskakis, D., Karachalios, N., Kevrekidis, P.G., Palmero, F. (eds.) Localized Excitations in Nonlinear Complex Systems, pp. 317–331. Springer International Publishing, Cham (2014)
4. Archilla, J.F.R., Kosevich, YuA, Jiménez, N., Sánchez-Morcillo, V.J., García-Raffi, L.M.: Ultradiscrete kinks with supersonic speed in a layered crystal with realistic potentials. Phys. Rev. E **91**(2), 022912 (2015)

5. Archilla, J.F.R., Kosevich, Yu.A., Jiménez, N., Sánchez-Morcillo, V.J., García-Raffi, L.M.: A supersonic crowdion in mica. In: J.F.R. Archilla, N. Jiménez, V.J. Sánchez-Morcillo, L.M. García-Raffi (eds.) Quodons In Mica: Nonlinear Localized Travelling Excitations In Crystals, Springer Series in Materials Science, vol. 221, pp. 69–96 (2015)
6. Archilla, J.F.R., Russell, F.M.: On the charge of quodons. Lett. Mater. **6**, 3–8 (2016)
7. Camacho, J.M., Sosa, V.: Alternative method to calculate the magnetic field of permanent magnets with azimuthal symmetry. Rev. Mex. Fis. **59**, 8–17 (2013)
8. Deshpande, V.V., Bockrath, M.: The one-dimensional Wigner crystal in carbon nanotubes. Nat. Phys. **4**(4), 314–318 (2008)
9. Griffiths, D.J.: Introduction to Electrodynamics, 3 edn. Prentice Hall (2007)
10. Homann, A., Melzer, A., Peters, S., Piel, A.: Determination of the dust screening length by laser-excited lattice waves. Phys. Rev. E **56**(6), 7138–7141 (1997)
11. Jackson, J.D.: Classical Electrodynamics, 3 edn., p. 190 WileyJohn Wiley and Sons (1999)
12. Jiménez, N.: Nonlinear acoustic waves in complex media. Ph.D. thesis, Universitat Politècnica de València, València, Spain (2015). https://doi.org/10.4995/Thesis/10251/53237
13. Kittel, C.: Solid State Physics, 8 edn. John Wiley and Sons (2004)
14. Kosevich, YuA: Nonlinear sinusoidal waves and their superposition in anharmonic lattices. Phys. Rev. Lett. **71**(13), 2058–2061 (1993)
15. Kosevich, YuA, Khomeriki, R., Ruffo, S.: Supersonic discrete kink-solitons and sinusoidal patterns with magic wave number in anharmonic lattices. Europhys. Lett. **66**(1), 21–27 (2004)
16. Matveev, K.A., Andreev, A.V., Pustilnik, M.: Equilibration of a one-dimensional Wigner crystal. Phys. Rev. Lett. **105**(4), 046401 (2010)
17. Mehrem, A.: Nonlinear acoustics in periodic media :from fundamental effects to applications. Ph.D. thesis, Universitat Politècnica de València, València, Spain (2017). https://doi.org/10.4995/Thesis/10251/80289
18. Molerón, M., Leonard, A., Daraio, C.: Solitary waves in a chain of repelling magnets. J. Appl. Phys. **115**(18), 184901 (2014)
19. Nosenko, V., Avinash, K., Goree, J., Liu, B.: Nonlinear interaction of compressional waves in a 2D dusty plasma crystal. Phys. Rev. Lett. **92**(8), 085001 (2004)
20. Peyrard, M., Pnevmatikos, S., Flytzanis, N.: Discreteness effects on non-topological kink soliton dynamics in nonlinear lattices. Phys. D **19**(2), 268–281 (1986)
21. Pnevmatikos, St, Flytzanis, N., Remoissenet, M.: Soliton dynamics of nonlinear diatomic lattices. Phys. Rev. B **33**(4), 2308–2321 (1986)
22. Poggi, P., Ruffo, S.: Exact solutions in the FPU oscillator chain. Phys. D **103**(1–4), 251–272 (1997)
23. Porras, D., Marquardt, F., Von Delft, J., Cirac, J.I.: Mesoscopic spin-boson models of trapped ions. Phys. Rev. A **78**(1), 010101 (2008)
24. Raizen, M.G., Gilligan, J.M., Bergquist, J.C., Itano, W.M., Wineland, D.J.: Ionic crystals in a linear Paul trap. Phys. Rev. A **45**(9), 6493 (1992)
25. Remoissenet, M.: Waves called solitons: concepts and experiments. Springer Science & Business Media (2013)
26. Russell, F.M., Eilbeck, J.C.: Evidence for moving breathers in a layered crystal insulator at 300 K. Europhys. Lett. **78**(1), 10004 (2007)
27. Russell, F.M., Zolotaryuk, Y.O., Eilbeck, J.C., Dauxois, T.: Moving breathers in a chain of magnetic pendulums. Phys. Rev. B **55**(10), 6304–6308 (1997)
28. Savin, A.V., Zolotaryuk, Y.O., Eilbeck, J.C.: Moving kinks and nanopterons in the nonlinear Klein-Gordon lattice. Phys. D **138**(3), 267–281 (2000)

Kinetics of Annealing: Basic Relationships and Nonlinear Effects

Pavel A. Selyshchev and Pavel M. Bokov

Abstract The thermal annealing of radiation-induced interstitial clusters is analysed, taking into account the nonlinear feedback between the defect density, the rate of annealing, and the temperature (thermal-concentration feedback). The discussion covers isothermal and isochronous annealing regimes, a change in cluster size distribution during the annealing, and the travelling wave of annealing. It is shown that the thermal-concentration feedback leads to a stronger than exponential dependence of the number of annealed defects on time, and is the mechanism of the self-sustained annealing and its propagation. Furthermore, the travelling wave of annealing can be unstable with respect to oscillations of the propagation rate and the temperature profile. The reason for this instability is the preheating of an as yet un-annealed area of metal.

Keywords Thermal annealing · Radiation-induced clusters · Thermal-concentration feedback · Self-sustained annealing · Travelling wave of annealing

1 Introduction

It is well known that the degradation of materials due to irradiation reduces the operating life of nuclear facilities [19]. Radiation affects materials in many ways, but the main reason for their degradation is radiation-induced defects, which cause changes in material microstructure and properties. One of the most common and efficient ways of recovering radiation damaged metals is by thermal annealing [4].

P. A. Selyshchev
Department of Physics, University of Pretoria, Private bag X20, Hatfield 0028, South Africa
e-mail: selyshchev@gmail.com

P. M. Bokov (✉)
Radiation Science Department, The South African Nuclear Energy Corporation SOC Ltd (Necsa), Building 1900, P.O. Box 582, Pretoria 0001, South Africa
e-mail: pavel.bokov@necsa.co.za

J. F. R. Archilla et al. (eds.), *Nonlinear Systems, Vol. 2*, Understanding Complex Systems, https://doi.org/10.1007/978-3-319-72218-4_12

The state of the metal after irradiation is metastable because the irradiated sample is an open system far from thermodynamic equilibrium [14]. The flux of high-energy particles produces different types of defects (both point- and extended ones, such as dislocation loops) in the crystal lattice. A thermal generation of these defects is impossible because they require a large amount of energy for their formation. For example, as a result of the creation of one interstitial atom, the energy of the crystal increases by a few electronvolts; subsequent formation of interstitial loops and voids requires hundreds and thousands of electronvolts for each loop or void [2, 7, 19]. Further formation of radiation defects leads to an even higher growth of the athermal energy of the crystal, caused by the creation of defects.

After irradiation, the radiation-induced material condition starts to relax towards equilibrium. The crystal structure of the metal begins to recover as a result of the thermal decomposition of extended low-mobile defects and due to the diffusion of point defects. Since all aforementioned processes are thermally activated, the relaxation rate depends strongly on temperature. Therefore, the set of relaxation processes leading to the restoration of the original properties of the metal is referred to as *annealing* whereas annealing of a given class of defects means their disappearance. For defects to anneal, each of them should be provided with a certain amount of energy, referred to as the *activation energy*, E_a. At low temperatures defects with a low activation energy are annealed, e.g. interstitial atoms, while at higher temperatures defects with a higher E_a are annealed. For clusters of defects, if the process is not limited by the migration of particles in a crystal with the subsequent recombination, this energy is the binding energy of the defects in the cluster. For clusters of interstitial atoms in metals the binding energy can reach several electronvolts [11, 19]. In the case of a large binding energy of a cluster, its thermal decomposition becomes unlikely, and the annealing of the cluster is determined by the recombination with mobile vacancies.

If the temperature of the crystal is too low, then the probability for a defect to obtain an amount of energy comparable to the activation energy is very small, and annealing does not occur, i.e. defects of this type, despite the fact that they are not in equilibrium, remains stable at this temperature. The state of the metal after irradiation is therefore metastable, although essentially non-equilibrium. This is schematically shown in Fig. 1.

In addition, annealing of radiation-induced defects is one of the few ways of obtaining information about the characteristics of these defects. Two types of thermal annealing experiments are usually performed: *isothermal* ones, in which a sample is kept at a constant temperature for some, usually long, periods of time; and *isochronous* ones, when the sample is subjected to different increasing temperature values during the same period of time.

In the case of isochronous experiments, defects with increasing activation energy are annealed sequentially and six stages (of annealing) are usually distinguished [4]. These stages are identified based on a change of physical characteristics that are sensitive to defects of the crystal, for example, conductivity or hardening. The interpretation of annealing stages is not unequivocal [4, 7]. Stage I is associated with the recombination of Frenkel pairs, located at small distances from each other due

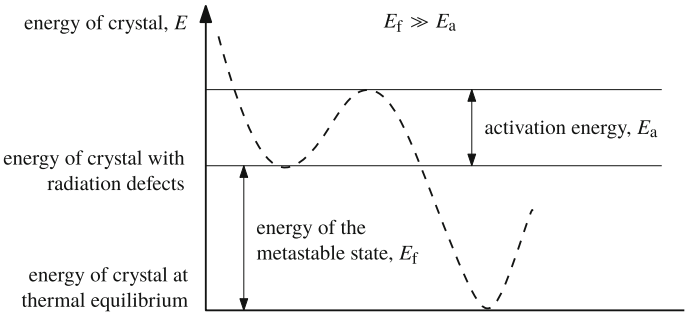

Fig. 1 Schematic of an irradiation-damaged material in a metastable state

to the mobility of the interstitial atoms. Stage II is associated with the movement of interstitial atoms to more distant sinks (such as dislocations, pores, formations of a second phase, dislocation loops, external surfaces, grain boundaries). Stage III is associated with the processes of decay of clusters, for example, the release of interstitial atoms from impurity traps (e.g. complexes of interstitial and impurity atoms), which could be formed in the crystal either during the irradiation or at Stage I. Stage IV corresponds to the beginning of the migration of vacancies to sinks and the formation of clusters of vacancies. In Stage V the recrystallization processes occur which involve an intensive migration of defects to the surface of the material, and other restructuring. Stage VI is detected in the range 0.33–0.45 of the melting temperature for bcc and 0.4–0.53 for fcc crystals when studying the change of strength characteristics in the process of annealing of irradiated metals. This stage is linked to the annealing of hardening radiation defects; the activation energy of the process is close to the activation energy of recrystallization of the metal. Annealing of a small fraction (not more than 10%) of increase in yield strength occurs at a lower temperature than that of Stage V.

As a rule, in order to identify the activation energies of a particular process (migration of a defect or its decay), the temperature at which a change in a particular characteristic happens is used. Of no less importance but, because of the difficulties of interpretation, much less frequently used, is the dynamics of changes of this characteristics, which reflects the transformation in the structure of radiation damage (change in the density of different types of defects).

The kinetics of annealing of each defect class at a given temperature is a multistage and complex process since the result of annealing depends essentially on the microstructure of the metal and on the structure of defects created by the irradiation, as well as on their interaction.

Defects can interact directly, for example through deformation fields, or indirectly, due to the thermal-concentration feedback between the metal temperature and the rate of their annealing [13, 14]. Since the energy of irradiated material is the sum of two components: a *thermal* one, which corresponds to the temperature of the material, and an *athermal* one, which is stored in radiation-induced defects, then

upon annealing the latter is converted into heat and the temperature of the material increases. In turn, the temperature increase leads to the acceleration of annealing of defects (mainly due to the exponential dependence of the diffusion of mobile defects on temperature), which causes a further increase in temperature. As a result, a feedback between the rate of annealing of radiation defects, the generation of heat accompanying the annealing, and the temperature, is established. Under certain conditions, this feedback leads to the development of a *self-sustained annealing* which can significantly alter its overall kinetics. In particular, it can lead to the development of *self-oscillations* [18] of temperature and of defect density and to propagation of annealing *travelling waves* [3, 14, 16].

2 Homogeneous Annealing of Defects of a Single Type

For a better understanding of phenomena taking place in the processes of annealing, let us consider a single-stage annealing of defects of a single type. If the initial distribution of temperature and of defects over the sample are uniform, a homogeneous annealing of defects will take place. This means that the rate of annealing is equal at any point of space, the density of defects decreases but remains homogeneous, and any fluxes of defects and energy are absent.

2.1 Isothermal Annealing

Consider defects of a given type, k. The evolution of their density (defects m^{-3}), n_k, is described, in the case of isothermal annealing, by the equation

$$\frac{\mathrm{d}n_k}{\mathrm{d}t} = -\frac{n_k}{\tau_k} \,. \tag{1}$$

Given an initial value $n_{k,0}$, the density of defects thereby decreases monotonically according to the exponential law

$$n_k = n_{k,0} \exp\left(-t/\tau_k\right) \,, \tag{2}$$

with a characteristic time τ_k, which depends on temperature. For instance, in the case of an activation process, the characteristic time is given by the Arrhenius law

$$\frac{1}{\tau_k} = \beta_0^k \exp\left(-\frac{E_{\mathrm{a},k}}{k_\mathrm{B} T}\right) \,, \tag{3}$$

where β_0^k is a parameter which depends on the properties of the material, $E_{a,k}$ is the activation energy of annealing, T is the absolute temperature and k_B is the Boltzmann constant.

If the annealing of defects of different types is not linked via a common kinetics, it may be described with a few activation processes; in which case the concentration of defects of each type monotonically decreases according to the exponential law. As a rule, defects of different types are annealed at different temperatures, which correspond to their respective activation energies.

2.2 Isochronous Annealing

The evolution of the defect density in isochronous annealing is described by (1), but the temperature does not remain constant, and increases with time. We will consider two regimes of temperature change: stepwise and continuous.

In the first regime, starting at the time t_0 and continuing until t_1 the temperature is maintained constant and equal to T_1, then it abruptly rises to T_2, and is again kept constant during the time interval from t_1 to t_2, etc. During the time interval from t_{j-1} to t_j, the temperature is equal to T_j. In this case, the dependence of the density of defects on time has the form

$$n_k(t) = n_{k,0}\left[\prod_{i=1}^{j}\exp\left(\frac{t_{i-1}-t_i}{\tau_k(T_i)}\right)\right]\exp\left(\frac{t_j-t}{\tau_k(T_j)}\right), \quad \text{for } t > t_j\ , \tag{4}$$

where t_j is the time of a temperature increase which is closest to, but not exceeding, t. From the structure of (4) we see that, due to the Arrhenius dependence of the lifetime on temperature, the rate of annealing and the number of annealed defects of this type have a sharp maximum for a certain temperature: for the early low-temperature "steps" the annealing rate is negligibly small and the corresponding exponent in (4) is almost equal to one. However, at steps with high temperature, nothing is left to anneal. Therefore, a characteristic of the material sensitive to this type of defects should display a drastic change. It may enable us to identify the activation energy corresponding to this annealing stage, and the type of the annealed defects.

In the second regime the temperature increases linearly with time: $T(t) = T_0 + \dot{T}t$. The decrease in the density of defects is now described by the following expression

$$n_k(t) = n_{k,0}\exp\left(-\frac{\beta_0^k E_{a,k}}{k_B\dot{T}}\left[-\frac{e^x}{x} + \mathrm{Ei}\,(x)\right]\right)\Bigg|_{x=-a_1}^{x=-a_2},$$

where $a_1 = E_{a,k}/k_B T_0$, $a_2 = E_{a,k}/k_B\left(T_0 + \dot{T}t\right)$ and $\mathrm{Ei}\,(x)$ is a special function called the *exponential integral* and is defined by the Cauchy principal value of the integral [12]:

$$\mathrm{Ei}\,(x) = -\mathrm{v.p.}\int_{-x}^{\infty}\frac{\mathrm{e}^{-\xi}}{\xi}\mathrm{d}\xi = \mathrm{v.p.}\int_{-\infty}^{x}\frac{\mathrm{e}^{\xi}}{\xi}\mathrm{d}\xi\ , \quad x > 0\ . \tag{5}$$

2.3 Adiabatic Annealing: The Thermal-Concentration Feedback

An isothermal annealing requires heat removal to accompany the process. Otherwise the change of the temperature leads to a change of the characteristic annealing time, which turns to be time-dependent. In this case two equations are required to describe the annealing kinetics: one for the concentration (1) and one for the temperature:

$$\rho c\frac{\mathrm{d}T}{\mathrm{d}t} = \theta_k\frac{n_k}{\tau_k}\ . \tag{6}$$

Here ρ is the material density, c is the specific heat capacity and the product ρc is the volumetric heat capacity; θ_k is the energy released by the annealing of one defect.

The system of Eqs. (1) and (6) has an integral which represents the conservation of the total energy of the material, E_0:

$$\rho cT + \theta_k n_k = E_0\ . \tag{7}$$

After introducing dimensionless defect density (v), temperature (w), time ($\bar{t}$) and the dimensionless parameter α, which is the ratio of heat release to activation energy:

$$v = \frac{n_k}{n_{k,0}}\ , \quad w = \frac{k_\mathrm{B}T}{E_{\mathrm{a},k}}\ , \quad \bar{t} = \beta_0^k t \quad \text{and} \quad \alpha = \frac{k_\mathrm{B}\theta_k n_{k,0}}{\rho c E_{\mathrm{a},k}}\ ,$$

we obtain, instead of (1) and (6), the system:

$$\frac{\mathrm{d}v}{\mathrm{d}\bar{t}} = -v\mathrm{e}^{-1/w}\ , \tag{8}$$

$$\frac{\mathrm{d}w}{\mathrm{d}\bar{t}} = \alpha v\mathrm{e}^{-1/w}\ , \tag{9}$$

subject to the initial conditions

$$v(\bar{t}=0) = v_0 = 1\ ,$$
$$w(\bar{t}=0) = w_0\ .$$

The energy conservation relationship (7) can be rewritten as

$$\alpha v + w = \alpha v_0 + w_0 = w_\infty\ , \tag{10}$$

where $v_\infty = v(\bar{t} \to \infty) = 0$ and $w_\infty = w(\bar{t} \to \infty) = \alpha v_0 + w_0 = \alpha + w_0$.

Substituting αv from (10) to (9) and solving the resulting differential equation, one obtains a relationship between w and $\bar{t}$:

$$\bar{t} = \mathrm{Ei}\left(\frac{1}{w}\right) - \mathrm{Ei}\left(\frac{1}{w_0}\right) + \mathrm{e}^{1/w_0}\left[\mathrm{Ei}\left(\frac{1}{w_0} - \frac{1}{w_\infty}\right) - \mathrm{Ei}\left(\frac{1}{w} - \frac{1}{w_\infty}\right)\right] . \quad (11)$$

The growth of temperature with time, as described by (11), is illustrated in Fig. 2 for parameter values corresponding to aluminium: $T_0 = 300\,\mathrm{K}$, $E_{\mathrm{a},k}/k_\mathrm{B} = 5\,802\,\mathrm{K}$, $\theta_k n_{k,0}/\rho c = 180\,\mathrm{K}$ and $\beta_0^k = 10^7\,\mathrm{s}^{-1}$. The temperature dependence on time has a shape of the smoothed step function. A rapid (faster than exponential) temperature growth is observed in the beginning. The rate of annealing thereby increases, reaches the maximum and starts to decrease: the temperature slowly approaches its stationary value w_∞. The temperature value at the inflection point, w_*, is a positive solution of the quadratic equation

$$w_*^2 + w_* - w_\infty = 0 . \quad (12)$$

The maximum rate of temperature increase is achieved at the inflection point $\bar{t}_* = \bar{t}(w_*)$ and is $\left(\mathrm{d}w/\mathrm{d}\bar{t}\right)|_{\bar{t}=\bar{t}_*} = w_*^2\mathrm{e}^{-1/w_*}$. The temperature growth can therefore be approximated with a linear function in the vicinity of the inflection point (recall that at the inflection point $(\mathrm{d}^2w/\mathrm{d}\bar{t}^2)|_{\bar{t}=\bar{t}_*} = 0$ and the second order term vanishes):

$$w(\bar{t}) = w_* + w_*^2\mathrm{e}^{-1/w_*}\left(\bar{t} - \bar{t}_*\right) .$$

For typical parameters of metals (heat capacity, heat conductivity, energy of formation and migration of defects) the difference between w_∞ and w_* does not exceed 20%, i.e. the temperature quickly approaches a value close to the maximum and after that it practically does not change.

The dependence of defect density on time is a vertically flipped and scaled version of the temperature curve (see Fig. 2, the left graph). This is expected from the energy conservation relationship described by (7) and (10).

The initial ($\bar{t} \to 0$) growth of dimensionless temperature (and, accordingly, the reduction in defect density) can be approximated by the exponential dependence

$$w(\bar{t}) = w_0 + \left(\frac{w_\infty - w_0}{w_\infty - w_0 - w_0^2}\right)\left(-1 + \mathrm{e}^{\bar{t}/\bar{\tau}_0}\right) , \quad (13)$$

with characteristic time $\bar{\tau}_0$:

$$\bar{\tau}_0 = \left(\frac{w_0^2}{w_\infty - w_0 - w_0^2}\right)\mathrm{e}^{1/w_0} . \quad (14)$$

The terminal ($\bar{t} \to \infty$) part of temperature growth (and of corresponding defect decay) can be approximated by the dependence

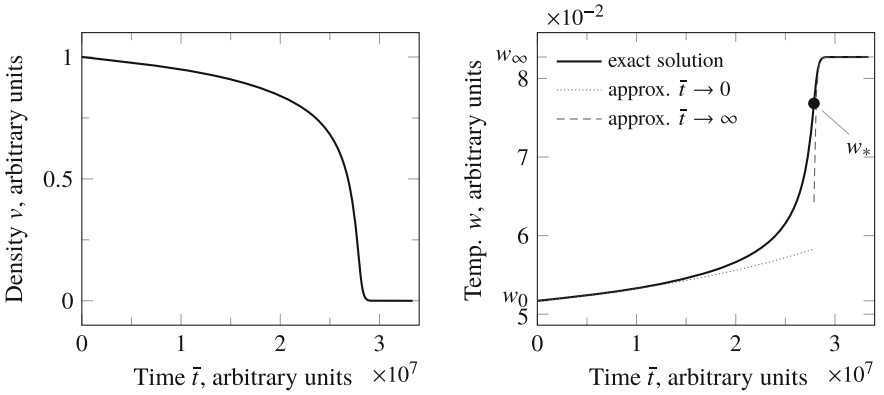

Fig. 2 Homogeneous adiabatic annealing of irradiation defects for a material with parameters corresponding to aluminium (presented for dimensionless variables). The left graph illustrates the dependence of defect density on time. The right graph shows the dependence of the material temperature on time, as well as the approximations for $\bar{t} \to 0$ and $\bar{t} \to \infty$, shown with dotted and dashed lines respectively, and the inflection point, w_*

$$w(\bar{t}) = w_\infty \left(1 - \frac{w_\infty - w_b}{w_\infty} \mathrm{e}^{-(\bar{t}-\bar{t}_b)/\bar{\tau}_\infty}\right) , \tag{15}$$

with characteristic time

$$\bar{\tau}_\infty = \mathrm{e}^{1/w_\infty} , \tag{16}$$

where parameters $\bar{t}_b$ and w_b are defined from an additional condition that for some, sufficiently large $\bar{t}_b$, $w\left(\bar{t}_b\right) = w_b$.

The ratio between $\bar{\tau}_\infty$ and $\bar{\tau}_0$ depends on the initial temperature and the amount of energy stored in defects. If the stored energy is small, the characteristic times are comparable and the accelerating annealing of defects is not observed. In this case the process is described by the more gradually growing part of the curve above the inflection point. Otherwise $\bar{\tau}_\infty \gg \bar{\tau}_0$: for instance, for activation energy $E_{\mathrm{a},k} = 0.3\,\mathrm{eV}$ with initial and final temperatures 300 and 600 K respectively, $\bar{\tau}_\infty/\bar{\tau}_0 \approx 10^4$.

2.4 *Influence of Energy Dissipation*

When the energy dissipation is taken into account, Eq. (6), and correspondingly Eq. (9), are transformed to

$$\rho c \frac{\mathrm{d}T}{\mathrm{d}t} = \theta_k \frac{n_k}{\tau_k} - \rho c \frac{T - T_\mathrm{e}}{\tau_\mathrm{h}} \quad \text{or} \quad \frac{\mathrm{d}w}{\mathrm{d}\bar{t}} = \alpha v \mathrm{e}^{-1/w} - h\,(w - w_\mathrm{e}) ,$$

where T_e is the environment temperature, τ_h is the characteristic time of heat transfer, w_e is the dimensionless environment temperature and $h = (\beta_0^k \tau_h)^{-1}$. Equations (1) and (8) do not change.

If the annealed sample transfers heat to the surrounding environment, its total energy is not preserved and relation (7) is not satisfied. Accordingly, Eqs. (7) and (10) are replaced by

$$\frac{dT}{dt} = \frac{\theta_k}{\rho c}\frac{n_k}{\tau_k} - \frac{T - T_e}{\tau_h} \quad \text{or} \quad \frac{d(\alpha v + w)}{d\bar{t}} = -h(w - w_e) , \tag{17}$$

which describe the decrease of the total energy of the sample. As a rule, in practice the annealing temperature is kept constant, at least for a fixed period of time, so one may assume that $T_0 = T_e$ (and $w_0 = w_e$, respectively).

Depending on the ratio between the energy dissipation and the energy release during the annealing of defects, the process occurs in different ways. Indeed, if the heat removal dominates and the density of defects decreases slowly during the annealing, the temperature of the sample remains constant and approximately equal to $T_e \approx T_0$. The density of defects decreases in accordance with the exponential law (3) with a characteristic time $\tau_k(T_0)$. Conversely, if the heat removal is low, then the total energy of a material during the annealing process remains constant, the temperature begins to rise, the annealing self-accelerates due to the thermal-concentration feedback, and exponential decrease in the concentration changes to a more rapid, step-like one. The growth of temperature happens in a similar way, it reaches a maximum value and begins to decrease. The density of defects continues to gradually decrease at a lower rate in accordance with a decrease in temperature.

Thereby, if the thermal-concentration feedback is activated, almost all defects are annealed during the time within which the contribution of the heat removal is negligible. This time is significantly smaller than $\tau_k(T_0)$, because the time of annealing depends on the temperature exponentially.

3 Heterogeneous Annealing of Defects of a Single Type

Inhomogeneous distribution of temperature and of defects mainly causes the heat flux; as a first approximation, the diffusion of defects can be neglected because of their low mobility. Taking into account the thermal conductivity, and considering for simplicity a one-dimensional geometry, (6) and (9) take the form

$$\rho c \frac{\partial T}{\partial t} = \theta_k \frac{n_k}{\tau_k} + \kappa \frac{\partial^2 T}{\partial x^2} \quad \text{or} \quad \frac{\partial w}{\partial \bar{t}} = \alpha v e^{-1/w} + \chi \frac{\partial^2 w}{\partial x^2} , \tag{18}$$

where κ is the thermal conductivity coefficient and $\chi = \kappa/(\rho c \beta_0^k)$. Instead of (10) we have $\iiint (\alpha v + w)\, dV = w_\infty V$, where V is the volume of the sample.

Even if the initial temperature distribution and the density of defects are uniform, it may cease to be so because of the loss of stability. Let $\hat{v}(\bar{t})$ and $\hat{w}(\bar{t})$ be homogeneous solutions of (8) and (9); and $\delta v(x,\bar{t})$ and $\delta w(x,\bar{t})$ be their inhomogeneous perturbations, which we present in the form: $\delta v(x,\bar{t}) = \delta v(\bar{t})\mathrm{e}^{\mathrm{i}kx}$ and $\delta w(x,\bar{t}) = \delta w(\bar{t})\mathrm{e}^{\mathrm{i}kx}$, where $\mathrm{i} = \sqrt{-1}$ is the imaginary unit and k is the wavenumber (spatial frequency). Substitution of $w(x,\bar{t}) = \hat{w}(\bar{t}) + \delta w(x,\bar{t})$ and $v(x,\bar{t}) = \hat{v}(\bar{t}) + \delta v(x,\bar{t})$ to (8) and (18) yields

$$\frac{\partial \delta v}{\partial \bar{t}} = -\mathrm{e}^{-1/\hat{w}}\delta v(\bar{t}) - \frac{\hat{v}}{\hat{w}^2}\mathrm{e}^{-1/\hat{w}}\delta w(\bar{t}) \,, \tag{19}$$

$$\frac{\partial \delta w}{\partial \bar{t}} = \alpha \mathrm{e}^{-1/\hat{w}}\delta v(\bar{t}) + \left(\frac{\alpha\hat{v}}{\hat{w}^2}\mathrm{e}^{-1/\hat{w}} - \chi k^2\right)\delta w(\bar{t}) \,. \tag{20}$$

Coefficients of the linear system (19)–(20) are bounded functions of time since $0 \le \hat{v}(t) \le 1$ by definition, $w_0 \le \hat{w}(t) \le w_\infty$, $0 \le \mathrm{e}^{-1/\hat{w}} \le 1$ and $0 \le \hat{v}\mathrm{e}^{-1/\hat{w}}/\hat{w}^2 \le v_0/w_0^2$. This allows us to assess the stability of $\hat{v}(t)$ and $\hat{w}(t)$ (the evolution of small perturbations) locally near some point in time, by "switching on" the perturbation at this time point and assuming the coefficients of the equations being constant. Then, a damping ratio λ satisfies the equation

$$\lambda^2 + \left(\mathrm{e}^{-1/\hat{w}} - \frac{\alpha\hat{v}}{\hat{w}^2}\mathrm{e}^{-1/\hat{w}} + \chi k^2\right)\lambda + \chi k^2 \mathrm{e}^{-1/\hat{w}} = 0 \,. \tag{21}$$

The uniform distribution of temperature and of defect density during the annealing process will be asymptotically stable, and the perturbed distribution is stable if $\mathrm{Re}\,(\lambda) < 0$, i.e. when the condition $\left(1 - \alpha\hat{v}/\hat{w}^2\right)\mathrm{e}^{-1/\hat{w}} + \chi k^2 > 0$ is fulfilled. As expected, the thermal conductivity stabilizes the uniform distribution: the instability develops primarily with regard to the long-wave perturbation. The spatial structure of the evolving perturbation will be determined by the shape of the annealed sample and the conditions at its boundary. For $k = 0$ the bifurcation value of w coincides with the inflection value w_* obtained for isothermal homogeneous annealing (condition (12)). Thus, the instability of the uniform distribution should be expected when a large amount of energy is stored in defects and the thermal energy is low.

4 Annealing Wave as a Result of Thermal-Concentration Feedback

In this section we consider a travelling wave of annealing, which may arise due to the thermal-concentration feedback [15]. We assume an ideal situation where the temperature of the metal, in which the wave is initiated, is equal to absolute zero. Formally this means that the relaxation time approaches infinity, and the defects are in a stationary state. This assumption is crucial for a mathematical description of the

travelling wave regime, because, as a result of annealing, the system transits from one stationary state to another.[1] A similar model of travelling waves was applied to describe combustion waves (chemical reactions) [17, 20, 21].

Consider for simplicity the annealing dynamics of defects of a single type, and infinite one-dimensional geometry. The evolution of defect density n (the index k is omitted) and of absolute temperature T is described by a system of equations:

$$\frac{\partial n}{\partial t} = -\frac{n}{\tau(T)} , \tag{22}$$

$$\rho c \frac{\partial T}{\partial t} = \kappa \frac{\partial^2 T}{\partial x^2} + \theta \frac{n}{\tau(T)} . \tag{23}$$

Here, as in previous sections, x is the spatial variable, t is time, ρc denotes the volumetric heat capacity of the material, κ is the thermal conductivity coefficient and θ is the thermal energy released in the annealing of one defect. The characteristic lifetime of defects, τ, depends on temperature according to the Arrhenius equation:

$$\frac{1}{\tau(T)} = \beta_0 \exp\left(-\frac{E_a}{k_B T}\right) , \tag{24}$$

where E_a is the activation energy of the transition from a metastable state to equilibrium, k_B is the Boltzmann constant and β_0 is the pre-exponential factor.

If we neglect the energy dissipation then, due to annealing, the density of defects decreases to zero, and the homogeneous distribution of temperature establishes with a value given by the energy conservation:

$$T_\infty = \frac{\theta n_0}{\rho c} . \tag{25}$$

Such a distribution may settle in the process of homogeneous spontaneous annealing of defects along with the ordinary thermal conductivity. This is a slow process, it is realized under conditions in which a thermal-concentration feedback is not activated.

Otherwise, the development of thermal-concentration instability causes a rapid[2] process of defect annealing, referred to as travelling wave, in which the density of defects and the temperature are almost constant throughout the sample and sharply change in a narrow region, we will call it the *annealing zone*, that moves with a constant speed. In this zone the density of defects falls to zero, and the temperature value increases to T_∞.. This is depicted in Fig. 3.

Since the annealing takes place in a narrow region of space, we can assume that it occurs on a surface that we will refer to as *annealing front*. Let us define the speed

[1] In a real life situation the temperature of the material is positive and the radiation-damaged crystal is not in a stationary state, since the lifetime of the defects is finite.

[2] The assumption of a sharp dependence of the annealing rate on temperature for the Arrhenius function (24) means a greater value of the activation energy E_a.

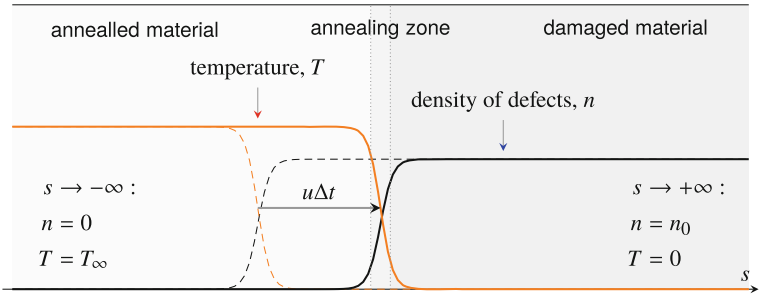

Fig. 3 Schematic of annealing wave. The wave propagates from the annealed material on the left to the damaged material on the right with a constant speed u. Temperature and defect density profiles at a given time t (solid line) and previous time $(t - \Delta t)$ (dashed line) are presented in orange and black, respectively. The density of defects and the temperature are constant throughout the sample except for the annealing zone

of the annealing front, u, as a volume of damaged material in which the defects are annealed per unit time per unit surface. To determine u we use the coordinate system in which the annealing front is at rest, i.e., we introduce a new independent variable $s = x - ut$. Then (22) and (23) transform to ordinary differential equations:

$$-u\frac{\mathrm{d}n}{\mathrm{d}s} = -\frac{n}{\tau(T)}\,, \tag{26}$$

$$-u\rho c\frac{\mathrm{d}T}{\mathrm{d}s} = \kappa\frac{\mathrm{d}^2T}{\mathrm{d}s^2} + \frac{\theta n}{\tau(T)}, \tag{27}$$

subject to the boundary conditions:

$$\begin{aligned} s \to -\infty : &\qquad n = 0, &\qquad T = T_\infty, \\ s \to +\infty : &\qquad n = n_0, &\qquad T = 0. \end{aligned}$$

As was already discussed, the annealing of defects happens in a narrow zone in the vicinity of the front. In this zone the temperature changes from the finite value T_∞ on the annealed side of the material – from the annealing zone the heat is transferred by the thermal conduction – to a value equal to zero on the side of the un-annealed damaged material, where the thermal equilibrium is reached. A rapid change of the temperature gradient on a short spatial interval means a greater contribution of the thermal conduction. For this reason, the contribution of the advective heat flow (i.e. the term on the left-hand side of (27)) is small[3] when compared with the contribution of the thermal conduction, and a simplified equation

[3]The temperature difference is small in the annealing zone since, due to the strong dependence of the annealing rate on temperature, the bulk of defects are annealed at a maximum temperature T_∞ [21].

$$\kappa \frac{\mathrm{d}^2 T}{\mathrm{d}s^2} + \frac{\theta n}{\tau(T)} = 0 \tag{28}$$

can be considered in the annealing zone. Turning T into the independent variable and making the substitution $\kappa \mathrm{d}T/\mathrm{d}s = \zeta$, gives

$$\zeta \frac{\mathrm{d}\zeta}{\mathrm{d}T} + \kappa \frac{\theta n}{\tau(T)} = 0. \tag{29}$$

Integrating (29) from 0 to T_∞ yields the heat flux from the annealing front:

$$\kappa \frac{\mathrm{d}T}{\mathrm{d}s} = \sqrt{2\kappa\theta \int_0^{T_\infty} \frac{n}{\tau(T)} \mathrm{d}T} \ . \tag{30}$$

The total amount of heat released as a result of annealing per unit time and removed by the heat conduction, is equal to the energy stored in defects, which carried by the flow of un-annealed substance (in our coordinate system, the material moves with a speed equal to the speed of the annealing front). Therefore, we can write

$$\sqrt{2\kappa\theta \int_0^{T_\infty} \frac{n}{\tau(T)} \mathrm{d}T} = \theta n_0 u \ , \tag{31}$$

from which we obtain the speed of the annealing front

$$u = \sqrt{\frac{2\kappa}{\theta} \int_0^{T_\infty} \frac{n}{\tau(T)} \mathrm{d}T} \ . \tag{32}$$

Formula (32) indicates that the speed of the annealing wave depends on the integral of the rate of heat production and, thereby, is associated with the activation energy and other kinetic characteristics of the material with defects.

Numerical estimations presented in [15] show that the speed of the annealing wave varies, depending on the model parameters, in the range from a few centimetres to a few meters per second. These assessments are highly inaccurate because of approximations used in the evaluation of the integral in (32). Nevertheless, accounting for the thermal-concentration feedback provides a correct description of physical phenomena, demonstrates the possibility in principle of the annealing wave and gives the correct qualitative dependence.

Accounting for the energy dissipation leads to the violation of conservation of enthalpy in the system; after the passage of the annealing wave the temperature will drop to an ambient value. The annealing wave will have the form of a moving peak with a steep front and a more gentle descent, caused by the heat sink, unlike the sigmoid (smoothed step) shape that occurs in a system without energy dissipation [9]. Therefore, the material will be subjected to an elevated temperature in a

narrower spatial region and for a shorter time, which can, to some extent, prevent the temperature-induced phase and structural transformations in the material and, consequently, changes of its properties during the annealing process.

5 The Kinetics of Accumulation and of Annealing of Interstitial Clusters: Basic Equations

Interstitial clusters are created in the process of irradiation of a material with high-energy particles. They significantly affect the mechanical and physical properties of the material as they act as stoppers for the moving of dislocations, and they redistribute the flows of point defects. Clusters can be created directly in cascades [1] and emerge both heterogeneously and homogeneously. With further irradiation the clusters grow and their size distribution changes. As a rule, there is a tendency for the formation and growth of one or more maxima of the distribution [7, 8]. Therefore, after the termination of irradiation, the material contains clusters of a certain size.

With the cessation of the irradiation begins decomposition of clusters. However, since the activation energy of their decay may be quite large, a high-temperature annealing is required for a more effective dissolution of clusters and the recovery of material properties.

Consider an ensemble of clusters of different sizes, each consisting of several interstitial atoms. It is known that with the exception of bi- and tri-interstitials, the interstitial clusters are dislocation loops, which can slide under the action of applied stress, but do not show a diffusion mobility. Clusters can grow and decompose. The growth of the clusters is associated with the merger of mobile, usually small clusters or with their absorption by large immobile clusters. Thermal decay of a cluster requires not only for the corresponding bonds to be broken, but also the possibility of withdrawal of parts of the disintegrated cluster to some distance from each other. For this reason it is most likely for the cluster to emit single interstitial atoms lying on the edge of the loop. In addition to the decay of the cluster, reduction of its size is caused by the absorption of vacancies by the cluster, i.e. the recombination of mobile vacancies with one of the atoms of the cluster. In the case of decay the total number of interstitial atoms (both free and included in the cluster) is preserved, while one interstitial atom disappears at each act of recombination. Therefore, even if the density of vacancies is maintained constant, the decay and recombination should be considered independently and described in the kinetic equations by different terms. Interstitial atoms are also irreversibly absorbed by various sinks: dislocations, grain boundaries, etc. The thermal emission of interstitial atoms by the sinks is negligible because of their high formation energy.

Let us write kinetic equations for the density of clusters of different sizes. We will, in accordance with experimental data, assume that clusters containing more than m interstitial atoms are unstable and are not formed. The value of m depends on the type and dose of radiation and on the properties of irradiated material. Therefore,

clusters of maximum size contain m interstitial atoms; hence m cluster types and m equations for their density are considered.

Clusters containing k interstitial atoms will be, for the sake of brevity, called k-clusters, their density will be denoted by n_k. In these notations $n_1 = n_\mathrm{i}$ is the density of interstitial atoms. We assume that the cluster size may decrease as a result of the successive emission of one interstitial atom or capture of one vacancy: for example, a k-cluster is formed when a $(k+1)$-cluster emits an interstitial atom. In the kinetic equations given below, the first process is described by the term $(-n_k/\tau_k)$, and the second one by $(-\gamma_k n_k n_\mathrm{v})$. The decay of the cluster consisting of two interstitial atoms leads to the appearance of two unbound interstitial atoms.

The growth of a cluster occurs through sequential inclusions of interstitial atoms: for example, a k-cluster is formed when an interstitial atom is attached to a $(k-1)$-cluster. This is described in the kinetic equations by the term $(\alpha_{k-1} n_{k-1} n_\mathrm{i})$.

Radiative generation of interstitial atoms, vacancies or (in a cascade irradiation) their small clusters is described by the corresponding terms, which are assumed to be specified and dependent on characteristics of both radiation and irradiated material (the masses of its constituent atoms and bonds between them). In the equations written below, the generation of Frenkel pairs with a constant rate K is assumed.

Therefore the system of equations describing the radiation-induced kinetics of vacancies and interstitial clusters takes the form

$$
\begin{aligned}
\frac{\mathrm{d}n_\mathrm{v}}{\mathrm{d}t} &= K - \frac{n_\mathrm{v} - n_\mathrm{v}^\mathrm{e}}{\tau_\mathrm{v}} - \gamma_1 n_\mathrm{i} n_\mathrm{v} - \sum_{k=2}^{m} \gamma_k n_k n_\mathrm{v} \ , \\
\frac{\mathrm{d}n_\mathrm{i}}{\mathrm{d}t} &= -2\alpha_1 n_\mathrm{i}^2 - \sum_{k=3}^{m-1} \alpha_k n_k n_\mathrm{i} - \gamma_1 n_\mathrm{i} n_\mathrm{v} + \gamma_2 n_2 n_\mathrm{v} - \frac{n_\mathrm{i}}{\tau_\mathrm{i}} + 2\frac{n_2}{\tau_2} + \sum_{k=3}^{m} \frac{n_k}{\tau_k} \ , \\
\frac{\mathrm{d}n_2}{\mathrm{d}t} &= -\alpha_2 n_2 n_\mathrm{i} + \frac{n_3}{\tau_3} + \gamma_3 n_3 n_\mathrm{v} + \alpha_1 n_\mathrm{i}^2 - \frac{n_2}{\tau_2} - \gamma_2 n_2 n_\mathrm{v}, \qquad (33) \\
&\vdots \\
\frac{\mathrm{d}n_{m-1}}{\mathrm{d}t} &= -\alpha_{m-1} n_{m-1} n_\mathrm{i} + \frac{n_m}{\tau_m} + \gamma_m n_m n_\mathrm{v} + \alpha_{m-2} n_{m-2} n_\mathrm{i} - \frac{n_{m-1}}{\tau_{m-1}} - \gamma_{m-1} n_{m-1} n_\mathrm{v} \ , \\
\frac{\mathrm{d}n_m}{\mathrm{d}t} &= \alpha_{m-1} n_{m-1} n_\mathrm{i} - \frac{n_m}{\tau_m} - \gamma_m n_m n_\mathrm{v} \ .
\end{aligned}
$$

Here n_v is the density of vacancies, α_k is the growth rate coefficient of a k-cluster and γ_k is the coefficient of vacancy recombination with k-clusters (both α_k and γ_k depend on temperature); $\tau_\mathrm{v}^{-1} = z_\mathrm{v} \rho_\mathrm{d} D_\mathrm{v}$ and $\tau_\mathrm{i}^{-1} = z_\mathrm{i} \rho_\mathrm{d} D_\mathrm{i}$ are the inverse lifetimes of vacancies and of interstitial atoms with respect to moving to sinks; ρ_d is the density of these sinks, z_i is the preferential interstitial absorption; $D_\mathrm{v} = D_\mathrm{v}^0 \exp(-E_\mathrm{m}^\mathrm{v}/k_\mathrm{B}T)$, $D_\mathrm{i} = D_\mathrm{i}^0 \exp(-E_\mathrm{m}^\mathrm{i}/k_\mathrm{B}T)$ are diffusion coefficients and E_m^v, E_m^i are migration energies of vacancies and of interstitial atoms, respectively. $n_\mathrm{v}^\mathrm{e} = n_\mathrm{v}^0 \exp(-E_\mathrm{f}^\mathrm{v}/k_B T)$ is the density of vacancies at a thermal equilibrium, E_f^v is the energy of vacancy formation, and N is the number of lattice sites per unit volume of the crystal.

It is known [13, 15] that the interdependence between temperature, rate of annealing and concentration of defects can significantly modify the kinetics of annealing and results in the emergence of qualitatively new regimes. The activation of the thermal-concentration feedback in the irradiated crystal leads to the development of self-oscillations of the crystal temperature and of the defect density [13]. In the case of annealing, this interdependence gives rise to an annealing wave [15]. Accounting for the thermal-concentration feedback in the kinetics of cluster density evolution (as during irradiation and during annealing after irradiation) leads to the need to extend the system (33) with an equation for the temperature variation:

$$\begin{aligned}\rho c\frac{\partial T}{\partial t} &= \kappa\frac{\partial^2 T}{\partial x^2} + \frac{\theta_\mathrm{i} n_\mathrm{i}}{\tau_\mathrm{i}} + \frac{\theta_\mathrm{v} n_\mathrm{v}}{\tau_\mathrm{v}} - \sum_{k=2}^{m}\frac{\theta_k n_k}{\tau_k} + (\theta_\mathrm{i}+\theta_\mathrm{v})\,\gamma_1 n_\mathrm{i} n_\mathrm{v} \\ &+ \sum_{k=2}^{m}(\theta_\mathrm{i}+\theta_\mathrm{v}-\theta_k)\,\gamma_k n_k n_\mathrm{v}\ .\end{aligned} \tag{34}$$

Here θ_i and θ_v are the energies released in absorption by a sink of an interstitial atom and of a vacancy, respectively, their values are approximately equal to the energies of formation of the respective defects. θ_k is the thermal energy required to activate the emission of an interstitial atom by a k-cluster, its magnitude is approximately equal to the binding energy of an interstitial atom in a k-cluster.

At the annealing stage it is often possible to neglect the growth of the cluster because in this case, the irradiation is absent and the density of the interstitial atoms is negligibly small. The density of vacancies during annealing can be set equal to the density of thermal vacancies n_v^e, which remains constant for a fixed temperature. Then one can disregard the energy release associated with the disappearance of vacancies in the process of recombination of vacancies with interstitial atoms within the cluster since a new vacancy is immediately generated instead of a disappeared one at the expense of this energy.

In such a case the system (33) and (34) simplifies, equations become linear and take the form

$$\begin{aligned}\frac{\mathrm{d}n_\mathrm{i}}{\mathrm{d}t} &= -\gamma_1 n_\mathrm{i} n_\mathrm{v}^\mathrm{e} + \gamma_2 n_2 n_\mathrm{v}^\mathrm{e} - \frac{n_\mathrm{i}}{\tau_\mathrm{i}} + 2\frac{n_2}{\tau_2} + \sum_{k=3}^{m}\frac{n_k}{\tau_k}\ , \\ \frac{\mathrm{d}n_2}{\mathrm{d}t} &= -\frac{n_2}{\tau_2} - \gamma_2 n_2 n_\mathrm{v}^\mathrm{e} + \frac{n_3}{\tau_3} + \gamma_3 n_3 n_\mathrm{v}^\mathrm{e}\ , \\ &\vdots \\ \frac{\mathrm{d}n_{m-1}}{\mathrm{d}t} &= -\frac{n_{m-1}}{\tau_{m-1}} - \gamma_{m-1} n_{m-1} n_\mathrm{v}^\mathrm{e} + \frac{n_m}{\tau_m} + \gamma_m n_m n_\mathrm{v}^\mathrm{e}\ , \\ \frac{\mathrm{d}n_m}{\mathrm{d}t} &= -\frac{n_m}{\tau_m} - \gamma_m n_m n_\mathrm{v}^\mathrm{e}\ ,\end{aligned} \tag{35}$$

and

$$\rho c \frac{\partial T}{\partial t} = \kappa \frac{\partial^2 T}{\partial x^2} + \frac{\theta_\mathrm{i} n_\mathrm{i}}{\tau_\mathrm{i}} - \sum_{k=2}^{m} \frac{\theta_k n_k}{\tau_k} + \theta_\mathrm{i} \gamma_1 n_\mathrm{i} n_\mathrm{v}^\mathrm{e} + \sum_{k=2}^{m} (\theta_\mathrm{i} - \theta_k)\, \gamma_k n_k n_\mathrm{v}^\mathrm{e} \,. \tag{36}$$

By introducing new effective lifetimes of clusters which take the recombination into account, the annealing of clusters can be formally seen as their decay.

Using (33) we obtain for the decline of the full number of interstitial atoms, both unbound and bound in clusters, in the process of annealing the following expression

$$\frac{\mathrm{d}}{\mathrm{d}t}\left(\sum_{k=1}^{m} k n_k\right) = -\sum_{k=1}^{m} \gamma_k n_k n_\mathrm{v}^\mathrm{e} - \frac{n_\mathrm{i}}{\tau_\mathrm{i}} \,, \tag{37}$$

which shows that the decrease of interstitial atoms is due to all the processes of recombination and movement of the unbound interstitial atoms to sinks. The decline in the total number of clusters, including interstitial atoms, is described by the formula

$$\frac{\mathrm{d}}{\mathrm{d}t}\left(\sum_{k=1}^{m} n_k\right) = -\gamma_1 n_\mathrm{i} n_\mathrm{v}^\mathrm{e} - \frac{n_\mathrm{i}}{\tau_\mathrm{i}} + \sum_{k=2}^{m} \frac{n_k}{\tau_k} \,, \tag{38}$$

the decrease in the number of clusters consisting of k or more atoms is determined by the number of k-clusters

$$\frac{\mathrm{d}}{\mathrm{d}t}\left(\sum_{k=1}^{m} n_k\right) = -\gamma_k n_k n_\mathrm{v}^\mathrm{e} - \frac{n_k}{\tau_k} \,.$$

As will be shown below, if the decay of clusters is predominant, and the role of recombination is negligible, the kinetics of annealing is determined by the clusters with the greatest lifetimes. On the contrary, with the dominance of recombination, the effective lifetime depends weakly on the cluster size, especially for large clusters.

6 Estimation of Kinetic Coefficients

Formation and accumulation of clusters depend on the kinetic coefficients. The latter are functions of the cluster size. For example, the probability of emission of an interstitial atom by a cluster is proportional to the number of atoms which occupy the edge of the dislocation loop.

Obtaining of kinetic coefficients is a difficult problem, because they depend on material properties, on the physical processes occurring in the material, as well as on the irradiation conditions. Without claiming to be its comprehensive solution, we

estimate the kinetic coefficients that describe the formation and decay of clusters (interstitial dislocation loops) in solids.

Let us clarify the definition of values to be used in future. The energy of formation of a defect (vacancies, $E_{\mathrm{f}}^{\mathrm{v}}$, interstitial atoms $E_{\mathrm{f}}^{\mathrm{i}}$, or k-cluster, E_{f}^{k}) is the difference between the energies of the crystal with and without the defect. The binding energy of a k-cluster, E_k^{b}, is the difference between the energies of the crystal containing the k-cluster and the crystal containing k interstitial atoms which are far away from each other. If the crystal contains several defects, it is assumed that the distance between them is large enough to neglect their interaction; in other words, a material with a not very high defect density is considered. The binding energy of the interstitial atoms of a k-cluster, E_k^{b1}, is the difference between the energies of the crystal containing the k-cluster and the crystal with a $(k-1)$-cluster and the interstitial atom that is far away from that $(k-1)$-cluster. The energy of cluster formation is not only the interaction energy between the atoms which form the cluster: it also includes the interaction energy of atoms of the cluster with atoms of the crystal which surround the cluster. The considered energies satisfy the following relations

$$\begin{aligned} E_{\mathrm{f}}^{k} &= E_{\mathrm{f}}^{k-1} + E_{\mathrm{f}}^{\mathrm{i}} + E_k^{\mathrm{b1}} \,, \\ E_{\mathrm{f}}^{k} &= k E_{\mathrm{f}}^{\mathrm{i}} + E_k^{\mathrm{b}} \,, \\ E_k^{\mathrm{b}} &= \sum_{j=2}^{k} E_j^{\mathrm{b1}} \,. \end{aligned} \tag{39}$$

A negative value of the binding energies, E_j^{b1} and E_k^{b}, means that the k-cluster is unstable with respect to the decomposition into k interstitial atoms or with respect to the emission of the interstitial atom, respectively.

At the thermal equilibrium state the probability of growth of the k-cluster ($k \to k+1$) is equal to the probability of the thermal-stimulated decay of the $(k+1)$-cluster. Therefore, we can write $\alpha_k n_k^{\mathrm{e}} n_{\mathrm{i}}^{\mathrm{e}} = n_{k+1}^{\mathrm{e}} / \tau_{k+1}$, from what follows that the growth rate coefficient of the k-cluster is

$$\alpha_k = \frac{n_{k+1}^{\mathrm{e}}}{n_k^{\mathrm{e}} n_{\mathrm{i}}^{\mathrm{e}}} \frac{1}{\tau_{k+1}} \,. \tag{40}$$

The values of the equilibrium densities of vacancies, of interstitial atoms and of their k-clusters are given by: $n_{\mathrm{i}}^{\mathrm{v}} = N \exp(-E_{\mathrm{f}}^{\mathrm{v}} / k_{\mathrm{B}} T)$, $n_{\mathrm{i}}^{\mathrm{e}} = N \exp(-E_{\mathrm{f}}^{\mathrm{i}} / k_{\mathrm{B}} T)$ and $n_k^{\mathrm{e}} = (N/k) \exp(-E_{\mathrm{f}}^{k} / k_{\mathrm{B}} T)$ respectively, where $E_{\mathrm{f}}^{\mathrm{v}}$, $E_{\mathrm{f}}^{\mathrm{i}}$, and E_{f}^{k} are their respective energies of formation; N is the number of lattice sites per unit volume of the crystal.

Substituting the expression for the equilibrium densities in (40), we obtain the relation connecting the growth rate coefficient of the k-cluster with the lifetime of the $(k+1)$-cluster:

$$\alpha_k = \frac{1}{\tau_{k+1}} \frac{k}{N\,(k+1)} \exp\left(-\frac{E_{\mathrm{f}}^{k+1} - E_{\mathrm{f}}^{k} - E_{\mathrm{f}}^{\mathrm{i}}}{k_{\mathrm{B}} T} \right) \text{ or } \alpha_k = \frac{1}{\tau_{k+1}} \frac{k}{N\,(k+1)} \exp\left(-\frac{E_{k+1}^{\mathrm{b1}}}{k_{\mathrm{B}} T} \right) . \tag{41}$$

The decay of the cluster happens due to the emission of one atom from the edge of the dislocation loop and its moving to a distance which is approximately equal to the radius of the dislocation core. To leave the cluster, the atom must overcome the potential barrier which is equal to its binding energy with the cluster. (It is supposed that only the peripheral atoms may come out). Thus, the lifetime of the cluster increases as its binding energy grows. In this case, the lifetime of the k-cluster can be represented as

$$\tau_k = A(k) \exp\left(E_k^{\mathrm{b1}} / k_{\mathrm{B}} T\right). \tag{42}$$

The pre-exponential factor is equal to the lifetime of the cluster with zero binding energy. It is proportional to the time of moving of an atom from the dislocation loop at a distance of the order of the radius of the dislocation core by means of diffusion and is inversely proportional to the fraction of edge atoms: $A(k) = (k/k_L)\, r_0^2/D_{\mathrm{i}}$, where r_0 is the radius of the dislocation core and k_L is the number of edge atoms of the dislocation loop. This number can be represented as $k_L = (2/a)\sqrt{k\pi\Omega/b}$, where a is the interatomic distance (period of the crystal lattice), Ω is the atomic volume and b is the Burgers vector. Thus, the expression for the lifetime of the cluster takes the form:

$$\tau_k = \frac{ar_0^2}{2D_{\mathrm{i}}}\sqrt{\frac{bk}{\pi\Omega}} \exp\left(\frac{E_k^{\mathrm{b1}}}{k_{\mathrm{B}}T}\right) = \frac{ar_0^2}{2D_{\mathrm{i}}}\sqrt{\frac{bk}{\pi\Omega}} \exp\left(\frac{E_{\mathrm{f}}^k - E_{\mathrm{f}}^{k-1} - E_{\mathrm{f}}^{\mathrm{i}}}{k_{\mathrm{B}}T}\right).$$

The binding energy $E_k^{\mathrm{b1}} = E_{\mathrm{f}}^k - E_{\mathrm{f}}^{k-1} - E_{\mathrm{f}}^{\mathrm{i}}$ depends on the difference between the energies of formation of the k- and $(k-1)$-cluster. Let us write this difference of energies as a function of the changing of energy of links between atoms of the cluster and changing of the linear tension energy at the edge of the dislocation loop (the magnitude of this energy is equal to the elastic energy of the dislocation loops [5]).

The energy of the linear tension on the edge of the dislocation loop is given by $E_L = 2\pi R\mu b^2$, where μ is the shear modulus. The radius of the loop, R, is a function of the number of its atoms k: $R = \sqrt{k\Omega/(\pi b)}$. Then the binding energy of an interstitial atom and k-cluster becomes $E_k^{\mathrm{b1}} = \mu b\sigma(\sqrt{k} - \sqrt{k-1}) - E_{\mathrm{i1}} - E_{\mathrm{f}}^{\mathrm{i}}$. Here E_{i1} is the energy of the broken links as a result of the separation of an atom; $\sigma = \sqrt{4\pi\Omega b}$ is a parameter introduced to render formulas less cumbersome. Both E_{i1} and $E_{\mathrm{f}}^{\mathrm{i}}$ do not depend on the cluster size. Let $C = C(T) = \exp\left[-(E_{\mathrm{i1}} + E_{\mathrm{f}}^{\mathrm{i}})/k_{\mathrm{B}}T\right]$ then the lifetime of the cluster as a function of its size is

$$\tau_k = \frac{abr_0^2}{D_{\mathrm{i}}\sigma}\sqrt{k}C \exp\left[\frac{\mu b\sigma\left(\sqrt{k} - \sqrt{k-1}\right)}{k_{\mathrm{B}}T}\right]. \tag{43}$$

Using (41) we get the coefficient of the rate of cluster growth:

$$\alpha_k = \frac{D_\mathrm{i}\sigma\sqrt{k}}{N(k+1)abr_0^2} C^{-2} \exp\left[-\frac{2\mu b\sigma\left(\sqrt{k+1}-\sqrt{k}\right)}{k_\mathrm{B}T} \right] . \tag{44}$$

The lifetime of a cluster increases and the coefficient of the rate of cluster growth decreases as the size of the cluster (dislocation loop) grows.

The growth of a cluster may be represented as two consecutive processes: the diffusion (α_k^d), and the reaction (α_k^r). Since these processes are separated in time, their rates satisfy the ratio:

$$\frac{1}{\alpha_k} = \frac{1}{\alpha_k^\mathrm{d}} + \frac{1}{\alpha_k^\mathrm{r}} \quad \rightarrow \quad \alpha_k = \frac{\alpha_k^\mathrm{d}\alpha_k^\mathrm{r}}{\alpha_k^\mathrm{d} + \alpha_k^\mathrm{r}} .$$

Let us consider α_k^r and α_k^d in more detail.

The application of Smoluchowski's relation yields

$$\alpha_k^\mathrm{d} = 4\pi R(k) \left(D_\mathrm{i} + D_k\right) ,$$

where D_k is the diffusion coefficient of the k-cluster; for interstitial loops it can be set equal to zero. To determine it we use the Arrhenius relation:

$$\alpha_k^\mathrm{r} = \frac{S(k)\left(D_\mathrm{i} + D_k\right)}{a} \exp\left(-\frac{E_\mathrm{a}^\mathrm{i}}{k_\mathrm{B}T} \right) ,$$

where $S(k) = 2\pi R(k) b$ is the active surface that absorbs defects and E_a^i is the activation energy of the attaching interstitial atoms to the cluster. This energy barrier is related to the deformation of the neighbouring atomic planes when the interstitial atom attaches to the cluster (to the dislocation loop).

After corresponding substitutions, the coefficient of the rate of cluster growth takes the form:

$$\alpha_k = \frac{\left(D_\mathrm{i} + D_k\right)\sigma\sqrt{k}}{\left(D_\mathrm{i} + D_k\right)\sigma\sqrt{k} + a\exp\left(E_\mathrm{a}^\mathrm{i}/k_\mathrm{B}T\right)} . \tag{45}$$

Comparing the obtained expression with (44), we get the activation energy of the joining of interstitial atoms to the cluster as a function of k:

$$E_\mathrm{a}^\mathrm{i} = k_\mathrm{B}T \ln\left[\left(D_\mathrm{i} + D_k\right)\sigma\sqrt{k}\left(\frac{Nr_0^2C^2b}{D_\mathrm{i}\sigma} \frac{(k+1)^{3/2}}{k} \mathrm{e}^{2\mu b\sigma\left(\sqrt{k+1}-\sqrt{k}\right)/k_\mathrm{B}T} - 1 \right) \right] . \tag{46}$$

The activation energy increases with increasing k, at large k it grows like $\ln(k)$.

The recombination rate coefficient, γ_k, characterizes the rate of recombination of a vacancy with an interstitial atom or a k-cluster. To obtain γ_k, let us take into account that the process of capture of an interstitial atom by a cluster is similar to the process of capture of a vacancy. The dependence of activation energy of the recombination,

$E_{\mathrm{a}}^{\mathrm{v}}$, on k coincides with $E_{\mathrm{a}}^{\mathrm{i}}$ as a function of k up to the ratio of dilatational volumes, but has the opposite sign:

$$E_{\mathrm{a}}^{\mathrm{v}} = -k_{\mathrm{B}}T\frac{\Delta V_{\mathrm{v}}}{\Delta V_{\mathrm{i}}}\ln\left[(D_{\mathrm{i}}+D_k)\,\sigma\sqrt{k}\left(\frac{Nr_0^2C^2b}{D_{\mathrm{i}}\sigma}\,\frac{(k+1)^{3/2}}{k}\mathrm{e}^{2\mu b\sigma\left(\sqrt{k+1}-\sqrt{k}\right)/k_{\mathrm{B}}T}-1\right)\right], \tag{47}$$

where ΔV_{v} and ΔV_{i} are dilatational volumes of a vacancy and of an interstitial atom, respectively. The negative sign of activation energy is caused by the fact that the recombination decreases the tension of the elastic field near the edge of the dislocation loops.

Since the recombination as well as the growth of the cluster can be represented by a sequence of processes of diffusion and reaction, carrying out a similar argument for the recombination rate coefficient of vacancies with an interstitial atom of the k-cluster we obtain

$$\gamma_k = \frac{(D_{\mathrm{v}}+D_k)\,\sigma\sqrt{k}}{(D_{\mathrm{v}}+D_k)\,\sigma\sqrt{k}+a\exp\left(E_{\mathrm{a}}^{\mathrm{v}}/k_{\mathrm{B}}T\right)}\,, \tag{48}$$

where the activation energy of recombination is described by (47). This relation shows that the recombination rate coefficient, γ_k, increases as the number of atoms in the cluster, k, grows.

Thus, we obtained all the coefficients describing the kinetics of growth and decay of interstitial clusters. As the size of the cluster increases, the lifetime of the cluster grows, the growth rate coefficient decreases and the recombination rate coefficient increases. Therefore, starting from a certain m, the cluster growth rate becomes negative (cluster decays). The m-cluster for which the growth rate equals zero is determined by the relationship:

$$\alpha_m n_m n_{\mathrm{i}} = \frac{n_{m+1}}{\tau_{m+1}} + \gamma_{m+1}n_{m+1}n_{\mathrm{v}}\,. \tag{49}$$

The growth rate as a function of k has a sharp peak at some $k = k^*$. Depending on the physical characteristics of the metal, the values of k^* lie in the range between 2 and 10. According to [1], the cascade irradiation can form small clusters with a number of atoms both smaller and bigger than k^*. Clusters having a size of the order of k^* quickly grow to a size of m, near which α_k varies slightly ($\alpha_k \approx \alpha_m$), and k-clusters with $k < k^*$ decay. Therefore, if α_{k^*} is large, we can assume that only interstitial atoms and m-clusters are formed in a cascade. This will be used in the future.

The expressions for the kinetic coefficients are simplified for a large size of the clusters:

$$\tau_k = C_\tau\sqrt{k}\,,\quad \alpha_k = C_\alpha\frac{\sqrt{k}}{k+1}\,,\quad \gamma_k = C_\gamma\frac{k\sqrt{k}}{k+1}\,,$$

where $C_\tau \approx 7\times10^2$ s, $C_\alpha \approx 2\times10^{10}\,\mathrm{m^3\,s^{-1}}$, $C_\gamma \approx 7\times10^4\,\mathrm{m^3\,s^{-1}}$.

The resulting formulas for the kinetic coefficients are approximate. They are obtained for an elastic medium assuming a perfect geometric shape of dislocation loops and equal average binding energy for atoms at the edge of the cluster. Accounting for the crystal structure of the material, the structure and size of the bonds between atoms in the core of the dislocation, dislocation kinks and jogs leads to the fact that the probability of the emission of atoms by a cluster is not the same for each atom. A change of cluster size due to the absorption or emission of an atom can lead to a significant change in the structure of the dislocation loop edge, including a noticeable change in the probability of thermal emission of weakly bound atoms. The consequence of the aforementioned is a local nonmonotonicity of generally monotonic dependence of the kinetic coefficients on the size of the cluster. As shown below, this can significantly change the size distribution of the clusters.

7 Evolution of Cluster Size Distribution in the Process of Annealing

As follows from (37), the total number of interstitial atoms, both unbound and bound in clusters, decreases monotonically during the annealing process. Of no less importance is the change of cluster distribution in size associated with the annealing. Indeed, the decay of each cluster is accompanied by the emission of an interstitial atom, which leads to a decline in the number of large clusters and the growth of small ones.

Let us consider the kinetics of cluster decay, when the recombination can be neglected and the lifetime of a cluster of a certain size, for example of a k'-cluster, is much longer than the lifetimes of larger clusters, i.e. $\tau_{k'} \gg \tau_k$ for $k' < k \leq m$. Using this difference in lifetimes, one can build two approximations. The first one is for time periods shorter than the minimum lifetime of clusters with $k > k'$. In this case, the decay of k'-clusters can be neglected. Then, as a result of decomposition of larger clusters, the density of k'-clusters monotonically increases by the total density of larger clusters, i.e. to $n_{k',\mathrm{tot}} = \sum_{k \geq k'}^{m} n_k$.

On the contrary, at times greater than the lifetime of k'-clusters (i.e. for $t > \tau_{k'}$), the larger clusters can be considered to have disintegrated and their density assumed to be zero. Along with this, the density of the k'-clusters decreases exponentially from the value $n_{k',\mathrm{tot}}$.

Consequently, the density of k'-clusters increases rapidly, reaches a maximum value then decreases monotonically to zero. The change in the distribution of cluster sizes (i.e. over k) produces a maximum close to k'. Hence at long times, which are typical for the study of annealing, it is possible to restrict the consideration to clusters with large lifetimes, the size of which is less than a certain finite size. The distribution of size for this type of clusters has several maxima.

In order to understand the way the distribution in size of clusters evolves, let us consider as an example the decay of clusters consisting of k and $k + 1$ interstitial

atoms with densities n_1 and n_2, respectively. Equations describing the annealing (decay) of the two types of clusters have the form

$$\begin{aligned} \frac{dn_1}{dt} &= -\frac{n_1}{\tau_1} + 2\frac{n_2}{\tau_2} , \\ \frac{dn_2}{dt} &= -\frac{n_2}{\tau_2} . \end{aligned} \tag{50}$$

Consider a case when $\tau_1 \neq \tau_2$. Then the change in the density of each type of cluster is described by equations

$$n_2 = n_{2,0}\mathrm{e}^{-t/\tau_2} , \tag{51}$$

$$n_1 = n_{1,0}\mathrm{e}^{-t/\tau_1} + \frac{\tau_1 n_{2,0}}{\tau_2 - \tau_1}\left(\mathrm{e}^{-t/\tau_2} - \mathrm{e}^{-t/\tau_1}\right) , \tag{52}$$

where $n_{1,0}$ and $n_{2,0}$ are the initial (for $t = 0$) densities of clusters. If the inequality $\tau_2 n_{1,0} < \tau_1 n_{2,0}$ is satisfied, then the change of density n_1 in time has a maximum as illustrated in Fig. 4 on the left. The maximum value of n_1 is

$$\begin{aligned} n_1^{\max} = &\left\{\frac{\tau_2}{\tau_1}\left[1 - \frac{n_{1,0}}{n_{2,0}}\left(\frac{\tau_2}{\tau_1} - 1\right)\right]\right\}^{-\tau_2/(\tau_2-\tau_1)} \\ &\times \left\{n_{1,0} + \frac{\tau_1 n_{2,0}}{\tau_2 - \tau_1}\left(\left[\frac{\tau_2}{\tau_1}\left(1 - \frac{n_{1,0}}{n_{2,0}}\left(\frac{\tau_2}{\tau_1} - 1\right)\right)\right]^{-\tau_1/\tau_2} - 1\right)\right\} . \end{aligned} \tag{53}$$

The time at which $n_1^{\max}$ is achieved is

$$t_{\max} = \frac{\tau_1 \tau_2}{\tau_2 - \tau_1} \ln\left(\frac{\tau_2}{\tau_1}\left[1 - \frac{n_{1,0}}{n_{2,0}}\left(\frac{\tau_2}{\tau_1} - 1\right)\right]\right) .$$

If $\tau_1 \gg \tau_2$ then $n_1^{\max} \approx n_{1,0} + n_{2,0}$, in accordance with our previous discussions. Otherwise (i.e. when $\tau_2 n_{1,0} > \tau_1 n_{2,0}$) density n_1 decreases monotonically as shown in Fig. 4 on the right.

Approximations for long and short times can be easily obtained from (52). If $\tau_1 \ll \tau_2$ then $n_1 \approx (n_{1,0} + n_{2,0})\exp(-t/\tau_1)$. In the case when $\tau_2 n_{1,0} > \tau_1 n_{2,0}$ then, for short times $t \ll \tau_1$, we get an exponential decay $n_1 = n_{1,0}\exp(-t/\tau_1)$ with the characteristic time τ_1. At long times $t \gg \tau_2$ we get an exponential decay $n_1 = (\tau_1/\tau_2)n_{2,0}\exp(-t/\tau_2)$ with a characteristic time τ_2. In the opposite case, $\tau_2 n_{1,0} > \tau_1 n_{2,0}$, and for $t \gg \tau_1$, the value of n_1 decreases exponentially with the characteristic time τ_2: $n_1 = (\tau_1/\tau_2)n_{2,0}\exp(-t/\tau_2)$.

In the case of clusters with a greater number of different sizes, the kinetics of their decay for a large time is determined by the clusters with relatively long lifetimes. The change in the density of these clusters exhibits the same features as were observed above. This is illustrated with examples given in Fig. 5, which shows the kinetics of the decay of clusters consisting of ten or less atoms. It is specifically these long-

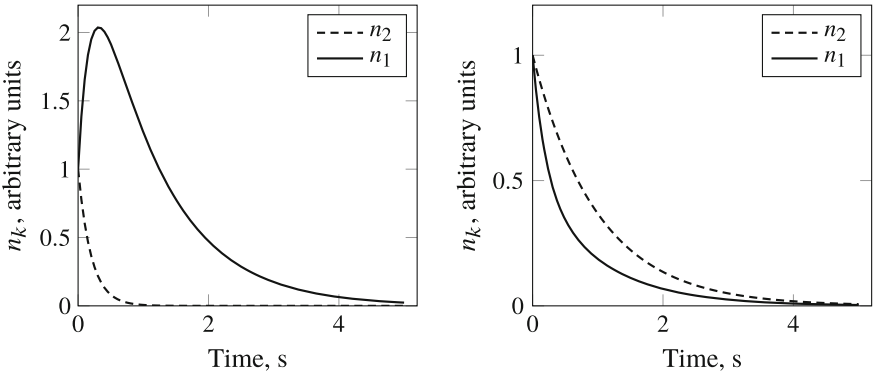

Fig. 4 Normalized densities of clusters consisting of k- and $(k+1)$-interstitial atoms (n_1 and n_2, respectively), as functions of time for initial densities $n_{1,0} = n_{2,0} = 1$, and lifetimes $\tau_1 = 1\,\mathrm{s}$ and $\tau_2 = 0.2\,\mathrm{s}$ (left), and $\tau_1 = 0.2\,\mathrm{s}$ and $\tau_2 = 1\,\mathrm{s}$ (right)

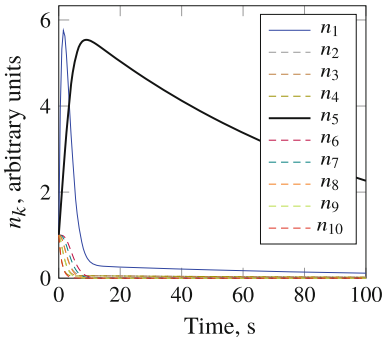

Fig. 5 The kinetics of the decay of clusters consisting of ten or less atoms with the corresponding normalized densities $n_{10}, n_9, \ldots, n_1$. Lifetimes of all clusters are equal to 1 s, except for the 5-cluster with $\tau_5 = 100\,\mathrm{s}$. Initial values of all n_k are equal to one. Maxima are observed for $n_5(t)$ and for $n_1(t)$, i.e. for clusters with the longest lifetime (5-cluster) and for interstitial atoms, respectively

lived clusters that are most prevalent in the material and are responsible for the modifications of its properties.

Measurements and calculations have shown that the binding energy of clusters is often quite large, 2 to 3 eV per interstitial atom. Therefore the lifetime of the cluster will remain quite large even for temperatures close to the melting point. In this case, the annealing of the clusters will occur mainly due to thermal recombination of vacancies with interstitial atoms within the clusters. As shown above, the values of the recombination rate coefficients, and consequently, the effective lifetimes of clusters with similar sizes are close, especially for large clusters. In this case, one can assume that $\gamma_{k+1} \approx \gamma_k = \gamma$, $1/\tau = \gamma n_{\mathrm{v}}^{\mathrm{e}}$ and we obtain for the density of the clusters

$$n_2 = n_{2,0} \exp\left(-\gamma n_{\mathrm{v}}^{\mathrm{e}} t\right) , \tag{54}$$

$$n_1 = \left(n_{1,0} + \gamma n_{\mathrm{v}}^{\mathrm{e}} n_{2,0}\right) \exp\left(-\gamma n_{\mathrm{v}}^{\mathrm{e}} t\right) . \tag{55}$$

Function $n_1(t)$ has a maximum if condition $n_{2,0} > n_{1,0}$ is satisfied.

8 Self-Sustained Annealing of Radiation-Induced Defects

In the process of annealing of the interstitial atoms and their complexes [3], as well as of interstitial clusters, the energy stored by the crystal as a result of their formation is converted into heat. Since all the kinetic coefficients depend exponentially on temperature, the thermal-concentration nonlinear feedback may emerge, thus leading to the self-sustained propagation of defect annealing.

Consider a situation where the crystal contains only m-clusters and their lifetime is much longer than the lifetimes of the all clusters of smaller size. This means that we can assume that a m-cluster immediately decays into m interstitial atoms, which are absorbed by the sinks. The system (35)–(36) can therefore be simplified and written in the form:

$$\begin{aligned} \frac{\partial n_m}{\partial t} &= -\frac{n_m}{\tau_m(T)} , \\ c\rho \frac{\partial T}{\partial t} &= \kappa \frac{\partial^2 T}{\partial x^2} + \theta \frac{n_m}{\tau_m(T)} , \\ n_{m-1} &= n_{m-2} = \cdots = n_2 = n_{\mathrm{i}} = 0 , \end{aligned} \tag{56}$$

where $\theta = m\theta_{\mathrm{i}} - E_m^{\mathrm{b}} = m\theta_{\mathrm{i}} - \sum_{k=1}^{m} \theta_k$.

The resulting system is, up to notations, the same as (22)–(23), hence we will omit index m for the sake of brevity. However, when simulating annealing in real life, it is not possible to set the temperature of the irradiated sample to zero. This is of fundamental importance, as in this case the state of the sample before annealing is not stationary: there is spontaneous thermal annealing with a slow but nonzero rate – that is known as the "cold-boundary problem" (for detail see [20] and the references therein). Under this condition the system of equations (56) does not have a travelling wave solution. A perturbation (i.e. an increase in temperature), created on the boundary, propagates through the sample due to thermal-concentration feedback but its magnitude gradually reduces because of the spontaneous annealing of defects. The study of such a process requires the use of numerical methods.

This numerical study should be performed for a specific finite geometry and prescribed initial and boundary conditions. As before, we select, for the sake of simplicity, an one-dimensional geometry and consider a finite sample of length L. We are looking for the distribution of the density of defects n and of the temperature T over $x \in [0, L]$ as functions of time t, i.e. $n(t, x)$ and $T(t, x)$. The evolution of these quantities for $t \geq 0$ is described by the coupled set of Eq. (56) with the

temperature-dependent lifetime given by the Arrhenius relationship (24). This mathematical problem can be classified as a reaction-diffusion system in the limit where the defect diffusion coefficient is set to zero. We consider a thermally isolated system and apply the homogeneous Von Neumann boundary conditions[4]

$$\left.\frac{\partial T}{\partial x}\right|_{x=0} = \left.\frac{\partial T}{\partial x}\right|_{x=L} = 0 \,. \tag{57}$$

We assume that there is some prescribed distribution of defects and temperature at the initial moment $t = 0$. In this study the initial density of defects is chosen to be equal to n_0 over the whole interval:

$$n\,(t = 0, x) = n_0 \,, \quad x_0 \le x \le L \,. \tag{58}$$

The initial temperature is $T_0 > 0$ everywhere except for a narrow near-surface layer of size x_0 at the left boundary, where the temperature is increased to $T_1 > T_0$:

$$T\,(t = 0, x) = \begin{cases} T_1, & 0 \le x \le x_0 \,; \\ T_0, & x_0 \le x \le L \,. \end{cases} \tag{59}$$

The geometry of the problem and initial distributions of the defect density and of the temperature are schematically presented in Fig. 6.

The non-linear problem (24), (56)–(59) was solved numerically by applying both the Crank–Nicolson and the Implicit Euler finite difference schemes. These discretisation schemes result in a system of nonlinear equations, which was solved with Newton iterations at each time step. The Jacobian matrix used in the Newton method was obtained analytically and the system of linear equations was also analytically reduced to a tridiagonal form, which can be efficiently solved with the Thomas algorithm.

Calculations were performed for materials with characteristics of aluminium and steel. Geometrical parameters were chosen as follows: $L = 10\,\text{cm}$ and $x_0 = 1\,\text{mm}$. However, in order to investigate mechanisms and features of a self-sustained radiation defect annealing propagation, the parameters were varied in wide ranges.

The numerical studies have shown, that depending on material properties and initial conditions (temperature and defect density values) the self-sustained annealing can proceed in two different regimes. In the first regime the annealing front, soon after some initial transient, propagates at a constant speed and both temperature and defect density have smooth, monotonic sigmoid-shaped profiles that almost do not vary with time. This regime was observed, for instance, in the case of aluminium, when T_0 is set to a room temperature of 300 K and the temperature of the preheated layer $T_1 = 700\,\text{K}$. The temperature and defect density profiles in this case are shown

[4]In principle the same zero flux condition across the borders holds for the density of defects. But this condition is satisfied automatically because we consider a problem in which the diffusion of defects is negligibly small.

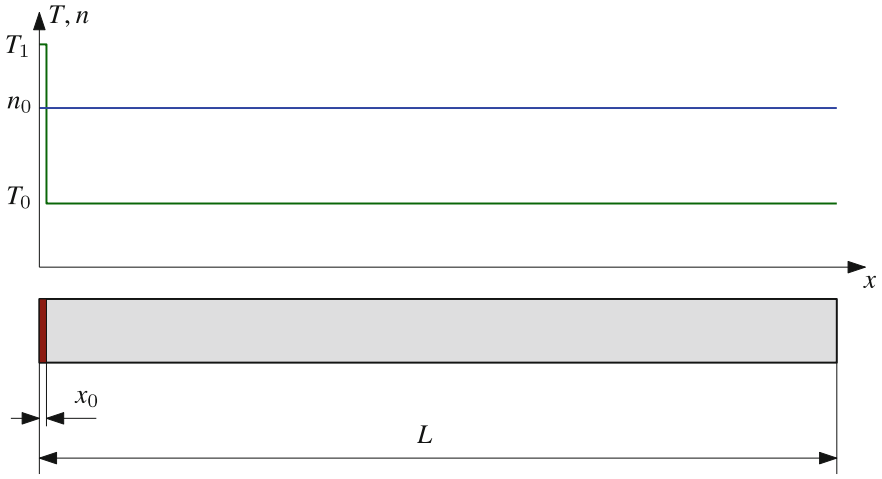

Fig. 6 Geometry of the problem (bottom) and initial temperature and defect density distributions (top)

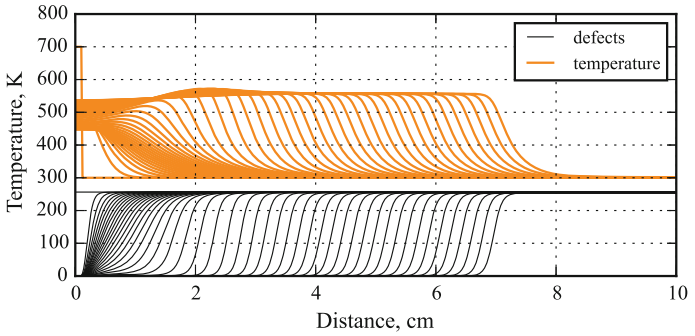

Fig. 7 Example of self-sustained annealing propagation with monotonic temperature, (top) and defect density (bottom) profiles. The defect density after multiplying by a constant factor $\theta/c\rho$ is reported. Material parameters correspond to aluminium

in Fig. 7 for initial 2.5 s. Note that in the figure the defect density is reported after multiplying by a constant factor $\theta/\rho c$. The resulting quantity has a physical meaning of the temperature increase of an isolated piece of material after all the defects have been annealed. Other parameters used in the example are $E_a/k_B = 6\,383\,\mathrm{K}$, $\theta n_0/\rho c = 256\,\mathrm{K}$, $\kappa = 220\,\mathrm{W\,m^{-1}\,K^{-1}}$ and $\beta_0 = 1 \times 10^7\,\mathrm{s^{-1}}$.

In the second regime, the self-sustained annealing propagates at a speed which oscillates around some average value that lies in a range from one to several centimetres per second. Along with this, a substantial deviation of the temperature profile from the sigmoid shape occurs in a narrow annealing zone. The temperature experiences periodic and, generally, non-harmonic oscillations, during which it can exceed its asymptotic value, T_∞. The shape of the defect density profile does not change

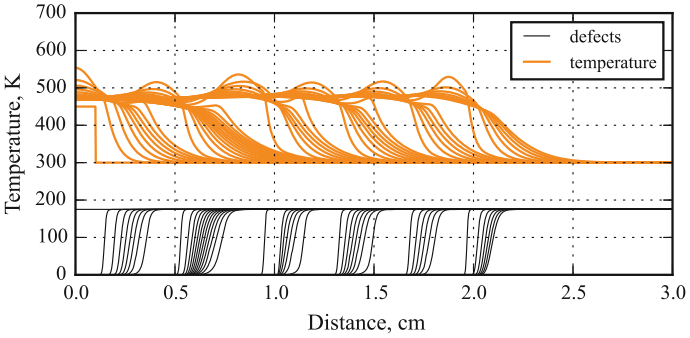

Fig. 8 Example of pulsing self-sustained annealing propagation with temperature (top) and normalised defect density (bottom) profiles dependent on time and space. The defect density after multiplying by a constant factor $\theta/c\rho$ is reported. Material parameters correspond to steel

so drastically: it remains essentially sigmoid-like although its tilt slightly oscillates. Such behaviour of the temperature and of the defect density in the annealing zone may apparently be associated with an instability caused by the pre-heating of the non-annealed material. Since the majority of defects is annealed at a temperature almost equal to T_∞, in first approximation, the wave propagation can be considered step by step. Namely, due to the energy release in the process of defect annealing, a non-annealed region adjacent to the front is heated up to a temperature value close to T_∞ with a subsequent annealing of defects in this area. Then the adjacent non-annealed layer warms up, etc. If the front moves with a constant speed, the depth of the heated layer must be constant. However, if, as the result of a fluctuation, more defects are annealed, then more energy is released and a larger area warms up, which leads to a further increase in the number of annealed defects and a loss of stability of the annealing propagation.

A mathematical justification for a similar instability was given, for example in [6, 10], where the Evans function method was employed to examine the linear stability problem. It has been shown that the solution, which corresponds to the travelling wave, becomes unstable as the result of a Hopf bifurcation. The Hopf bifurcation develops via a Bogdanov–Takens bifurcation, and leads to oscillations in the shape of the travelling wave. However, our results for the propagation of defect annealing show development of oscillations only for the temperature part of the travelling wave and for the speed of wave propagation.

The oscillating regime of annealing propagation was observed for a material with the parameters of steel. T_0 is set to a room temperature of 300 K again and the temperature of the preheated layer $T_1 = 450$ K. The remaining parameters used in this example are $E_a/k_B = 15\,090$ K, $\theta n_0/\rho c = 175$ K, $\kappa = 74.5\,\mathrm{W\,m^{-1}\,K^{-1}}$ and $\beta_0 = 6.4 \times 10^{16}\,\mathrm{s^{-1}}$. The temperature and defect density profiles for the first 3 cm and 1 s, calculated in this case, are shown in Fig. 8. In this figure one can clearly see oscillations of the front speed and temperature.

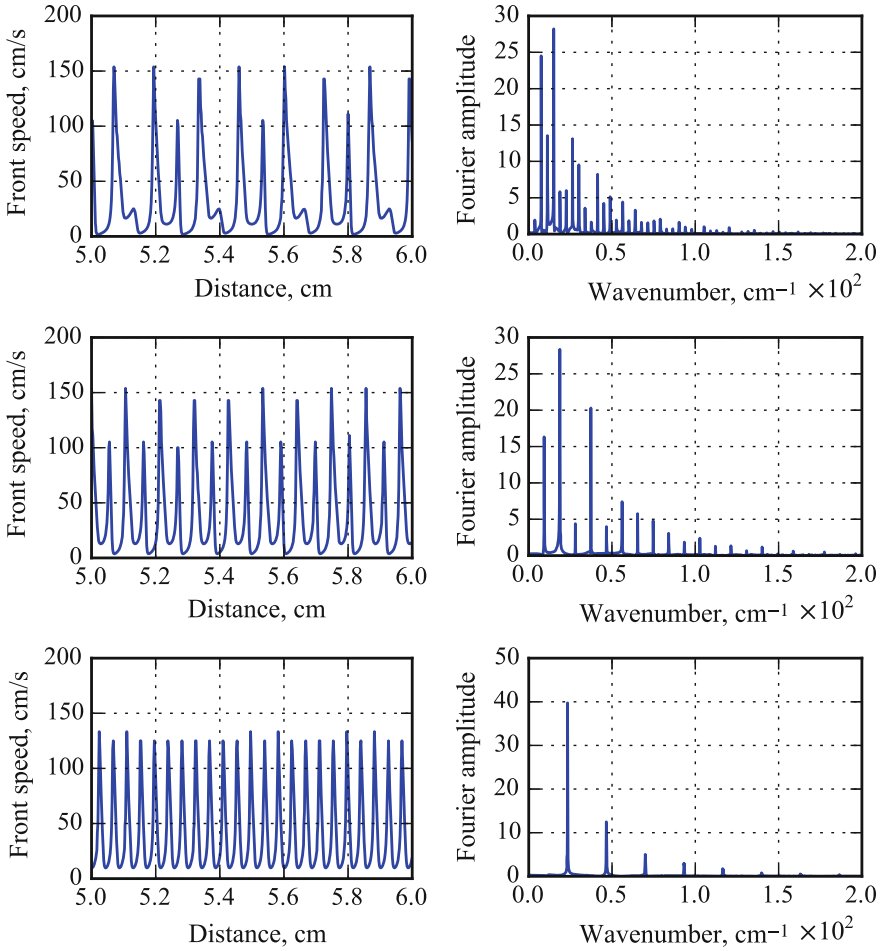

Fig. 9 Dependence of the annealing propagation speed on space (left) and the corresponding spatial Fourier spectra (right) for different values of initial temperature, T_0. Graphs on the top correspond to $T_0 = 330$ K, graphs in the middle—$T_0 = 340$ K, and graphs in the bottom—$T_0 = 350$ K

It is therefore of interest to study the dependence of the frequency of speed oscillations on the initial temperature of the material T_0, which was varied in the range from 300 to 375 K with steps of 10–20 K. In each calculation the parameters of iron were used, and graphs of the annealing front speed as functions of time, $u(t)$ and of space, $u(x)$, were built. Also, spatial and temporal spectra of the velocity were obtained by applying the discrete Fourier transform.

The results of the calculations corresponding to the different initial temperature values of 330, 340 and 350 K, are presented in Fig. 9 for spatial, and in Fig. 10 for temporal dependencies, respectively. In these figures the temporal and spatial intervals are chosen to reveal the structure of the oscillations, and the initial point of

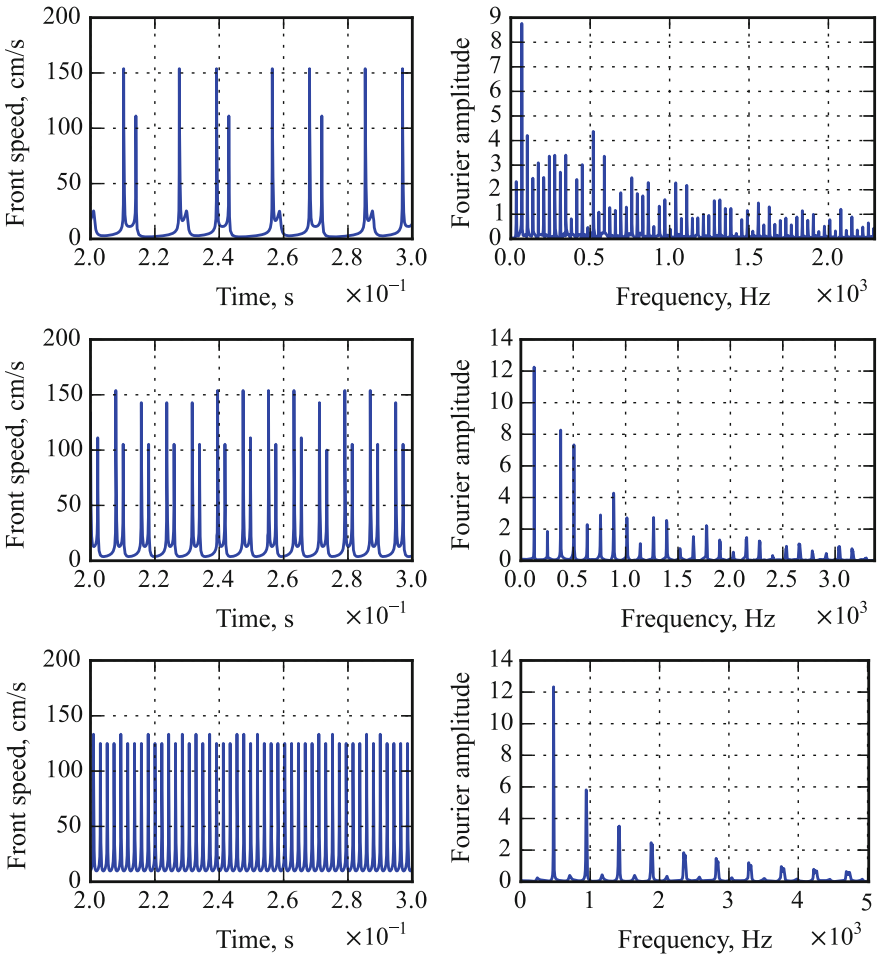

Fig. 10 Dependence of the annealing propagation speed on time (left) and the corresponding frequency spectra (right) for different values of initial temperature, T_0. Graphs on the top correspond to $T_0 = 330$ K, graphs in the middle—$T_0 = 340$ K, and graphs in the bottom—$T_0 = 350$ K

the interval—to minimize the influence of initial and boundary conditions. As one can see on the graphs, in the studied temperature interval, as the initial temperature grows, the frequency of oscillation slightly increases but the number of harmonics with significant amplitudes decreases. Temporal oscillations have a more complex structure than spatial ones, what is reflected in the number of significant harmonics observed in the graphs.

9 Summary

The analysis of thermal annealing of radiation-induced defects is of both fundamental and practical importance to the radiation material science. Annealing is an effective way to repair materials from radiation-induced damage. Additionally, it can be used to determine what kinds of defects are present in the metal, and obtain their characteristics.

Annealing is a complex, multi-step process, which involves the ensemble of defects of different types, as well as their interactions. A key role in the kinetics of annealing is played by clusters with relatively long lifetimes. Their accumulation in the metal during the process leads to a change in the cluster size distribution, and makes a major contribution to the duration of annealing.

Depending on the temperature regime of the annealing process, one distinguishes between isothermal and isochronous annealing. The properties of their kinetics depend on non-linear interactions and feedbacks, which are intrinsic to the metal microstructure. One of these interactions occurs due to the redistribution of fluxes of point defects between sinks (clusters, dislocations, etc.). This redistribution happens because the rate of absorption of point defects by clusters (in other words the rate of growth of clusters) depends on the size of the cluster. The redistribution of fluxes leads to the acceleration of the growth of big clusters and the deceleration of the growth of small ones. Preference in the absorption of interstitial atoms compared to the absorption of vacancies also depends on the size of the cluster. In general, big clusters can grow by virtue of the dissolution of small ones, due to these interactions. This leads to the appearance of several strong maxima in the size distribution of clusters.

Another nonlinear interaction is thermal-concentration feedback. This leads to a stronger than exponential dependence of the number of annealed defects on time, and is the mechanism of propagation of self-sustained annealing. The profile of the propagation depends on the annealing conditions and the state of the metal at the beginning of the annealing. Depending on the conditions, the propagation of annealing may be impossible, or the profile of propagating annealing may look like a smooth step, or the rate of propagation and the profile of annealing may oscillate in time and space. The reason for the development of the more complex propagation regime is an instability which is connected with the preheating of an as yet unannealed area of metal.

References

1. Bacon, D.J., de la Rubia, T.D.: Molecular dynamics computer simulations of displacement cascades in metals. J. Nucl. Mater. **216**, 275–290 (1994)
2. Bakaev, A.V., Zhurkin, E.E.: Characterization of radiation defects in austenitic alloys. St. Petersb. Polytech. Univ. J.: Phys. Math. **2**(194), 37–45 (2014). (In Russian)

3. Bokov, P.M., Selyshchev, P.A.: Propagating self-sustained annealing of radiation-induced interstitial complexes. IOP Conf. Ser-Mat. Sci. **110**(1), 012,055 (2016)
4. Bondarenko, G.G.: Radiation Physics, Structure and Strength of Solids. BKL Publishers, Moscow (2016). (In Russian)
5. Friedel, J.: Dislocations. Addison-Wesley Series in Metallurgy and aterials. Pergamon Press, New York (1967)
6. Gubernov, V.V., Kolobov, A.V., Polezhaev, A.A.: Pulsating regimes of flames propagation in a model with chain-branching reaction. Comput. Res. Model. **1**(3), 273–280 (2009). (In Russian)
7. Ivanov, L.I., Platov, Y.M.: Radiation Physics of Metals and Its Applications. Cambridge International Science Publishing, Cambridge (2004)
8. Kiritani, M.: Microstructure evolution during irradiation. J. Nucl. Mater. **216**, 220–264 (1994)
9. McIntosh, A.C., Weber, R.O., Mercer, G.N.: Non-adiabatic combustion waves for general Lewis numbers: wave speed and extinction conditions. ANZIAM J. **46**(1), 1–16 (2004)
10. Mercer, G.N., Sidhu, H.S., Weber, R.O., Gubernov, V.: Evans function stability of combustion waves. SIAM J. Appl. Math. **63**(4), 1259–1275 (2003)
11. Morishita, K., Sugano, R., Wirth, B.D., de La Rubia, T.D.: Thermal stability of helium-vacancy clusters in iron. Nucl. Instrum. Meth. B **202**, 76–81 (2003)
12. Press, W.H., Teukolsky, S.A., Vetterling, W.H., Flannery, B.P.: Numerical Recipes in FORTRAN. The Art of Scientific Computing, 2nd edn. Cambridge University Press, Cambridge (1992)
13. Selishchev, P.A., Sugakov, V.I.: Self-organization phenomena in impure irradiated crystals. Radiat. Eff. Defect. S. **133**(3), 237–245 (1995)
14. Selyshchev, P.A.: Self-Organization in Radiation Physics. R&C Dynamics, Moscow (2008). (In Russian)
15. Selyshchev, P.A.: Propagation of self-reinforcing annealing of radiation defects. In: Bondarenko, G.G. (ed.) Proceedings of the XXIV International Conference Radiation Physics of Solids, pp. 589–594. GNU NII PMT, Moscow (2014). (In Russian)
16. Selyshchev, P.A., Bokov, P.M.: Peculiarity of self-sustained annealing of irradiated metals. In: Bondarenko, G.G. (ed.) XXVI International Conference on Radiation Physics of Solid State, pp. 453–462. Sevastopol, Republic of Crimea (2016). (In Russian)
17. Vasil'ev, V.A., Romanovskii, Y.M., Yakhno, V.G.: Autowave Processes. Nauka, Moscow (1980). (In Russian)
18. Velichko, I.S., Selishchev, P.A., Sugakov, V.I.: The influence of the radiation induced changes of sample properties to the temperature autooscillations. Nucl. Phys. At. Energ. **10**(2), 185–192 (2009). (In Russian)
19. Was, G.S.: Fundamentals of Radiation Materials Science: Metals and Alloys. Springer Science and Business Media, Berlin (2007)
20. Weber, R.O., Mercer, G.N., Sidhu, H.S., Gray, B.F.: Combustion waves for gases (Le $= 1$) and solids (Le $\to \infty$). Proc. R. Soc. Lond. A **453**(1960), 1105–1118 (1997)
21. Zeldovich, I.A., Barenblatt, G.I., Librovich, V.B., Makhviladze, G.M.: Mathematical Theory of Combustion and Explosions. Consultants Bureau, New York (1985)

Moving Embedded Solitons in the Discrete Double Sine-Gordon Equation

Yaroslav Zolotaryuk and Ivan O. Starodub

Abstract The soliton mobility in the discrete double sine-Gordon (DDbSG) equation is investigated. This equation is used as a model of various physical applications, including the arrays of small Josephson junctions. In particular, it describes the array of asymmetric three-junction superconducting quantum interference devices (SQUIDs) with one junction in one arm of the SQUID and two junctions in another arm of it. The DDbSG equation is investigated both in the hamiltonian limit and in the presence of dissipation and dc bias. The existence of perfectly localized *embedded solitons* that can propagate with some selected values of velocity has been demonstrated numerically with the help of the pseudo-spectral method. The embedded soliton existence diagram is constructed on the parameter plane. The signatures of the embedded solitons on the current-voltage curves of the array are discussed.

Keywords Kinks · Embedded solitons · Josephson junctions · Peierls–Nabarro potential · Discreteness · Discrete sine-Gordon equation · Discrete double sine-Gordon equation · Discrete nonlinear Klein–Gordon equation

1 Introduction

Solitons are ubiquitous in nature [46]. According to the standard mathematical definition, solitons have three crucial properties. They are (i) spatially localized, (ii) propagate with the constant shape and velocity and (iii) collide elastically. This is true for the systems that are integrable with the inverse scattering transform method. If the system is non-integrable, in the continuum case the first two conditions are usually fulfilled, but the condition (iii) normally is not. If we turn to discrete systems, the condition (ii) holds or not depending on the type of the solitary waves and depending

Y. Zolotaryuk (✉) · I. O. Starodub
Bogolyubov Institute for Theoretical Physics, National Academy of Sciences of Ukraine,
vul. Metrologichna 14-B, Kiev 03680, Ukraine
e-mail: yzolo@bitp.kiev.ua

I. O. Starodub
e-mail: starodub@bitp.kiev.ua

J. F. R. Archilla et al. (eds.), *Nonlinear Systems, Vol. 2*, Understanding Complex Systems, https://doi.org/10.1007/978-3-319-72218-4_13

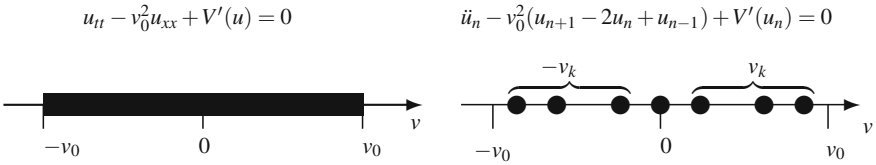

Fig. 1 Velocity spectrum for kinks in the typical continuous Klein–Gordon equation (left) and its discrete analogue (right)

on the system properties. If one takes topological solitons, their mobility in discrete media is generally suppressed [41]. The reason for this is the resonance between the topological soliton and the linear spectrum of the system. More precisely, for any topological soliton velocity a plane wave with the same phase velocity can be excited. This does not happen in the continuous systems, where solitons and phonons occupy different velocity sectors. The supersonic acoustic solitons in the lattices with anharmonic intersite interaction usually do not have this resonance problem, because their speed exceeds the speed of phonons [24].

Since the early numerical studies of the topological soliton mobility in discrete media [41] researches have focused their efforts on the different ways to obtain free *discrete* soliton motion. Apart from the discrete integrable systems [38], two main paths have been undertaken in that direction.

In the first case, the main focus has been made on finding conditions when the Peierls–Nabarro (PN) barrier becomes zero [25, 30, 49]. This can be achieved, for example, by the special discretization of the continuous system [7, 18, 32, 47, 48].

Another direction, to which the present article also belongs, is to find exact solitary travelling-wave solutions that propagate freely along the lattice. In the pioneering paper by Schmidt [45] a discrete nonlinear Klein–Gordon (DNKG) class model has been constructed with an exact localized kink solution in the explicit form for one value of velocity. This approach has been generalized in [23]. Later it has been demonstrated that in many discrete kink-bearing systems there exist exact moving topological solitons. This has been shown first numerically in [1, 44] for the Peyrard–Remoissenet model [40], and later for the double-Morse model [31]. Later a number of more rigorous analytical results have followed [19, 39]. The main result of this research can be briefly summarized by Fig. 1.

Suppose there is a kink-bearing nonlinear Klein–Gordon model $u_{tt} - v_0^2 u_{xx} + V'(u) = 0$ with the potential $V(u)$ that has at least two equivalent minima, and its discrete analogue $\ddot{u}_n - v_0^2(u_{n+1} - 2u_n + u_{n-1}) + V'(u_n) = 0$. Then, if the topological solitons of these equations are considered, the former has the continuous velocity spectrum $v \in [-v_0, v_0]$, while the velocity spectrum of the latter is discrete. An important point is that the velocities of the discrete nonlinear Klein–Gordon model may be non-zero. Further extension of these results have been made on the discrete models with anharmonic inter-particle interactions [5, 6, 57], where moving supersonic kinks were found. The existence of non-topological discrete moving solitons was reported in [34, 36].

These moving solitons that exist for some selected values of velocity are discrete *embedded* solitons. According to the initial definition [16], embedded solitons are solitons that exist despite the resonance with the linear spectrum of the underlying system. Moving lattice solitons fit perfectly into this definition because they exist despite the fact that for any soliton velocity a linear wave with the same phase velocity can be excited. Apart from the discrete media, they also exist in various continuous systems like the sine-Gordon [15] and the double sine-Gordon equations [10] with the fourth order (u_{xxxx}) dispersion term. This term drastically changes the linear dispersion law and, as a result, the resonance between the soliton, moving with any velocity, and the linear waves becomes unavoidable. Also, the models with nonlocal dispersion, where the second order dispersion term u_{xx} is replaced by the term $\hat{U}u$ with $\hat{U}$ being some integral operator, can support embedded solitons [2–4].

In this article we are going to study the properties of embedded solitons in the array of Josephson junctions that is described by the discrete double sine-Gordon equation. Also we will demonstrate how these solitons can be observed experimentally.

The article is organized as follows. The next section the model and the equations of motion are described. In the Sect. 3 the static and dynamic properties of embedded solitons in the hamiltonian limit are investigated. The Sect. 4 is focused on the soliton motion in the presence of dissipation and external bias. Discussions and conclusions are given in the last section.

2 Discrete Double Sine-Gordon Equation

Discrete double sine-Gordon (DDbSG) equation is written as

$$\ddot{\phi}_n - \kappa\,(\phi_{n+1} - 2\phi_n + \phi_{n-1}) + \frac{2}{1+2\eta}\left(\eta \sin\phi_n + \sin\frac{\phi_n}{2}\right) = 0\,,\ \ n = 1, 2, \ldots\,. \tag{1}$$

It emanates from the discrete nonlinear Klein–Gordon (DNKG) type Hamiltonian

$$H = \sum_{n=1}^{N}\left[\frac{\dot{\phi}_n^2}{2} + \frac{\kappa}{2}(\phi_{n+1} - \phi_n)^2 + V(\phi_n)\right], \tag{2}$$

$$V(\phi) = \frac{2}{1+2\eta}\left[\eta(1-\cos\phi) + 2\left(1 - \cos\frac{\phi}{2}\right)\right]. \tag{3}$$

The dot in Eq. (1) denotes the differentiation with respect to time, κ is the discreteness constant and η is the shape parameter that controls the on-site potential $V(\phi)$. If $0 \le \eta \le 1/2$ the potential V has only one minimum in the interval $-2\pi < \phi \le 2\pi$ with $V(0) = V(4\pi) = 0$. If $\eta > 1/2$ a pair of local minima appear for $\phi = \pm\pi$. They remain local for any $\eta > 0$, i.e. $V(2\pi) > V(0)$. The discrete sine-Gordon (DSG) equation is restored in two limits, $\eta = 0$ and $\eta = +\infty$. In the former case the DSG equation is 4π-periodic while in the latter case it is $2\pi-$periodic. There

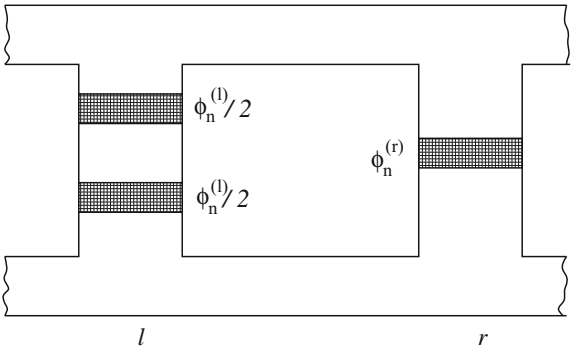

Fig. 2 Schematic view of the SQUID array. White colour stands for the superconducting electrodes and the insulating barriers are marked by grey. Reproduced with permission from [56]. Copyright (2015) by American Physical Society

exists a number of physical systems that can be modelled by the double sine-Gordon (DbSG) equation, including ultrashort optical pulses that propagate in degenerate media [20], spin waves in superfluid ^{3}He [33], nonlinear waves in the XY model with piezoelectric coupling [43], asymmetric arrays of Josephson junctions (JJs) [37], arrays of the superconductor-ferromagnet-superconductor (SFS) or superconductor-ferromagnet-insulator-superconductor (SFIS) junctions [26, 27], etc. The adequate description of the last two systems requires an essentially discrete approach while for the rest it was sufficient to work with the continuum DbSG equation. Properties of the continuous DbSG equation have been studied extensively in [17].

Let us focus on the asymmetric array of JJs, first introduced in [37]. The elementary cell of such an array is an asymmetric three-junction SQUID (superconducting quantum interference device) with two junctions in its left arm and one junction in its right arm, as shown in Fig. 2. The elementary cell of this array is asymmetric, but the whole array is not, because it remains mirror-symmetric with respect to the center of any one-junction or two-junction arm. Generally, it is well-known that any periodic chain of two alternating elements $\cdots - A - B - A - B - \cdots$ is mirror-symmetric. For the more detailed scheme one might consult the original paper [37]. The dynamics of each junction is described by the Josephson phases, $\phi_n^{(l,r)}(t)$. They are the phase difference between the phases of the wave-functions of the superconducting electrodes of the junction. The superscripts l and r stand for the left and right arms of the SQUID, respectively. If the loop size is small the single phase difference $\phi_n = \phi_n^{(l)} = \phi_n^{(r)}$ can be introduced [37]. The array is studied within the resistively and capacitively shunted junction model (the RCSJ-model)[8]. Based on this model and with the help of the Kirchhoff laws and the Josephson laws [8] the equations of motion of such an array have been derived in Ref. [37]. The physical meaning of the parameters κ and η of Eq. (1) is as follows:

Discreteness constant κ: is responsible for the inductive coupling between the cells of the array and equals $\kappa = \frac{\Phi_0}{2\pi L I_c}$, where $\Phi_0 = \frac{\pi\hbar}{e}$ is the magnetic flux quantum, L_J is the elementary cell inductance and $I_c = I_c^{(r)} + \frac{I_c^{(l)}}{2}$ with $I_c^{(l,r)}$ being the critical currents through the left and right arms of the cell, respectively.

Asymmetry parameter η: The ratio $\eta = \frac{I_c^{(r)}}{I_c^{(l)}} > 0$ of the critical currents that describes the left-right asymmetry of the SQUID.

At this point the physical meaning of the limits $\eta \to 0$ and $\eta \to +\infty$ can be explained. In the former case the left arm of the SQUID dominates as $I_c^{(r)} \to 0$, while in the latter case only the right arm works, $I_c^{(l)} \to 0$. In both cases we arrive to the standard JJ array where the left-right asymmetry of the elementary cell disappears. The SFS or SFIS junction array consists of the parallel small junctions and is similar to the standard JJ array [50, 51, 53], but its current-phase relation has an additional second-harmonic term: $I_s(\phi) = I_1^{(c)} \sin\phi + I_2^{(c)} \sin 2\phi$. The respective equations of motion for this system will be again the DDbSGE which can be reduced to the Eq. (1) after the elementary substitution $\phi \to 2\phi$.

If the dissipative effects due to the normal electron flow are taken into account, the term $\alpha\dot{\phi}_n$ should be added to the l.h.s of Eq. (1). Introduction of the uniformly applied dc bias is achieved by the constant term in the r.h.s. of that equation. More details will be given in Sect. 4. The physical meaning of the soliton in the JJ arrays is the following [8, 50]: it carries the magnetic flux quantum and is also known in the literature as *fluxon* or Josephson vortex.

The dispersion law has the form typical for the discrete nonlinear Klein–Gordon equations:

$$\omega_L(q) = \sqrt{1 + 4\kappa \sin^2 \frac{q}{2}}\,. \tag{4}$$

Note that it depends solely on the coupling constant κ and does not depend on the asymmetry parameter η. In fact, the dispersion law for the standard DSG equation has exactly the same form.

The boundary conditions will be specified in the next sections.

3 Hamiltonian Limit

In this section we study the soliton mobility in the hamiltonian limit $\alpha = 0$ of the non-driven array $\gamma = 0$. Therefore, the system is described by the DDbSG Eq. (1).

3.1 Sliding Velocities

We are interested in the topological travelling wave (TW) solutions that propagate along the lattice with the constant shape and velocity:

$$\phi_n(t) = \phi(n - vt) \equiv \phi(z)\ ,\ \ z \equiv n - vt\,. \tag{5}$$

Thus, the TW solution must satisfy the differential-delay equation with the advance and delay terms:

$$v^2\phi''(z) - \kappa\,[\phi(z+1) + \phi(z-1) - 2\phi(z)] + V'[\phi(z)] = 0\,. \tag{6}$$

This equation is to be solved numerically with the help of the pseudo-spectral method, developed in [21, 22, 28]. The unknown solution

$$\phi(z) \simeq \phi_0(z) + \sum_{n=0}^{k} c_n \sin\left(\frac{2\pi n}{L} z\right)\,, \tag{7}$$

is represented as a superposition of the initial approximation $\phi_0(z)$ and the Fourier series. The purpose of the function $\phi_0(z)$ is also to satisfy the anti(kink) boundary conditions. The problem will be solved on the finite domain $z \in [-L/2, L/2]$, where the residue $\phi(z) - \phi_0(z)$ is supposed to be antisymmetric. This is what we need if we study the annular JJ array, for which the periodic boundary conditions (with L being the length of the lattice) is a natural situation. If we are interested in the localized solution on the infinite interval, the solution (7) is an excellent approximation, provided the characteristic width of the solitary wave $\sim \mu^{-1} \ll L$ and the number of modes k in the expansion is large enough. The expansion (7) is substituted into Eq. (6) and the interval $z \in [-L/2, L/2]$ is broken into k collocation points. Consequently, the differential equation (6) turns into the nonlinear algebraic equation for the set of coefficients c_i, $i = 1, 2, \ldots k$, which can be solved with the Newton iteration method.

We are interested in the localized solutions with decaying tails

$$\phi(z) \to \begin{cases} 0\,, & z \to -\infty \\ 4\pi Q\,, & z \to +\infty\,, \end{cases} \tag{8}$$

where Q is the topological charge.

Numerical solution of Eq. (6) yields the following results. There exist two types of TW solutions. The first one is the partially delocalized bound state of the soliton with the non-decaying oscillating plane wave asymptotics, also known as *nanopteron* [11]. These solutions appear to be the natural consequence of the resonance that takes place between the soliton and the plane waves (4). In other words, for any soliton moving with some velocity v there exist at least one plane wave with the same phase velocity v because there is always at least one root of the equation

$$vq - \omega_L(q) = 0\,. \tag{9}$$

The reason of this behaviour of the roots of Eq. (9) is based on the existence of the gap in the linear spectrum (4). If such gap is absent, as it happens for the acoustic chains with anharmonic interaction and without the on-site potential, there will be no real roots of Eq. (9) except the trivial one $q = 0$ (provided the soliton is supersonic

($|v| > 1$). As a result, discrete acoustic supersonic solitons exist as exact solutions of acoustic lattices and form a one-parametric family of solutions [22, 24]. The second type of solutions are localized moving solitons (8) that exist for some selected values of v.

The well-known conventional discrete models like DSG or discrete ϕ^4 equation have only nanopterons [13, 41]. However, in the DDbSG equation there exists at least one velocity for which the TW solution has no oscillating tail. These are embedded solitons which are known to exist in a number of discrete systems [1, 31, 39, 44, 45]. Embedded soliton existence is clearly demonstrated in Fig. 3, where we present the results of the numerical solution of Eq. (6). In that figure the dependence of the amplitude A of the plane wave in the nanopteron tail is plotted as a function of the soliton velocity. In the panel (a) the $A(v)$ functions are given for fixed discreteness $\kappa = 0.4$ and for the different values of the asymmetry. In the panel (b) the asymmetry is fixed to $\eta = 0.75$ while the discreteness is varied. The clear result is a very sharp minimum at certain value of velocity. Note that there is no such minima for the curve 1 in the panel (a). With high degree of certainty we can claim that $A = 0$ at this velocity. In addition, we have done calculations with other values of the period L in the Fourier expansion (7) and this velocity value does not depend on L. Further on it will be referred to as the *sliding* velocity, because the soliton slides along the lattice without causing any radiation. The insets in the panels (a) and (b) show the soliton profiles at the sliding velocity (marked by black) as well as the nanopteron profiles with oscillating tails (marked by red). In the panel (c) the parameter values are fixed to $\eta = 5$, $\kappa = 1$. Here the existence of three embedded solitons with different velocities is demonstrated. The shapes of these solitons are given in Fig. 4. The fastest one [see Fig. 4a, b] looks very much similar to those in the insets of Fig. 3a, b. Note that its velocity profile $\phi'(z)$ has only one maximum. The second solution, shown in Fig. 4c, d, has three inflexion points in the core of the soliton profile and the velocity profile has two maxima and one minimum between them. Finally, the slowest soliton is presented in Fig. 4e, f and its velocity profile is even more complex. It has three maxima, two big ones and the small one in between them. We shall briefly comment on these solutions. The asymmetry parameter value $\eta = 5$ means that we are quite close to the 2π DSG limit of (3). In other words, the local well in the potential $V(\phi)$ at $\phi = 2\pi$ is very deep and very close to the global minimum at $\phi = 0$. Then the solutions, presented in Fig. 4 can be treated as being very close to the bound states of two solitons in the ordinary DSG model, first reported in [41] and later investigated numerically by the pseudospectral method in [1, 44]. They exhibit the same structural properties, including the oscillations in the centre of the $\phi'(z)$ profile. Numerical simulations [56] with the embedded solitons, obtained by the pseudo-spectral method have shown their dynamical stability.

Yet another observation can be made from Fig. 3. Everywhere away from the sliding velocity the dependences $A(v)$ have rather shallow minima separated by the sharp maxima. Especially well these maxima can be seen in the panel (a). In fact, they are not maxima but the singularities that appear because the numerical scheme is not able to find a solution with the appropriate wavelength. This is a consequence of the boundary conditions and these singularities depend on the length L. For the

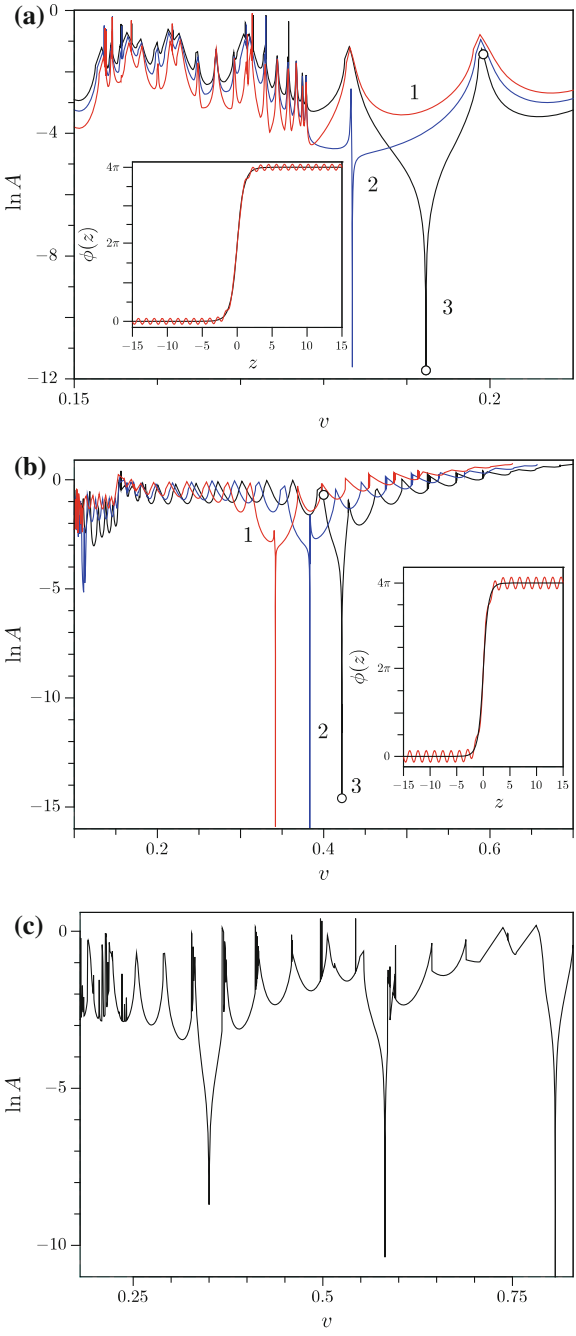

Fig. 3 **a** Dependence of the tail amplitude A on the moving soliton velocity $\kappa = 0.4$, $\eta = 0.26$ (curve 1, red), $\eta = 0.27$ (curve 2, blue) and $\eta = 0.28$ (curve 3, black). The inset shows the soliton profile for $v = 0.192302$ (red) and $v = 0.1992$ (black). Respective position of these solutions on the $A(s)$ curve are marked by $\circ$; **b** The same for the fixed $\eta = 0.75$ and $\kappa = 0.5$ (black,1), $\kappa = 0.45$ (2, blue) and $\kappa = 0.4$ (3, red), the soliton profiles shown in the inset correspond to $v = 0.4219$ (black) and $v = 0.4$ (red); **c** The same for $\eta = 5$, $\kappa = 1$. The length of the interval is $L = 30$ for all cases

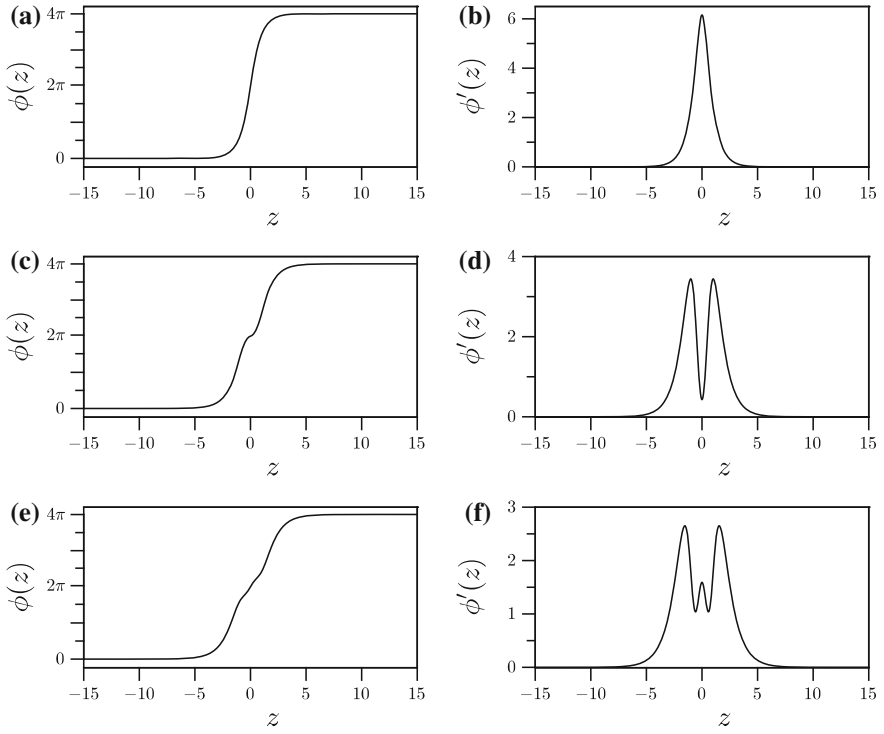

Fig. 4 Profiles of the embedded solitons that correspond to the zeroes of the $A(s)$ dependence in Fig. 3c. The soliton velocities are $v = 0.806421$ (**a**, **b**), $v = 0.581933$ (**c**, **d**) and $v = 0.35$ (**e**, **f**)

velocity that lies between the two adjacent singularities the nanopteron solution has a certain fixed number of small-amplitude wavelength that fit into the interval $[-L/2, L/2]$. The wavelength equals $2\pi/q$ where the wavenumber q is the root of Eq. (9). In the case of several roots there exist several nanopteron solutions with different wavelengths.

Finally, we discuss the dependence of the embedded soliton velocity on the system parameters as well as existence diagram on the parameter plane (η, κ). These dependencies are given in Fig. 5. The dependence of the sliding velocity v_k $(k = 1, 2, \ldots)$ on the asymmetry parameter η for two different values of κ is plotted in Fig. 5a. For the larger κ the soliton velocity is larger, which is no surprise because less discrete lattices sustain more mobile kinks. As we have learned from the Figs. 3c and 4, the velocity spectrum for the fixed parameter values can have more than one sliding velocity. Therefore, all existing sliding velocities have been plotted in Fig. 5a for both values of κ. The black lines correspond to $\kappa = 1$ and the red ones to $\kappa = 0.5$. The difference between the different branches that belong to the same κ is demonstrated in Fig. 4. The dependencies $v_k(\eta)$ do not fall down to the zero velocity but terminate at some fixed velocity value. Such behaviour is in complete accordance with the

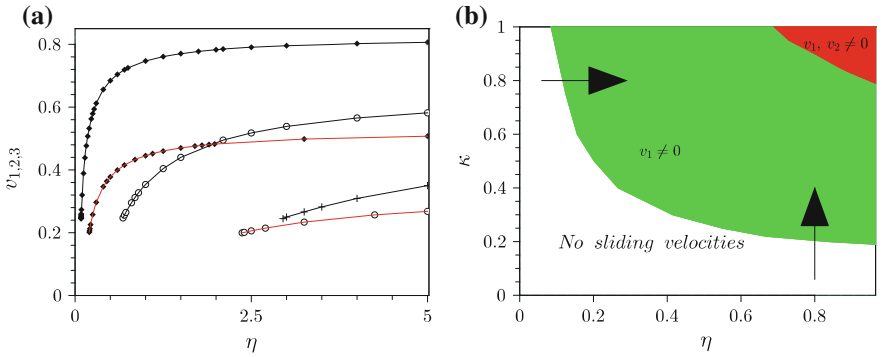

Fig. 5 **(Left)** The value of the sliding velocity v_k $(k = 1, 2, 3)$ as a function of the asymmetry parameter η for different values of the coupling constant: $\kappa = 1$ (black) and $\kappa = 0.5$ (red). Different markers correspond to the different velocity branches v_k. The solid lines are the guides for an eye. **(Right)** The existence diagram on the parameter plane (κ, η). One sliding velocity exists in the green area, two sliding velocities exist in the red area and there is no sliding velocities in the white area. All results were obtained for $L = 30$

results of Ref. [1] where the bottom limit for the value of the kink sliding velocity has been established. According to this criterion, an embedded soliton cannot exist if for its velocity value v the Eq. (9) has more than one root. It is easy to see that for $\kappa = 1$ there is only one root if $v > 0.2444$. Otherwise, for the smaller values of v there are three or more roots, but never one. The lowest sliding velocity value for all three branches is in good accordance with $v \simeq 0.24$. Similarly one can observe good accordance for $\kappa = 0.5$, where the lowest bond is $v \simeq 0.1906$.

Suppose one parameter of the pair (η, κ) is fixed and we slowly increase another one. Then, for some critical parameter value, an embedded soliton appears. This is illustrated in Fig. 3a, where small change of η causes a sudden appearance of the sliding velocity. Therefore, it is possible to draw a curve on the (η, κ) plane, that separates the area where no embedded soliton is possible (either because the coupling is too weak to support soliton motion or η is too small so that we are effectively in the DSG limit) from the area, where at least one embedded soliton exists. These areas are shown by white and green in Fig. 5b, respectively. If both η and κ are large enough, two embedded solitons can exist, as shown by the red section of the upper right corner of the existence diagram. For very large values of η and for small κ the existence diagram may look more complex. This is because for the small values of κ there exist many disjointed intervals on the velocity axis, where Eq. (9) has only one root. Thus, it is possible that several solitons with different sliding velocities coexist. As a result, the existing diagram for $\eta \gg 1, \kappa \ll 1$ may look more complex than just the green-white borderline.

3.2 Static Properties

Taking into account the results on the previous subsection, it is necessary to discuss the application of the well-known concept of the Peierls–Nabarro (PN) potential to this problem. It is well known that the PN potential models the influence of the lattice on the topological soliton mobility [13]. For weakly discrete lattices the PN potential can be introduced perturbatively, see, for example, [29] or the references in the review [13]. As a result, the discrete equation that is governed by the DNKG hamiltonian of the type (2) is approximated by the newtonian equation of motion $M_s \ddot{X}_c + V'_{PN}(X_c) = 0$, where M_s is the soliton mass, $X_c(t)$ is its center of mass, and $V_{PN}(X) = V_{PN}(X + 1)$ is the PN potential, which is, obviously, periodic.

The PN barrier is defined as

$$\Delta E_{PN} = \left| \max_{X\in[0,1]} V_{PN}(X) - \min_{X\in[0,1]} V_{PN}(X) \right| , \tag{10}$$

It is the amount of energy, required for the soliton to travel one lattice site. The dependence of the PN barrier on the asymmetry parameter η is presented in Fig. 6. It appears that the dependence has a clear minimum and the value of ΔE_{PN} decreases significantly comparing to the DSG limit ($\eta = 0$). This decreasing constitutes several orders of magnitude. The PN barrier never disappears completely, however can be barely visible on the graph, as for $\kappa = 0.5$, $\eta \in [0.12, 0.14]$. It is important to note that near the minimum of $\Delta E_{PN}(\eta)$ the static kink solutions undergo a transition, coined in [31] as *stability switching*. Within this transition the PN potential gradually changes, as shown in the left inset of Fig. 6. As η increases, its minima transfer from the half-integer values of X to the integer values of X. Inside this transition a new local minima appears for $X = n$, $n \in \mathbb{Z}$. It becomes deeper as η increases. At some point both the minima at n and $n + 1/2$ become equivalent. Eventually the minima at the half-integer value of X becomes the main one. This transition means that the stationary kink state which is centred between the sites (shown in the right inset by ○) loses its stability and the site-centred state (shown in the right inset by ⧫) becomes the minimum of the total lattice energy. The respective kink solutions undergo a cascade of the pitchfork bifurcations, for details see [31]. Multiple stability switchings for the DNKG models with the Peyrard–Remoissenet potential [40] and with the double-Morse potential [31] have been reported. There is an interesting observation (reported in [23, 31, 44] as well as in this article), that states that if the static DNKG model supports stability switching then the respective dynamical equation supports embedded solitons. No rigorous proof of this fact is known so far.

Thus, we see that the possibility of the free soliton motion is possible despite the non-zero PN barrier. Moreover, the minima of the PN barrier, seen in Fig. 6 lie in the white area of the existence diagram Fig. 5b.

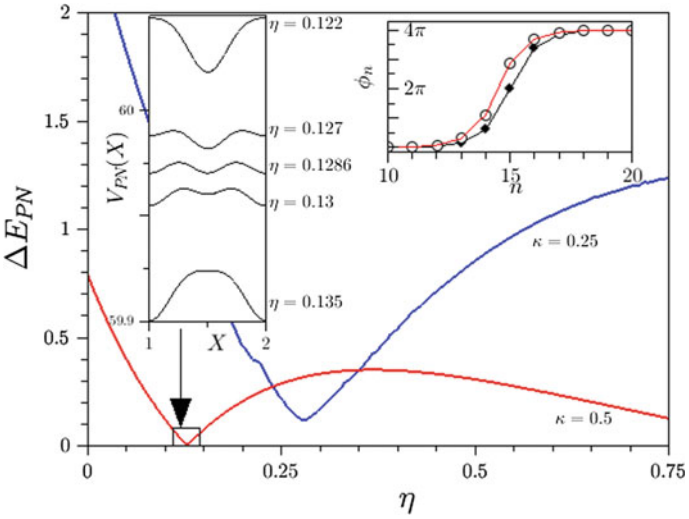

Fig. 6 Height of the Peierls–Nabarro potential as a function of the asymmetry parameter η for $\kappa = 0.25$ (blue) and $\kappa = 0.5$ (red). The left inset demonstrates the shape of the PN potential $V_{PN}(X)$ for the selected values of η and for the value of κ. The right inset shows the static soliton profiles that are local minima of the total energy at $\kappa = 0.5$, $\eta = 0.122$ (red,○) and $\eta = 0.135$ (black, ♦)

4 Dissipative Dynamics

Now we focus on more physically realistic situation when, the dissipation and external dc-bias are present. In that case the equations of motion (1) for the array should be complemented by the two following terms:

Dissipative term $\alpha\dot{\phi}_n$: takes into account the current of normal electrons across the junction.

Dc bias γ: takes into account external dc current, which is applied to each cell of the array.

As a result we shall work with the dissipative and biased DDbSG equation

$$\ddot{\phi}_n - \kappa\,(\phi_{n+1} - 2\phi_n + \phi_{n-1}) + \frac{2}{1+2\eta}\left(\eta \sin\phi_n + \sin\frac{\phi_n}{2}\right) + \alpha\dot{\phi}_n = \gamma,$$
$$n = 1, 2, \ldots, N\,. \tag{11}$$

The circular array is to be considered, thus, the boundary conditions read $\phi_n = \phi_{n+N} + 4\pi\,Q$, where Q is the total topological charge, i.e., the total number of kinks and anti-kinks trapped in the ring.

The current-voltage characteristics (CVCs) provide the necessary information about the JJ array dynamics and are accessible through experimental measurements. The average voltage drop is defined as

$$\bar{V} = \frac{1}{N}\sum_{n=1}^{N} \lim_{t\to\infty} \frac{1}{t}\int_0^t \dot{\phi}_n(t')dt' \,. \tag{12}$$

Since Eq. (11) is dissipative, we are going to deal with its attractor solutions. If there is a solution that corresponds to the soliton with certain Q that moves along the array with the constant velocity v, on the large times $t \gg \alpha^{-1}$ the Josephson phase $\phi_n(t)$ will receive the $4\pi Q$ increment every time the soliton passes the nth junction. As a result, this soliton will produce the average voltage drop $\bar{V} = 4Q\pi v/N$. Apart from the circular array one can consider the linear JJ array. The boundary conditions will be different, but the main physics will be the same. The soliton will travel along the array, bounce from the boundary and travel back with the velocity $-v$ and with the opposite topological charge. As a result, the phase $\phi_n(t)$ should receive the increment $8\pi Q$ after each visit of the site n by the soliton. The average voltage drop will be two times larger comparing to the circular array case, $\bar{V} = 8Q\pi v/N$.

The numerically obtained CVCs are given in Fig. 7. The coupling constant and the array size were fixed to $\kappa = 0.5$ and $N = 30$, respectively, while we have changed the asymmetry parameter η and the damping constant α. For the sake of brevity, we have chosen the system parameters in such a way that there is only one sliding velocity or no such velocities at all. Also, we have restricted ourselves to the one-soliton case $Q = 1$.

First we briefly recall the results of the continuum approximation [56]. In this approximation one can take the exact one-soliton solution [14, 17] $\phi(x,t) = 2\pi + 4\arctan\left\{(1+2\eta)^{-1/2}\sinh\left[(x-vt)/(1-v^2)^{1/2}\right]\right\}$ of the continuous double sine-Gordon equation $\phi_{tt} - \phi_{xx} + \frac{2}{1+2\eta}\left(\eta\sin\phi + \sin\frac{\phi}{2}\right) = 0$. Then the energy balance approximation [46] has to be applied. Its main point states that the total power $\bar{V}_c\gamma$, applied to the soliton is compensated by the dissipation, $\bar{V}_c\gamma = -P_{diss}$. The dissipative losses $P_{diss} = -\alpha\int_{-\infty}^{+\infty}\phi_t^2 dx$ can be easily calculated when the exact soliton solution is plugged in. As a result the following equation for the average voltage drop $\bar{V}_c$ is obtained:

$$\bar{V}_c = \sqrt{\kappa}\frac{4\pi v_\infty}{N} = \sqrt{\kappa}\frac{4\pi}{N}\left[1 + \Phi^2(\eta)\left(\frac{4\alpha}{\pi\gamma}\right)^2\right]^{-1/2}, \tag{13}$$

$$\Phi(\eta) = 1 + \frac{1}{\sqrt{2\eta(2\eta+1)}}\,\mathrm{arctanh}\sqrt{\frac{2\eta}{1+2\eta}}\,.$$

This formula is very similar to the well-known McLaughlin–Scott result for the soliton motion in the ordinary long JJ [35]. It is reduced to the McLaughlin–Scott formula in the both limits: $\eta \to 0$ and $\eta \to \infty$. The continuum version is plotted here mainly as a reference point, but appears to work surprisingly well even in this strongly discrete case.

Now we focus on the principal differences between the soliton mobility in discrete and continuous media. The numerically computed CVCs are shown in Fig. 7 by the different markers while the solid line corresponds to the CVC (13), obtained from

the continuum approximation. The soliton velocity in the continuous JJ is defined uniquely by the ratio γ/α and, as one can see in the CVCs in Fig. 7, the respective characteristics are continuous functions that pass through the origin. There are two main differences in the discrete case:

(i) the CVCs do not pass through the origin;
(ii) one continuous branch is replaced by the cascade of roughly parallel branches.

The first difference is the natural consequence of the discreteness, because some finite bias is always needed to overcome the lattice pinning. The second difference is caused by the boundary conditions and by the soliton coupling with the linear modes of the lattice. It has been observed in JJ arrays many times both experimentally [52, 54] and theoretically [12, 51, 55]. This issue has been partially discussed for the hamiltonian limit in Sect. 3.1. If the system is dissipative, the moving solitons become attractors. While moving along the lattice, the soliton excites the linear modes and forms a bound state that propagates with the same velocity. The wavelength of the linear mode is given by Eq. (9). Because of the periodic boundary conditions the phase locking in the array would occur if the finite number of the Josephson phase oscillations fit into one cycle of the soliton journey along the array. The phase locking means that the system settles on the periodic attractor that corresponds to the soliton that restores its shape and position completely after travelling around the array. In other words, a certain number of the linear modes wavelength should be fitted in the array. Each of the different branches of the CVC in Fig. 7 corresponds to the different number of these wavelengths. This can be observed in the inset in the panel (a) of that figure. One can easily see that soliton profiles that correspond to the different branches have different number of oscillations. The oscillations of the $A(s)$ dependence in Fig. 3 have the same nature.

Now we discuss how the embedded solitons manifest themselves on the current-voltage dependencies. It appears that there exists a significant difference between the CVCs of the array if the system supports embedded soliton and when it does not. In Fig. 7a the case of $\eta = 0.1$ is considered, and, according to Sect. 3.1, in the hamiltonian limit for this value of the asymmetry parameter there is no embedded solitons. On the contrary, for $\eta = 0.3$ [Fig. 7b], $\eta = 0.6$ [Fig. 7c] and for $\eta = 1.5$ [Fig. 7d] there exist one embedded soliton with the sliding velocity $v = 0.296835$, $v = 0.399493$ and $v = 0.469944$, respectively. For details see Fig. 5. In the first case [panel (a)] the CVC branches are distributed almost uniformly. In the case of $\eta = 0.3$ a small gap opens, but only for $\alpha = 0.02$. In the panel (c) and panel (d) one can easily spot the significant gap $V^-_{IVI} \le V \le V^+_{IVI}$ which will be called *inaccessible voltage interval* (IVI). This inaccessible interval appears to be more pronounced as η increases or when α is decreased. Moreover, if α is decreased significantly, its lower boundary, equals zero. The upper boundary, V^+_{IVI} tends to the value $4\pi v/N$, which is the voltage drop produced by the embedded soliton (marked by the red vertical line). We have further reduced α and computed the detuning $\varepsilon = |4\pi v_1/N - V^+_{IVI}|$. The value of this detuning parameter decreases with the decreasing of dissipation. For the lowest value of dissipation which we have used in our numerical analysis, $\alpha = 0.005$, the detuning value reached $\varepsilon \sim 10^{-3}$.

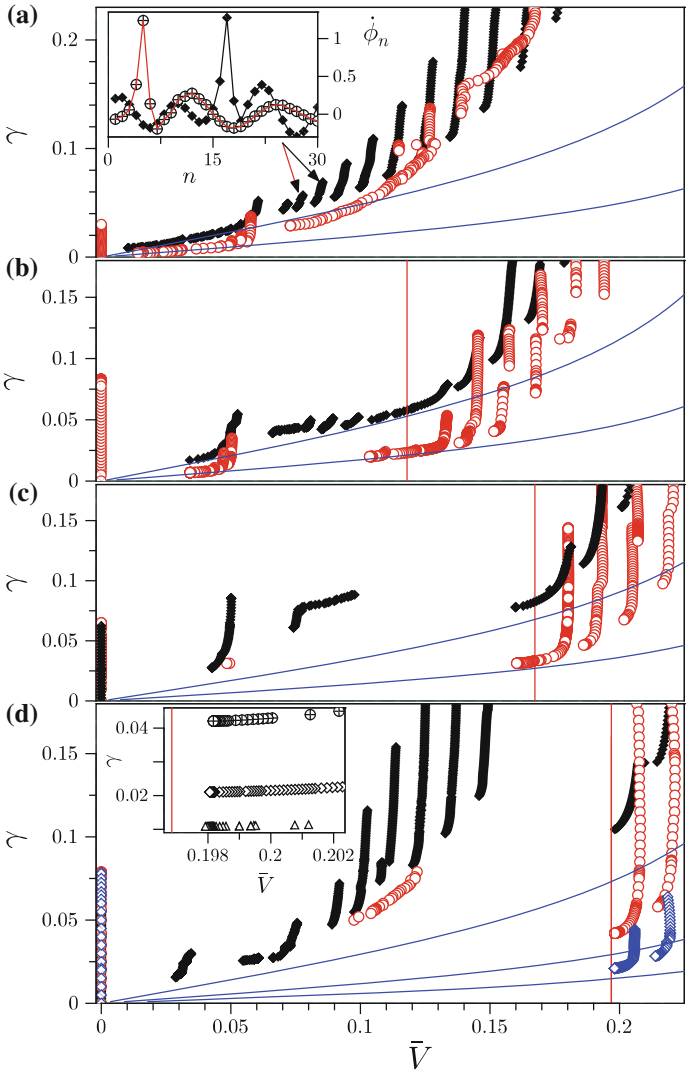

Fig. 7 CVCs for $\kappa = 0.5$, $N = 30$, $\alpha = 0.05$ (black ♦), $\alpha = 0.02$ (red ○), $\alpha = 0.01$ (blue ◇) and $\eta = 0.1$ (**a**), $\eta = 0.3$ (**b**), $\eta = 0.6$ (**c**) and $\eta = 1.5$ (**d**). The blue solid lines correspond to the respective CVC in the continuum limit. The red vertical lines in **b**–**d** are given by $4\pi v/N$, where v is the sliding velocity for the respective value of η. The inset in the panel **a** shows the different configurations of $\dot{\phi}_n$ at $\alpha = 0.05$. The configuration corresponding to the branch on the right is given by ♦, while ⊕ corresponds to the branch on the left. The inset in the panel **d** shows the details of CVCs in the neighbourhood of the sliding velocity for $\alpha = 0.02$ (⊕), $\alpha = 0.01$ (◇) and $\alpha = 0.005$ (Δ). Reproduced with permission from [56]. Copyright (2015) by American Physical Society

These results can be summarized as follows. If in the hamiltonian limit the SQUID array supports the embedded soliton that moves with velocity v, in the weakly driven and weakly dissipative array the system can sustain a regime of soliton that moves with the velocity close to v. Thus, the average voltage drop in this limit is defined by the sliding velocity and is far from zero. If the system does not support embedded solitons, its behaviour in the limit $\alpha \to 0, \gamma \to 0$ is different: the CVC ends up close to the origin, as shown in Fig. 7a. Of course, it cannot exactly pass through the origin due to discreteness.

Finally, we remark on the character of the dynamics that takes place when the soliton travels around the array. The CVCs of the array appear to be almost vertical (with the small bend at the low voltage end). As the zero voltages are approached, the length of the branches decreases and they become more horizontal. However, there exist some isolated branches that fall out of the general picture. For example, in the panel (c) one can observe an isolated branch with $\bar{V} \sim 0.07 \div 0.1$ for the dissipation value $\alpha = 0.05$. A small isolated branch for $\alpha = 0.02$ can be observed in the panels (c) at $\bar{V} \sim 0.05$ and (d) (at $\bar{V} \sim 0.05 \div 0.13$). In order to understand the nature of the dynamics that correspond to the different CVC branches we have calculated the largest Lyapunov exponent of the system as a function of the dc bias γ. The Benettin algorithm [9] was used. Three branches from the current-voltage dependence for $\alpha = 0.05$, given in Fig. 7c, have been investigated. Two branches lie just below the IVI gap (one is isolated and another one is approximately vertical) and one branch is situated just above the IVI with the voltages $\bar{V} \sim 0.16 \div 0.18$. All three branches have been traced from the top to the bottom and the largest Lyapunov exponent has been plotted as a function of the bias current in Fig. 8. The black line (1) corresponds to the branch just above the IVI. Since for the non-bounded trajectories of the autonomous systems there is always a zero Lyapunov exponent, we conclude that soliton dynamics on this branch is regular. The Lyapunov exponent for the isolated branch is zero approximately for its vertical part and becomes positive when the branch becomes strongly tilted. Finally, the vertical branch (the closest to the origin) has regular dynamics in its upper part and then undergoes complex transitions from chaotic dynamics to regular and back.

5 Summary

In this article we have discussed the properties of discrete embedded solitons in the double sine-Gordon lattice. The respective equation belongs to the class of discrete nonlinear Klein–Gordon (DNKG) equations and is used to model a number of wave phenomena in condensed matter physics. In particular, the array of asymmetric three-junction SQUIDs with two junctions in its left arm and one junction in its right arm is described by the DDbSG equation. If these arms are equivalent, the array is described by the standard DSG equation. The asymmetry parameter $\eta = I_c^{(r)}/I_c^{(l)}$ is introduced as a measure of how far the system is from the DSG equation. The DSG equation is

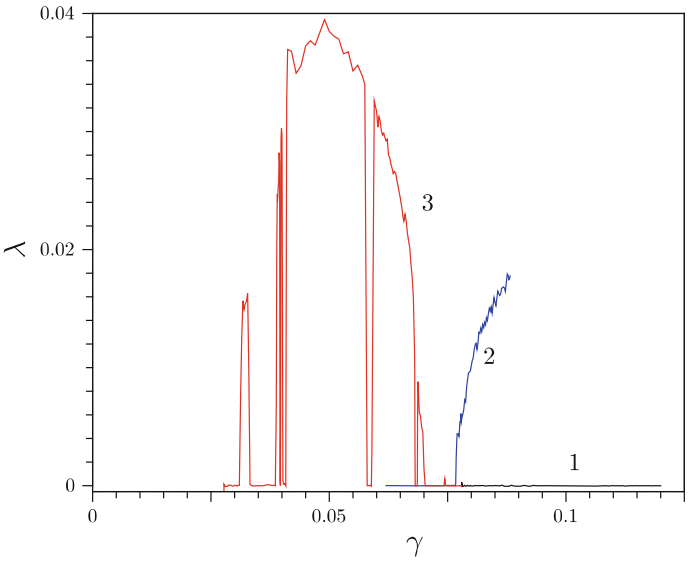

Fig. 8 Largest Lyapunov exponent as a function of bias for three branches of the current-voltage dependence, given in Fig. 7c. The parameters are: $\kappa = 0.5$, $\alpha = 0.05$ and $\eta = 0.6$. Different lines correspond to the different branches of the CVC. See text for details. Reproduced with permission from [56]. Copyright (2015) by American Physical Society

restored in the limits $\eta = 0$ and $\eta = +\infty$. The DDbSG equation also describes the array of SFS ans SFIS junctions [26, 27].

In the hamiltonian limit it was possible to identify the set of soliton velocities (so-called *sliding* velocities), for which free propagation is possible. These propagating solitons exist despite the obvious resonance with the phonons of the system and, thus, belong to the class of embedded solitons. We have calculated the PN barrier as a function of the discreteness constant and the asymmetry parameter η. The PN barrier appears to be nonzero, however, its dependence on the system parameters is non-monotonic with a clear minimum as a function of η. Thus, free soliton propagation is not directly connected with the existence of the PN barrier. This non-monotonicity is attributed to the phenomenon of the stability switching [31]. The stability switching is the alteration of the kink ground-state from the inter-site centred to the site-centred configuration (and back) when the coupling constant or some shape parameter is varied. It does not happen for the DSG equation and for the discrete ϕ^4 model. As far as we know, all DNKG-type models that have stability switching also support moving embedded solitons. We are not aware of any mathematically rigorous proof of this fact and, therefore, consider it as a prospective direction of the future research.

For the biased and damped DDbSG equation we have shown how the moving embedded solitons manifest themselves on the current-voltage curve (CVC) of the array. The main signature of the embedded soliton motion in the array is the

forbidden interval of voltages. The upper boundary of this interval equals approximately $4\pi v_*/N$, where v_* is the embedded soliton velocity.

The bound states of two or more topological solitons of the DSG equation also behave like moving embedded solitons [1, 41, 44]. They have been observed experimentally in the circular JJ array [42]. The parameter η connects two DSG equations, one with the nonlinear term $\sin(\phi/2)$ (at $\eta = 0$) and another one with $\sin\phi$ (at $\eta = +\infty$). Thus, in the limit $\eta = +\infty$ the bound state of two DSG solitons that connects 0 and 4π, gradually transforms into one embedded soliton of the DDbSG equation as η is decreased. Therefore, the embedded solitons of the DDbSG equation is a continuation of the DSG two-soliton bound state that persists into the domain of finite values of η.

Acknowledgments The authors acknowledge the support from the Ukrainian State Grant for Fundamental Research No. 0117U00236.

References

1. Aigner, A., Champneys, A., Rothos, V.: A new barrier to the existence of moving kinks in Frenkel–Kontorova lattices. Phys. D **186**(3–4), 148–170 (2003)
2. Alfimov, G.L., Korolev, V.G.: On multikink states described by the nonlocal sine-Gordon equation. Phys. Lett. A **246**, 429–435 (1998)
3. Alfimov, G.L., Eleonsky, V.M., Lerman, L.M.: Solitary wave solutions of nonlocal sine-Gordon equations. Chaos **8**, 257–271 (1998)
4. Alfimov, G.L., Medvedeva, E., Pelinovsky, D.E.: Wave systems with an infinite number of localized traveling waves. Phys. Rev. Lett. **112**, 054103 (2014)
5. Archilla, J.F.R., Kosevich, Y.A., Jimenez, N., Sanchez-Morcillo, V.J., Garcia-Raffi, L.M.: Moving excitations in cation lattices. Ukr. J. Phys. **58**, 646–656 (2013)
6. Archilla, J.F.R., Kosevich, Y.A., Jimenez, N., Sanchez-Morcillo, V.J., Garcia-Raffi, L.M.: Ultradiscrete kinks with supersonic speed in a layered crystal with realistic potentials. Phys. Rev. E **91**, 022912(12) (2015)
7. Barashenkov, I.V., Oxtoby, O.F., Pelinovsky, D.E.: Translationally invariant discrete kinks from one-dimensional maps. Phys. Rev. E **72**(3), 035602(R) (2005)
8. Barone, A., Paterno, G.: Physics and Applications of the Josephson Effect. Wiley, New York (1982)
9. Benettin, G., Galgani, L., Giorgilli, A., Strelcyn, J.M.: Lyapunov characteristic exponents for smooth dynamical systems and for hamiltonian systems; a method for computing all of them. part 1: theory. Meccanica **15**(1), 9–20 (1980)
10. Bogdan, M.M., Kosevich, A., Maugin, G.A.: Soliton complex dynamics in strongly dispersive medium. Wave Motion **34**, 1–26 (2001)
11. Boyd, J.P.: A numerical calculation of a weakly non-local solitary wave: the ϕ^4 breather. Nonlinearity **3**, 177 (1990)
12. Braun, O., Hu, B., Zeltser, A.: Driven kink in the Frenkel–Kontorova model. Phys. Rev. E **62**(3), 4235–4245 (2000)
13. Braun, O.M., Kivshar, Y.S.: Nonlinear dynamics of the Frenkel–Kontorova model. Phys. Rep. **306**(1–2), 2–108 (1998)
14. Campbell, D.K., Peyrard, M., Sodano, P.: Kink-antikink interactions in the double sine-Gordon equation. Phys. D **19**, 165–205 (1986)
15. Champneys, A., Kivshar, Y.S.: Origin of multikinks in dispersive nonlinear systems. Phys. Rev. E **61**, 2551–2554 (2000)

16. Champneys, A., Malomed, B., Yang, J., Kaup, D.: Embedded solitons: solitary waves in resonance with the linear spectrum. Phys. D **152–153**, 340–354 (2001)
17. Condat, C.A., Guyer, R.A., Miller, M.D.: Double sine-Gordon chain. Phys. Rev. B **27**, 474–494 (1983)
18. Dmitriev, S.V., Kevrekidis, P.G., Yoshikawa, N.: Discrete Klein–Gordon models with static kinks free of the Peierls–Nabarro potential. J. Phys. A Math. Gen. **38**, 7617–7627 (2005)
19. Dmitriev, S.V., Khare, A., Kevrekidis, P.G., Saxena, A., Hadžievski, L.: High-speed kinks in a generalized discrete ϕ^4 model. Phys. Rev. E **77**, 056603 (2008)
20. Dodd, R.K., Bullough, R.K., Duckworth, S.: Multisoliton solutions of nonlinear dispersive wave equations not soluble by the inverse method. J. Phys. A Math. Gen. **8**(7), L64 (1975)
21. Duncan, D., Eilbeck, J., Feddersen, H., Wattis, J.: Solitons on lattices. Phys. D **68**, 1–11 (1993)
22. Eilbeck, J.C., Flesch, R.: Calculation of families of solitary waves on discrete lattices. Phys. Lett. A **149**, 200 (1990)
23. Flach, S., Zolotaryuk, Y., Kladko, K.: Moving lattice kinks and pulses: An inverse method. Phys. Rev. E **59**(5), 6105–6115 (1999). https://doi.org/10.1103/PhysRevE.59.6105
24. Friesecke, G., Wattis, J.A.D.: Existence theorem for solitary waves on lattices. Commun. Math. Phys. **161**, 391 (1994)
25. Gochev, I.G.: Contribution to the theory of plane domain walls in a ferromagnet. Sov. Phys. JETP **58**, 115–119 (1983)
26. Goldobin, E., Koelle, D., Kleiner, R., Buzdin, A.: Josephson junctions with second harmonic in the current-phase relation: properties of φ junctions. Phys. Rev. B **76**, 224523 (2007)
27. Golubov, A.A., Kupriyanov, M.Y., Il'ichev, E.: The current-phase relation in Josephson junctions. Rev. Mod. Phys. **76**, 411–469 (2004)
28. Hochstrasser, D., Mertens, F.G., Büttner, H.: An iterative method for the calculation of narrow solitary excitations on atomic chains. Phys. D **35**, 259 (1989)
29. Ishimori, Y., Munakata, T.: Kink dynamics in the discrete sine-Gordon system. A perturbational approach. J. Phys. Soc. Jpn. **51**, 3367 (1982)
30. Jensen, M., Bak, P., Popielewicz, A.: Pinning-free soliton lattices and bifurcation in a discrete double-well model: exact results. J. Phys. A Math. Gen. **16**, 4369–4375 (1983)
31. Karpan, V.M., Zolotaryuk, Y., Christiansen, P.L., Zolotaryuk, A.V.: Discrete kink dynamics in hydrogen-bonded chains: the one-component model. Phys. Rev. E **66**(6), 066603 (2002)
32. Kevrekidis, P.G.: On a class of discretizations of Hamiltonian nonlinear partial differential equations. Phys. D **183**, 68–86 (2003)
33. Maki, K., Kumar, P.: Magnetic solitons in superfluid ^{3}He. Phys. Rev. B **14**, 118–127 (1976)
34. Malomed, B.A., Fujioka, J., Espinosa-Cern, A., Rodrguez, R.F., Gonzlez, S.: Moving embedded lattice solitons. Chaos **16**(1), 013112 (2006)
35. McLaughlin, D.W., Scott, A.C.: Perturbation analysis of fluxon dynamics. Phys. Rev. A **18**(4), 1652 (1978)
36. Melvin, T.R.O., Champneys, A.R., Kevrekidis, P.G., Cuevas, J.: Radiationless traveling waves in saturable nonlinear schrödinger lattices. Phys. Rev. Lett. **97**, 124101 (2006)
37. Nishida, M., Kanayama, T., Nakajo, T., Fujii, T., Hatakenaka, N.: Bound fluxon pair in one-dimensional squid array. Phys. C **470**, 832–834 (2010)
38. Orfanidis, S.J.: Discrete sine-Gordon equations. Phys. Rev. D **18**, 3822–3827 (1978)
39. Oxtoby, O., Pelinovsky, D.E., Barashenkov, I.V.: Travelling kinks in discrete ϕ^4 models. Nonlinearity **19**, 217–235 (2006)
40. Peyrard, M., Remoissenet, M.: Solitonlike excitations in a one-dimensional atomic chain with a nonlinear deformable substrate potential. Phys. Rev. B **26**, 2886 (1982)
41. Peyrard, M., Kruskal, M.D.: Kink dynamics in the highly discrete sine-Gordon system. Phys. D **14**, 88 (1984)
42. Pfeiffer, J., Schuster, M., Abdumalikov Jr., A.A., Ustinov, A.V.: Observation of soliton fusion in a Josephson array. Phys. Rev. Lett. **96**, 034103(4) (2006)
43. Remoissenet, M.: Non-linear excitations in a compressible chain of dipoles. J. Phys. C Solid State **14**(11), L335 (1981)

44. Savin, A.V., Zolotaryuk, Y., Eilbeck, J.C.: Moving kinks and nanopterons in the nonlinear Klein–Gordon lattice. Phys. D **138**(3–4), 265–279 (2000)
45. Schmidt, V.H.: Exact solution in the discrete case for solitons propagating in a chain of harmonically coupled particles lying in double-minimum potential wells. Phys. Rev. B **20**, 4397–4405 (1979)
46. Scott, A.C.: Nonlinear Science: Emergence and Dynamics of Coherent Structures. Oxford Texts in Applied and Engineering Mathematics (Book 8). Oxford University Press, Oxford (2003)
47. Speight, J.: A discrete system without a Peierls - Nabarro barrier. Nonlinearity **10**, 1615–1625 (1997)
48. Speight, J.M., Ward, R.S.: Kink dynamics in a novel discrete sine-Gordon system. Nonlinearity **7**, 125 (1994)
49. Speight, M., Zolotaryuk, Y.: Kinks in dipole chains. Nonlinearity **19**(6), 1365–1382 (2006)
50. Ustinov, A.V.: Solitons in Josephson junctions. Phys. D **123**(1–4), 315–329 (1998)
51. Ustinov, A.V., Cirillo, M., Malomed, B.A.: Fluxon dynamics in one-dimensional Josephson-junction arrays. Phys. Rev. B **47**, 8357–8360 (1993)
52. Ustinov, A.V., Cirillo, M., Larsen, B.H., Oboznov, V.A., Carelli, P., Rotoli, G.: Experimental and numerical study of dynamic regimes in a discrete sine-Gordon lattice. Phys. Rev. B **51**, 3081–3091 (1995)
53. van der Zant, HSJ, Orlando, T.P., Watanabe, S., Strogatz, S.H.: Kink propagation in a highly discrete system: observation of phase locking to linear waves. Phys. Rev. Lett. **74**(1), 174–177 (1995)
54. Watanabe, S., Strogatz, S.H., van der Zant, H.S.J., Orlando, T.P.: Whirling modes and parametric instabilities in the discrete sine-Gordon equation: experimental tests in Josephson rings. Phys. Rev. Lett. **74**, 23 (1995)
55. Watanabe, S., van der Zant, H.S.J., Strogatz, S.H., Orlando, T.P.: Dynamics of circular arrays of Josephson junctions and the discrete sine-Gordon equations. Phys. D **97**, 429–470 (1996)
56. Zolotaryuk, Y., Starodub, I.O.: Fluxon mobility in an array of asymmetric superconducting quantum interference devices. Phys. Rev. E **91**, 013202 (2015)
57. Zolotaryuk, Y., Eilbeck, J.C., Savin, A.V.: Bound states of lattice solitons and their bifurcations. Phys. D **108**, 81 (1997)

Index

J. F. R. Archilla et al. (eds.), *Nonlinear Systems, Vol. 2*, Understanding Complex Systems, https://doi.org/10.1007/978-3-319-72218-4